



DUCT WALL IMPEDANCE CONTROL AS AN ADVANCED CONCEPT FOR ACOUSTIC SUPPRESSION

N76-37.28

Unclass
48377

G3/71

(NASA-CR-134998) DUCT WALL IMPEDANCE
CONTROL AS AN ADVANCED CONCEPT FOR ACOUSTIC
SUPPRESSION Final Report (Lockheed-Georgia
Co.) 361 p HC \$7.50
CSCI 2.0

BY
PETER D. DEAN
AND
BRIAN J. TESTER

NOVEMBER 1975

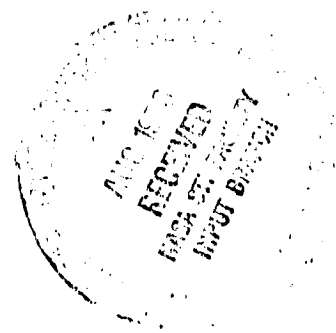
THE LOCKHEED GEORGIA COMPANY
MARIETTA, GEORGIA

LG76ER0132

PREPARED FOR

NATIONAL AERONAUTICS AND SPACE ADMINISTRATION

NASA-LEWIS RESEARCH CENTER
CONTRACT NAS3-18554



1. Report No. CR-134998	2. Government Accession No.	3. Recipient's Catalog No.
4. Title and Subtitle Duct Wall Impedance Control as an Advanced Concept for Acoustic Suppression	5. Report Date November 1975	6. Performing Organization Code
7. Author(s) Peter D. Dean and Brian J. Tester	8. Performing Organization Report No.	10. Work Unit No.
9. Performing Organization Name and Address Lockheed-Georgia Company A Division of Lockheed Aircraft Corporation 86 South Cobb Drive Marietta, Georgia 30063	11. Contract or Grant No. NAS3-18554	13. Type of Report and Period Covered Final Contract Report
12. Sponsoring Agency Name and Address National Aeronautics and Space Administration Washington, D. C. 20548	14. Sponsoring Agency Code	
15. Supplementary Notes Project Manager : Dr. Kenneth Baumeister, V/STOL and Noise Division NASA Lewis Research Center, Cleveland, Ohio 44135		
16. Abstract This report describes models of and tests on an acoustic duct liner system which has the property of controlled-variable acoustic impedance. This is achieved by the use of a novel concept which uses the effect of steady air flow through a multi-layer, locally reacting, resonant-cavity absorber. The scope of this work was limited to a "proof of concept." The test of the concept was implemented by means of a small-scale, square-section flow duct facility designed specifically for acoustic measurements, with one side of the duct acoustically lined. The test liners were designed with the aid of previously established duct acoustic theory and a semi-empirical impedance model of the liner system. Over the limited range tested, the liner behaved primarily as predicted, exhibiting significant changes in resistance and reactance, thus providing the necessary concept validation.		
17. Key Words (Suggested by Author(s)) Flow Duct Acoustics Acoustic Treatment Engine Duct Noise Suppression Sound Absorbent Duct Liners	18. Distribution Statement Unclassified - Unlimited	
19. Security Classif. (of this report) Unclassified	20. Security Classif. (of this page) Unclassified	21. No. of Pages 22. Price

NASA CR-134998

DUCT WALL IMPEDANCE CONTROL AS AN
ADVANCED CONCEPT FOR ACOUSTIC SUPPRESSION

by

Peter D. Dean
Brian J. Tester

November 1975

Prepared under Contract NAS3-18554 by
LOCKHEED-GEORGIA COMPANY
Marietta, Georgia

for

NATIONAL AERONAUTICS AND SPACE ADMINISTRATION
Lewis Research Center
Cleveland, Ohio

SUMMARY

This report describes models of and tests on an acoustic duct liner system which has the property of controlled-variable acoustic impedance. This is achieved by the use of a novel concept which uses the effect of steady air flow through a multi-layer, locally reacting, resonant-cavity absorber. The scope of this work was limited to a "proof of concept." The test of the concept was implemented by means of a small-scale, square-section flow duct facility designed specifically for acoustic measurements, with one side of the duct acoustically lined. The test liners were designed with the aid of previously established duct acoustic theory and a semi-empirical impedance model of the liner system. Over the limited range tested, the liner behaved primarily as predicted, exhibiting significant changes in resistance and reactance, thus providing the necessary concept validation.

CONTENTS

	Page
1. INTRODUCTION	1
2. DESCRIPTION OF CONCEPT	3
3. ANALYTICAL STUDY	5
3.1 Introduction	5
3.2 Attenuation Contour Plots	5
3.3 Liner Impedance Model	8
3.4 Model Parametric Considerations	23
4. EXPERIMENTAL STUDY	41
4.1 Verification of Impedance Model	41
4.1.1 Introduction	41
4.1.2 Apparatus	41
4.1.3 Impedance Analysis Methods	46
4.1.4 Test Results	49
4.2 Verification of Concept	59
4.2.1 Introduction	59
4.2.2 Liner Design Considerations and Specifications	59
4.2.3 Apparatus	63
4.2.4 Analysis Methodology	75
4.2.5 Test Results	75
5. CONCLUDING REMARKS	117
APPENDIX A PLOTS OF CONTOURS OF CONSTANT ATTENUATION FOR FIRST TWO MODES OF PROPAGATION IN A SQUARE DUCT WITH ONE SIDE ACOUSTICALLY LINED AT VARIOUS REDUCED FREQUENCIES AND DUCT GRAZING-FLOW MACH NUMBERS	119
APPENDIX B MATHEMATICAL OUTLINE OF PREDICTION FORMULATIONS FOR IMPEDANCE EVALUATION IN THE PRESENCE OF BIAS OUTFLOW AND GRAZING FLOW	221
APPENDIX C EVALUATION OF OVERALL ACOUSTIC IMPEDANCE AT SURFACE OF A MULTI-LAYER, LOCALLY REACTING, RESONANT-CAVITY LINER SYSTEM	225

CONTENTS (Cont'd)

	Page
APPENDIX D EFFECTS OF BIAS FLOW ON IMPEDANCE OF MULTI-CAVITY LINER AT VARIOUS REDUCED FREQUENCIES, GRAZING-FLOW VELOCITIES, FACING SHEET POROSITIES AND CAVITY DEPTHS	229
APPENDIX E THE CALCULATION OF NORMAL INCIDENCE IMPEDANCE IN A STANDING WAVE TUBE	275
APPENDIX F CALCULATION OF ACOUSTIC IMPEDANCE FOR A LOCALLY REACTING RESONANT CAVITY TYPE TRIPLE-LAYER LINER SYSTEM	277
APPENDIX G AXIAL SOUND PRESSURE AND PHASE TRAVERSES ON CENTERLINE OF TEST FLOW DUCT AT VARIOUS FREQUENCIES AT VARIOUS COMBINATIONS OF TWO EXTREMES OF BIAS FLOW (MACH NUMBER = 0.0 AND 0.15) AND GRAZING FLOW (MACH NUMBER = 0.0 AND 0.25)	279
APPENDIX H SOUND PRESSURE AND PHASE TRAVERSES WITHIN UPSTREAM AND DOWNSTREAM SECTIONS OF FLOW DUCT LINER AT VARIOUS FREQUENCIES AT VARIOUS COMBINATIONS OF TWO EXTREMES OF BIAS FLOW (MACH NUMBER = 0.0 AND 0.015) AND GRAZING FLOW (MACH NUMBER = 0.0 AND 0.25)	329
REFERENCES	359

1. INTRODUCTION

The pressing need to reduce aircraft noise is a widely recognized and highly challenging problem. Recent advances in engine design, particularly in fan-jet applications, have partially alleviated the situation, but it remains evident that further improvements in noise reduction are urgently required. From the mid 1960's, some industrial and academic organizations responded to the problem of noise generated within the engine by means of a theoretical study of attenuation in flow ducts, which defined and explained the influence on modal propagation of both duct fluid flow and liner wall impedance. Many aerospace companies also emphasized materials evaluation programs to the extent that, through a proper combination of analytical models with empirical qualifications, the aerospace industry can successfully produce duct liner designs for particular applications to commercial turbo-fan engines. Thus, the main thrust of development is now to improve the *efficiency* of acoustic liner materials and that is the goal of the work described here. In this context, "efficiency" can be defined, for a specific range of engine operation conditions, as an increase in attenuation over existing liner designs and/or an increase in effective bandwidth.

The efficiency, or degree of optimization, is governed by factors which are dependent on the basic characteristics of actual engine application and operation: (1) variable operating range giving variable source distributions which are generally unknown quantities; (2) variable mean flow environments; and (3) severe weight, size, engine performance degradation, and cost constraints. The first two factors define the limitations of existing liner design, with the design aim of obtaining the maximum insertion loss possible for any arbitrary engine condition.

The source distribution, which determines the modal spectra, is rarely known and is difficult to measure; while the aerodynamic conditions such as the mean velocity and temperature profiles can usually be specified with adequate accuracy. It has been established that the liner impedance is not only a function of liner design but that it also depends on the local sound pressure level and properties of the local aerodynamic flow (often called the "grazing flow" effect). Both of these effects are inadequately described by empirical models. Thus, it is impossible to specify accurately the liner impedances required as input to the theoretical models.

It is clear that the optimum suppressor performance (an appropriately specified maximum insertion loss) for a given treated area cannot be obtained with a liner impedance distribution guided by theoretical models alone. Neither can it be obtained from empirical data taken from flow duct facilities, since the spatial distribution of the aero-engine acoustic sources cannot be faithfully reproduced in such facilities. The only feasible method of determining the optimum impedance distribution is to perform tests on a range of liners installed in a reduced- or full-scale version of the engine. However, this approach demands a time-consuming, expensive engine test program in which segments of duct lining are replaced and interchanged until an

optimum suppressor performance is attained at one particular engine operating condition. Once this is achieved, the procedure would have to be repeated if the suppressor is required to be effective at two engine operating conditions. There would inevitably be a compromise, since the acoustic source intensity and distribution and the aerodynamic conditions will differ at the two operating conditions. To overcome these limitations, the liner must be "tuned" after installation such that the maximum insertion loss can be achieved for an arbitrary engine condition. Since the insertion loss, or duct attenuation, is a direct function of the liner impedance, it is necessary to have direct, in situ control of the liner impedance.

The aim of this work is to show that the impedance of the liner can essentially be controlled after installation. It has long been known that steady bias air flow through perforated sheet-metal material will increase the acoustic resistance (the real part of the impedance) from the zero through-flow, or bias flow, value (ref. 1). However, the imaginary part of the impedance (the reactance) is only slightly affected by bias flow. A concept is described which uses these known effects in a multi-cavity liner configuration such that controlled changes in reactance and resistance can be effected. The practical use of this concept depends only on the availability of a supply of compressed air at a controlled pressure, and a slight design modification of the liner configuration to allow injection of steady air flow. Since aero-engine design has met similar requirements in the past, such as for de-icing and boundary layer control applications, this major requirement is eminently practicable and presents no real obstacle to the application of the proposed concept.

2. DESCRIPTION OF CONCEPT

For a single-layer locally reacting liner system, the total resistance is dominated by facing-layer resistance, and hence resistance control by bias flow is possible. However, since the total reactance is dominated by the cavity reactance, the changes in facing-layer reactance with bias flow will have little effect on the system reactance. However, consider the multi-layer configuration shown in Figure 1. The total reactance is a function of the cavity depths and of the resistance of the intermediate layer separating the two cavities. This effect can be envisaged by considering two extremes. First, when the intermediate layer is a rigid impervious plate, the reactance is solely a function of cavity depth (d_1). Then, if the intermediate layer is acoustically transparent, the reactance is a function of the total cavity depth ($d_1 + d_2$). Thus, a range of reactance is possible if the intermediate layer resistance is varied between the two extremes with bias flow. In practice, this effect is complicated by the fact that the impedance of the duct facing layer will also be changed by the bias flow. As a general rule, however, the total resistive changes can be controlled within the desired bounds simply by using a facing layer which is considerably less sensitive to bias flow than the intermediate layer.

A two-layer system is preferred for ease of analysis and fabrication, since only two facing-sheet porosities and two cavity depths have to be considered in design optimization.* The classical two-layer system would be terminated at the liner rear-wall with a rigid, impervious layer. However, to introduce bias flow through the two porous layers, the rigid back wall must be replaced with a third porous layer. This layer should have a relatively high acoustic flow resistance to minimize its effect on the two-layer system. Further, a plenum must be included behind the porous layer to ensure an even distribution of air flow throughout the system. While it would be ideal for the rear layer and plenum to be acoustically decoupled from the two-layer system, this cannot be fully realized in practice, as will be discussed later. This is not a serious shortcoming, since the system can be analyzed as a three-layer liner without a significant increase in complexity.

The potential of this basic concept must now be substantiated. This will be done by means of an analytical acoustic model of a simple lined duct system which will be used to define a series of bench-type laboratory tests aimed at validating the concept.

*It is possible that many layers and depths can be used.

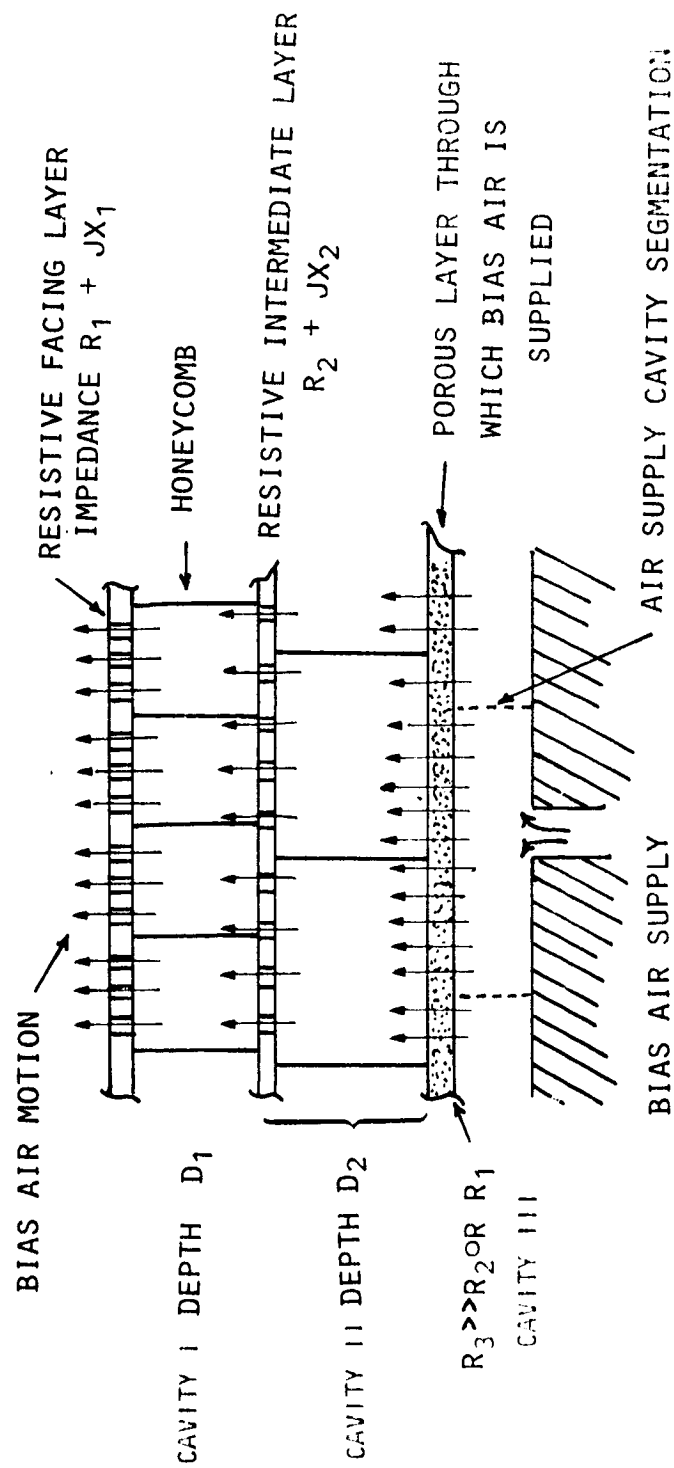


Figure 1 Variable Impedance Liner Concept

3. ANALYTICAL STUDY

3.1 Introduction

The first goal of the analytical program was to model the acoustics of the "proof-of-concept" test duct such that an estimate of the attenuation rates for the first two duct modes could be obtained as a function of wall impedance and duct flow velocity. This information would enable an "optimum" impedance to be defined, thus ultimately guiding the design of a test liner. The second part of the analytical study was to produce a workable impedance model of the multi-layer liner system incorporating the effects of bias flow. This model was to be used to design the liner component parts for the "proof-of-concept" tests.

It should be noted that the analytical work was done primarily to guide the liner design; associated analytical studies of the concept were incidental rather than comprehensive in nature.

3.2 Attenuation Contour Plots

The aim of this part of the study was to develop the computational facility to generate plots of contours of constant attenuation, in the impedance plane, for the first two duct modes. These plots are an essential part of the design of the liner system, the prime objective being to maintain any particular value of attenuation as defined by the proper choice of duct wall impedances appropriate to the desired frequency and flow velocity condition.

A large number of plots of contours of constant attenuation were required to determine the specific effects of the relevant parameters: frequency and duct flow velocity. Thus, a computational system was set up to display the attenuation contours on a computer-graphics system, with the option of a plot print-out on a line printer. This proved to be an extremely convenient system, as the effect of parameter changes could be almost instantly displayed, examined, and printed for future reference.

In the computer program, the plug flow equation [as described in Morse and Ingard (ref. 2)] was solved for the modal propagation constants, the input parameters consisting of duct grazing flow Mach number, duct wall impedance, and reduced frequency (K). The simplification of this analysis system over other more complex shear solutions (e.g. Pridmore-Brown type solutions) has been shown by Ko (ref. 3) to be justified for propagation with flow (i.e. the exhaust configuration) and a sufficient approximation for "thin" boundary layers with low grazing flows for upstream propagation (see Ko (ref. 3) and Schauer (ref. 4)). Therefore, for the purposes of the present investigation only plug flow calculations were utilized and other, more critical, analytical aspects of the problem were emphasized instead (e.g. wall impedance modeling).

The duct configuration chosen for this study is lined on one side, as shown in Figure 2. The reduced frequency (K) is related to the free space wave number (k) by $K = kd$, where d is the duct width. In the experimental case, $d = 7.62$ cms (3 inches); thus $K = 2\pi fd/c$, where f = frequency and c = speed of sound. That is, for $K = 1$ and $c = 34,400$ cms per second, the frequency becomes 718 Hz. The parameter of reduced frequency is particularly convenient for the normalization of impedance values on the complex plane, as the branch points remain in the same relative position on the contour plots, regardless of the frequency being considered. The frequencies covered in the analysis were based on 1/3-octave center frequencies from 315 Hz to 4000 Hz, with supplemental values corresponding to integer values of K. The duct Mach number values chosen were 0.0, 0.125, 0.25, and 0.5. For reference, the equivalent frequencies and K numbers are given in Table I and the resulting attenuation contour plots for the first two modes are reproduced in Appendix A. (Note: In some references, η is used instead of K, the two being related by $K = 2\pi\eta$.)

f	K	f	K
315	.439	1436	2.000
400	.557	1600	2.228
500	.696	2000	2.786
630	.877	2154	3.000
718	1.000	2500	3.482
800	1.114	2872	4.000
1000	1.393	3150	4.387
1250	1.741	3590	5.000

Table I Equivalent Frequencies and Reduced Frequencies (K Number)

In the analysis computation, the most convenient method of definition of mode separation was to define a line of constant reactance from the branch point to the zero resistance axis. This simplified the computation of the modal attenuation contours, as ambiguities in this region in the solution are conveniently minimized or avoided for most parameter configurations of interest. Also, in examining the contour plots it should be noted that both the acoustic resistance and reactance are multiplied by scale factors (SR and SX respectively) and divided by the reduced frequency (K). This scaling was used for convenience in plotting on the computer graphics system and the line printer to permit scale expansion as required.*

For zero flow, the position of the branch point will not change with frequency (K), as the branch point** (or optimum impedance point) solution is $(0.3 - .24j) \times K$. This observation is only approximate when flow is introduced

*In Figure 3, for example, the first mode branch point is located at the physical coordinates of $.60 - .24j$, which corresponds to a normalized distance and reactance (both normalized to $c = 0.1$ and -1.1 , respectively).

**The definition of the optimum impedance used here is that impedance associated with the branch point at which the attenuation of the first two modes are equal.

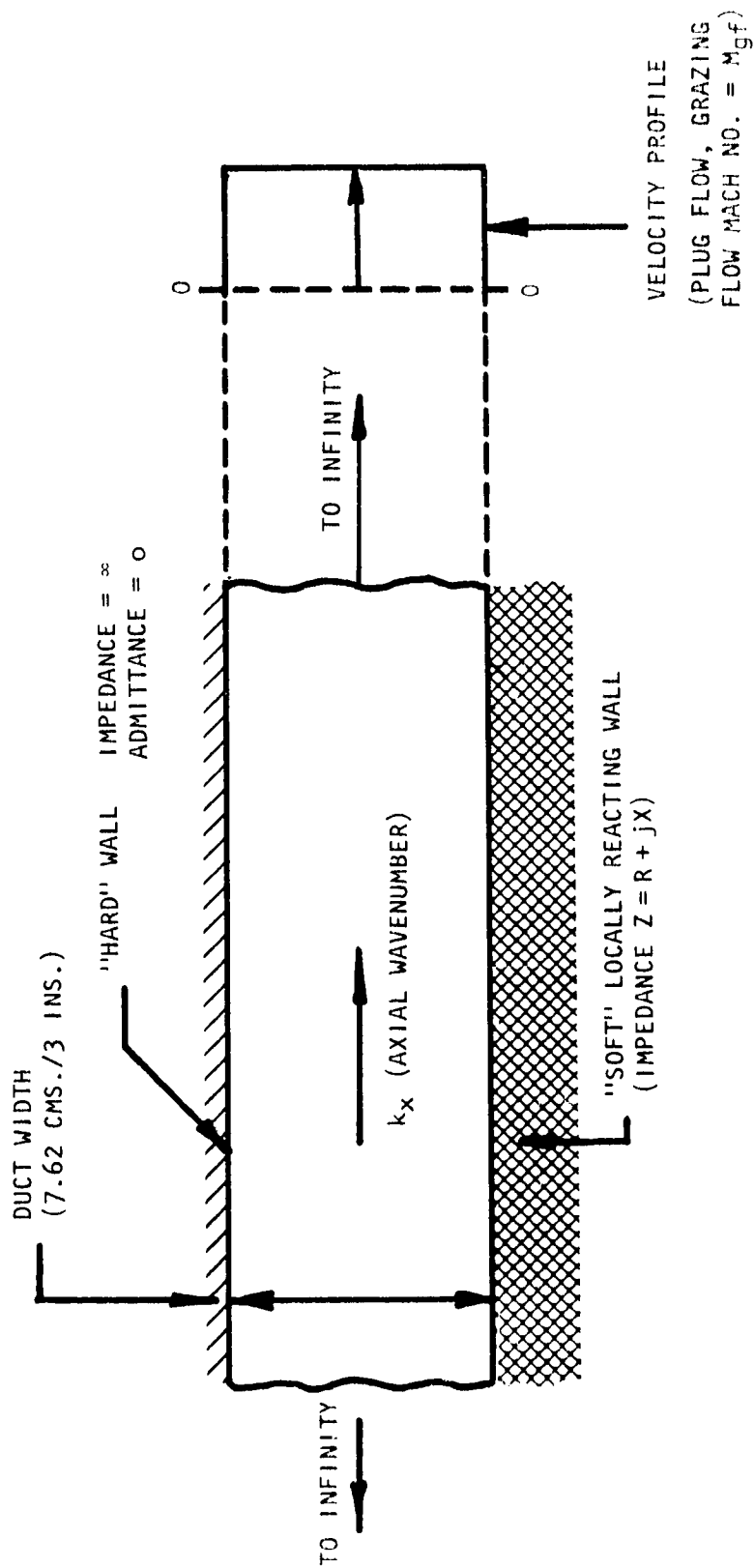


Figure 2 Configuration of Infinite Two-Dimensional Duct Used in Analytic Attenuation Model

but still results in plots which have consistent features. Figures 3 to 8 (covering selected frequencies for the zero flow duct condition) that, as the frequency increases, the peak attenuation reduces and the contour separation increases. From the information on the curves it is possible to define, for any given bounds of design impedance, what the expected range of attenuation rates would be for any given frequency.

The effects of duct Mach number are illustrated in Figures 5 and 9 through 14 for various reduced frequencies. As the Mach number increases for upstream propagation, the branch point moves to a more negative value of reactance and a more positive value of resistance, while for downstream propagation, the branch point moves to a more positive value of reactance and less positive value of resistance compared with the zero-flow case. At the branch point impedance both modes combine to form a pressure pattern that attenuates approximately at its maximum possible decay rate. However, any small deviation from the branch point impedance will result in a dramatic change of attenuation both in absolute value and relative values between the two modes, thus allowing one mode to dominate (that which is least attenuated).

Thus, it is evident that the design of a liner for a complex source distribution in frequency and space, plus variable mean flow conditions, involves the consideration of a large number of attenuation contour plots.

In this concept validation study, considering the practical difficulty of mode identification based on sound pressure measurements in the duct, it is highly desirable to maintain the attenuation rate of the second mode at a much greater value than that of the first mode. This ensures that the measured pressure decay rate is dominated by that of the first mode. This is particularly desirable in the situation where a complex source is present or where modal scattering at impedance boundaries occurs.

Thus, for concept validation, it is desirable that the test liner impedance *not* be either at the branch point or near a region where closely spaced attenuation contours exist. In practice, however, as will be shown in Section 4, such desirable conditions were difficult to achieve in every case tested.

3.3 Impedance Model of Liner

3.3.1 Introduction

An enormous amount of work has been done during the past 20 years on the analysis and prediction of the impedance properties of perforated-plate, resonant-cavity liners. This section will briefly discuss the significant parameters and detail the development of the impedance model considered most suitable for achieving the program goal: proof of the feasibility of controlling the acoustic impedance of the lining by means of bias air flow.

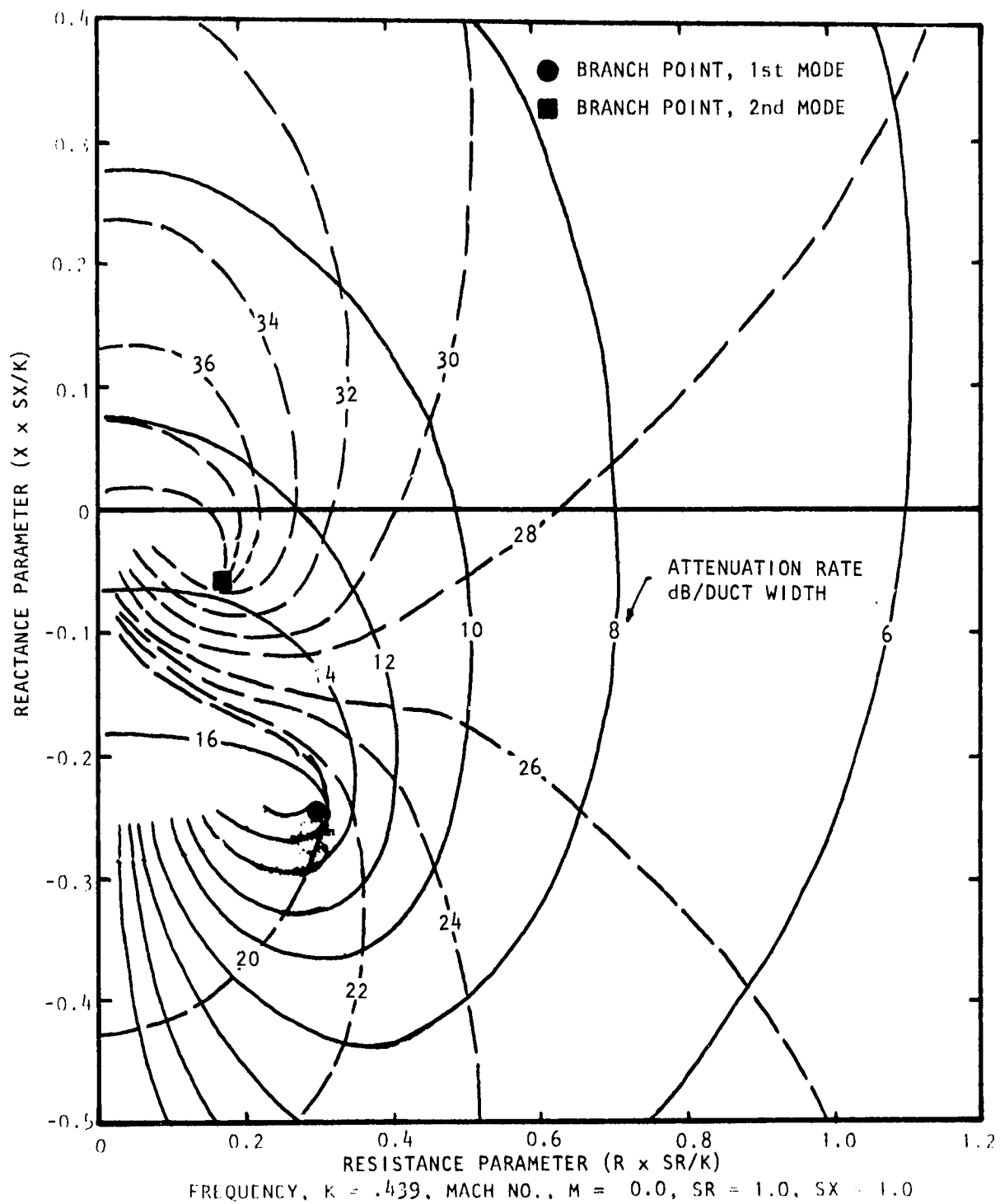


Figure 3 Contours of Constant Attenuation for First Two Modes of Propagation (First Mode —, Second Mode ----)

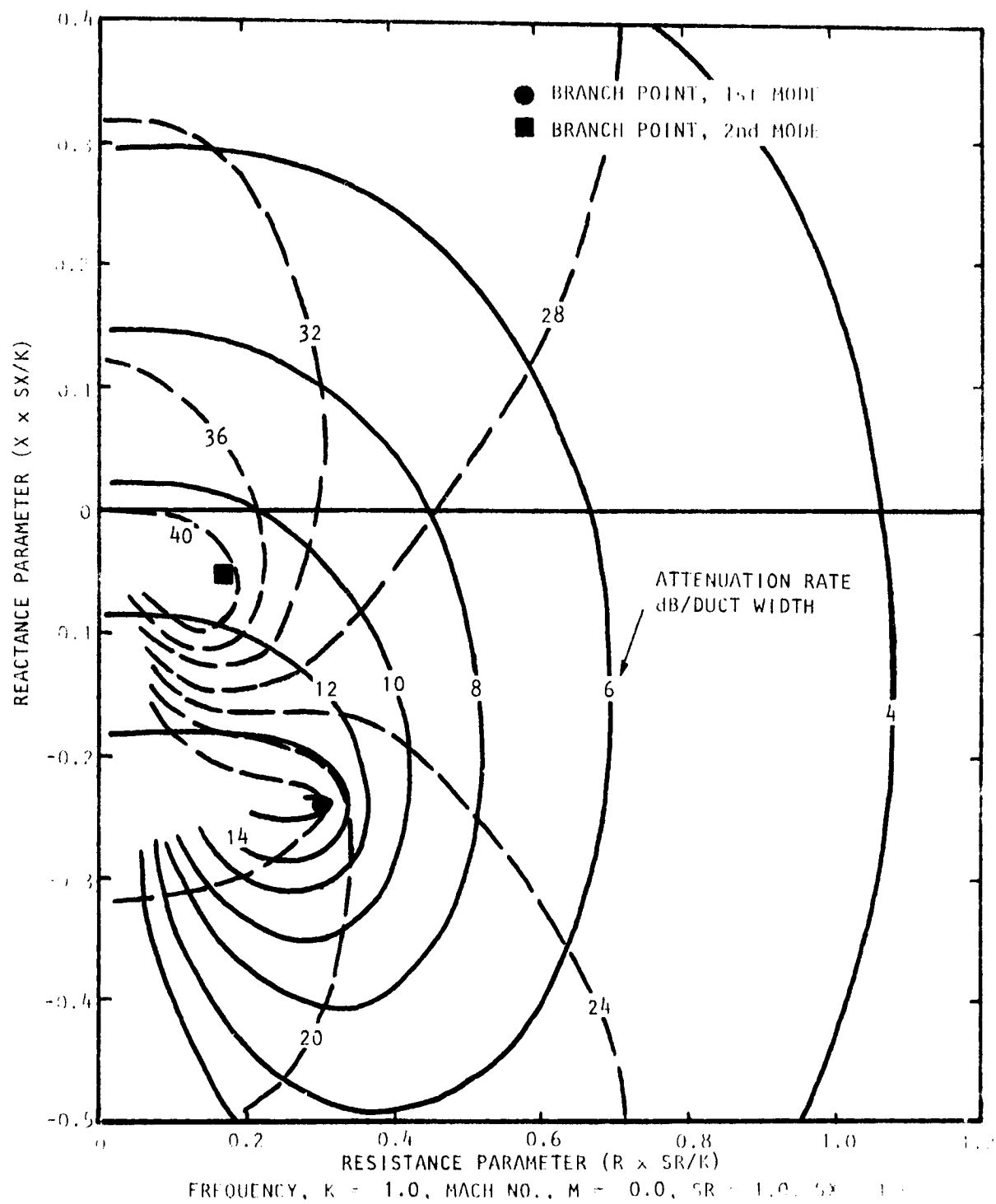


Figure 4 Contours of Constant Attenuation for First Two Modes of Propagation (First Mode —, Second Mode ---)

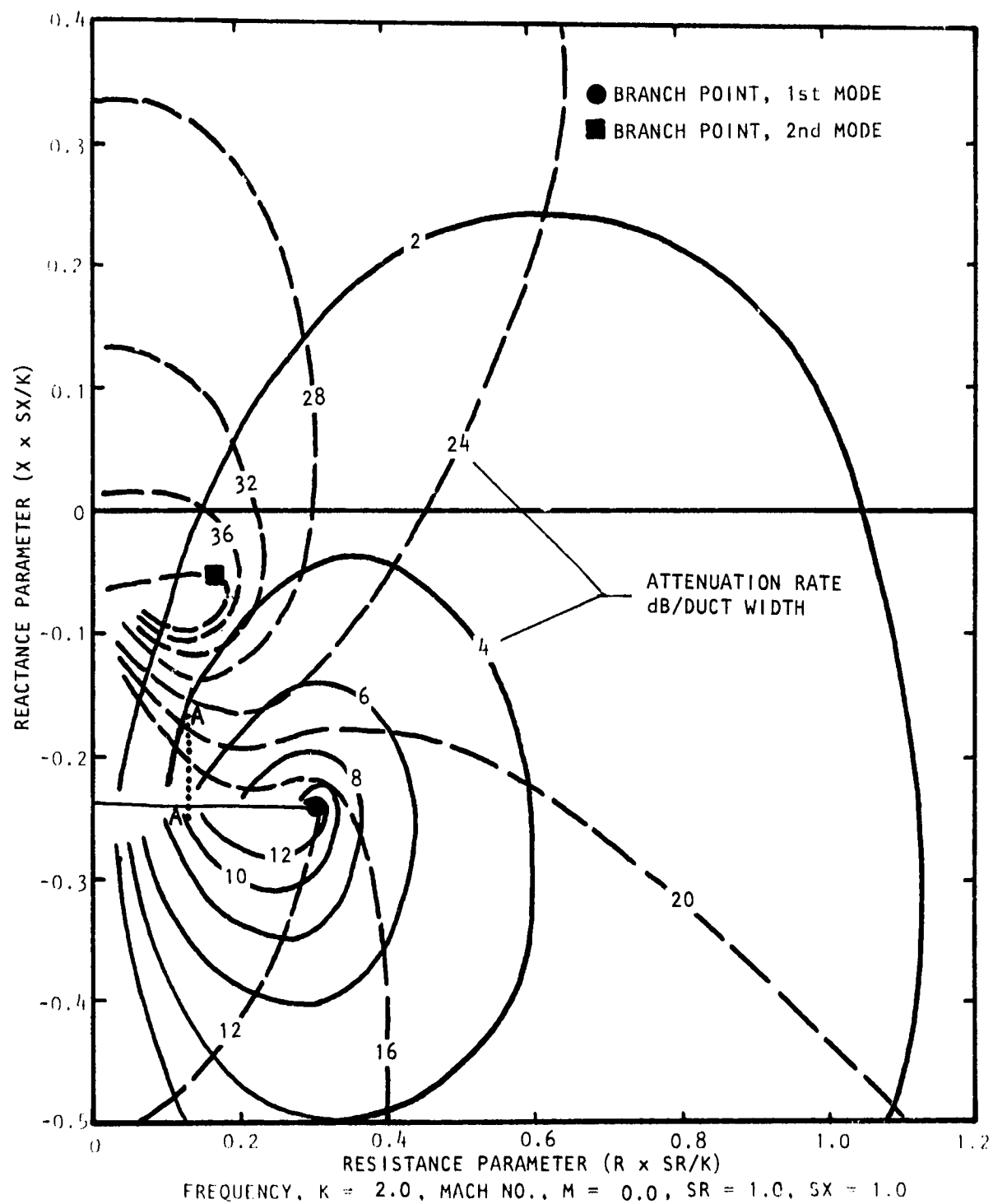


Figure 5 Contours of Constant Attenuation for First Two Modes of Propagation (First Mode —, Second Mode ----)

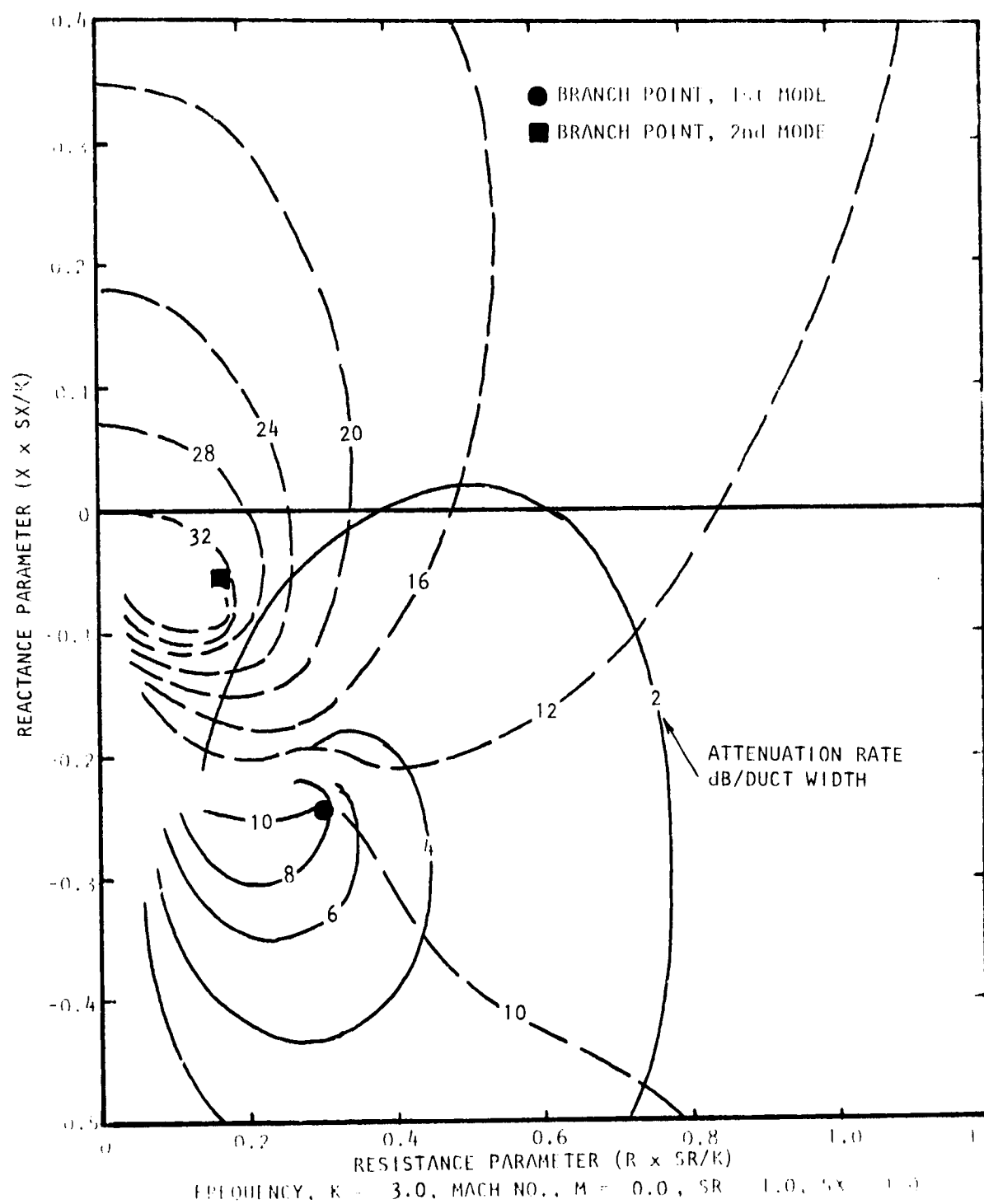


Figure 6 Contours of Constant Attenuation for First Two Modes of Propagation (First Mode —, Second Mode ---)

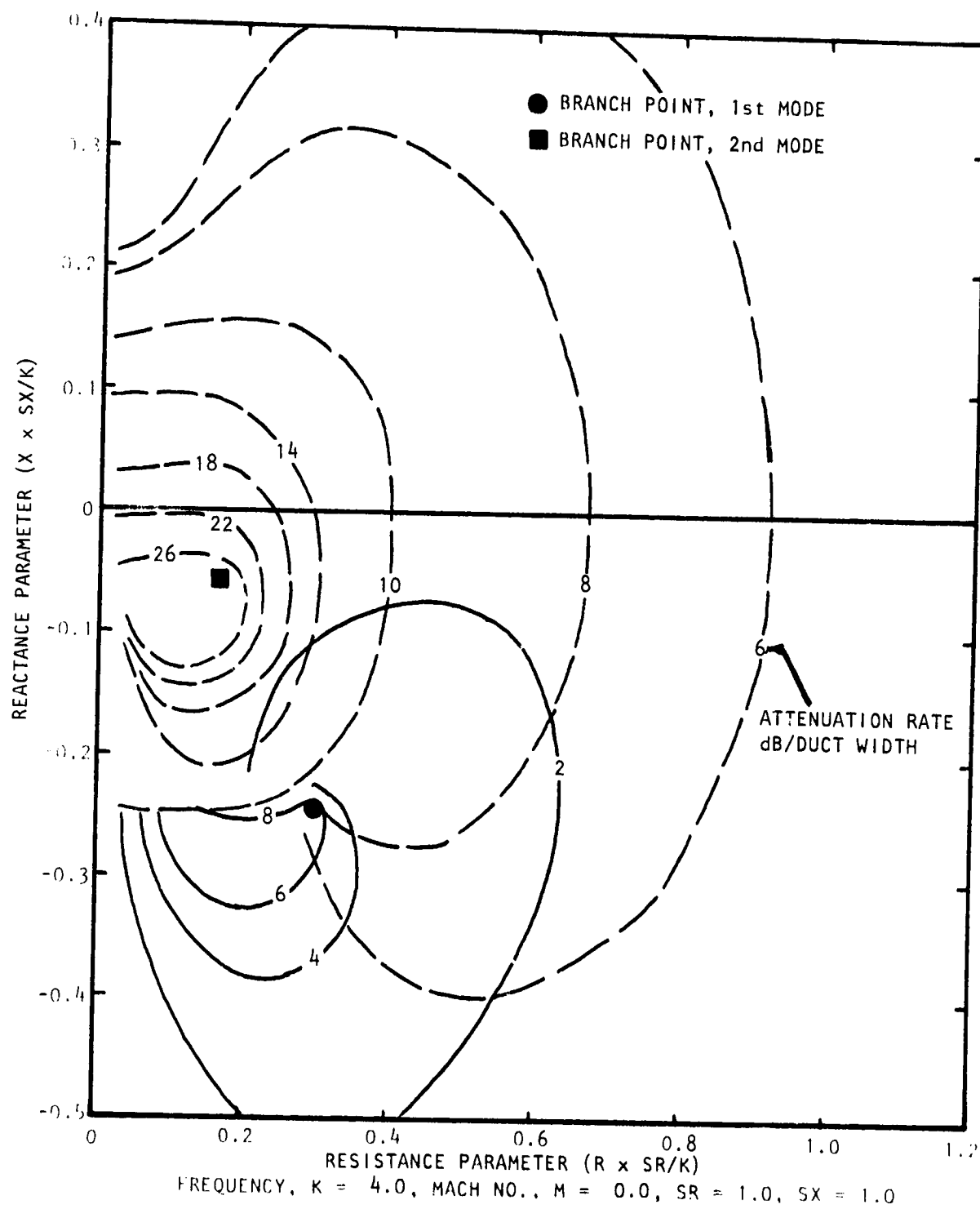


Figure 7 Contours of Constant Attenuation for First Two Modes of Propagation (First Mode —, Second Mode ----)

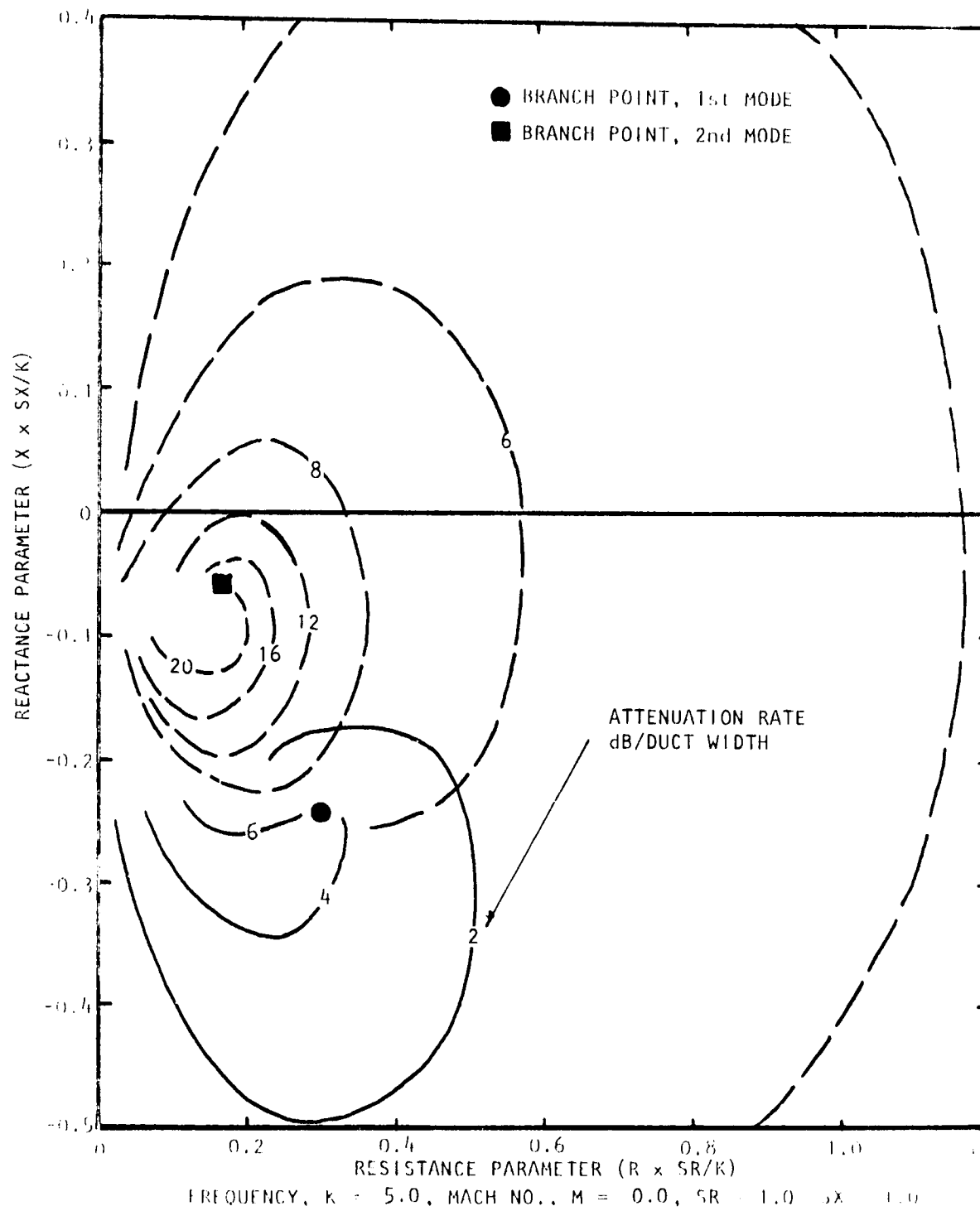


Figure 8 Contours of Constant Attenuation for First Two Modes of Propagation (First Mode —, Second Mode ---)

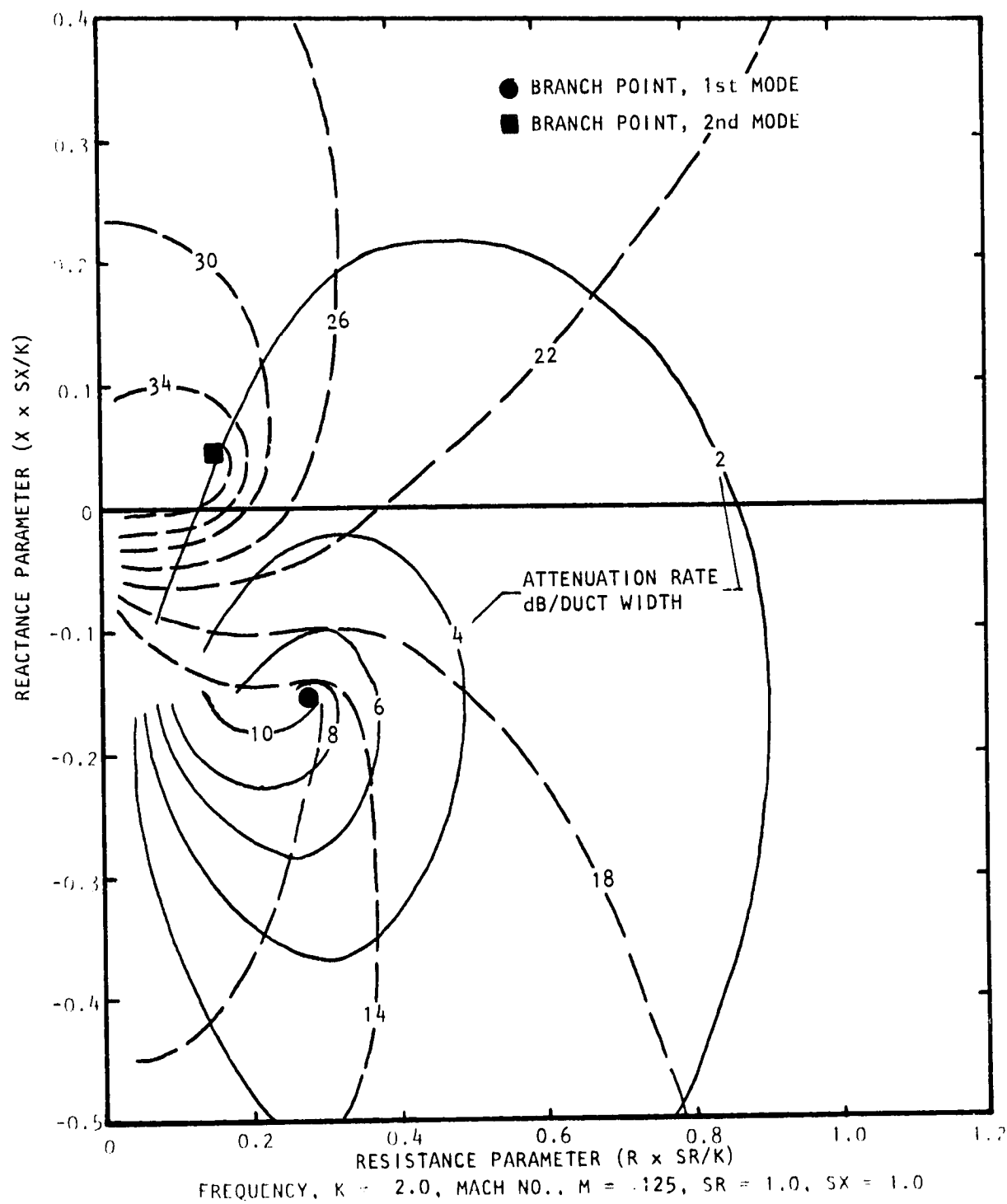


Figure 9 Contours of Constant Attenuation for First Two Modes of Propagation (First Mode —, Second Mode ----)

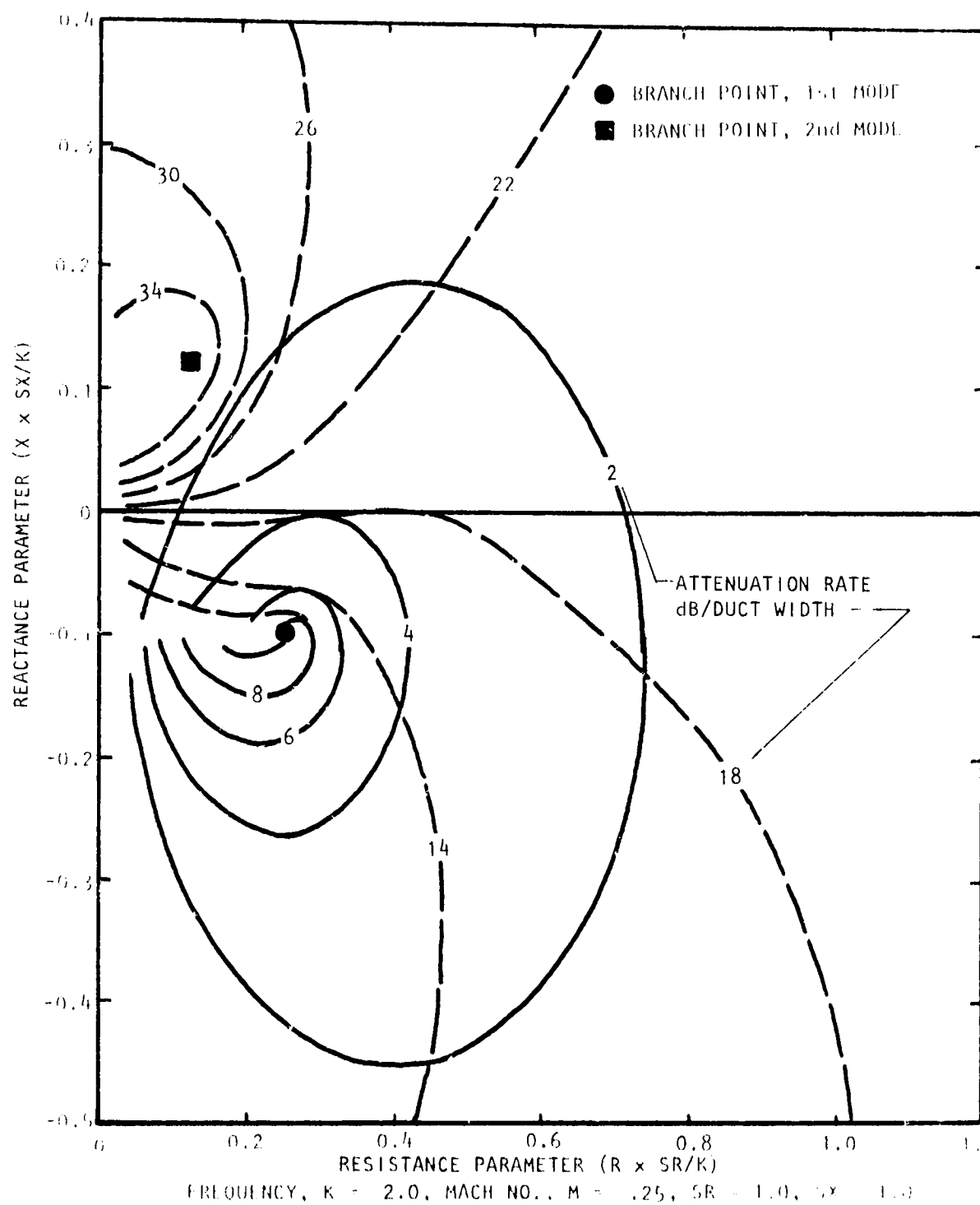


Figure 10 Contours of Constant Attenuation for First Two Modes of Propagation (First Mode —, Second Mode ---)

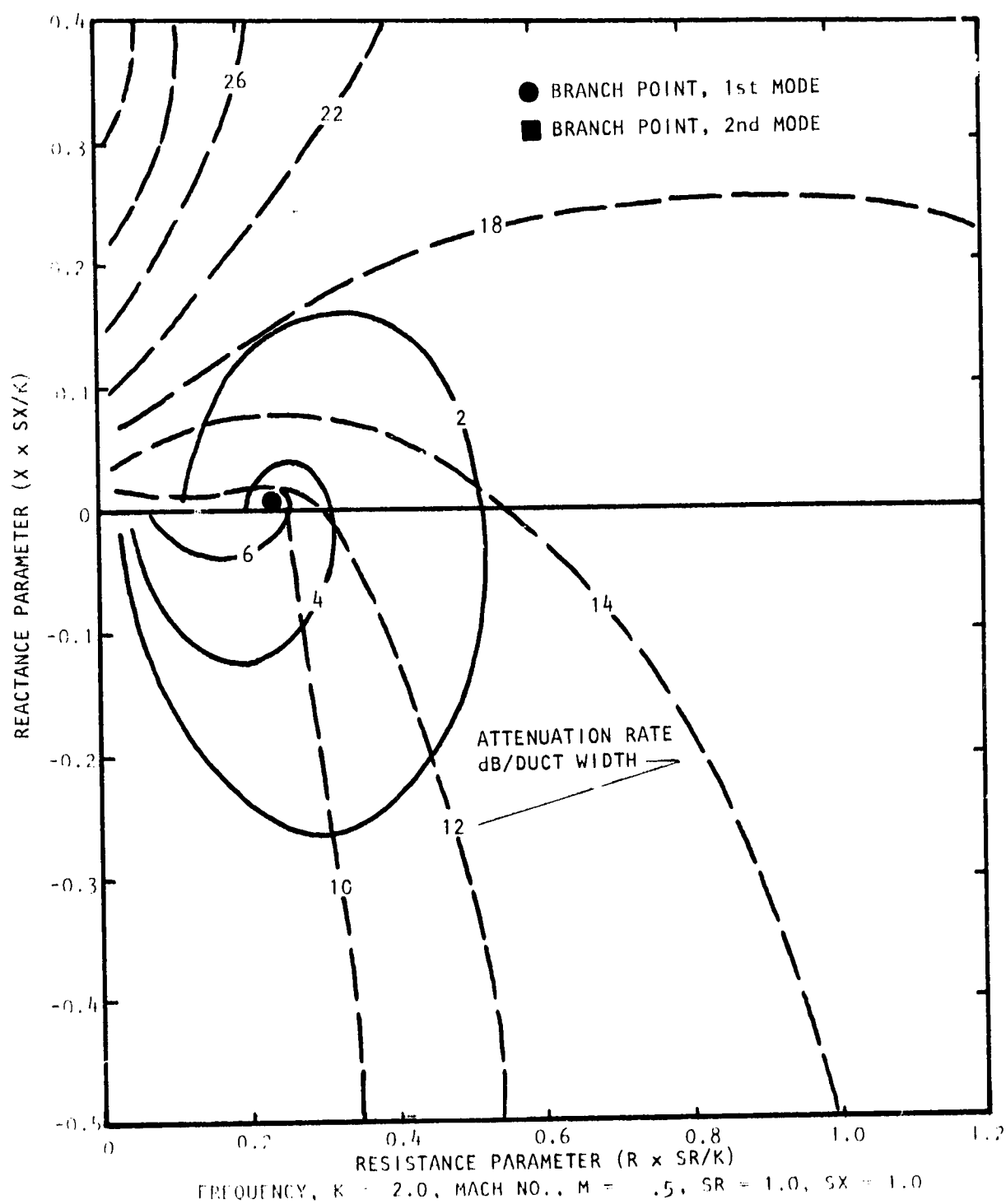


Figure 11 Contours of Constant Attenuation for First Two Modes of Propagation (First Mode —, Second Mode ---)

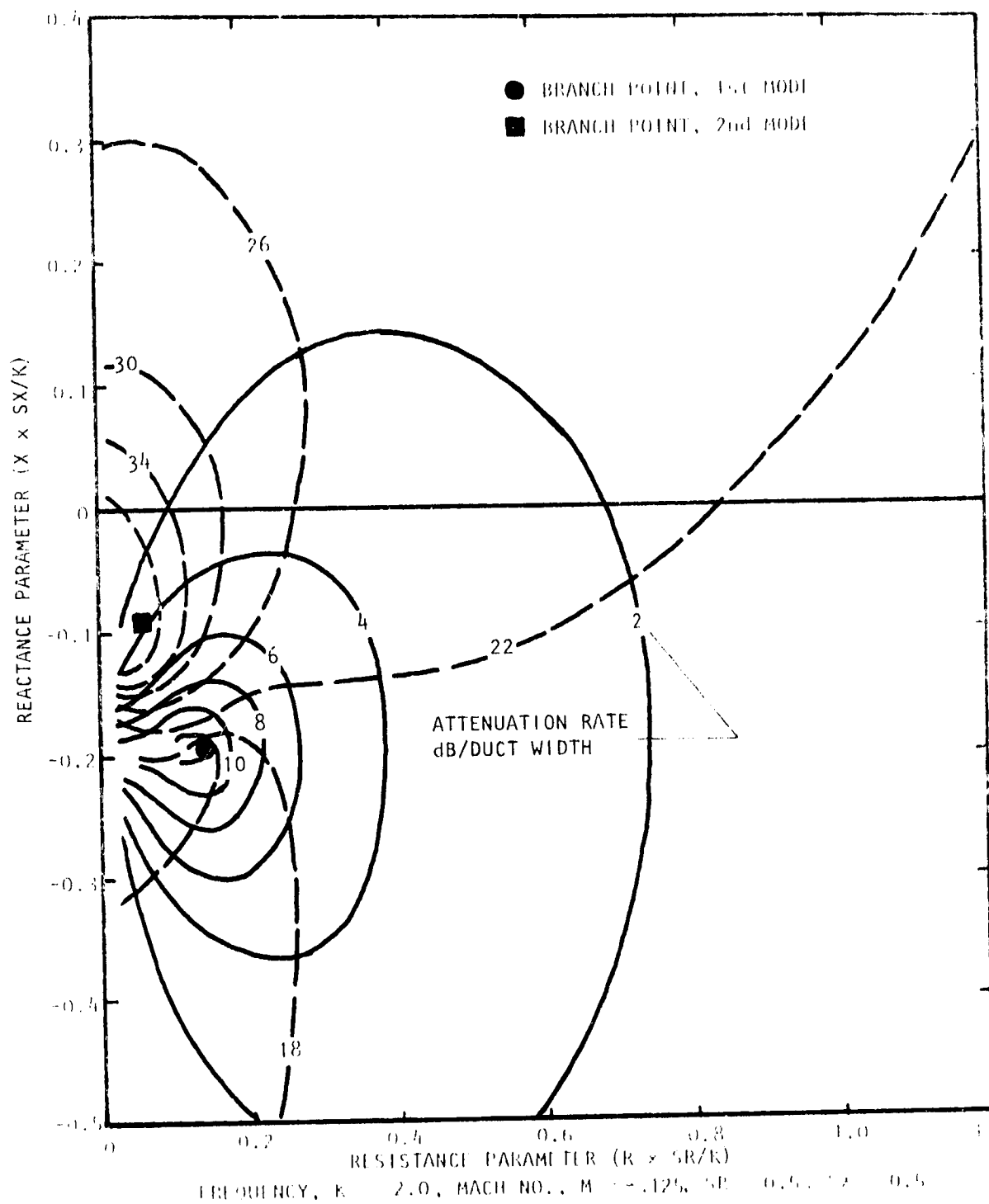


Figure 12 Contours of Constant Attenuation for First Two Modes of Propagation (First Mode ---, Second Mode - - -)

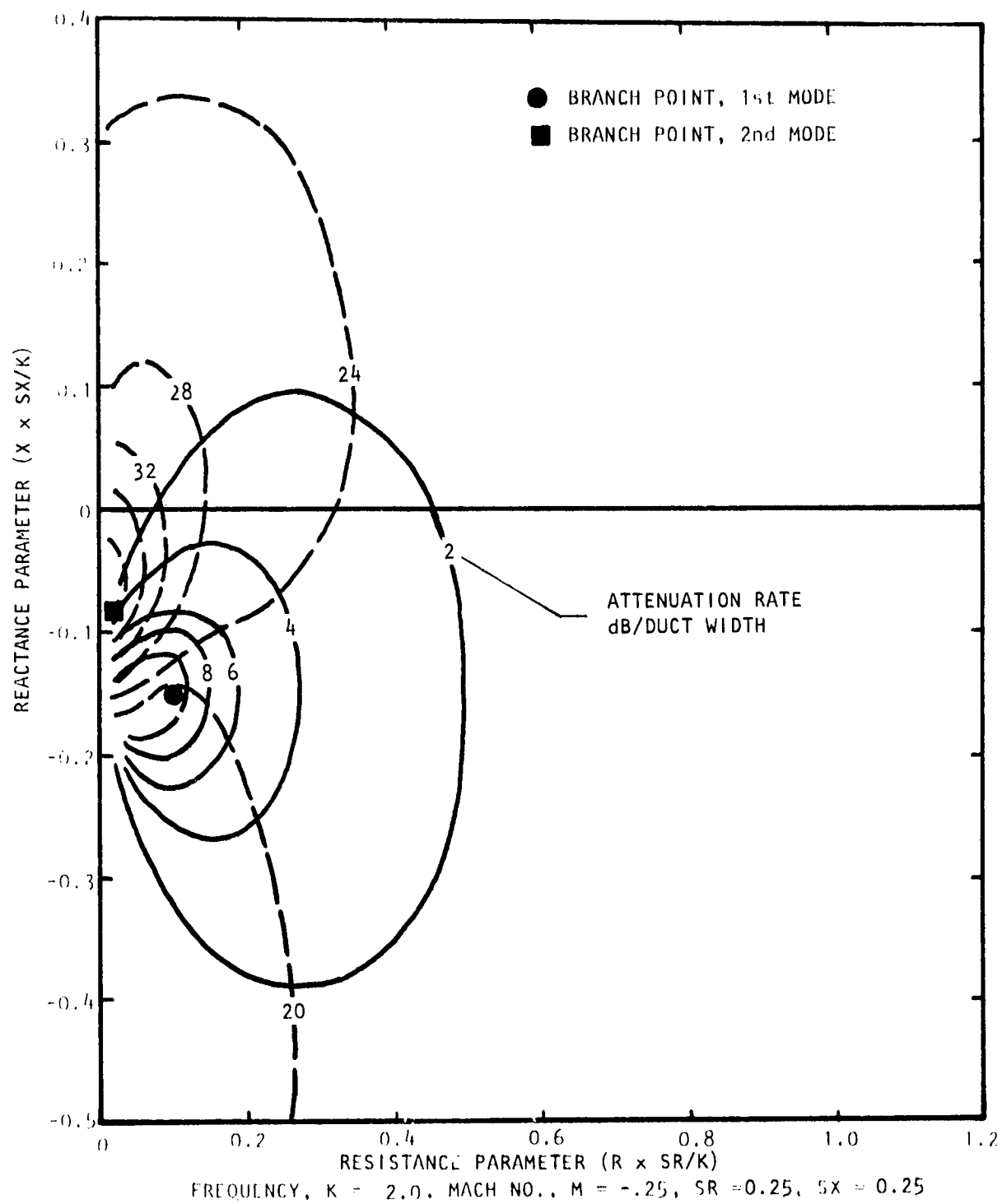


Figure 13 Contours of Constant Attenuation for First Two Modes of Propagation (First Mode —, Second Mode ----)

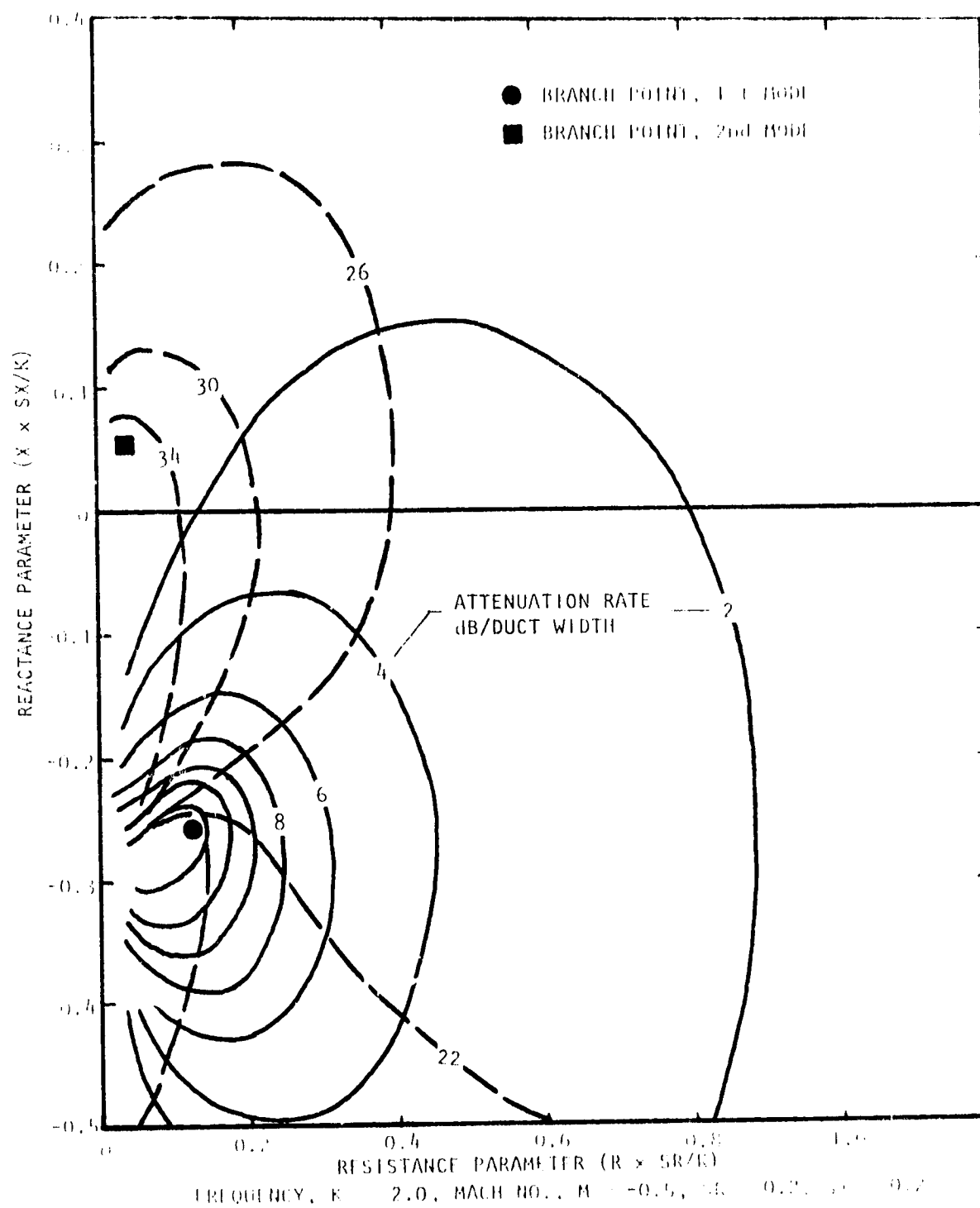


Figure 14 Contours of Constant Attenuation for First Two Modes of Propagation (First Mode —, Second Mode - -)

3.3.2 Requirements of the Model

The basic purpose of the impedance model is to obtain a simple relationship between the liner impedance and the bias flow Mach number. The impedance of the liner in its basic conceptual form can be determined from the individual impedances associated with the basic component parts. Ideally, the liner system is considered to consist of two cavities (I and II as shown in Figure 15) with porous facing layers which have individual impedances which must be defined by the model. Four independent acoustic component characteristics of this ideal liner system must be considered: (1) the facing layer resistance (R_1) and reactance (X_1), (2) the reactance of cavity I, (3) the intermediate layer resistance (R_2) and reactance (X_2), and (4) the reactance of cavity II. In practice, however, the mechanical requirements of the bias air supply introduce a third cavity whose purpose is to ensure a uniform bias air distribution. Thus, because of the finite value of the acoustic impedance of the air supply plenum and distribution control layer, this third cavity must also be taken into account. The influence of the air supply pipework in this third cavity will be ignored, since the system consists of a large number of very small holes through which choked flow passes, with negligible effect on the overall absorption of the third cavity.

The duct facing layer is to be treated as a special case in that the effect of grazing flow on the impedance must be accounted for. This effect is complicated by the fact that bias inflow or outflow interacts with the grazing flow to modify the impedance. This is the first of three major influences on the resistance of the facing layers which must be considered in the model. The second influence is the effect of the bias flow itself, which must be assumed uniform along the liner section, by design, although axial variations are theoretically possible. The third influence is the effect of nonlinear sound pressure levels, complicated by the fact that, as the sound wave is attenuated down the duct, the influence will decrease in magnitude. Some experimental evidence points to an acceptable equivalence between nonlinear SPL effects and bias flow effects; this is expected, since the physical mechanism of dissipation in each case is related to the particle velocity through the perforate holes. Thus, although it is considered desirable to incorporate this effect into the model, for the purpose of this work, this influence is tacitly assumed to be incorporated in the bias flow effect and not a specific model requirement.

In summary, the model must be capable of evaluating the impedance at a particular reduced frequency (K), for a particular grazing flow Mach number (M_{GF}), and bias approach Mach number (M_i), in terms of the impedance properties of the individual component parts. These impedance properties must be defined in terms of the physical properties of the liner: (1) the number of layers; (2) perforated facing sheet parameters of open area (or porosity σ), hole diameter (d_h), and plate thickness (e); and (3) the individual layer cavity depths (d).

In addition, there will be some practical constraints on the liner system. For example, perforated sheet can be readily obtained in only a limited range of porosities, cavity depths must be convenient to use in the test liner, and there must be reasonable ease of manufacture. The model is

thus not required to incorporate an optimization routine for impedance evaluation, as in all probability there probably would be a multiplicity of solutions.

3.3.3 Description of the Model

The model is developed in two logical steps. The first step is the definition of the impedance characteristics of the component parts, while the second step combines the component impedances in the multi-layer configuration, resulting in the required evaluation of the total liner impedance.

The simplest component part to evaluate is the impedance of the respective cavities. The model assumed that each cavity behaves only as a pure reactance; e.g., it takes the familiar form $\cot(kd)$, where k is the free space wave number and d the cavity depth for a single cavity system.

Evaluation of the perforated facing sheet impedance is considerably more complex. The simplest approximation for the *resistive* part of a perforated material is the well-known fact that the resistance (R) is proportional M_i/σ^2 , where M_i is the incident bias Mach number and σ is the perforate porosity. The constant of proportionality for this D.C. flow case is often given as between 0.7 and 1.0; however, for acoustic excitation it can be justified as being closer to 2.0, which is somewhat closer to the experimentally observed value. However, this simple form results in values of resistance that are far too small for small bias flows (e.g. as M_i approaches zero, then R approaches zero), and the more complex and comprehensive formulation of Hersh and Rogers (ref. 5) is of use. They have developed an improved orifice impedance model which accounts for both the linear and nonlinear regimes of acoustic excitation, which compares quite accurately with observed impedance measurements such as those of Ingard and Ising (ref. 6). The basic assumption in the use of this quasi-steady, hydrodynamic model (outlined mathematically in Appendix B) is that the acoustic velocities can be replaced by bias flow velocities (the case of zero bias flow being approximated with an incident bias Mach number of 0.001).

The resistance model developed for this work does not define a transfer point between the two approaches; instead it combines the two with a resulting smooth curve of resistance changes with bias flow.

The reactive part of the impedance of the layer facing sheets was also evaluated using the model of Hersh and Rogers (ref. 5) (the exact formulation is outlined in Appendix B).

The facing sheet of the outermost layer is a special case in that its impedance is affected by the presence of the duct air flow, the so-called "grazing-flow" effect. Rogers and Hersh (ref. 7) have investigated this effect and produced a model which considers the interaction of both bias flow and grazing flow. The case of outflow, corresponding to the proposed test configuration, is particularly simplified in that Rogers and Hersh show that the resistance collapses onto a single curve when plotted in terms of an effective discharge coefficient versus orifice to grazing flow velocity ratio. Thus, the resistive changes are incorporated into the model in terms directly

proportional to the grazing flow, but with the discharge coefficient dependent on the ratio of bias flow Mach number to grazing flow Mach number.

Their model shows that, when the bias outflow velocity greatly exceeds the grazing flow velocity, the effects of grazing flow induced resistance are negligible. In fact, it has been established experimentally [see Rice (ref. 8), for example] that grazing flow induced resistance dominates and holds the overall resistance constant up to a value of the velocity ratio (bias to grazing flow) of 0.3, after which the bias flow induced resistance dominates. Thus, the model computes the two situations and assigns the larger value of the resistance for each value of the bias flow velocity. Although the reactive changes of the duct facing sheet with grazing flow were not incorporated in the liner impedance formulation due to a lack of a reliable empirical model, this omission is not considered serious. Indeed, there is some evidence that increasing grazing flow will add a small positive component to the facing sheet reactance [see Dean (ref. 9)], which will, in turn, be reduced as the bias flow is increased [as determined by Guess (ref. 10)]. The resulting duct facing layer reactance approaches that of Hersh's model as the bias flow is increased. Thus, the reactance model of Hersh and Robers will be sufficiently accurate for this investigation.

Special consideration in the model had to be given to the facing sheet of the air supply cavity. The concept recognized the physical necessity of its existence, and the model requires that the acoustic impedance contribution must be considered, with the restriction that the physical configuration of the air supply cavity and facing sheet be an invariant quantity. In fact, the facing layer was chosen to be a fiber metal with a nominal flow resistance of about 80 rayls (C.G.S.). Only its resistive component was used in the model and was taken to be identical to the D.C. values measured by means of a flow bench facility; that is, the resistance of this layer was taken to be in direct proportion to the bias flow Mach number, as given in Appendix B.

Finally, all the component parts of the separate layer impedances must now be combined so as to evaluate the total liner impedance as seen by the duct acoustic field. Rschevkin (ref. 11) provides the means to combine the impedances of the individual layers through a convenient recurrence relationship (given in Appendix C for reference) which holds for an arbitrary number of layers. Indeed, the computer program, which calculates the component impedances and the total liner impedance, was set up such that the number of layers was a defined variable, recognizing the possibility of more complex liner systems.

3.4 Model Parametric Considerations

The parameters which control the impedance of the multi-layer system are grazing-flow Mach number, perforate porosity, and cavity depth. As the effect of each parameter on system impedance is highly interactive with that of the other parameters, it is extremely difficult to visualize the specific effect of a change of any one of them on the system impedance. However, some generalizations can be made.

The effect of grazing flow is the simplest to classify. An increase in grazing-flow Mach number results in an increase in resistance (and not reactance) of the multi-layer system.

Second, in a system with fixed cavity depths, the effect of a decrease in the *ratio* of intermediate to facing layer porosities will effectively result in a decoupling of the intermediate layer at a *lower* value of bias flow Mach number. The consequence of this decoupling is a more rapid decrease of reactance with bias flow.

Similarly, for given perforate porosities, an increase in the ratio of intermediate to facing cavity depths will result in a larger reduction in reactance over the same bias flow range.

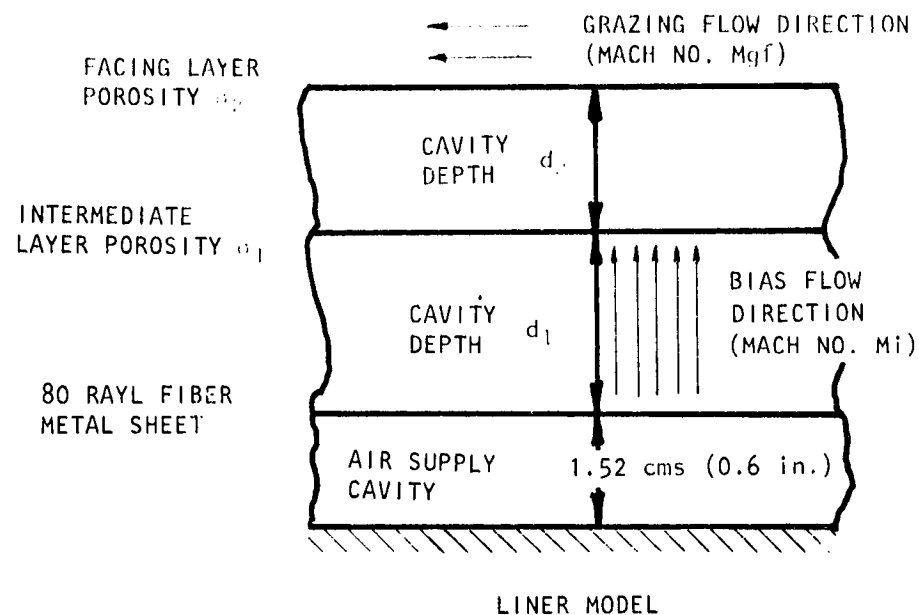
A rather thorough computer study was made of the effects of these three parameters on system impedance, and the complete set of results is included in Appendix D for a comprehensive range of frequencies. The reduced frequency K was varied from 0.5 to 5.0 (which is equivalent to 360 Hz to 3.6 KHz, respectively). The resistance and reactance coordinates are scaled such that these plots can be compared with (or overlayed on) the attenuation contour plots in such a way that a change in one of the parameters can be related easily to a change in attenuation. Figure 15 shows both the impedance model liner configuration and the coding of the bias flow symbols used on the subsequent bias flow impedance characteristic plots.

It is possible to categorize the response of the basic double-layer liner system (as shown in Figure 15) into three regions, based on their relative positions on the impedance plane, corresponding to increasing values of reduced frequency K .

The first region, broadly classified as that area where the impedance characteristic lies below and just above zero reactance axis, is illustrated in Figures 16 to 18. (Zero reactance in this case can be defined as the first resonant frequency of the liner.) In this region the effect of bias flow is to reduce the reactance and increase the resistance.

In the second region, illustrated in Figures 19, 20, and 21, the bias flow characteristic is such that an increase of bias flow initially reduces the resistance; then at some point the rear cavity effectively becomes decoupled, and the resistance increases with increasing bias flow. This behavior usually occurs when the reduced frequency K is close to the second liner resonance point. If the zero bias reactance is *positive* (as in Figures 19 and 20, i.e. K just below the second resonance), an increase in the bias flow will reduce the reactance until a constant value is approached. At this point the rear cavity is effectively decoupled. If the zero bias reactance is *negative* (as in Figure 21, i.e. K just above the second resonance point), increasing bias flow will increase the reactance until the rear cavity is again decoupled, whereupon it remains constant.

The third region covers even higher values of K . In this region, increasing bias flow has the effect of increasing both resistance and reactance (as shown in Figures 22 and 23).



BIAS FLOW CODE

MACH NO.	SYMBOL
0.001	○
0.003	□
0.005	△
0.010	◇
0.015	◐
0.020	◑

- NOTE: 1) SYMBOL ARROW (►) DENOTES DIRECTION OF INCREASING BIAS FLOW
- 2) SR, SX ARE SCALE FACTORS ON RESISTANCE AND REACTANCE, RESPECTIVELY

Figure 15 Impedance Model Layout, Parameter Nomenclature and Bias Flow Symbol Coding for Figures 105 to 147

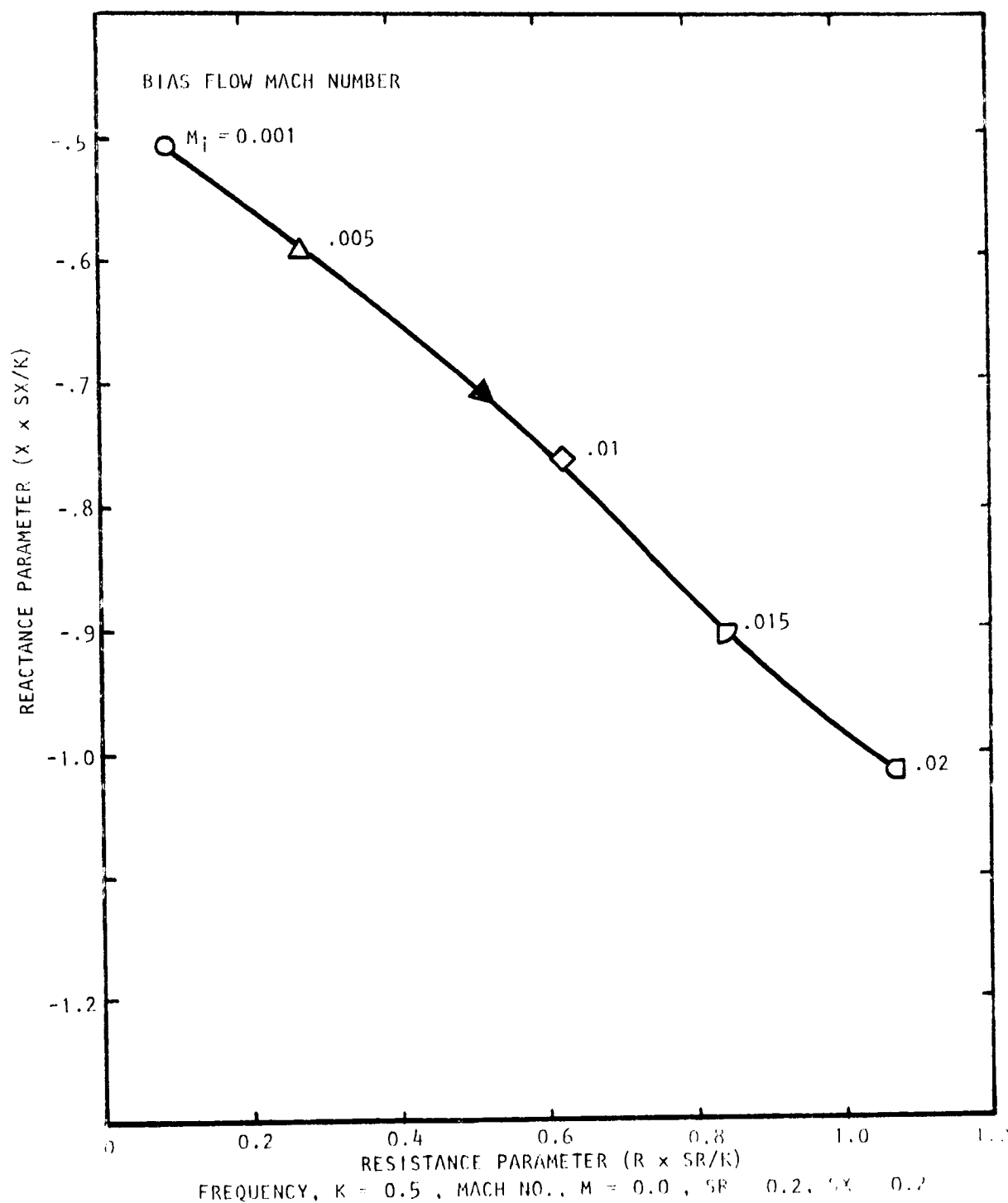


Figure 16 Effect of Bias Flow on Impedance of Multi-cavity Liner with Porosities $\sigma_1 = 10\%$, $\sigma_2 = 20\%$, and Cavity Depths $d = 3.81$ cms. (1.5 ins.) and $d = 3.81$ cms. (1.5 ins.)

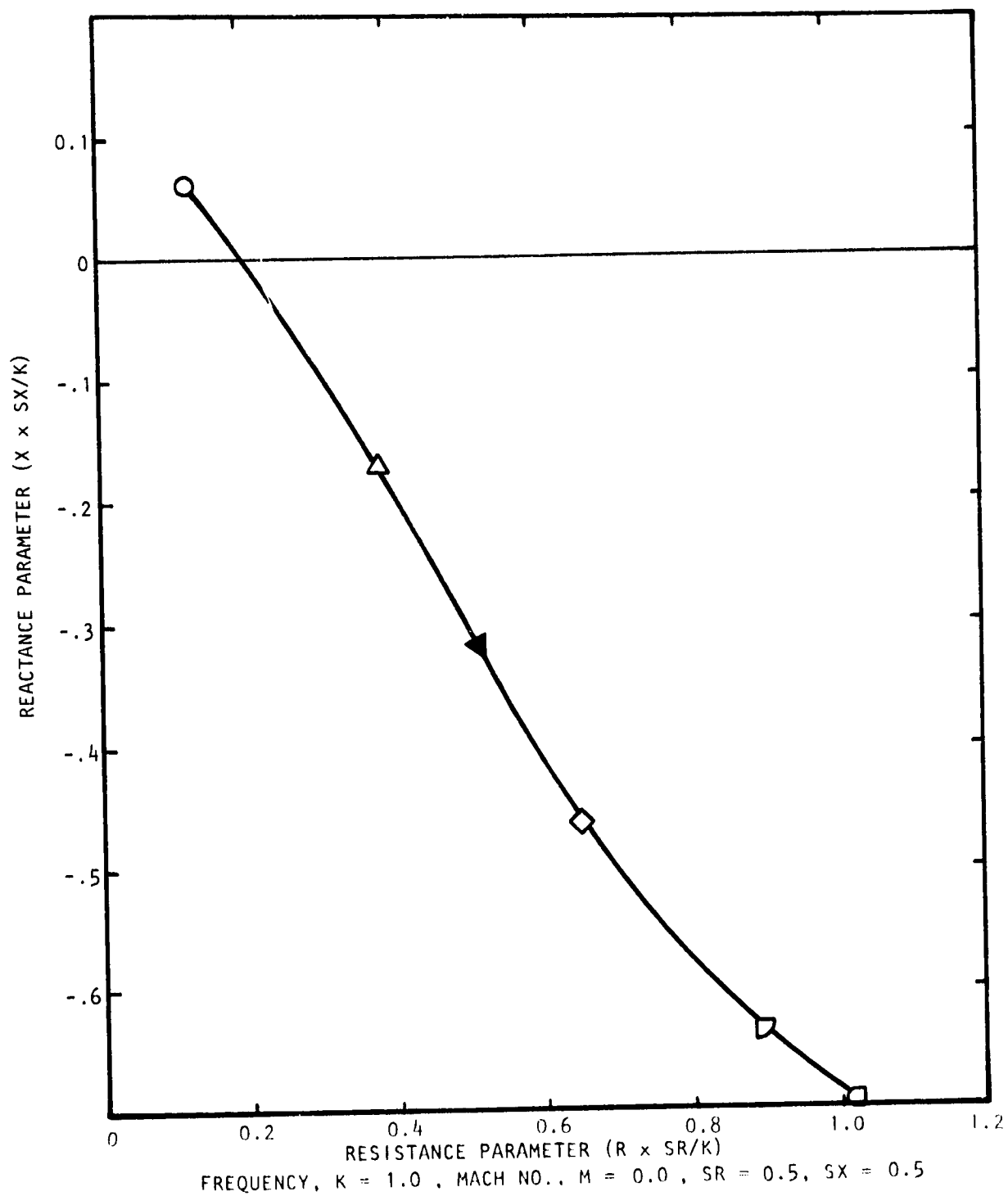


Figure 17 Effect of Bias Flow on Impedance of Multi-Cavity Liner with Porosities $\phi_1 = 10\%$, $\phi_2 = 20\%$, and Cavity Depths $d_1 = 3.81$ cms. (1.5 in.) and $d_2 = 3.81$ cms. (1.5 in.)

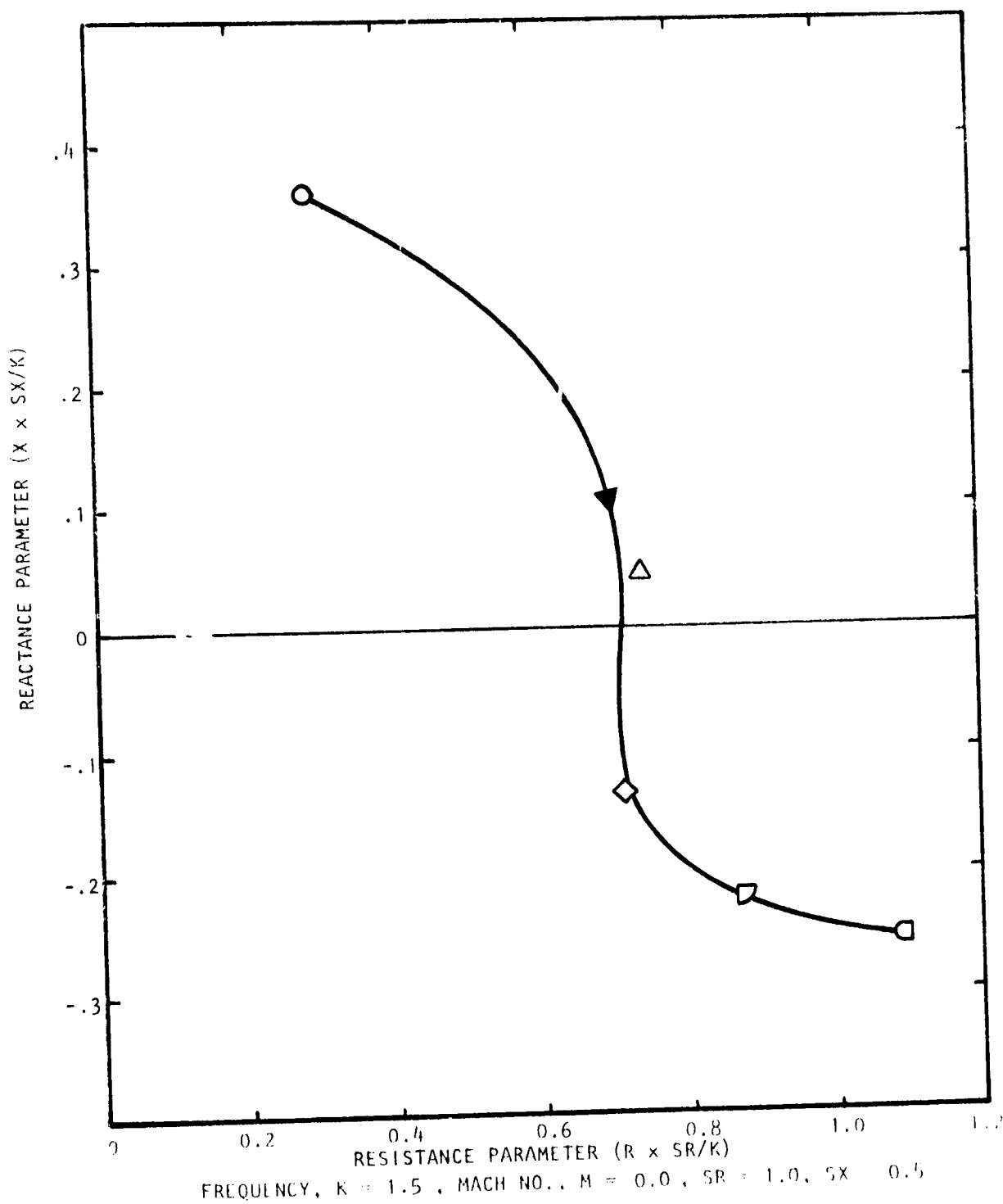


Figure 18 Effect of Bias Flow on Impedance of Multi-Cavity Liner with Porosities $\epsilon_1 = 10\%$, $\epsilon_2 = 20\%$, and Cavity Depths $d_1 = 3.81$ cms. (1.5 in.) and $d_2 = 3.81$ cms. (1.5 in.)

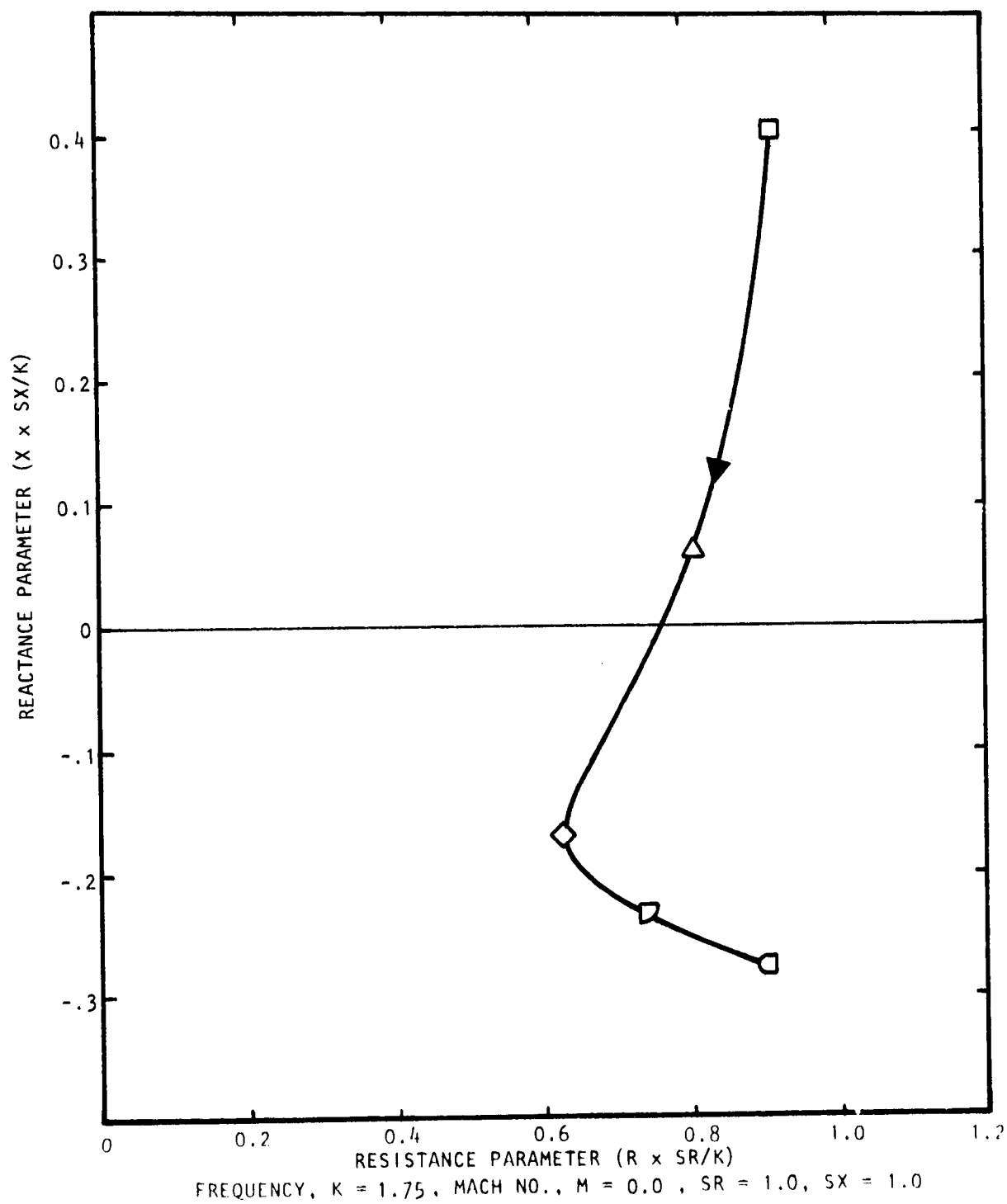


Figure 19 Effect of Bias Blow on Impedance of Multi-Cavity Liner with Porosities $\alpha_1 = 10\%$, $\alpha_2 = 20\%$, and Cavity Depths $d_1 = 3.81$ cms. (1.5 in.) and $d_2 = 3.81$ cms. (1.5 in.)

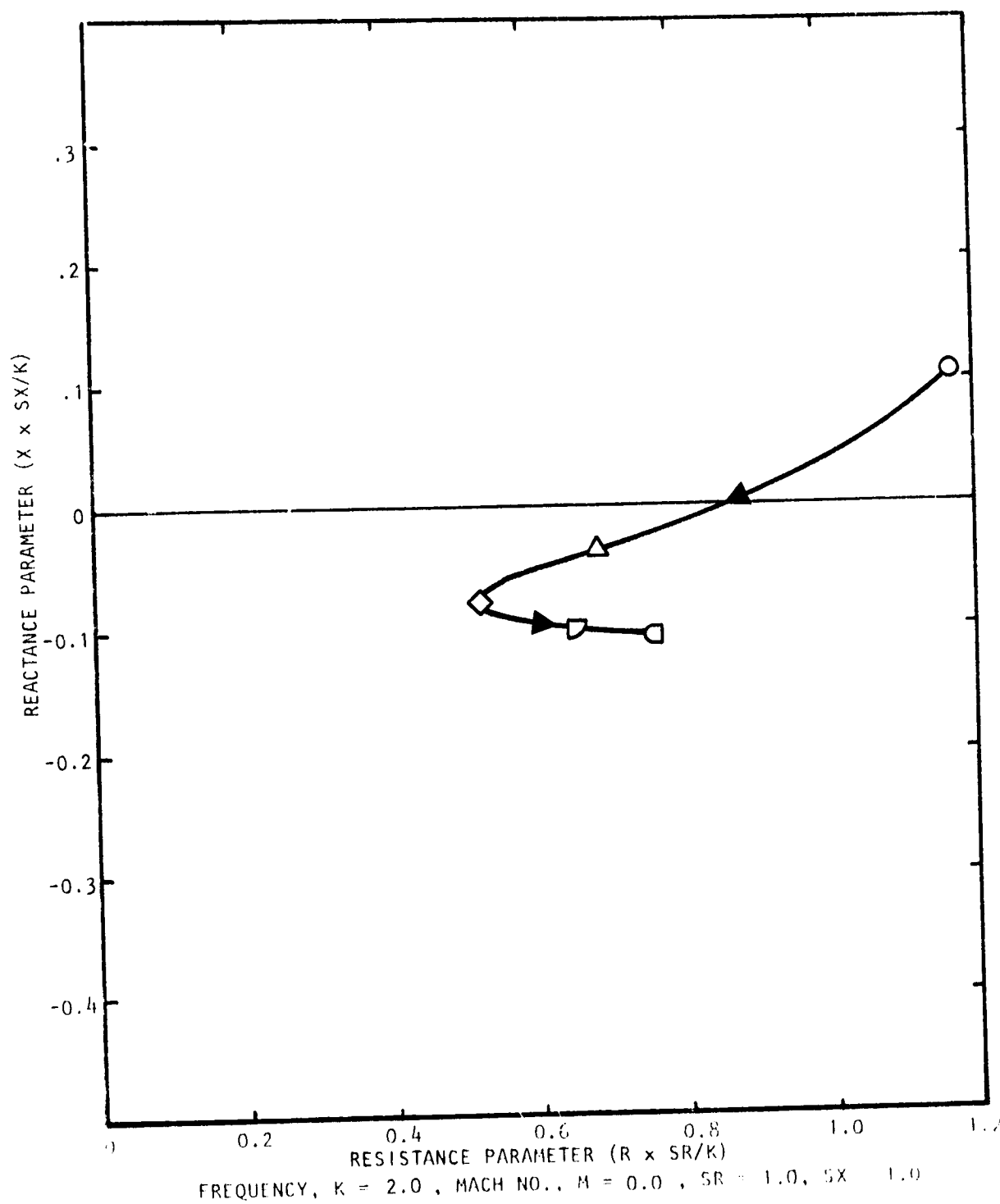


Figure 20 Effect of Bias Flow on Impedance of Multi-Cavity Liner with Porosities $\sigma_1 = 10$, $\sigma_2 = 20\%$, and Cavity Depths $d_1 = 3.81$ cms. (1.5 in.) and $d_2 = 3.81$ cms. (1.5 in.)

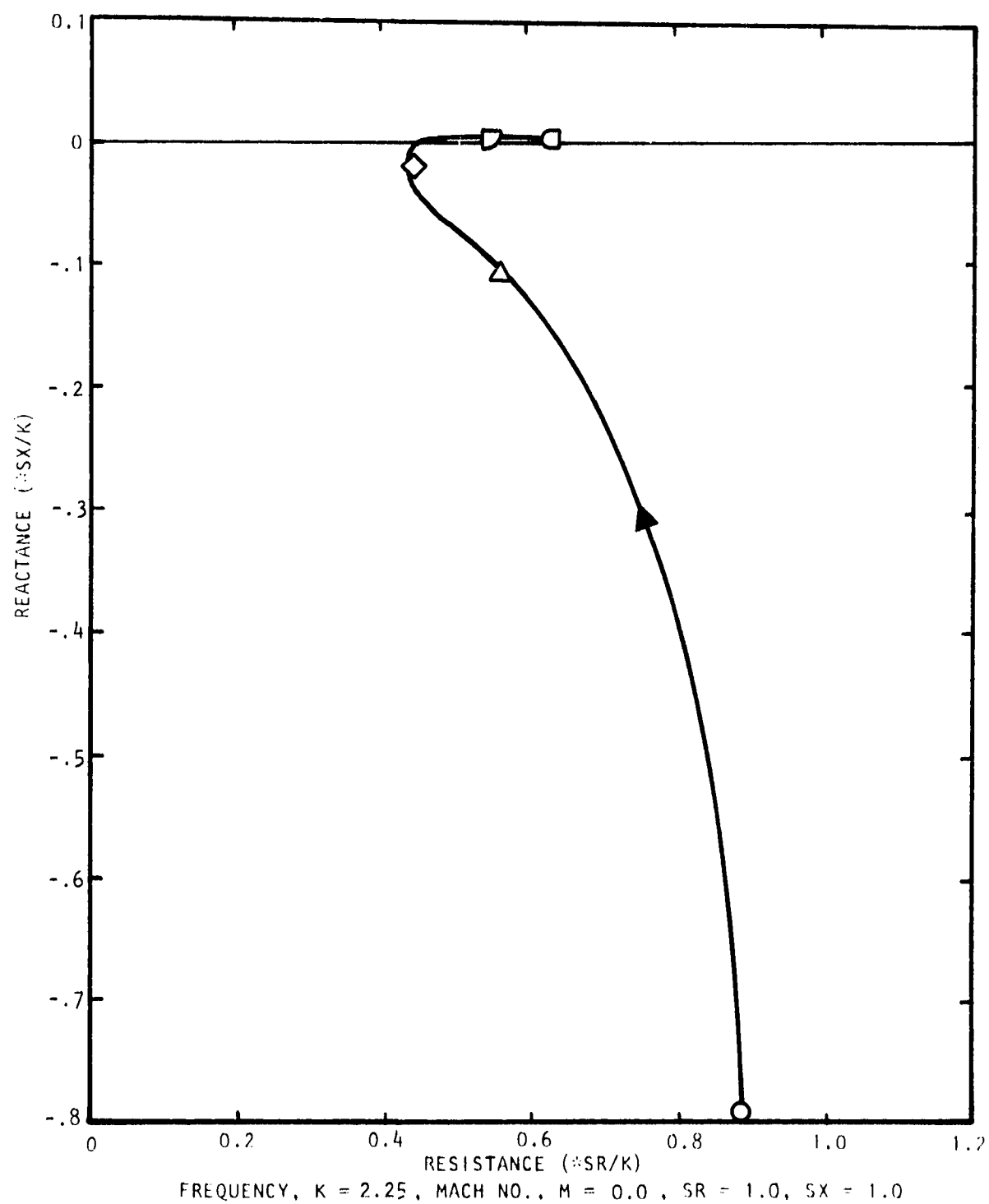


Figure 21 Effect of Bias Flow on Impedance of Multi-Cavity Liner with Porosities $\alpha_1 = 10\%$, $\alpha_2 = 20\%$, and Cavity Depths $d_1 = 3.81$ cms. (1.5 in.) and $d_2 = 3.81$ cms. (1.5 in.)

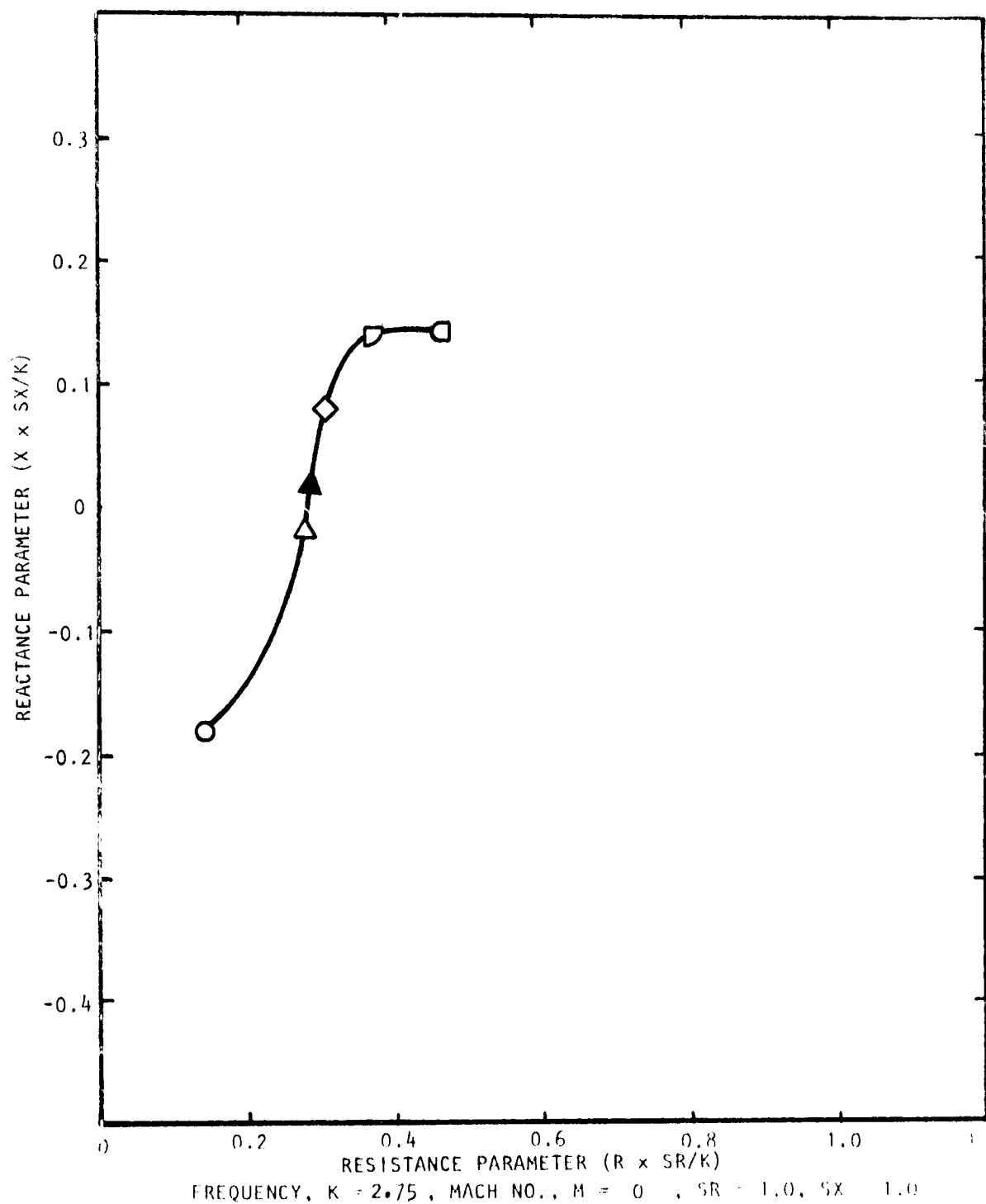


Figure 22 Effect of Bias Flow on Impedance of Multi-Cavity Liner with Porosities $\sigma_1 = 10\%$, $\sigma_2 = 20\%$, and Cavity Depths $d_1 = 3.81$ Cms. (1.5 in.) and $d_2 = 3.81$ Cms. (1.5 in.)

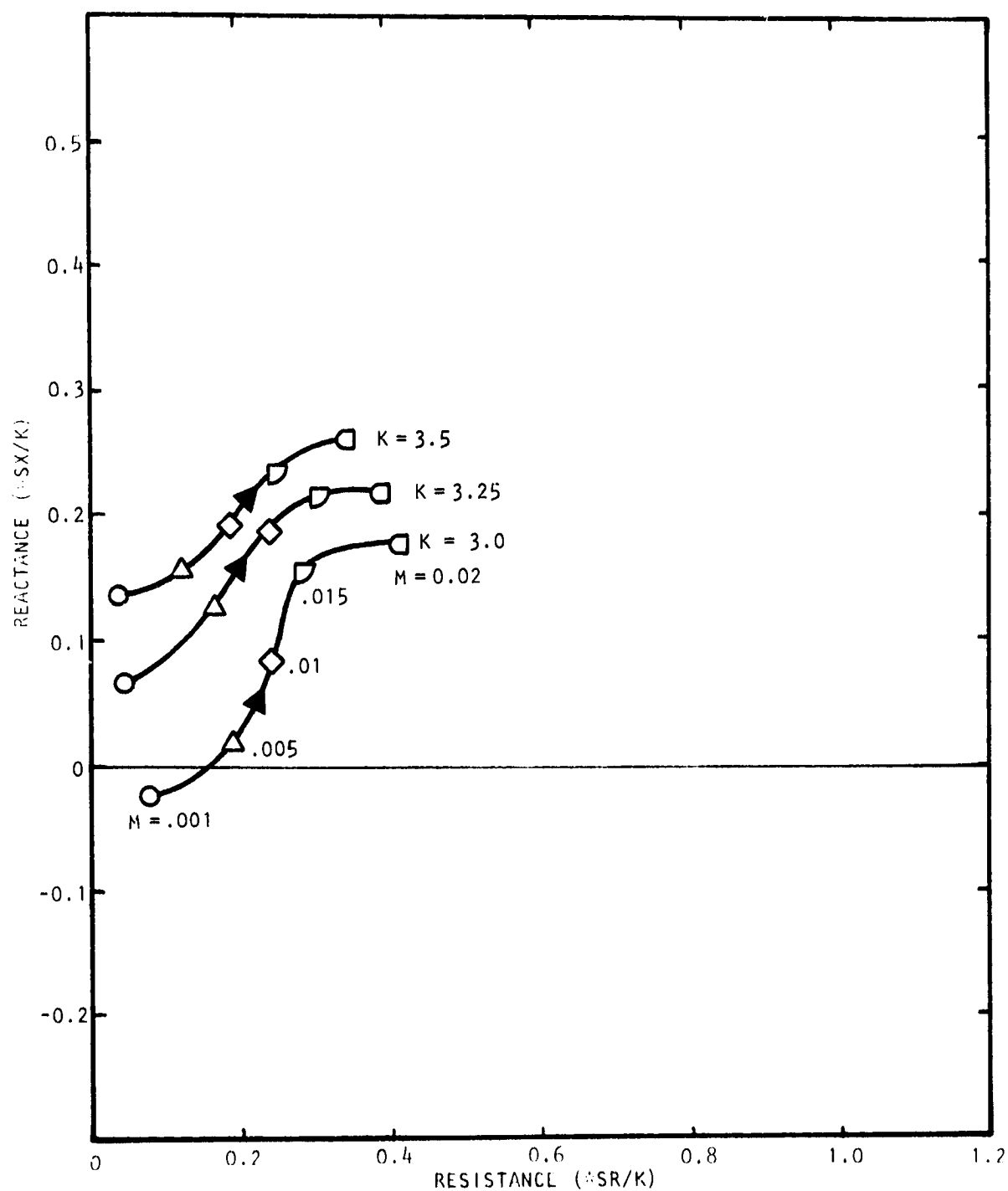


Figure 23 Effect of Bias Flow on Impedance of Multi-Cavity Liner with Porosities $\sigma_1 = 10\%$, $\sigma_2 = 20\%$, and Cavity Depths $d_1 = 3.81$ cms. (1.5 in.) and $d_2 = 3.81$ cms. (1.5 in.)

Within each generalized region, the bias flow characteristic for a fixed value of K can be widely varied by means of porosity and cavity depth changes. For example, consider Figures 17, 24, and 25. The difference between each case is simply that of porosity ratios between the intermediate and facing layer. From Figure 17 to 24 the ratio has changed from 0.5 to 1.0, and while the resistive part of the bias flow characteristic is essentially the same, the reactive changes have decreased by one third (note the scale factor change between plots). This is a direct effect of the more weakly decoupling behavior of the rear cavity. Conversely, compare Figures 17 and 25 (in the latter case the porosity ratio has been reduced to 0.25 by increasing the facing layer porosity); the reactive changes due to bias flow are almost identical to Figure 17, but the increasing resistance characteristic has been suppressed until it is virtually constant over a large range of bias flows. For similar comparisons at other frequencies, reference can be made to the bias flow characteristic plots given in Appendix D.

If the layer porosities are held constant and only the cavity depths permitted to change, the comparative situation can again be deduced from the plots given in Appendix D. In all cases the *total* cavity depth remains constant; only the relative cavity depths are changed. To consider a specific example, decreasing the rear cavity depth by half for $K=1.0$ (Figure 26) results in a slightly reduced overall resistance compared with Figure 17, but the reactance is reduced by about half at the maximum bias flow value. This is to be expected, as in the fully decoupled condition of the rear cavity, the liner overall reactance is a function of the facing cavity depth alone. Conversely again, if the facing layer cavity depth is reduced by half (as in Figure 27), at high bias flows much larger negative reactances will result, although with larger resistances when compared with Figure 17.

Similar effects can be observed by making similar comparisons at other frequencies (the plots are given by Appendix D). Thus, it is obvious that virtually any desired bias flow characteristic can be produced on the impedance plane, with the basic problem being the complex interaction of the three basic liner parameters: frequency, porosity, and cavity depth. A complication not explicitly discussed, but implicitly included in porosity effects, is comprised of the parameters of hole diameters and hole spacing.

Also presented in Appendix D are examples of the effect of grazing flow at two representative Mach numbers (0.25 and 0.5). This effect is characterized by a bodily shift of the bias flow characteristic to the right (the positive resistance direction) in the impedance plane. For example, at $K=1.0$, this effect is shown in Figures 17, 28, and 29, corresponding to grazing-flow Mach numbers of 0.0, 0.25, and 0.5, respectively. It must be remembered that this factor in the model is entirely empirical and may be severely modified, depending on the actual duct shear profiles encountered. Thus, the real-life effects on the bias flow characteristic may be quite different, and any predicted values should be used with caution, particularly at low values of bias flow.

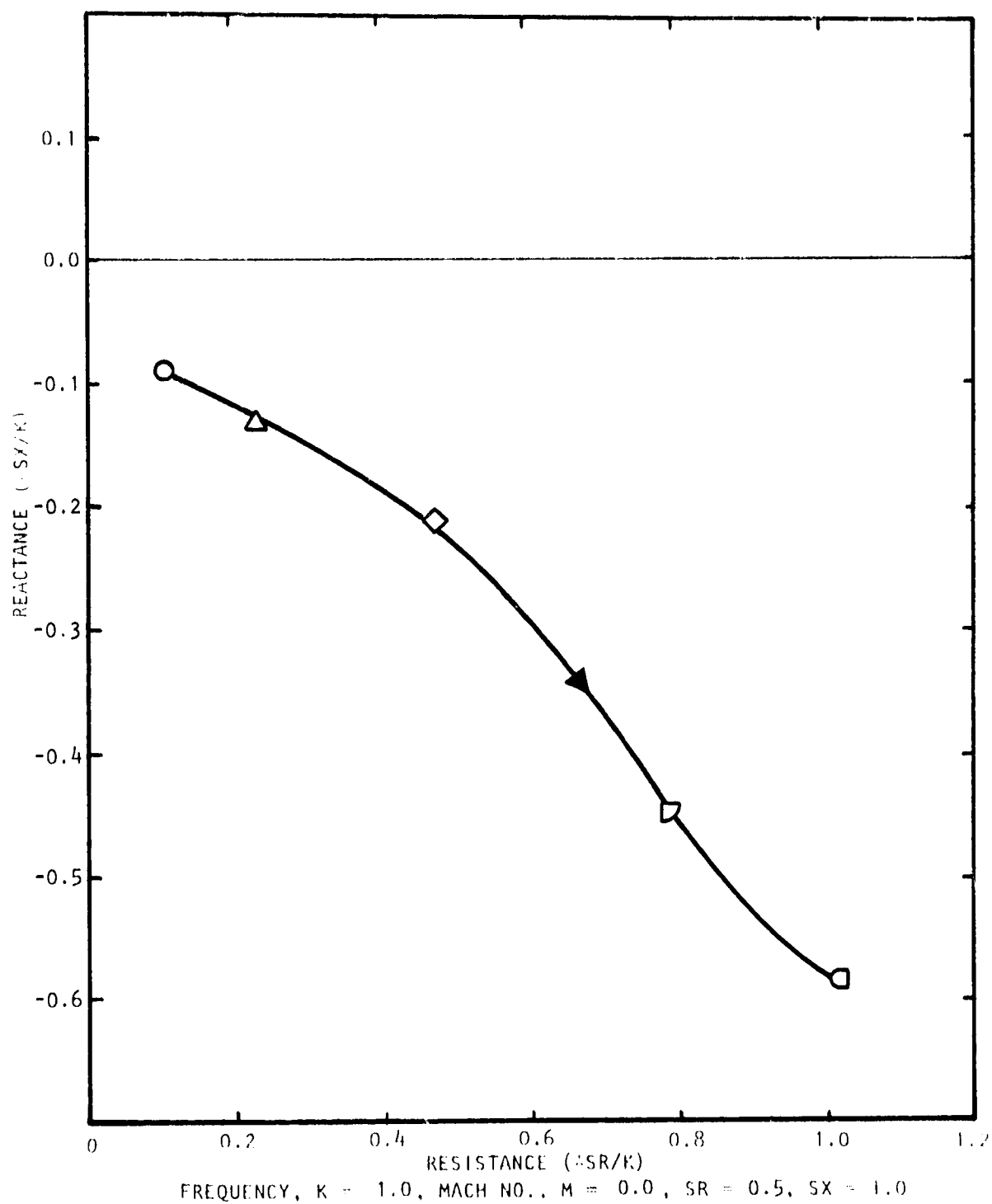
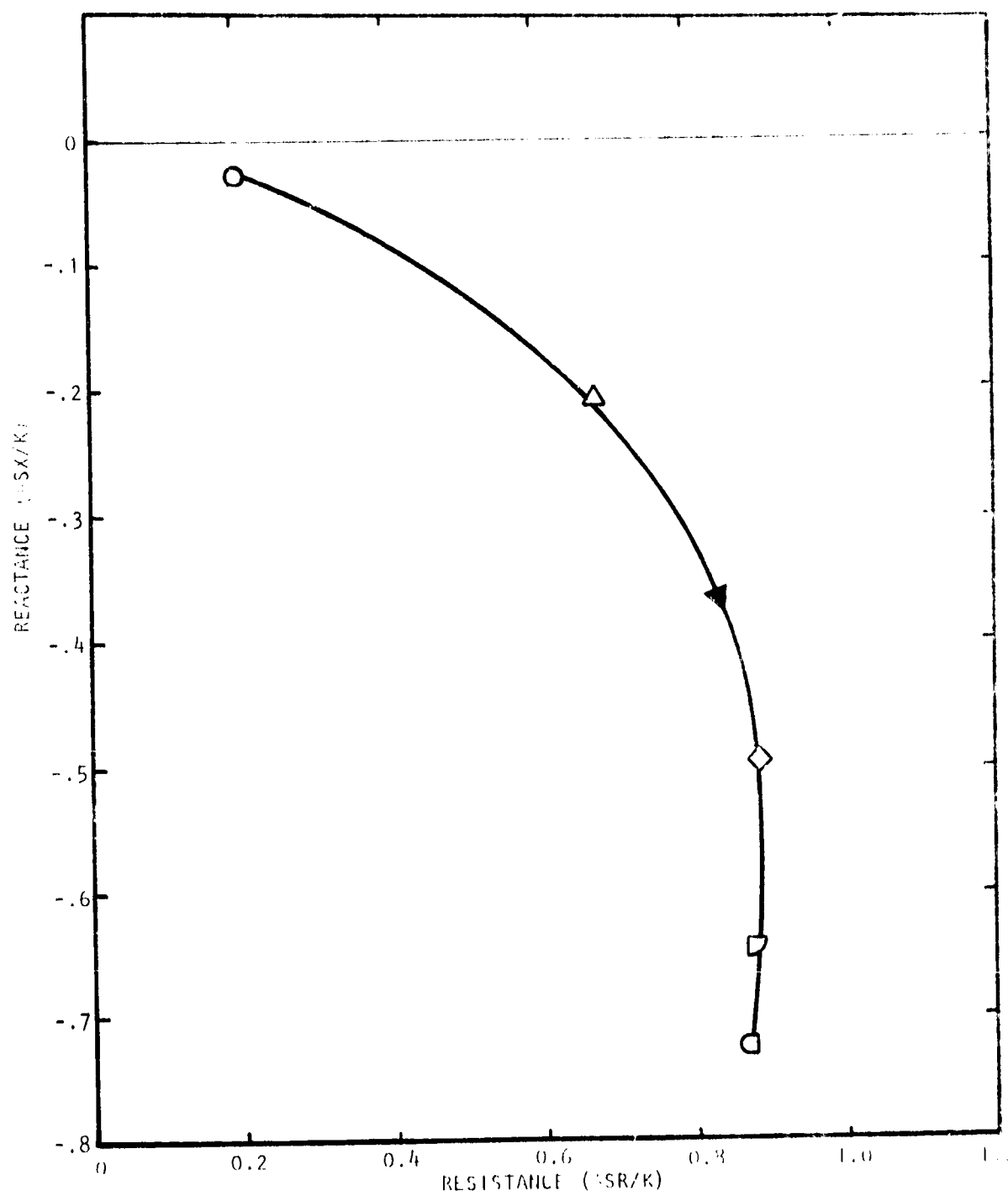
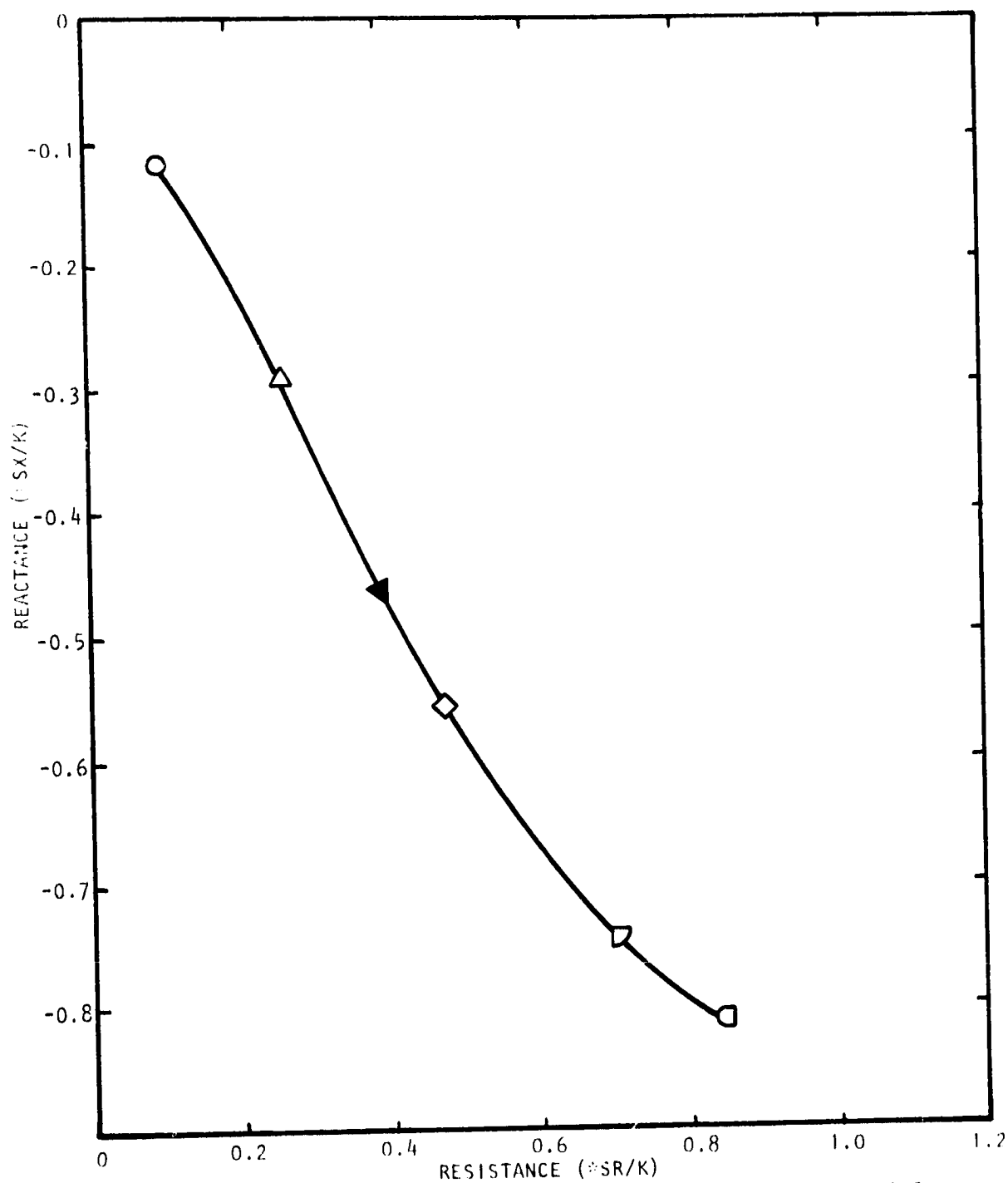


Figure 24 Effect of Bias Flow on Impedance of Multi-cavity Liner with Porosities $\sigma_1 = 20\%$, $\sigma_2 = 20\%$, and Cavity Depths $d_1 = 3.81$ cms. (1.5 in.) and $d_2 = 3.81$ cms (1.5 in.)



FREQUENCY, $K = 1.0$, MACH NO., $M = 0.0$, $SR = 1.0$, $5X = 0.5$

Figure 25 Effect of Bias Flow on Impedance of Multi-cavity Liner with Porosities $\sigma_1 = 10\%$, $\sigma_2 = 40\%$, and Cavity Depths $d_1 = 3.81$ cms. (1.5 in.) and $d_2 = 3.81$ cms. (1.5 in.)



FREQUENCY, $K = 1.0$, MACH NO., $M = 0.0$, $SR = 0.5$, $SX = 1.0$

Figure 26 Effect of Bias Flow on Impedance of Multi-cavity Liner with Porosities $\alpha_1 = 10\%$, $\alpha_2 = 20\%$, and Cavity Depths $d_1 = 1.91$ cms. (0.75 in.) and $d_2 = 5.72$ cms. (2.25 in.)

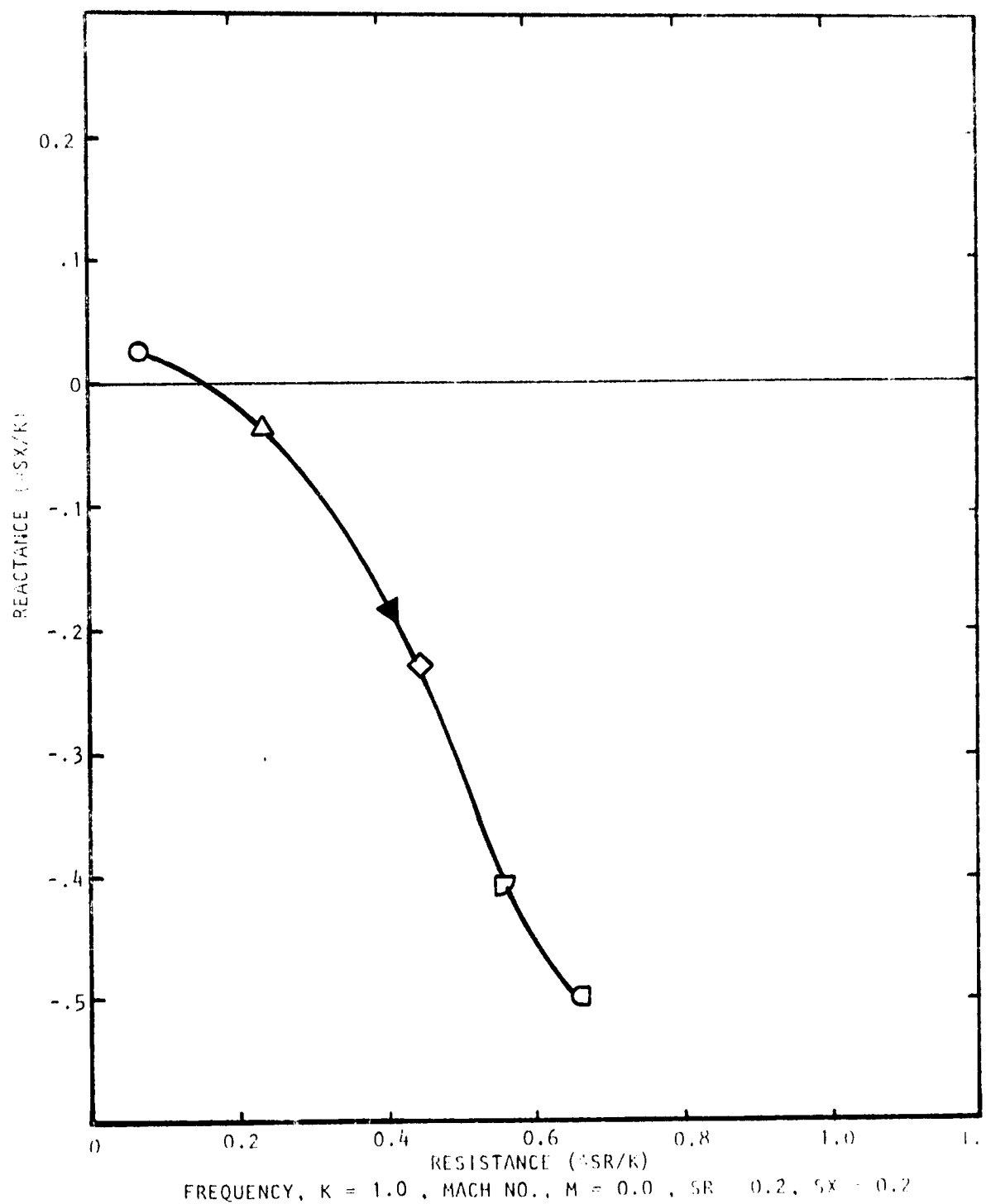
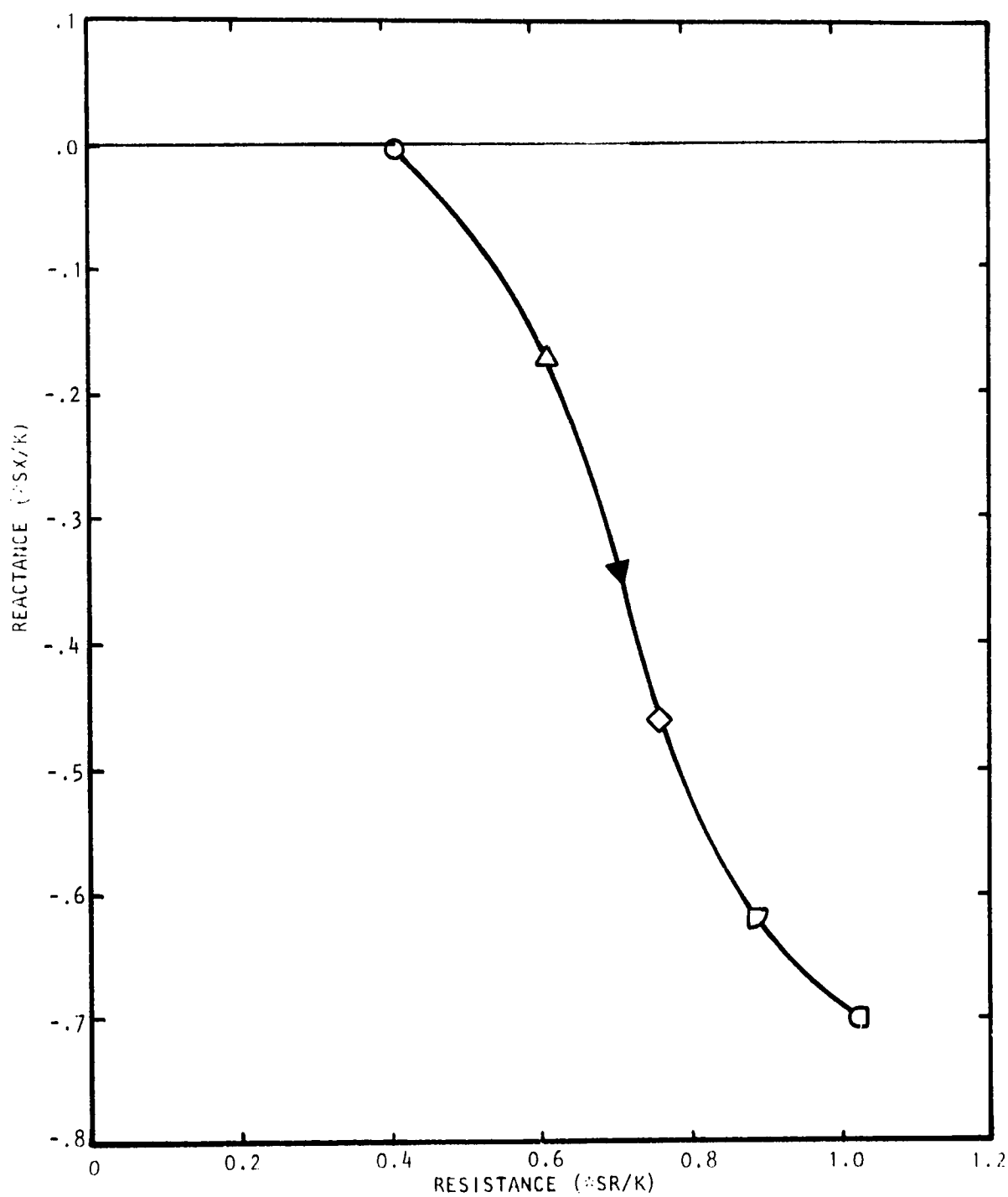
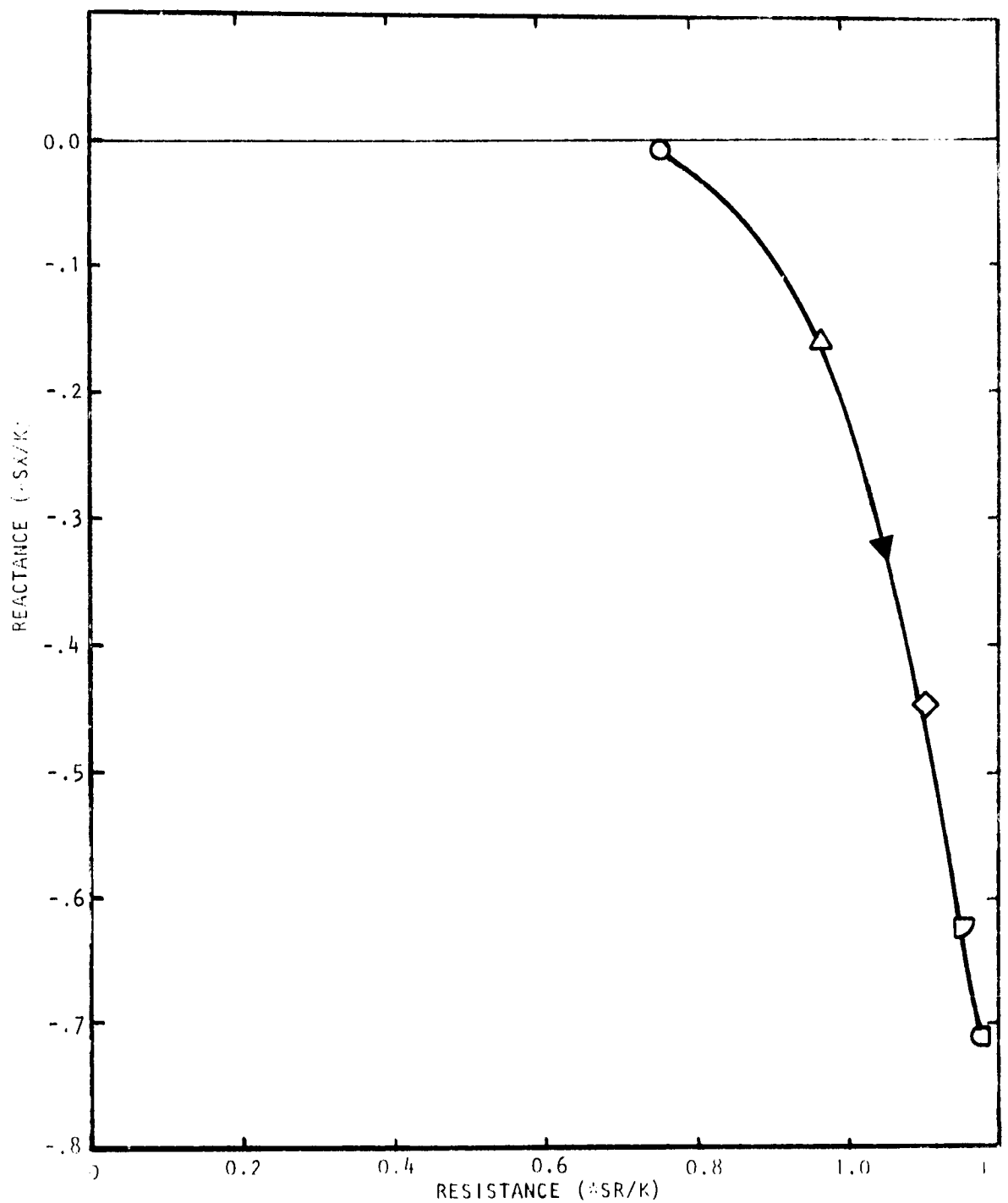


Figure 27 Effect of Bias Flow on Impedance of Multi-cavity Liner with Porosities $\sigma_1 = 10\%$, $\sigma_2 = 20\%$, and Cavity Depths $d_1 = 5.72$ cm. (2.25 in.) and $d_2 = 1.91$ cm. (0.75 in.)



FREQUENCY, $K = 1.0$, MACH NO., $M = .25$, $SR = 0.5$, $SX = 0.5$
 Figure 28 Effect of Bias Flow on Impedance of Multi-Cavity Liner with
 Porosities $\alpha_1 = 10\%$, $\alpha_2 = 20\%$, and Cavity Depths $d_1 = 3.81$ cms.
 (1.5 in.) and $d_2 = 3.81$ cms. (1.5 in.)



FREQUENCY, $K = 1.0$, MACH NO., $M = 0.5$, $SR = 0.5$, $SX = 0.5$

Figure 29 Effect of Bias Flow on Impedance of Multi-Cavity Liner with Porosities $\sigma_1 = 10\%$, $\sigma_2 = 20\%$, and Cavity Depths $d_1 = 3.81$ cms. (1.5 in.) and $d_2 = 3.81$ cms. (1.5 in.)

4. EXPERIMENTAL STUDY

4.1 Verification of Bias Flow Impedance Model

4.1.1 Introduction

The purpose of these tests was to verify the predicted effects of bias flow on the multi-layer system impedance by means of impedance measurements in a normal incidence standing-wave tube. In this configuration, all the parametric effects previously discussed can be studied in detail except those of grazing flow and nonlinear sound pressure levels.

The term "nonlinear sound pressure level" is perhaps misleading in that the nonlinearity effect is really a direct function of the acoustic velocity [see Melling (ref. 12)]. This is related to the SPL only by the specific acoustic impedance (ρc for a free-traveling wave). The study of this effect in a standing wave tube thus requires high acoustic velocities on the sample face. In the single-cavity situation, this condition is most easily achieved at a frequency such that resonance exists (i.e. the cavity depth is a quarter wavelength). At other frequencies, the standing wave structure is such that, for the *same* incident SPL, the acoustic velocities at the sample face will be lower, and it may be impossible to drive the source hard enough to maintain the necessary high acoustic velocities.

The situation becomes even more complex with a double-layer liner sample, as nonlinear acoustic velocities will not occur at the same time on both the surface and intermediate layers due to the complex wave structure within the sample. Thus, it is not practical or feasible to consider this effect within the bounds of the overall scope of this program.

4.1.2 Apparatus

The basic normal incidence impedance tube (or standing-wave tube) and signal processing system schematic diagram is presented in Figure 30. It is 7.62 cms (3 inches) square, and the duct standing wave is measured by means of an axially traversing microphone in the duct, recording via an X-Y plotter the necessary sound maxima and minima and their relative positions for use in the standard impedance formula. The less well-known in-situ impedance measurement technique uses a probe microphone which traverses from the rear to the front face of the liner system, recording the sound pressure and relative phase at various key points.

The bias air supply was derived from 100-psi filtered shop air fed via a manifold system to the rear cavity. As initial problems were experienced with excessive valve flow losses and noise, subsequent modifications were made to reduce the flow losses and the valve noise by means of a combination muffler and manifold system as shown in Figure 31. A Venturi meter measured the mean bias flow at a point near the tube source section (see Figure 32) such that the standing wave in the vicinity of the sample remained undisturbed. Since the mean flow in the tube never exceeded a Mach number of 0.025, any

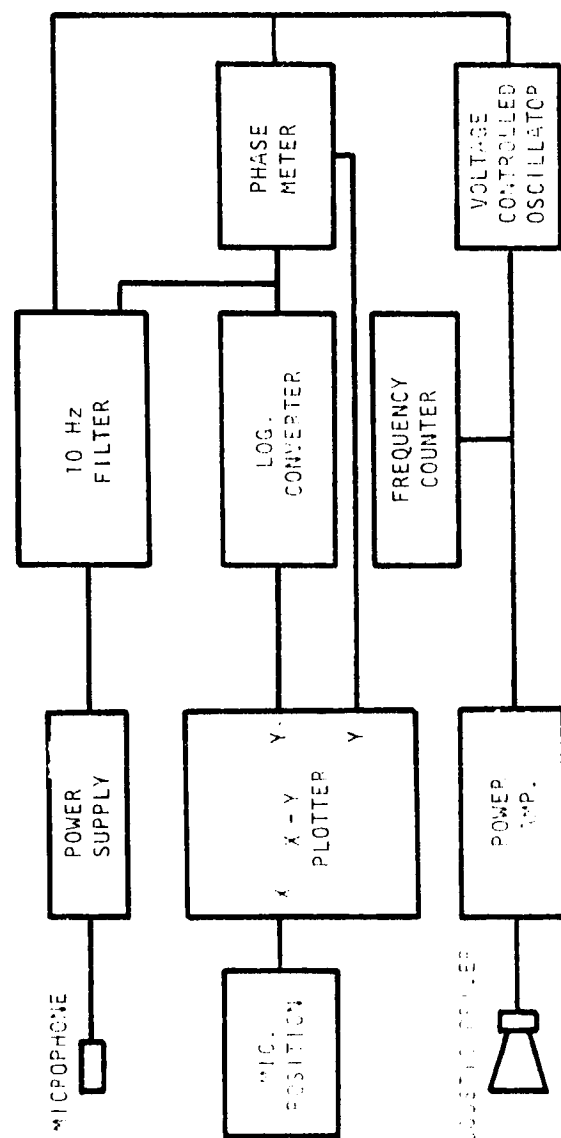
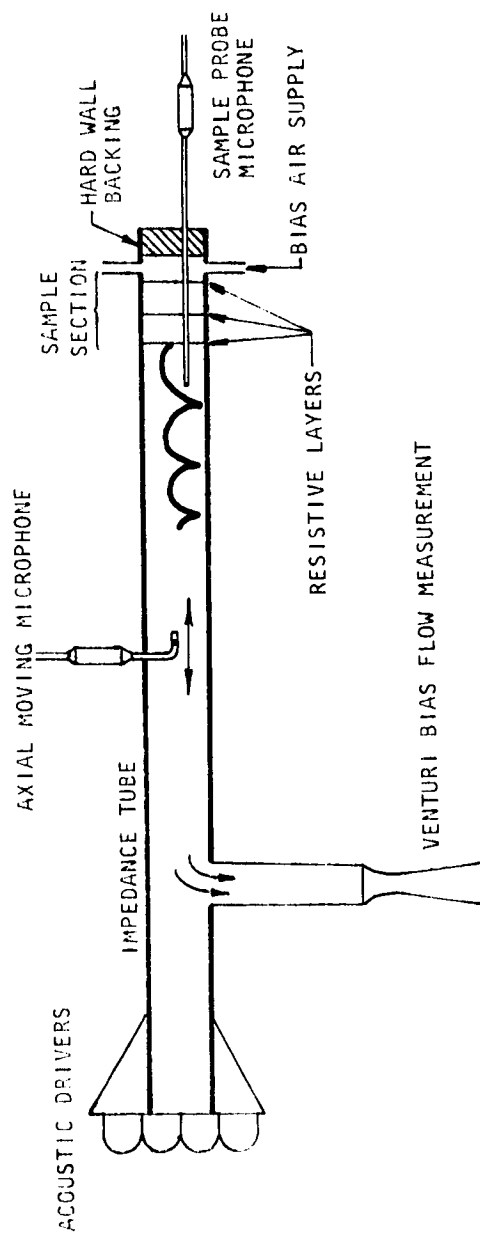


Fig. 1. Schematic diagram of the experimental setup for measuring bias flow through resistive layers.

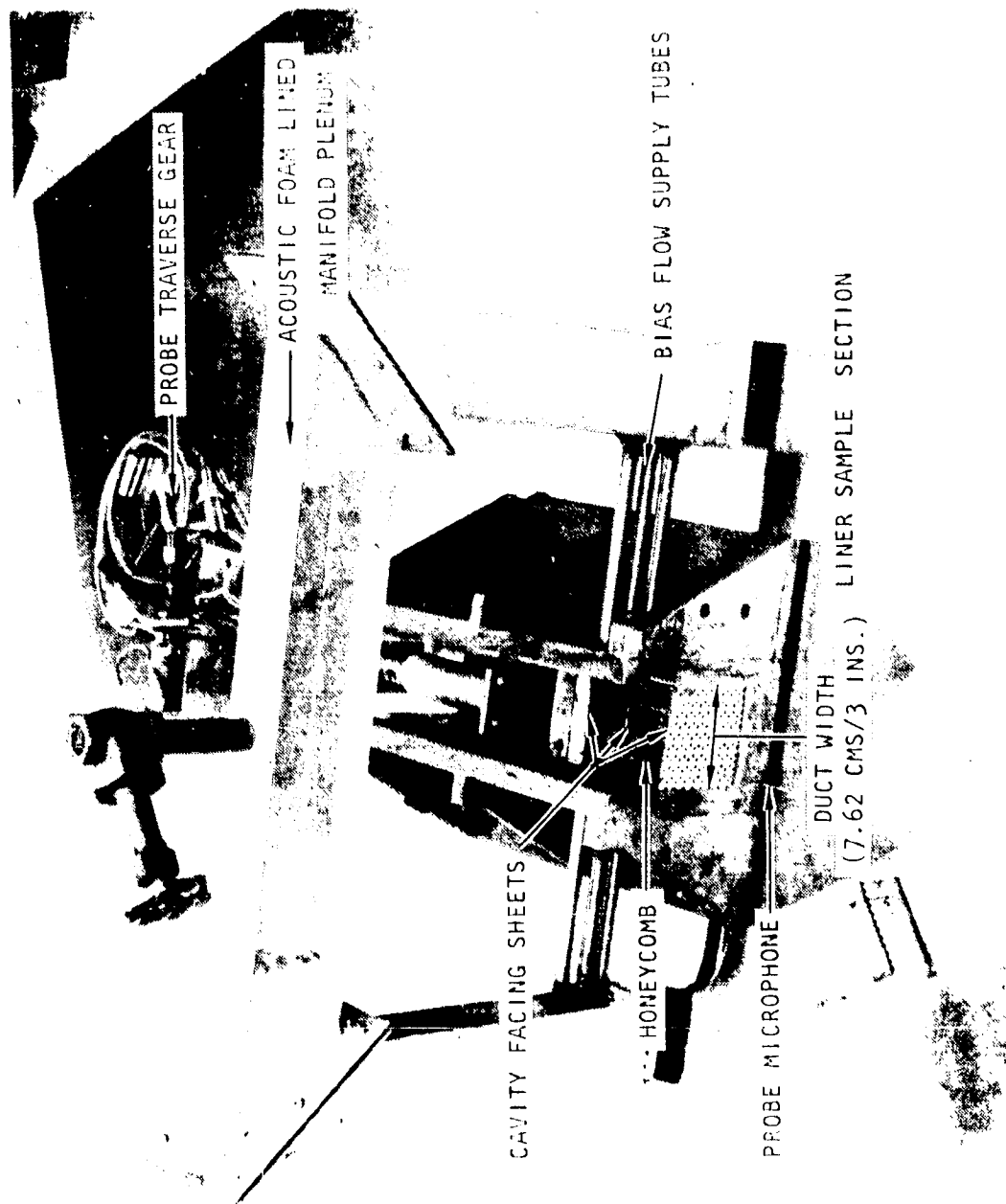


Figure 31(a) Normal Incidence Impedance Tube Sample Holder and
Bias Flow Manifold System

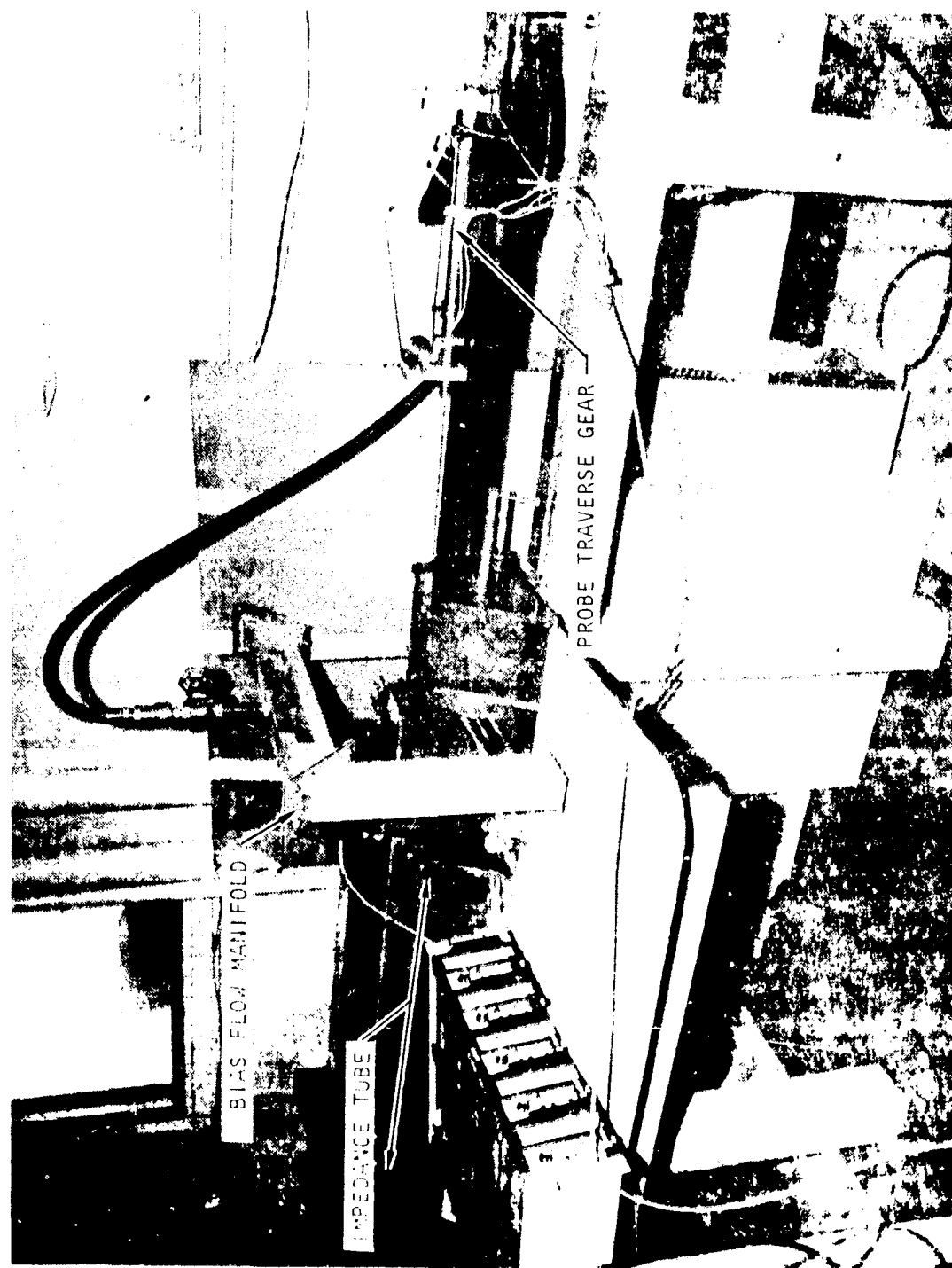


Figure 31(b) Liner Sample Holder Mounted on Rear of Impedance Tube

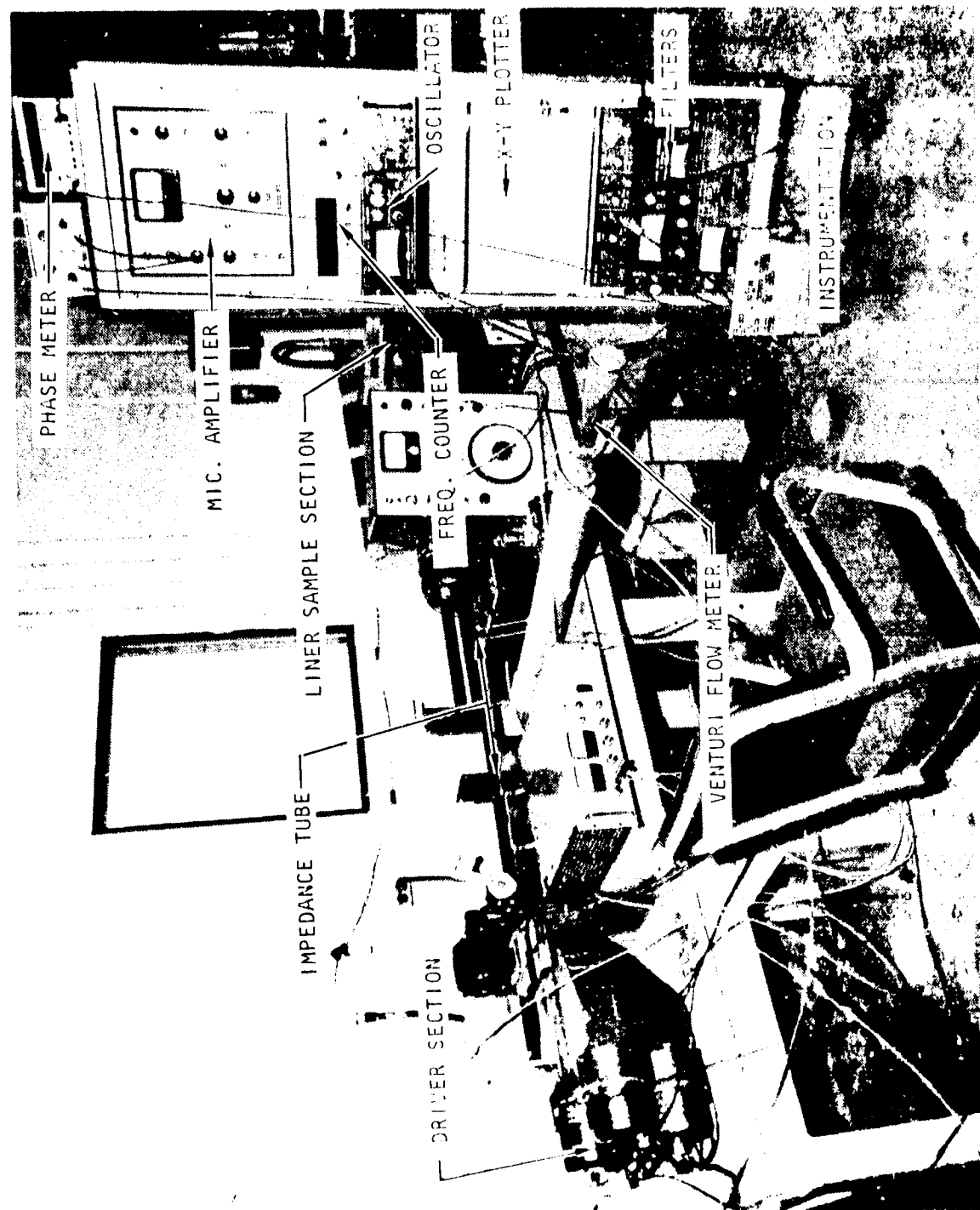


Figure 32 Overall View of Normal Incidence Impedance Tube and Analysis Instrumentation

convective corrections to the standing-wave tube theory were considered negligible.

The axially traversing microphone is mounted on an axially moving bar which constitutes the top of the duct. A 1/2-inch B&K microphone was used, with a probe microphone adapter, the probe sensing ports being on the duct centerline to extend the frequency range of the tube by cancellation of the first higher-order mode. The probe tip and sensing ports were patterned after a static pressure probe tube to minimize the turbulent effects of the bias flow over the probe tip. The microphone used to probe through the liner was also a 1/2-inch B&K coupled to a probe tube about 40 cms in length. The sensing holes were 15 cms from the closed tip, which incorporated a small length of acoustic foam to partially damp out the natural resonances of the probe tube system. The length of probe tube in front of the measurement holes was necessary so that the facing sheet porosity would not be affected by the presence of the probe, as would occur with an open-end tube. The probe tube was capable of approximately 20 cms of movement with appropriate position transducers and signal conditioning to match the X-Y plotter inputs. The probe traversing system is shown in Figure 33.

4.1.3 Impedance Analysis Methods

The standing-wave tube method has been a viable technique for determining acoustic impedance for over 45 years. Basically, it requires the measurement of the standing-wave ratio and the distance of the first minimum pressure point from the face of the sample, from which the complex impedance can be calculated. For convenient reference, the formula for calculating resistance (R) and reactance (X) are given in Appendix E.

The in-situ (or "two-microphone") impedance measurement technique is relatively new [see Dean (ref. 9)], especially in its current adaptation. It relies on the one-dimensionality of the acoustic wave motion inside the acoustic material. For the typical multi-layer construction involving use of honeycomb core material, this requirement is met up to very high frequencies. In fact, this method has one big advantage over the standing wave technique. Above the first duct mode cut-on frequency, the wave structure in the impedance tube consists of the superposition of multiple modes of propagation, each having a characteristic standing-wave pattern axially and transversely within the duct. Consequently, the pressure field measured by the probe microphone loses its regular classical one-dimensional standing wave pattern, due to the interference of the various modes. It thus becomes impossible to determine the sample impedance with the simple standing-wave formulae. However, since the construction of the liner ensures local reactivity (by means of honeycomb cavity dividers) to a much higher frequency, the sound field within the liner is essentially one-dimensional. Thus, the measurement of impedance can be made at much higher frequencies than with the standing-wave tube method. It is sensitive only to local pressure levels at the surface rather than the acoustic mode field incident on the liner sample.

With this method, as described in Appendix F, referring to the configuration shown in Figure 34, it is necessary to measure the sound pressure and

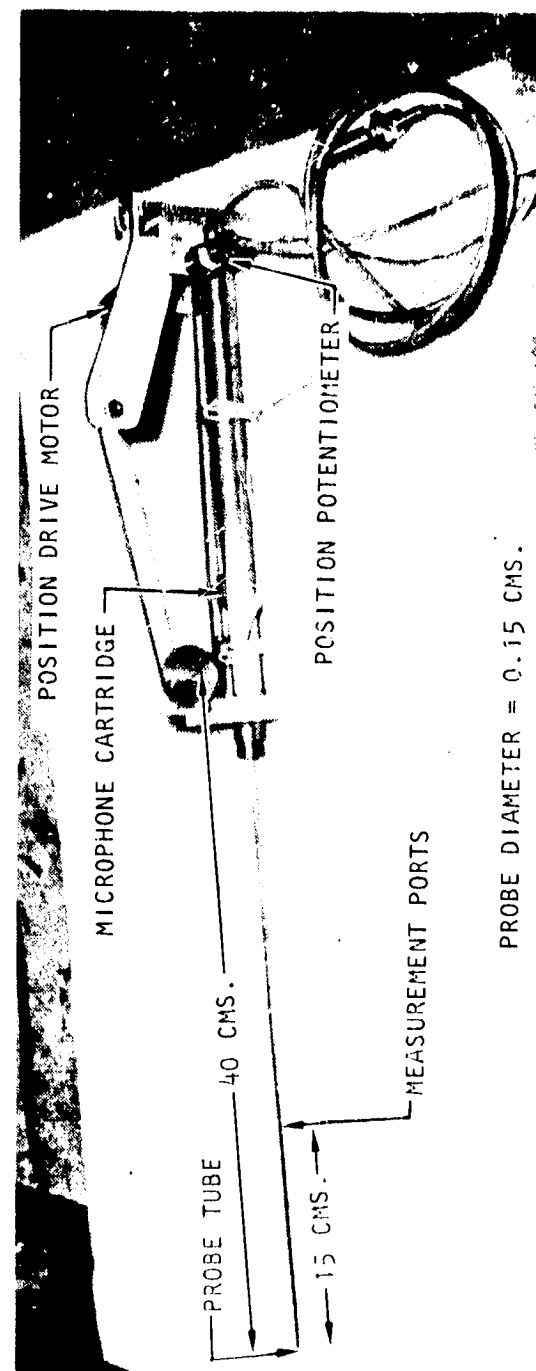


Figure 33 Probe Microphone and Associated Traverse Gear for In-Situ Impedance Measurements

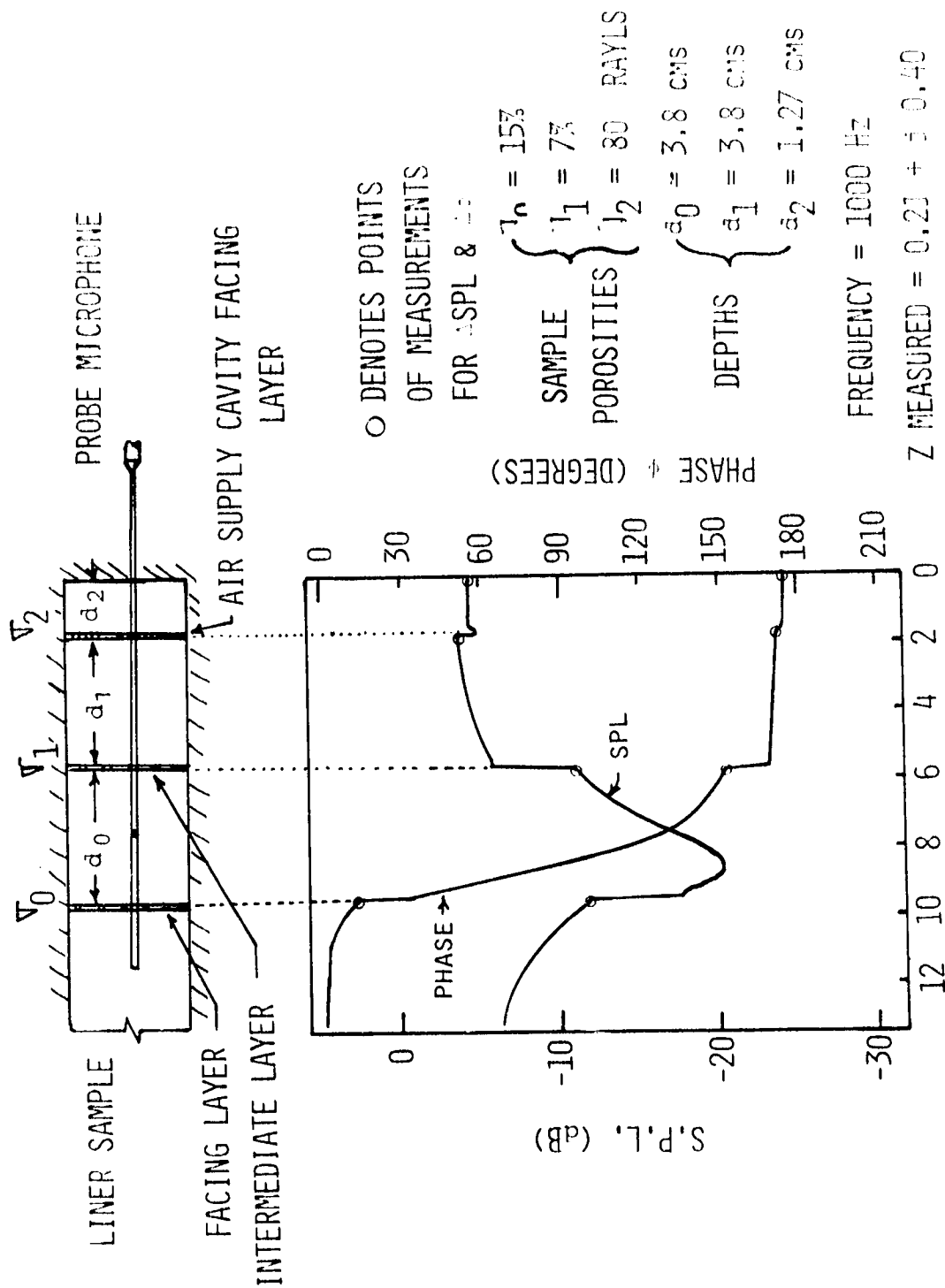


Figure 34 Example of "4 Microphone" Impedance Measurement Technique

phase (relative to the oscillator for convenience) at the front of each resistive layer and at the back wall. For the case of the single-layer cavity, two measurement points are required, thus resulting in the label "two-microphone" impedance method. However, as stated before and illustrated in Figure 34, the current adaptation provides a continuous SPL and phase distribution from front to back of the multi-layer system. With this plot, SPL and phase differences can be determined for application in the formulae of Appendix F.

4.1.4 Results of Tests

Comprehensive tests were conducted on five configurations in the normal incidence impedance tube. The first three were single layers, while the last two were of double-layer construction. It should be remembered that a "single" layer liner actually consists of two layers, the air supply cavity being the second layer. Similarly with the double-layer liners, these actually consist of three layers. Since the air supply cavity and its facing sheet are invariant for all the tests, the terms "single" and "double" are used as descriptors of the variable components of the liner.

Figures 35, 36, and 37 show the comparison between measured (by the standard impedance tube method) and calculated values of impedance for the three single-layer configurations: 17% and 7% porosity facing on an 80 rayl (nominal) fiber metal, all on a single cavity of 7.62 cms (3 inches) depth. These tests were conducted at four bias flow velocities.

It would be intuitively expected that the bias flow effects would be purely resistive in character, except perhaps near resonance. This is confirmed by measurements and analytical model evaluations. The comparison between test and prediction for both bias flow and frequency behavior is particularly close in Region I (defined in Section 3). The model tends to slightly overestimate the reactance magnitude at low frequencies, below the first resonance point. In both perforate configurations, the model tends to accentuate the resistive components such that the measured results are consistently lower. This may be due to inadequate sample edge sealing allowing some leakage of the bias air flow. Edge seals were improved in the double-layer tests, but the fact that the top of the test duct (a bar with the axial microphone incorporated in it as shown in Figure 31b) must move over the top of the sample liner, means that the top edge cannot be perfectly sealed.

Since the first cut-on frequency of the first higher order cross mode in the duct is about 2.2 KHz, the "three-microphone" method of impedance measurement was used at all frequencies higher than 2 KHz.

The impedance of fiber-metal sample (shown in Figure 37) could not be compared with the perforate-based model results; thus its predicted resistive behavior was based on its measured D.C. flow resistance, using a flow bench. Therefore, the close impedance comparison, particularly that of the resistive part, is to be expected.

The most critical test comparison, however, is that of the double-layer liner samples. Because of the importance of these validation tests, both the

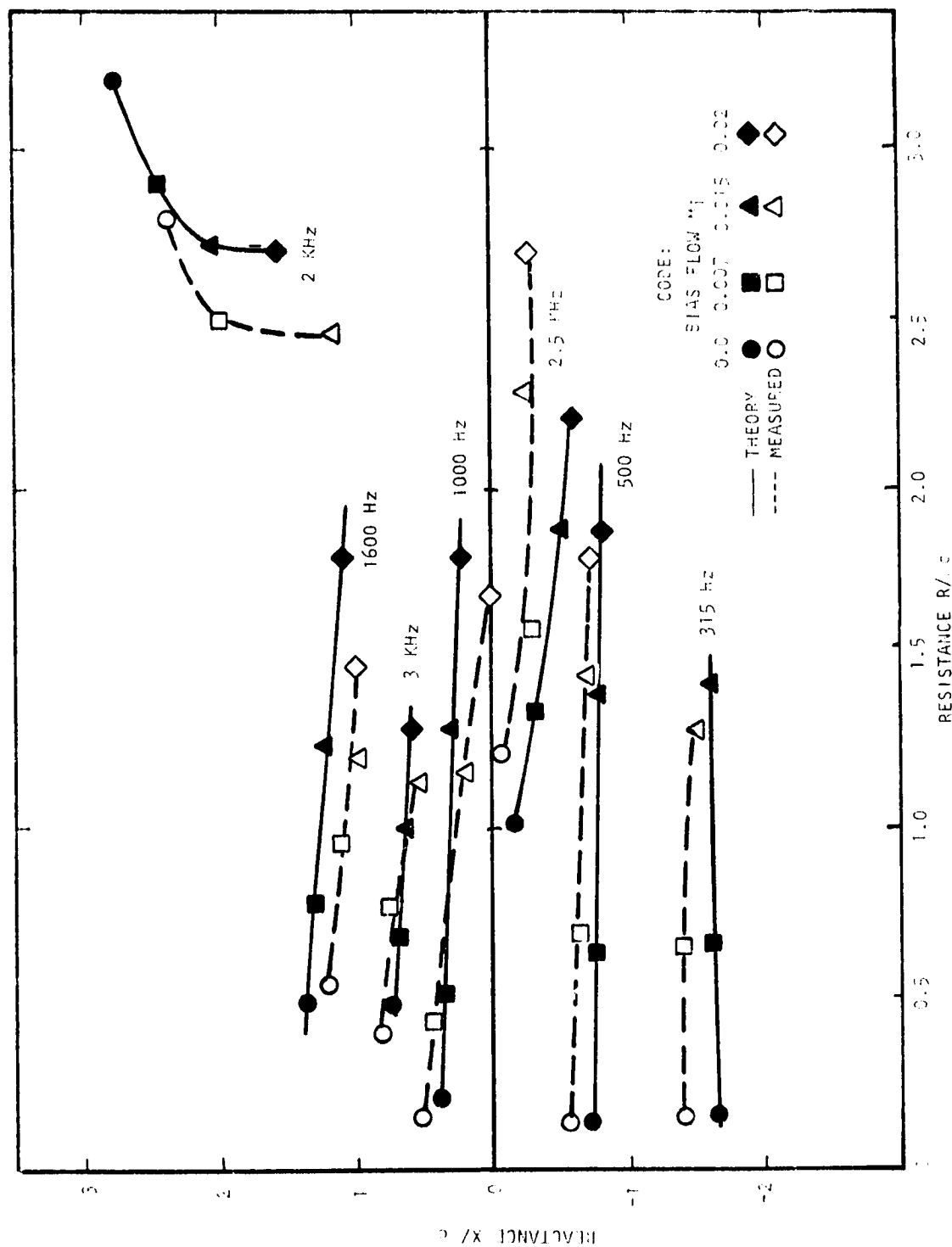


Figure 35 Comparison of Measured and Calculated Low Loss Coefficients for 100 Hz Bias Flow

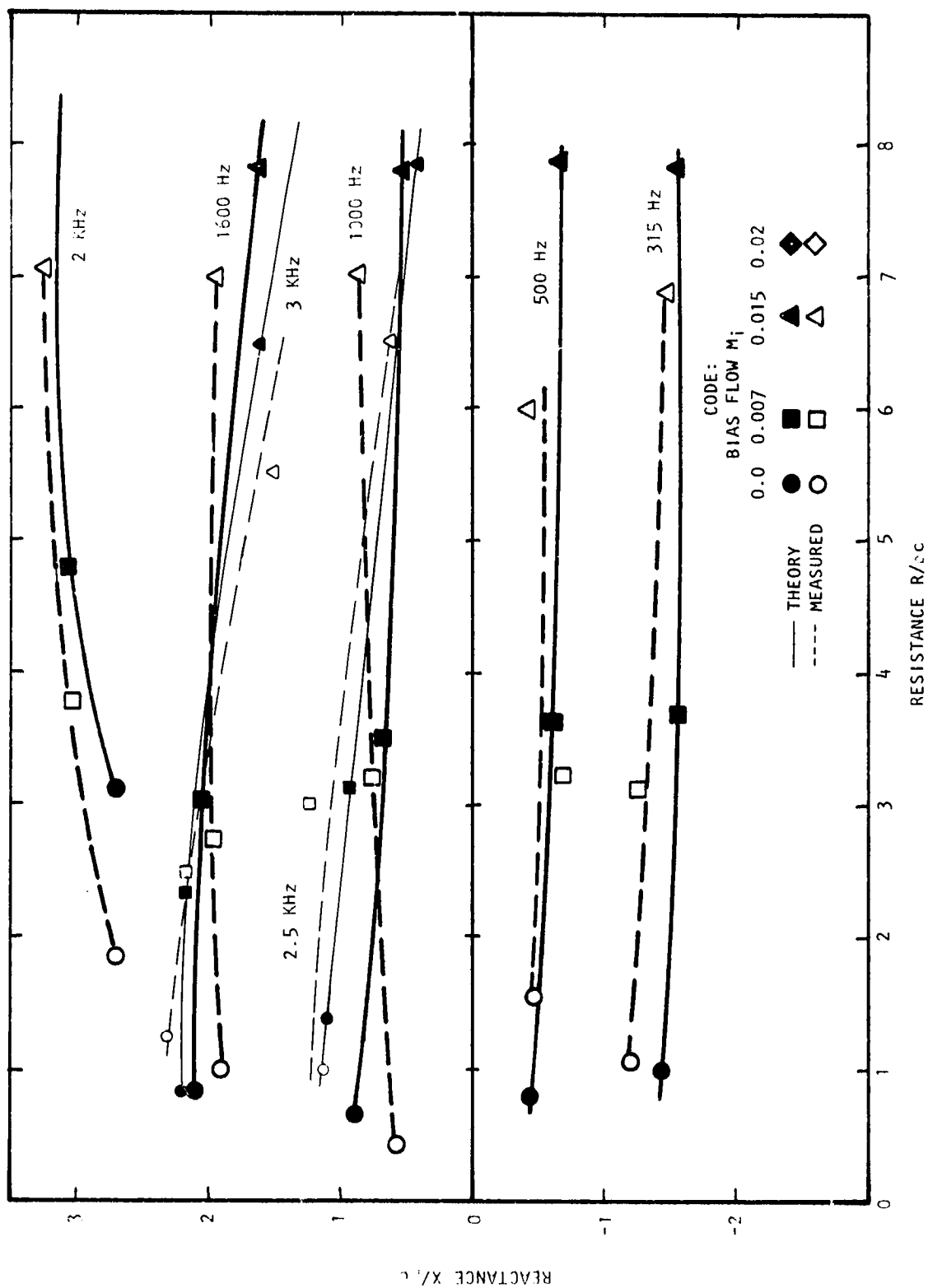


Figure 36 Comparison of Measured and Calculated Impedances for 7 Porosity Facing on 7.62 Cms. (3 in.) Cavity

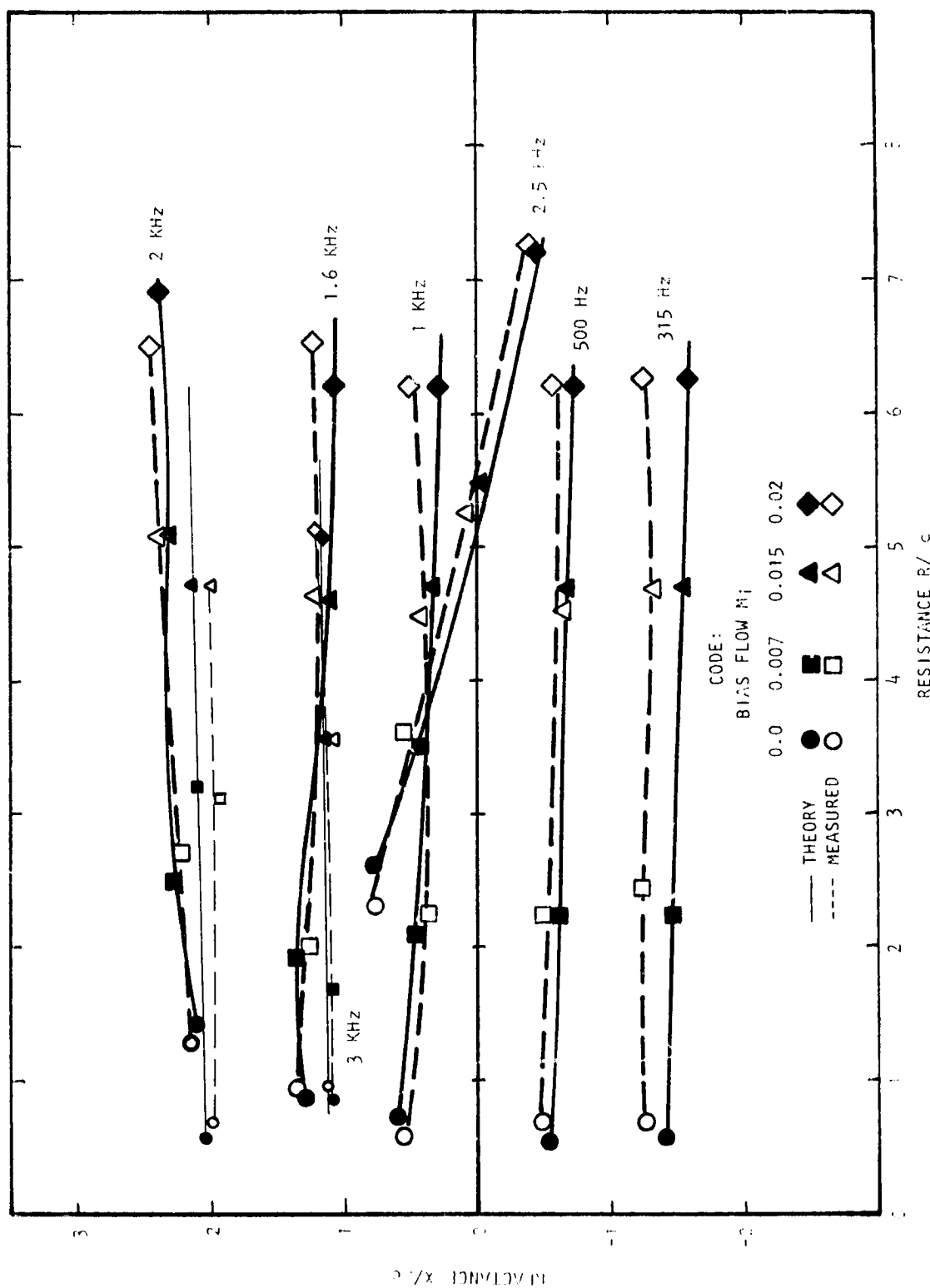


Figure 37 Comparison of Measured and Calculated Impedances for 30 R:1 Fiber Metal Facing on 7.62 C/s (3 in.) Cavity

standing-wave tube method and the "four-microphone" method of impedance evaluation were used throughout the frequency range of test (from 315 Hz to 3 KHz). In both test samples, the cavity depths of each layer were equal (for convenience) at 3.81 cms (1.5 inches) each. The first double-layer sample consisted of a facing layer of 22% porosity and an intermediate layer of 17% porosity. Figure 38 shows the comparison between measured and calculated impedances for this liner sample. Over the test frequency range from 315 Hz to 3 KHz with bias flows up to $M=0.02$, the agreement is excellent up to about 1250 Hz (Figure 38a). As the frequency is further increased to 1600 Hz, the bias flow characteristic is in Region II, near the second resonance point of the liner, where large changes on the impedance plane result from small frequency changes. In this region, the model begins to diverge from the experimental data for reasons which appear to be linked to the second resonance. The most likely cause of the deviation is local nonlinear dissipation. When the frequency moves up to 2 KHz (Figure 38b), the bias flow characteristic is now in Region III, and agreement improves significantly. There seems to be no general pattern of deviations between either of the measurement techniques and those predicted by the model. Some experimental scatter is evident, a particular problem being the high flow noise interference in the four-microphone technique at the highest bias flows tested ($M=0.02$). Figure 39 shows the comparison between measurements and the model for the second double-layer liner sample. The facing sheet porosity was 15% and the intermediate layer 7%, again with equal cavity depths of 3.81 cms (1.5 inches). Agreement again is very good, with the exceptions being once again in Region II (around the second resonance frequency point). There is a particularly large deviation between experiment and theory for the zero bias flow point at 1250 Hz in Figure 39; however, if the bias flow is increased to a Mach number of 0.007 (about 250 cms per second), the fit improves considerably. In Figure 40, sound pressure and phase traverses are given which correspond to frequencies near the second resonance point, and the behavioral clue seems to be pronounced pressure minima and, therefore, velocity maxima at the exact location of the intermediate layer. The deviation could be the result of SPL nonlinearities as a result of this velocity maximum at the intermediate facing layer. A similar error pattern occurs at 1600 Hz, except that the model now tends to underestimate the impedance rather than overestimate it. Higher frequency test points in Region III show satisfactory agreement once more, with close correlations between both measurement techniques and the impedance model.

The conclusion which can be drawn from these comparative tests is that the model will provide a satisfactory means of evaluating the impedance characteristics of a liner with changes in bias flow, with the proviso that estimations at frequency regions near the second resonance point should be treated with extreme caution. Fortunately, in most typical situations, this area of rapidly changing bias flow characteristics with frequency is usually less than several hundred Hertz wide, and consequently only a small percentage of the total frequency range to be considered.

It is interesting to note the ease with which virtually total decoupling of the second cavity occurs in Region II. For example, at both 1250 Hz and 1600 Hz in Figure 39, only a bias flow of Mach 0.007 is necessary to cause a massive shift of reactance to the single cavity value, after which any

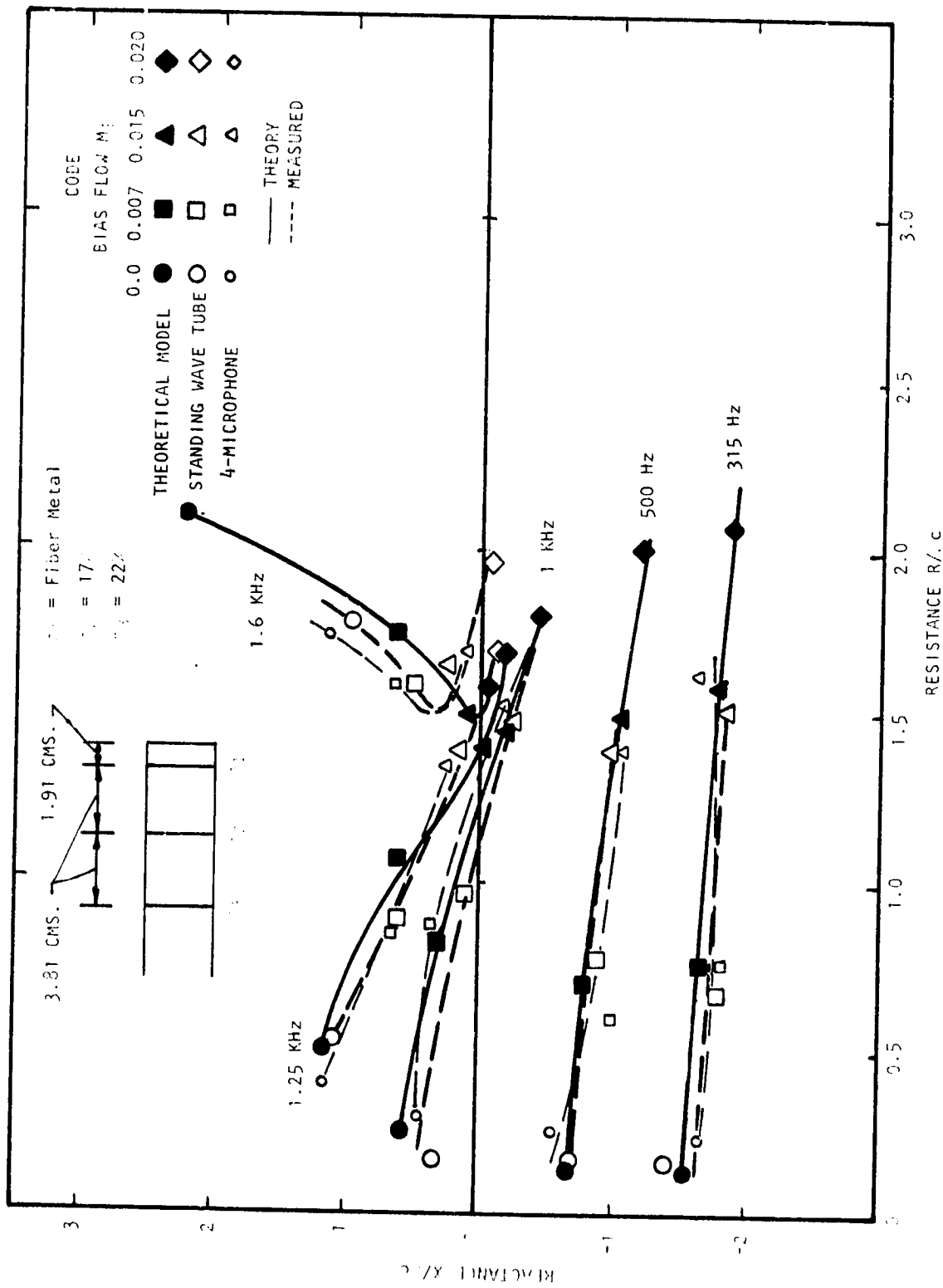


Figure 38 (a) Comparison of Measured and Calculated Impedances for Double Layer Sample: Facing Sheet Porosity 22, Intermediate Sheet 17, with Equal Cavity Depths of 3.81 CMS. 1.5 in.

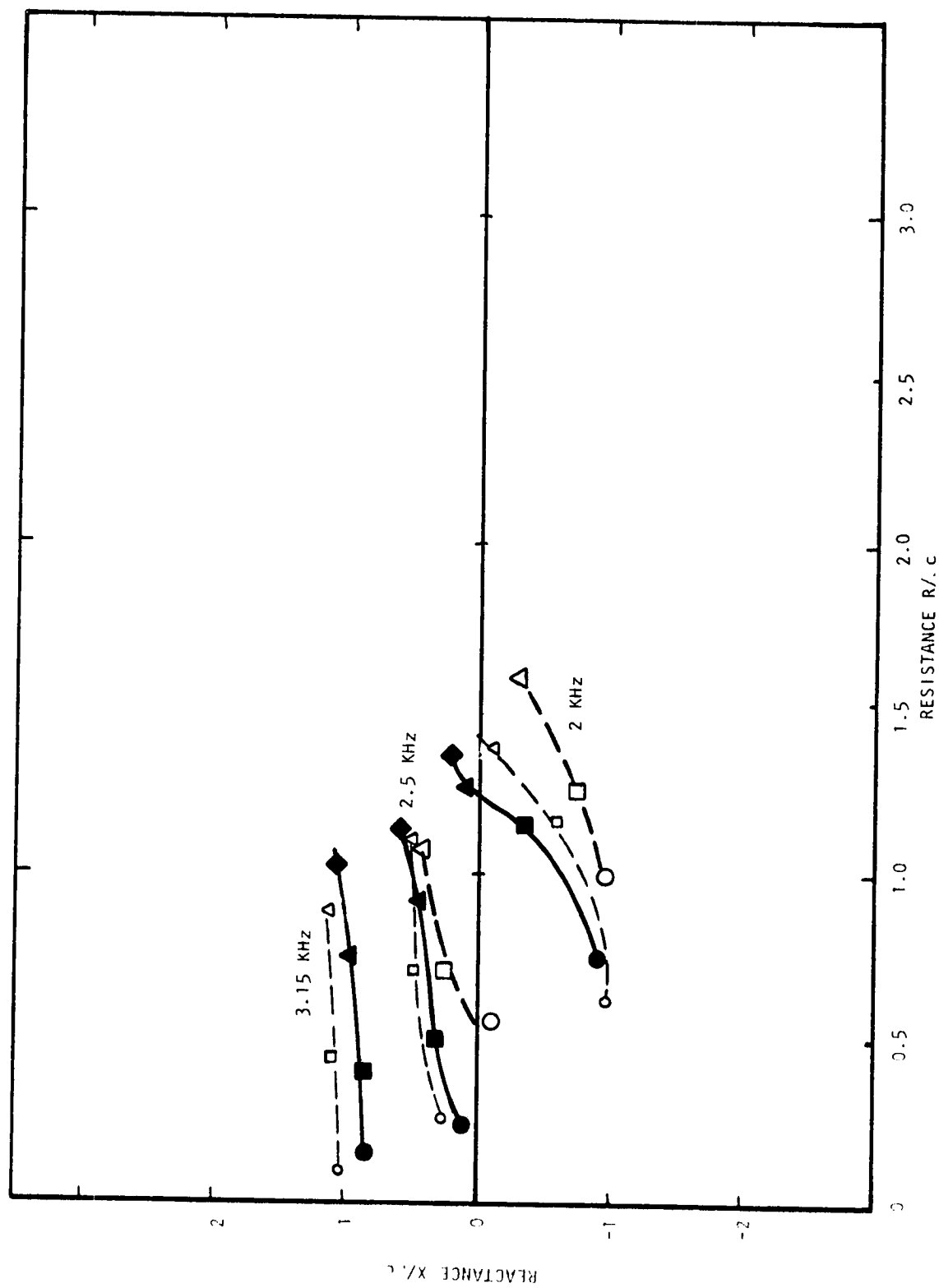


Figure 38 (b) Comparison of Measured and Calculated Impedances for Double Layer Sample: Facing Sheet Porosity 22%, Intermediate Sheet 17, With Equal Cavity Depths of 3.81 Cms. (1.5 in.)

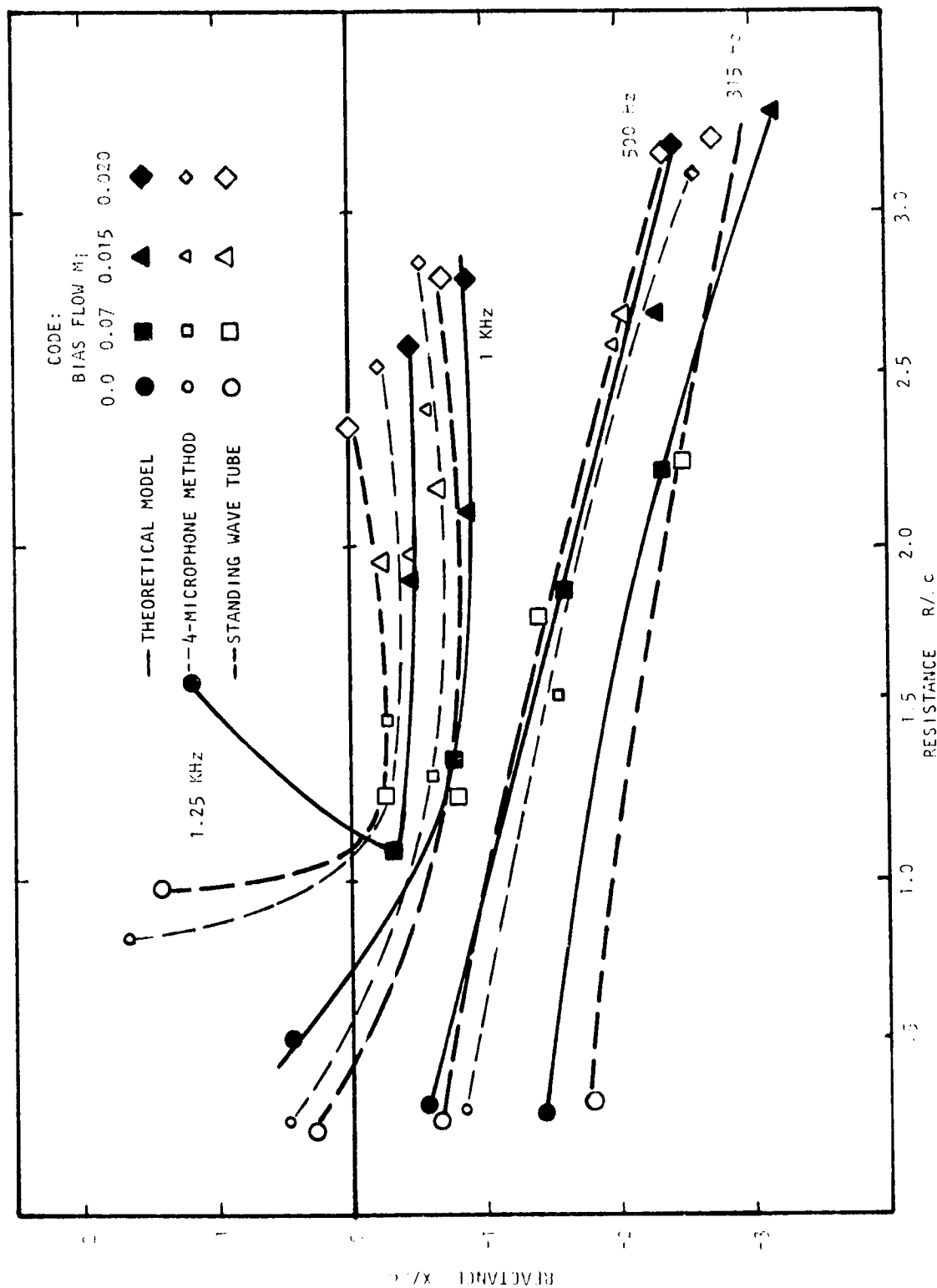


Fig. 1. Comparison of Measured and Calculated Impedances for Double Layer Sintered Electrode Porosity = 15% Interdigitated Electrode Equal Cavities of 0.11 cm x 0.15 cm

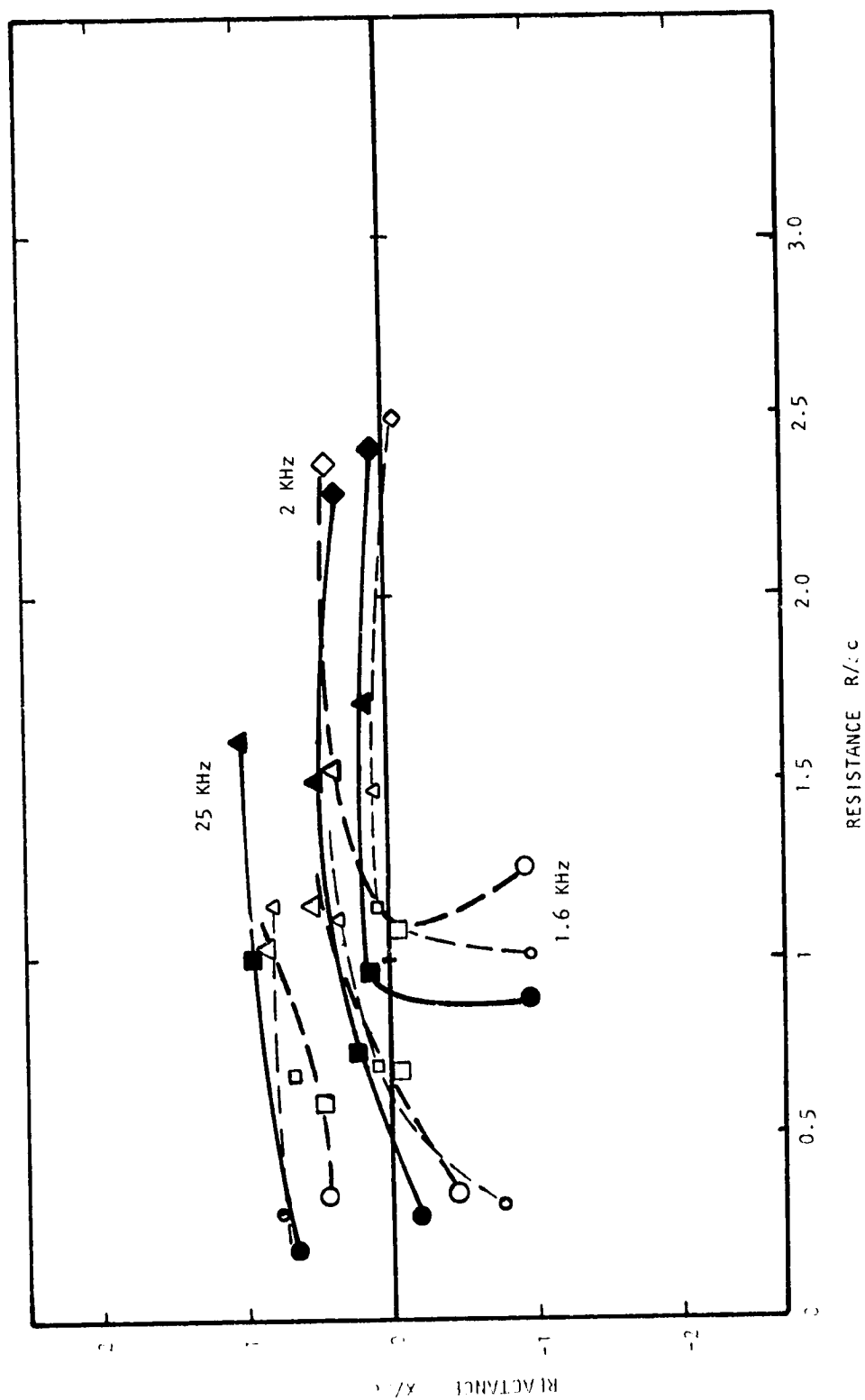


Figure 39(b) Comparison of Measured and Calculated Impedances for Double Layer Sample: Facing Sheet Porosity = 15%, Intermediate Sheet 7% with Equal Cavity Depths of 3.81 Cms. (1.5 in.)

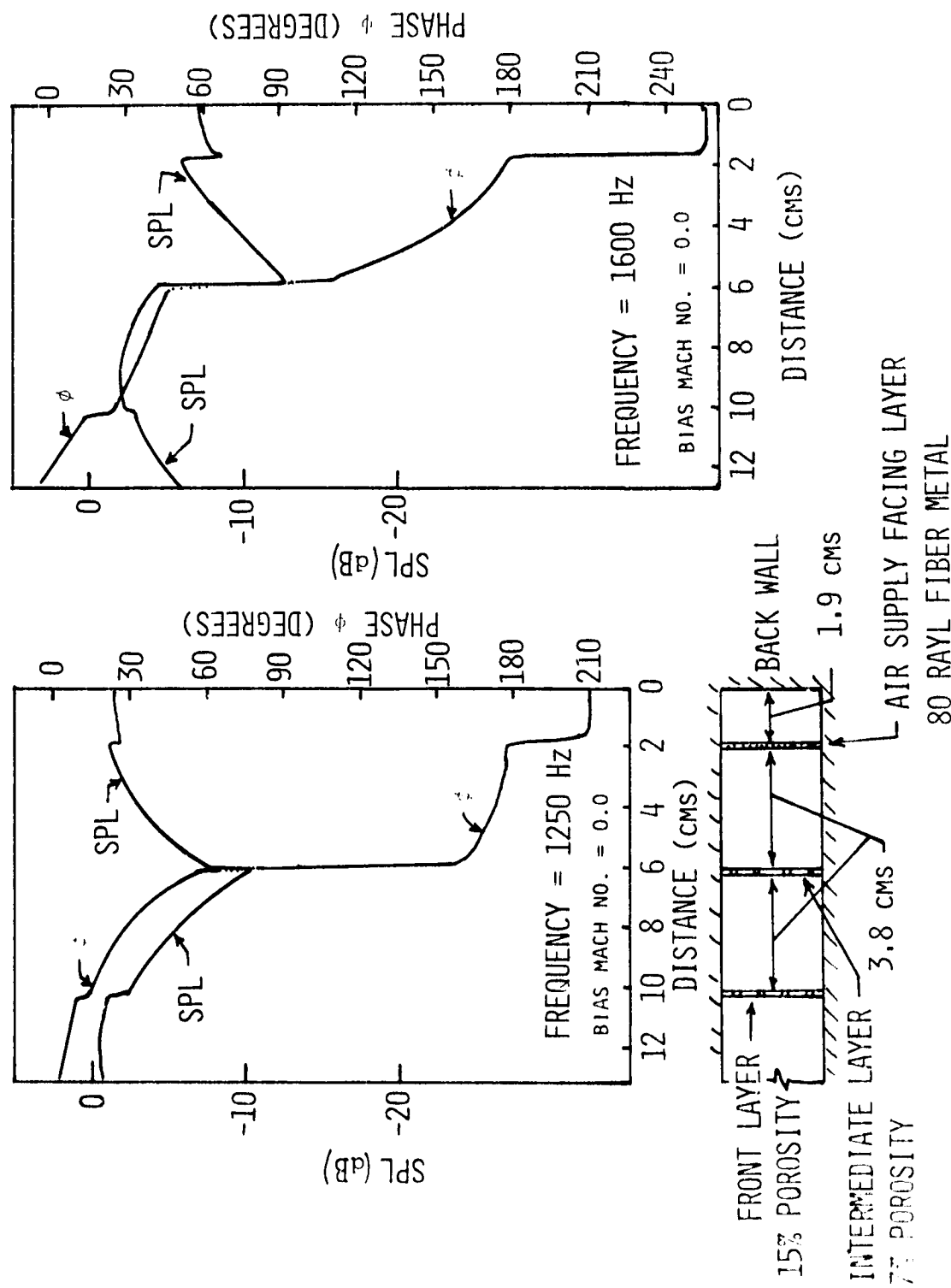


Figure 40 Example of Liner Pressure and Phase Traverses Near the Second Liner Resonance Frequency

increase in bias flow affects only the total resistance, the reactance of the system remaining effectively constant.

4.2 Verification of the Concept

4.2.1 Introduction

The grazing-flow propagation tests embody the basic objective of the entire program, i.e. to obtain a *proof of concept*. Specifically, does the bias flow actually control the attenuation *via* control of liner impedance as the theory predicts it should? The secondary consideration is the comparison of the absolute values of measured and theoretical attenuation, which itself is a measure of the prediction accuracy. Thus, the scope of these tests was defined such that the attainment of this aim would be a sufficient program end in itself. Because a very limited number of specific liners would be tested within the program time span, conclusions derived from these tests should not be treated as categorical results but as positive indications of concept viability.

4.2.2 Liner Design Considerations and Specifications

The initial steps in the design of a liner system, assuming a given duct geometry, involve the determination of the source distribution, the peak frequency involved, and the attenuation desired. In this feasibility study, to demonstrate the control of impedance experimentally, a single case was considered where the first or least attenuated mode of propagation, the plane wave (0,0) mode, is dominant. Thus, the frequency was chosen to ensure that all other modes were attenuated at a *much higher* rate than the first. The attenuation rate of the first mode should be as nearly optimum as possible in order to show that optimum impedance (and thus attenuation) can be maintained over a range of grazing flow conditions, but secondarily also to circumvent data interpretation problems due to interference from back reflections at the duct termination (when the modal attenuation is small). However, optimum attenuation requires that the liner impedance be close to the branch point value and in that vicinity the second mode has an attenuation rate comparable with that of the first mode. Thus, confusion in measurement interpretation can easily result at and near the optimum condition. In the attenuation contour plots on Figure 5, the highest rates of attenuation exist just below the branch line, and the contour lines are closely spaced. Thus, small changes in impedance will result in large attenuation changes, thereby creating practical difficulties in maintaining the correct impedance for the maximum attenuation. In Figure 5, for example, a reactive change of 0.1 ρc in position A-A results in the first mode attenuation rate changing from 10 dB duct width to 4 dB per duct width. There are regions below the branch line where the second mode (dashed contour lines in Figure 5) has attenuations comparable with those of the first mode. A reasonable compromise is to choose an impedance value, which then defines the attenuation rate, at a reactance point slightly above the branch line, and a resistance slightly greater than the branch point resistance. This region is desirable, since the rate of

change of attenuation with reactance is very small. This is particularly important in bias flow impedance control, since a particular value of reactance is inherently more difficult to achieve than a particular value of resistance. For a 7.62 cm (3 inch) square duct, the first cross mode cut-on frequency is about 2.2 KHz. Therefore, in order to minimize interference from this mode, a design frequency of about 1600 Hz, corresponding to a reduced frequency (K) of about 2.0 was chosen. The next step was to consider the attenuation contour plots, at this K number, for all values of grazing flow of interest.

A comparison of Figures 13, 5, and 10 shows that the attenuation contours are particularly susceptible to duct mean flow conditions. For example, the branch point has moved from $0.36 - 0.54j$ for a grazing flow Mach number of -0.25 (upstream propagation) to $0.30 - 0.24j$ at zero flow, and then to $0.25 - 0.11j$ for a grazing flow Mach number of $+0.25$. It is precisely this phenomenon which limits a static liner design.

It is instructive to use the complete set of attenuation contours in the grazing flow Mach number range of -0.5 to $+0.5$ (Figures 14, 13, 12, 5, 9, 10, and 11 corresponding to -0.5 , -0.25 , -0.125 , 0 , $+0.125$, $+0.25$, and $+0.5$ Mach numbers, respectively), and to construct a locus of desired constant attenuation points on the impedance plane as shown in Figure 41(a) with grazing flow as the variable parameter. In this figure, the locus corresponds to an attenuation of about 8 dB per duct width. The problem remaining is to attempt to match the liner variables of porosity and cavity depths such that bias flow effects on liner impedance will closely follow this locus. From consideration of the engine cycle, it would be desirable to require no bias flow at the maximum power engine condition and to use bias flow only while at idle or low power settings when excess air is available. As a general design philosophy, it is thus desirable to use maximum bias flow for the minimum grazing flow condition and to use minimum bias flow for the maximum grazing flow condition. From reference to Figure 41a for *downstream* propagation (positive Mach number), the liner bias flow characteristic must be such that the resistance increases and reactance decreases with increasing bias flow, while for *upstream* propagation, the converse exists: the resistance must decrease and the reactance increase with bias flow.

It is convenient to imagine the liner impedance as the sum of two component impedances, one the bias flow characteristic at zero grazing flow, the other a lumped resistive quantity associated with the grazing flow on the front facing layer of the liner. It is then possible to define that *downstream* propagation requires the liner bias flow characteristic to be in Region I (with the bias flow characteristic shape as shown in Figure 41b as line c-c). Thus, grazing flow will have the effect of a bodily movement of the characteristic to the right (as shown by c'-c') such that, at any value of grazing flow, a corresponding bias flow value will intersect the desired impedance locus. Similarly, upstream propagation requires the liner bias flow characteristics to be in Region III (with the bias flow characteristic shape as shown in Figure 41b as D-D). Again, grazing flow will shift the characteristic bodily to the right (as shown by D'-D') such that, again for any value of grazing flow, corresponding bias flow value will intersect the desired impedance locus. To accommodate this requirement at the same K number, it is

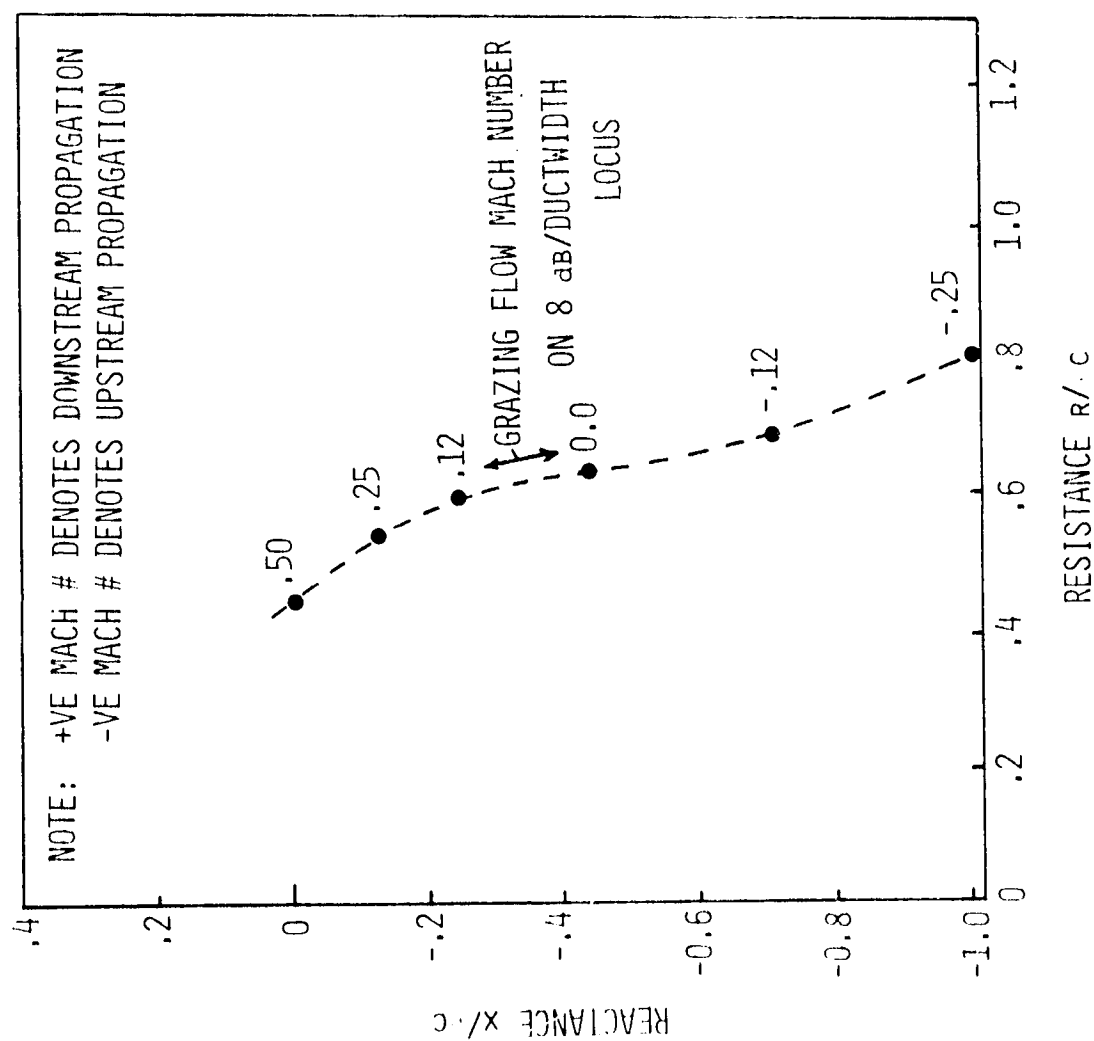


Figure 41(a) Locus of 8 dB per Duct Width Attenuation Constant on the Impedance Plane, with Respect to Grazing Flow Mach Number

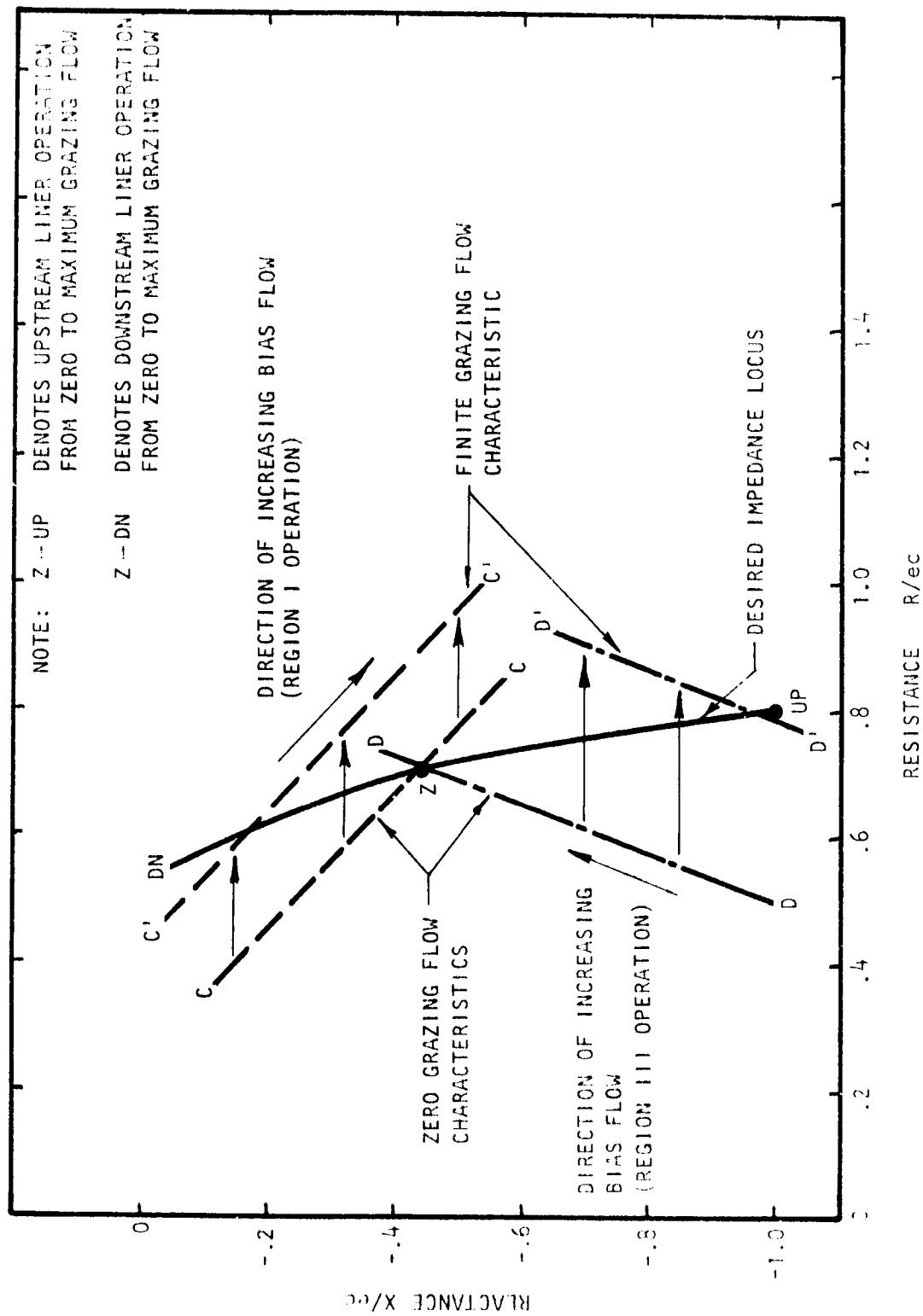


FIGURE 41. Impedance Characteristic Design Philosophy of Bias Flow Concept Operation

apparent that the upstream and downstream liners will have substantially different cavity depths and facing layer porosities, the upstream cavity depths in practice being almost twice as great as the downstream cavity depths. The actual choice of porosities and cavity depths was the result of a considerable amount of judicious trial-and-error evaluation with the impedance model. Since it was extremely difficult to match the liner impedances to the attenuation locus over the Mach number range from -0.5 to $+0.5$, the Mach number range of liner design was limited to -0.25 to $+0.25$. The procedure adopted was to choose the facing sheet porosities (commensurate with available stock materials) and to vary the cavity depths until the impedances for each operational extreme (zero bias flow with Mach $+0.25$ grazing flow, and Mach 0.015 bias flow with zero grazing flow) matched the respective points on the desired attenuation locus. The resultant test liner configurations are shown in Figures 42a and 42b, and the theoretically matched attenuation locus is shown in Figure 43.

4.2.3 Flow Duct Apparatus

The facility used for these tests incorporated the basic microphone traversing systems as used in the static impedance tube tests. The modifications are illustrated in Figures 44 and 45. The salient features incorporated are: (1) a central source section consisting of two 100-watt acoustic drivers excited, in phase, on opposite sides of the 7.62 cm (3 inch) square duct; and (2) the test liners upstream and downstream of the test section (and described below), each 12 duct widths in length, with duct lining only on one side. The upstream and downstream liners are divided into two sections, 45.72 cms (18 inches) in length, each with a separate bias air supply as sketched in Figure 44.

The preliminary performance tests were divided into two parts: fluid dynamic tests and acoustic tests. The fluid dynamic properties of the duct stream were measured at the duct entrance and exit (see Figure 44 for location) and consisted of wall static pressure measurements and velocity profile measurements. The velocity profiles and turbulence levels were measured with a hot-wire anemometer with the results as shown in Figure 46. It is apparent that considerable asymmetry existed due to acceleration of the air around the upstream pipe bends before entering the duct section. This defect was partially corrected by means of $1/8$ cell size honeycomb and screens placed upstream of the duct, but it became evident that perfect symmetry could be achieved only at the expense of duct performance. That is, the maximum attainable velocity was reduced due to the flow losses introduced by the flow conditioning elements.

The compromise final result is shown in Figure 47 as duct entrance and exit velocity profiles. The duct grazing mean flow calibration was set up such that a pitot probe on the duct centerline could be correlated to a mean velocity, derived from the velocity integral over the duct area assuming velocity profile symmetry.

The estimation of liner bias flow velocities was initially attempted with a downstream hot-wire traversing system. However, the hot-wire traverse gear

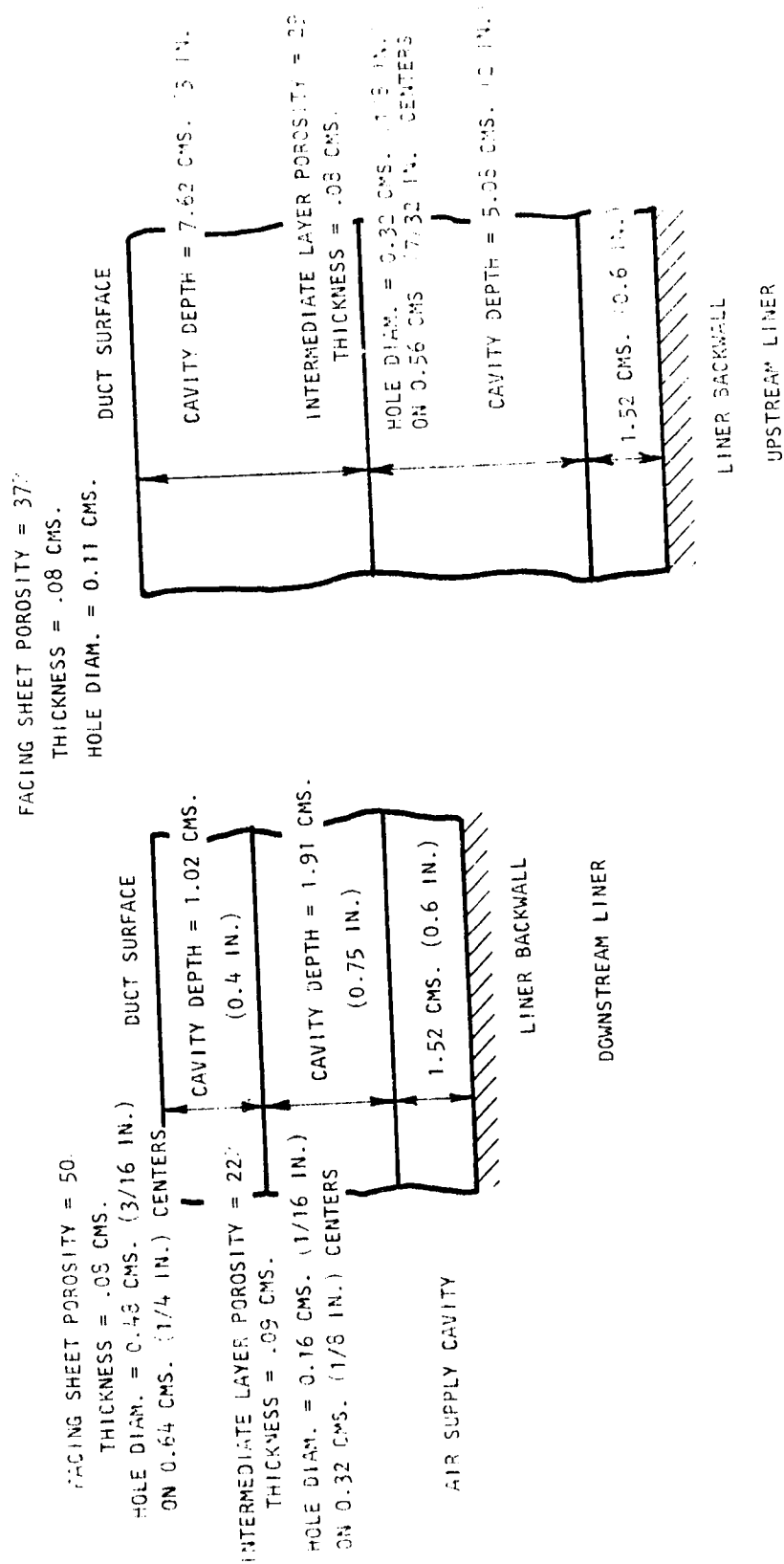


Figure 42 (a) Liner Configurations for Concept Validation in Grazing Flow
Test Duct Facility

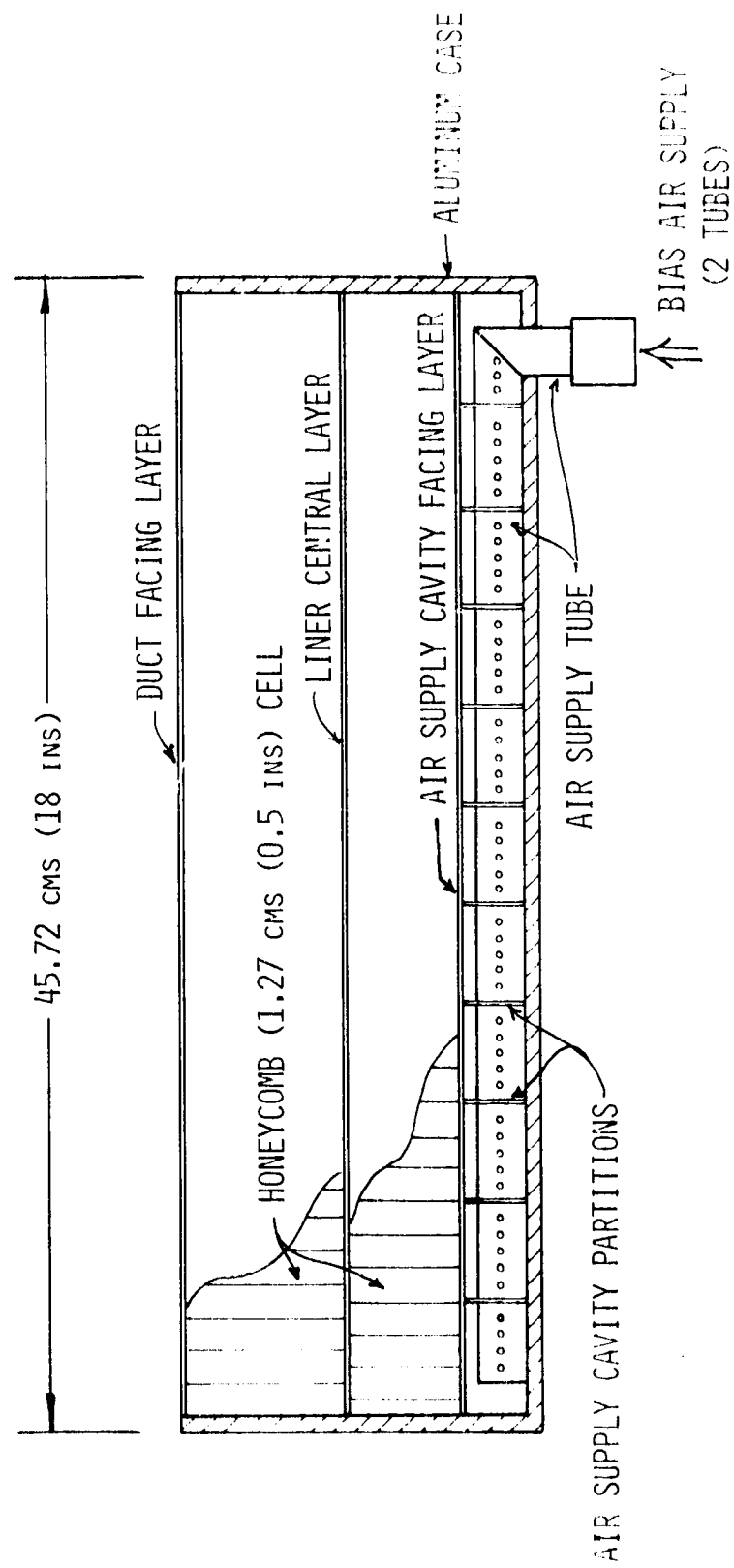


Figure 42(b) Bias Air Supply System on Sample Duct Liners

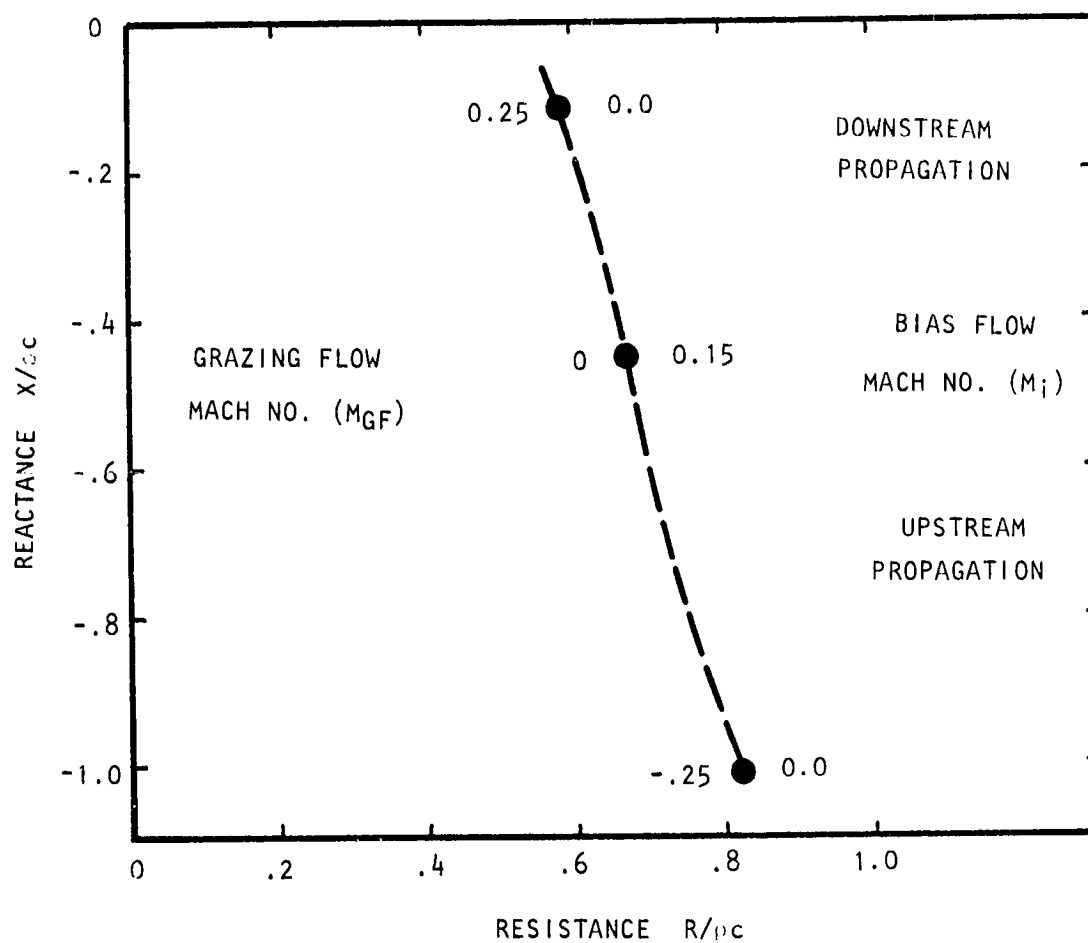


Figure 43 Impedance Model Attenuation Locus at $K=2.0$ for Test Liner Configuration of Figure 160 in Flow Duct Facility

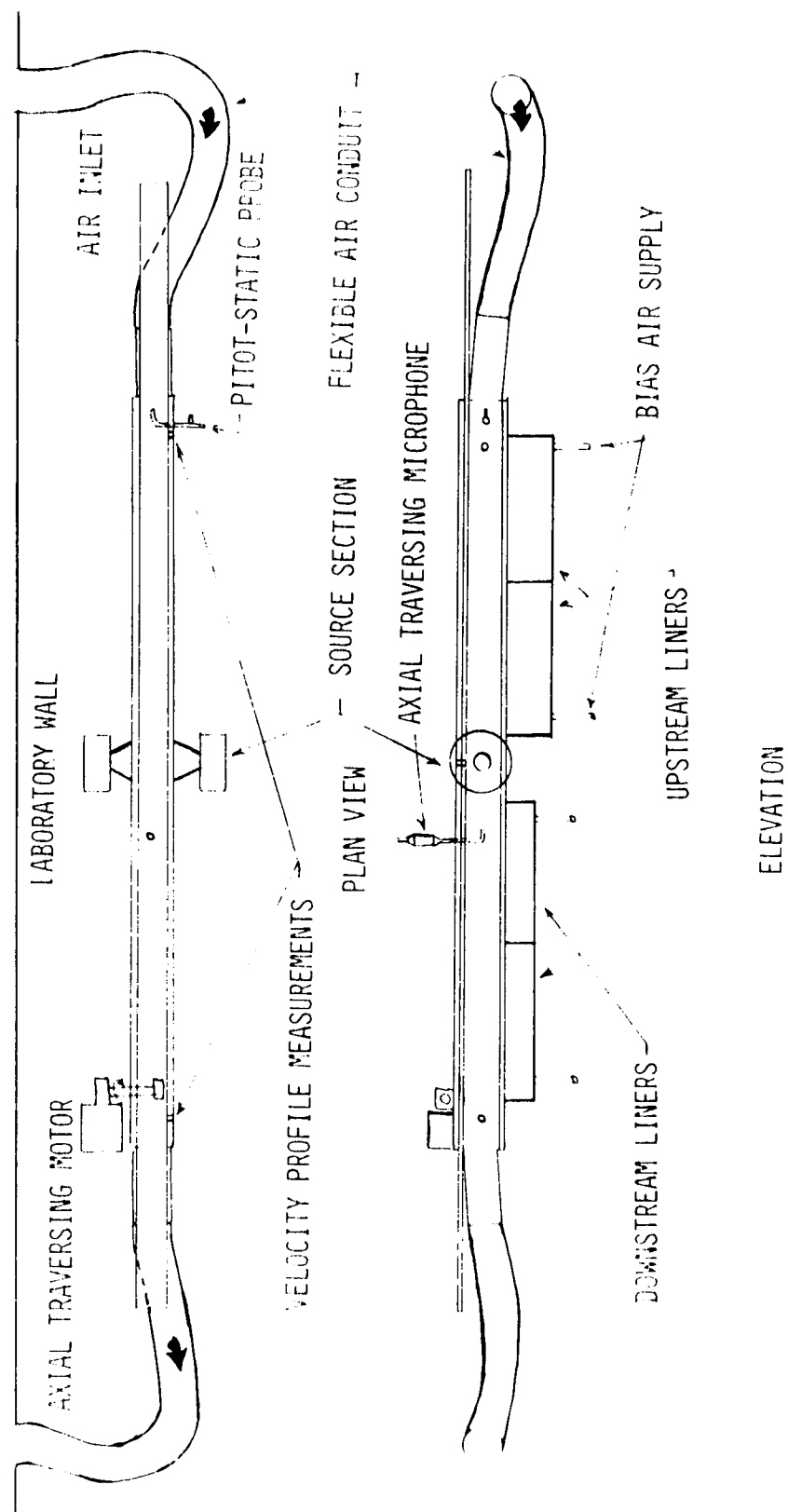


Figure 44 Schematic of Flow Duct Liner Test Facility

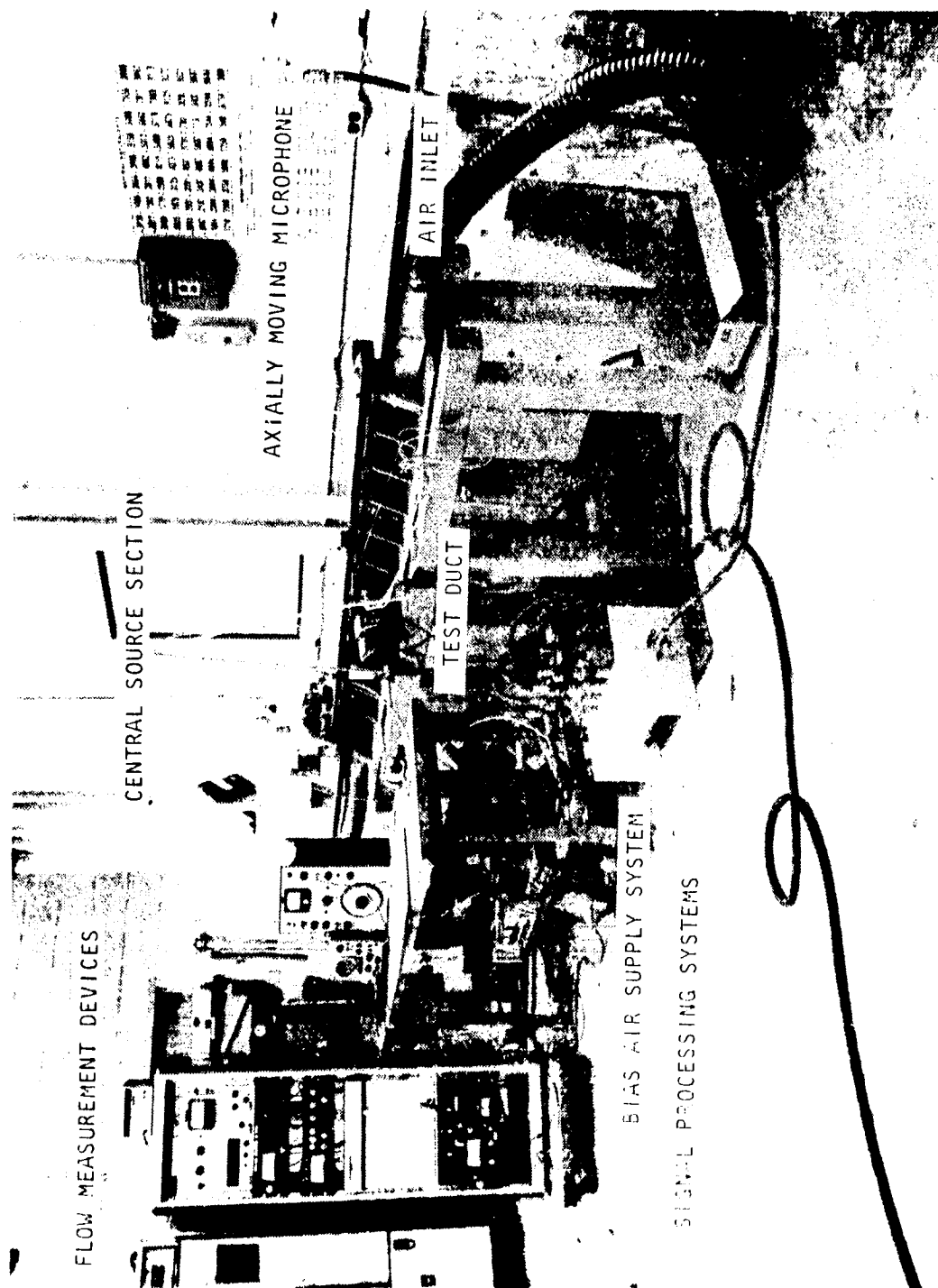


Figure 45(a) Overall Illustration of Flow Duct Liner Test Facility

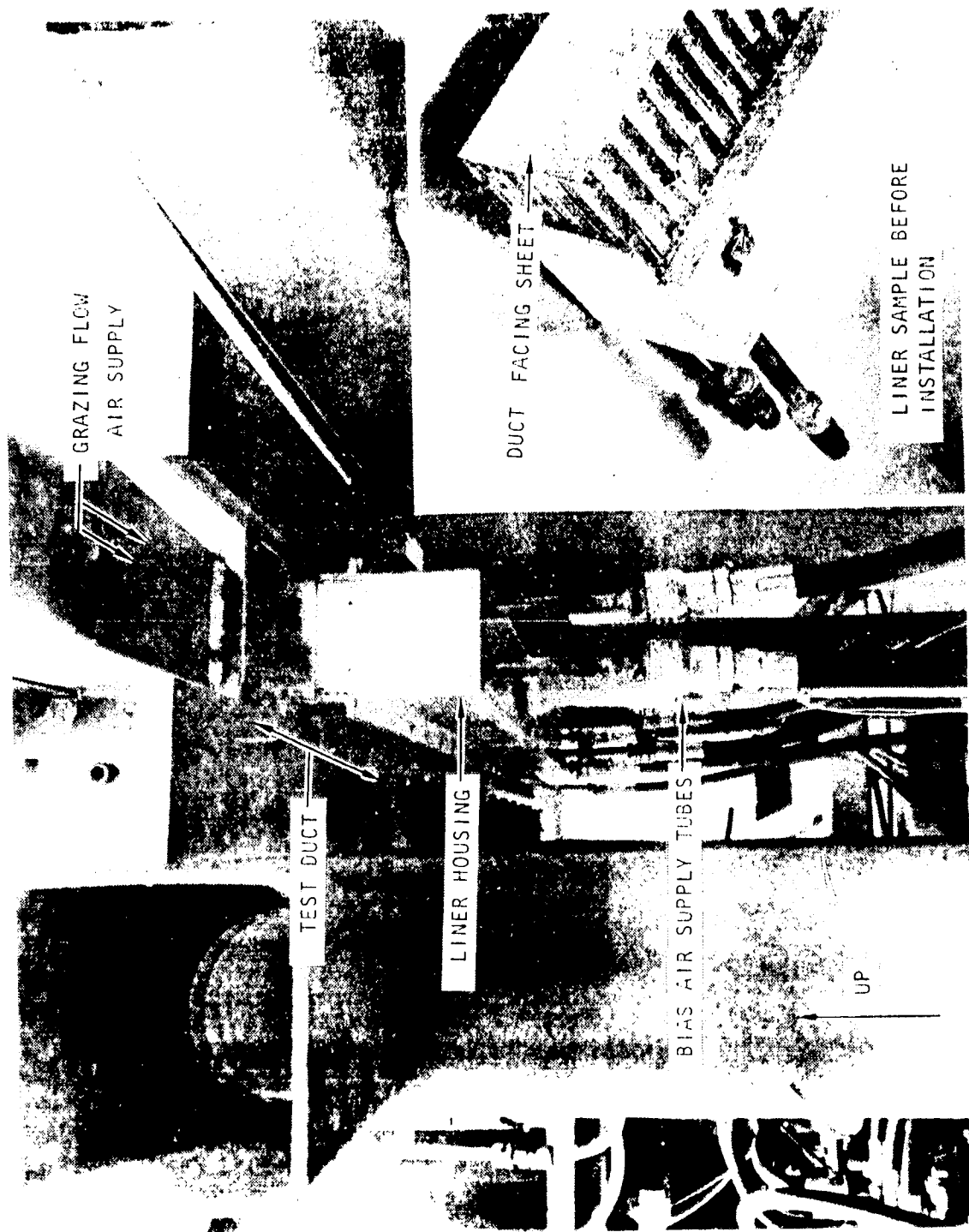


Figure 45(b) Acoustic Liners Mounted on Underside of Flow Test Duct

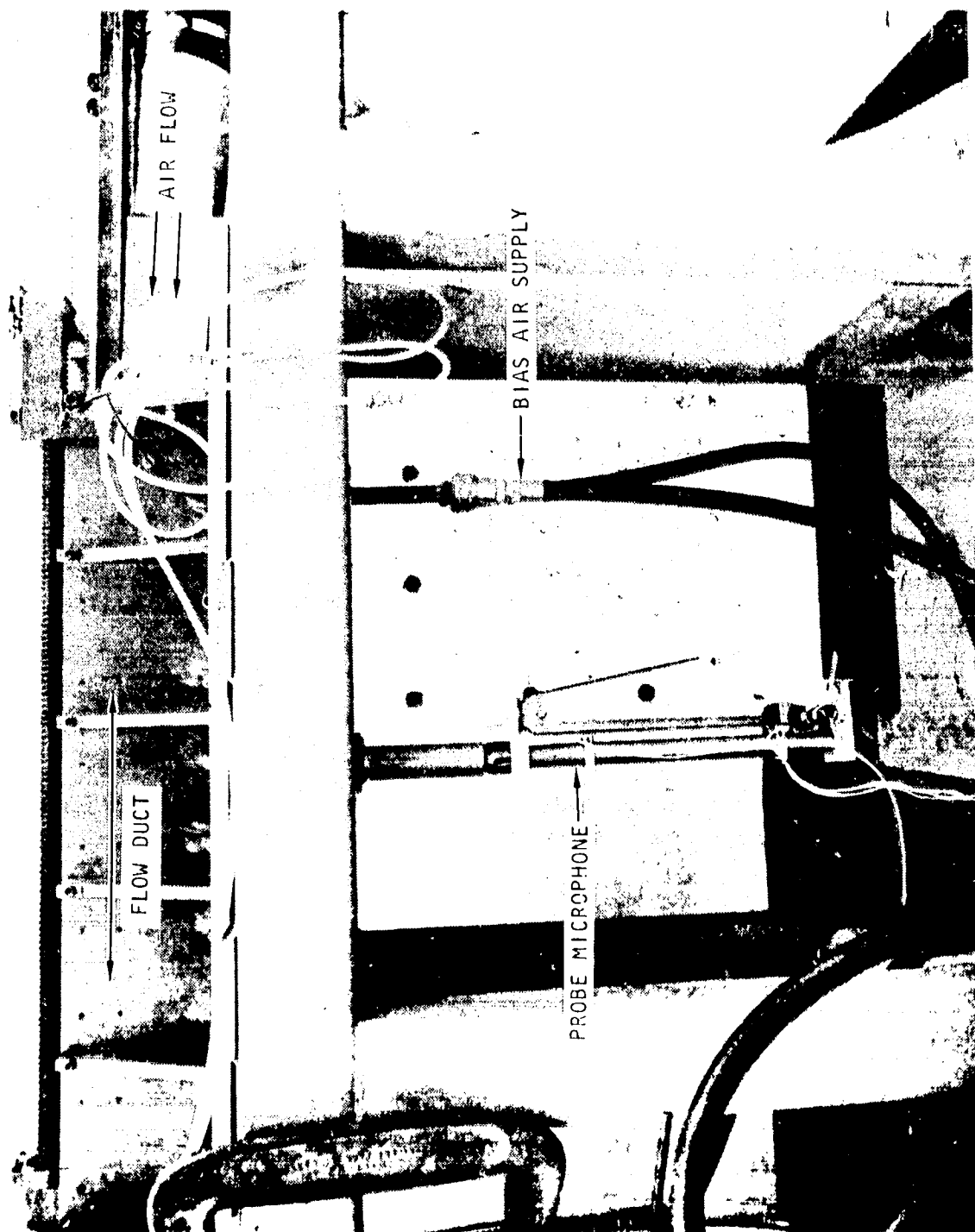


Figure 45(c) Probe Microphone Mounted on Test Duct Liner

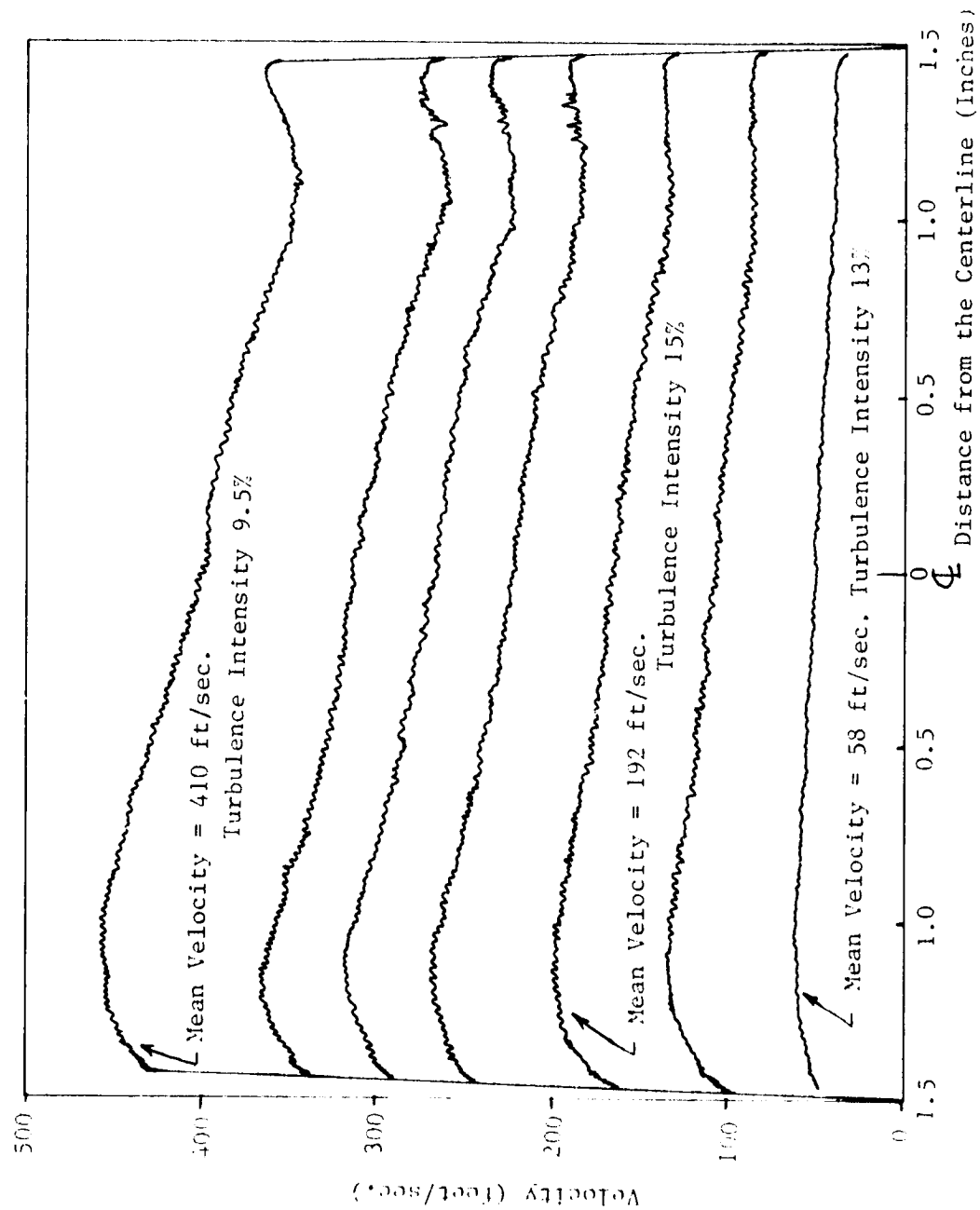


Figure 46 Initial Duct Entrance and Exit Velocity Profiles

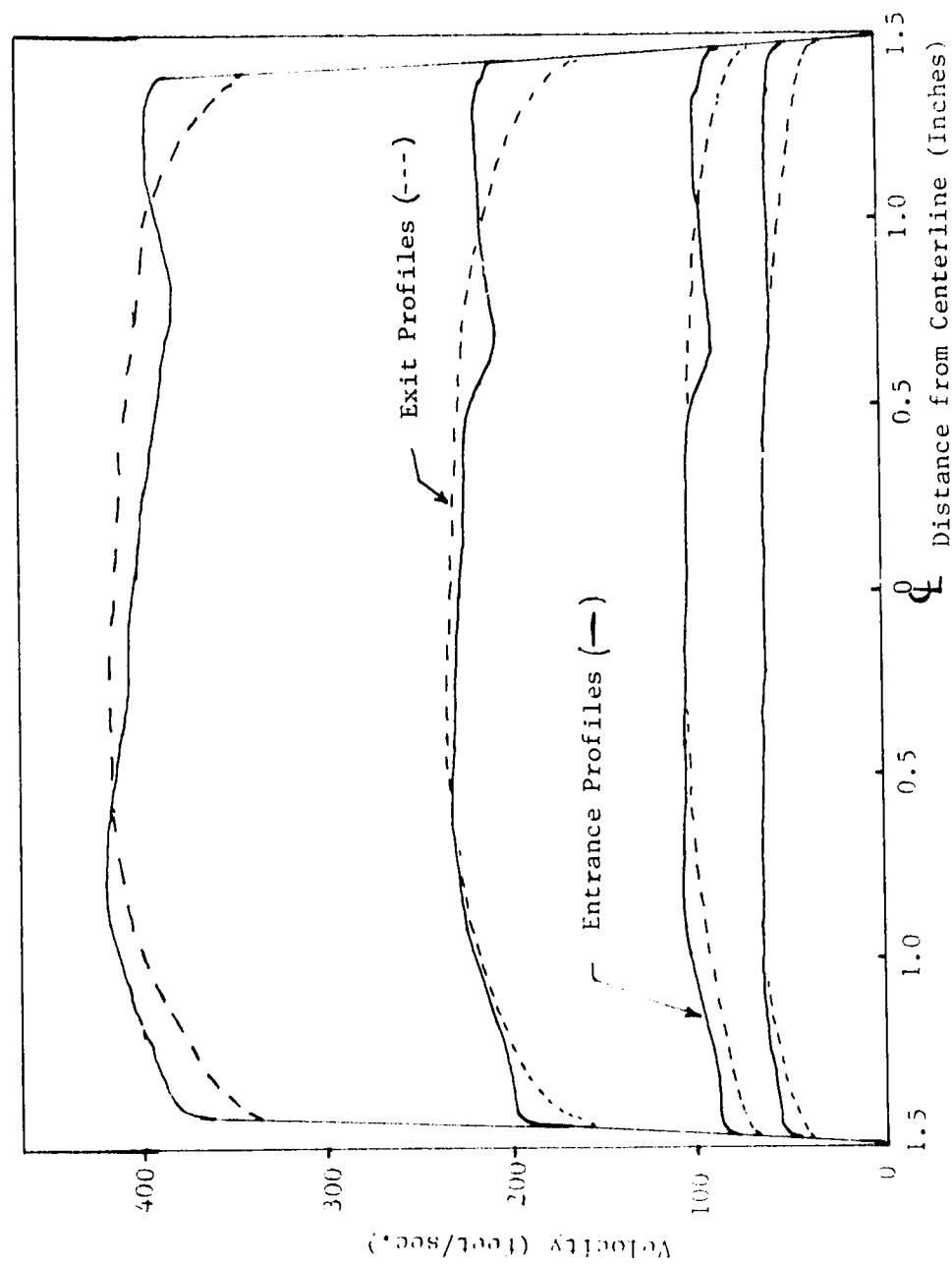


Figure 47 Typical Duct Entrance and Exit Velocity Profiles After Flow Conditioning Elements Inserted

could not completely map the air velocity over the duct cross-section. In addition, the fact that the liner was only on one side of the duct caused local bias flow distortions at the measurement point, invalidating the symmetry assumptions. Thus, in a more direct approach, a Venturi flow meter was used downstream of the test duct. The velocities thus measured were corrected for equivalent liner bias flow velocities (assuming incompressibility) and correlated to a manifold pressure reading controlled manually from a choked, constant-pressure air supply.

Two major measurement systems were used, each basically similar to those used for the normal incidence impedance tests. The first used the axial traversing duct microphone (as sketched earlier in Figure 30), which recorded the axial sound pressure and phase changes within the duct via an X-Y plotter. One complete axial sweep thus produced sufficient data to calculate the axial propagation constant for both upstream and downstream acoustic propagation. The second system was that associated with local in-situ impedance measurements at selected duct liner positions. The output was identical to that used in the normal incidence impedance measurement: an X-Y plot of sound pressure and phase through the entire liner and partially into the duct. The probe microphone was also identical to the normal incidence case, except that a solid probe extension was incorporated to support the probe by means of a hole in the opposite duct wall, which minimized probe flutter due to the duct grazing flow over the probe tube.

Two basic preliminary acoustic tests were undertaken, using a 1/4" B&K flush mounted microphone: (1) duct background noise levels measured in 1/3-octave bands for various grazing flow velocities up to 122 meters (400 feet) per second, and (2) source sound pressure levels over the same grazing flow velocities with discrete tone excitation at 1/3-octave center frequencies. As shown in Figure 48, over the operating frequency range of interest, there is a source signal-to-noise ratio in excess of 20 dB. This is further enhanced by the use of a 20 Hz tracking filter. It should be noted that, should the design attenuation of 8 dB per duct width be achieved then the implication is that over the entire liner duct length (12 duct widths in extent) a reduction of 96 dB would result. This would, of course, be outside the dynamic range of any existing instrumentation, and in a flow situation the signal would be deeply buried in flow-induced noise. Thus, it was anticipated that some attenuation measurements would have to be made over a limited axial range.

It is pertinent to mention two initial problems with the liner samples. First, as the perforate facing material must be bonded to the honeycomb core support structure, some perforate hole blockage by the bonding cement must be tolerated. It was originally estimated that about 5% of the holes would be blocked. Unfortunately, a higher number of holes were obstructed, and attempts to clear them manually were only partly successful. It was estimated that, in some areas on the downstream liners, the open area was reduced by 10 to 15%. The second initial problem was associated with the bias air supply cavity. It became apparent that the local reactivity assumption was invalidated due to flanking transmission of sound along the air supply cavity, which initially was not partitioned in order to encourage even distribution of bias air. This flanking transmission produced violent axial sound pressure fluctuations and nonsensical impedance measurements. These effects

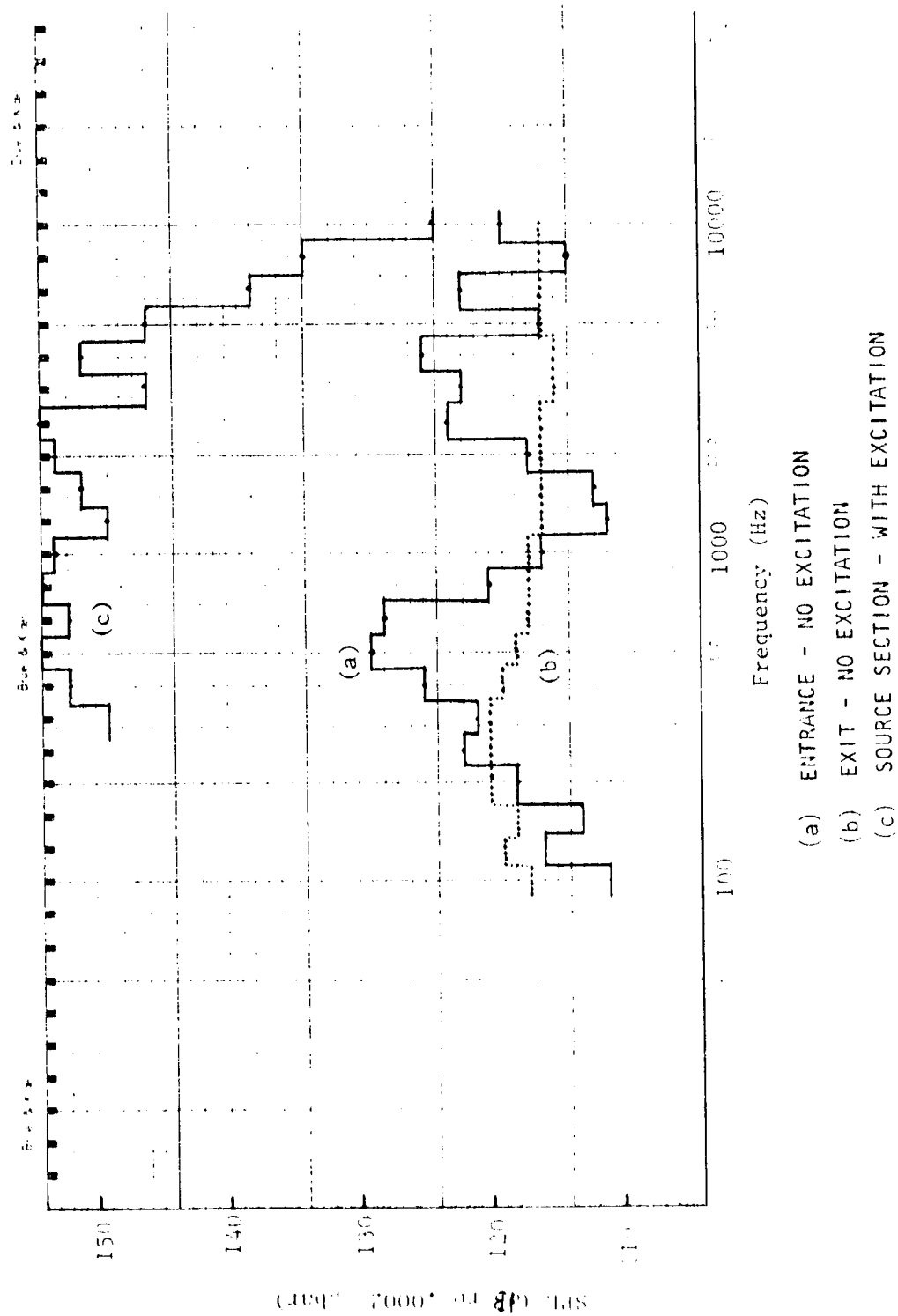


Figure 48 Flush Wall Microphone Spectra in Test Duct at 122 Meters/Sec. (400 feet/sec.) Mean Velocity

were cured by bias air supply cavity partitioning and careful cavity edge sealing with silicone rubber. The criterion for partition spacing was that the spacing should be much less than the wavelength of the highest frequency of interest in order to ensure local reactivity. It appears that careful attention to air supply cavity acoustic properties in any larger-scale liner design would be fundamentally necessary.

4.2.4 Analysis Methodology

As discussed in Section 4.1.3, sound pressure and relative phase were the measured duct acoustic quantities: under certain conditions a modal decay rate (in dB per duct width) and phase speed (nondimensionalized to free-space speed of sound and thus expressed as a Mach number M_ϕ) can be deduced from that measured data. Theoretically, the decay rate for a uniform wall impedance of infinite extent should be linear beyond a certain distance from the source. However, as will be shown, the practical necessity for the duct to be finite, and liner construction nonuniformities result in some nonlinear axial fluctuations in the sound pressure level. Thus, modal decay rates (ascribed to the liner) must be determined by allowing for these disturbances. In most cases, the liner termination standing-wave effects and initial near field structure close to the source section can be recognized*, and the desired uniform liner decay rate can be detected in the intermediate region. Similarly, the phase changes with axial distance will be locally disturbed. The phase velocity is determined from an estimate of the axial wavelength of the mode. Classically, the wavelength is defined as the axial distance necessary to result in 360 degrees change of phase, and thus is generally an easily measured quantity. However, particularly with downstream flow, this may not be possible to measure due to the wavelength elongation associated with convected propagation; in those cases an estimate was made from the rate of change of phase associated with the same region of measurement of the attenuation rate.

There are two possible approaches to verify the concept. The first is to use the liner predicted impedance and the attenuation analysis, which will result in predicted attenuation rates and phase velocities for direct comparison with the measured values. The second approach is to use the *measured* values of impedance and the attenuation analysis, which results in a desired attenuation rate and phase speed for direct comparison with the measurements. The decision to use the latter approach was based on the fact that the impedance model was not validated under grazing flow conditions and that the original intent in the use of the model was to provide a guide for the design of a liner suitable for the "proof of concept" goal of the program.

4.2.5 Flow Duct Test Results

Axial sound pressure and phase traverses were recorded using discrete frequency excitation at chosen 1/3-octave center frequencies from 315 Hz to

* See also, for illustration, the case of the 1/3-octave band at 315 Hz, where the axial pressure level is shown in Figure 4.1. The axial distance is in inches.

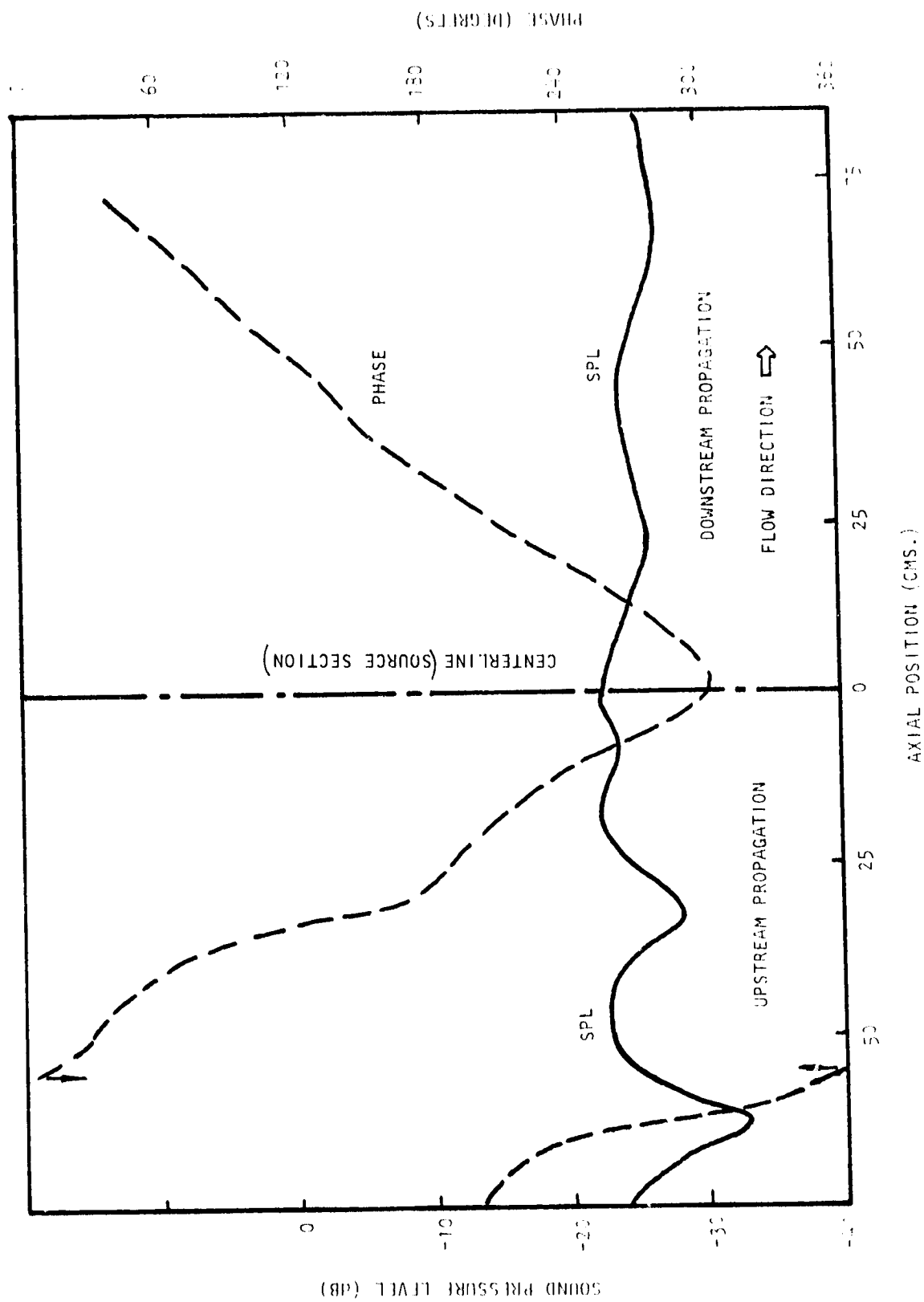


Figure 49 Axial Sound Pressure and Phase Traverses in Duct Centerline at 315 Hz. $B_{100} = 0.0$, Grating $B_{100} = 0.0$

3.15 KHz, with additional traverses at 1.4, 1.5, and 1.7 KHz to investigate more closely the frequency space around the liner design frequency. These traverses are shown in Appendix G. At the extremes of the frequency range tested, the duct attenuation rates are small, and large standing-wave effects are to be expected due to termination reflections. Indeed, some classic examples can be seen at 315 Hz in Figure 49 for the upstream case, and at 1250 Hz in Figure 50a and at 3.15 KHz in Figure 51. It should be kept in mind that the traverses show the effects of *both* liners, each having quite different construction geometries.

At each frequency, four extremes of grazing and bias flow conditions are shown, the figure nomenclature defined as follows: (a) zero grazing flow and zero bias flow; (b) zero grazing flow and bias flow Mach number equal to 0.015, (c) grazing flow Mach number equal to 0.25* and bias flow Mach number equal to 0.015, and (d) grazing flow Mach number equal to 0.25 and zero bias flow. The points of interest in these figures are: (1) the axial propagation constant (i.e., is the attenuation linear in slope, is the axial phase wavelength constant?), (2) comparison of attenuation rates between the cases of zero grazing flow with bias flow Mach number of 0.015, and zero bias flow with a grazing flow Mach number of 0.25 (i.e., do the measured attenuation rates agree with each other and with the theoretical design values?), and (3) comparison of attenuation rates between the cases of zero bias flow and ~~small~~ bias flows (i.e., Does the bias flow control the attenuation via impedance control as the theory predicts it should?). The third point is most vital, and a confirmation of this point implies a proof of concept which is the major objective of this work.

Figures 52, 53, and 54, representing frequencies tested at and on either side of the design point, present the relevant data to answer the above questions.

Figure 50, at 1250 Hz, represents the case several hundred Hertz below the design frequency. The most obvious point is that termination reflections are present which distort the axial sound pressure pattern more significantly than the phase pattern. Obviously, it becomes difficult to estimate attenuation slopes when significant reflection interferences are involved, as in Figure 50a. A graphical technique was adopted, consisting of an overlay on which a range of decay rates (in terms of dB per duct width) was plotted. The decay rate ascribed to the test case was then determined from the line of best fit, as shown, for example, on Figure 50a.

For all the cases of upstream propagation shown in Figure 50, the decay rate is less than 1.8 dB per duct width and appears to be only slightly affected by either bias or grazing flow, the combination of both producing

*The grazing flow Mach number was restricted to this value in conformity with the liner design limitations and also to reduce test time. It was felt that a further extension of the range of test conditions would be counterproductive or impair the conclusions or fundamental aim of the work.

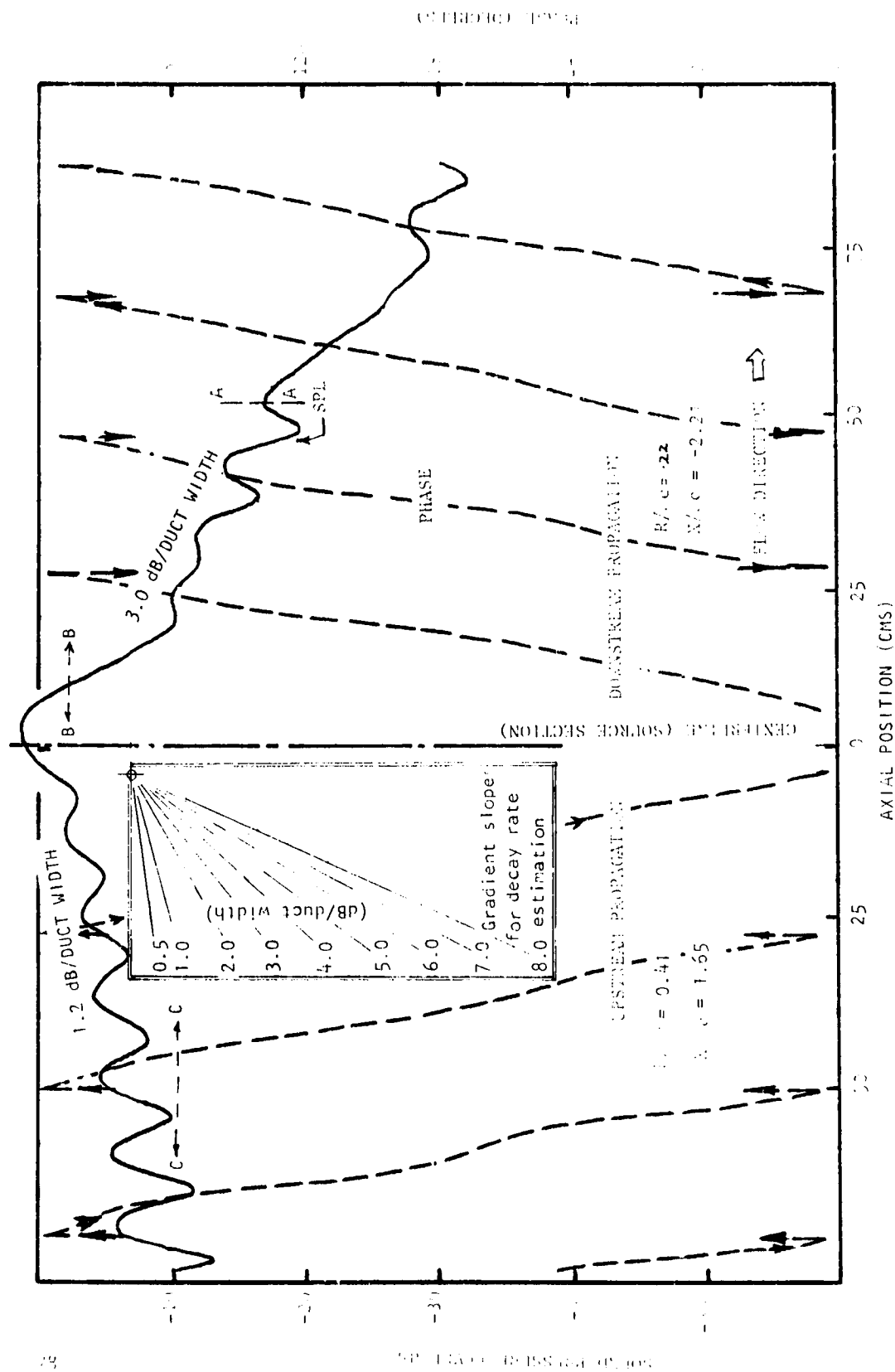


Figure 30 (a) Axial Sound Pressure and Phase Traverses at 1250 Hz. Bias Flow $M_1 = 0.0$. Grazing angle $\theta = 0^\circ$.

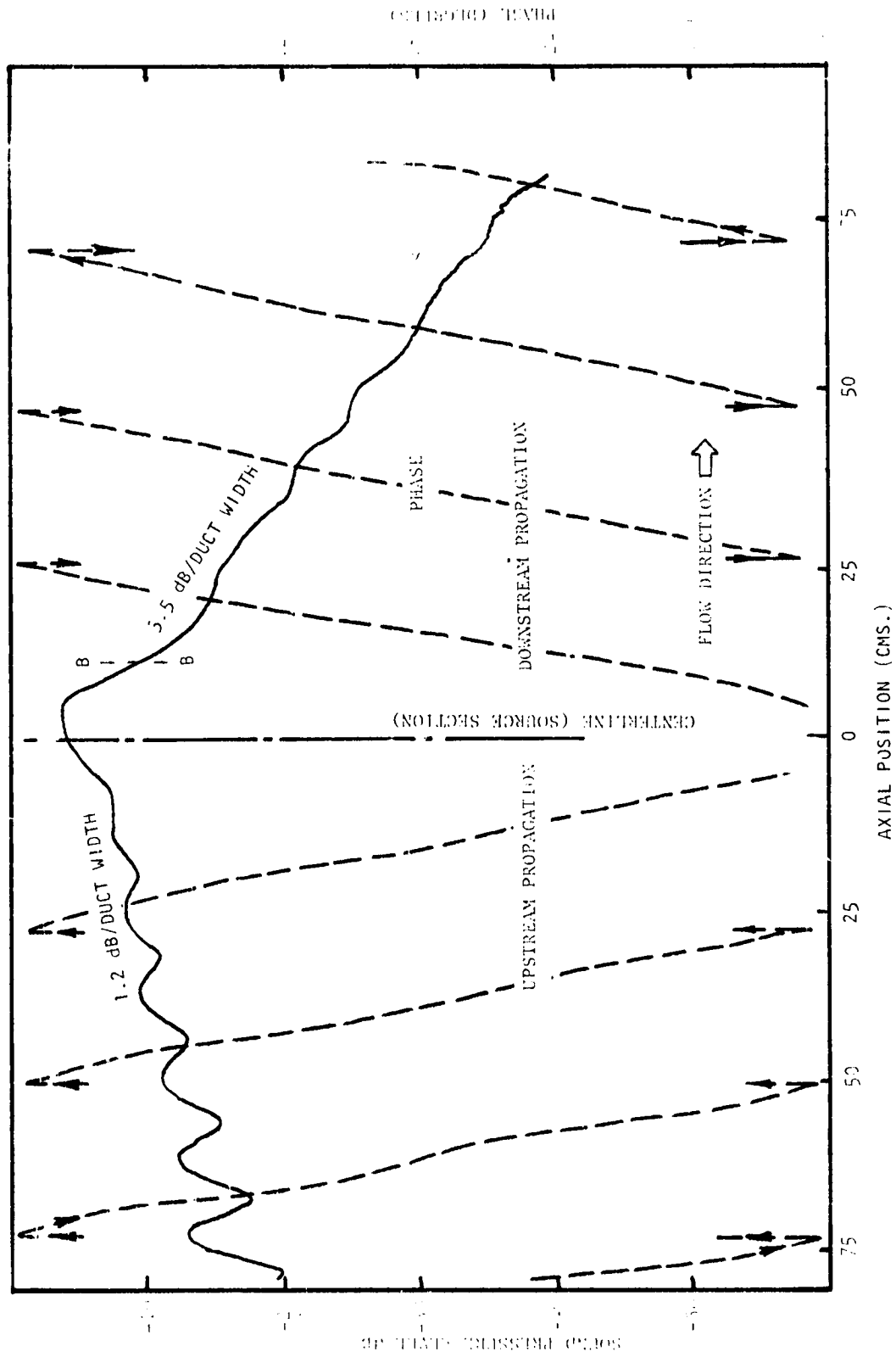


Figure 50(b) Axial Sound Pressure and Phase Traverses on Duct Centerline at 1250 Hz. Bias Flow $M_i = 0.015$, Grazing Flow $M_{GF} = 0.0$

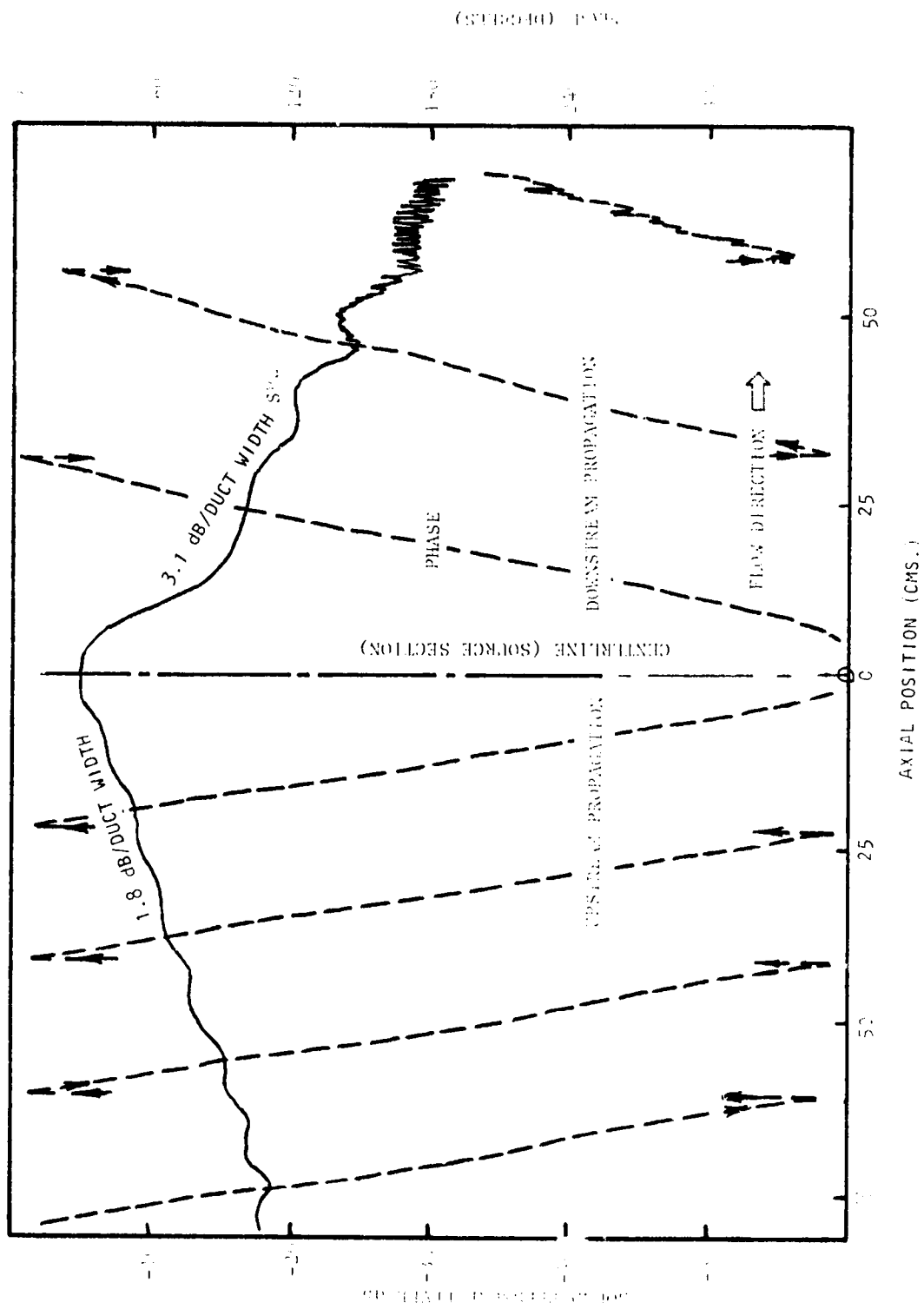


FIG. 1. Axial Sound Pressure and Phase Transitions in Duct Centerline
 at 100 Hz. Duct Length = 100 cm, Duct Diameter = 1.5 cm, Flow Rate = 0.05

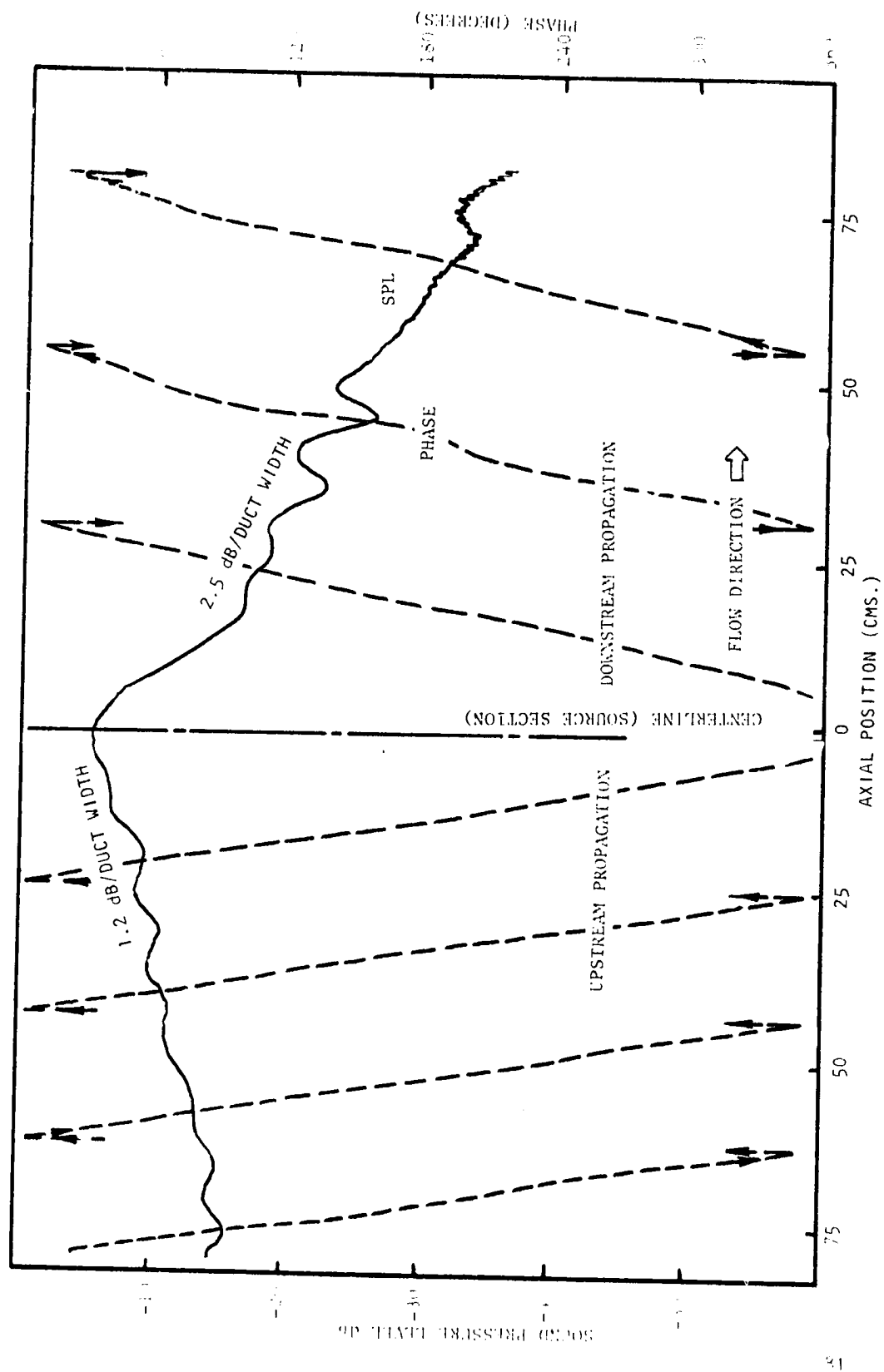


Figure 50(d) Axial Sound Pressure and Phase Traverses on Duct Centerline at 1250 Hz. Bias Flow $M_i = 0.0$, Grazing Flow $M_{GF} = 0.25$

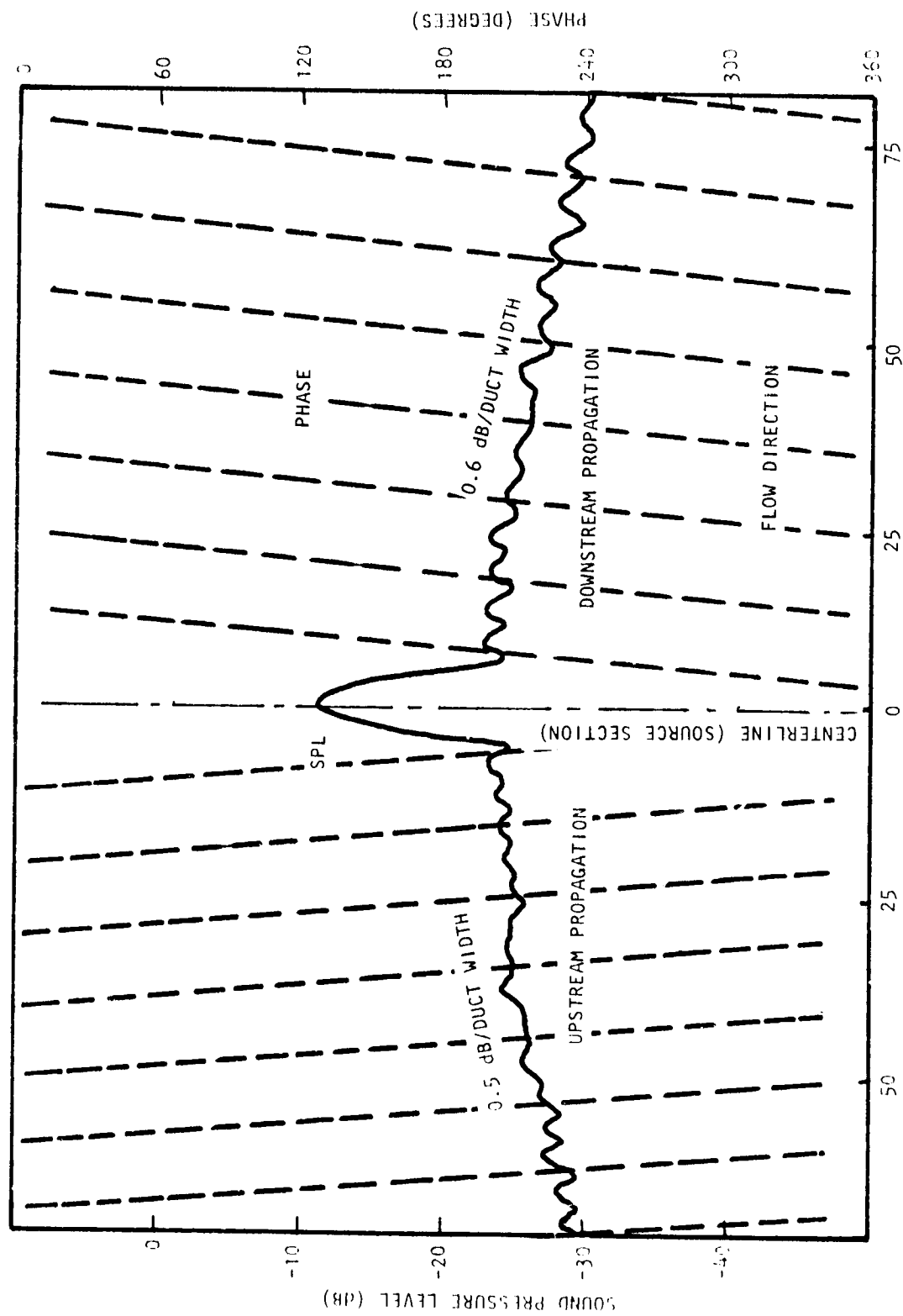


Figure 51 Axial Sound Pressure and Phase Traverses on Duct Centerline at 3.15 kHz. Bias Flow $M_i = 0.0$, Grazing Flow $M_{GF} = 0.0$

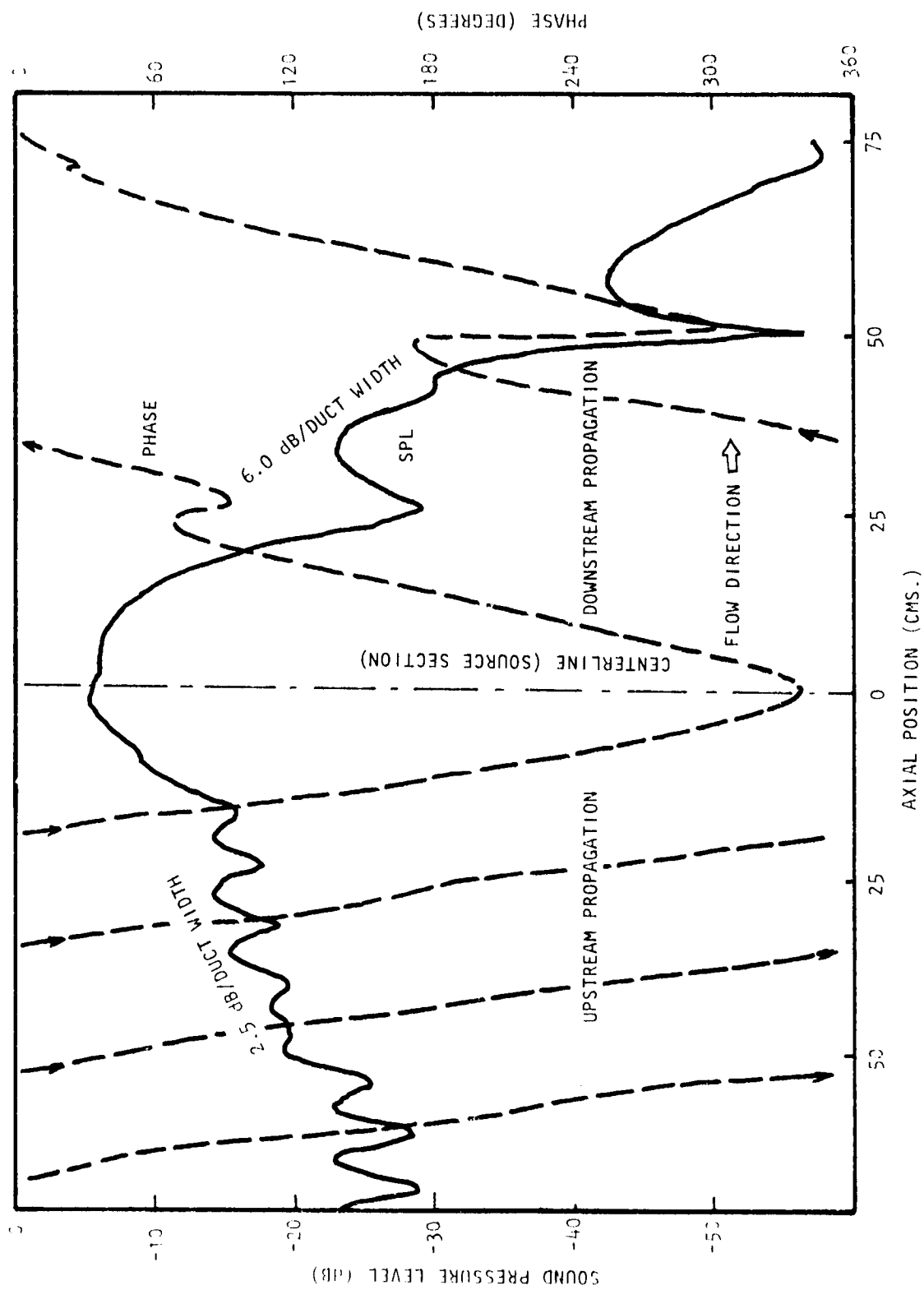


Figure 52 (a) Axial Sound Pressure and Phase Traverses on Duct Centerline at 1500 Hz. Bias Flow $M_1 = 0.0$, Grazing Flow $M_{GF} = 0.0$

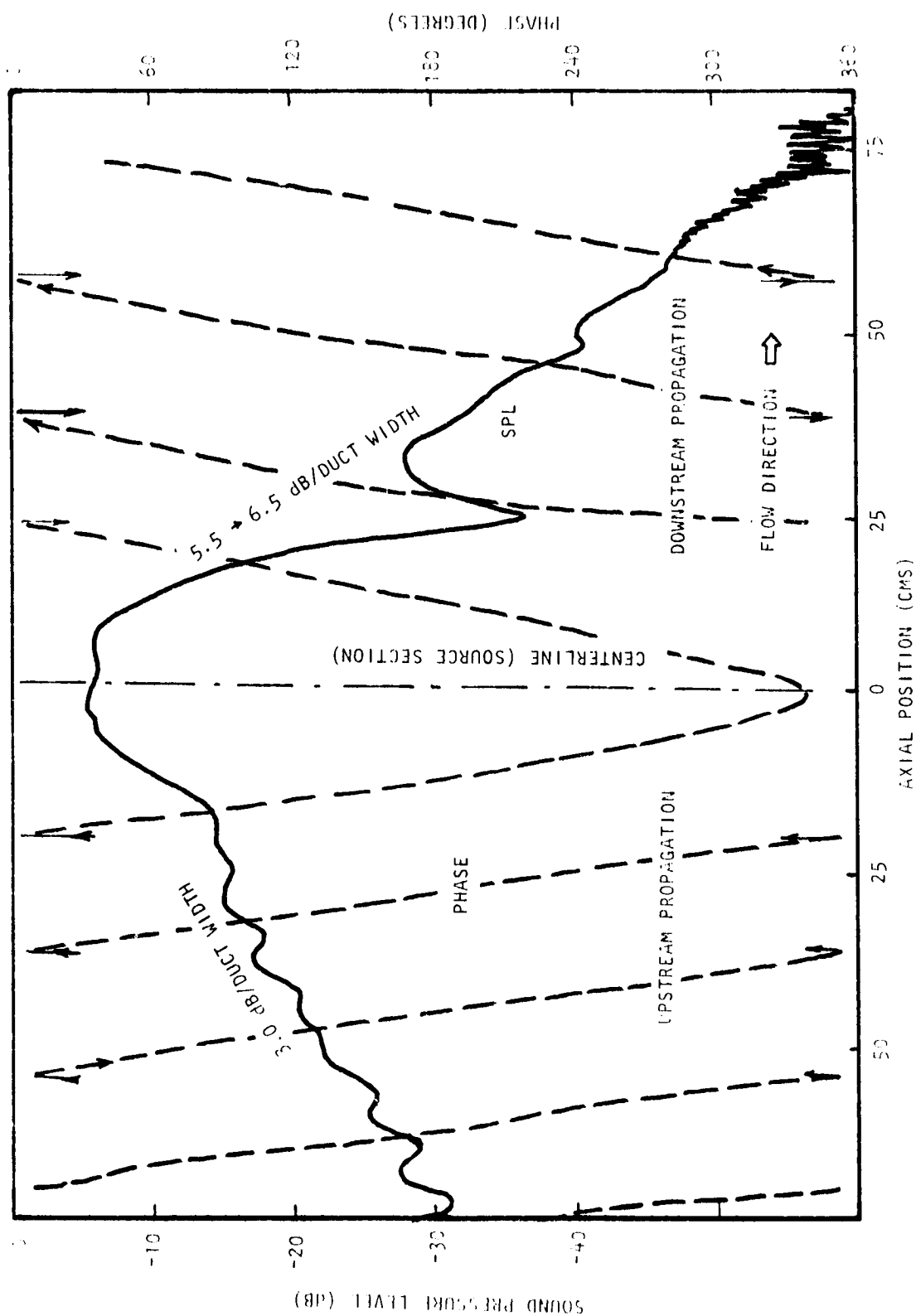


Figure 52(b) Axial Sound Pressure and Phase Traverses on Duct Centerline at 1500 Hz. Bias Flow $M_0 = 0.15$, Grazing Flow $M_{GF} = 0.0$

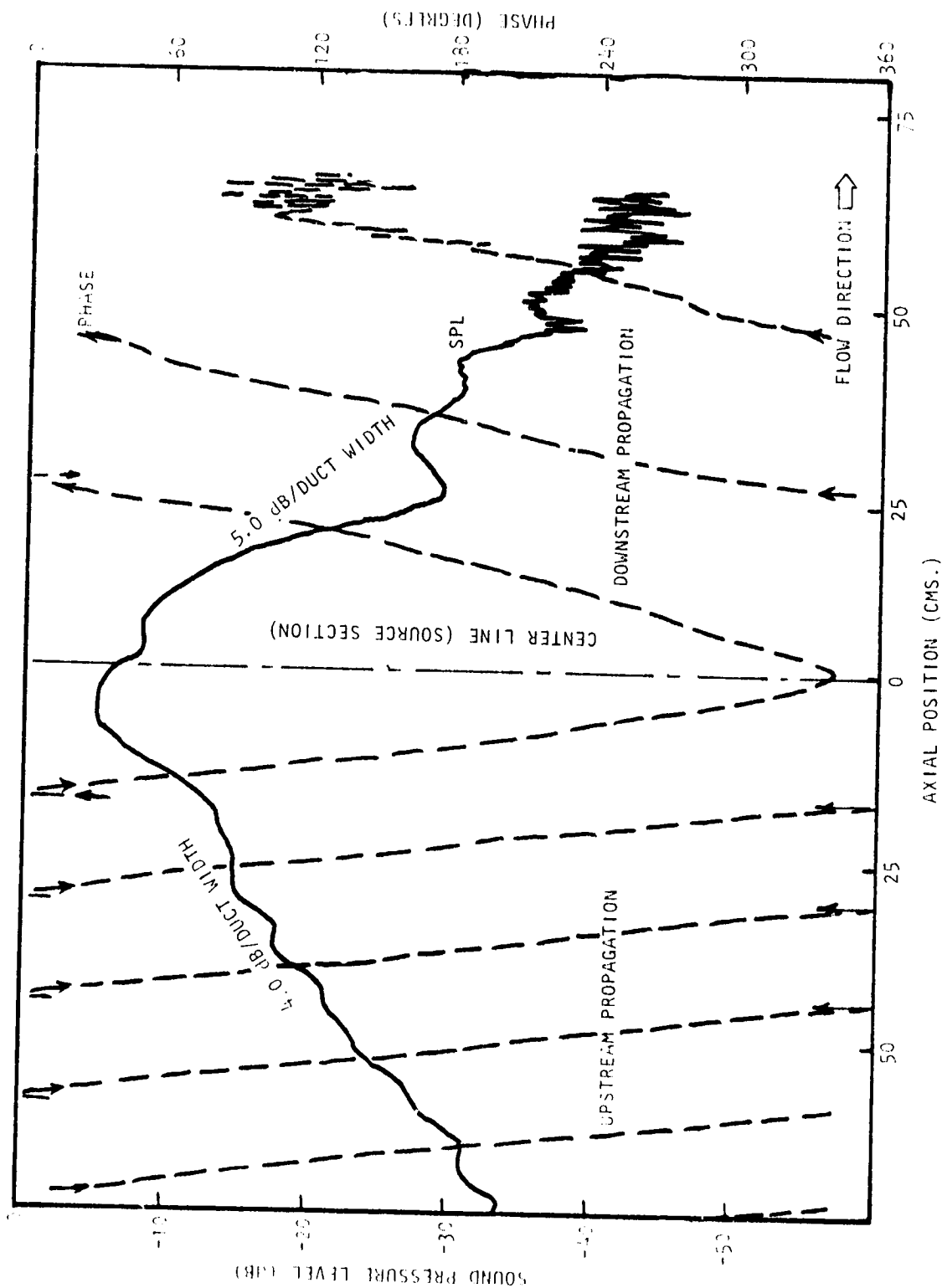


Figure 52(c) Axial Sound Pressure and Phase Traverses on Duct Centerline at 1500 Hz. Bias Flow $M_i = 0.015$, Grazing Flow $M_{GF} = 0.25$

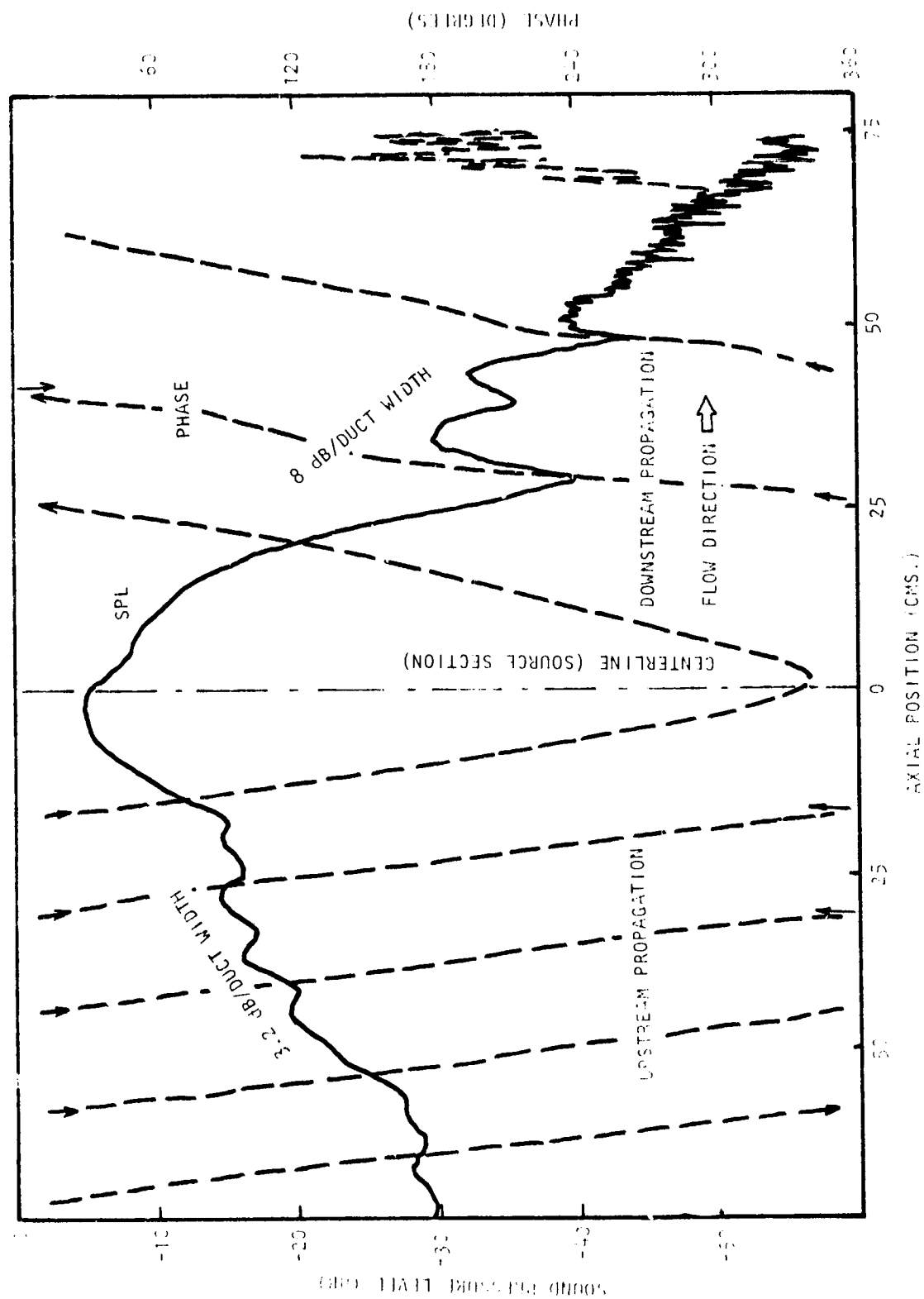


Figure 52-41 Axial Sound Pressure and Phase Traverses on Duct Centerline at 1500 Hz. Bias Flow $M_1 = 0.0$, Grating Flow $M_{GF} = 0.25$

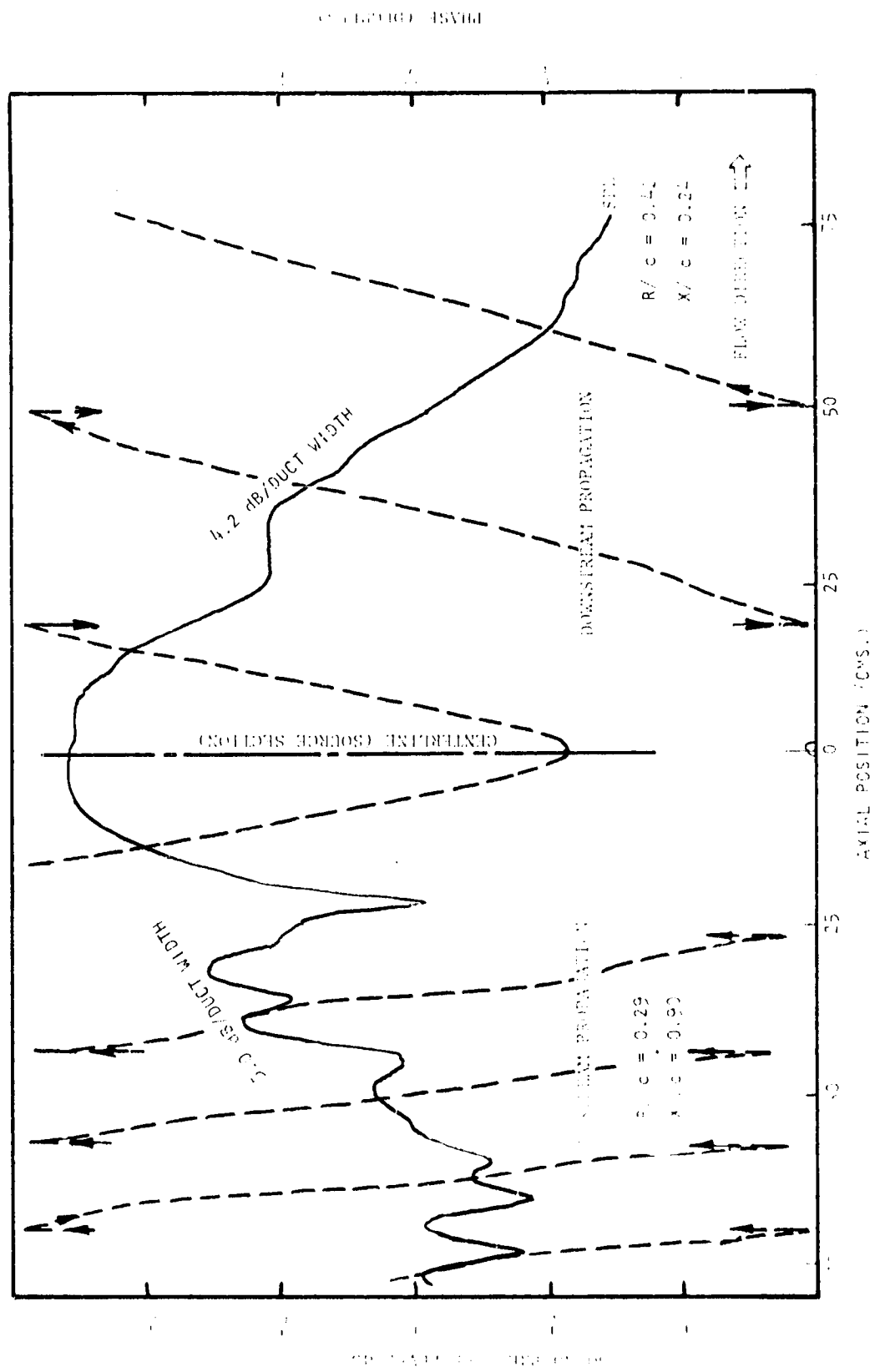


FIGURE 53 (a) Axial Sound Pressure and Phase Traverses in Duct Centerline
at 1600 Hz. $R/c = 0.29$, $X/c = 0.90$, $M = 0.0$, $M_{eff} = 0.0$

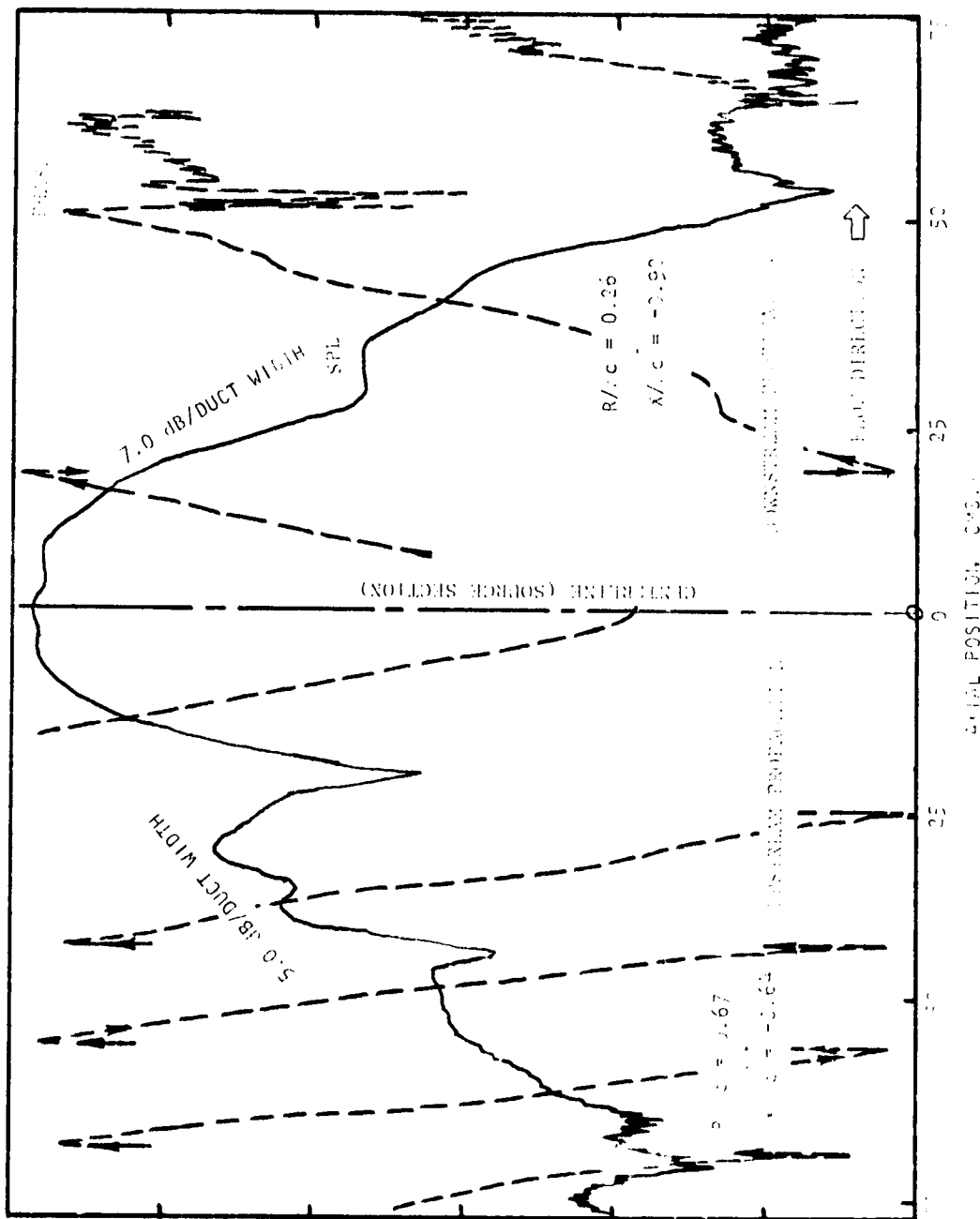


FIGURE 3. Static Pressure and Phase Traverses on Duct Centerline
at 100 Hz, $R/c = 0.26$, $X/c = -0.90$, Grazing Angle = 0°

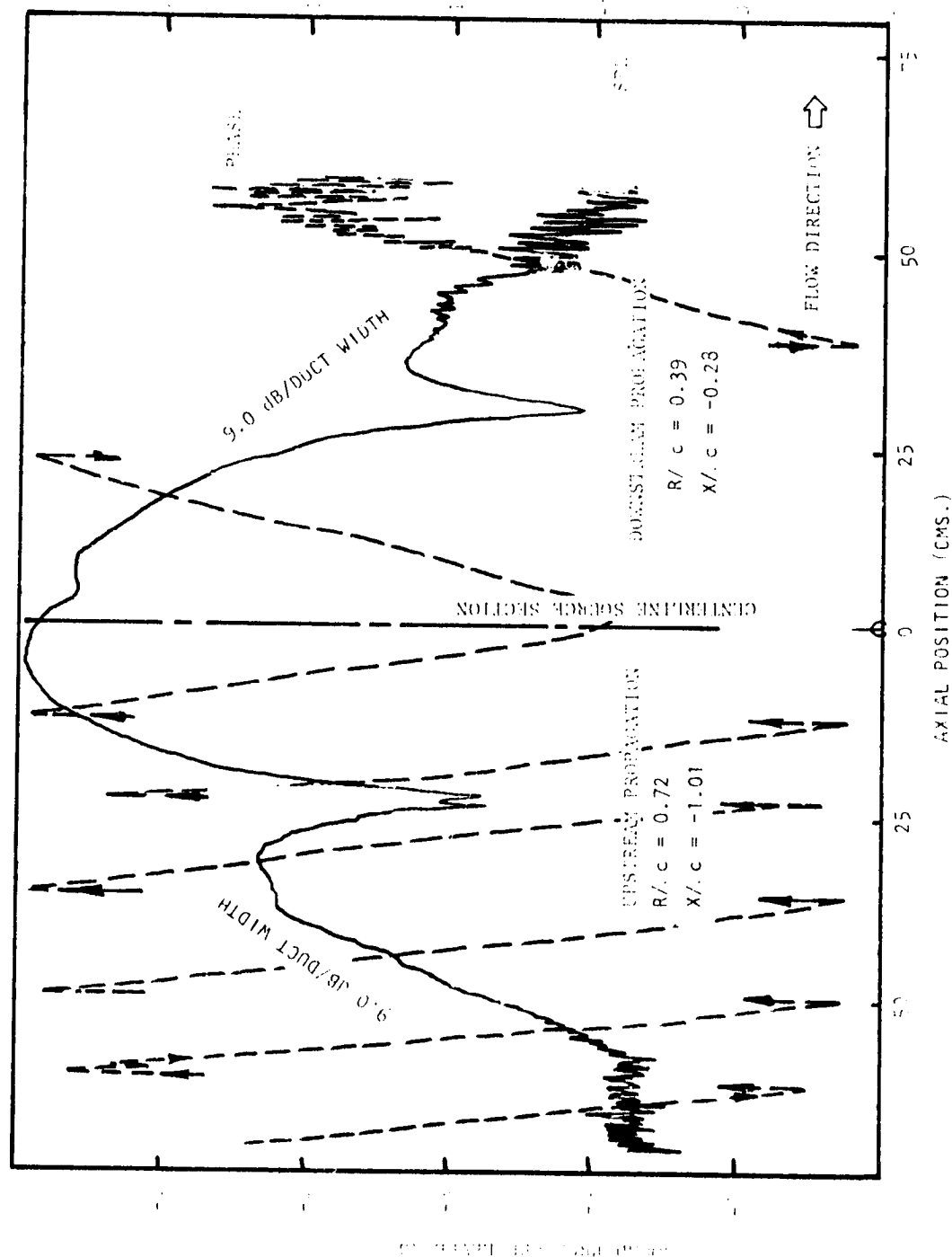
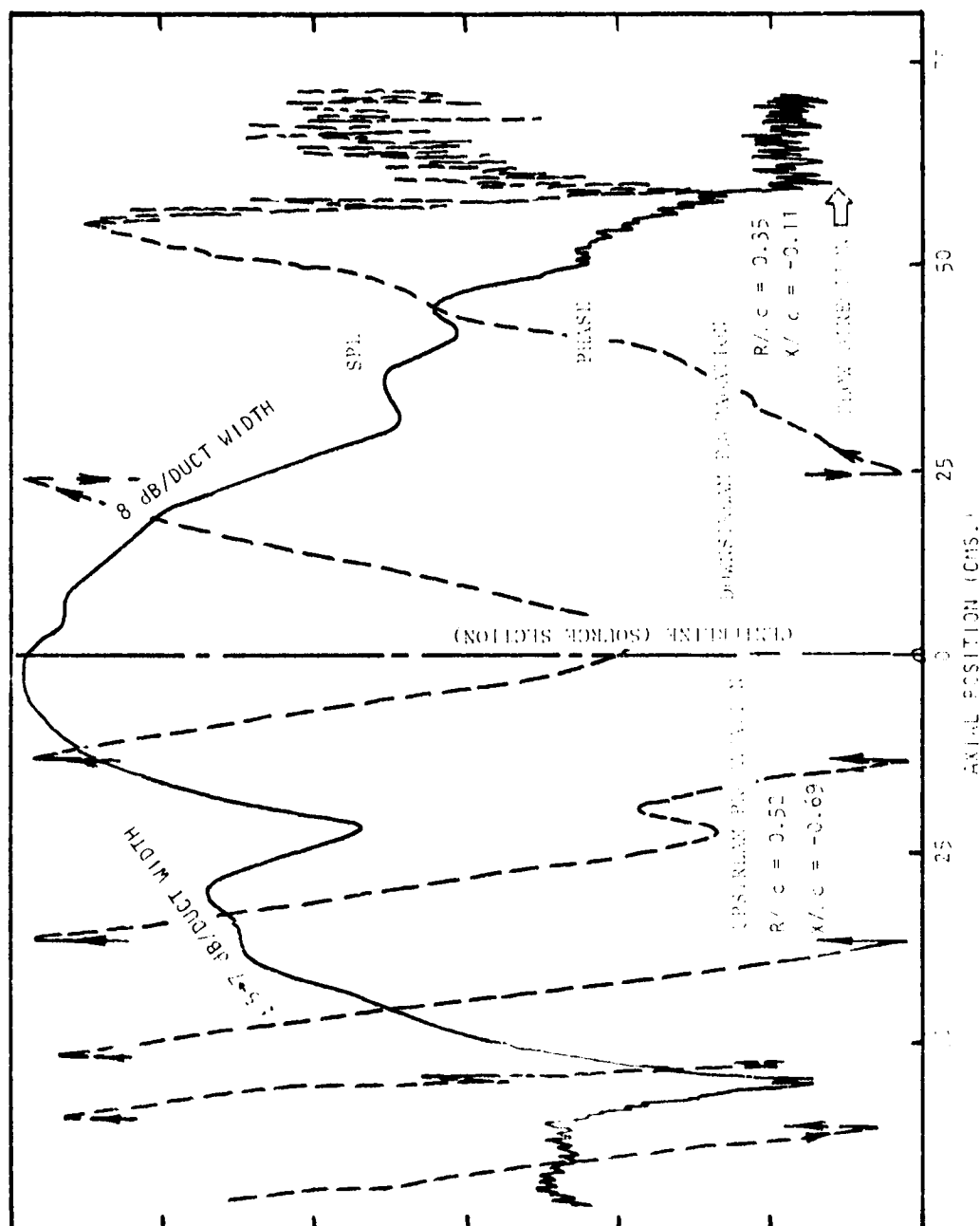


Figure 53(c) Axial Sound Pressure and Phase Traverses in Duct Centerline at 1600 Hz. Bias Flow $M_1 = 0.015$, Grating $EL = M_2 = 0.05$

PHASE (DEGREES)

[illegible]

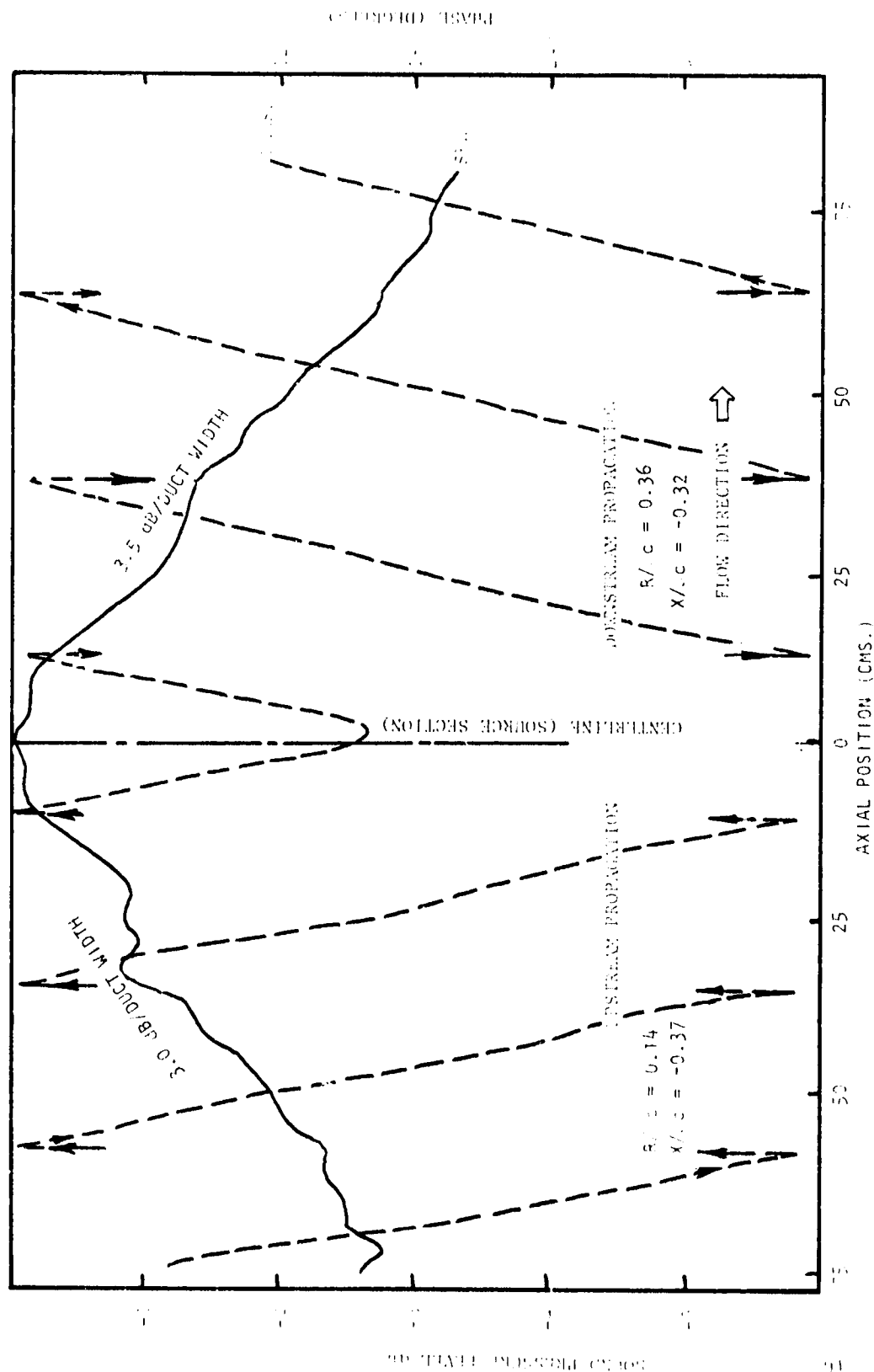


Figure 34 a) Axial Sound Pressure and Phase Traverses on Duct Centerlines at 1700 Hz. Bias Flow $M_1 = 0.0$, Grazing Flow $M_2 = 0.0$

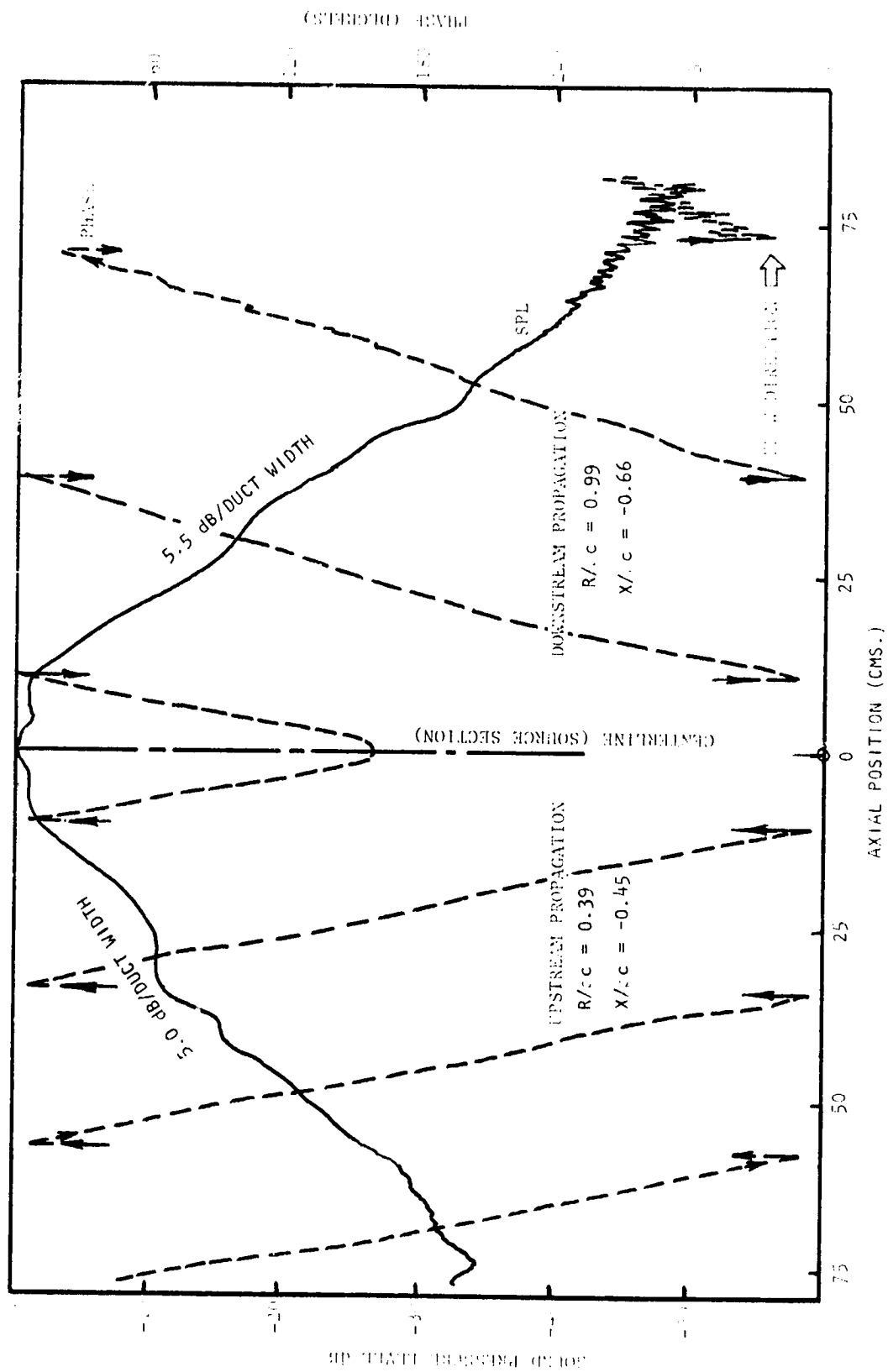


Figure 54(b) Axial Sound Pressure and Phase Traverses on Duct Centerline at 1700 Hz. Bias Flow $M_j = 1.015$, Grazing Flow $M_{GF} = 0.0$

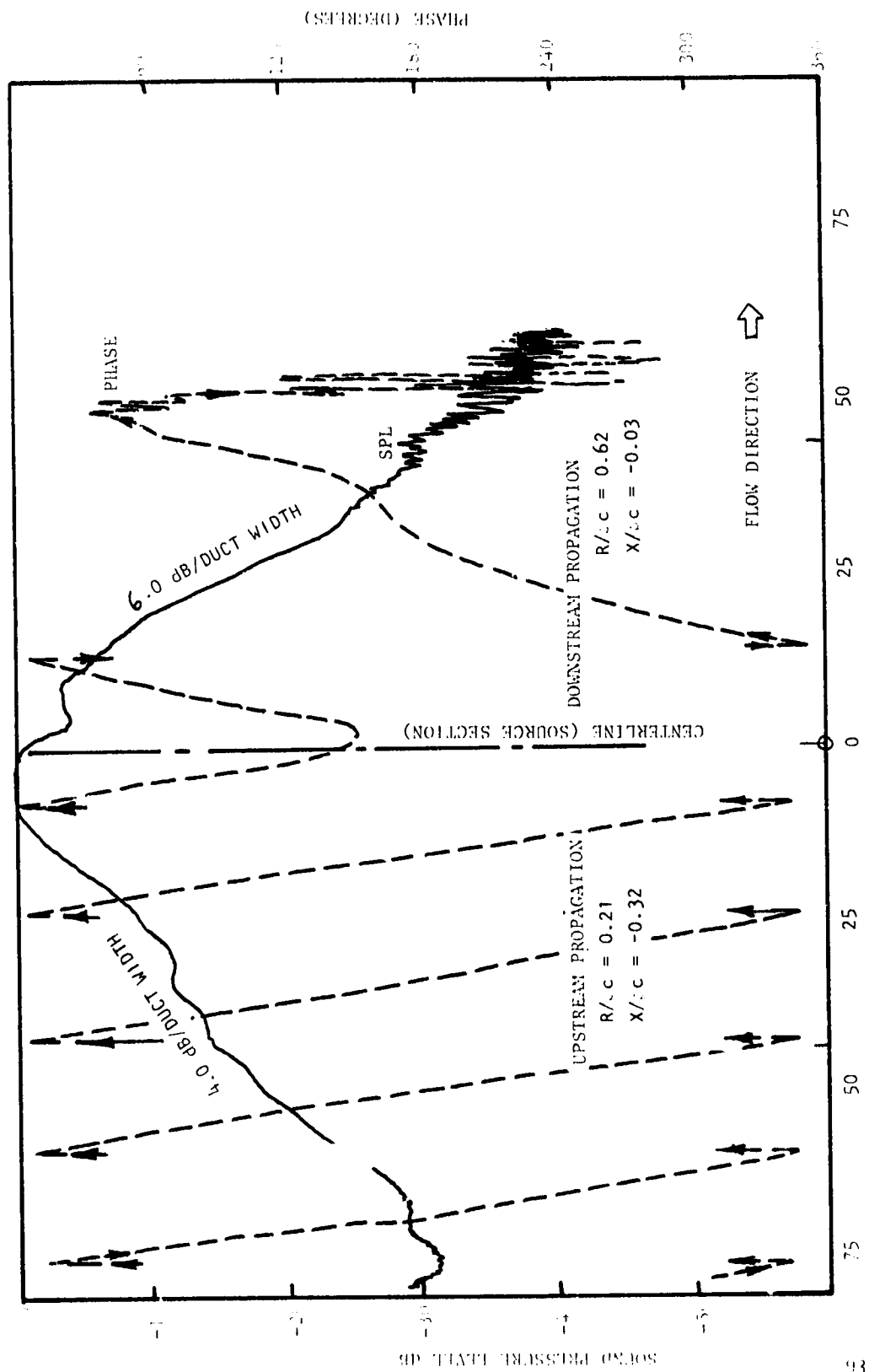


Figure 54(c) Axial Sound Pressure and Phase Traverses on Duct Centerline at 1700 Hz. Bias Flow $M_1 = 0.015$, Grazing Flow $M_G = 0.25$

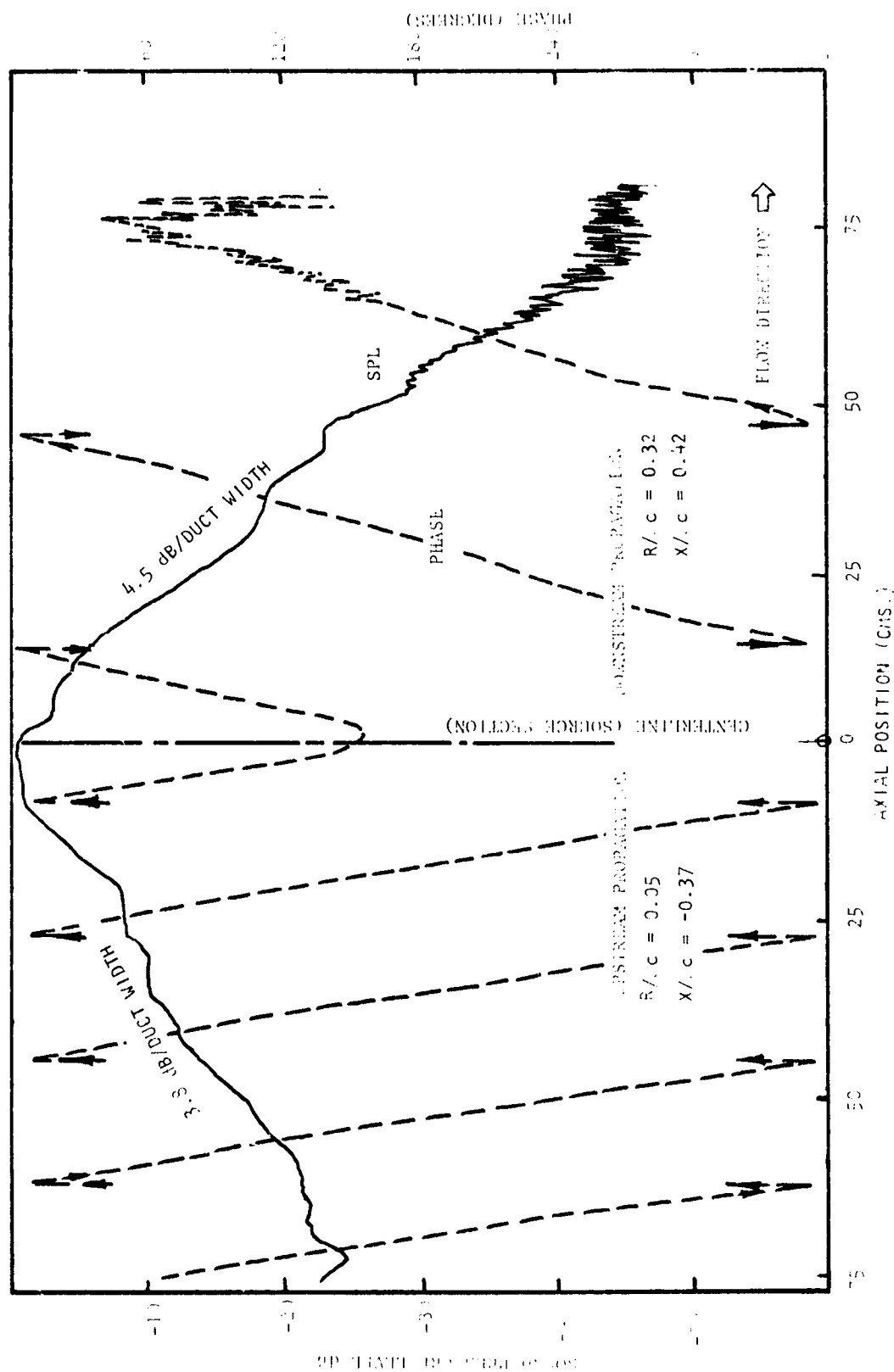


Figure 2-30. 2000 Hz, 60 dB SPL, Pressure and Phase Traverses on Duct Centerline. $R/c = 0.05$, $X/c = -0.37$ (UPSTREAM PROPAGATION); $R/c = 0.32$, $X/c = 0.42$ (DOWNSTREAM PROPAGATION). Flow $M_0 = 0.0$, Grazing Flow $M_{GF} = 0.25$.

the maximum decay rate. For downstream propagation*, at zero grazing flow, the effect of bias flow is to increase the attenuation rate from 3.0 to 3.5 dB per duct width (Figures 50a and 50b). While this may not appear large over the 12 duct widths of measurement, it represents some 6 dB overall, with a smoother decay curve due to the reduced interference of reflected waves. In the presence of grazing flow, the effect of bias flow also increases the attenuation by about 0.5 dB per duct width. One point of note on Figure 50a is that the downstream axial location A-A represents the junction between each 45.72 cm (18-inch) liner segment. This discontinuity resulted in an impedance mismatch with consequent reflections back towards the source. Subsequent examination revealed the cause to be a small air gap (about 1 mm) between the liner sections. An interesting nonlinear decay region (with peak decay rates of about 7 dB per duct width) occurred immediately downstream of the source section (see B-B in Figure 50b). This could be due to either a source near-field effect, or nonlinear high sound pressure level effects on the perforate facing sheet.

As the frequency increases, both upstream and downstream attenuations increase, with the effect of bias flow again being to smooth out the termination reflections. For example, at 1500 Hz in Figure 52b, and again in the upstream case, about 0.5 dB per duct width increase in attenuation rate is produced by bias flow. It is interesting to note that the addition of grazing flow to bias flow, Figure 52c, further improves the attenuation and shows the need for more resistive liner behavior. In the downstream case at 1500 Hz, however, there appears to be axially periodic interference patterns coupled with attenuation rates of about 6 dB per duct width. Past experience with duct mode interference patterns (ref. 13-15) points to secondary mode interference which is indicative of the liner impedance being near the optimum region of the branch point, where the first two modes have comparable large attenuation rates. Figure 52c shows that the combined resistive action of grazing flow and bias flow is sufficient to separate the two attenuation rates such that a reduced smoother decay pattern results.

An increase of frequency to 1600 Hz, the design condition, proves that the optimum condition is imminent. The downstream attenuation for zero grazing flow dramatically changes from 4.2 to 7 dB per duct width with the addition of bias flow of Mach number 0.015 (see Figures 53a and 53b). With a grazing flow Mach number of 0.25, the addition of bias flow only increases the attenuation from 8 to 9 dB per duct width, as shown in Figures 53d and 53c, respectively. However, this is precisely the design philosophy conceived in the first instance. That is, high levels of grazing flow should require little or no bias to achieve high attenuation rates, while low levels of grazing flow should need large amounts of bias flow to maintain the high attenuation rates.

For the upstream liner the situation is a little less clear. Although the end result of high attenuation is achieved, it is apparent that again the

*In the absence of grazing flow the downstream liner is defined to be that to the left side of the source in the schematic of Figure 4d and conversely for the upstream liner.

impedance is a little too close to the optimum (the branch point), and modal interference is present. The addition of bias flow in the zero grazing flow produces a finite overall increase in attenuation. This modal interference phenomenon dramatically illustrates the risk involved in designing a liner to have maximum attenuation rates near the branch point. It is quite possible that local variations in impedance could lead to this condition, which could be considered desirable in practice.

If the frequency is again slightly increased to 1700 Hz (see Figure 54), these modal interference effects disappear with only minor termination reflections present. Thus, the concept is now clearly operating as designed. The application of bias flow dramatically increases the attenuation rates at zero grazing flow from 3 to 5 dB per duct width in the upstream direction of propagation, as in Figures 54a and 54b, and 3.5 to 5.5 dB per duct width in the downstream direction. For both liners under the influence of a grazing flow Mach number of 0.25, as in Figures 54c and 54d, the bias flow increases the upstream attenuation by only 0.2 dB per duct width and downstream attenuation by 1.5 dB per duct width. As was expected, the liner impedance is dominated by the grazing flow. Thus, Figure 54 is a good example of the operational feasibility of the concept.

As the frequency is further increased, the impedance moves further away from the optimum and attenuation rates are correspondingly reduced, as shown for example, in Figure 55 at 2 KHz. However, bias flow effects can still be observed, particularly in the downstream liner case, where the frequencies are still within Region I of the general bias flow characteristic pattern and not too far removed from the liner first-resonance condition.

It is of interest to recall that the upstream liner was designed to operate in a region just above the second resonance frequency. Thus, it should be possible to observe attenuation peaks at a lower frequency, near the first resonance point. Figure 56, corresponding to 500 Hz, shows that this condition is imminent. Comparison of Figure 56a and 56b shows a marked increase in attenuation at zero grazing flow with increase in bias flow from 1 dB per duct width to 4 dB per duct width for the case of upstream propagation. With a grazing flow Mach number of 0.25 present, bias flow provides an increase in attenuation from 3.5 to about 4.0 dB per duct width, the obvious implication being that the dominant need of this liner is for more resistance, since the effects of bias flow and grazing flow on the attenuation rates are similar. Thus, in this case, as predicted, bias flow proved extremely effective in improving the attenuation characteristics for the liner at reduced grazing flow. Figure 56e is included to illustrate the effect of bias flow on each of the two upstream liner segments in isolation. The heavy line shows the decay rate with bias flow applied to the liner segment closest to the source section, within which the decay rate has increased from 1.5 to 4.0 dB per duct width. The thin line shows the effect of bias flow applied only to the furthest upstream liner segment, with similar enhancement of the decay rates. Somewhat surprisingly or perhaps fortuitously, overall attenuation is identical.

On all the attenuation plots, the simultaneous measurements of axial phase changes are shown superimposed. The first point to note is the wide differences possible in axial wavenumber (visualized as axial wavelength or

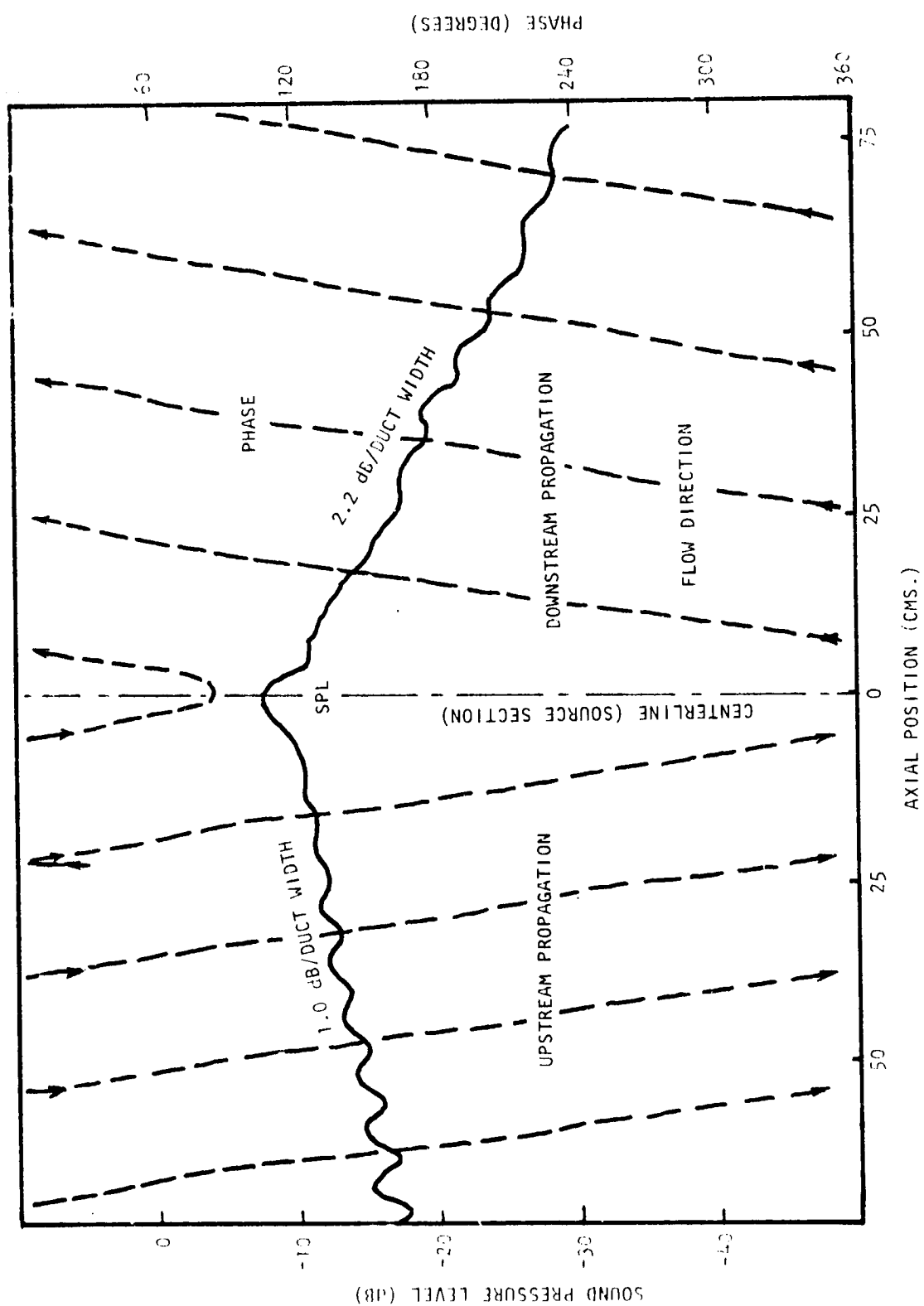


Figure 55(a) Axial Sound Pressure and Phase Traverses on Duct Centerline at 2 KHz. Bias Flow $M_i = 0.0$, Grazing Flow $M_{GF} = 0.0$

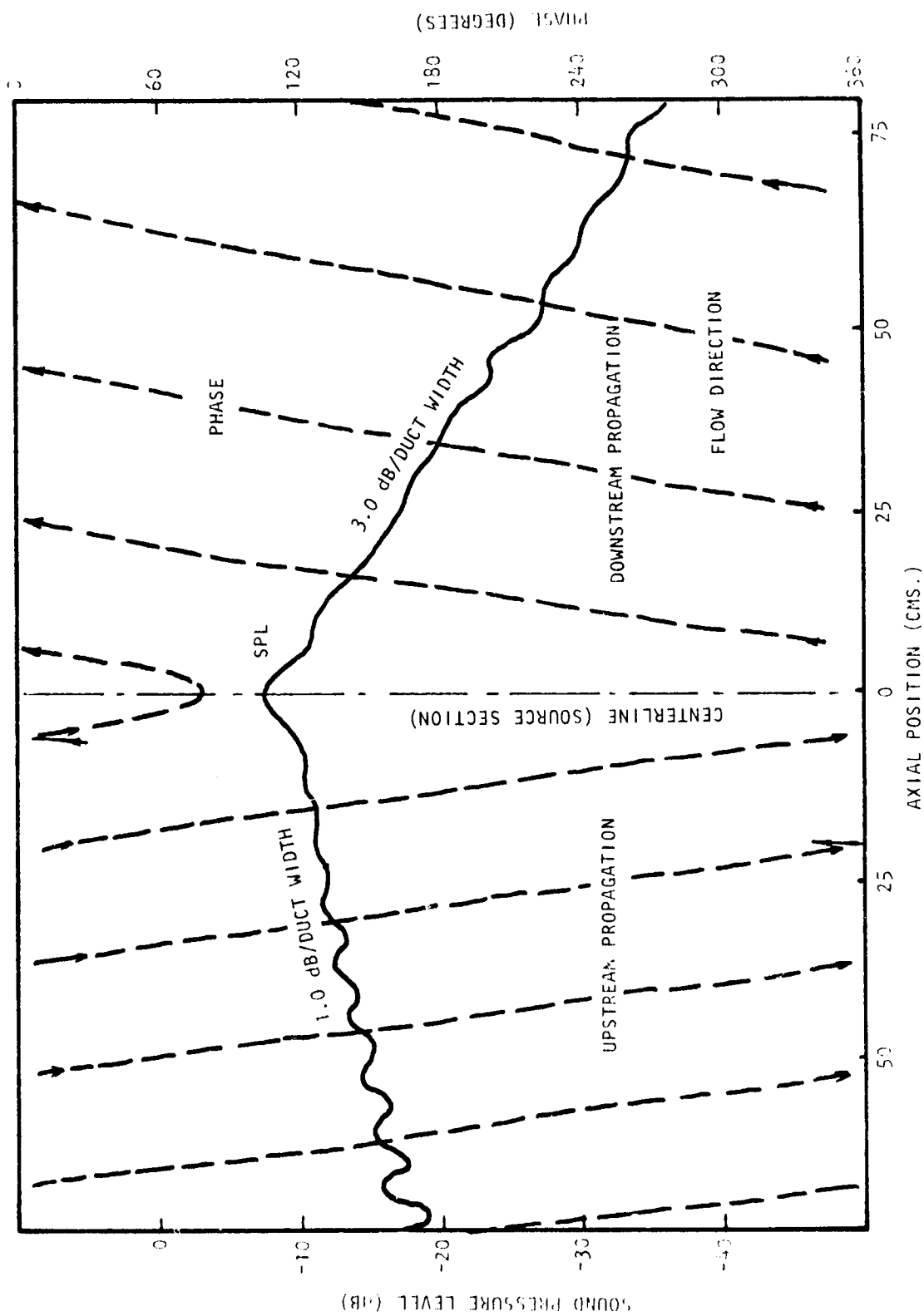


Figure 55(b) Axial Sound Pressure and Phase Traverses on Duct Centerline at 2 KHz. Bias Flow $M_0 = 0.015$, Grazing Flow $M_{GF} = 0.0$

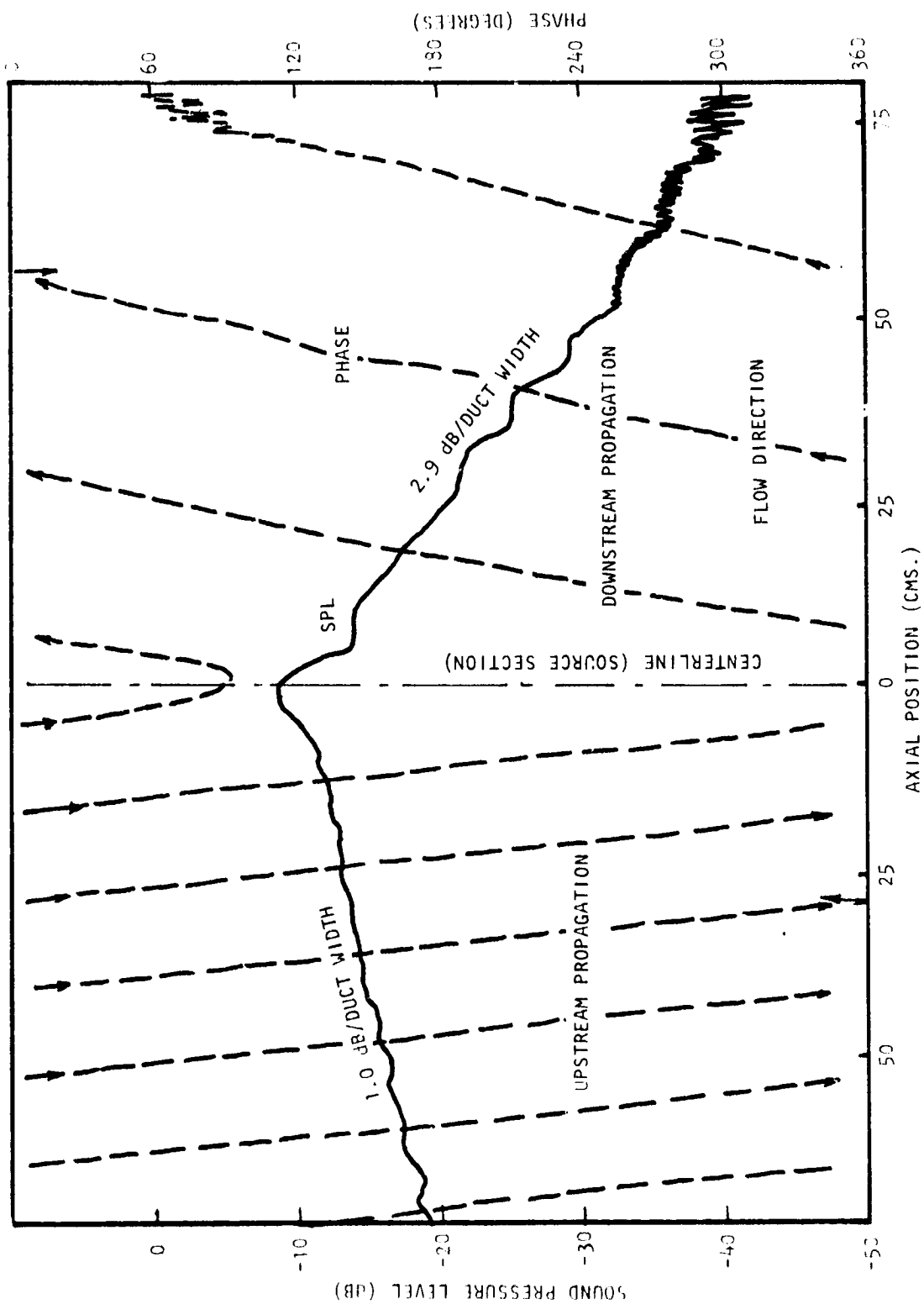


Figure 55(c) Axial Sound Pressure and Phase Traverses on Duct Centerline at 2 KHz. Bias Flow $M_i = 0.015$, Grazing Flow $M_{GF} = 0.25$

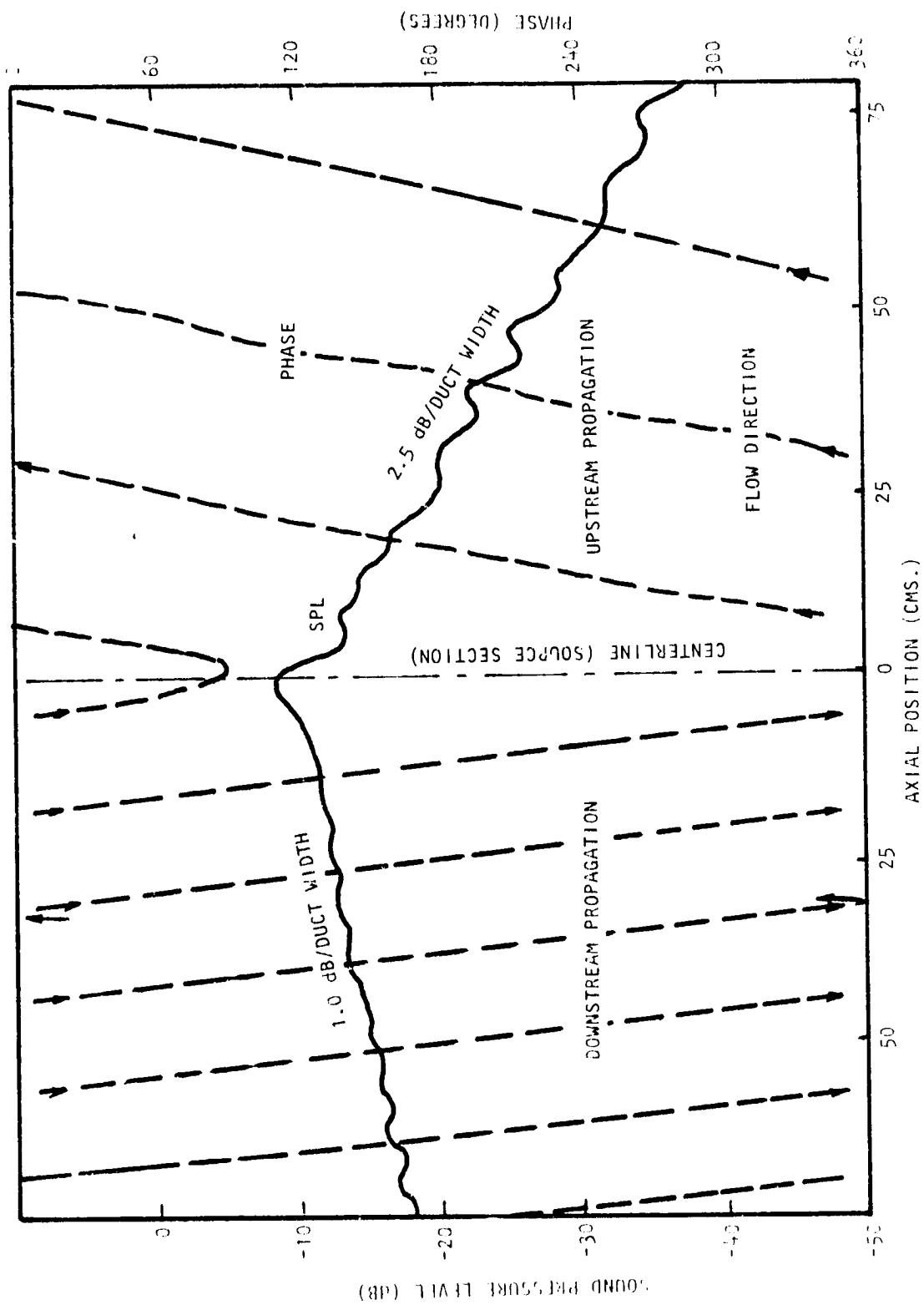
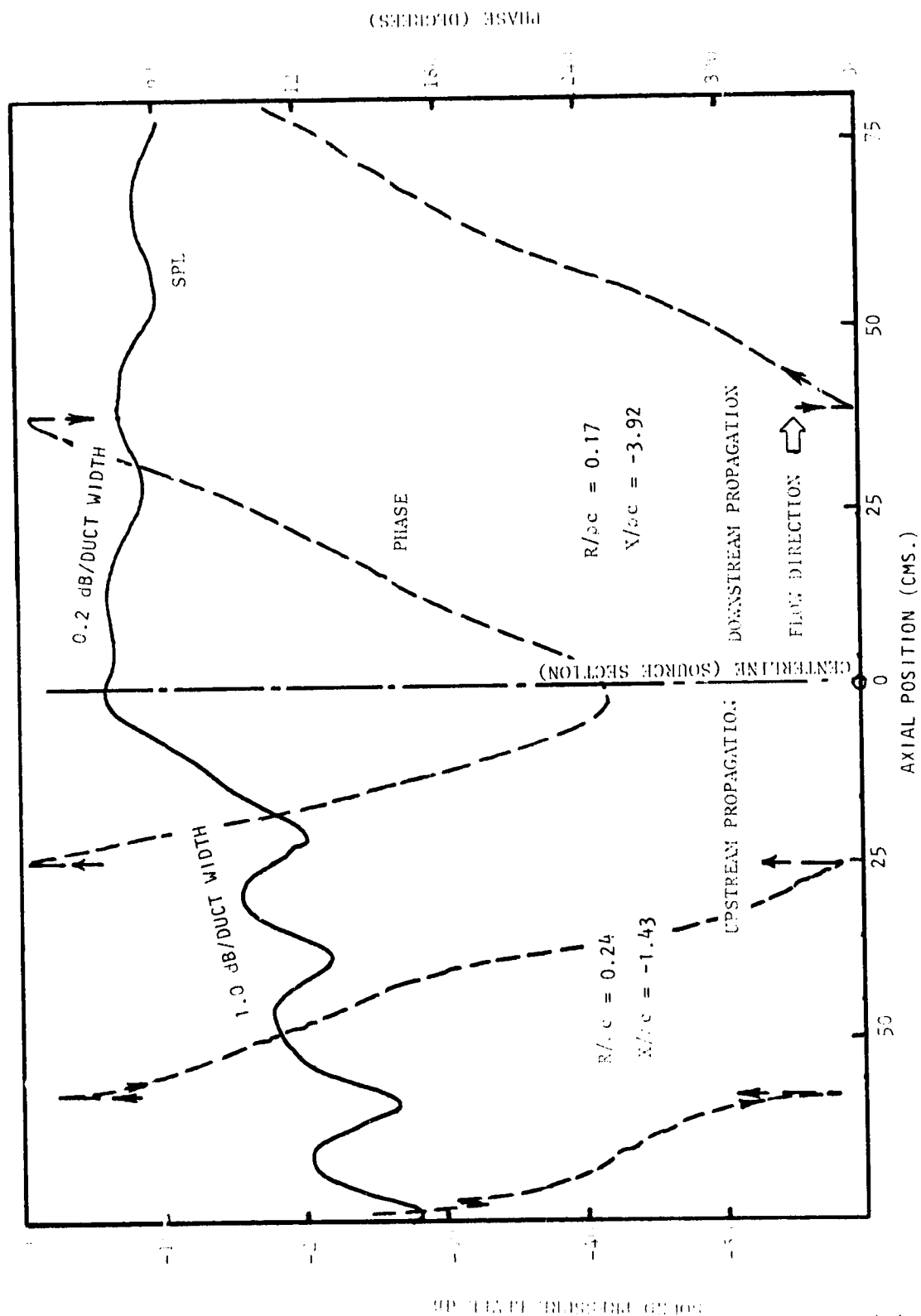


Figure 55(d) Axial Sound Pressure and Phase Traverses on Duct Centerline at 2 KHz. Bias Flow $M_i = 0.0$, Grazing Flow $M_{GF} = 0.25$



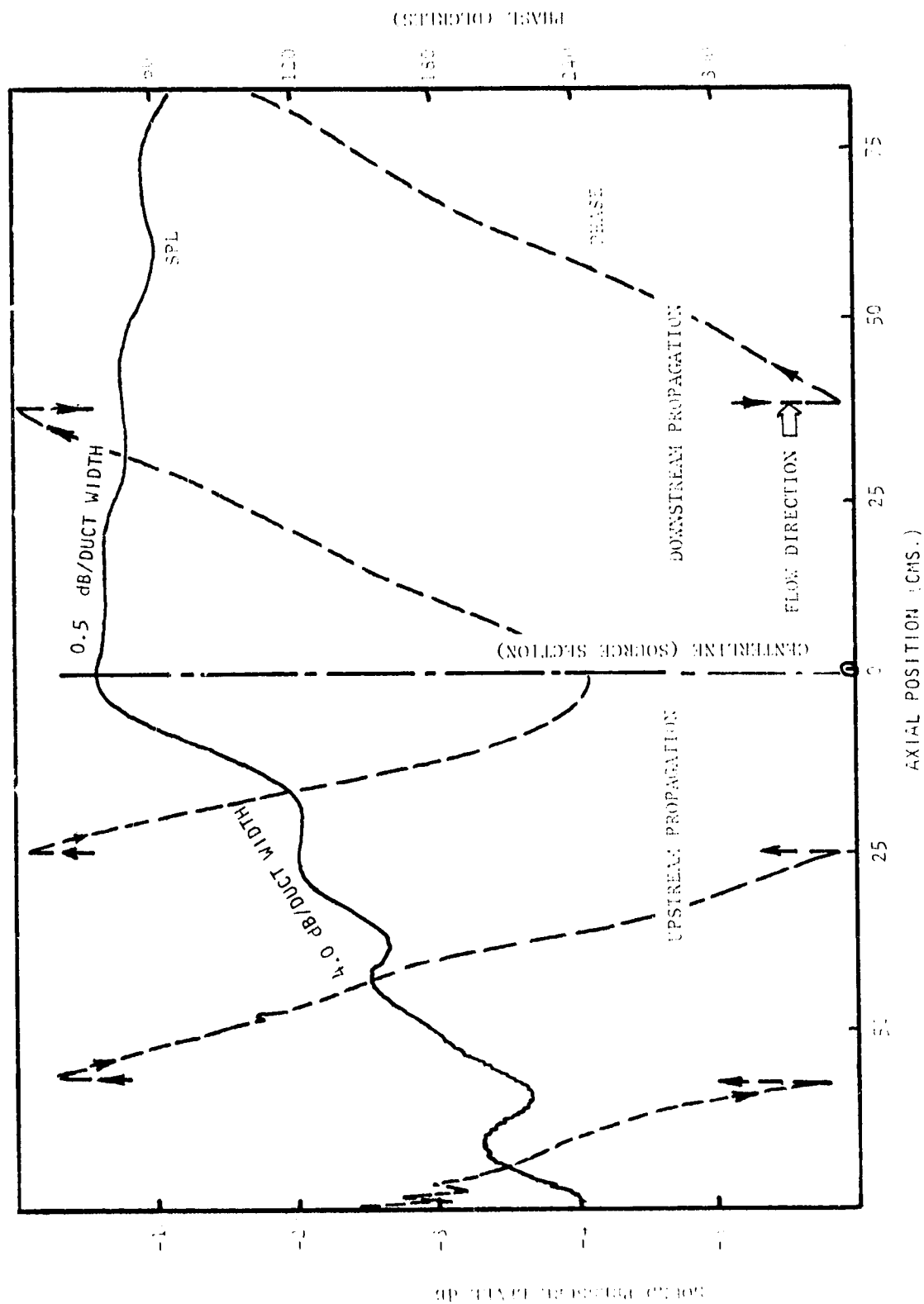


Figure 5615: Axial Sound Pressure and Phase Traverses on Duct Centerline at 500 Hz. Pipe Flow $Q = 0.015$ Grazing Flow $U_{gr} = 0.5$

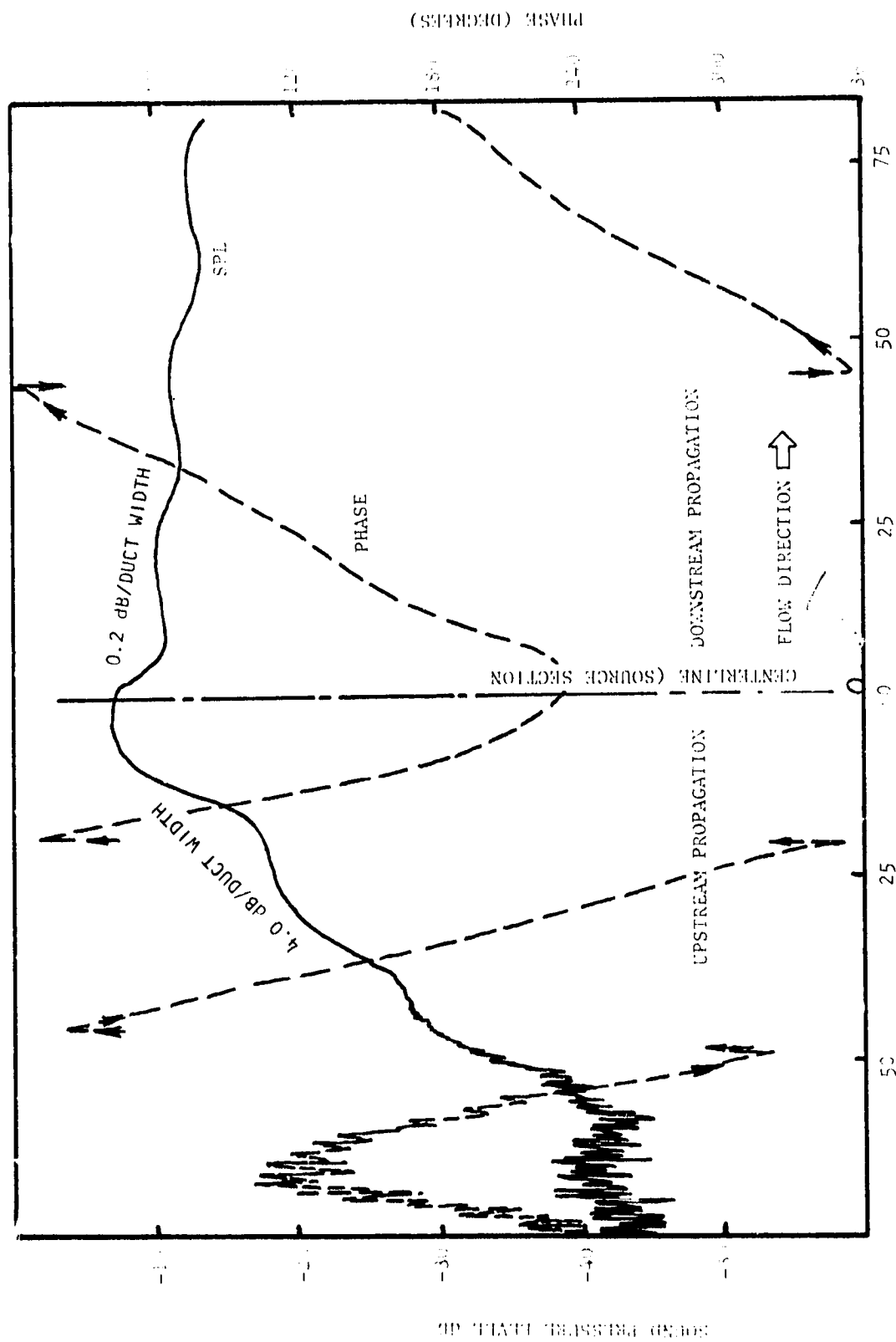


Figure 56(c) Axial Sound Pressure and Phase Traverses on Duct Centerline at 500 Hz. Bias Flow $M_1 = 0.015$, Grazing Flow $M_{GF} = 0.15$

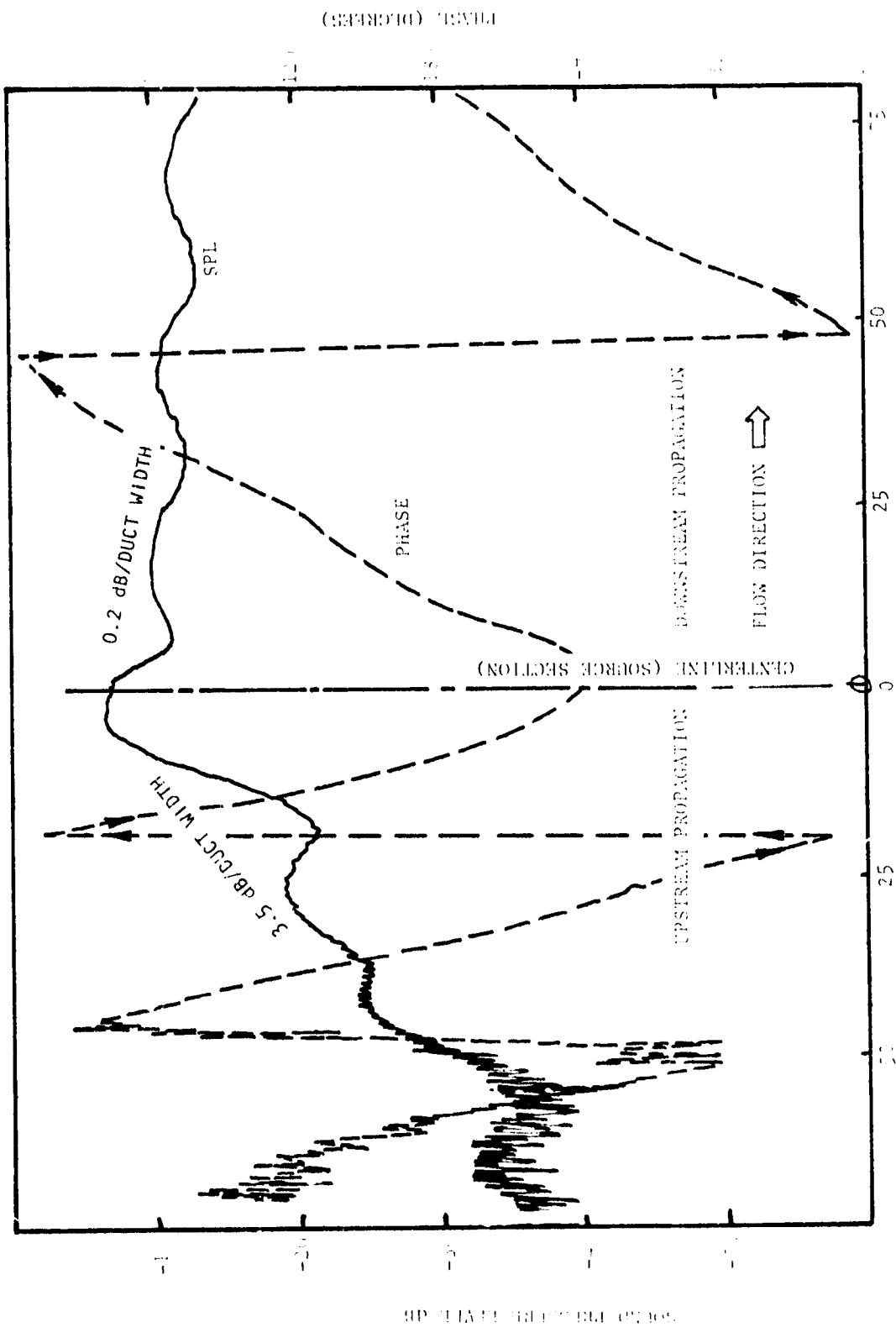


Figure 56(3) Axial Sound Pressure and Phase Traverses on Duct Centerline at 500 Hz. Bias Flow $M_1 = 0.0$, Grazing Flow $M_{g1} = 0.25$

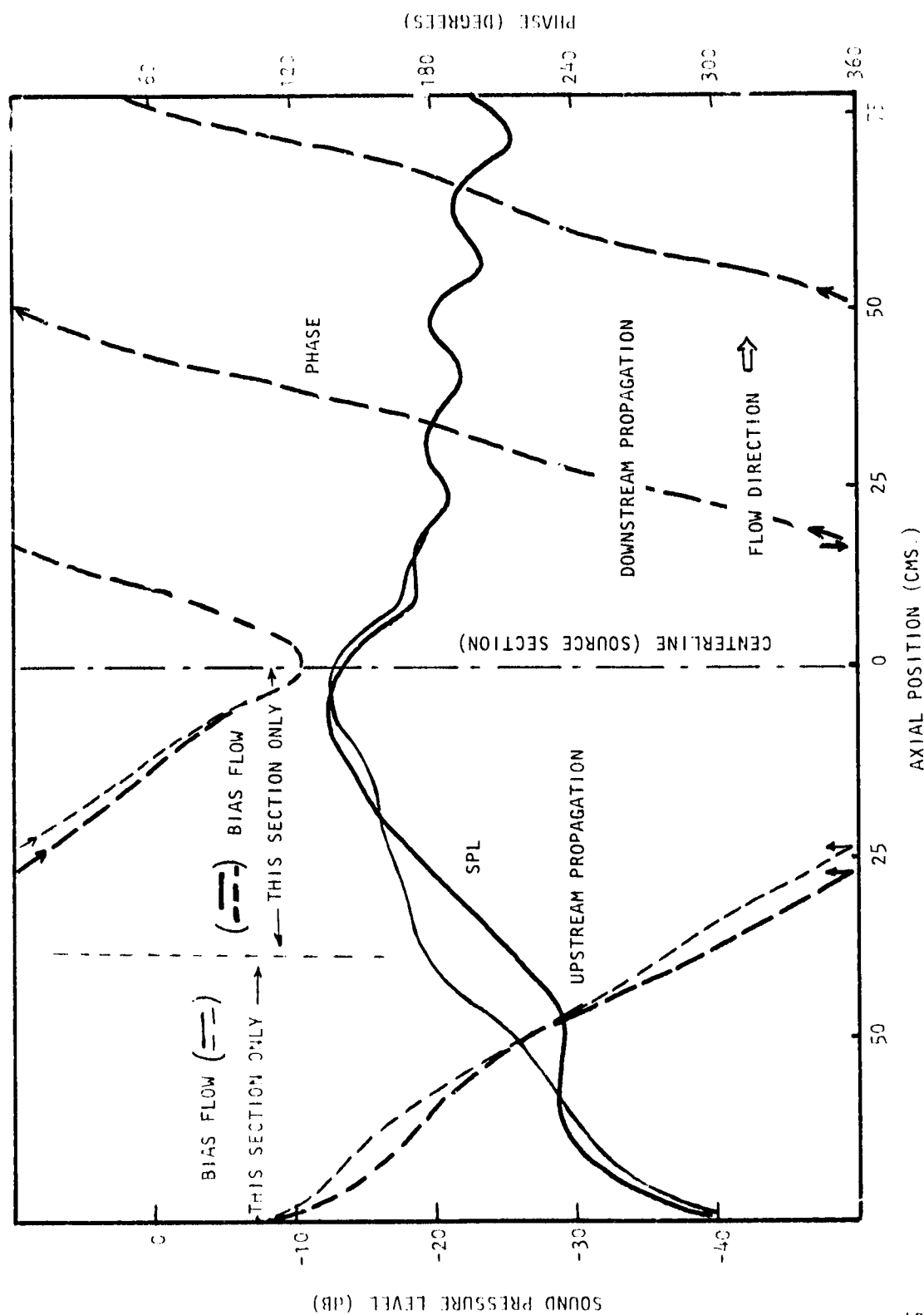


Figure 56(e) Axial Sound Pressure and Phase Traverses on Duct Centerline at 500 Hz. Bias Flow $M_i = 0.15$ Upstream Only, Grazing Flow $M_{GF} = 0$.

distance necessary to accommodate 360 degrees of phase change). The influence of the impedance boundary condition can be seen by comparison of the upstream and downstream liner cases in Figure 57 at 800 Hz with no grazing flow. The upstream wavelength is almost two and a half times as large as that of the downstream case. The virtually linear change of phase with axial distance implies a freely propagating wave (or single mode), with, in this case, a nearly uniform attenuation rate. The presence of standing waves, as in the downstream liner case of Figure 57, will produce *periodic* departures from linearity which result in more pronounced points of inflection, the larger the standing-wave ratio. In the limit, of course, such as is often seen in a standing-wave tube, perfect reflection will produce a step change of phase of 180 degrees in the nodal points. However, the important and often overlooked feature of these phase changes is that even if the phase rate of change with axial distance is not constant, since these phase changes are periodic, the measured axial wavelength remains essentially constant (i.e., the axial distance remains constant between two points 360 degrees apart in phase), provided the standing wave peak *difference* between successive interference cycles remains less than 1 or 2 dB. For more clarification of this point, see Plumblee *et al* (ref. 12).

The second point to note is the effect of convection on the phase speed. The addition of a Mach 0.25 grazing flow to Figure 56b results in a negligible attenuation change (see Figure 56c) for the upstream liner, but a considerably reduced wavelength. In simplistic terms, if the duct wall impedance were infinite, the wavelength would be reduced by a factor of $(1 - M_{GF})$. In fact, wall impedance and convection effects are linked [see Morse and Ingard (ref. 2)], but the axial wavelength can be a useful measurement as it is a fundamental part of the propagation constant.

To make realistic comparisons of theoretical and experimental propagation constants, an accurate estimate of the liner impedance is needed. In-situ impedance measurements were made on both liners for the four extremes of operation at three frequencies: 1250 Hz, 1.6 KHz, and 1.7 KHz (some cases at 500 Hz are also given). The sound pressure and phase traverses together with derived impedances are shown in Appendix H. The case of immediate interest is that of 1600 Hz, and Table II gives a comparison of measured and design impedances corresponding to the test case shown in Figures 58b and d, and 59b and d. In general, although agreement is reasonable, the measured resistances in the presence of grazing flow are lower than the design values. This inconsistency points to an inherent weakness in the impedance model and/or to defects in liner construction.

That the measured impedance values are substantially correct can be inferred from Table III, which compares measured and calculated attenuations and phase speeds at the design frequency using the measured in-situ impedance as the boundary condition for evaluation of the propagation constants. The agreement is remarkable, particularly in the zero grazing flow regime. In the presence of grazing flow, the attenuation rates agree quite well. However, the calculated phase velocities are all on the high side, which could be attributed to the inability of the "plug" flow model to account for wall shear effects. Another reason might be that impedance values measured in the presence of grazing flow may contain small errors to which the phase velocity is particularly sensitive.

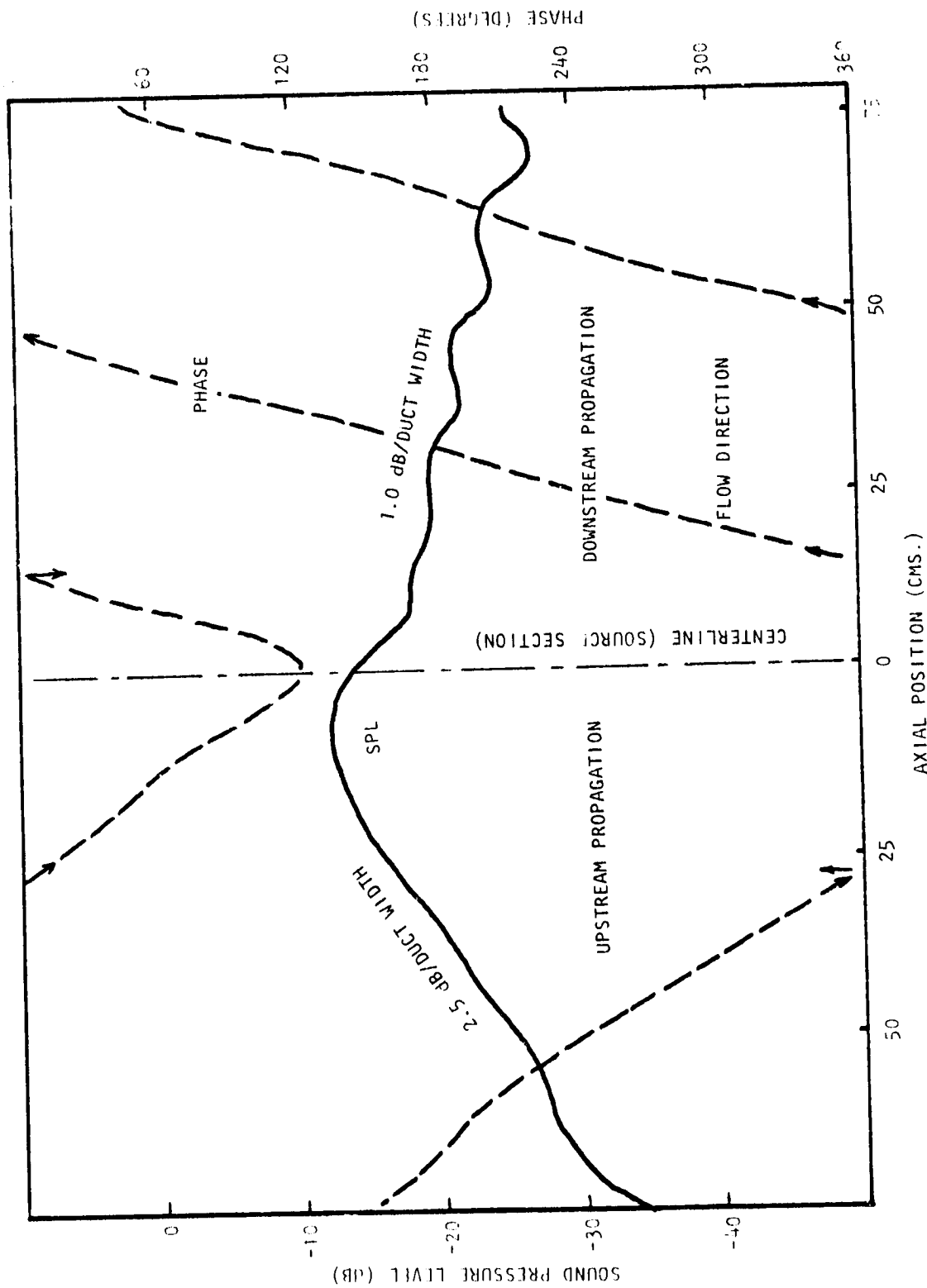


Figure 57 Axial Sound Pressure and Phase Traverses at Duct Centerline at 800 Hz. Bias Flow $M_1 = 0.015$, Grazing Flow $M_{GF} = 0.0$

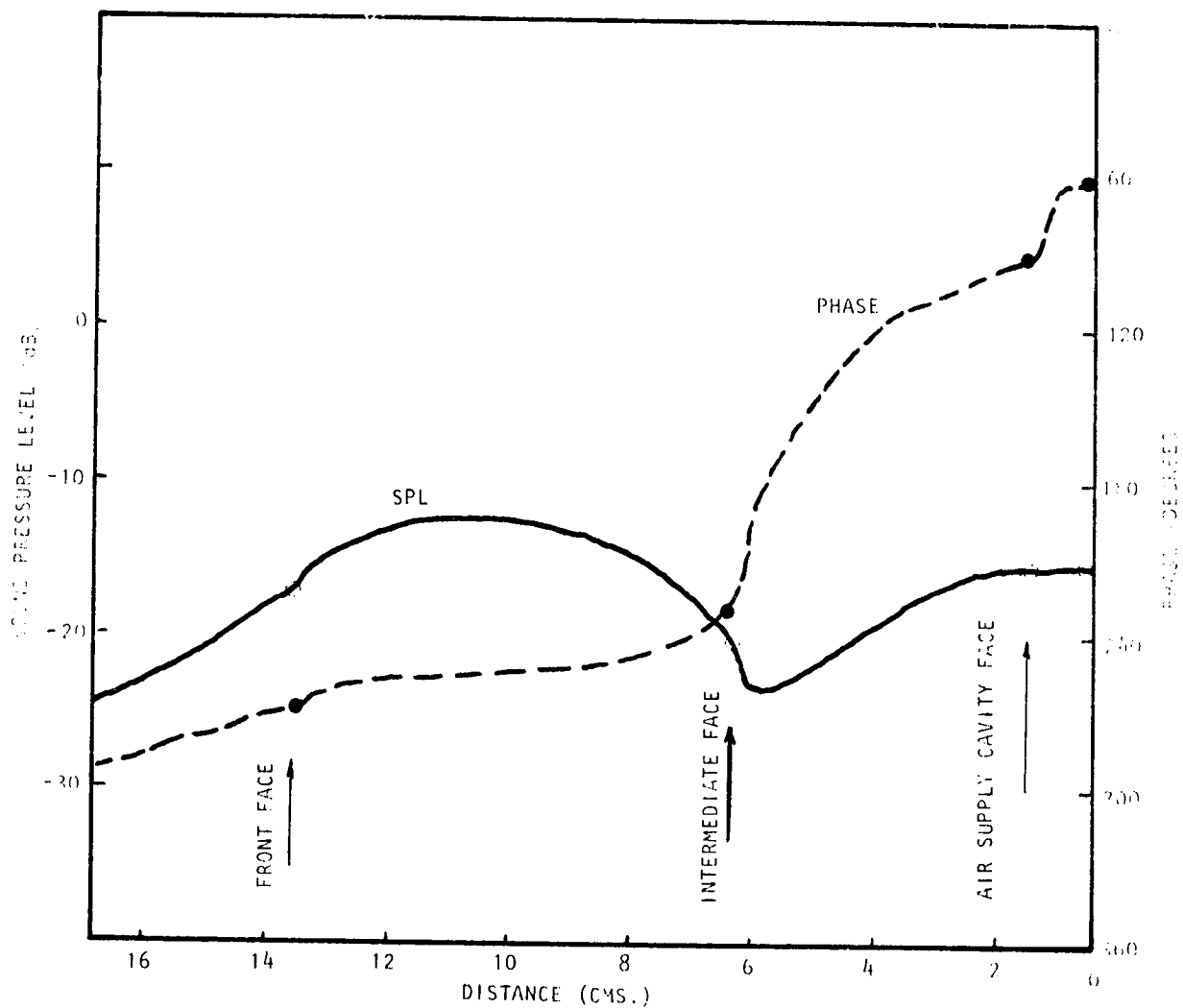


Figure 58(a) Sound Pressure and Phase Traverses within Upstream Liner at 1600 Hz. Bias Flow $M_b = 0.0$, Grazing Flow $M_{GF} = 0.0$

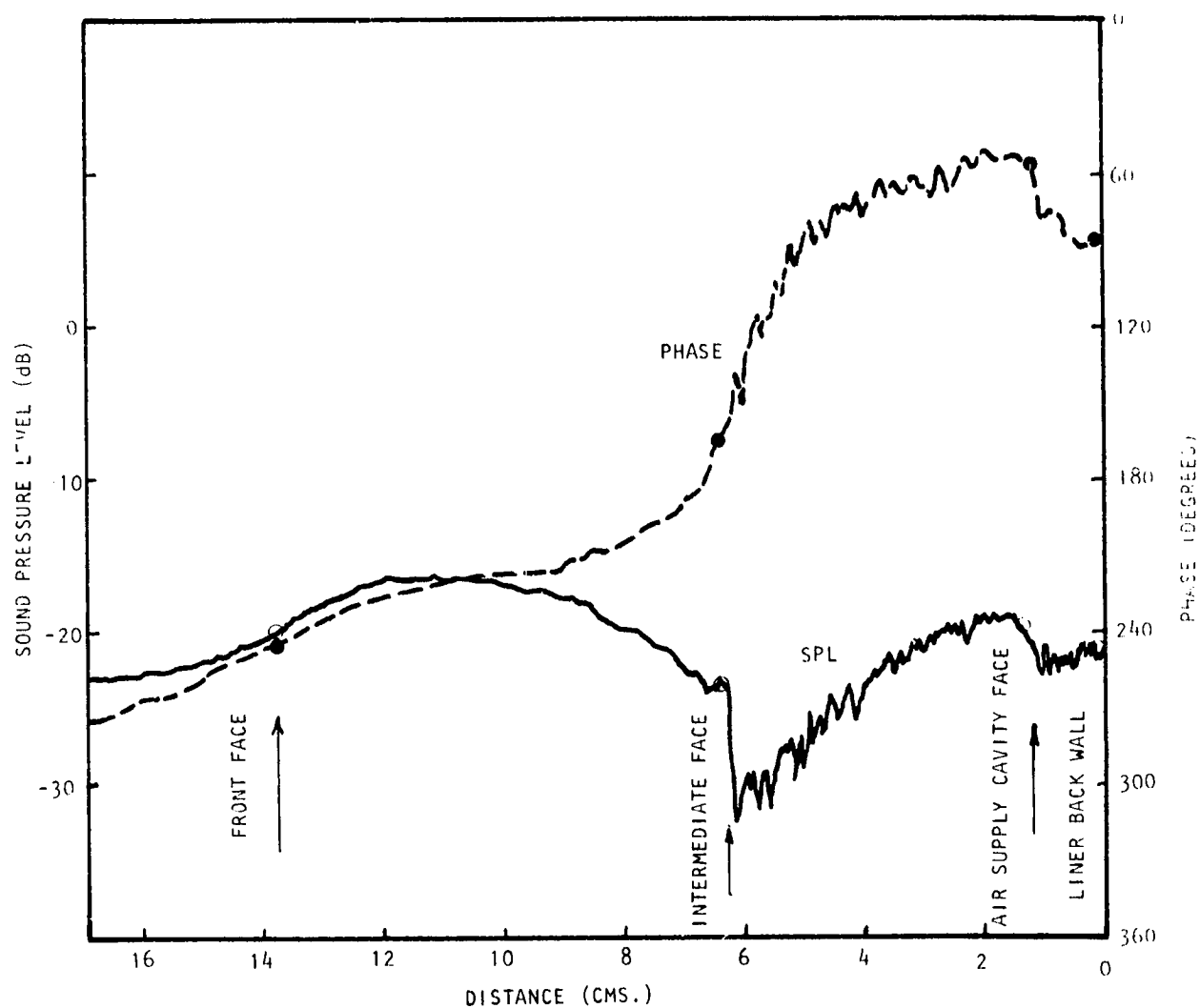


Figure 58(b) Sound Pressure and Phase Traverses within Upstream Liner at 1600 Hz. Bias Flow $M_i = 0.015$, Grazing Flow = 0.0

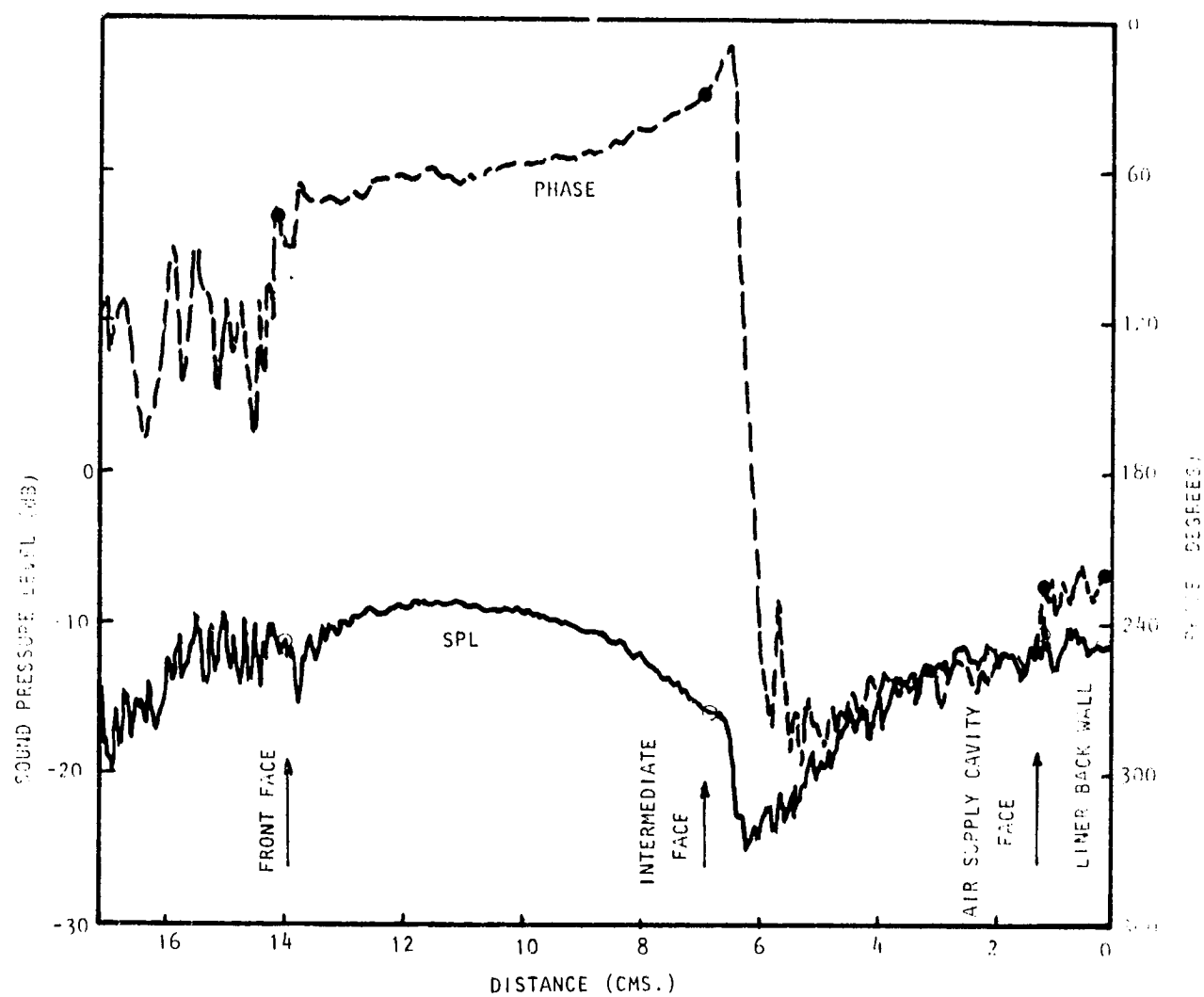


Figure 58(c) Sound Pressure and Phase Traverses within Upstream Liner at 1600 Hz. Bias Flow $M_j = 0.015$, Grazing Flow = 0.25

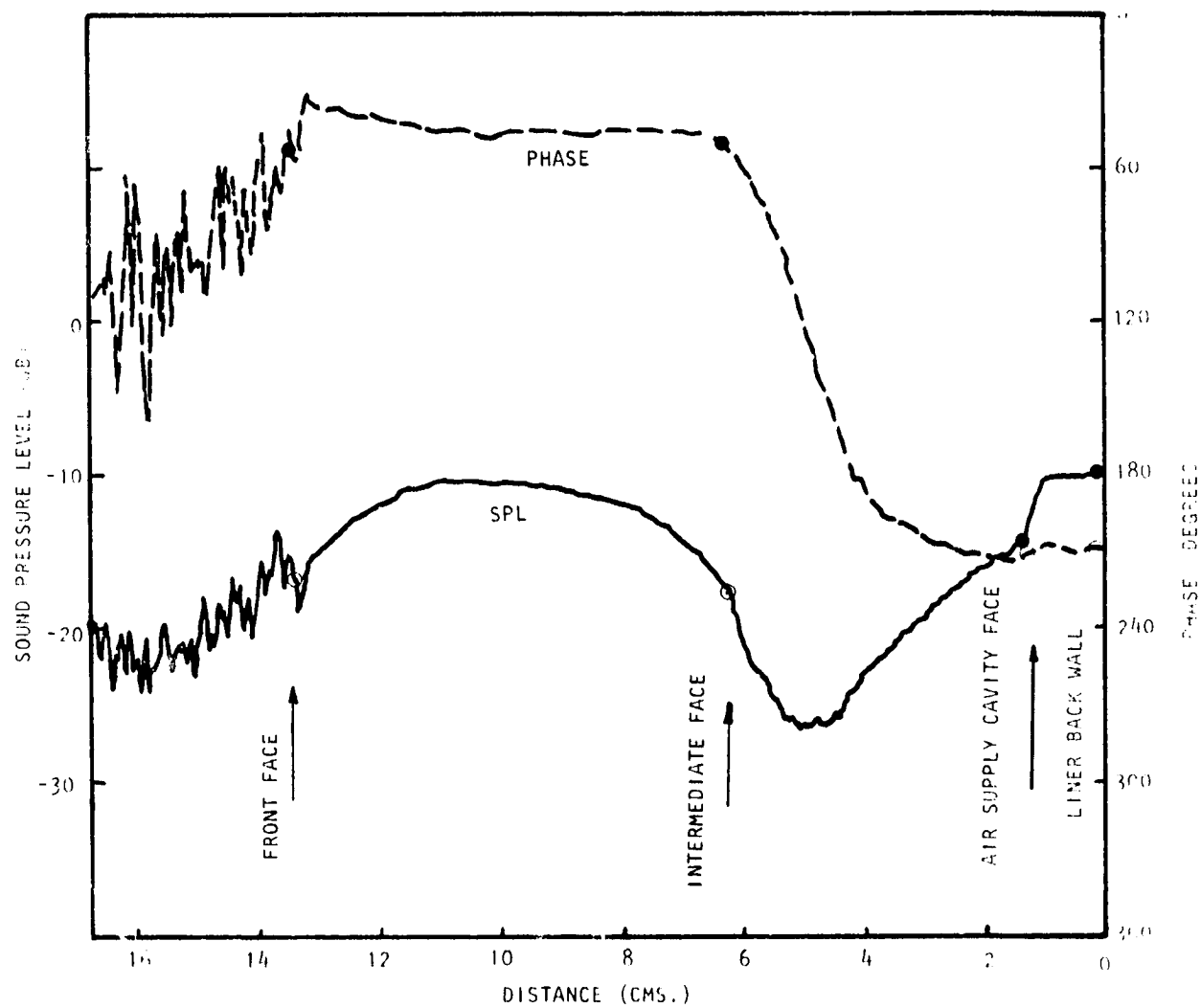


Figure 58(d) Sound Pressure and Phase Traverses within Upstream Liner at 1600 Hz. Bias Flow $M_i = 0.0$, Grazing Flow = 0.25

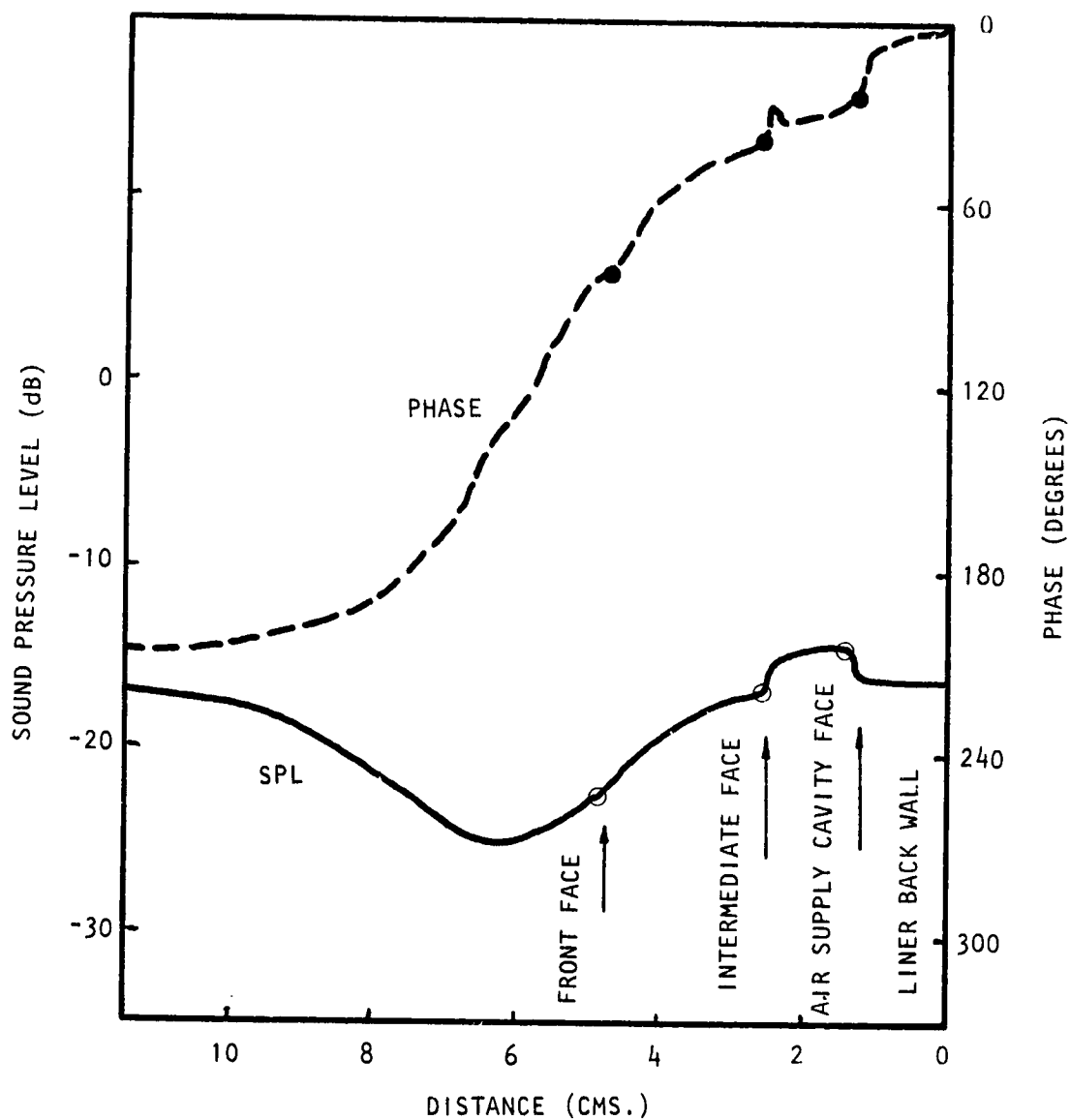


Figure 59(a) Sound Pressure and Phase Traverses within Downstream Liner at 1600 Hz. Bias Flow $M_i = 0.0$, Grazing Flow $M_{GF} = 0.0$

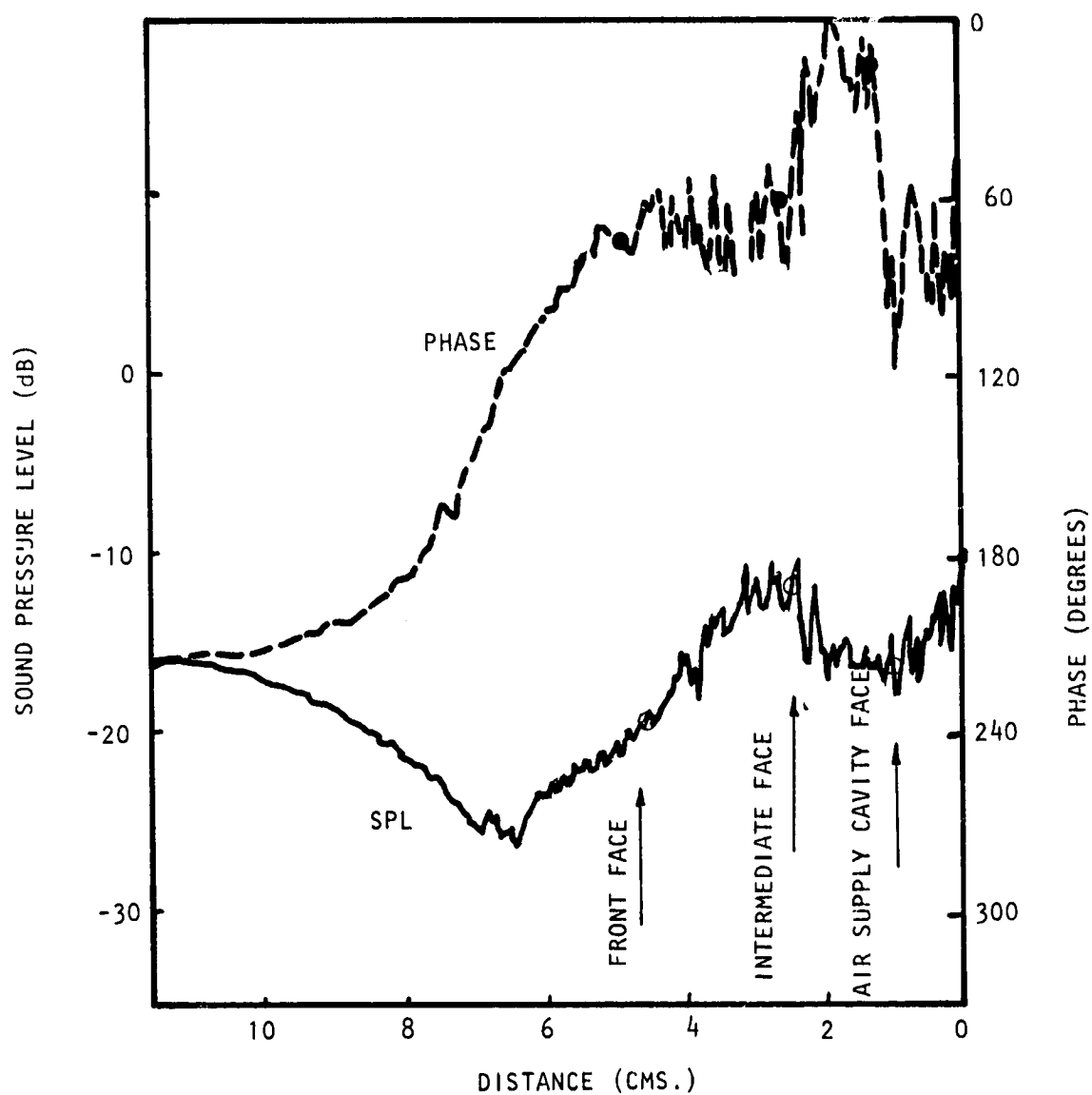


Figure 59(b) Sound Pressure and Phase Traverses within Downstream Liner at 1600 Hz, Bias Flow $M_i = 0.015$, Grazing Flow $M_{GF} = 0.0$

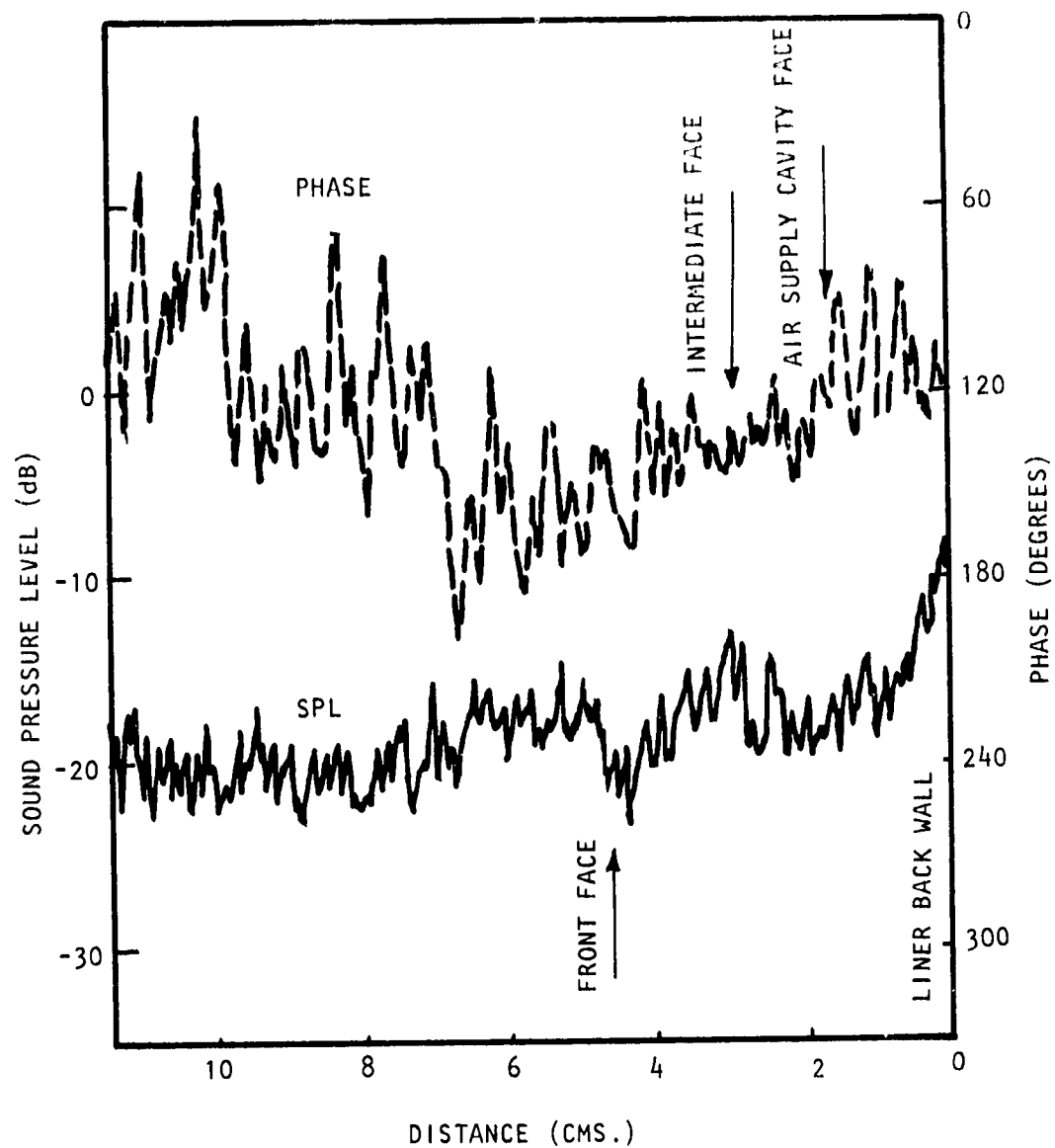


Figure 59(c) Sound Pressure and Phase Traverses within Downstream Liner at 1600 Hz. Bias Flow $M_i = 0.015$, Grazing Flow $M_{GF} = 0.25$

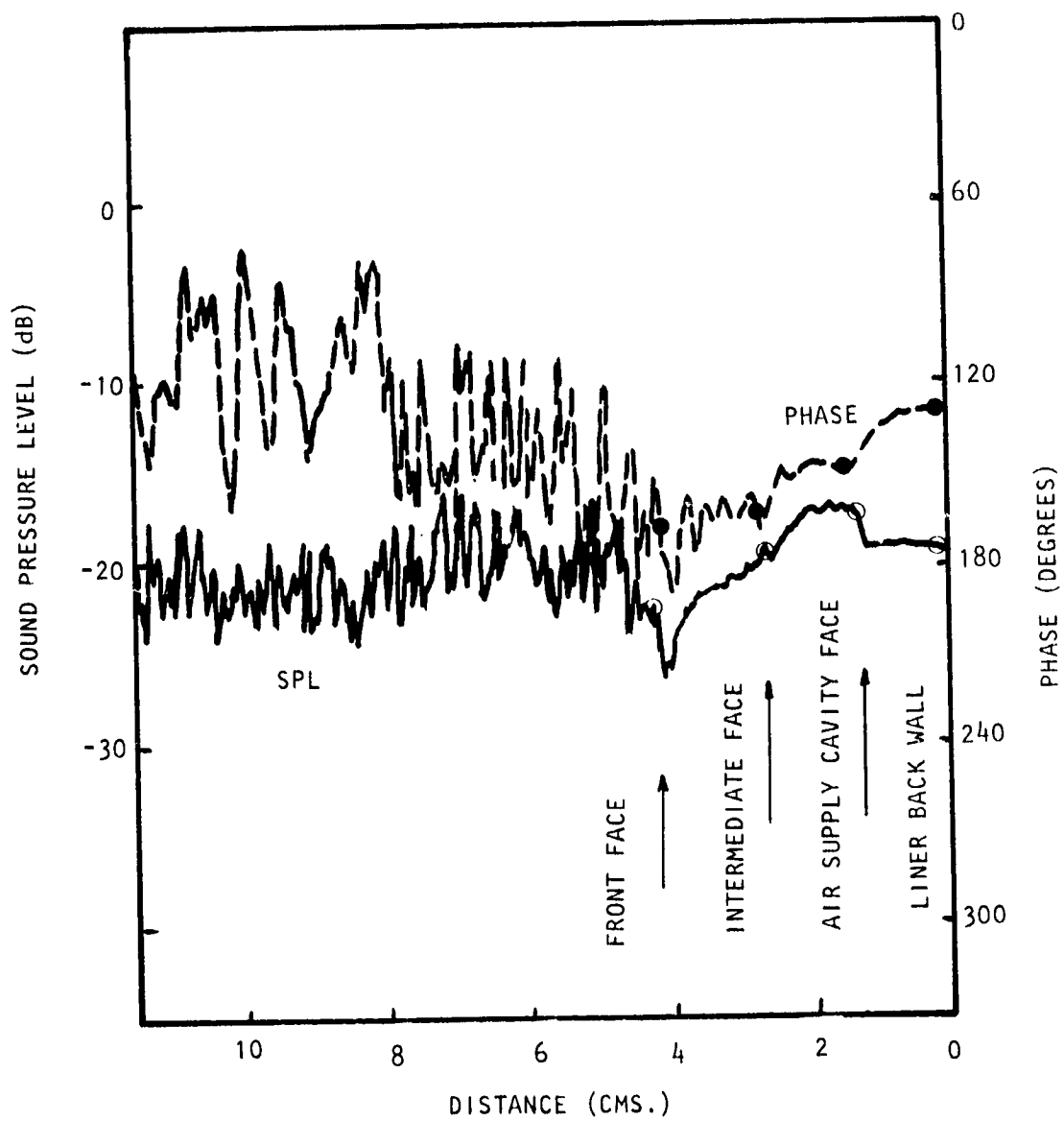


Figure 59(d) Sound Pressure and Phase Traverses within Downstream Liner at 1600 Hz. Bias Flow $M_i = 0.0$, Grazing Flow = 0.25.

	ZERO GRAZING FLOW BIAS FLOW, MACH 0.015		GRAZING FLOW, MACH 0.25 ZERO BIAS FLOW	
	Measured R/ ρc	Design R/ ρc X/ ρc	Measured R/ ρc X/ ρc	Design R/ ρc X/ ρc
Upstream Liner	0.67 - 0.64	0.61 - 0.45	0.52 - 0.69	0.80 - 0.95
Downstream Liner	0.26 - 0.90	0.61 - 0.45	0.35 - 0.11	0.55 - 0.11

Table II Comparison of Measured and Design Impedances
for Flow Test Duct Liners at 1600 Hz

	BIAS MACH 0.01 GRAZING MACH 0.0		BIAS MACH 0.0 GRAZING MACH 0.0		BIAS MACH 0.01 GRAZING MACH 0.25		BIAS MACH 0.0 GRAZING MACH 0.25	
	M ϕ *	α +	M ϕ	α	M ϕ	α	M	α
UPSTREAM LINER								
Measured	0.78	5.0	.68	5.0	0.77	9.0	0.80	6.0
Calculated	0.84	5.0	.72	4.0	1.00	10.5	1.11	5.8
DOWNSTREAM LINER								
Measured	1.88	7.0	1.63	4.2	1.42	9.0	1.30	8.0
Calculated	2.80	7.1	1.52	4.3	2.75	8.4	2.09	6.8

* (phase Mach number)

+ (attenuation dB/duct width)

Table III Comparison of Measured and Calculated Phase Speeds and
Attenuations in Test Duct at 1600 Hz

5. CONCLUDING REMARKS

The preceding sections have discussed an advanced acoustic suppression concept which enables the liner impedance to be varied, within limits, at will by means of external bias air flow. The viability of the concept has been successfully proved in a small-scale flow duct test facility by means of propagation constant measurements and local impedance measurements.

The test format was directed by the development of a simple impedance model of a double-layer resonant cavity liner configuration which delineated the parametric effects of liner bias air flow and provided a design guide for the flow duct tests. In addition, extensive use was made of the classical "plug flow" duct attenuation and propagation analysis as an integral part of the test liner design procedure.

Incorporated in the tests was the desirable, but not necessarily essential, philosophy of bias air use related to engine operation, which states that little bias air is needed for high grazing flows and that high bias air flows are needed to maintain attenuation at low grazing flows.

It is appropriate to consider the amount of air needed for a typical workable system. With a maximum bias flow Mach number of 0.02, at sea-level pressure and standard temperature, the mass flow needed would be approximately 8.2 kilograms per square meter per second (1.65 pounds per square foot per second). Thus, with an engine rated at about 50,000 pounds thrust (such as the Rolls Royce RB211), the total mass flow at takeoff would be about 430 kilograms (950 pounds) per second with an approach mass flow of about 270 kilograms (600 pounds) per second required. Thus, the percentage of total mass flow required for the liner bias flow, assuming a treatment of 9 square meters (about 100 square feet), would be about 12 percent for the approach condition. (These are gross conservative estimates which probably could be halved by careful design optimization.)

The bias flow concept described considered only the case of flow blown through the liner from the rear cavity to the duct itself. While it is recognized that this could be a practical advantage in the removal of ice, water, and other contaminants, the basic concept itself is *independent* of direction of bias flow, so boundary layer control by suction as well as blowing is possible. This implies the existing and hitherto unattained possibility that the acoustic treatment *could improve* engine efficiencies rather than the reverse.

Perhaps the most obvious potential advantages of the concept lie in the ability to "tune" the liner for maximum insertion loss, in place on the engine and over the entire operating envelope, thus obviating the need for expensive trial-and-error approaches that use many different lining types. An exciting variant of this "tuning" ability is the possibility of axial variation of impedance, either in a continuous manner, which could account for nonlinear sound pressure level effects, or step changes, in an axially segmented liner approach.

While the concept is not a universal panacea for the current problems of duct liner design, it offers remarkable promise of development into a practical means of improving the efficiency of real-life suppression systems in gas-turbine devices.

APPENDIX A

PLOTS OF CONTOURS OF CONSTANT ATTENUATION FOR
FIRST TWO MODES OF PROPAGATION IN A SQUARE DUCT
WITH ONE SIDE ACOUSTICALLY LINED AT VARIOUS REDUCED
FREQUENCIES AND DUCT GRAZING FLOW MACH NUMBERS

NOTE: Negative Mach numbers denote *upstream*
propagation of sound, positive Mach
numbers *downstream* propagation of sound.

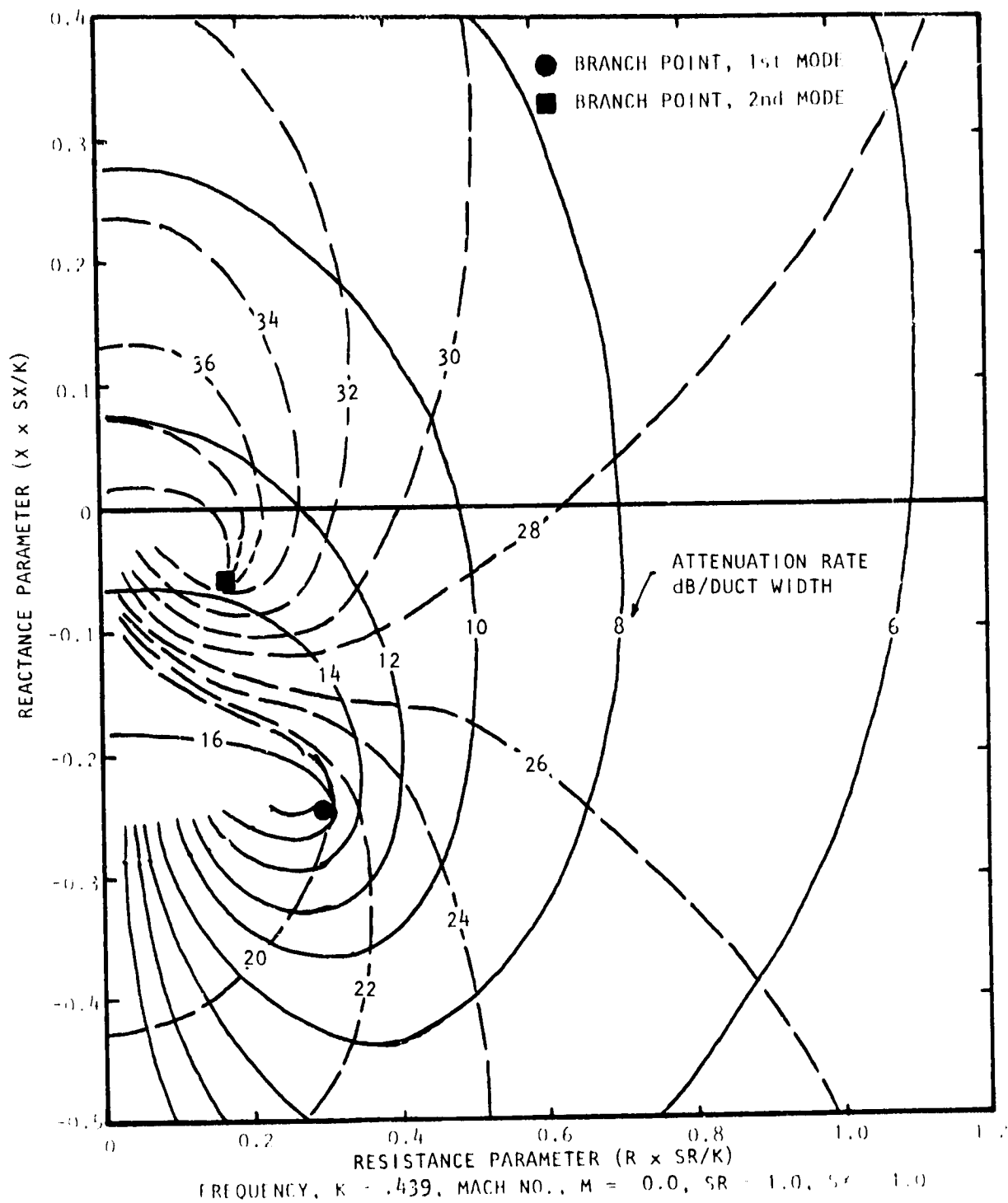


Figure A.1 Contours of Constant Attenuation for First Two Modes of Propagation (First Mode —, Second Mode ---)

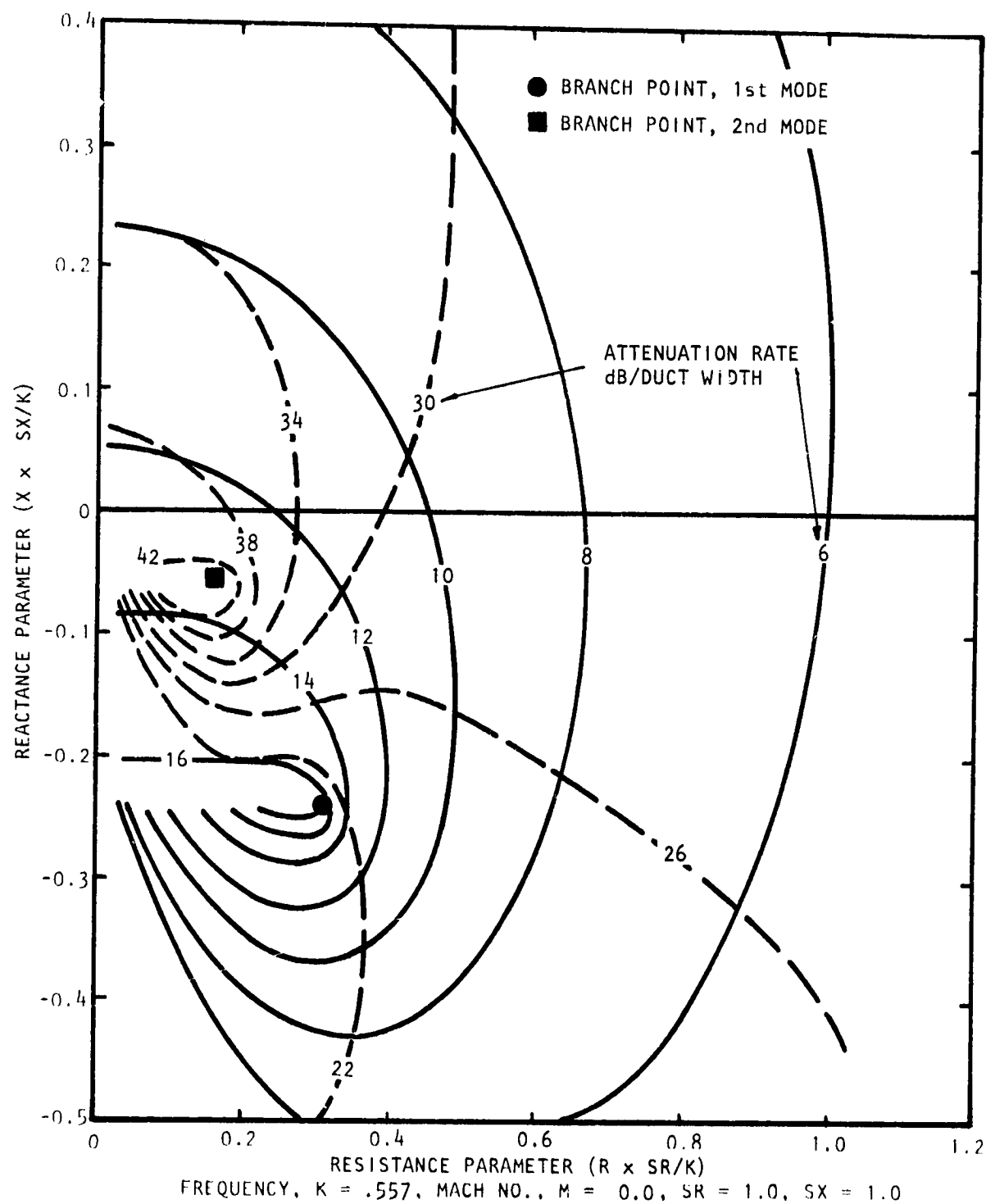


Figure A.2 Contours of Constant Attenuation for First Two Modes of Propagation (First Mode —, Second Mode ----)

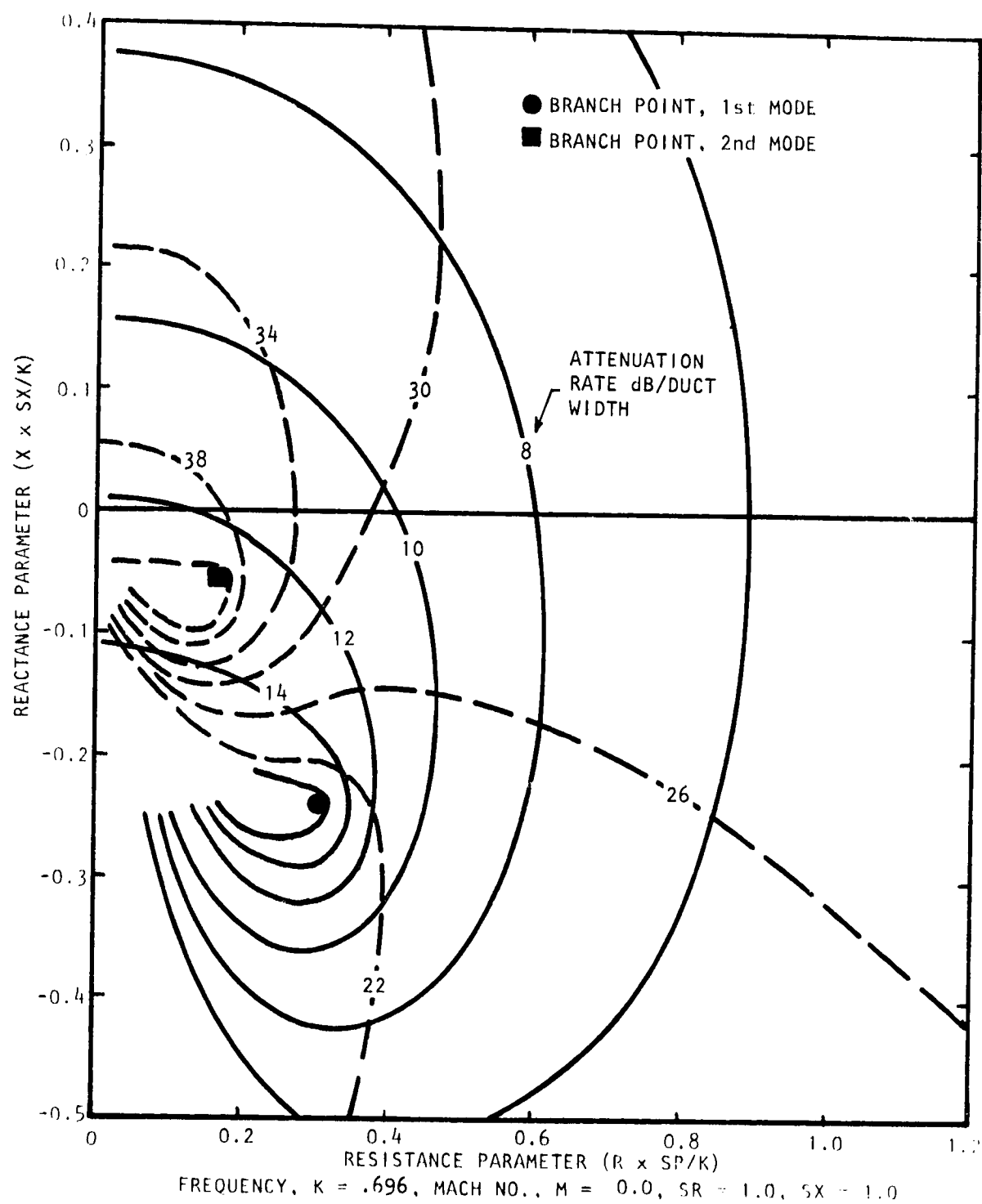


Figure A.3 Contours of Constant Attenuation for First Two Modes of Propagation (First Mode —, Second Mode ----)

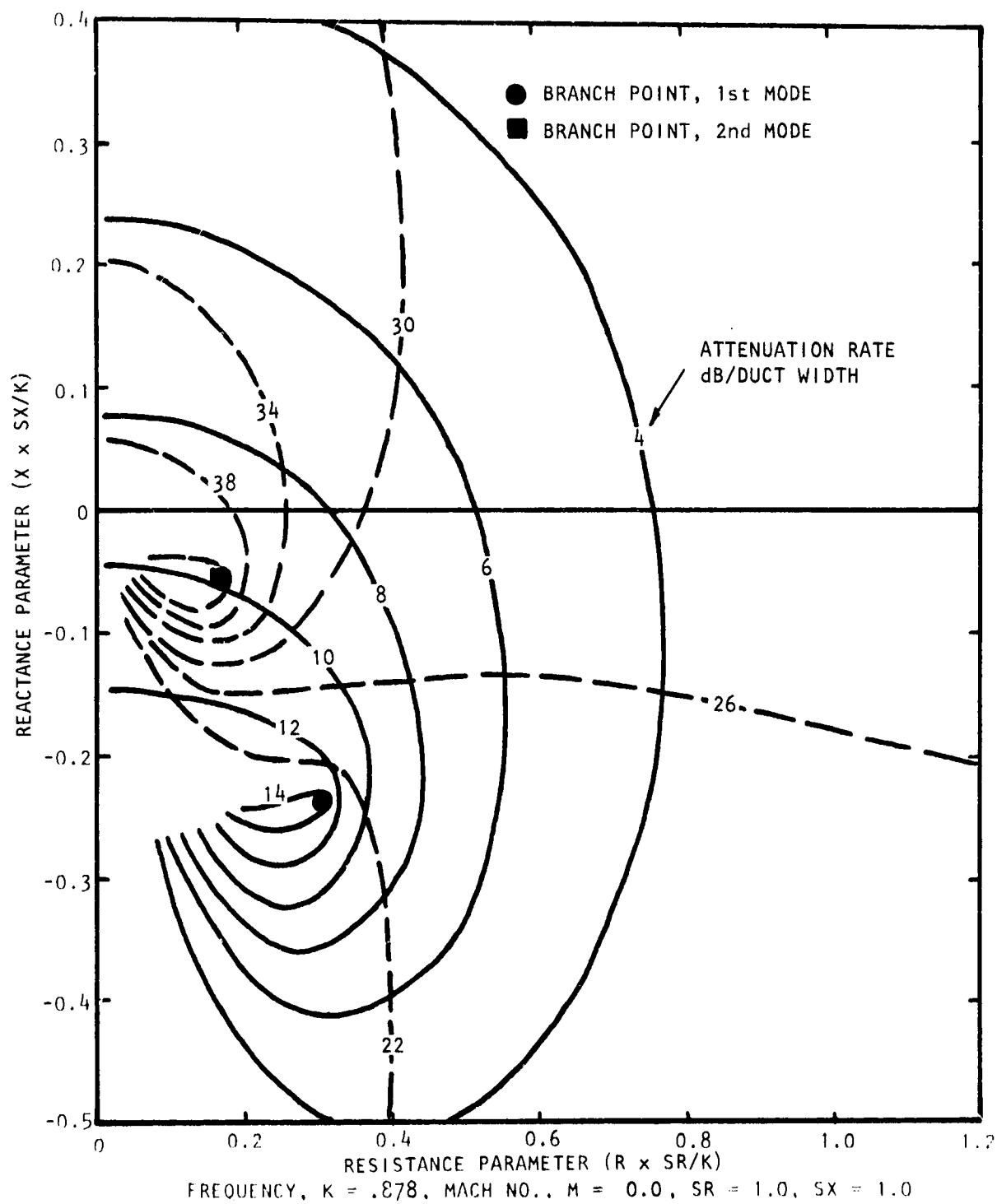


Figure A.4 Contours of Constant Attenuation for First Two Modes of Propagation (First Mode —, Second Mode ----)

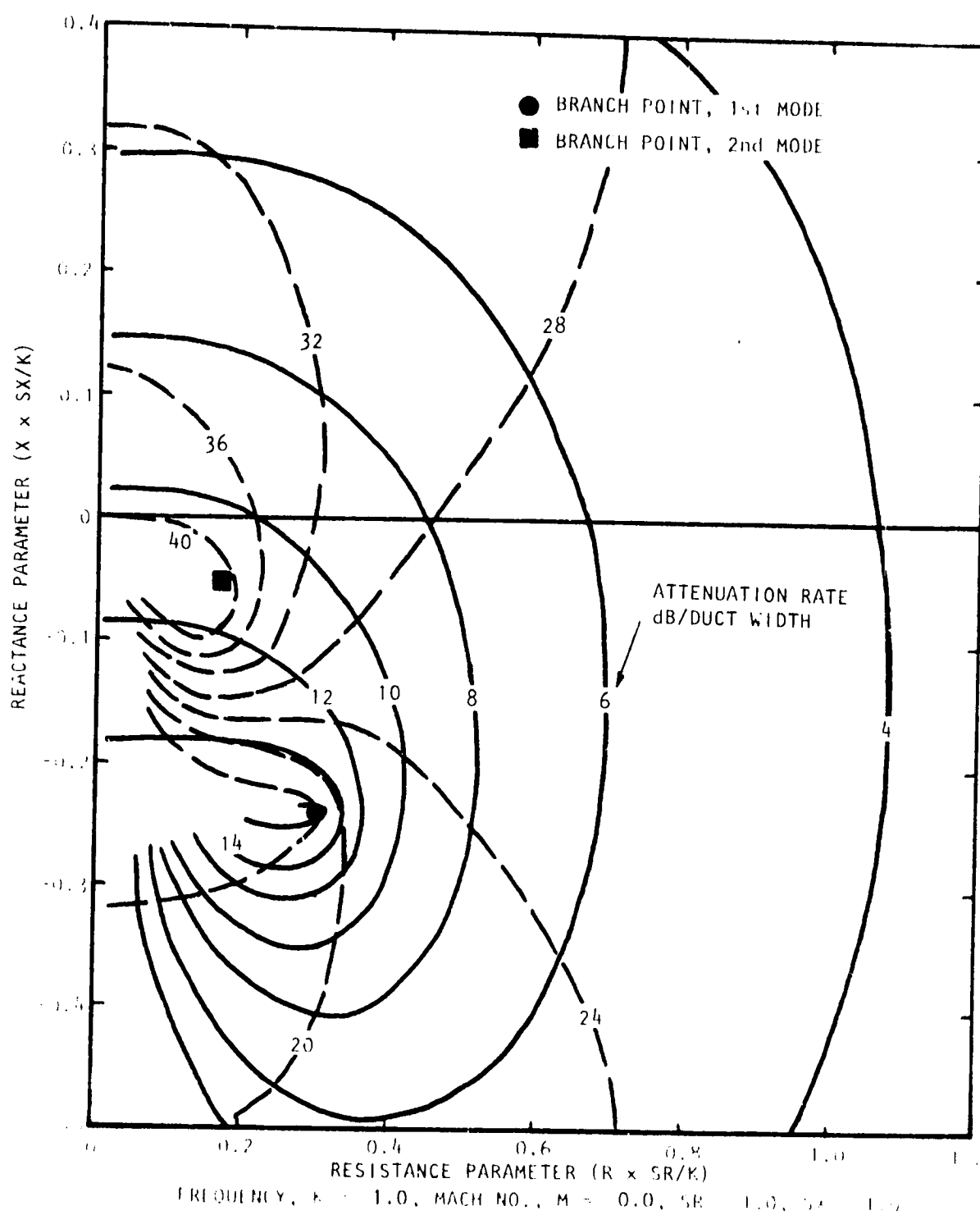


Figure A.5 Contours of Constant Attenuation for First Two Modes of Propagation (First Mode —, Second Mode ---)

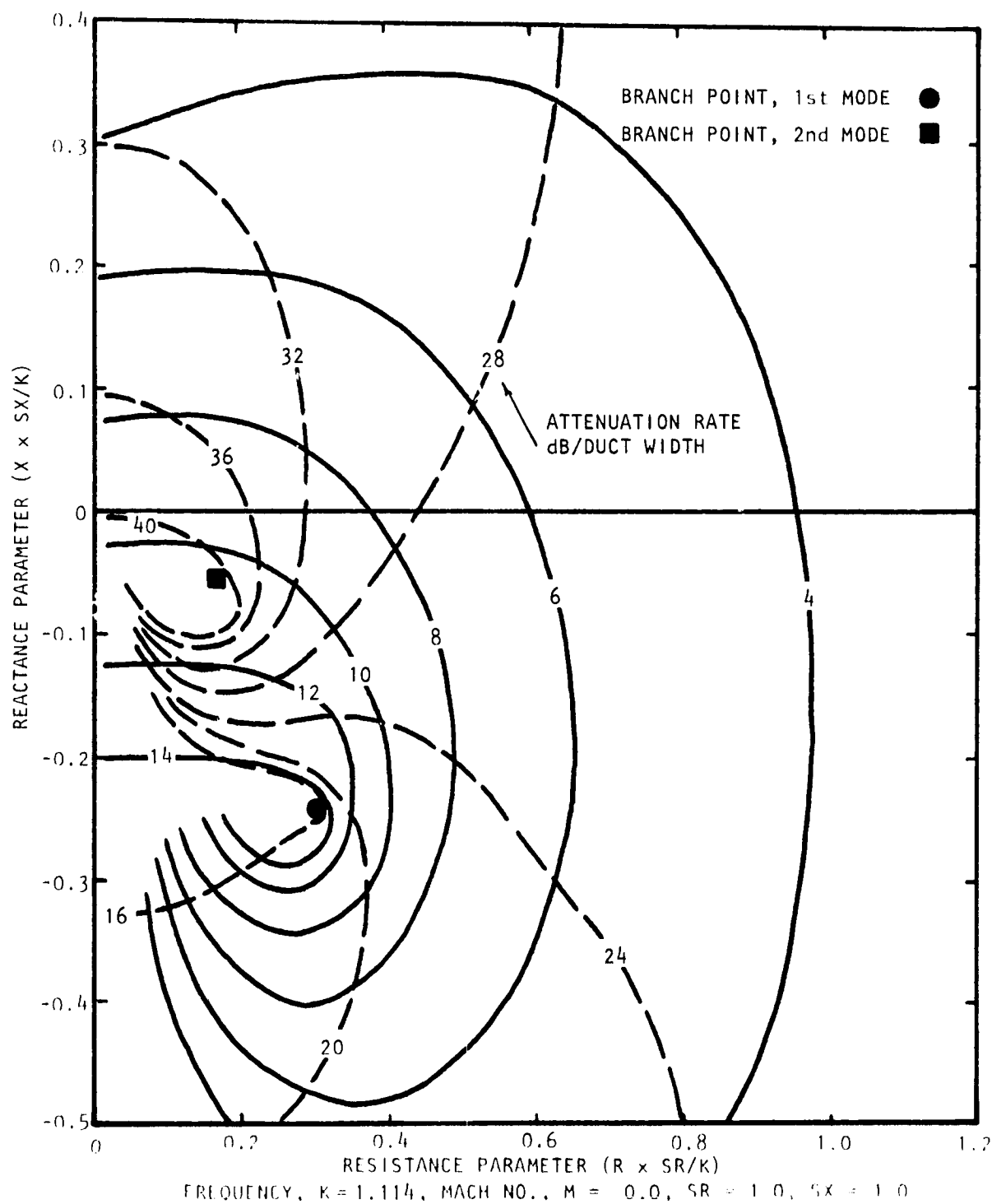


Figure A.6 Contours of Constant Attenuation for First Two Modes of Propagation (First Mode —, Second Mode ---)

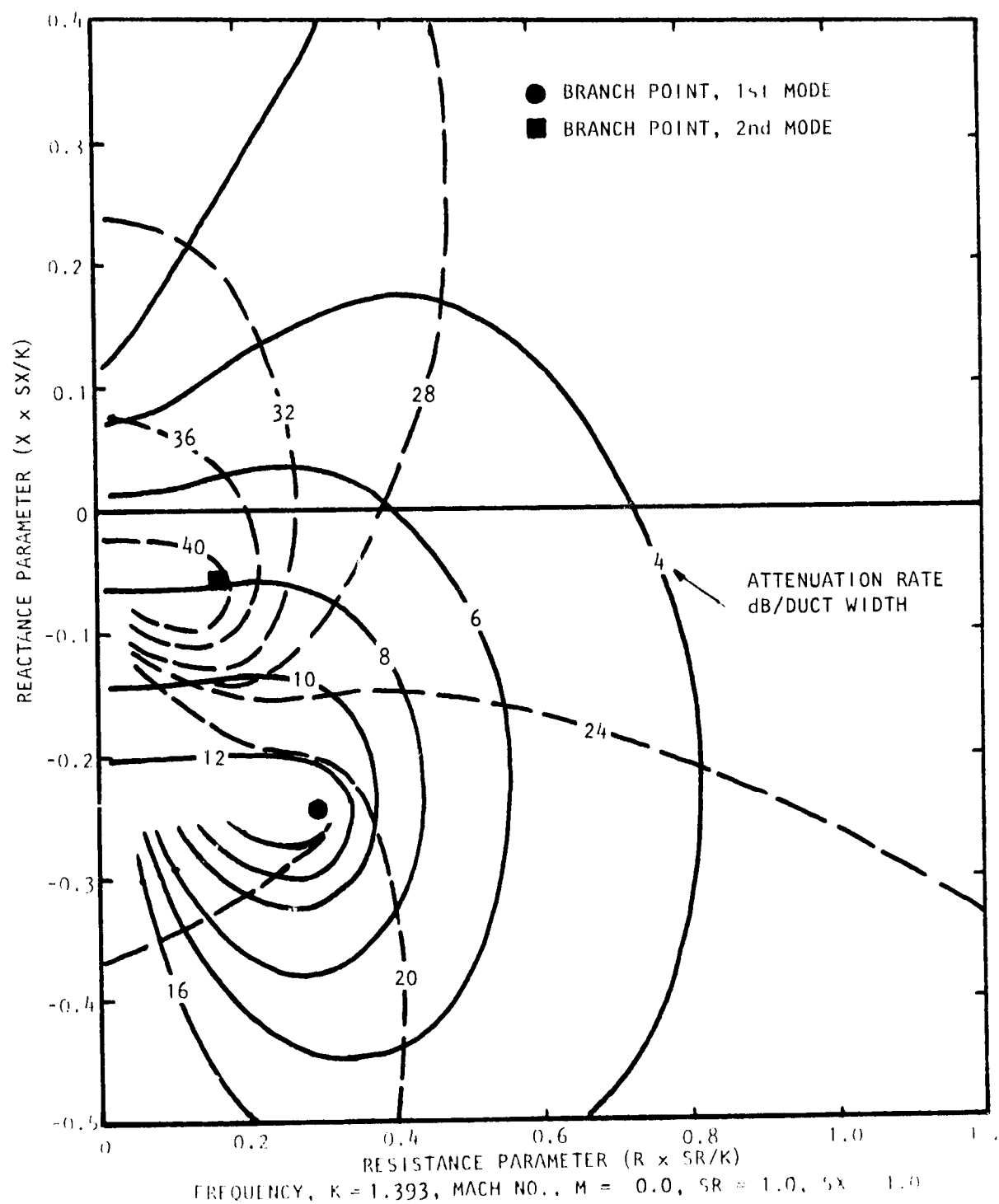


Figure A.7 Contours of Constant Attenuation for First Two Modes of Propagation (First Mode —, Second Mode ---)

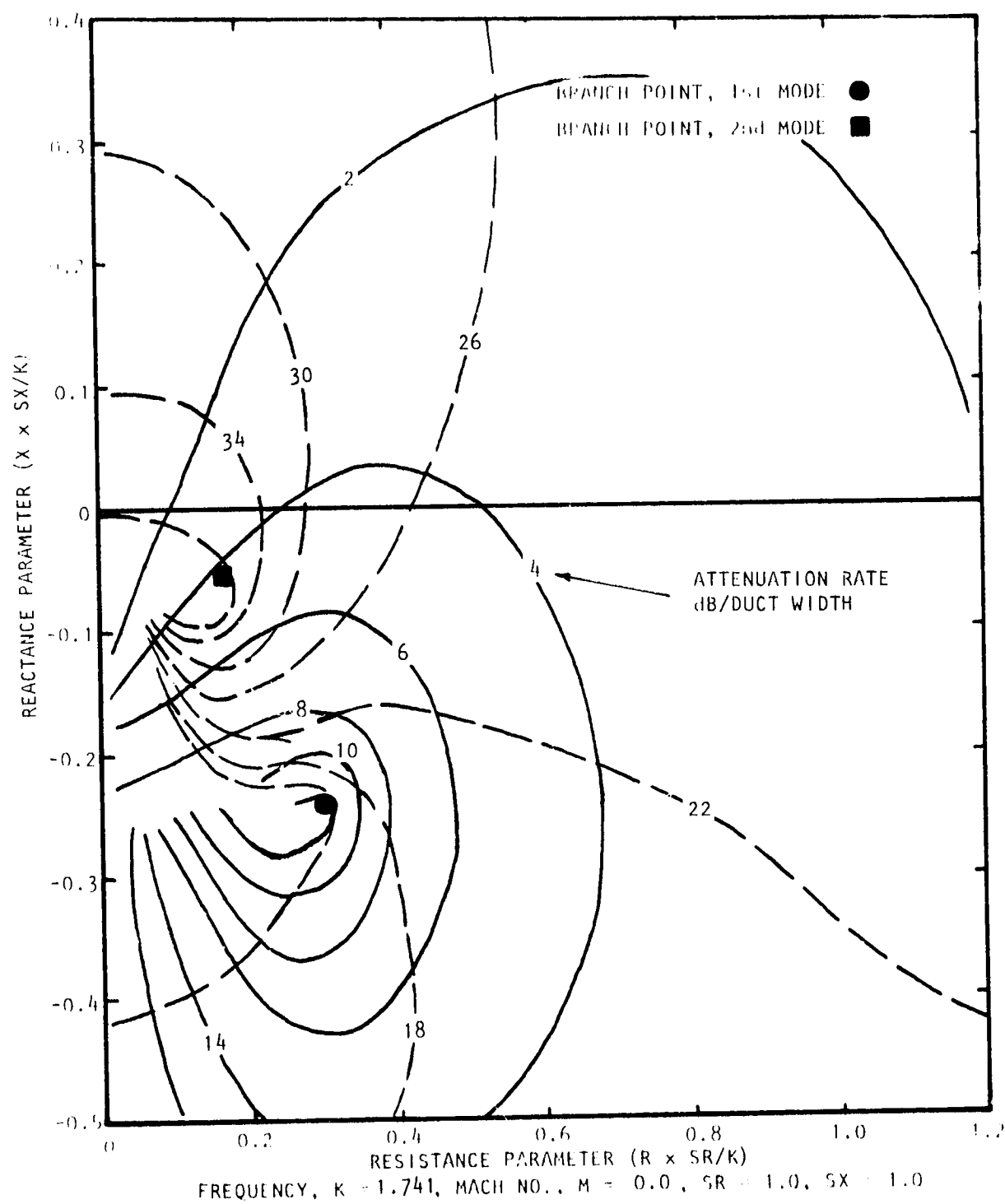


Figure A.8 Contours of Constant Attenuation for First Two Modes of Propagation (First Mode ---, Second Mode ----)

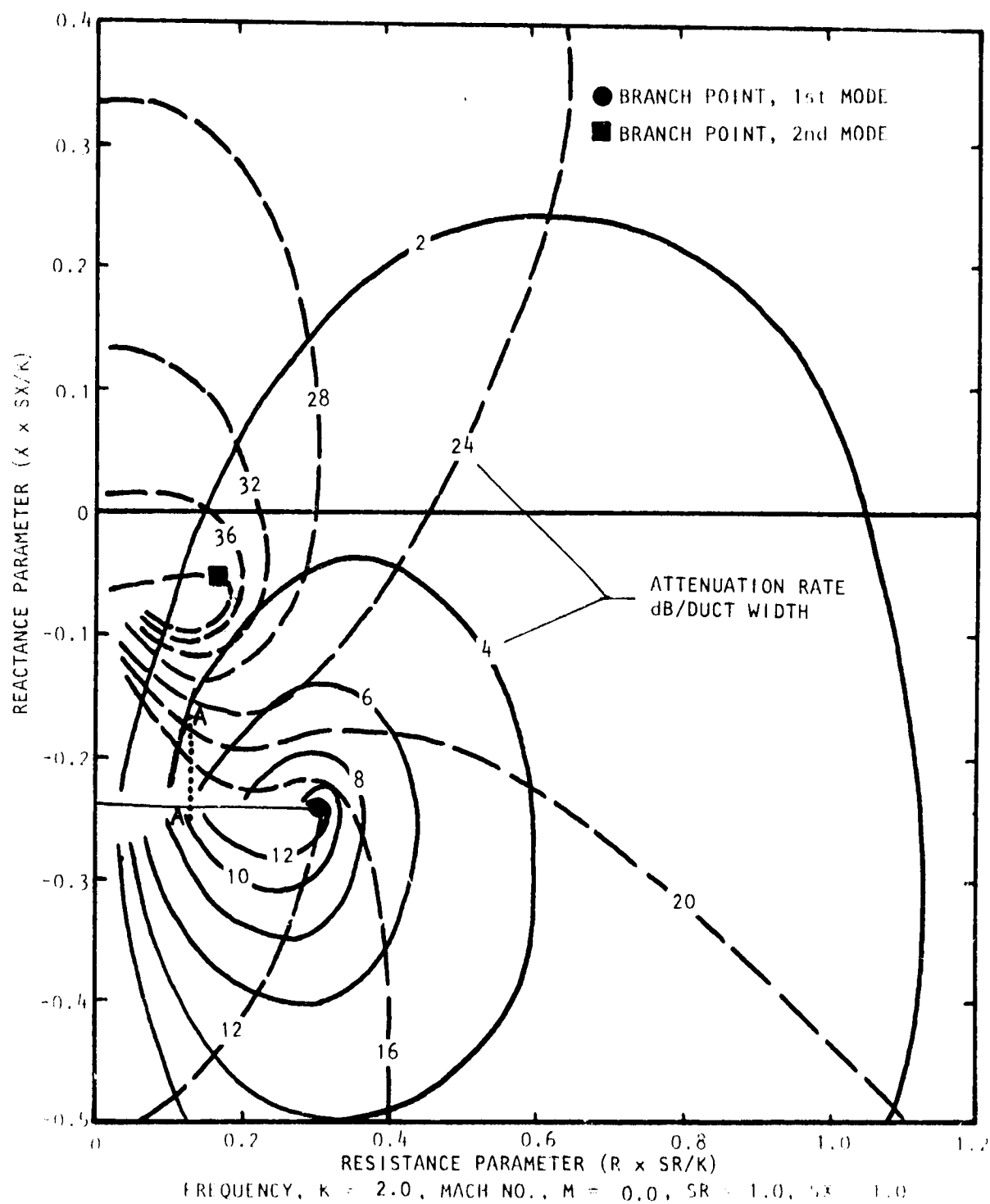


Figure A.9 Contours of Constant Attenuation for First Two Modes of Propagation (First Mode —, Second Mode ---)

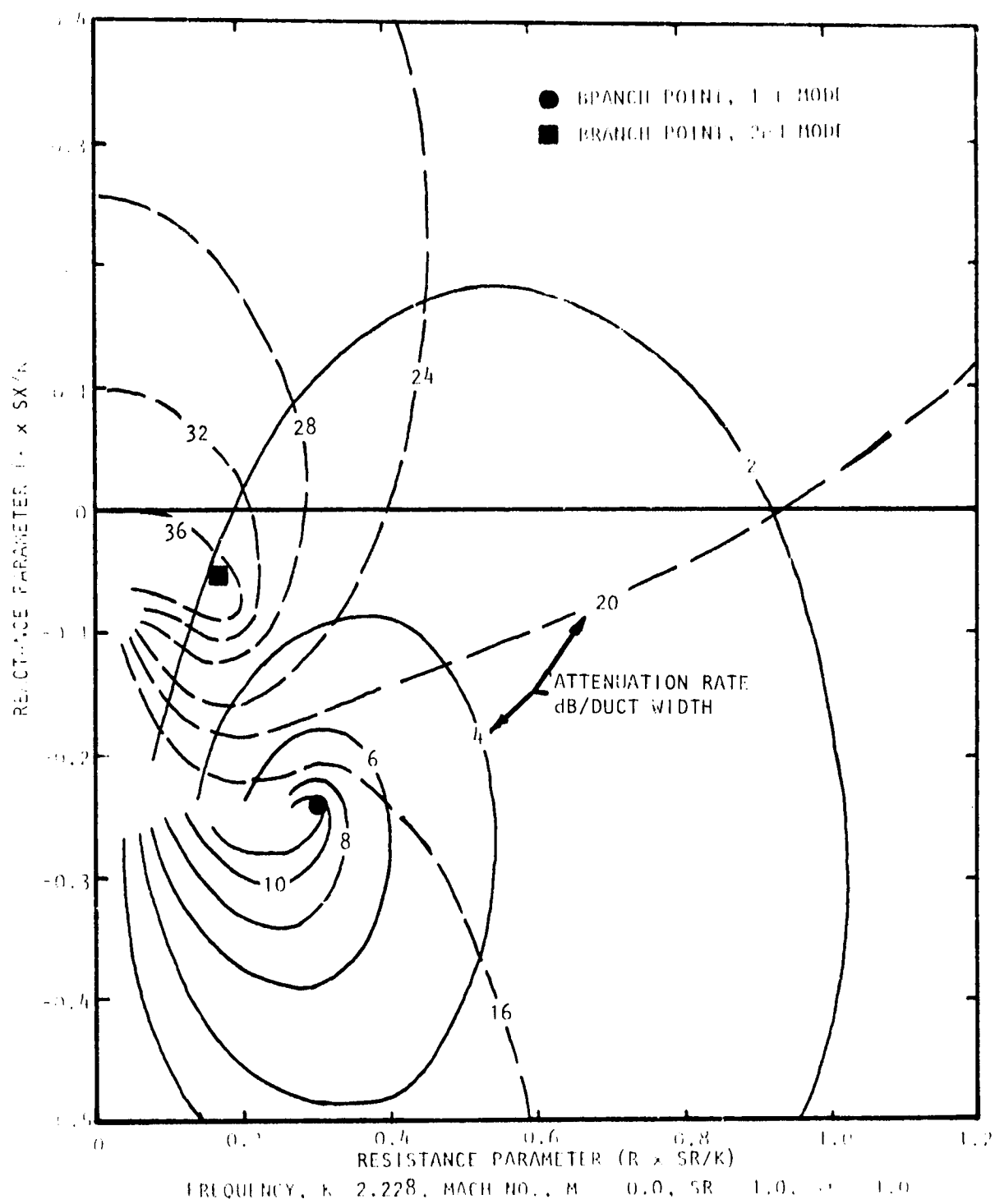


Figure A.10 Contours of Constant Attenuation for First Two Modes of Propagation (First Mode ———, Second Mode - - -)

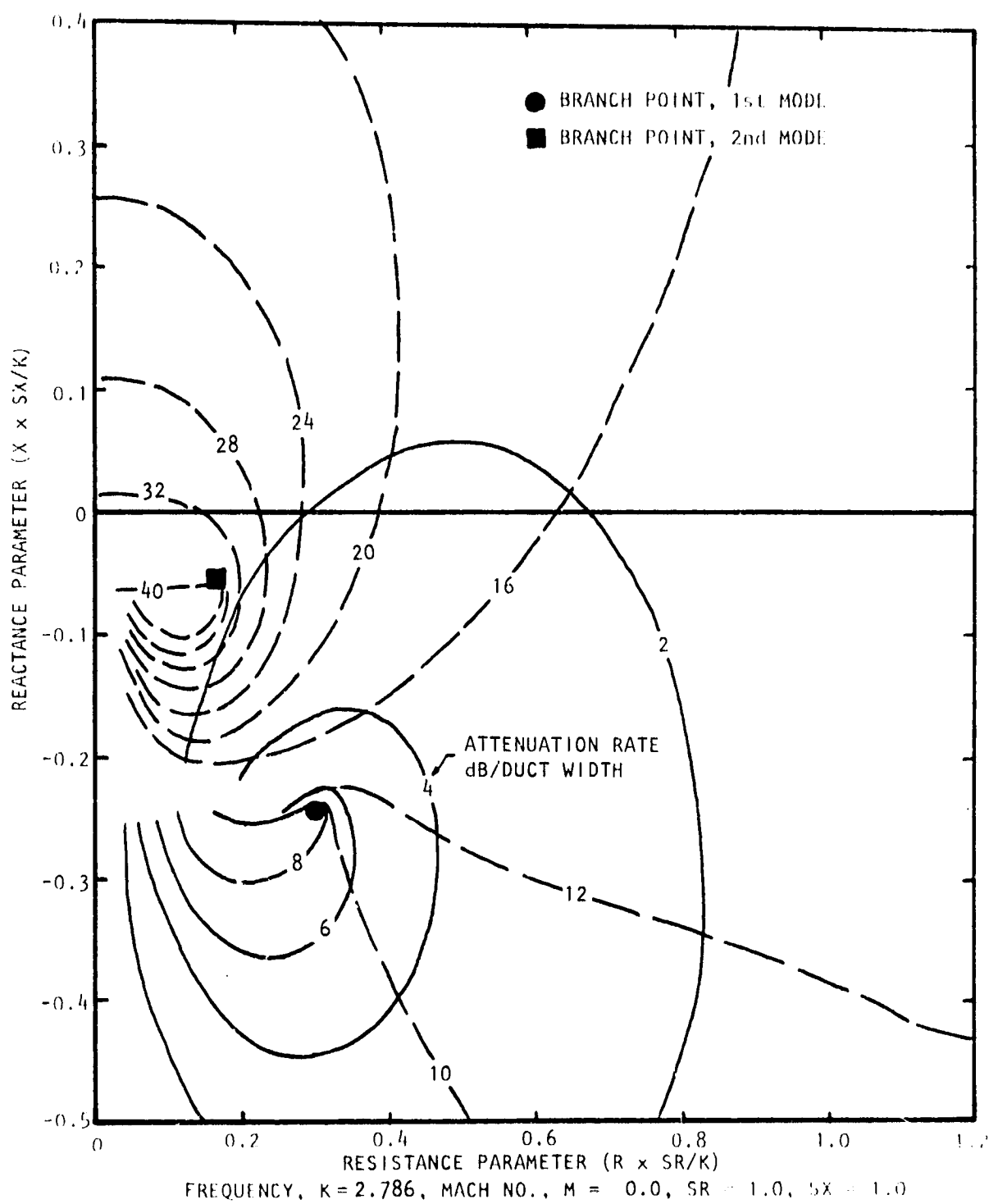


Figure A.11 Contours of Constant Attenuation for First Two Modes of Propagation (First Mode ———, Second Mode - - - -)

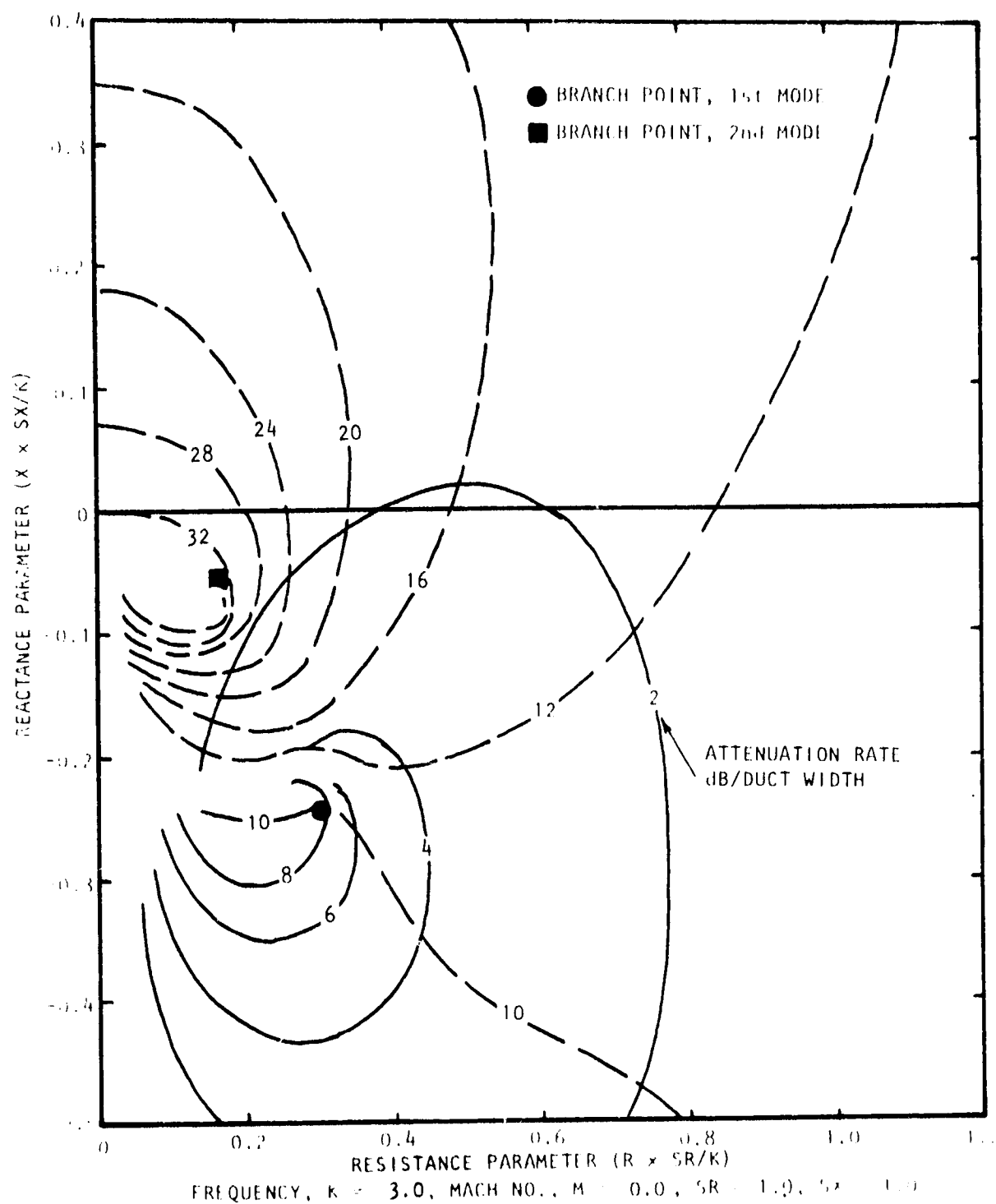


Figure A.12 Contours of Constant Attenuation for First Two Modes of Propagation (First Mode —, Second Mode ---)

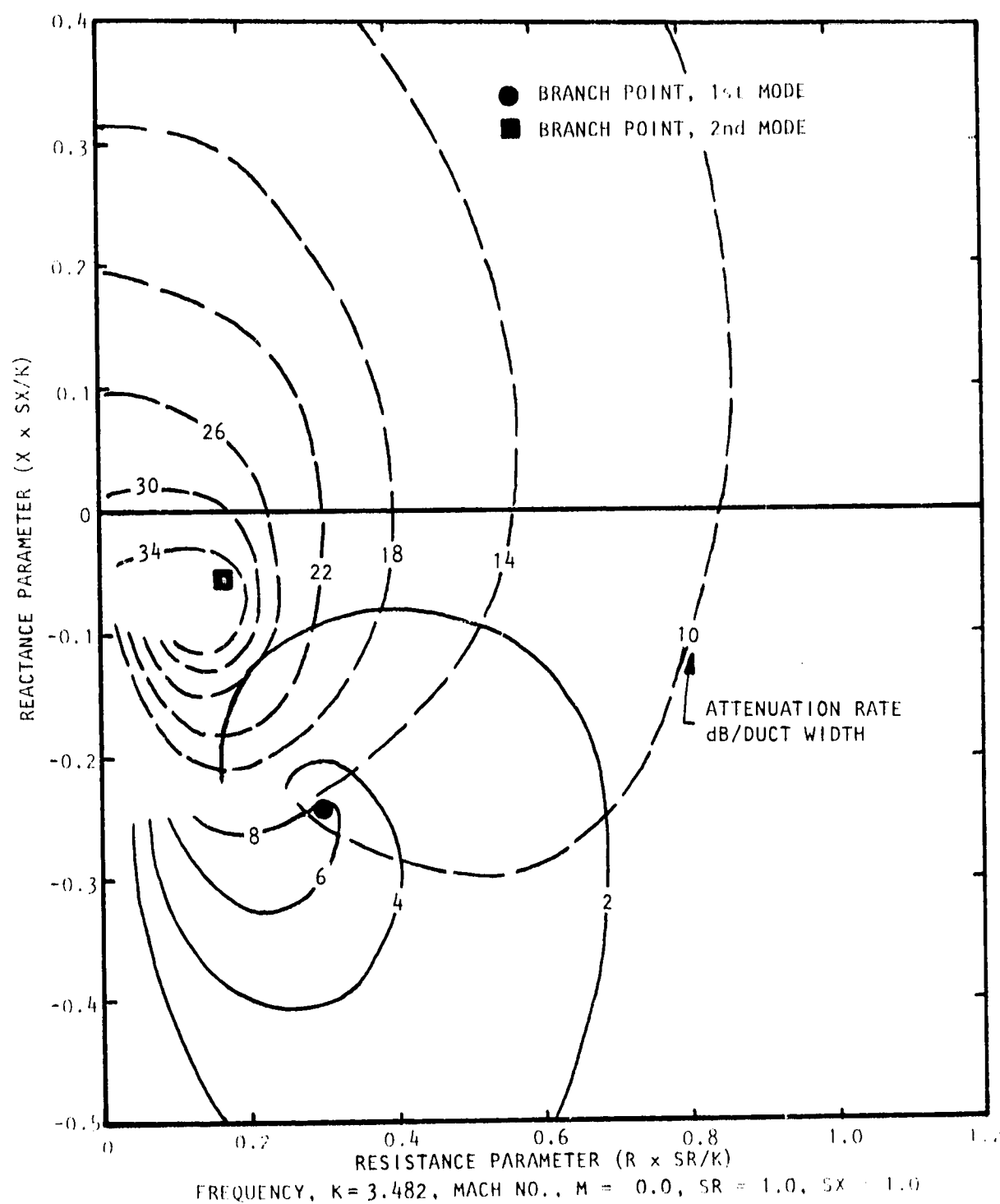


Figure A.13 Contours of Constant Attenuation for First Two Modes of Propagation (First Mode —, Second Mode ---)

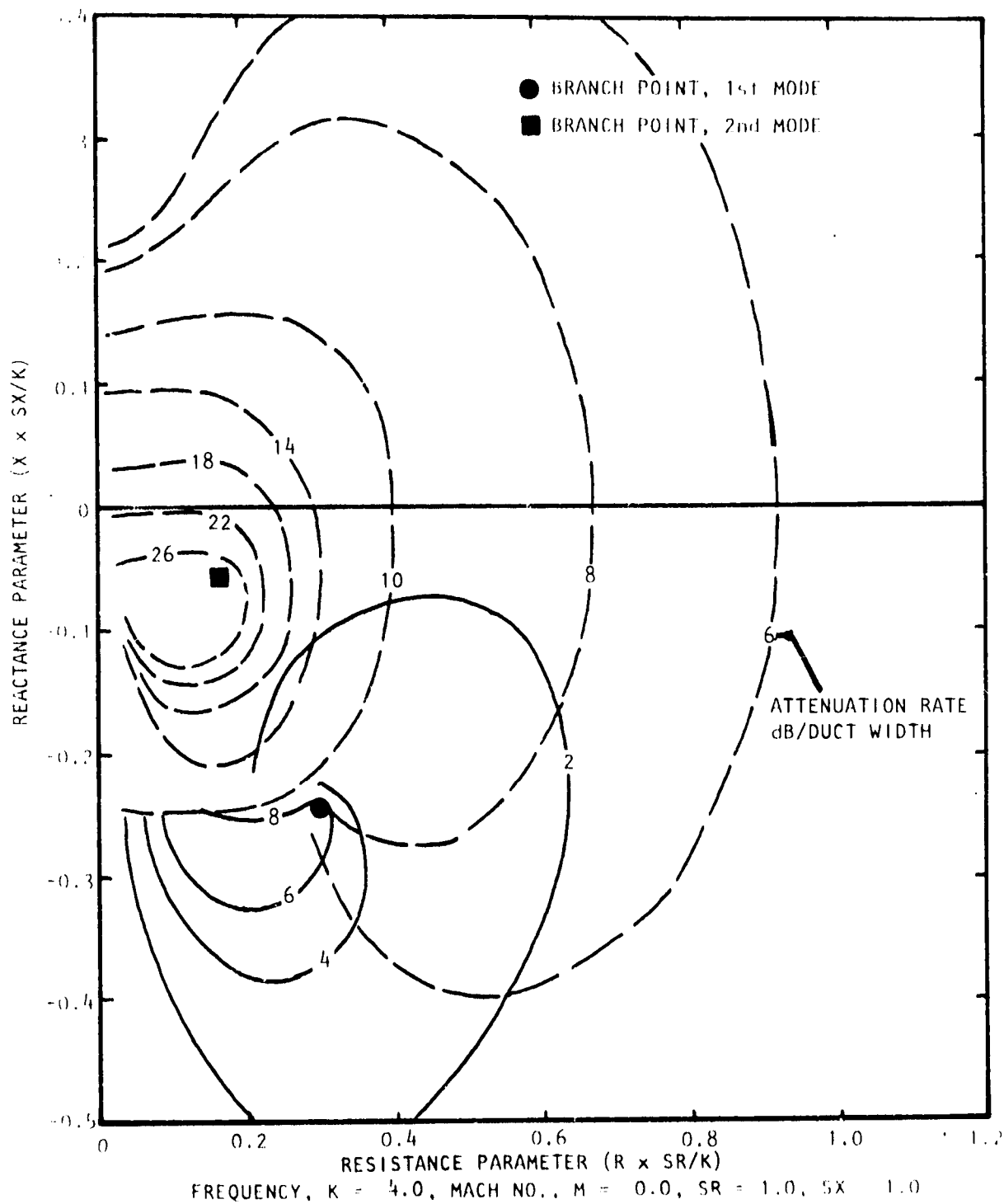


Figure A.14 Contours of Constant Attenuation for First Two Modes of Propagation (First Mode —, Second Mode ----)

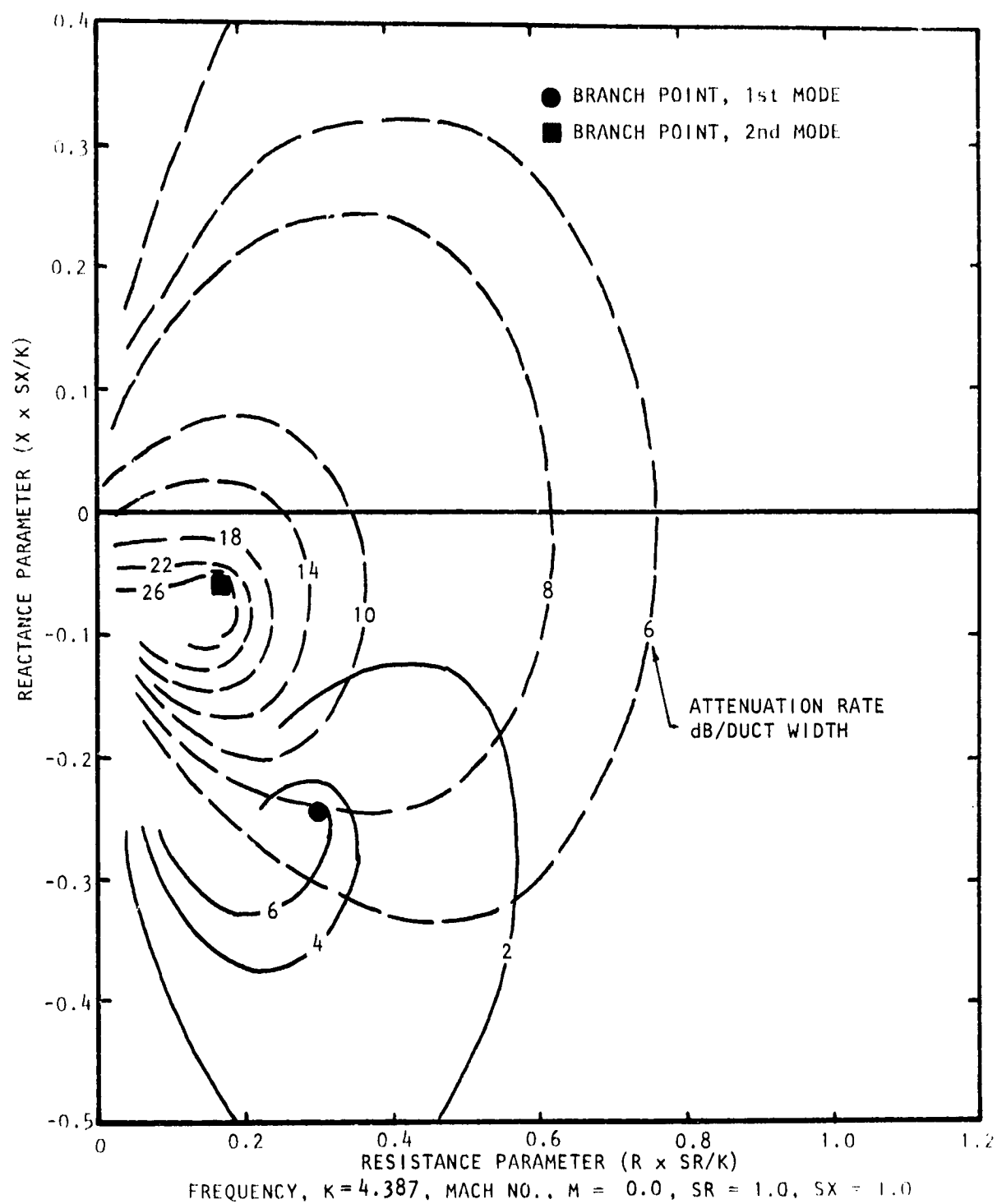


Figure A.15 Contours of Constant Attenuation for First Two Modes of Propagation (First Mode —, Second Mode ----)

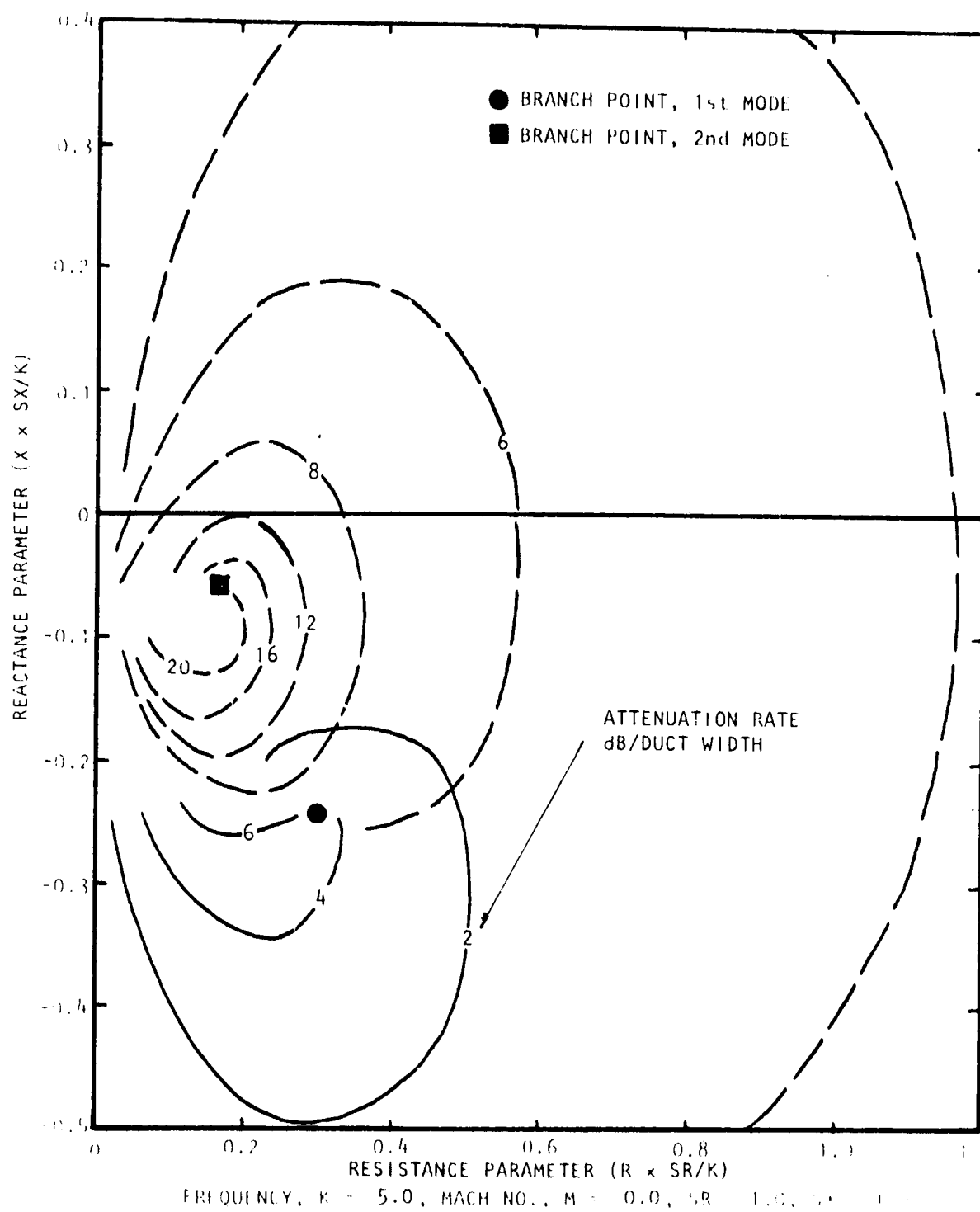


Figure A.16 Contours of Constant Attenuation for First Two Modes of Propagation (First Mode ---, Second Mode ----)

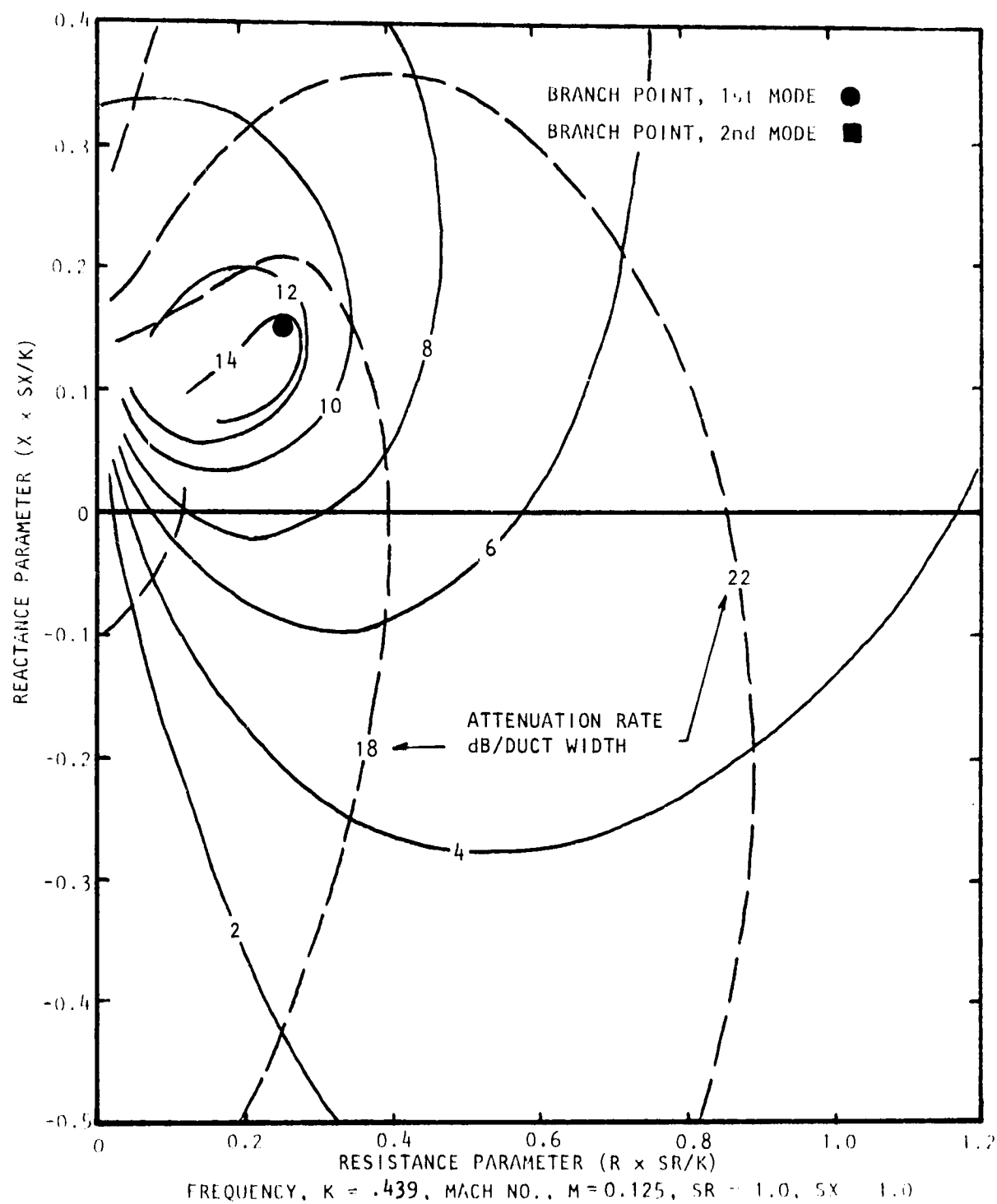


Figure A.17 Contours of Constant Attenuation for First Two Modes of Propagation (First Mode —, Second Mode ---)

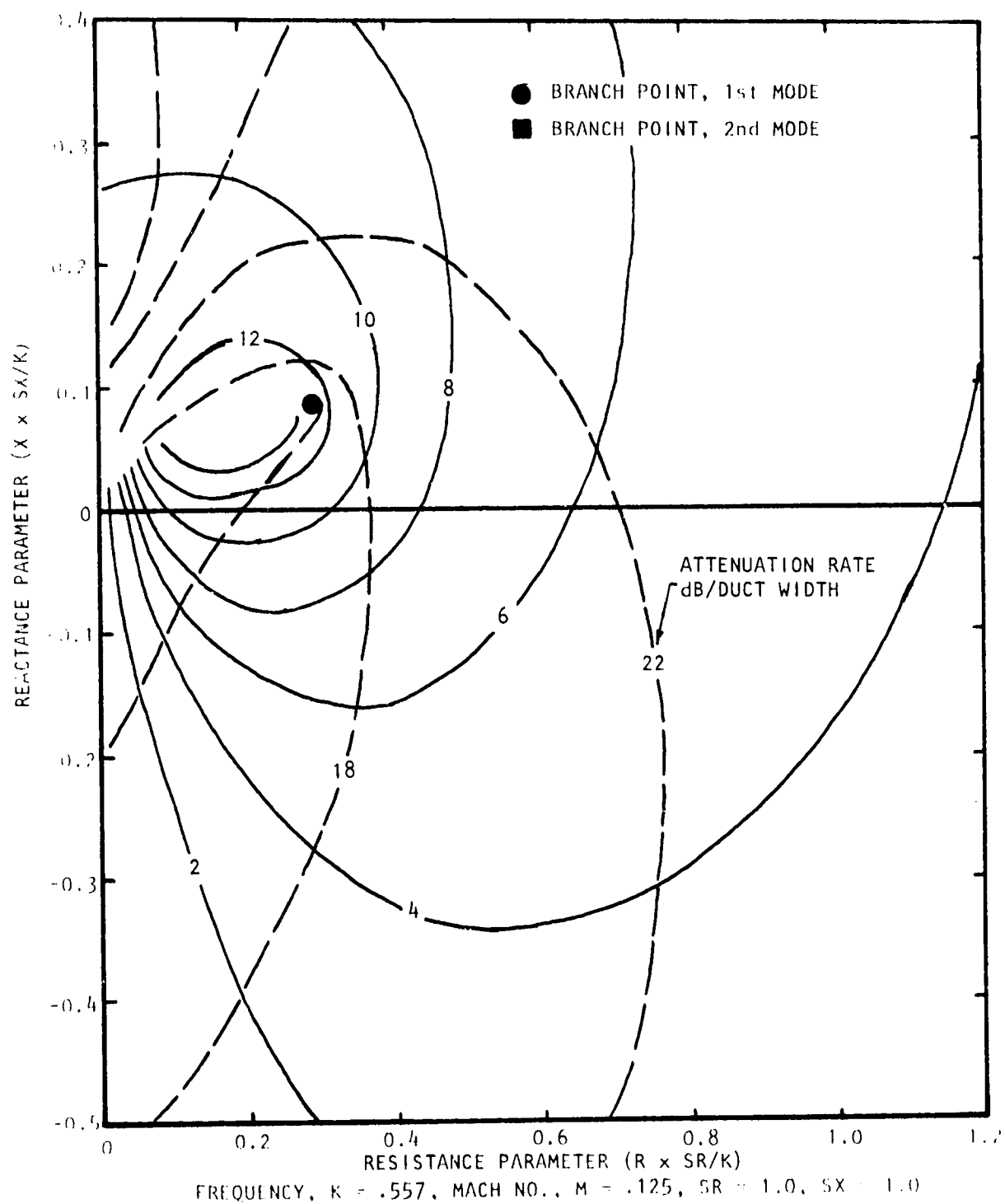


Figure A.18 Contours of Constant Attenuation for First Two Modes of Propagation (First Mode —, Second Mode ----)

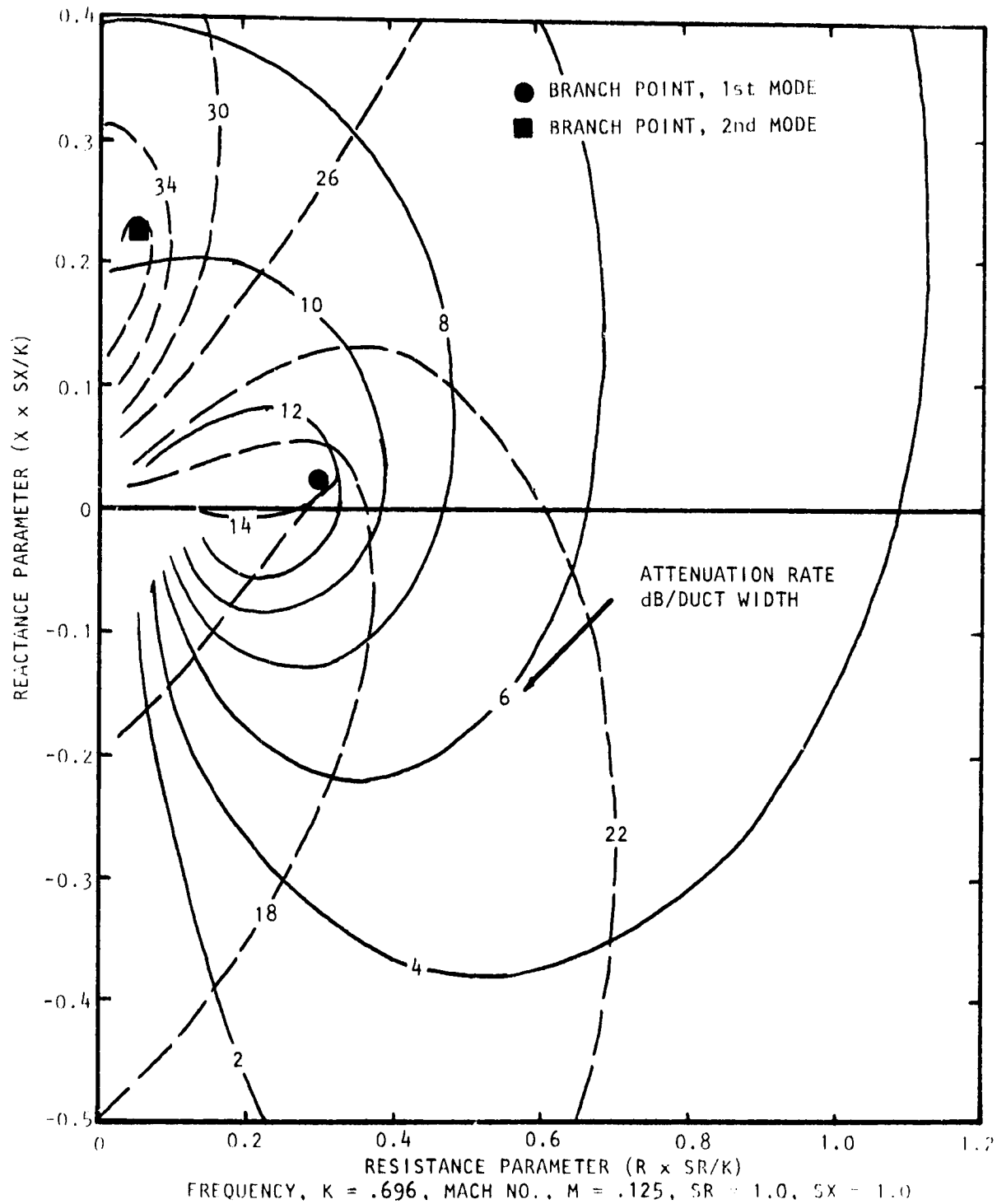


Figure A.19 Contours of Constant Attenuation for First Two Modes of Propagation (First Mode —, Second Mode ----)

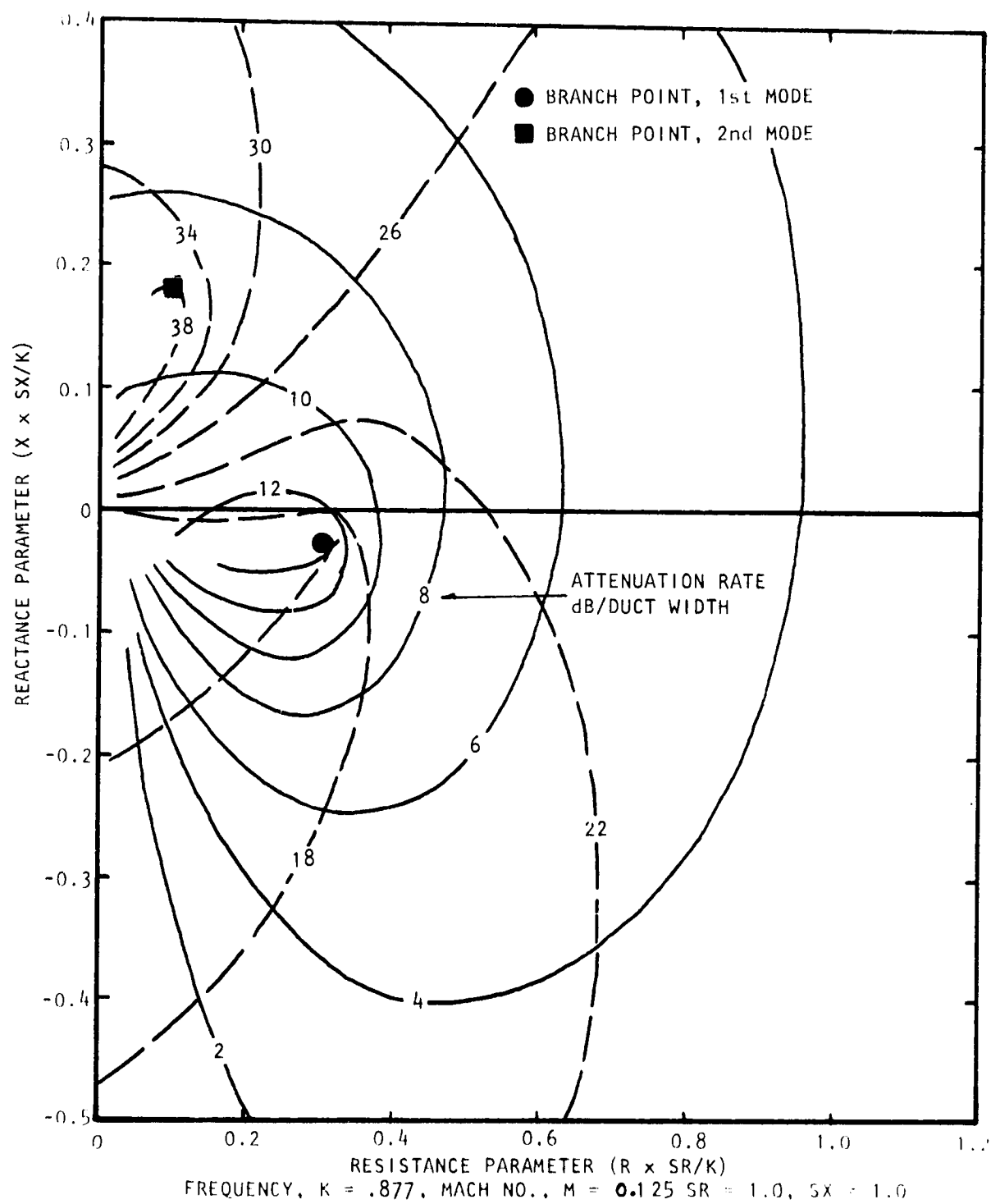


Figure A.20 Contours of Constant Attenuation for First Two Modes of Propagation (First Mode —, Second Mode ----)

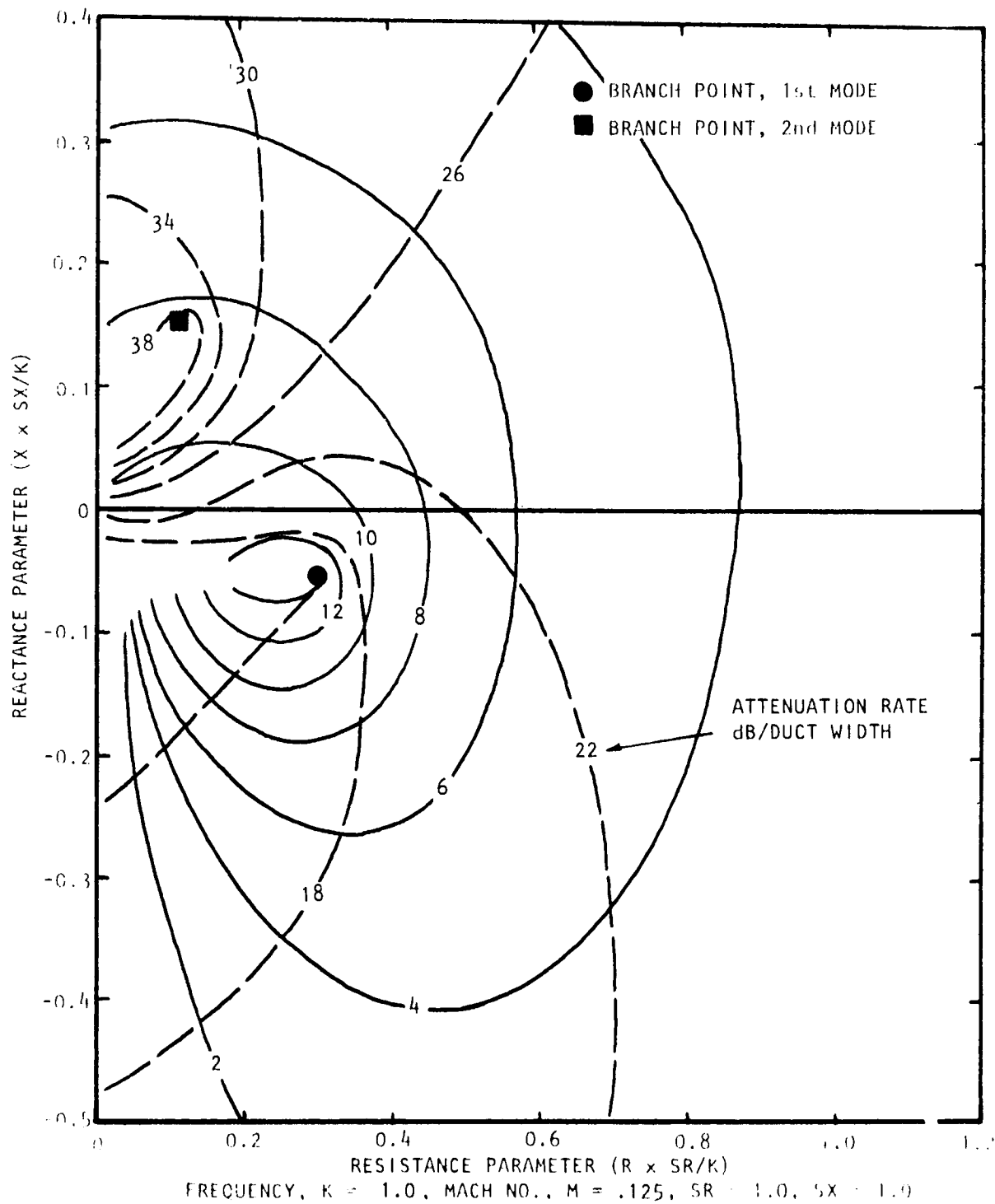


Figure A.21 Contours of Constant Attenuation for First Two Modes of Propagation (First Mode —, Second Mode ----)

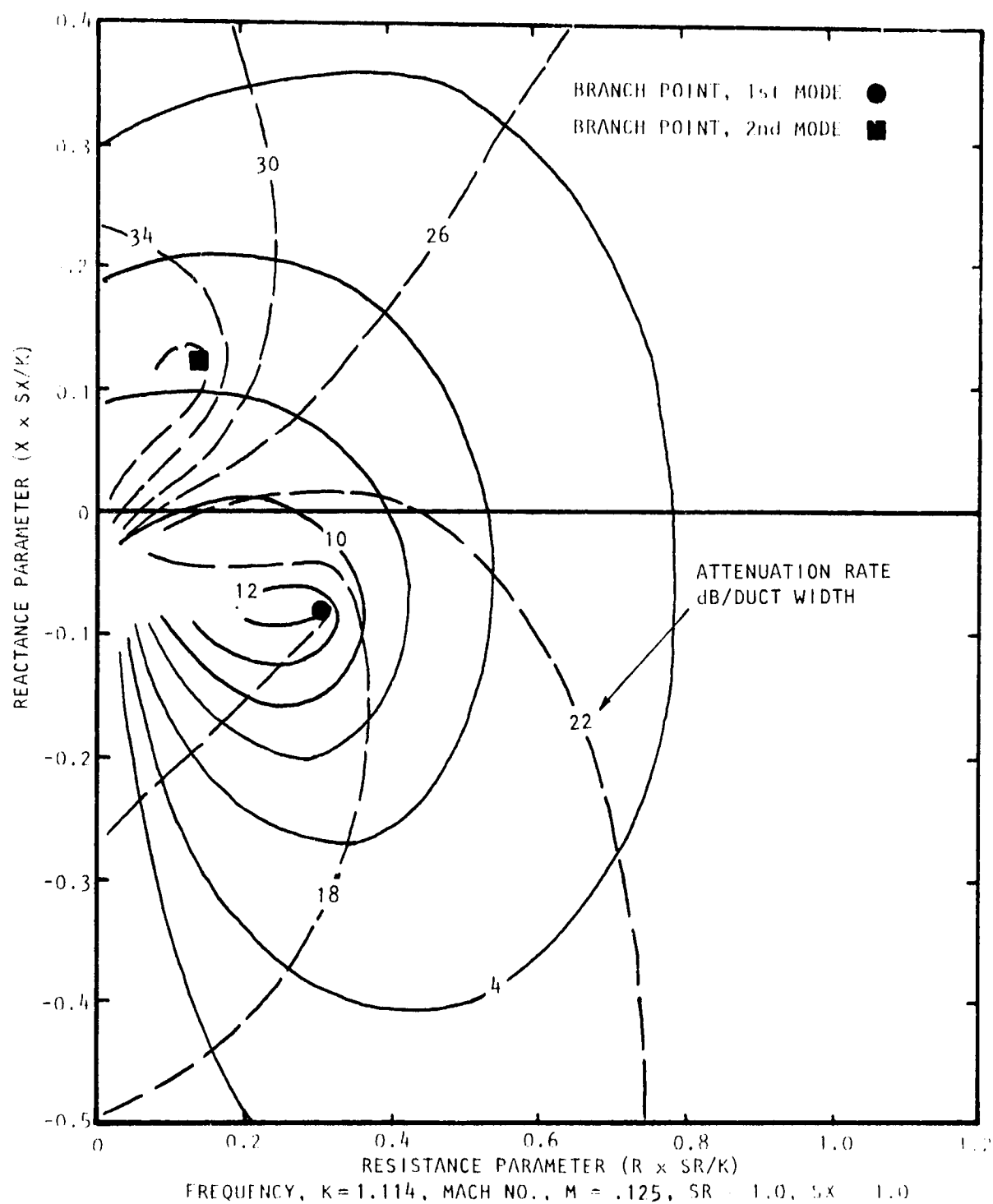


Figure A.22 Contours of Constant Attenuation for First Two Modes of Propagation (First Mode —, Second Mode ---)

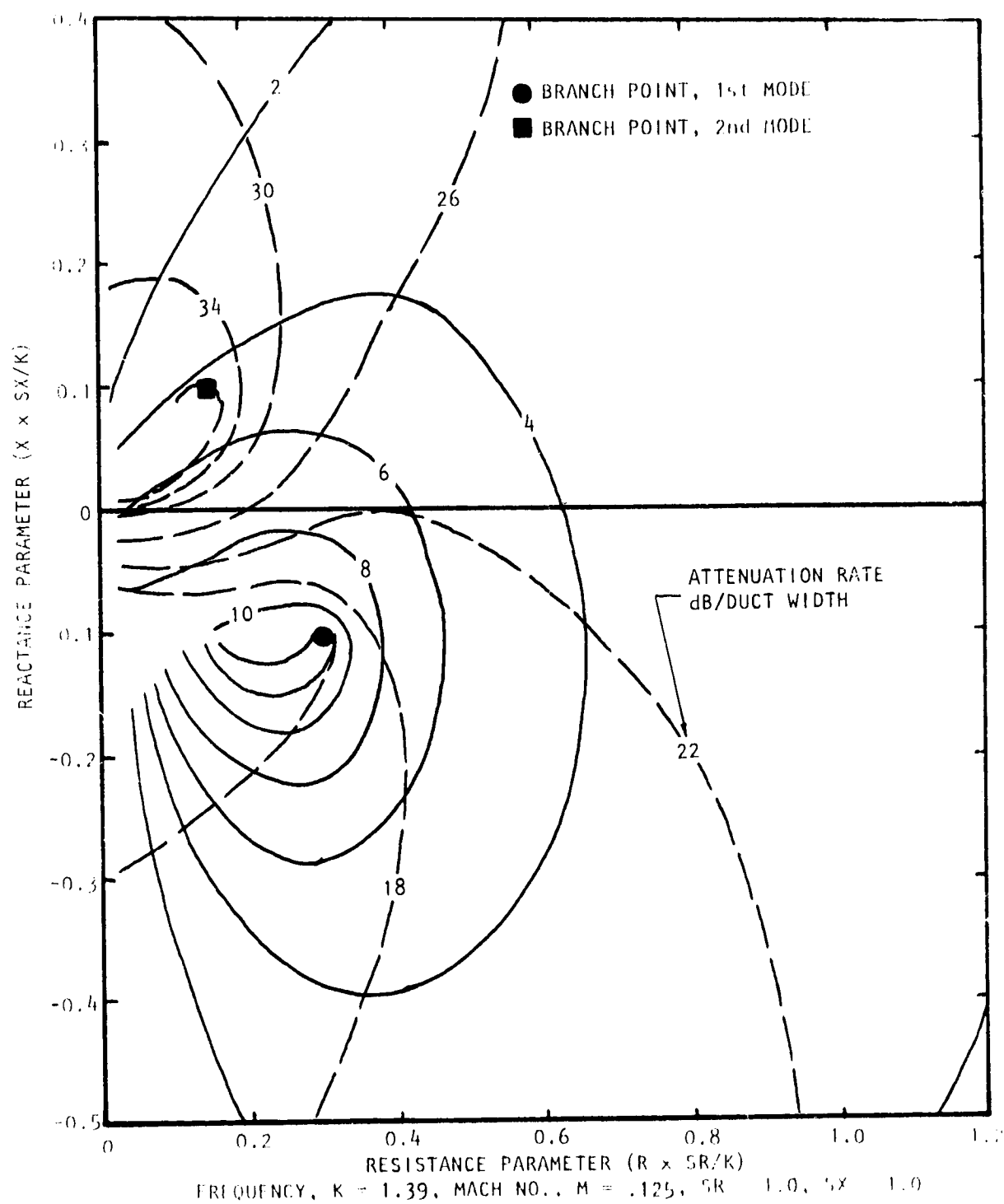


Figure A.23 Contours of Constant Attenuation for First Two Modes of Propagation (First Mode —, Second Mode ---)

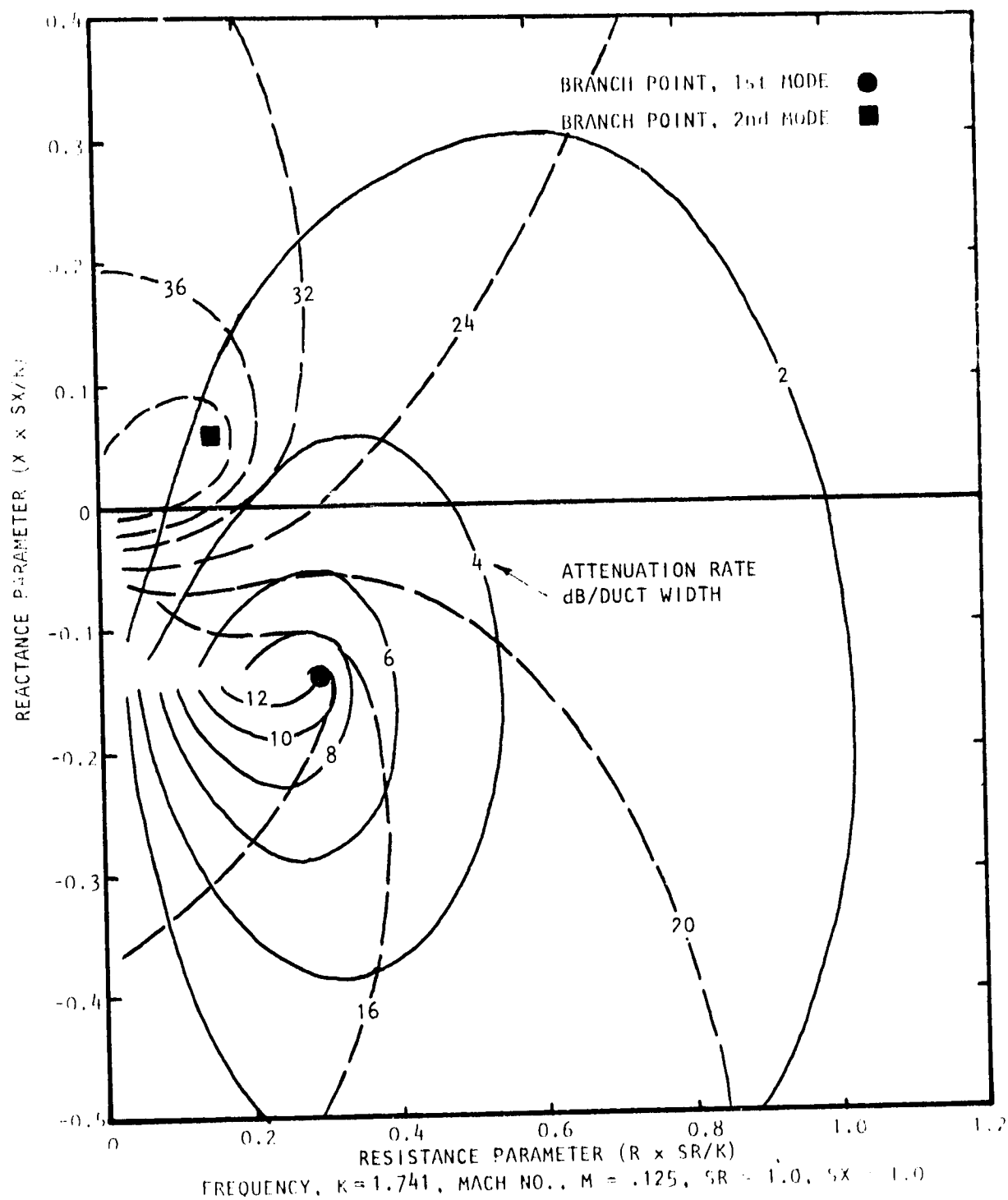


Figure A.24 Contours of Constant Attenuation for First Two Modes of Propagation (First Mode —, Second Mode ---)

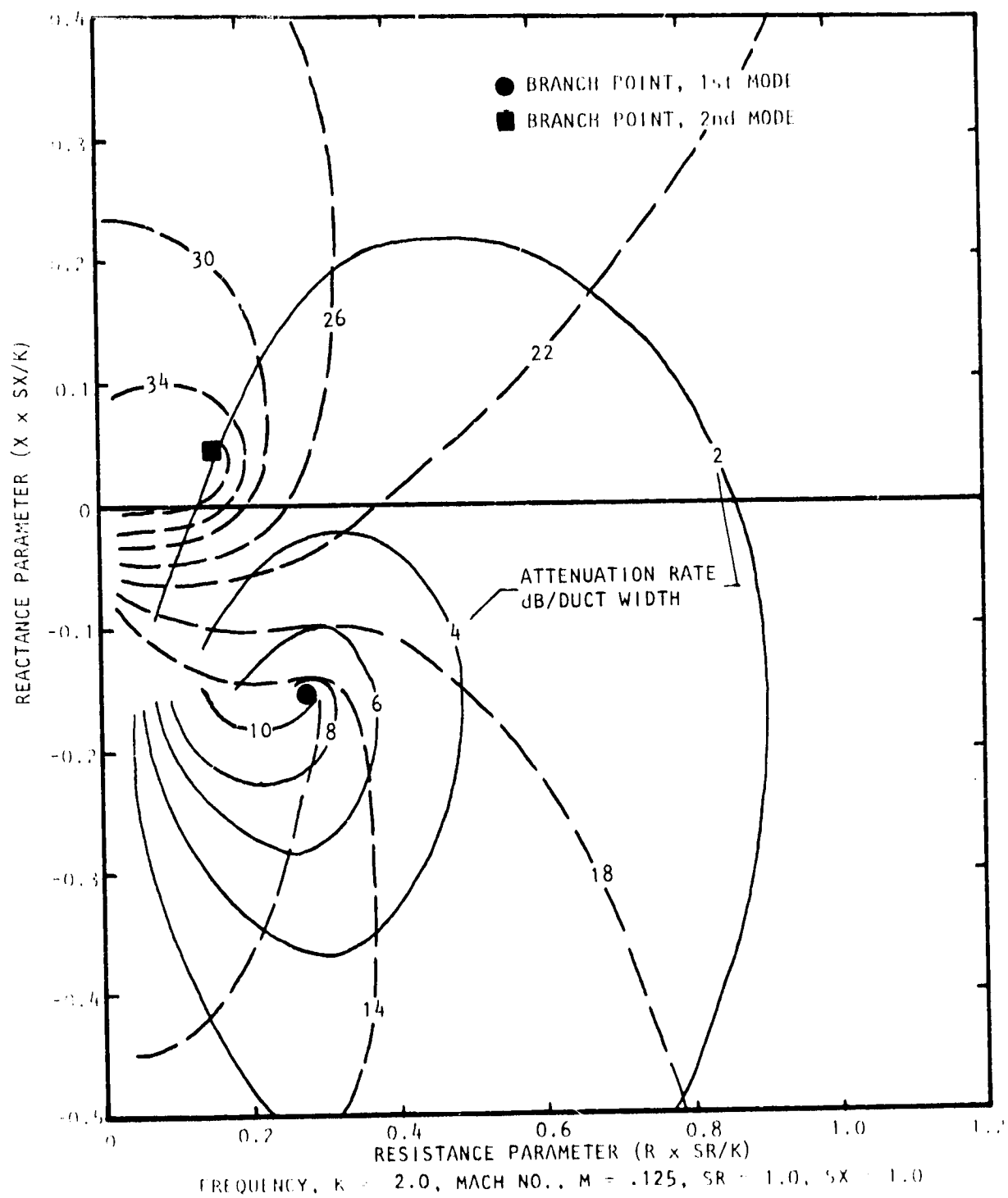


Figure A.25 Contours of Constant Attenuation for First Two Modes of Propagation (First Mode —, Second Mode ---)

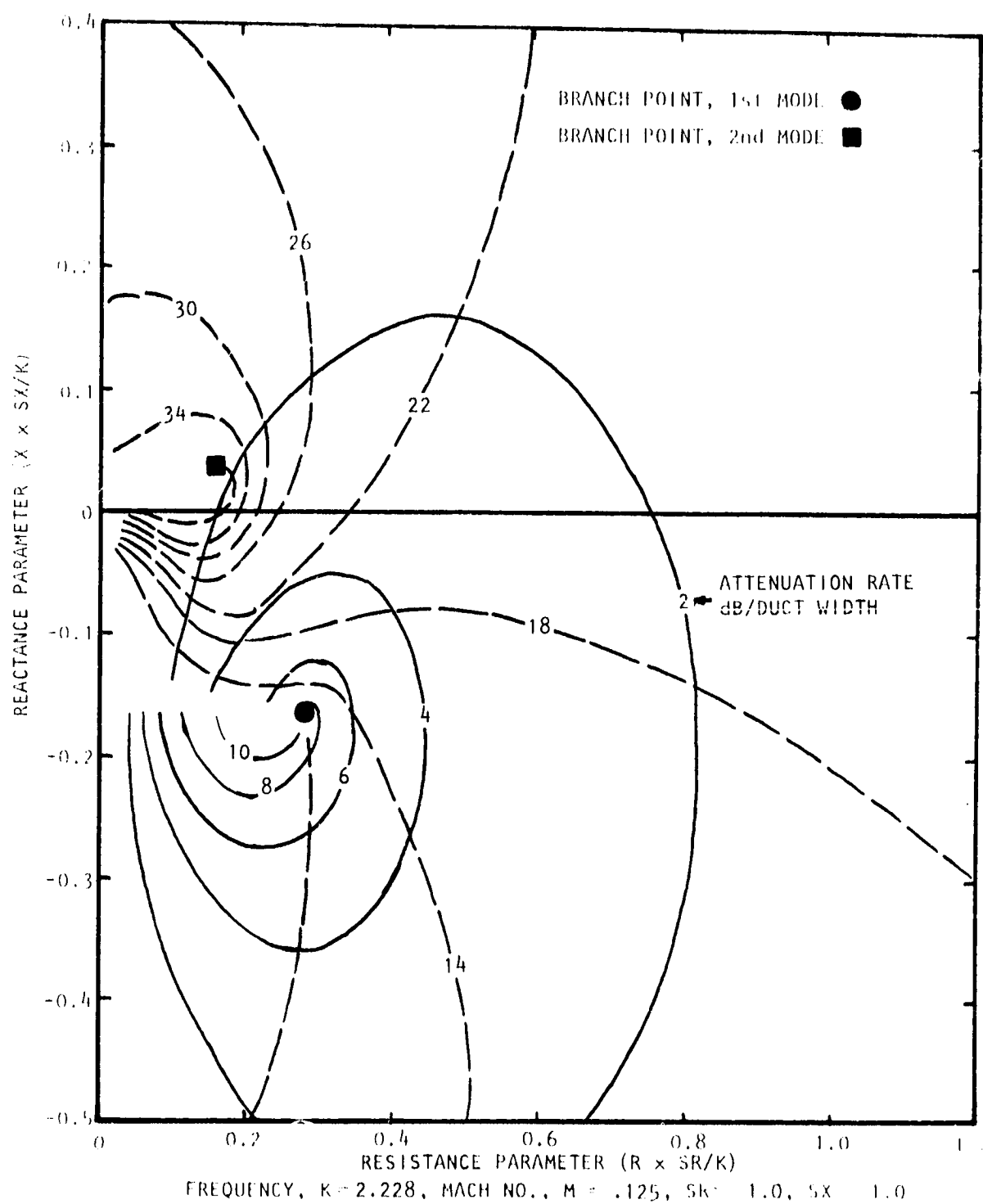


Figure A.26 Contours of Constant Attenuation for First Two Modes of Propagation (First Mode —, Second Mode ---)

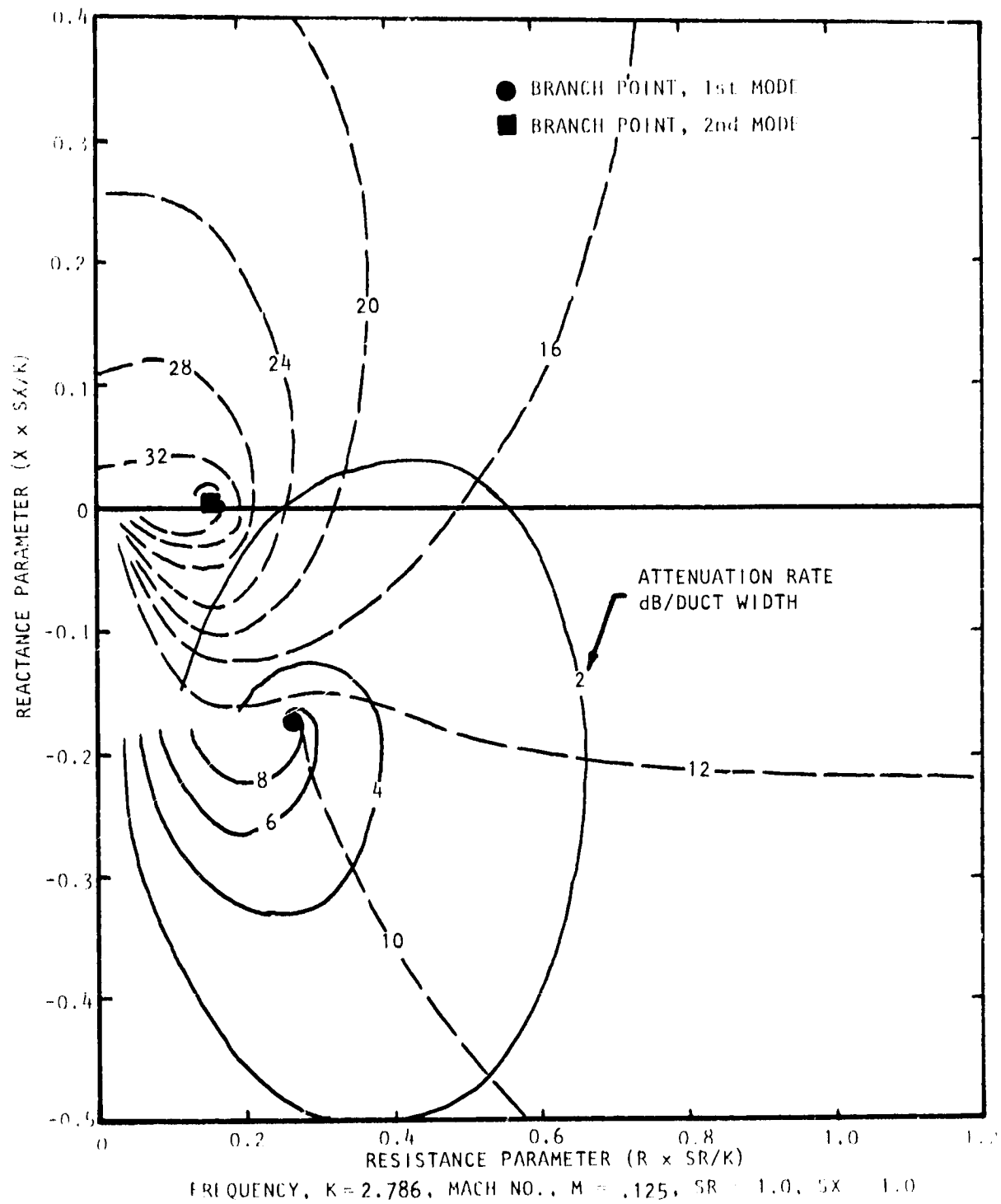


Figure A.27 Contours of Constant Attenuation for First Two Modes of Propagation (First Mode ———, Second Mode ----)

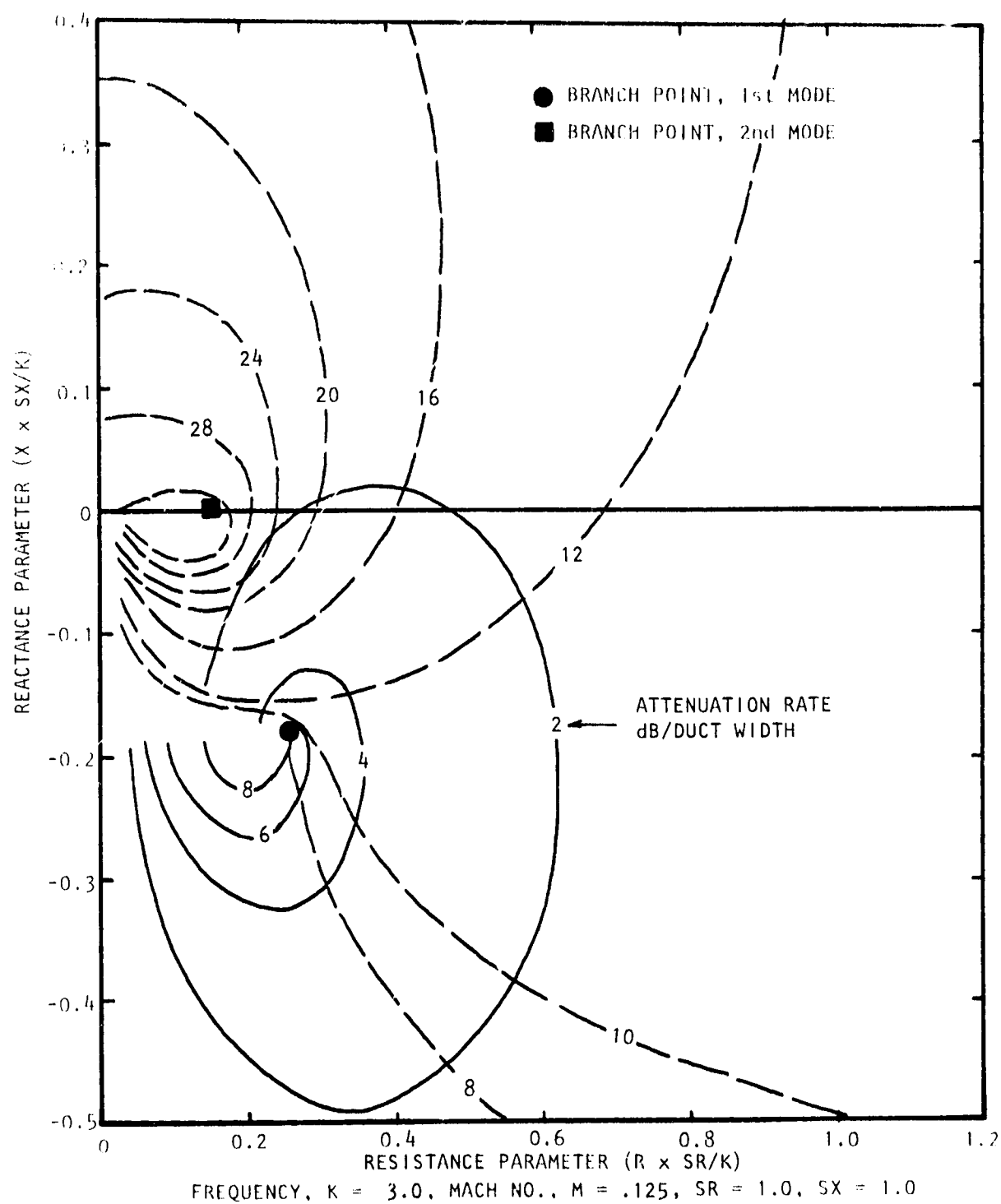


Figure A.28 Contours of Constant Attenuation for First Two Modes of Propagation (First Mode —, Second Mode ----)

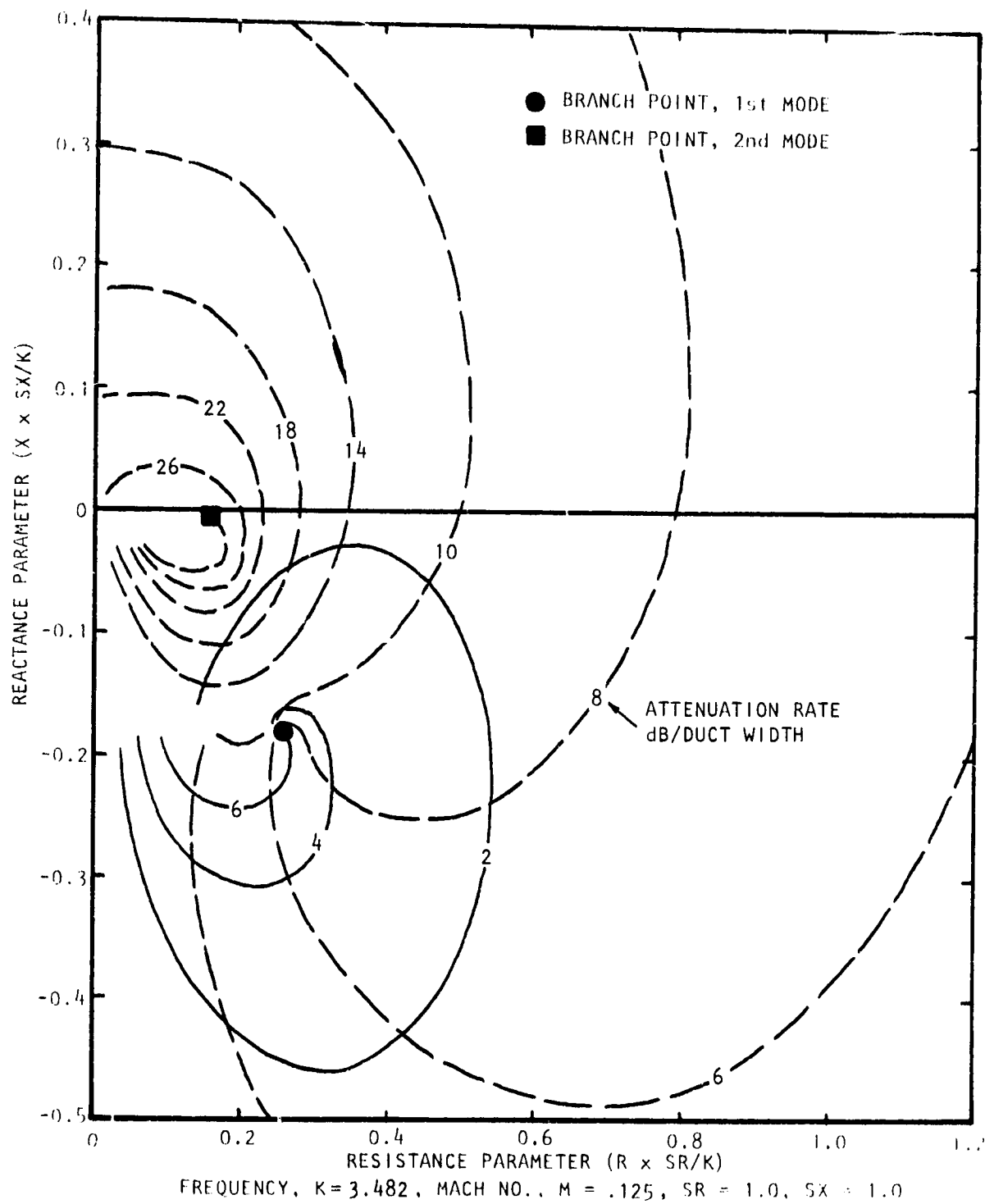


Figure A.29 Contours of Constant Attenuation for First Two Modes of Propagation (First Mode —, Second Mode ----)

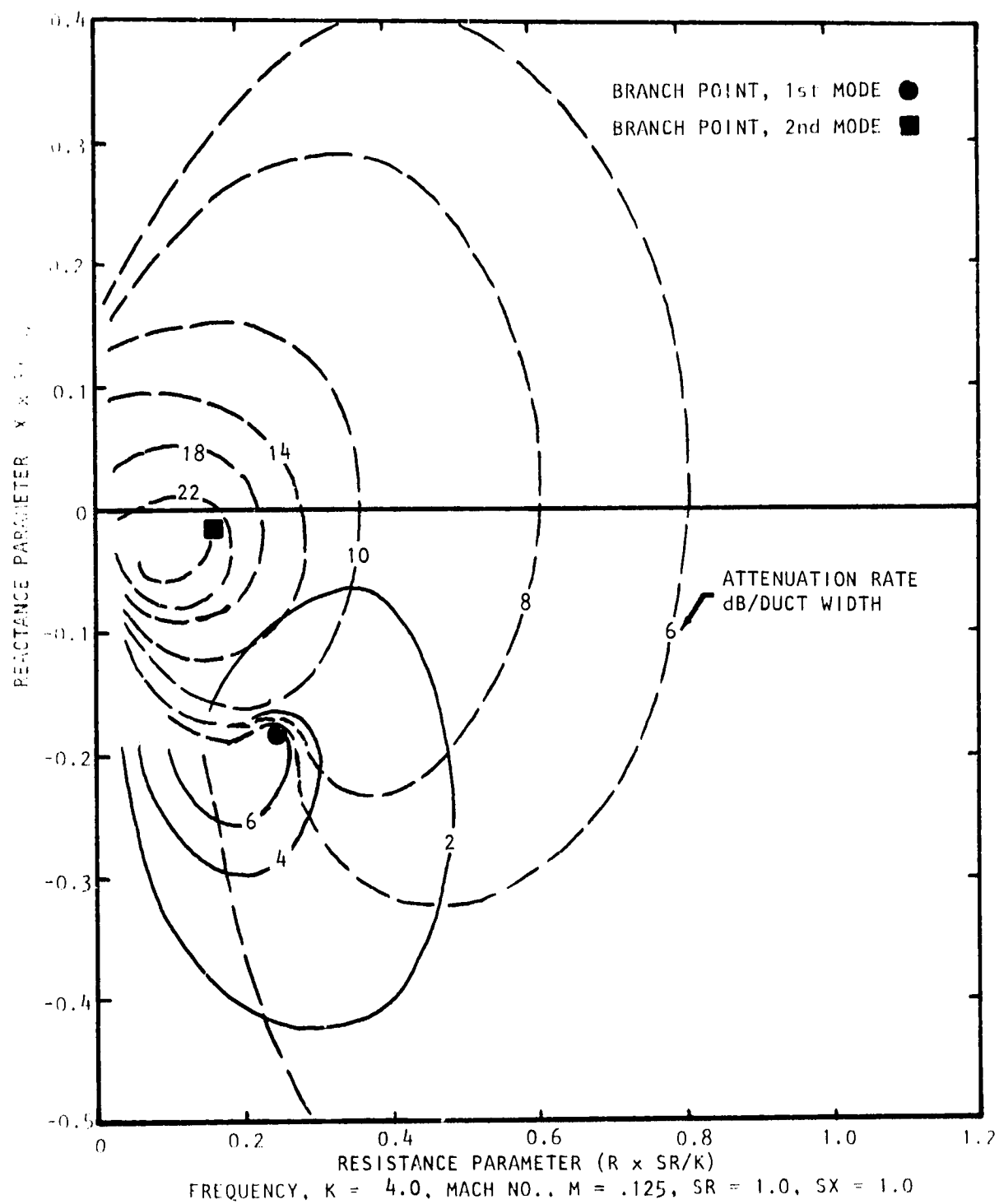


Figure A.30 Contours of Constant Attenuation for First Two Modes of Propagation (First Mode —, Second Mode ----)

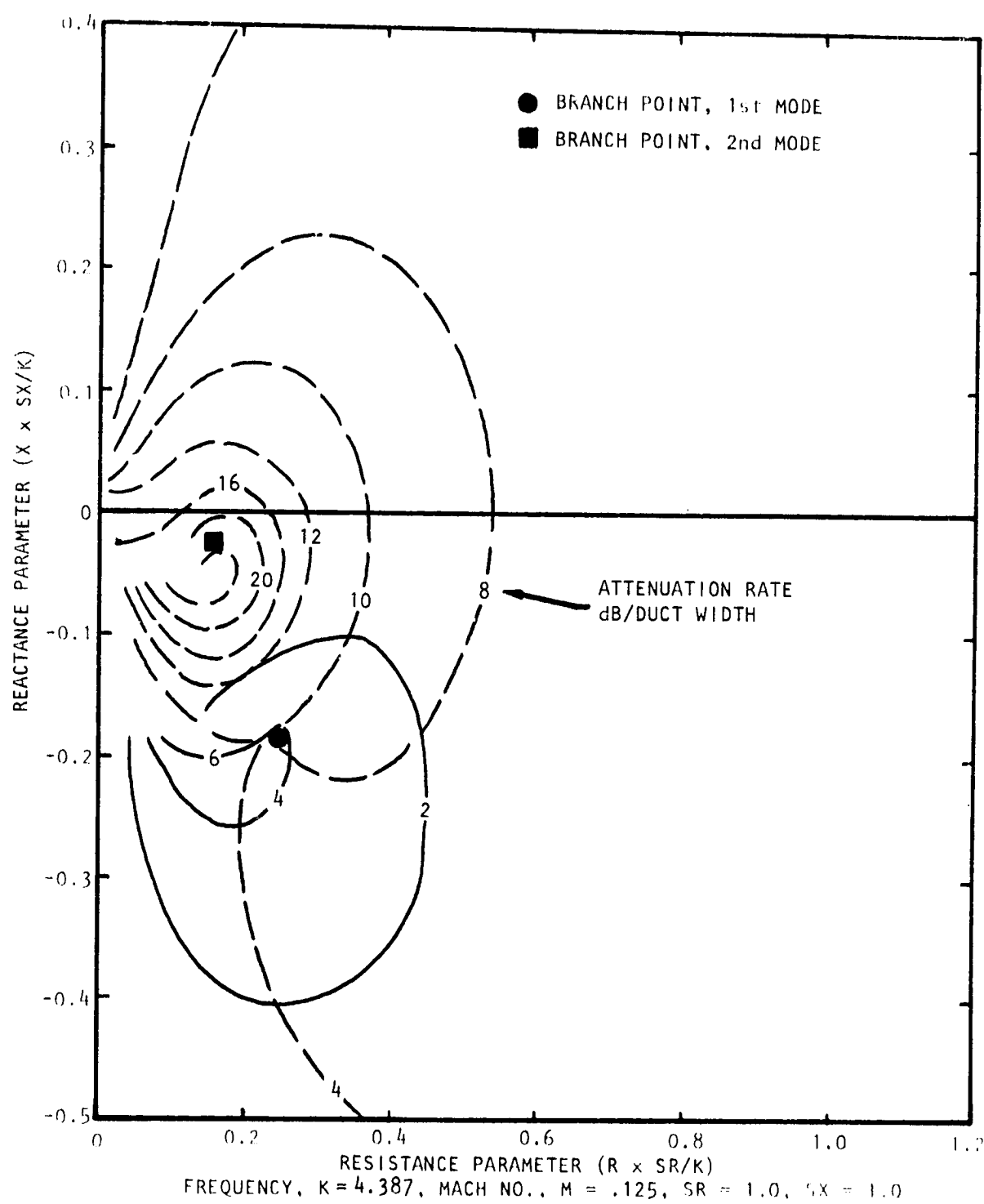


Figure A.31 Contours of Constant Attenuation for First Two Modes of Propagation (First Mode —, Second Mode ----)

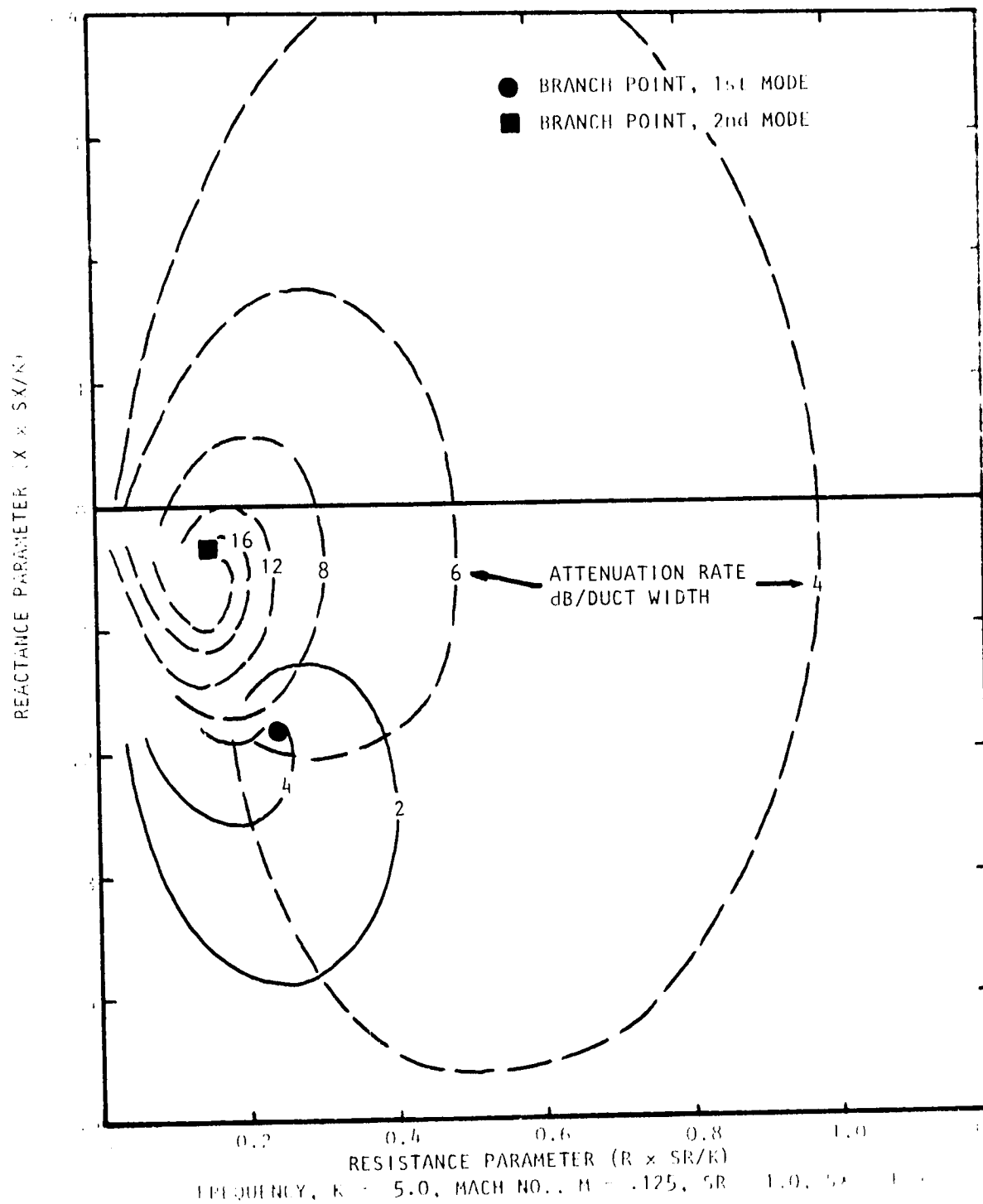


Figure A.32 Contours of Constant Attenuation for First Two Modes of Propagation (First Mode ---, Second Mode ----)

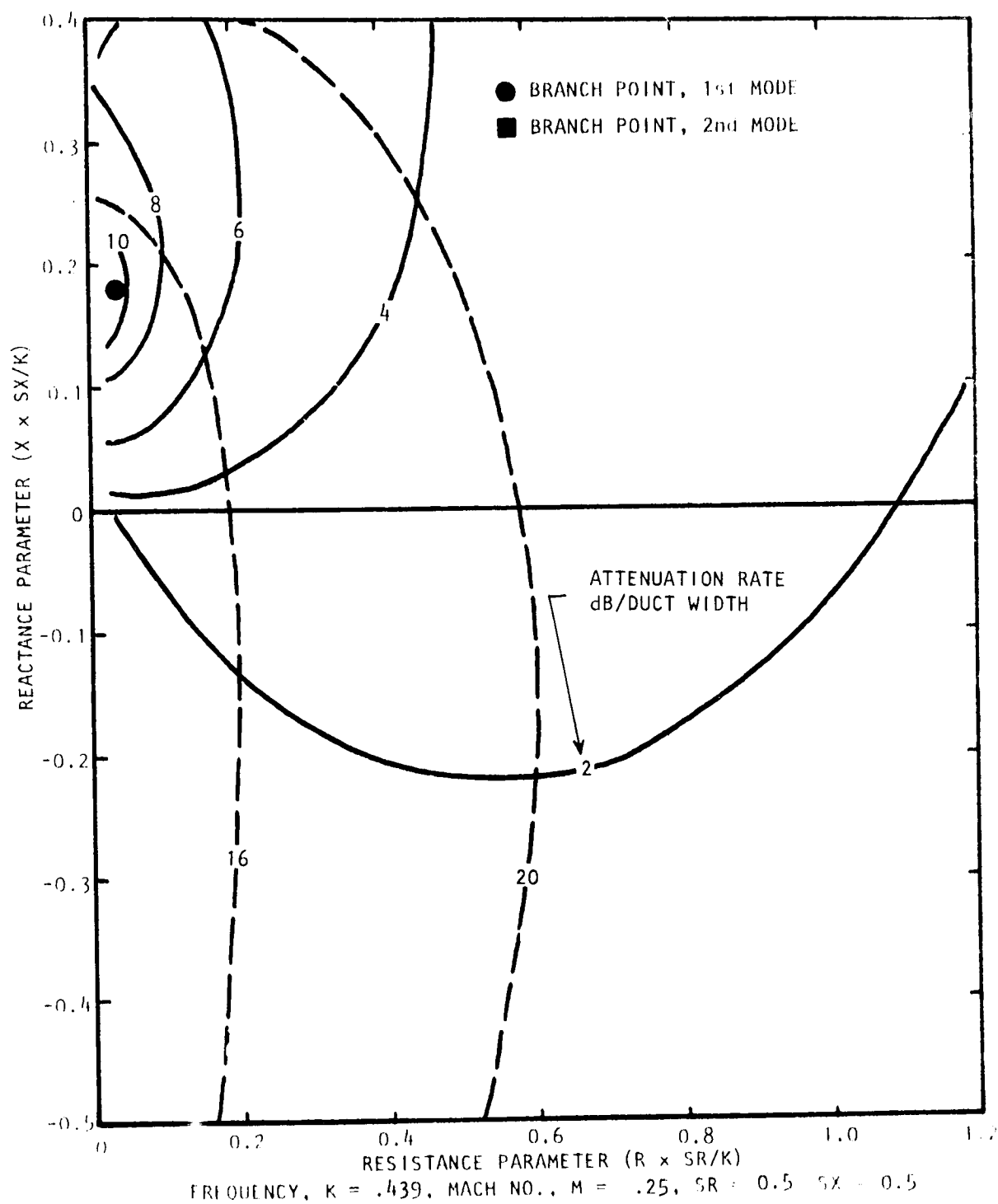


Figure A.33 Contours of Constant Attenuation for First Two Modes of Propagation (First Mode —, Second Mode ----)

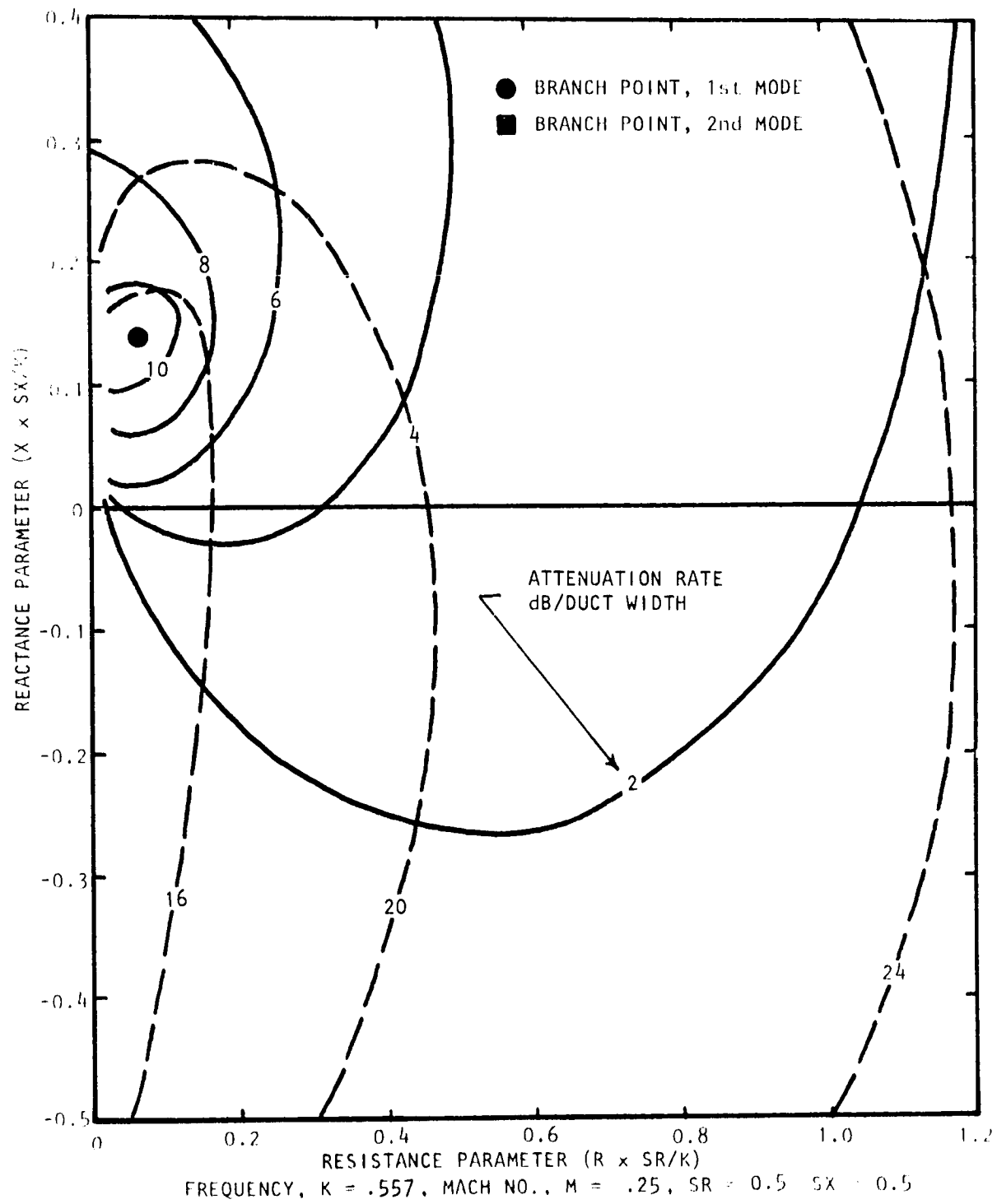


Figure A.34 Contours of Constant Attenuation for First Two Modes of Propagation (First Mode ———, Second Mode ----)

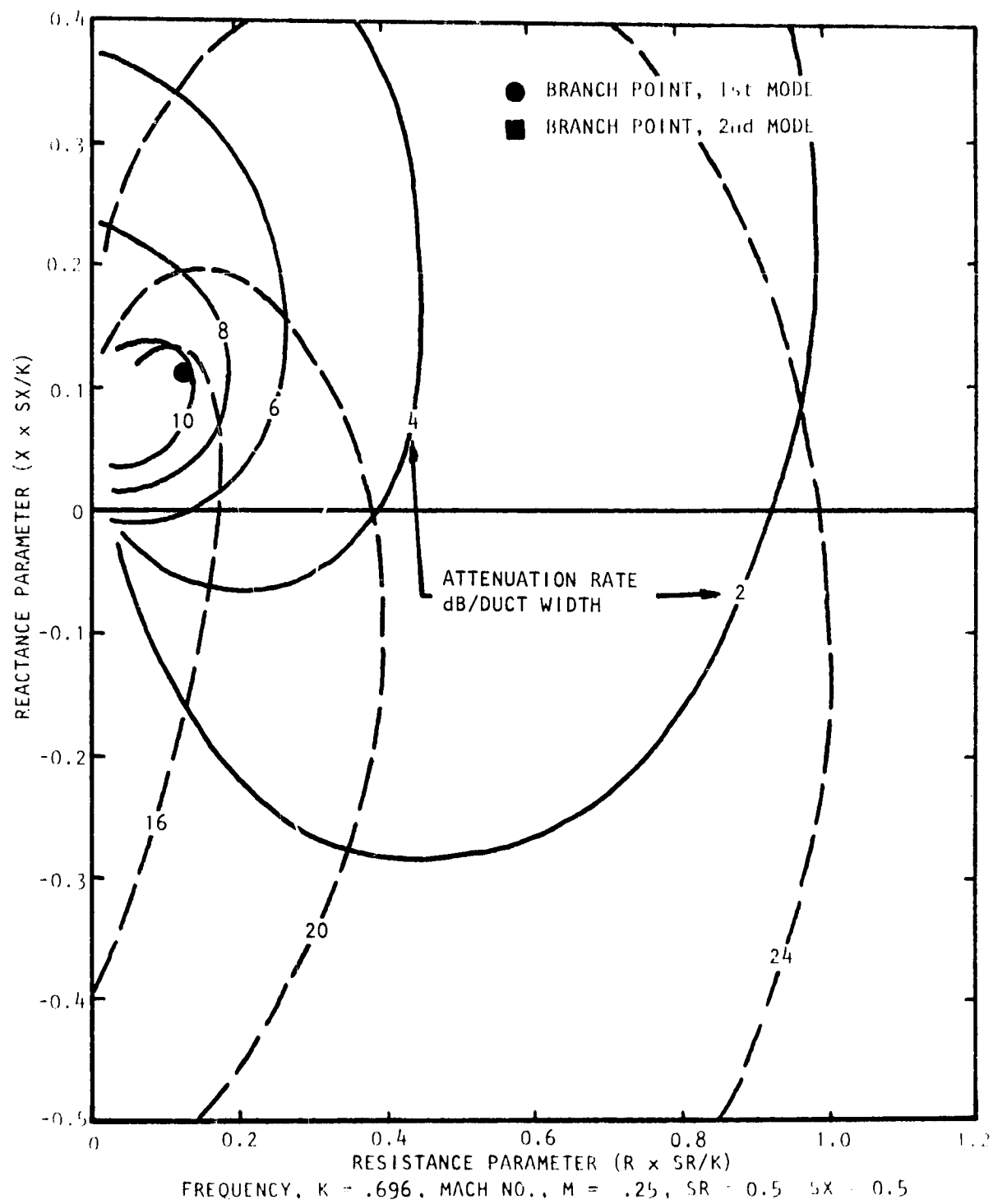


Figure A.35 Contours of Constant Attenuation for First Two Modes of Propagation (First Mode —, Second Mode ----)

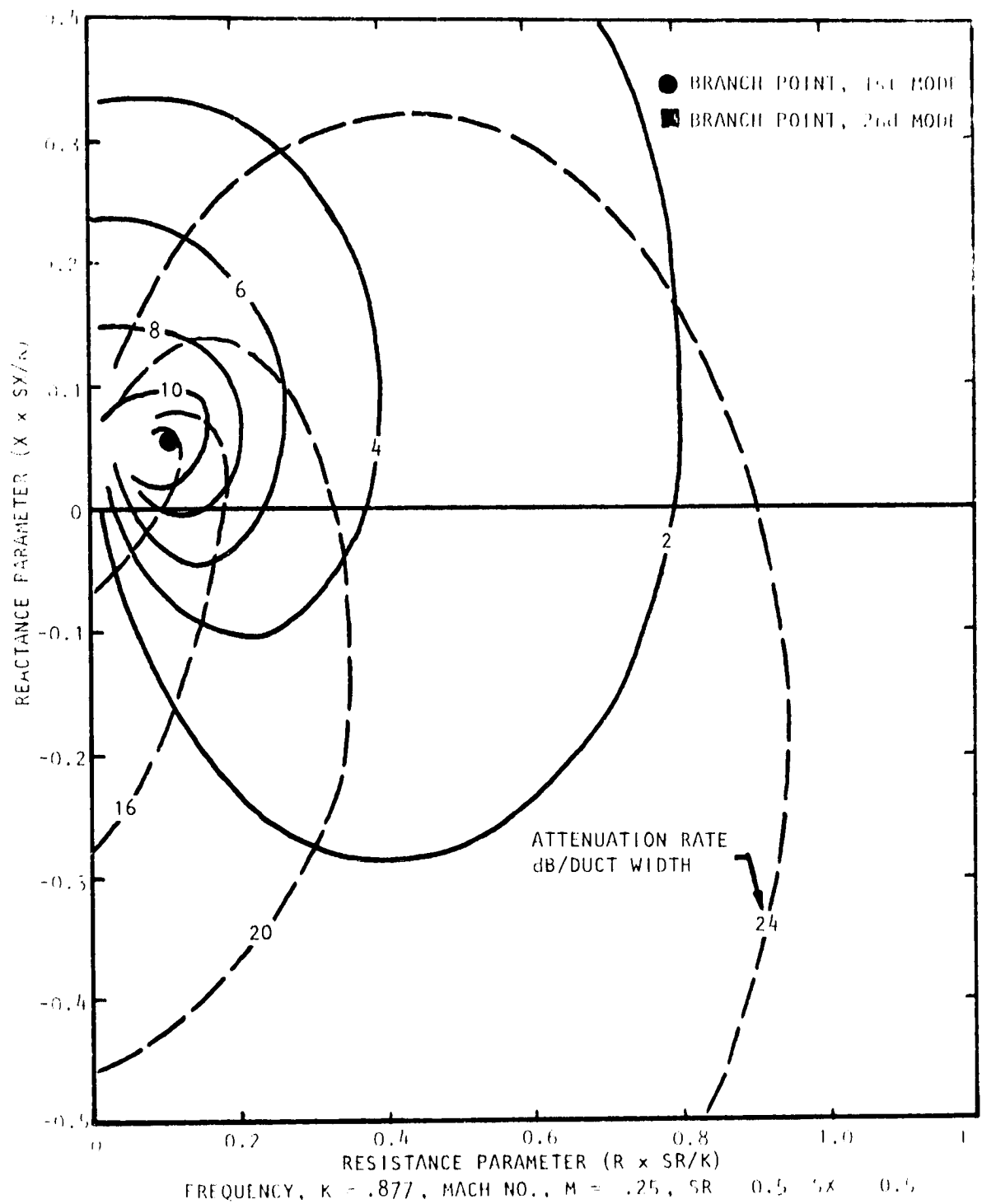


Figure A.36 Contours of Constant Attenuation for First Two Mode of Propagation (First Mode —, Second Mode ---)

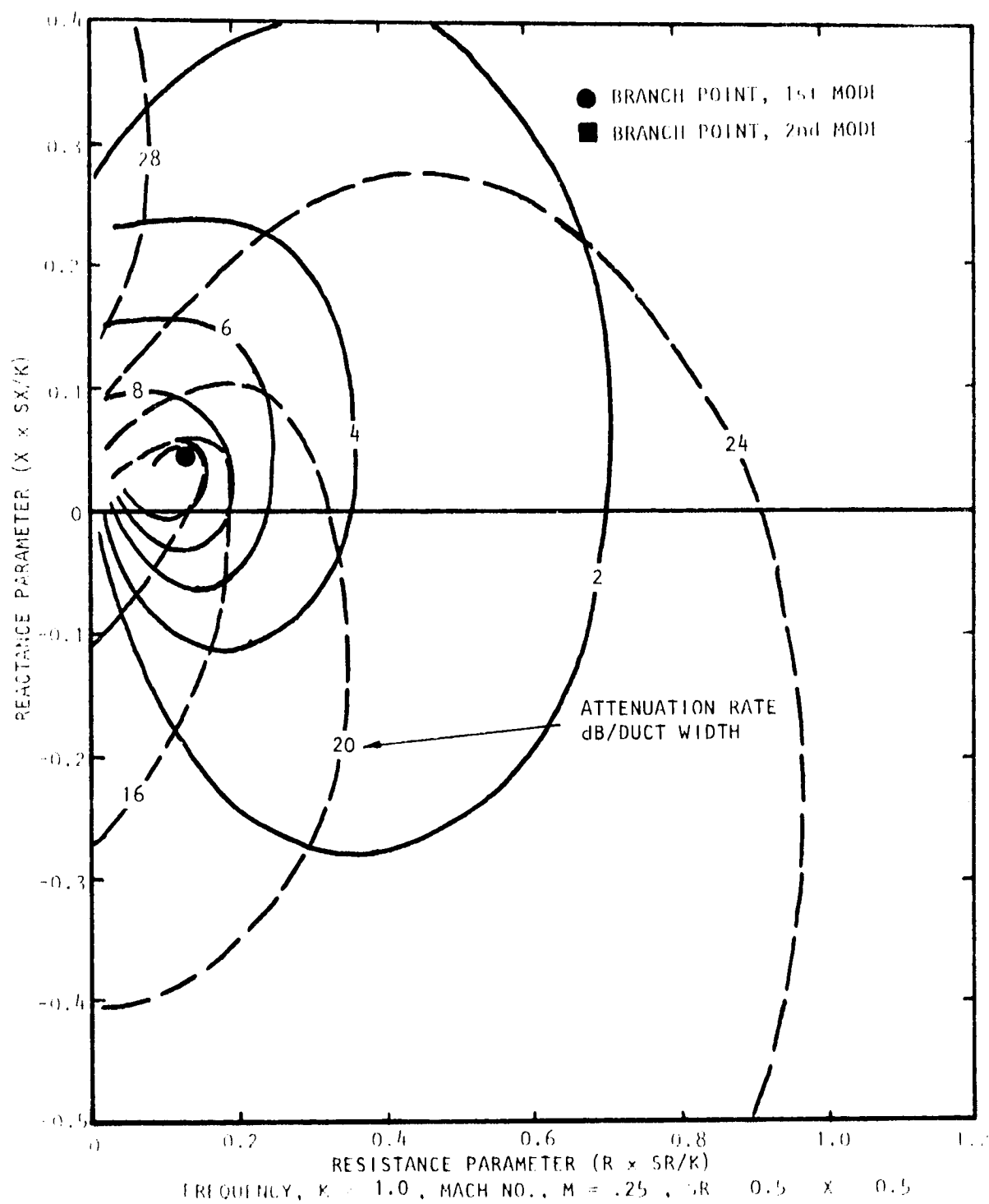


Figure A.37 Contours of Constant Attenuation for First Two Modes of Propagation (First Mode ———, Second Mode - - -)

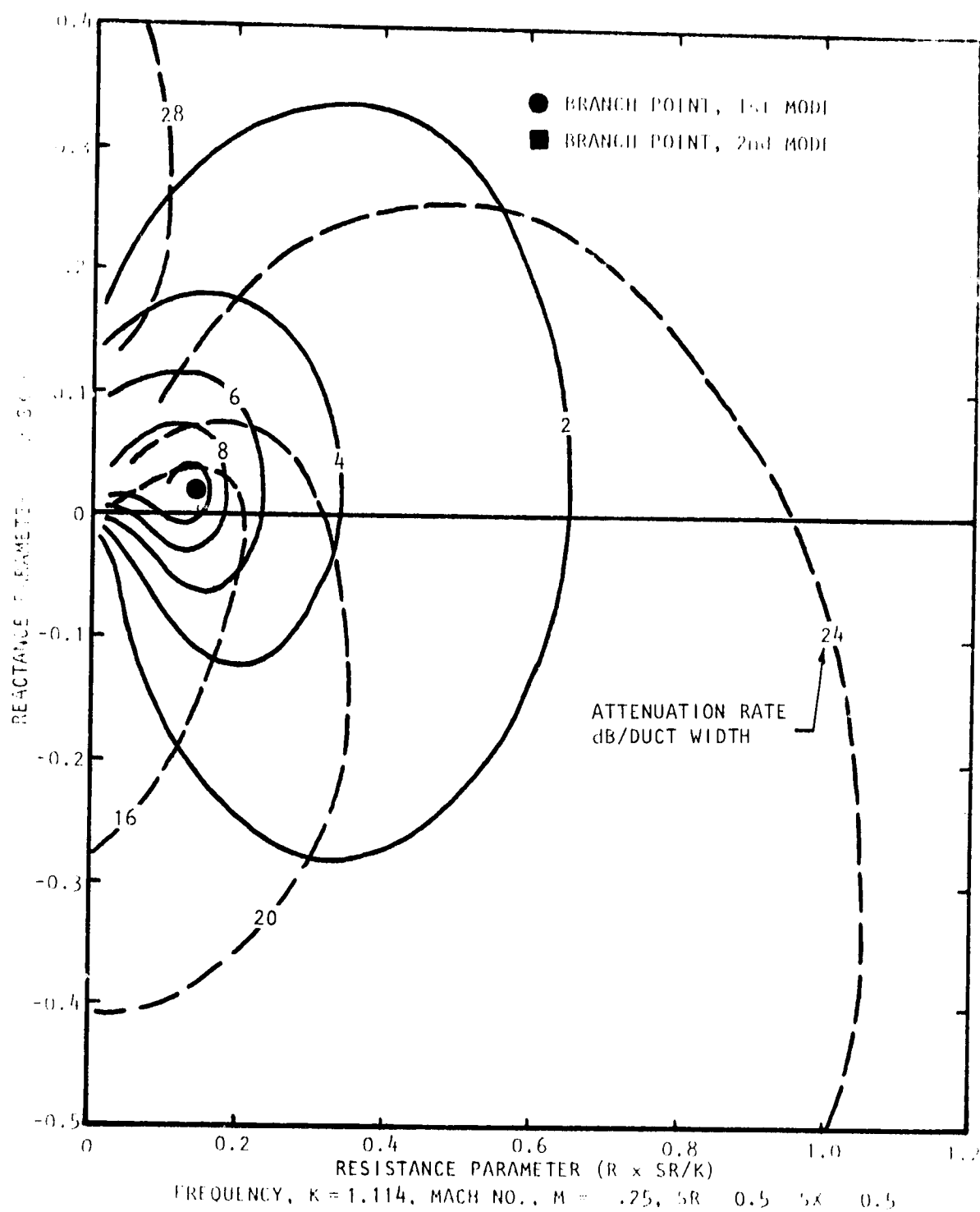


Figure A.38 Contours of Constant Attenuation for First Two Modes of Propagation (First Mode ———, Second Mode - - -)

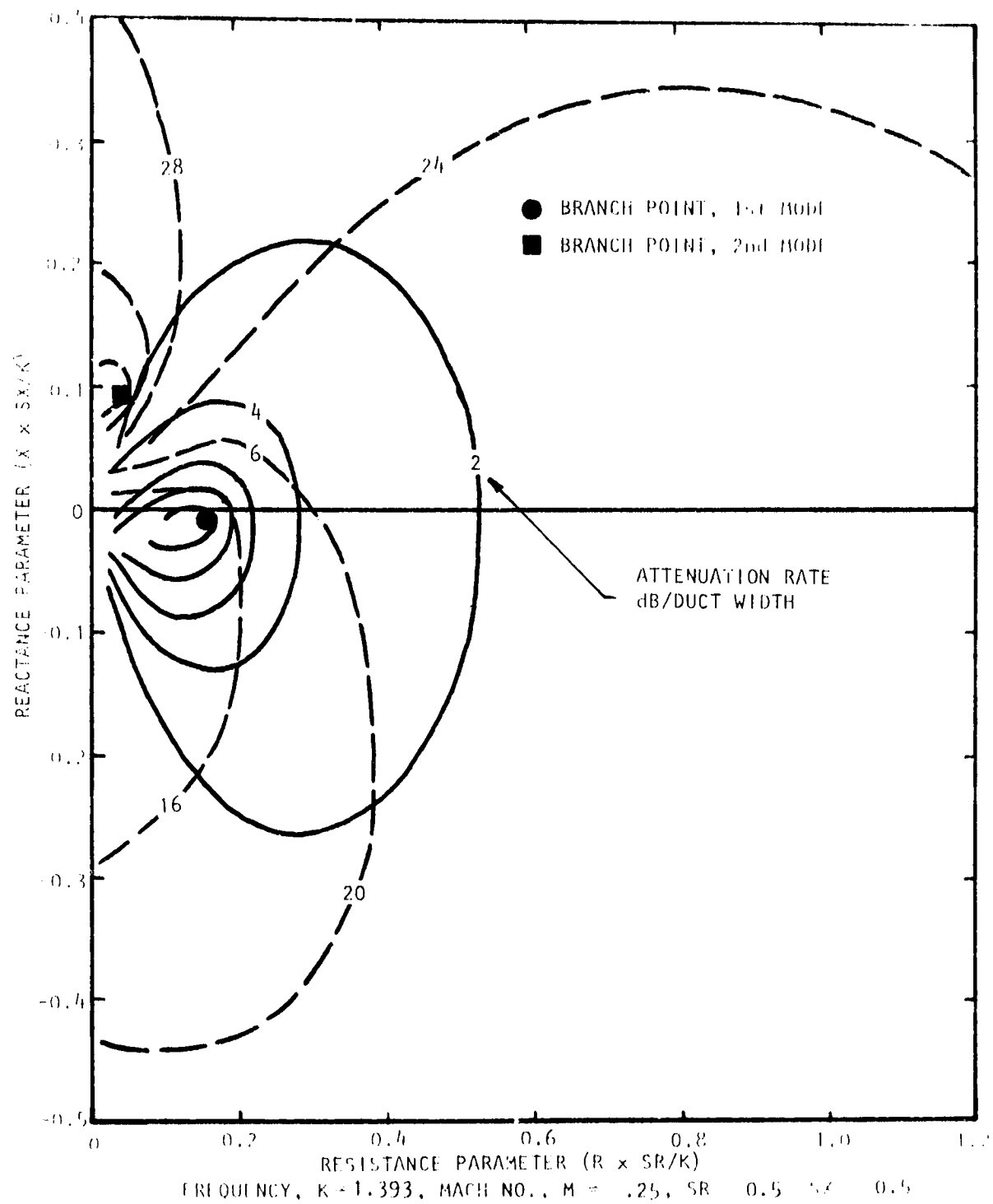


Figure A.39 Contours of Constant Attenuation for First Two Modes of Propagation (First Mode ---, Second Mode - - -)

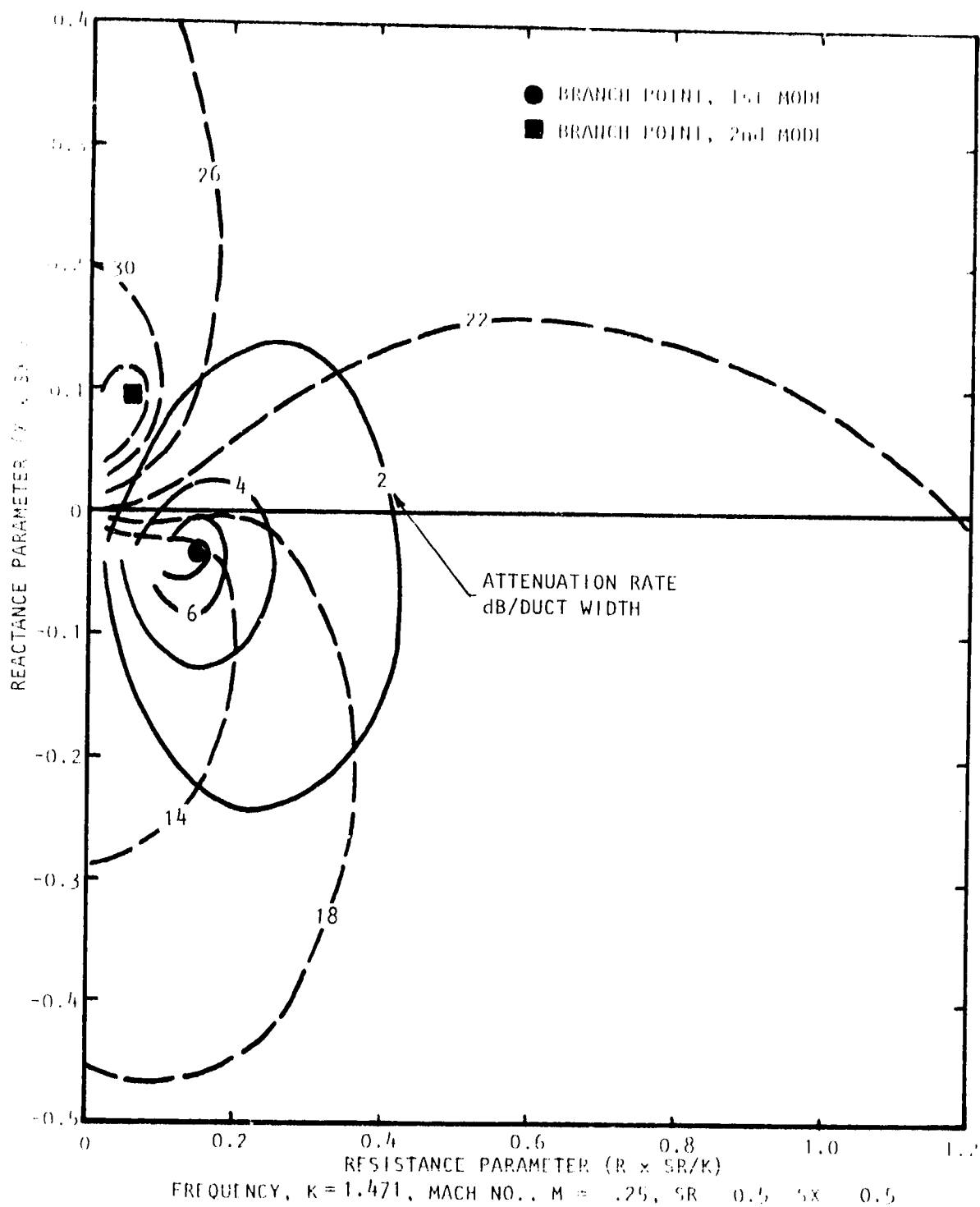


Figure A.40 Contours of Constant Attenuation for First Two Modes of Propagation (First Mode ———, Second Mode ----)

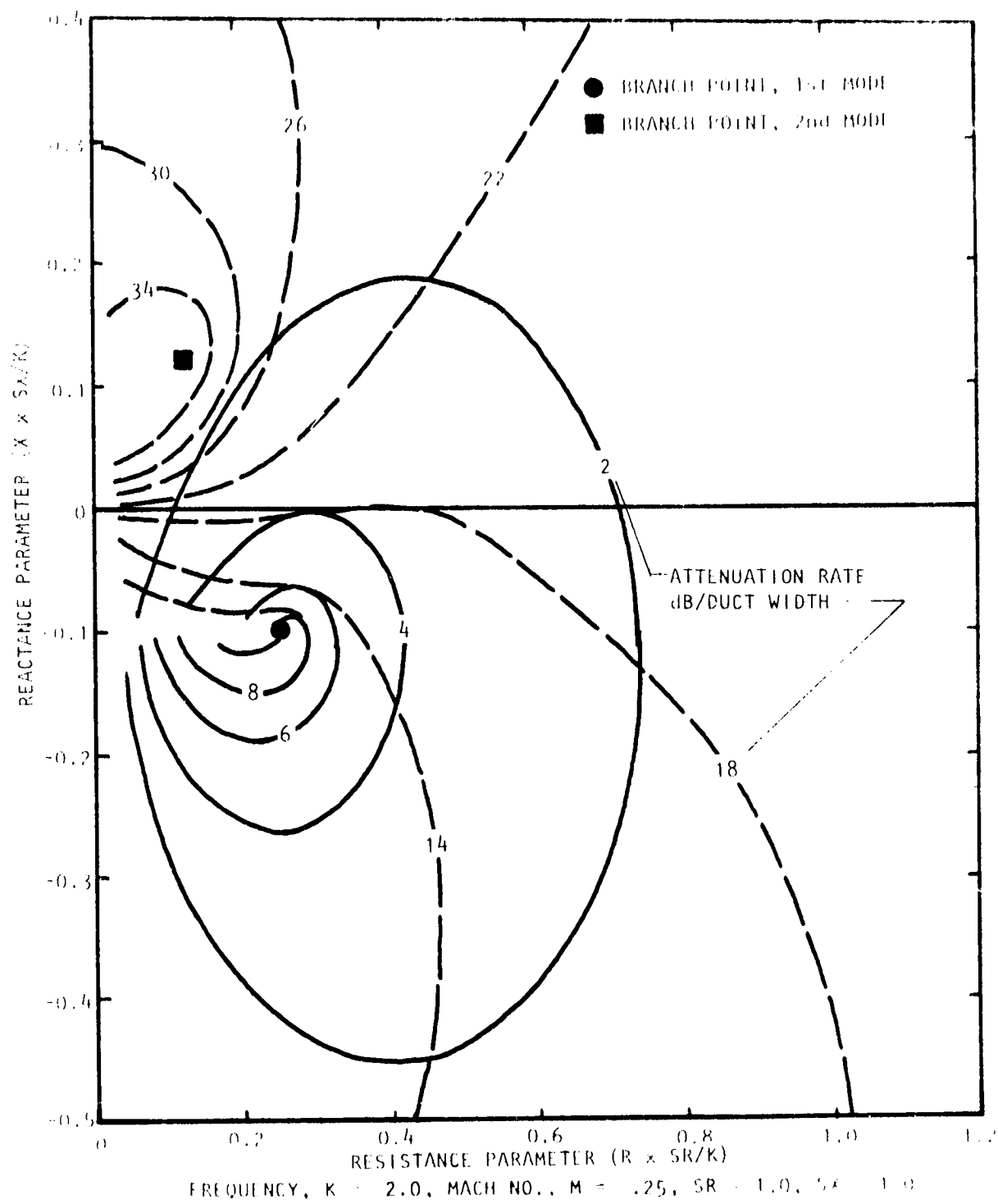


Figure A.41 Contours of Constant Attenuation for First Two Modes of Propagation (First Mode —, Second Mode ---)

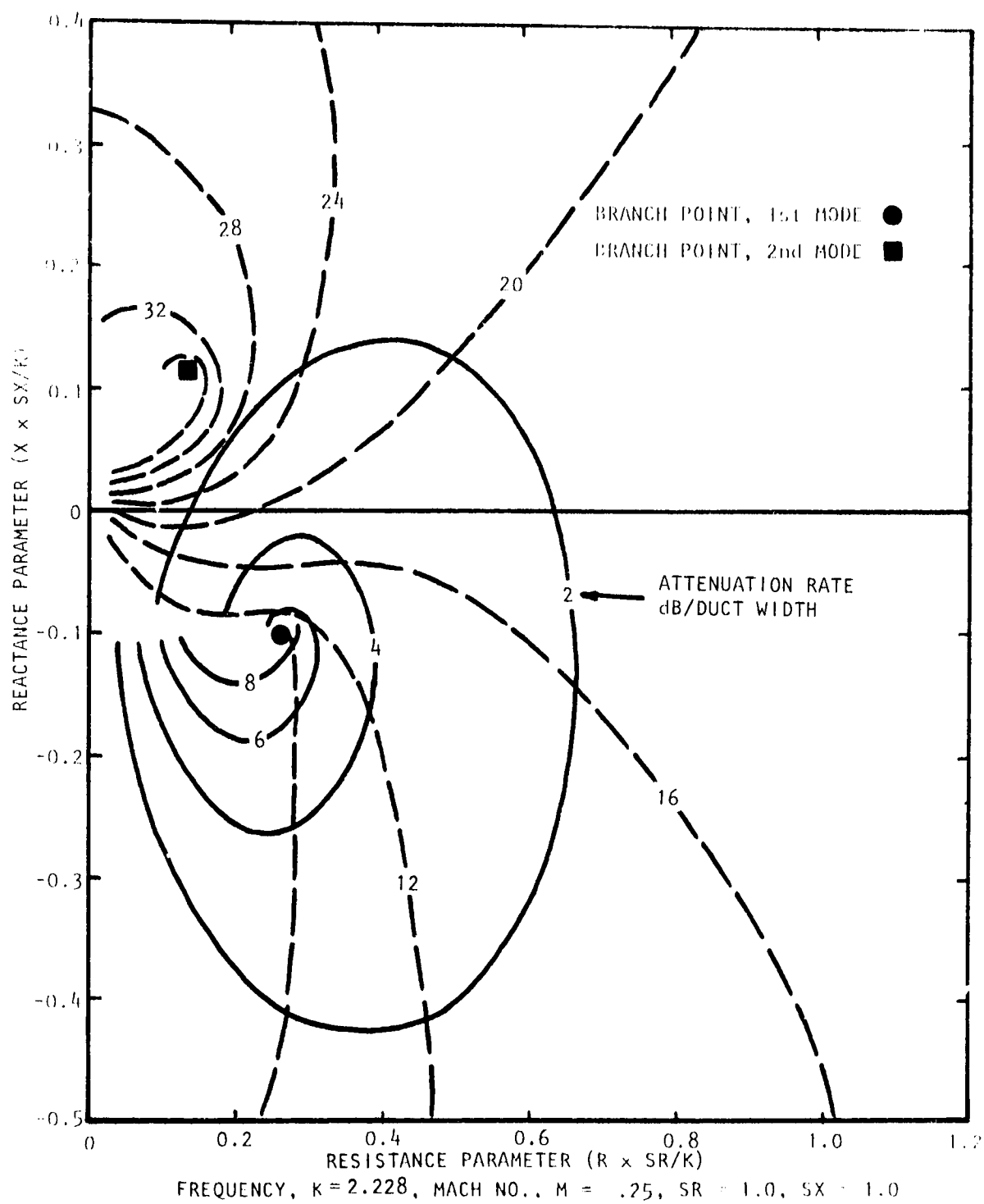


Figure A.42 Contours of Constant Attenuation for First Two Modes of Propagation. (First Mode —, Second Mode ---)

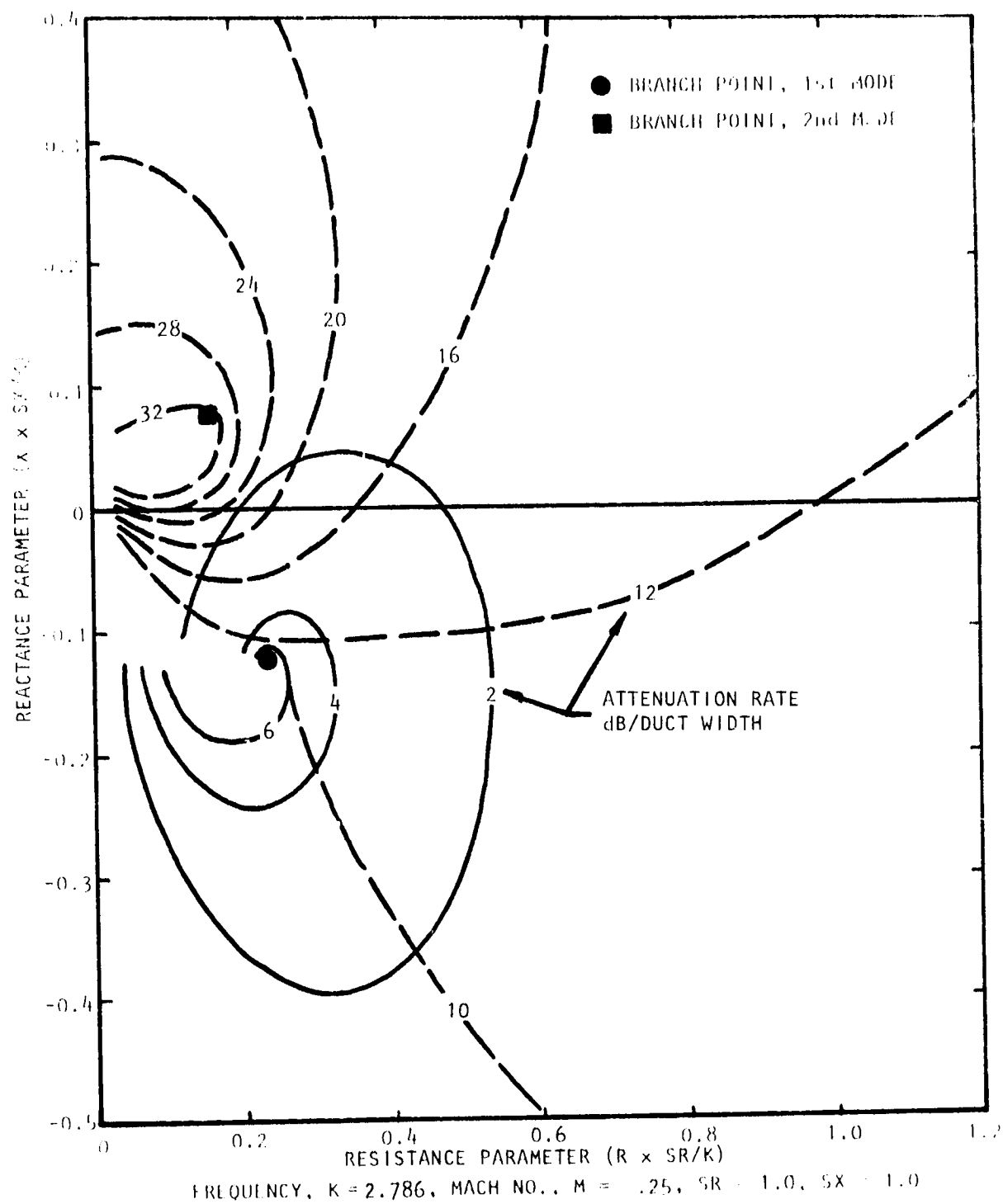


Figure A.43 Contours of Constant Attenuation for First Two Modes of Propagation (First Mode —, Second Mode ---)

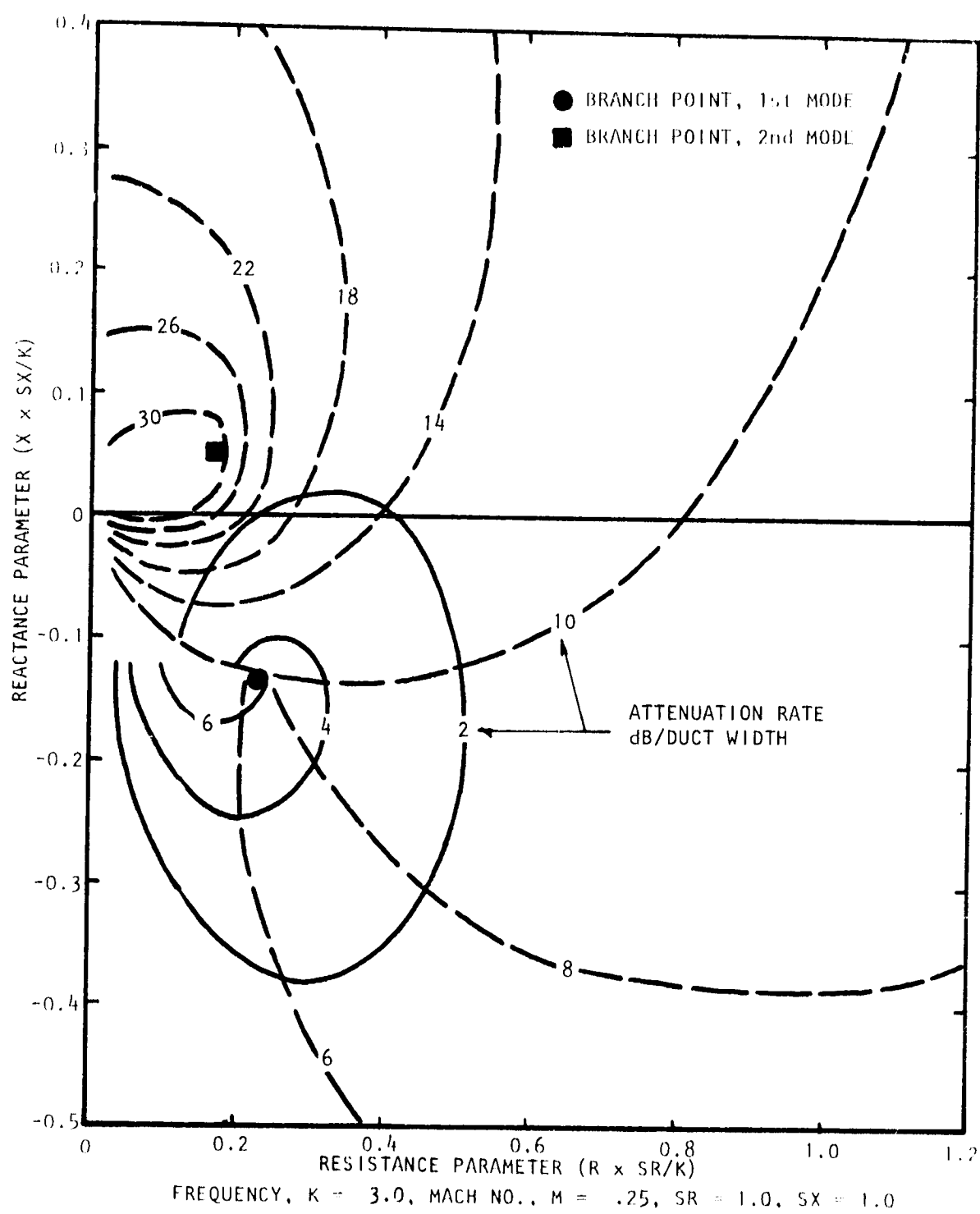


Figure A.44 Contours of Constant Attenuation for First Two Modes of Propagation (First Mode —, Second Mode ---)

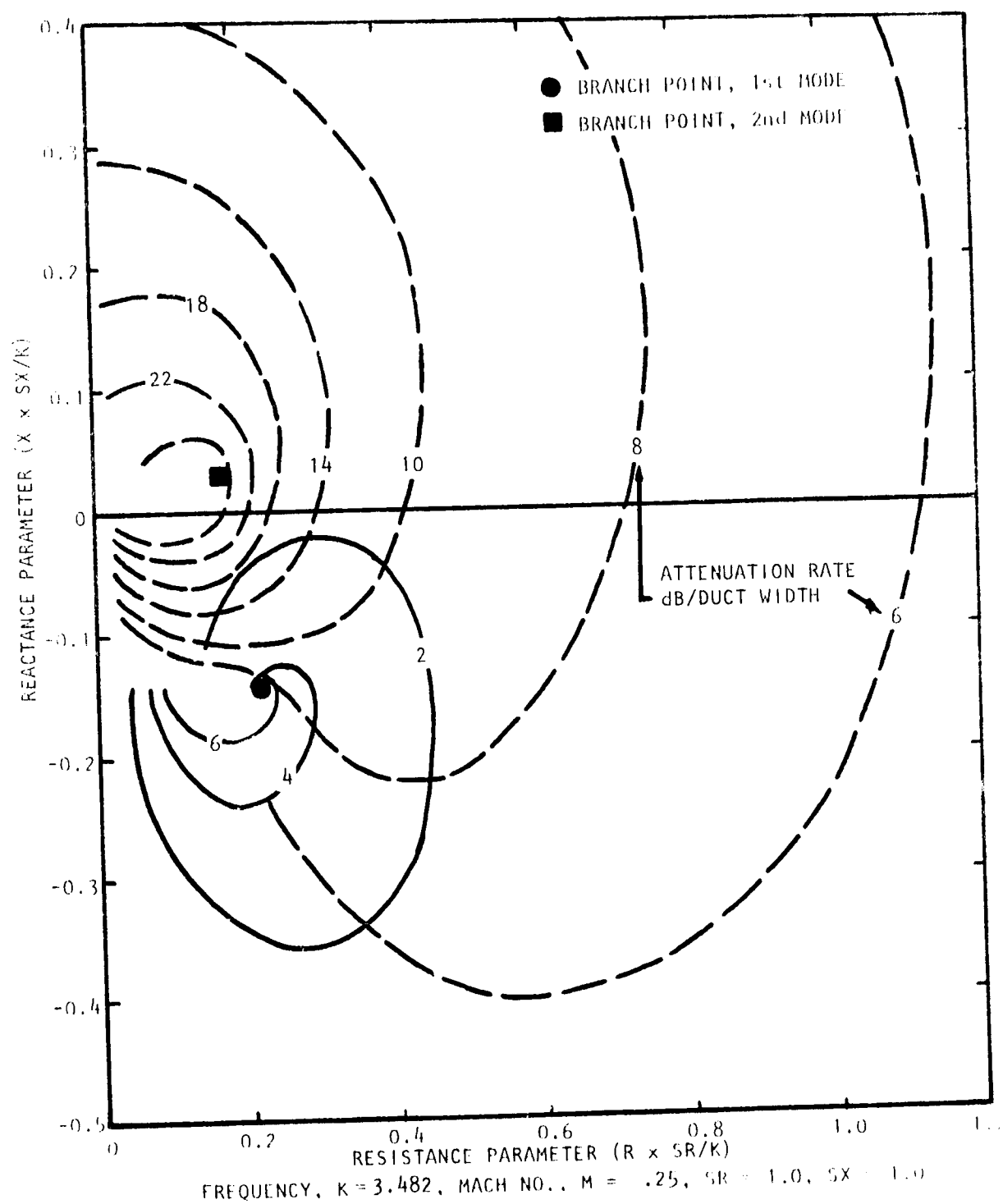


Figure A.45 Contours of Constant Attenuation for First Two Modes of Propagation (First Mode —, Second Mode ---)

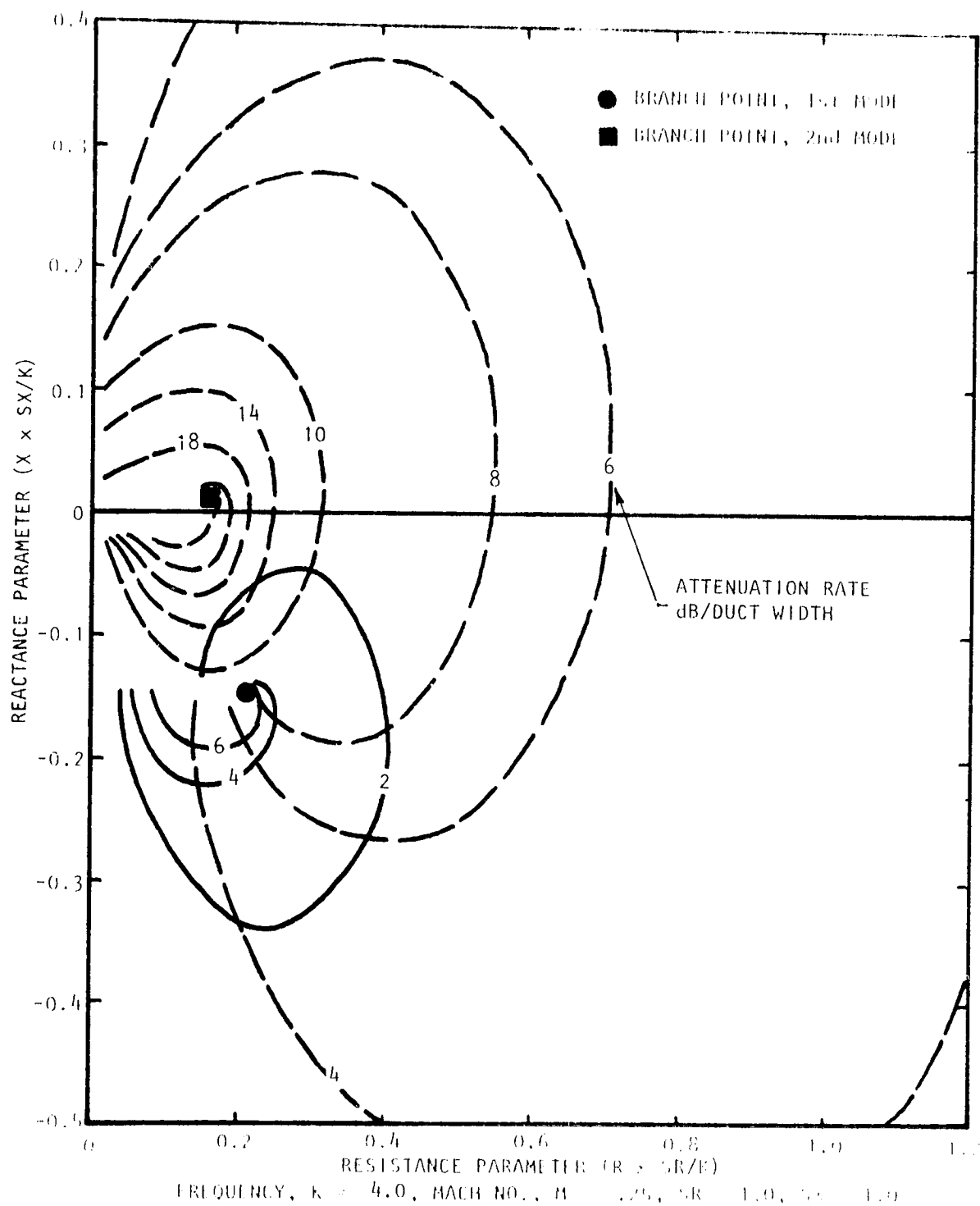


Figure A.46 Contours of Constant Attenuation for First Two Modes of Propagation (First Mode ---, Second Mode —)

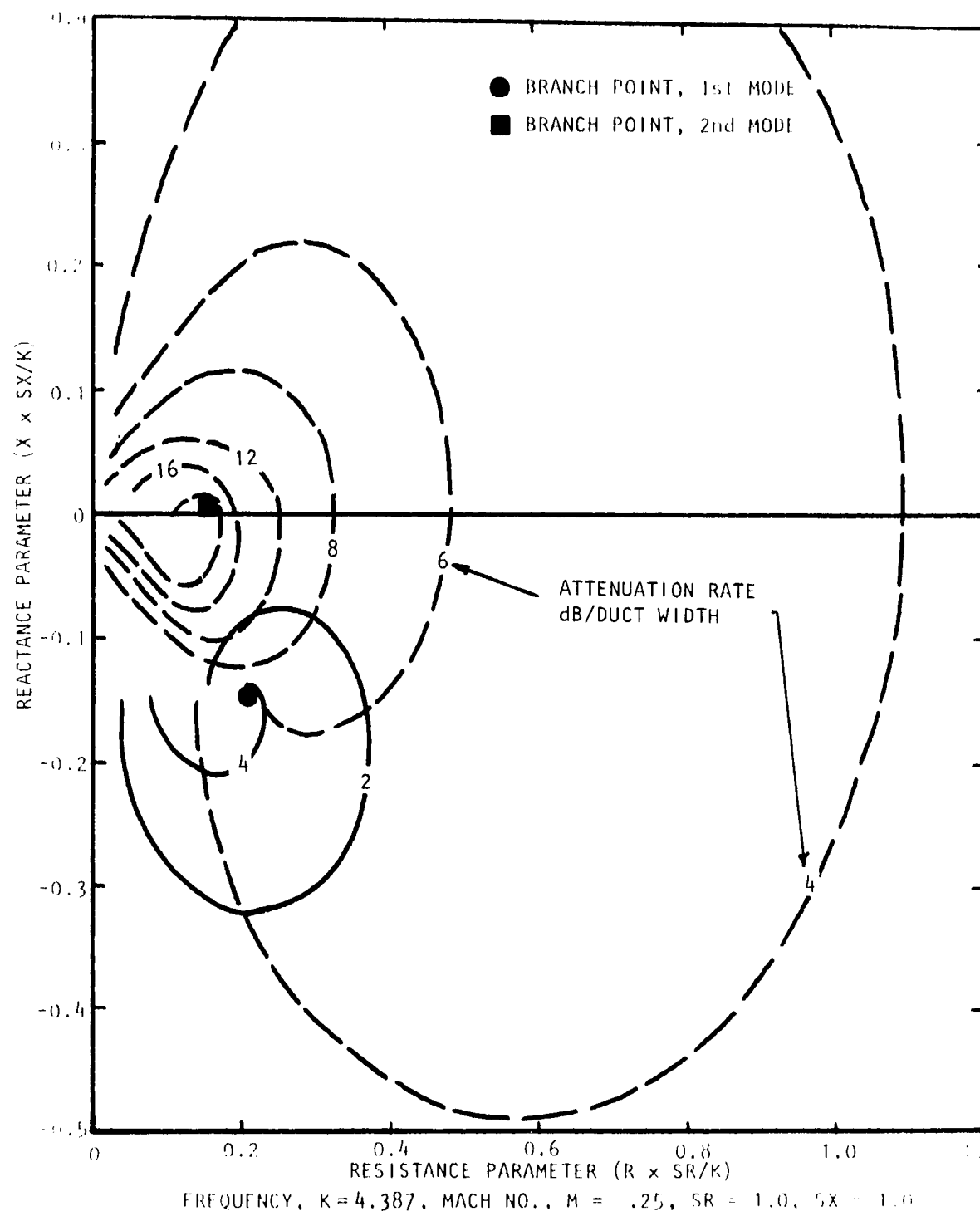


Figure A.47 Contours of Constant Attenuation for First Two Modes of Propagation (First Mode —, Second Mode ---)

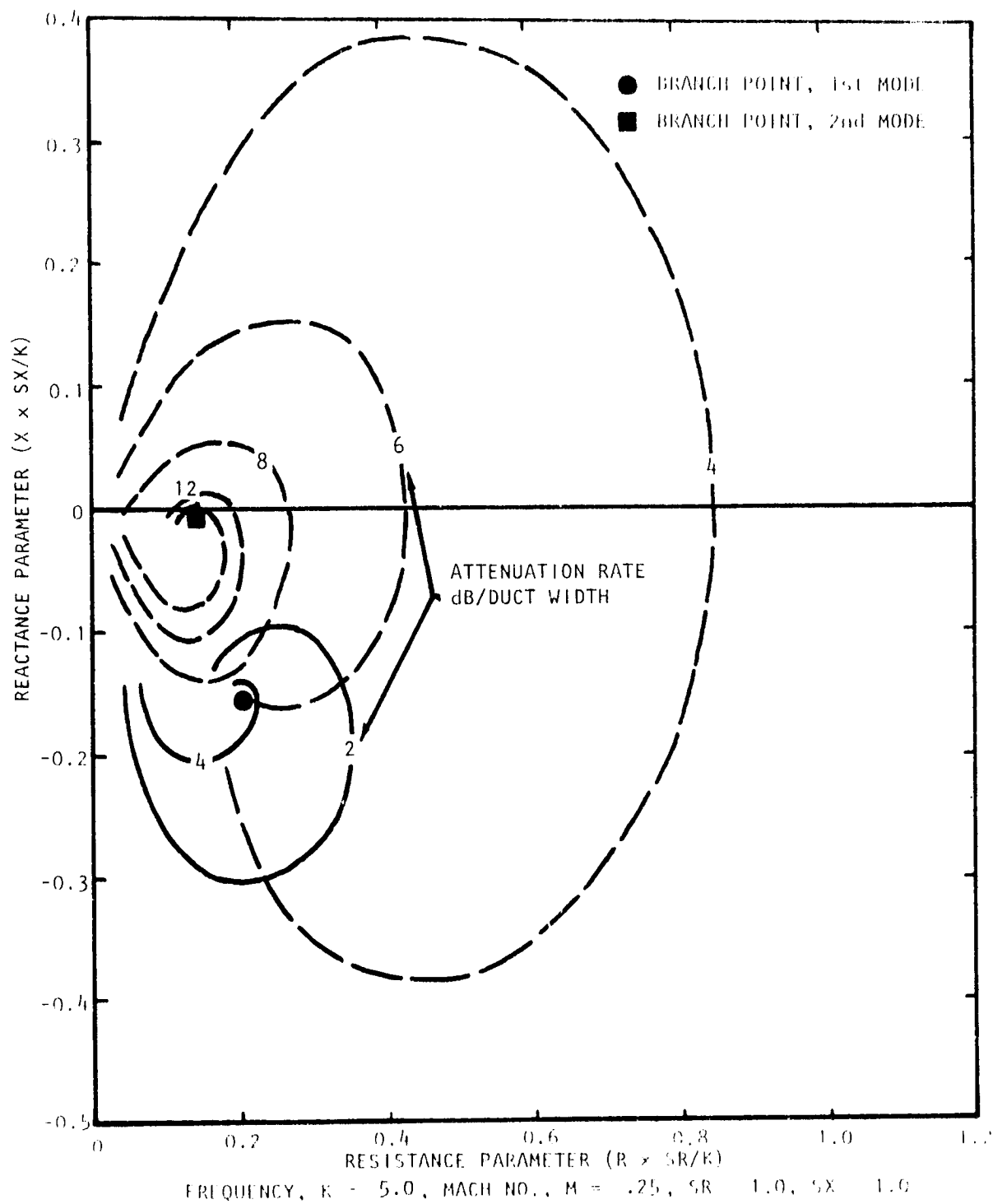


Figure A.48 Contours of Constant Attenuation for First Two Modes of Propagation (First Mode —, Second Mode ---)

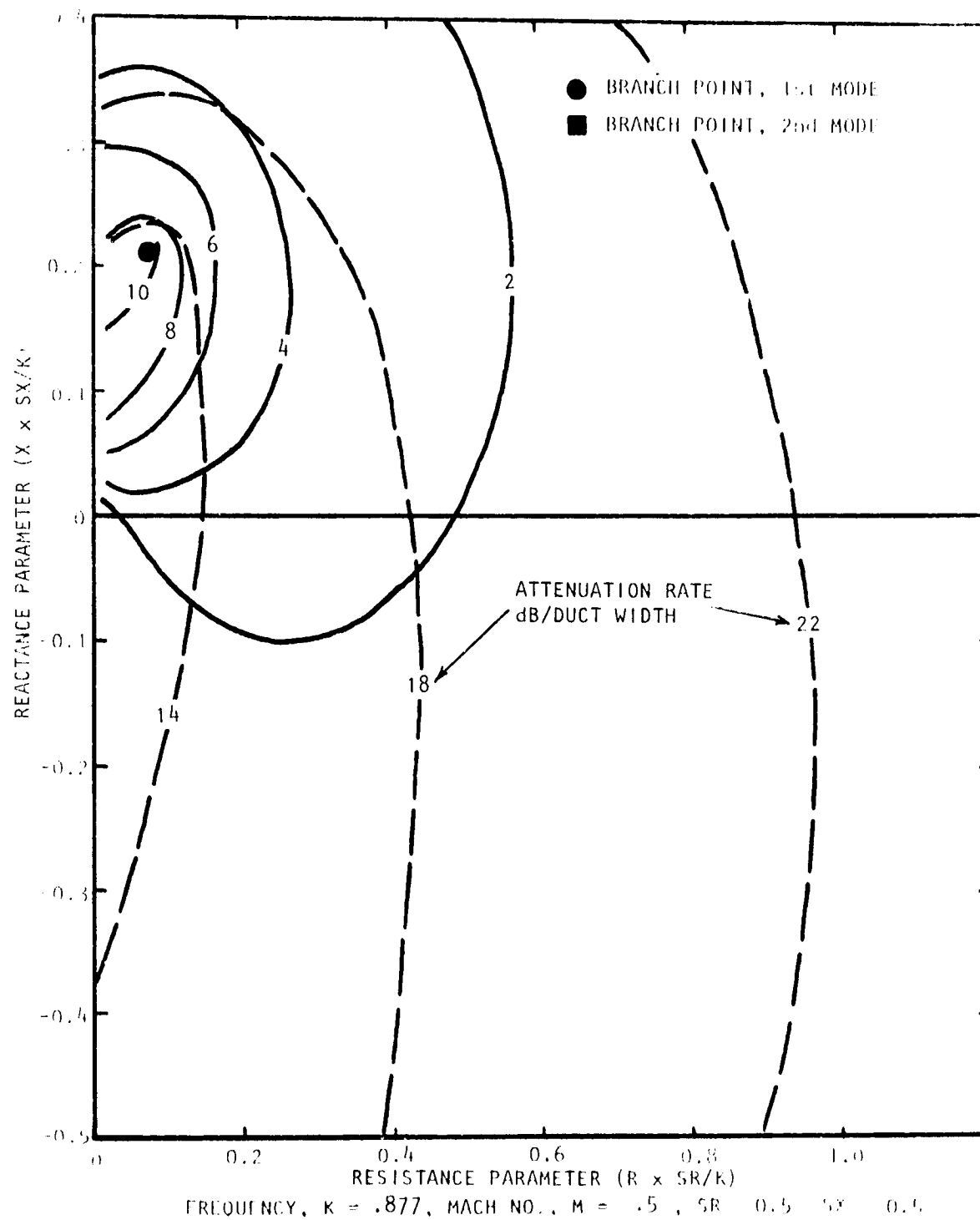


Figure A.49 Contours of Constant Attenuation for First Two Modes of Propagation (First Mode —, Second Mode ---)

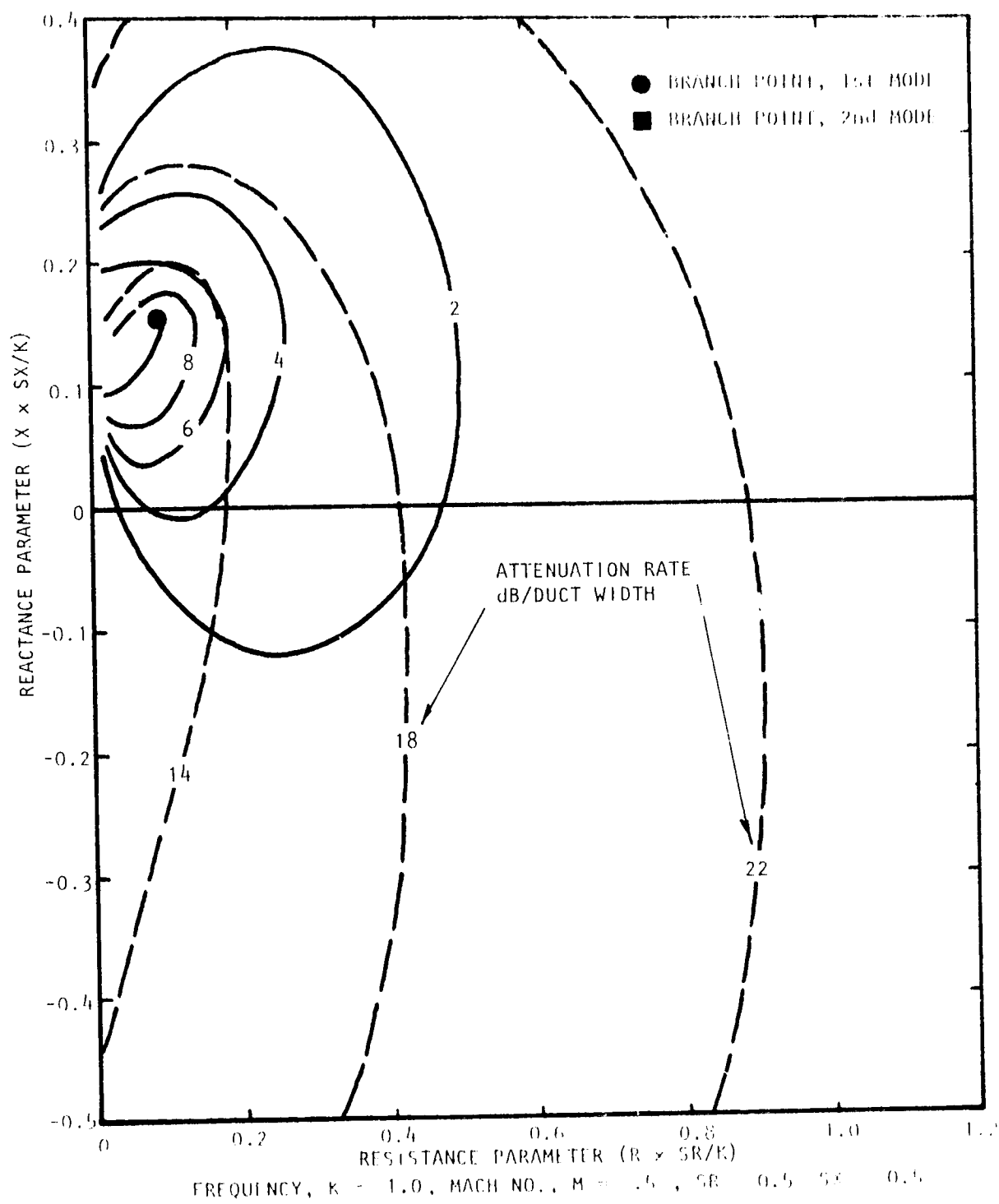


Figure A.50 Contours of Constant Attenuation for First Two Modes of Propagation (First Mode - - - , Second Mode - - -)

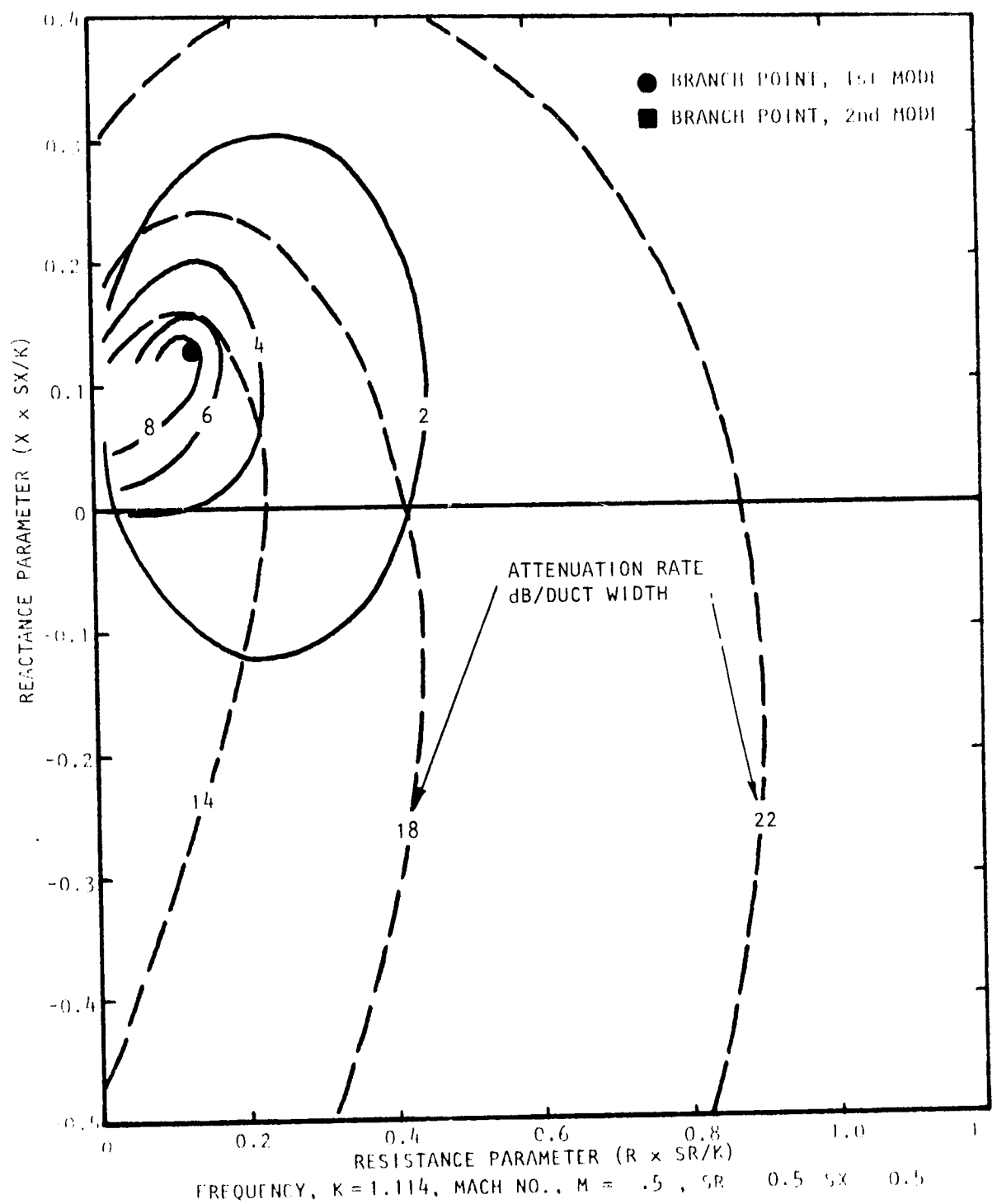


Figure A.51 Contours of Constant Attenuation for First Two Modes of Propagation (First Mode —, Second Mode ---)

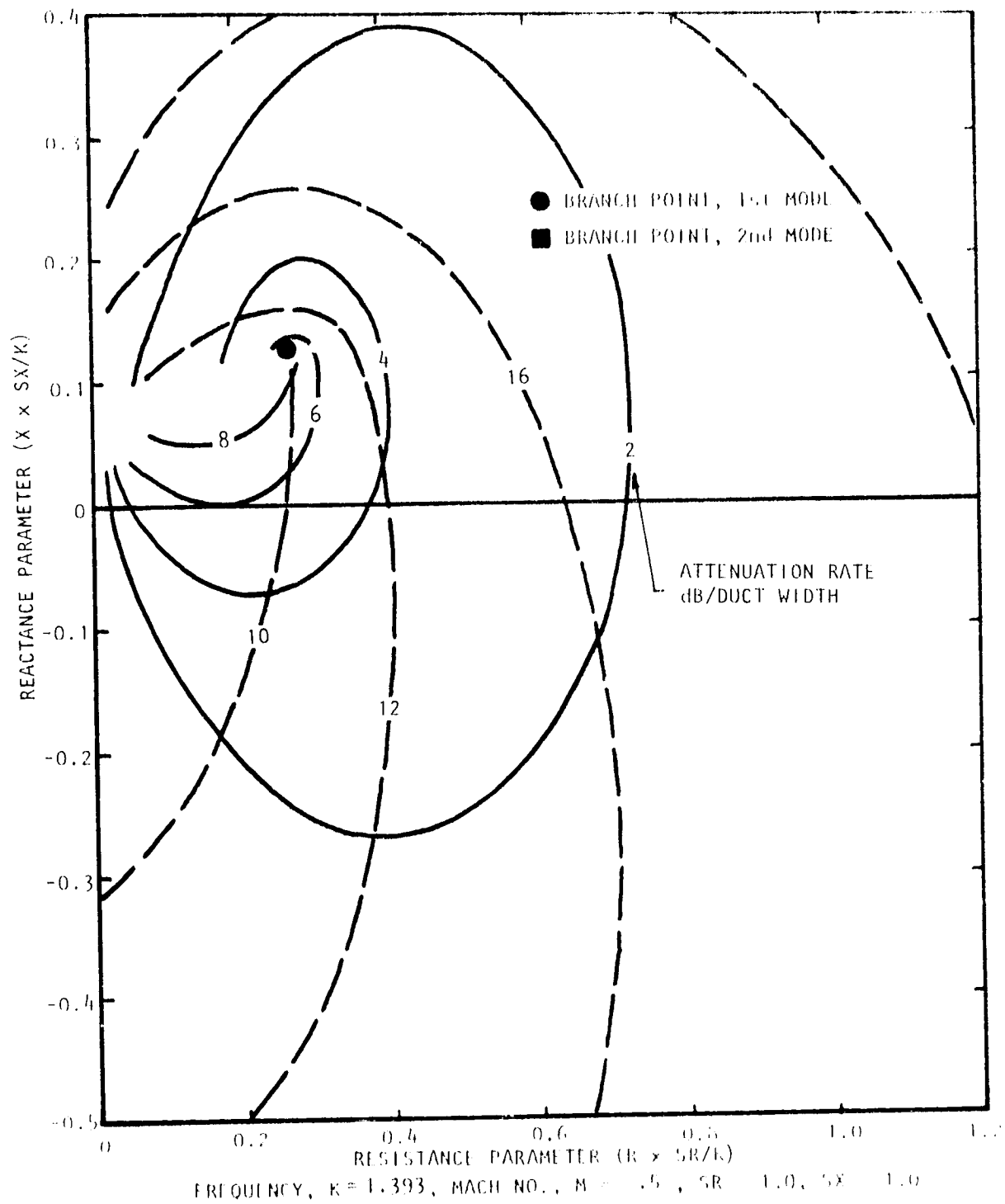


Figure A.52 Contours of Constant Attenuation for First Two Modes of Propagation (First Mode —, Second Mode ---)

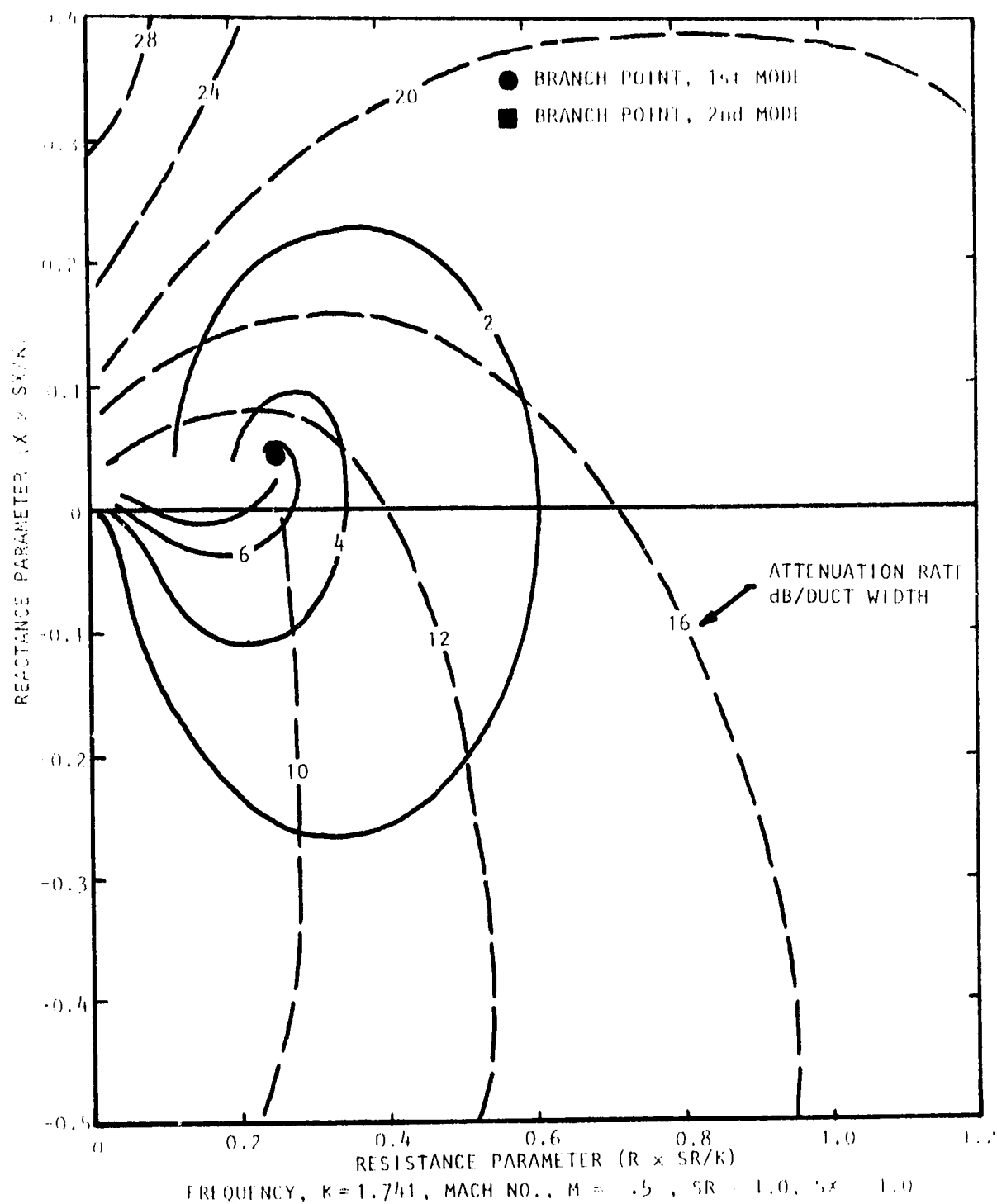


Figure A.53 Contours of Constant Attenuation for First Two Modes of Propagation (First Mode —, Second Mode - -)

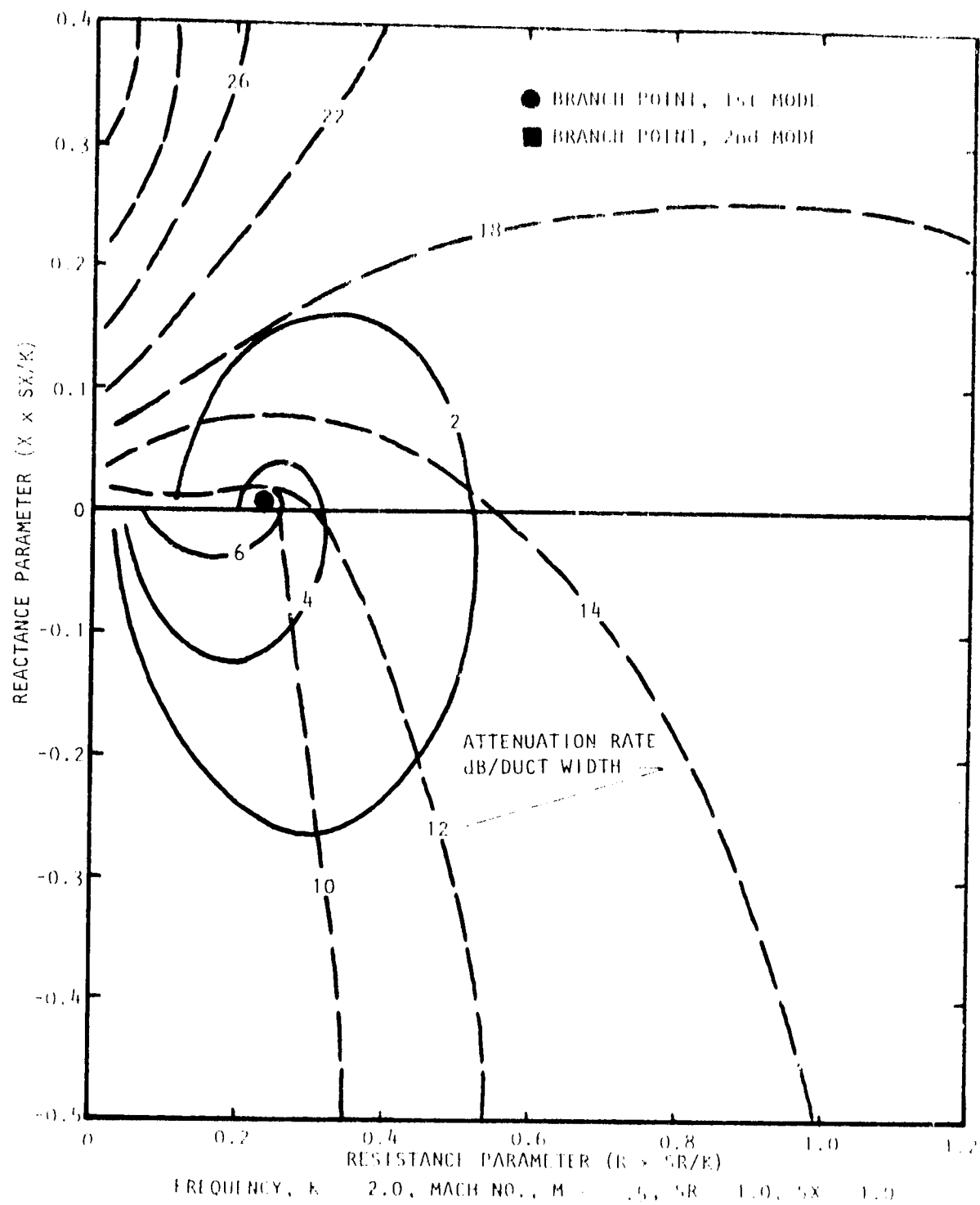


Figure A.54 Contours of Constant Attenuation for First Two Modes of Propagation (First Mode —, Second Mode - -)

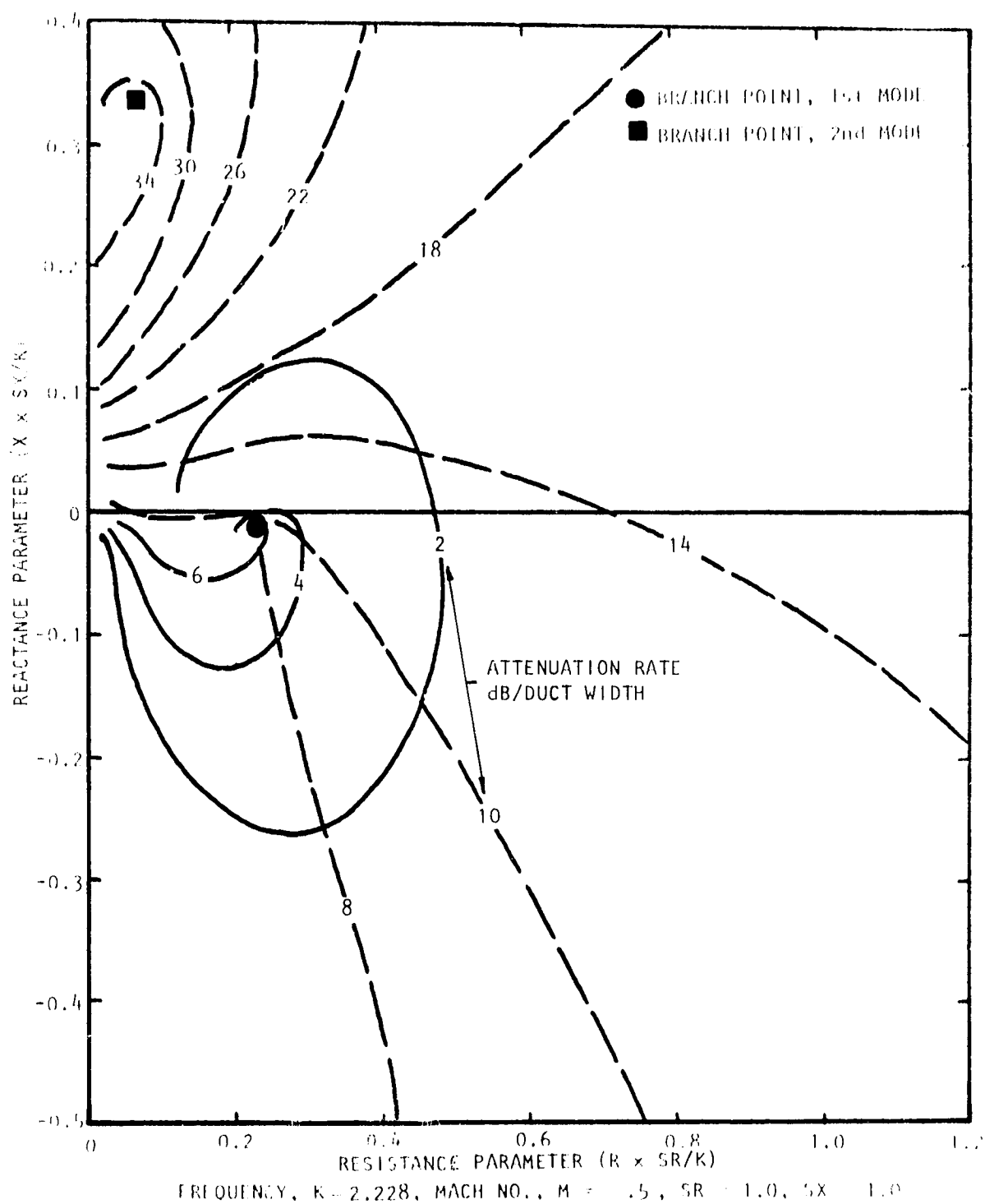


Figure A.55 Contours of Constant Attenuation for First Two Modes of Propagation (First Mode ———, Second Mode - - - -)

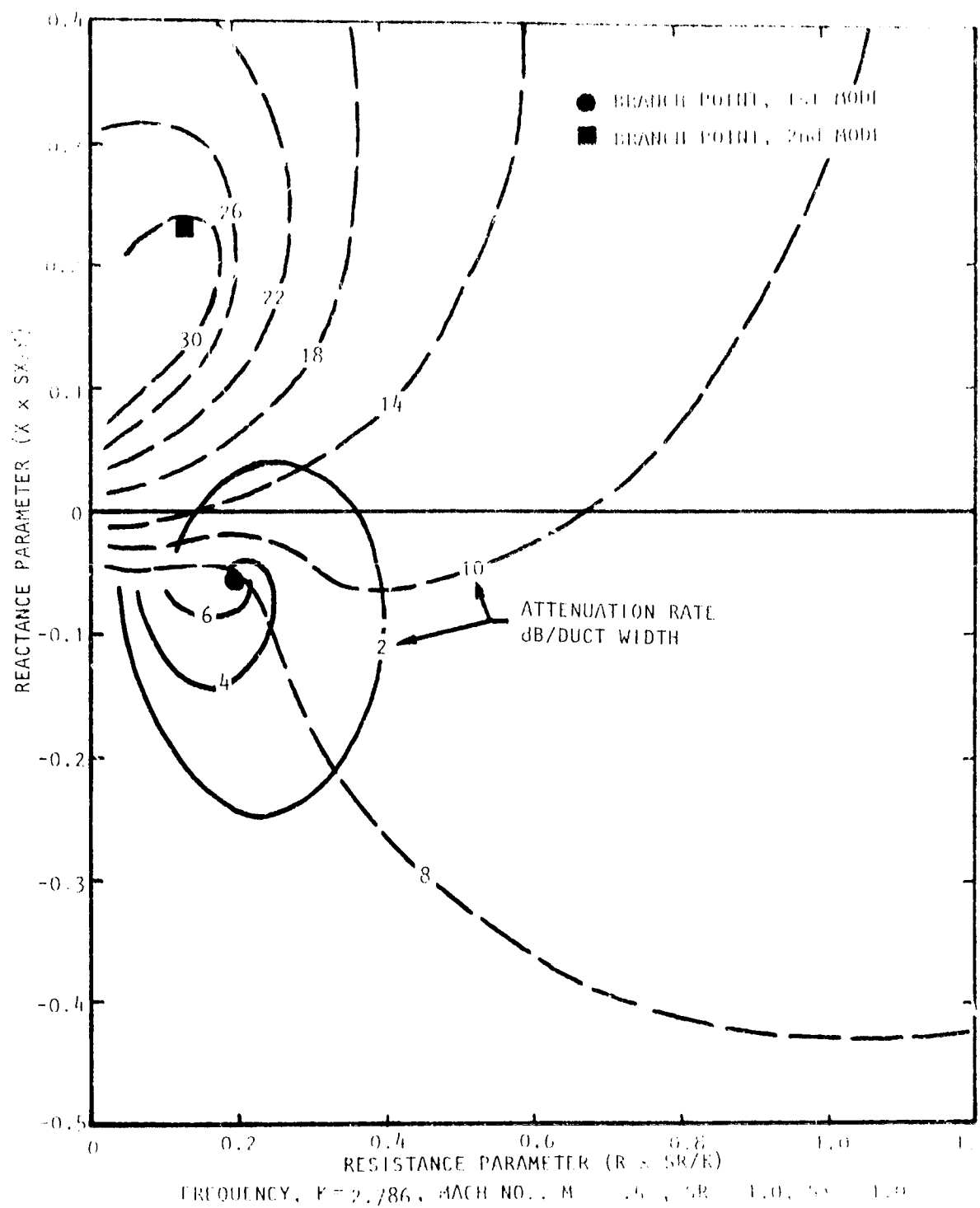


Figure A.56 Contours of Constant Attenuation for First Two Modes of Propagation (First Mode ---, Second Mode —)

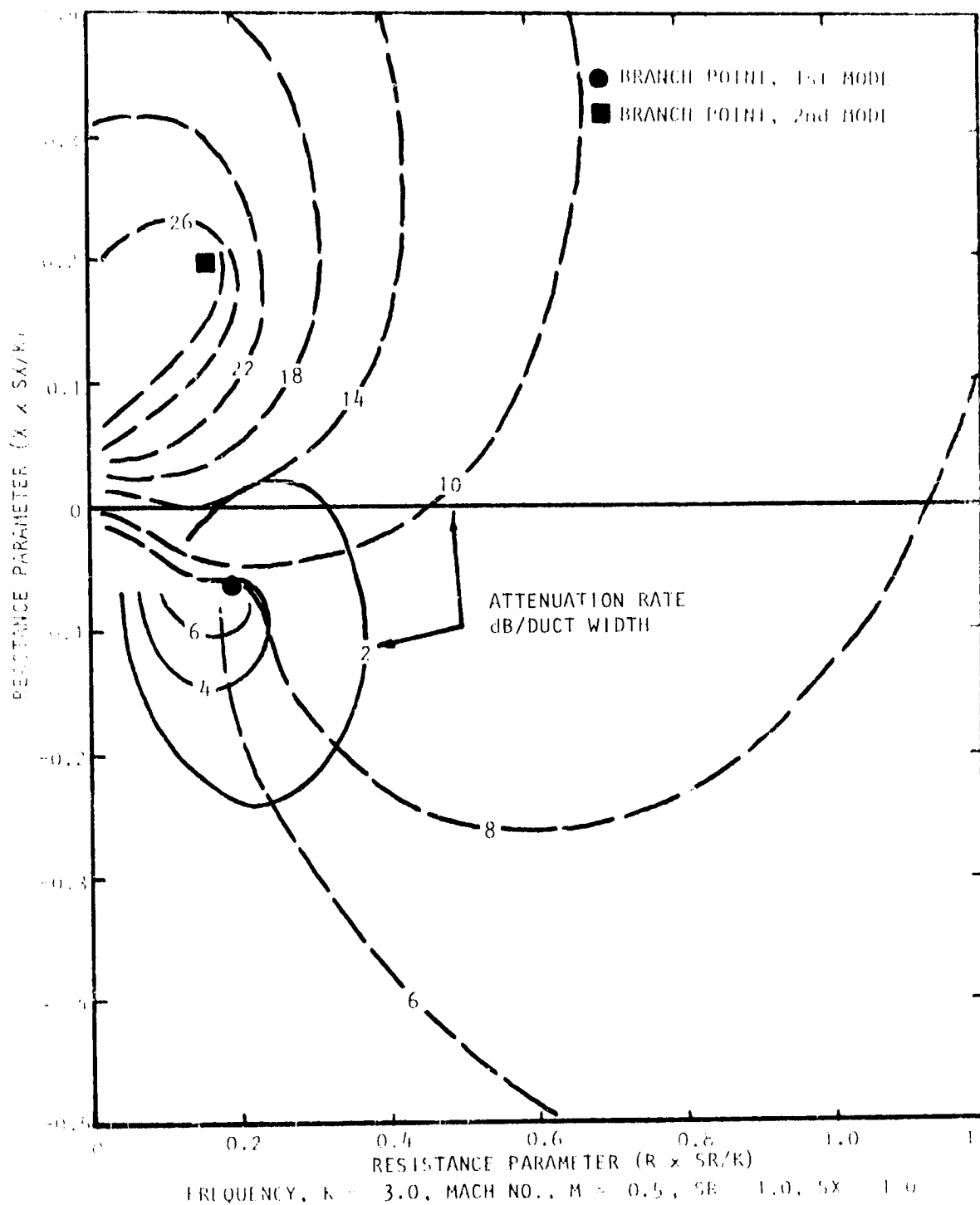


Figure A.57 Contours of Constant Attenuation for First Two Modes of Propagation (First Mode —, Second Mode ---)

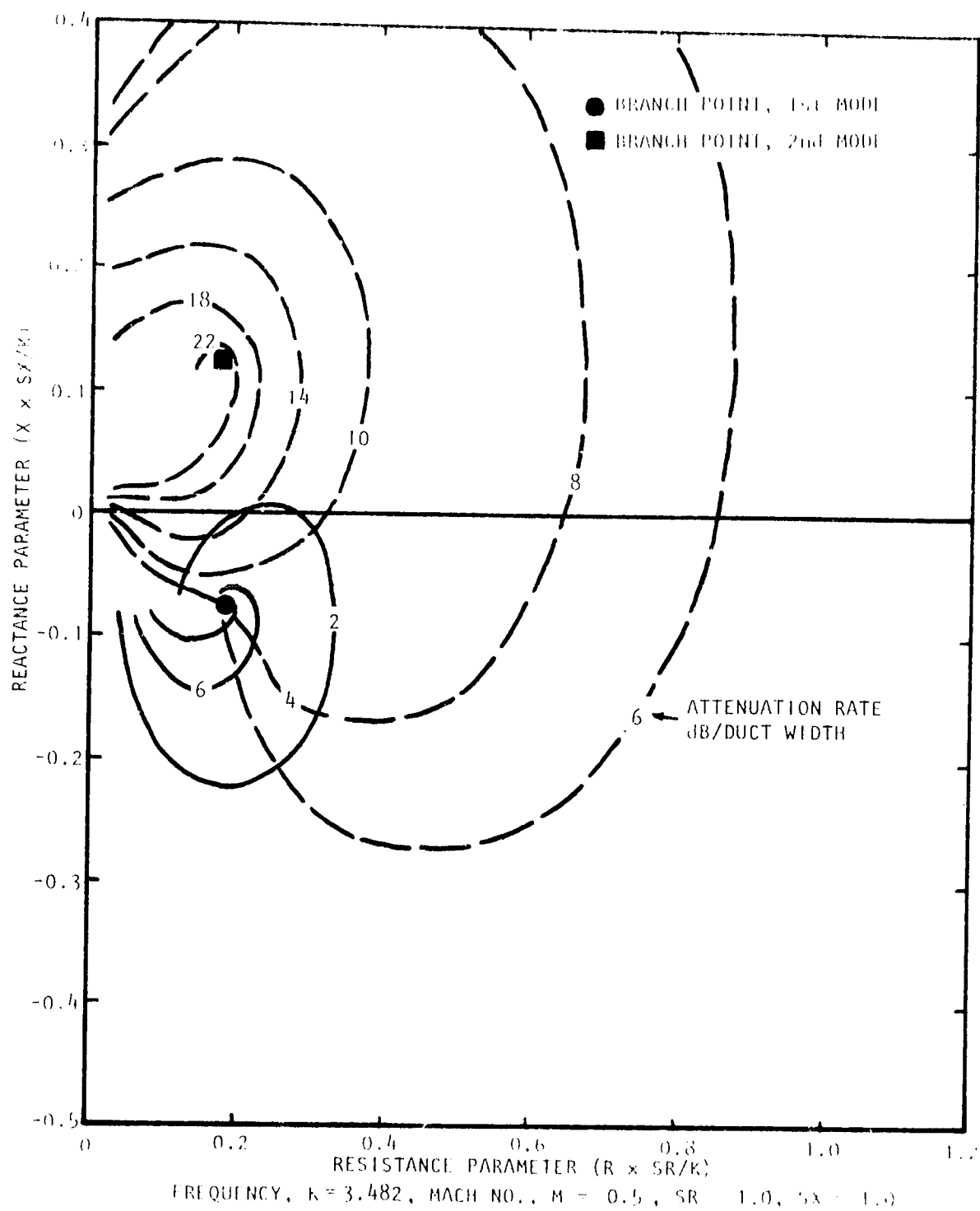


Figure A.58 Contours of constant attenuation for First Two Modes of Propagation (First Mode ---, Second Mode —)

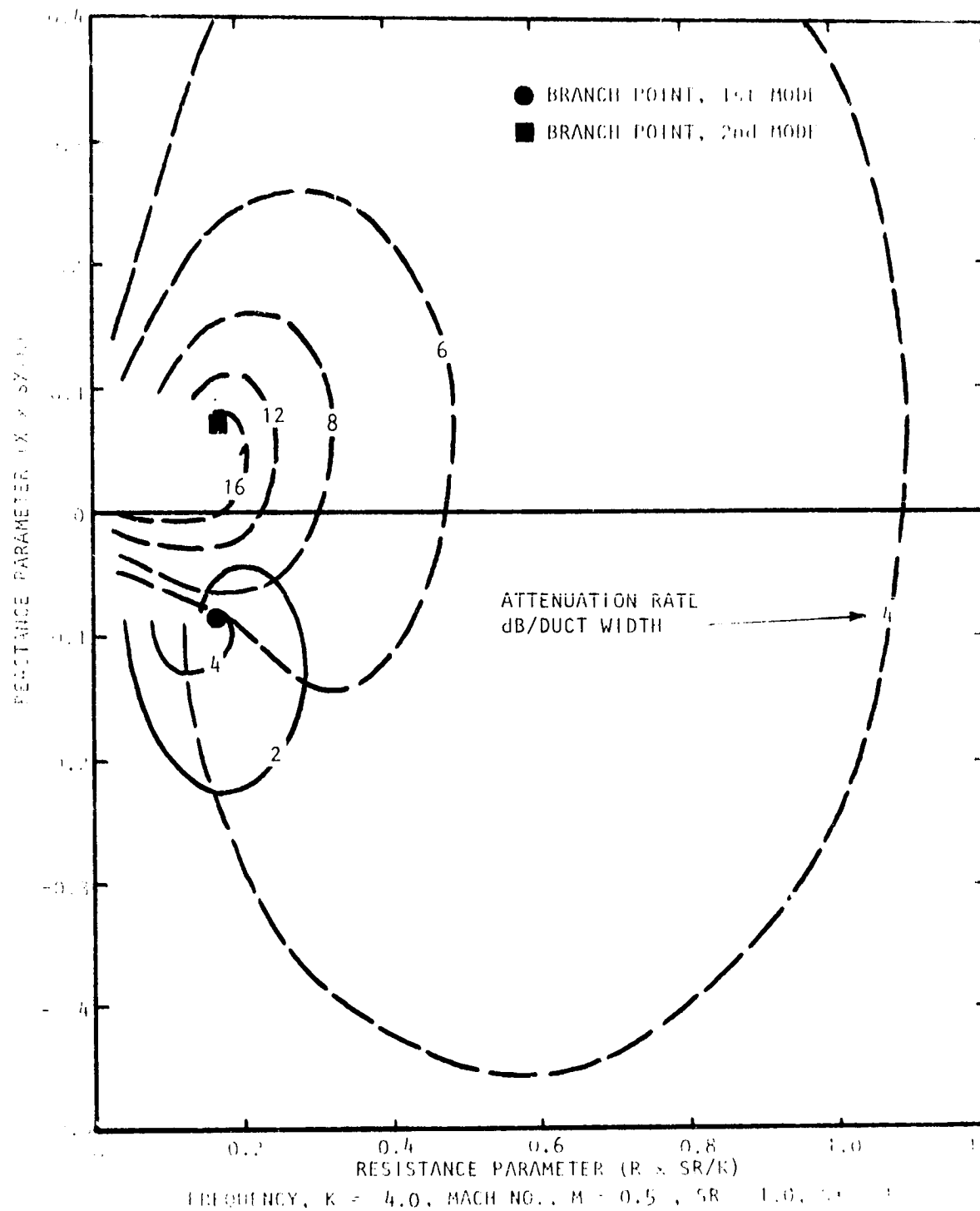


Figure A.59 Contours of Constant Attenuation for First Two Modes of Propagation (First Mode —, Second Mode ---)

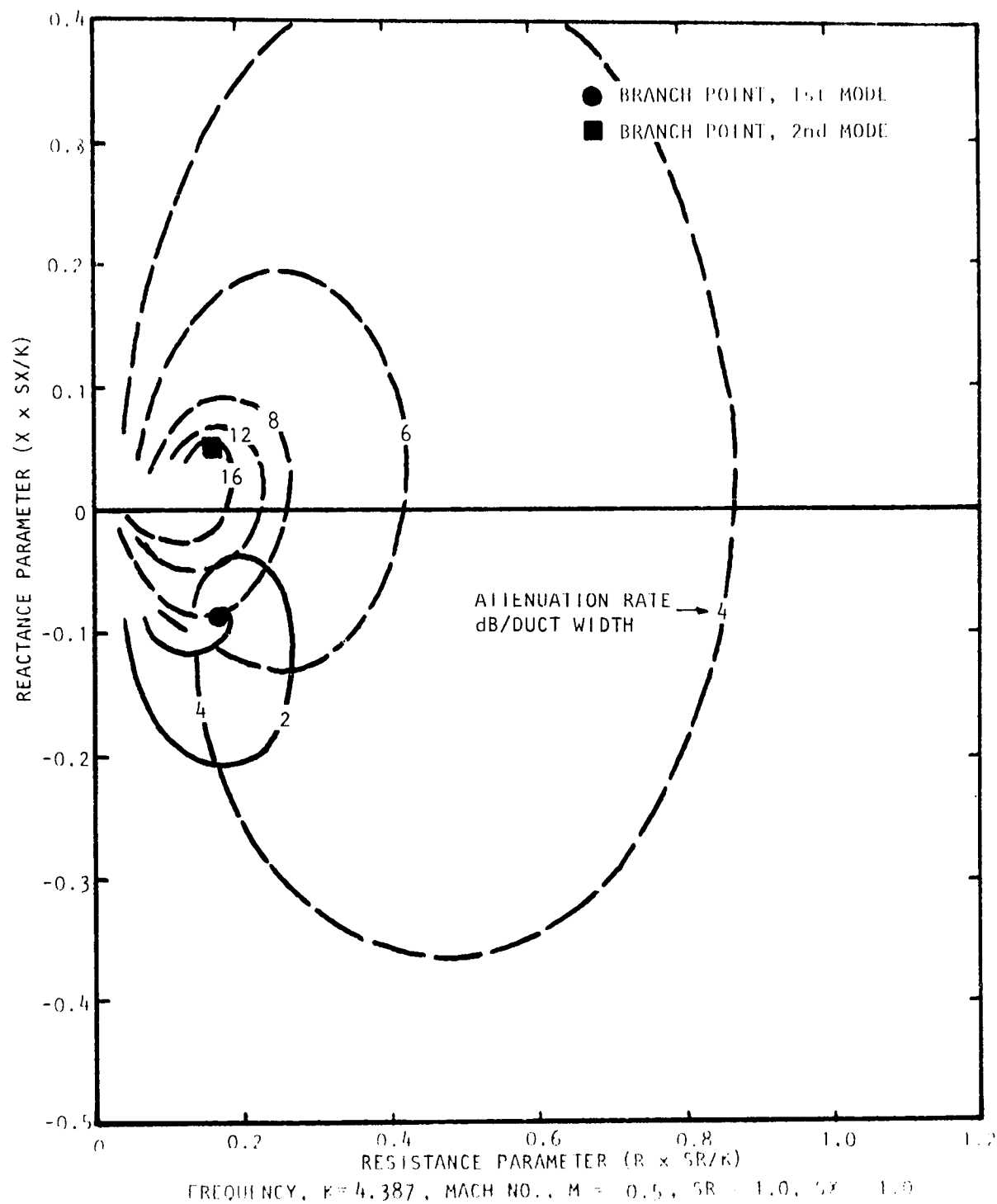


Figure A.60 Contours of Constant Attenuation for First Two Modes of Propagation (First Mode ---, Second Mode ----)

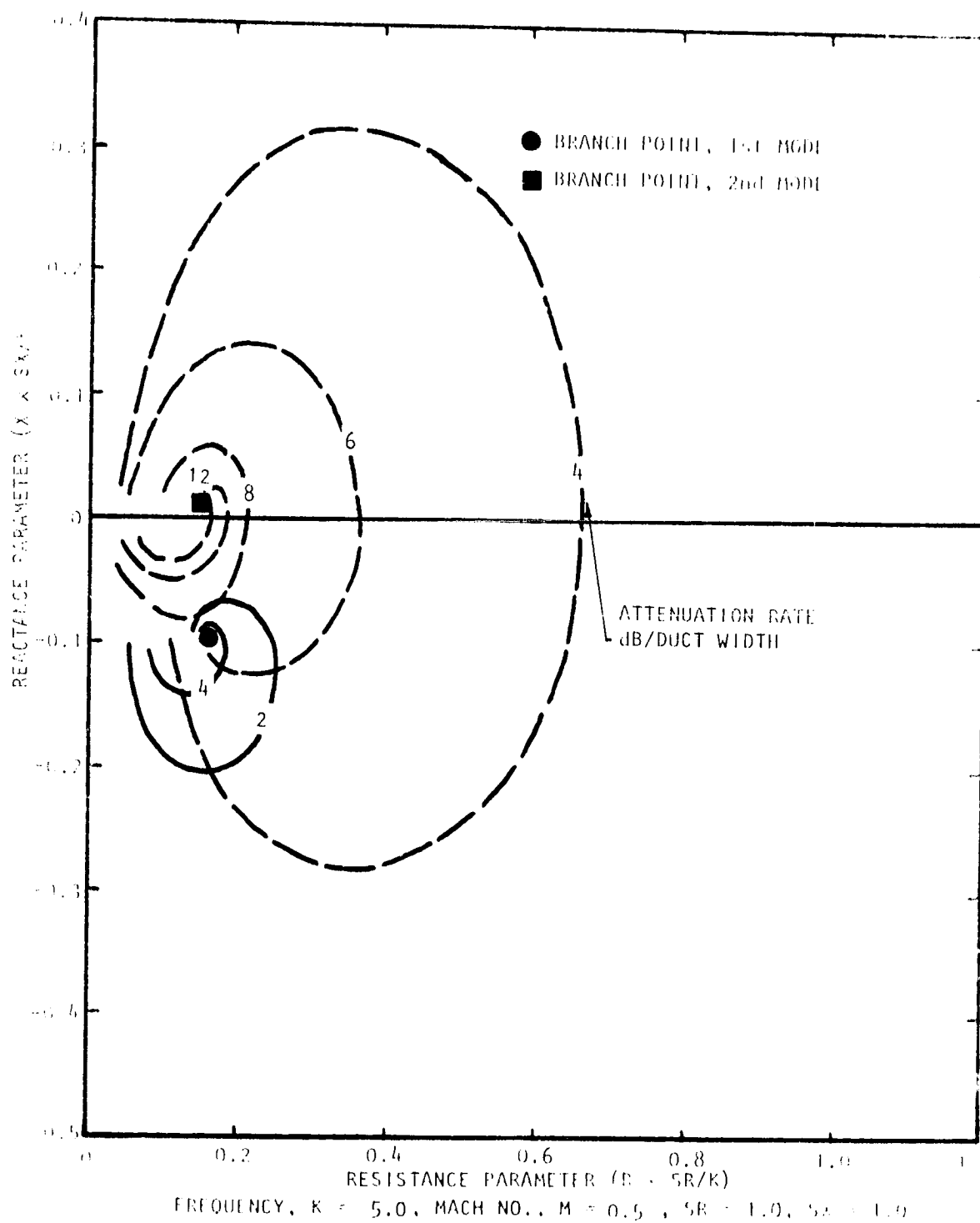


Figure 7.61 Contours of Constant Attenuation for First Two Modes of Propagation (First Mode ---, Second Mode —)

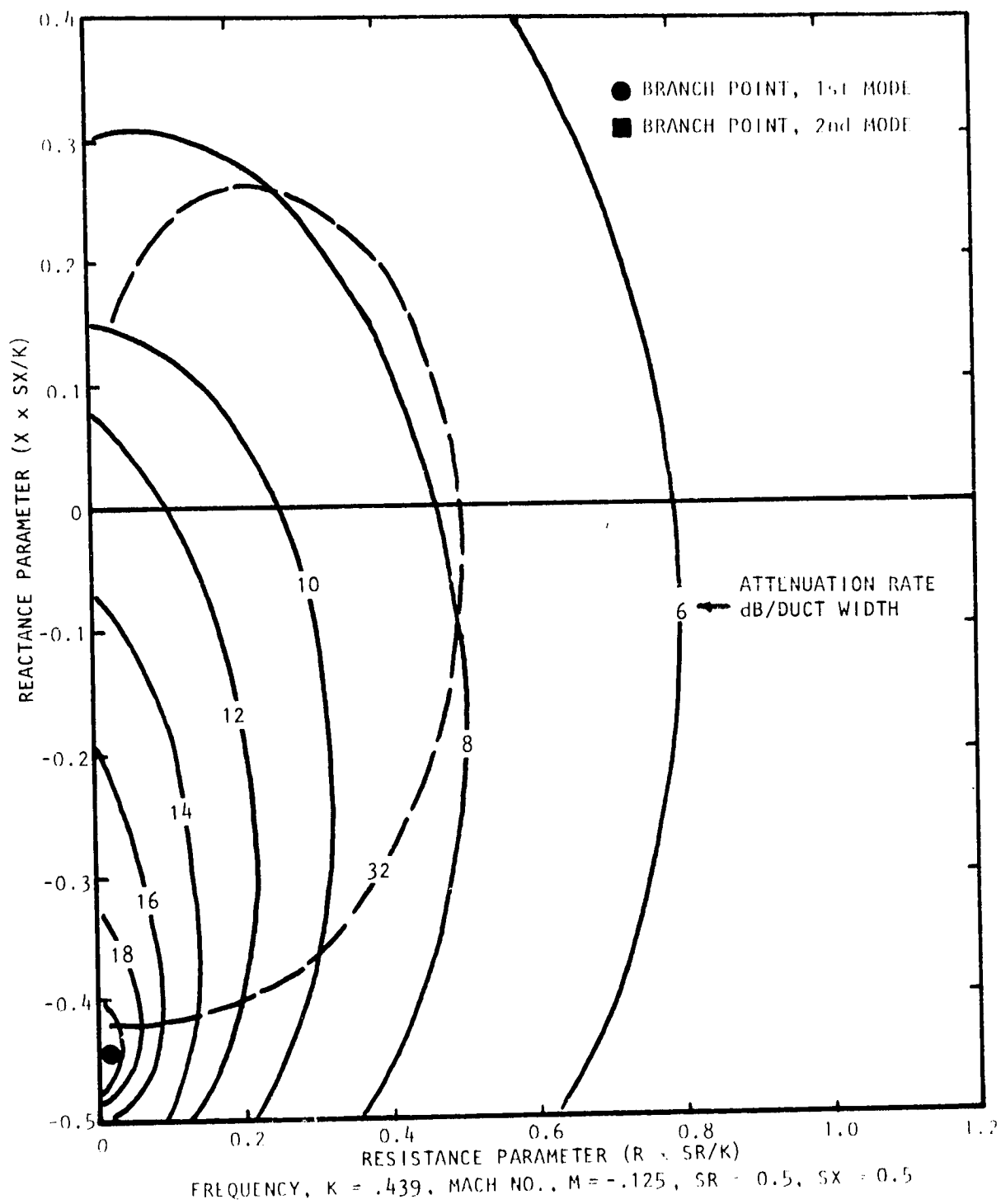


Figure A.62 Contours of Constant Attenuation for First Two Modes of Propagation (First Mode —, Second Mode ----)

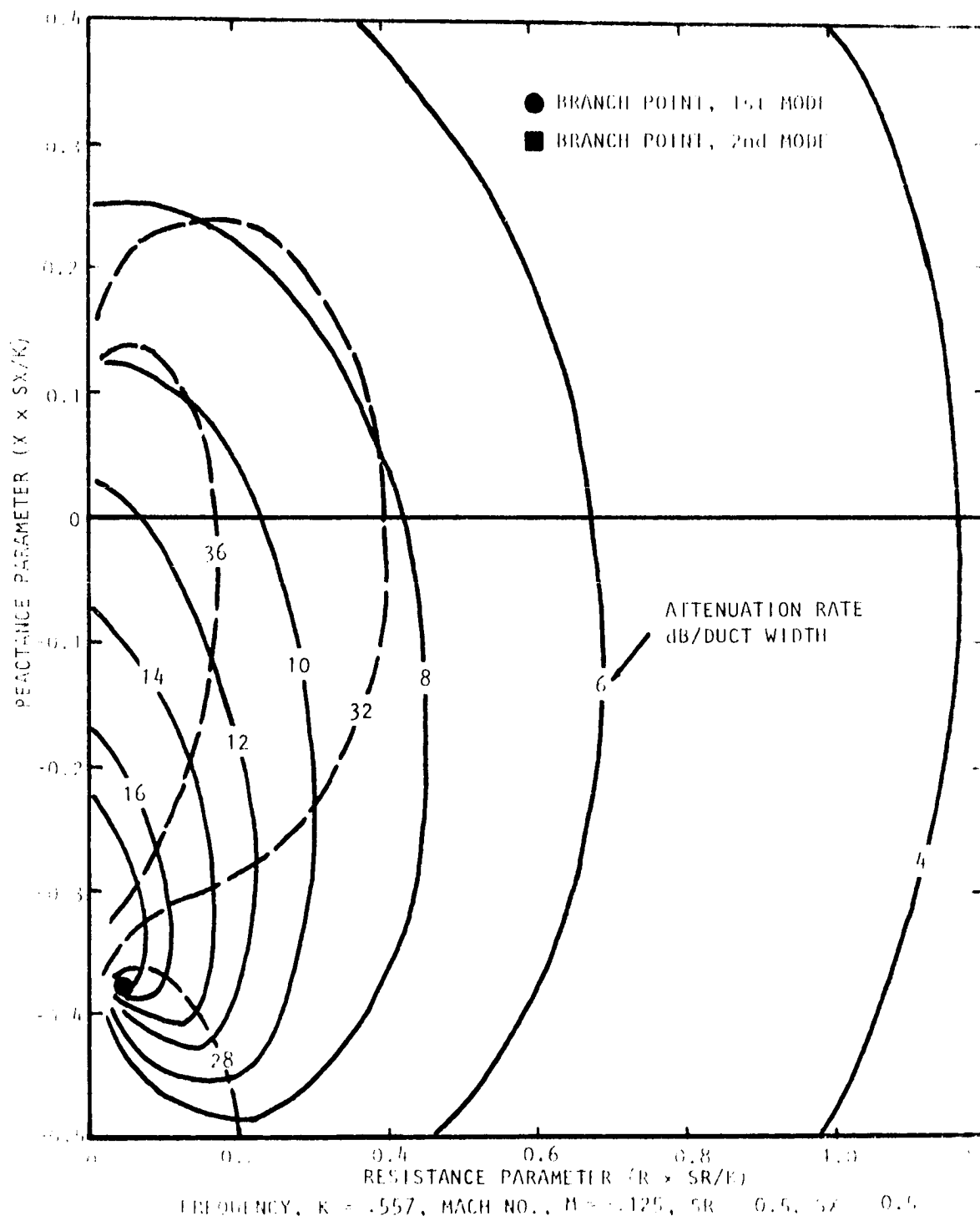


Figure A.63 Contours of Constant Attenuation for First Two Modes of Propagation (First Mode ---, Second Mode - - -)

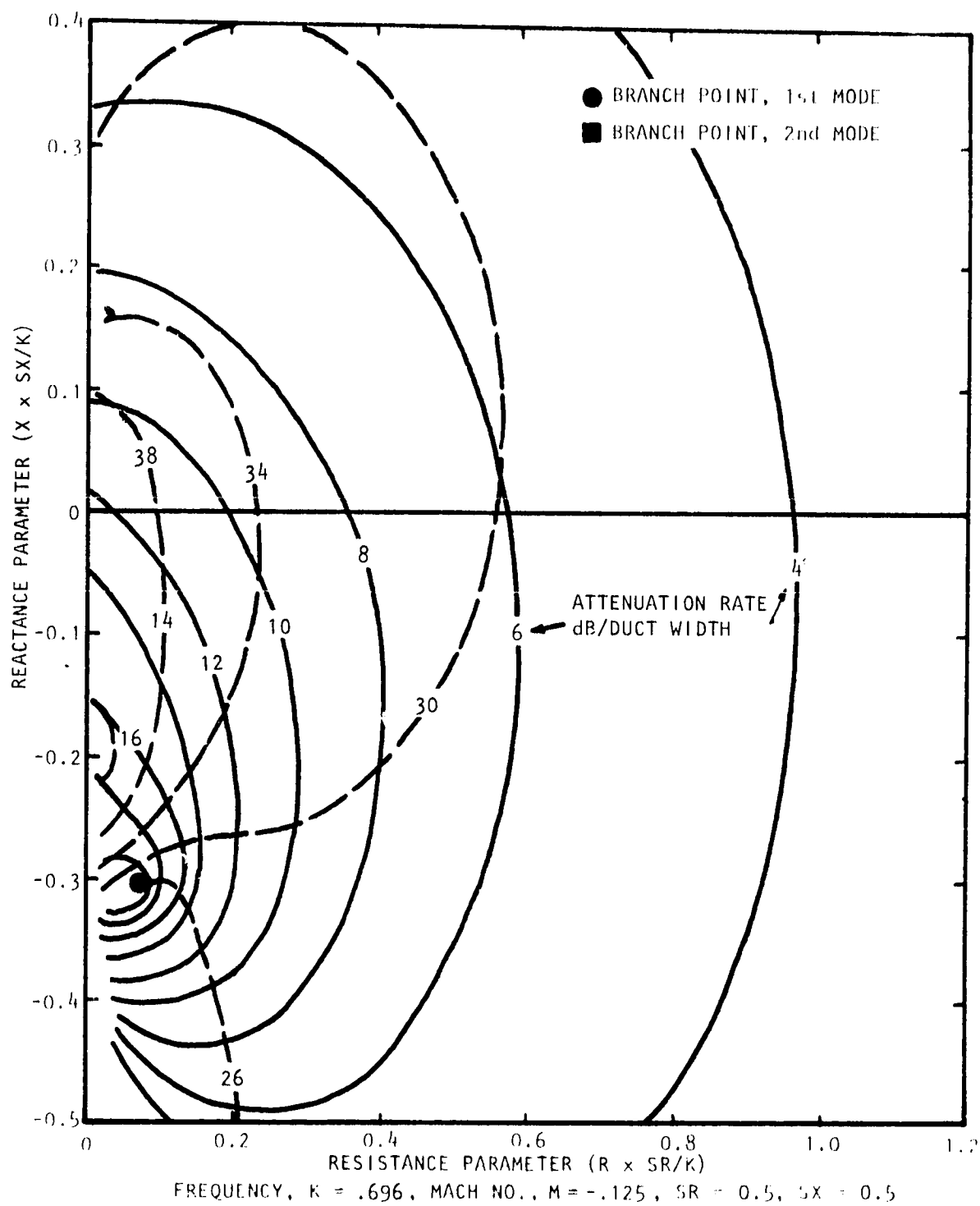


Figure A.64 Contours of Constant Attenuation for First Two Modes of Propagation (First Mode —, Second Mode ---)

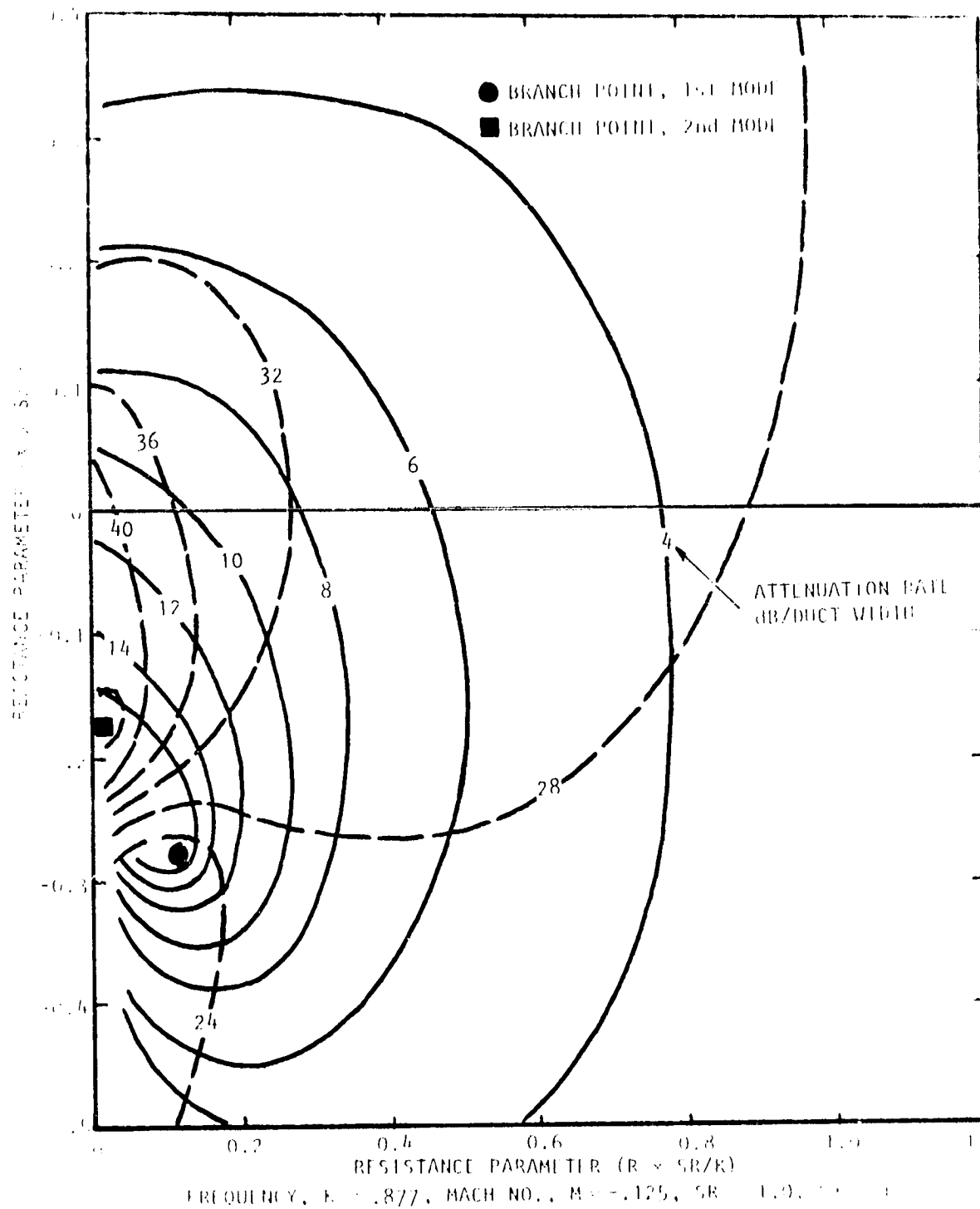


Figure A.65 Contours of Constant Attenuation for First Two Modes
 of Propagation (First Mode ---, Second Mode ----)

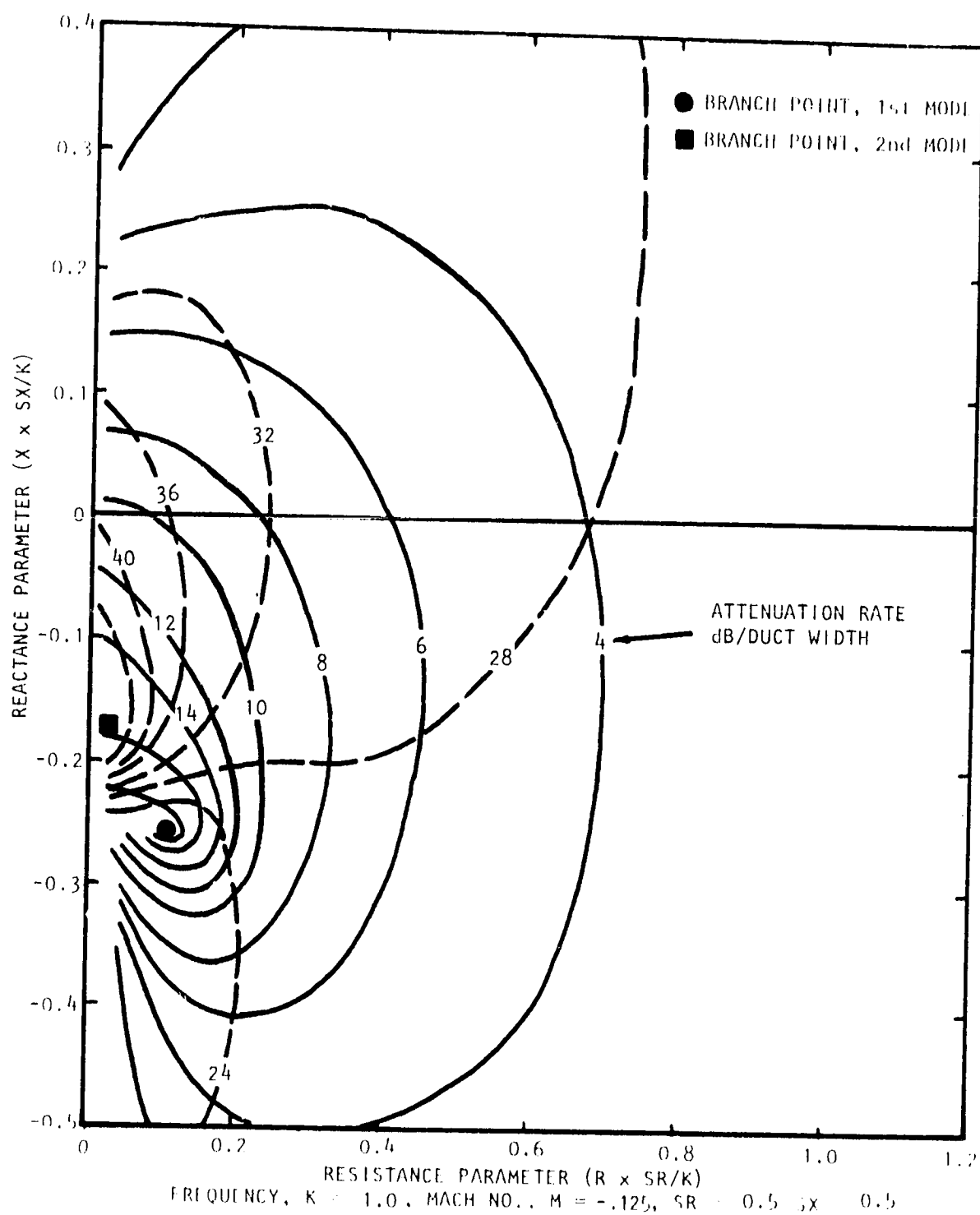


Figure A.66 Contours of Constant Attenuation for First Two Modes of Propagation (First Mode —, Second Mode ---)

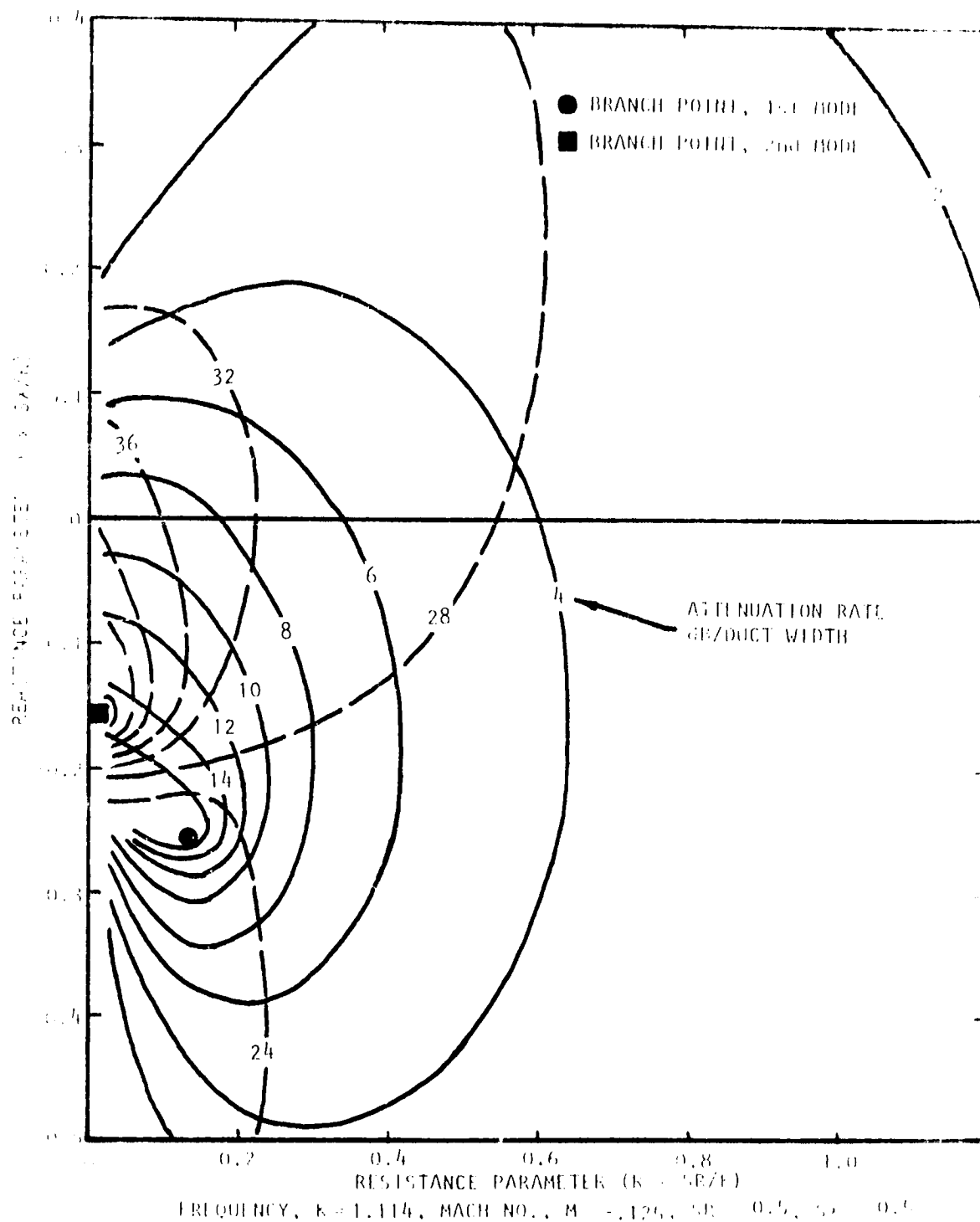


Figure A.6/ Contours of Constant Attenuation for First and Second Modes of Propagation (First Mode ---, Second Mode - - -)

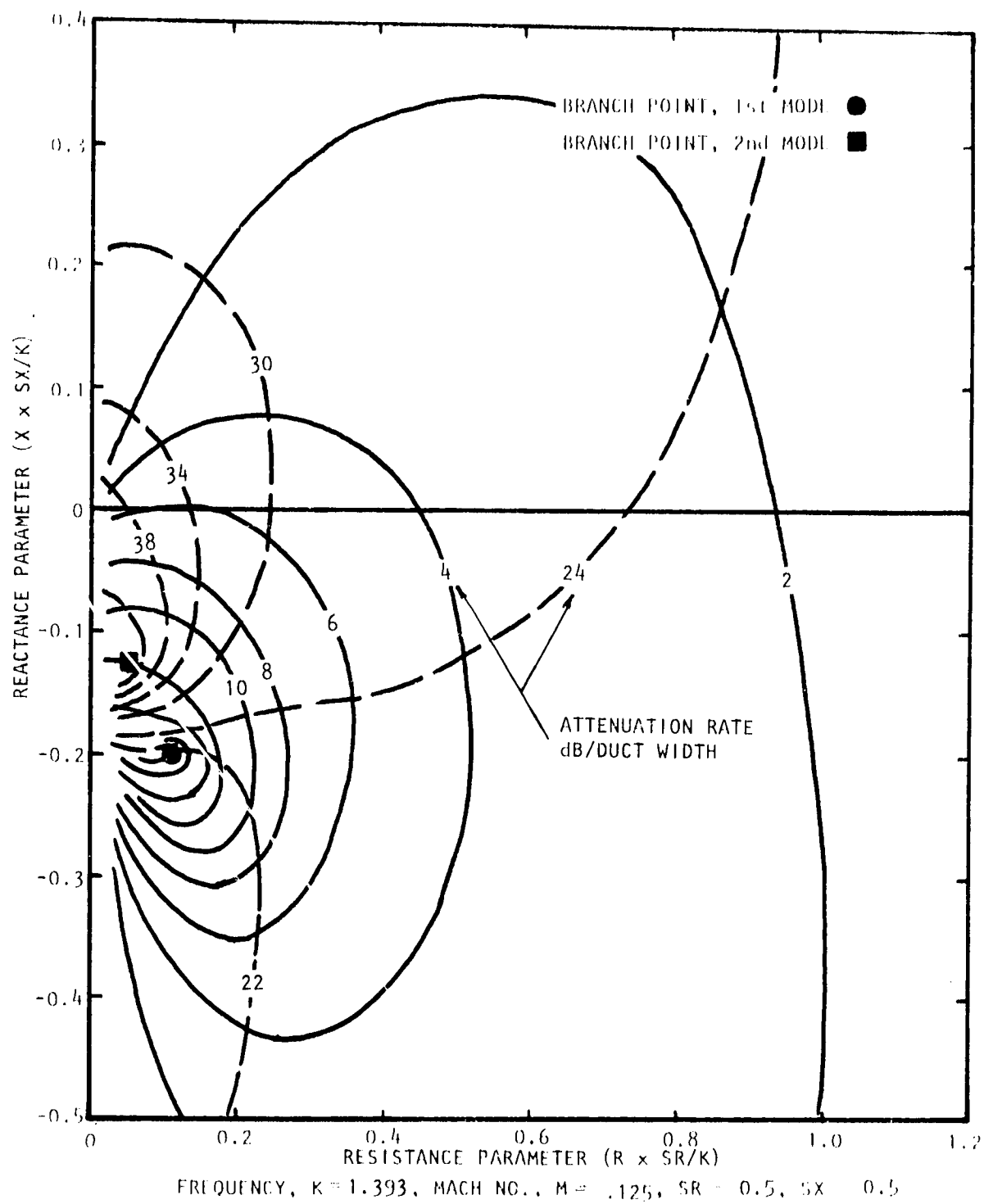


Figure A.68 Contours of Constant Attenuation for First Two Modes of Propagation (First Mode —, Second Mode ---)

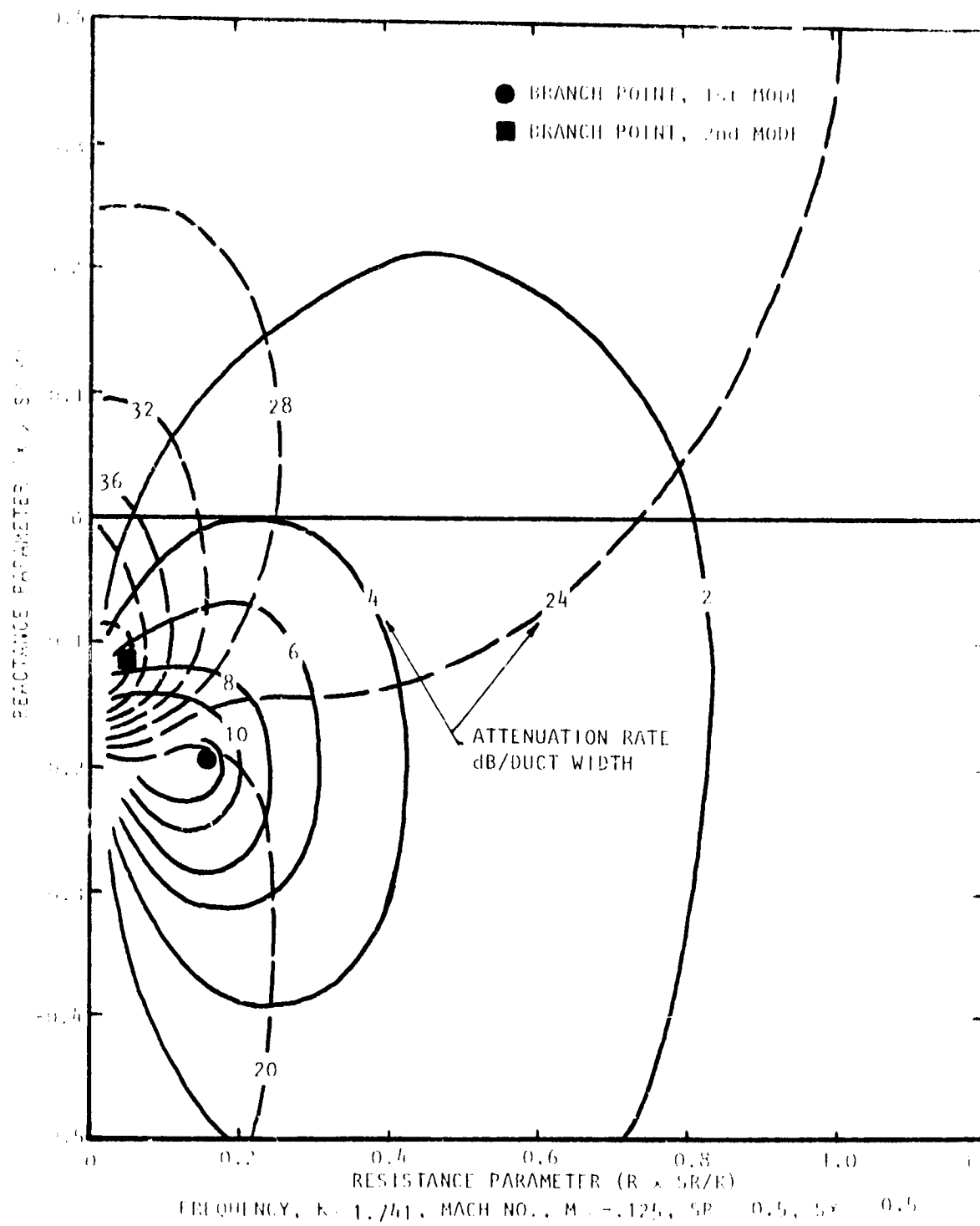


Figure A.69 Contours of Constant Attenuation for First Two Modes of Propagation (First Mode ---, Second Mode ----)

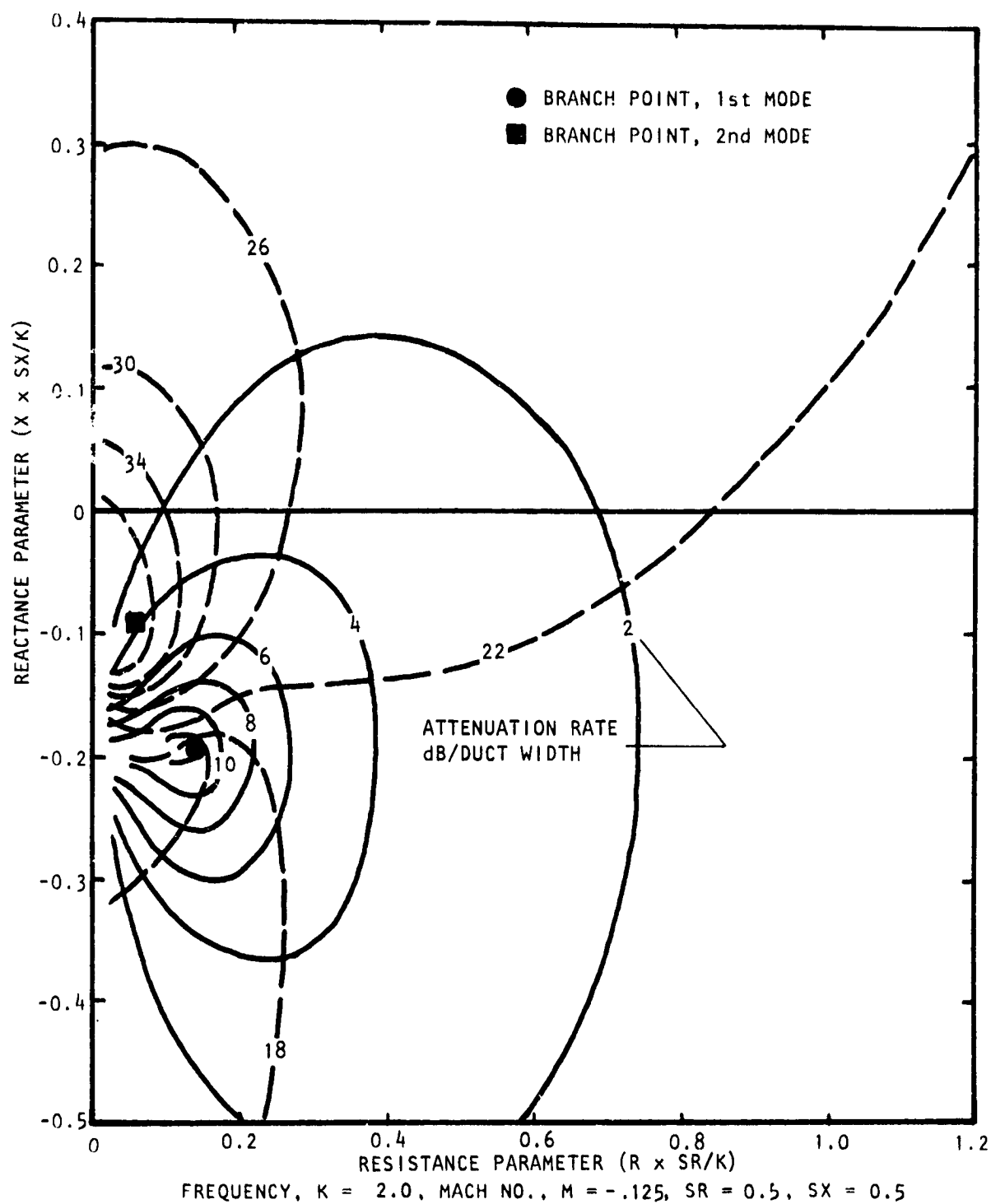


Figure A.70 Contours of Constant Attenuation for First Two Modes of Propagation (First Mode —, Second Mode ----)

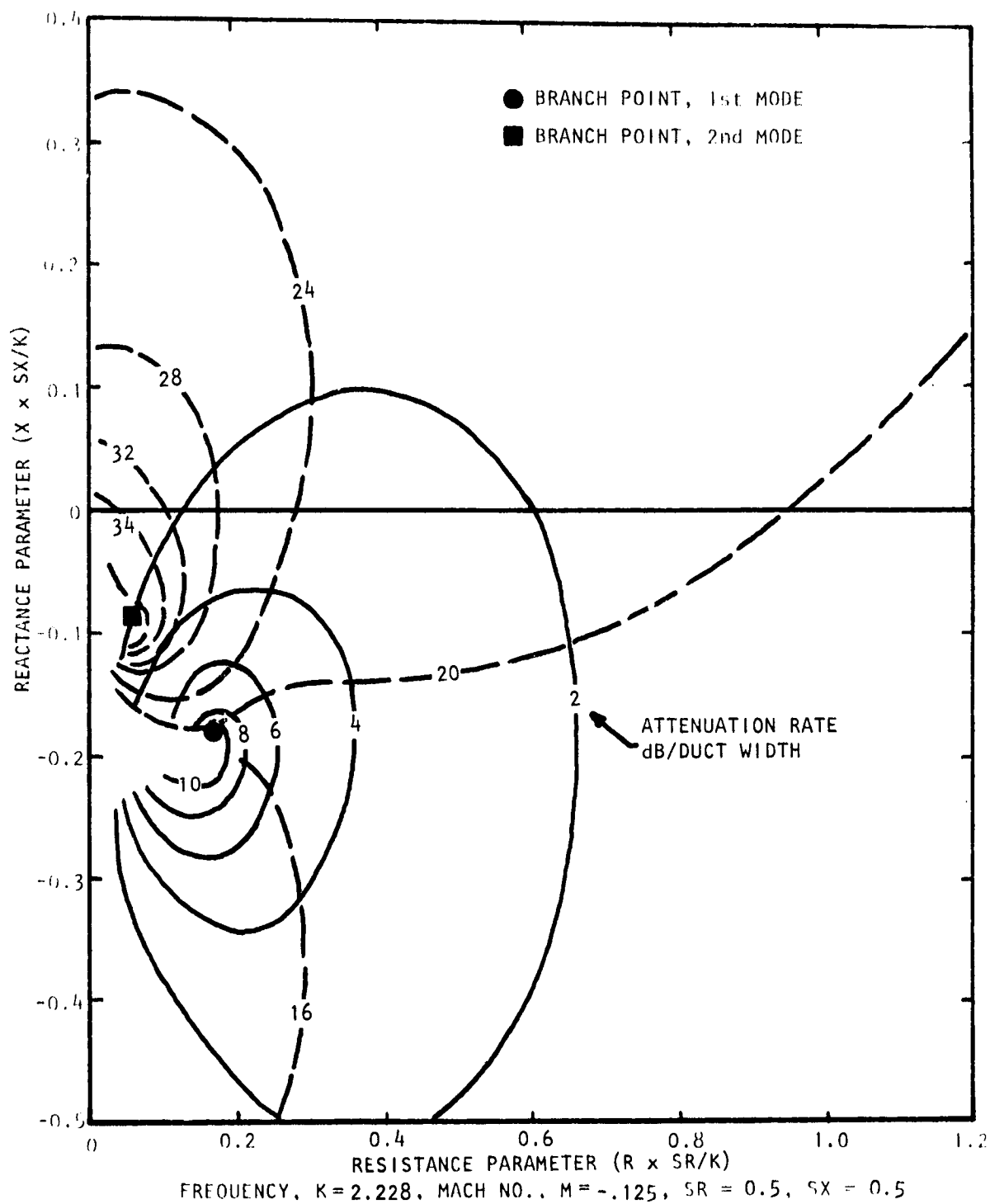


Figure A.71 Contours of Constant Attenuation for First Two Modes of Propagation (First Mode —, Second Mode ----)

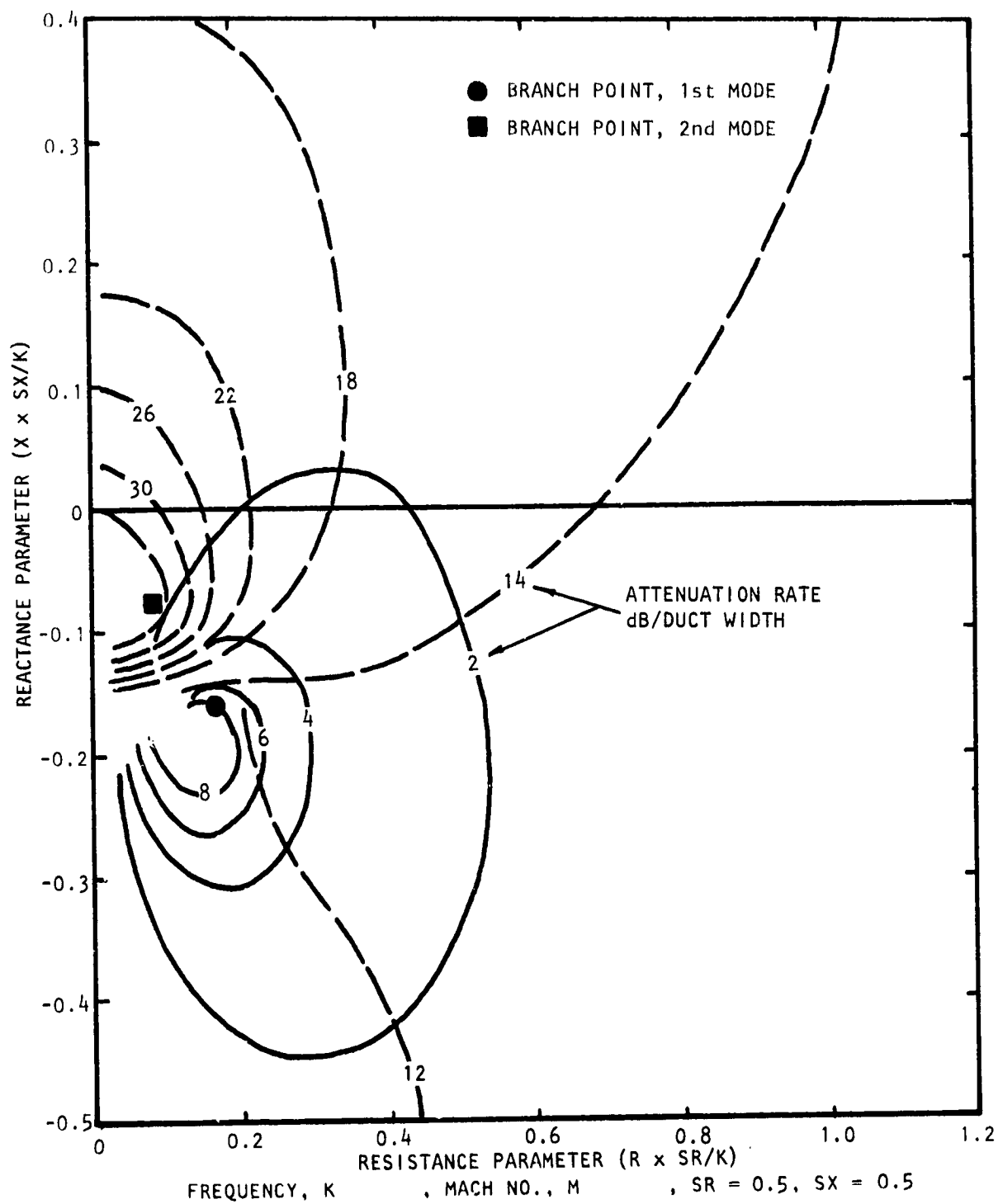


Figure A.72 Contours of Constant Attenuation for First Two Modes of Propagation (First Mode —, Second Mode ----)

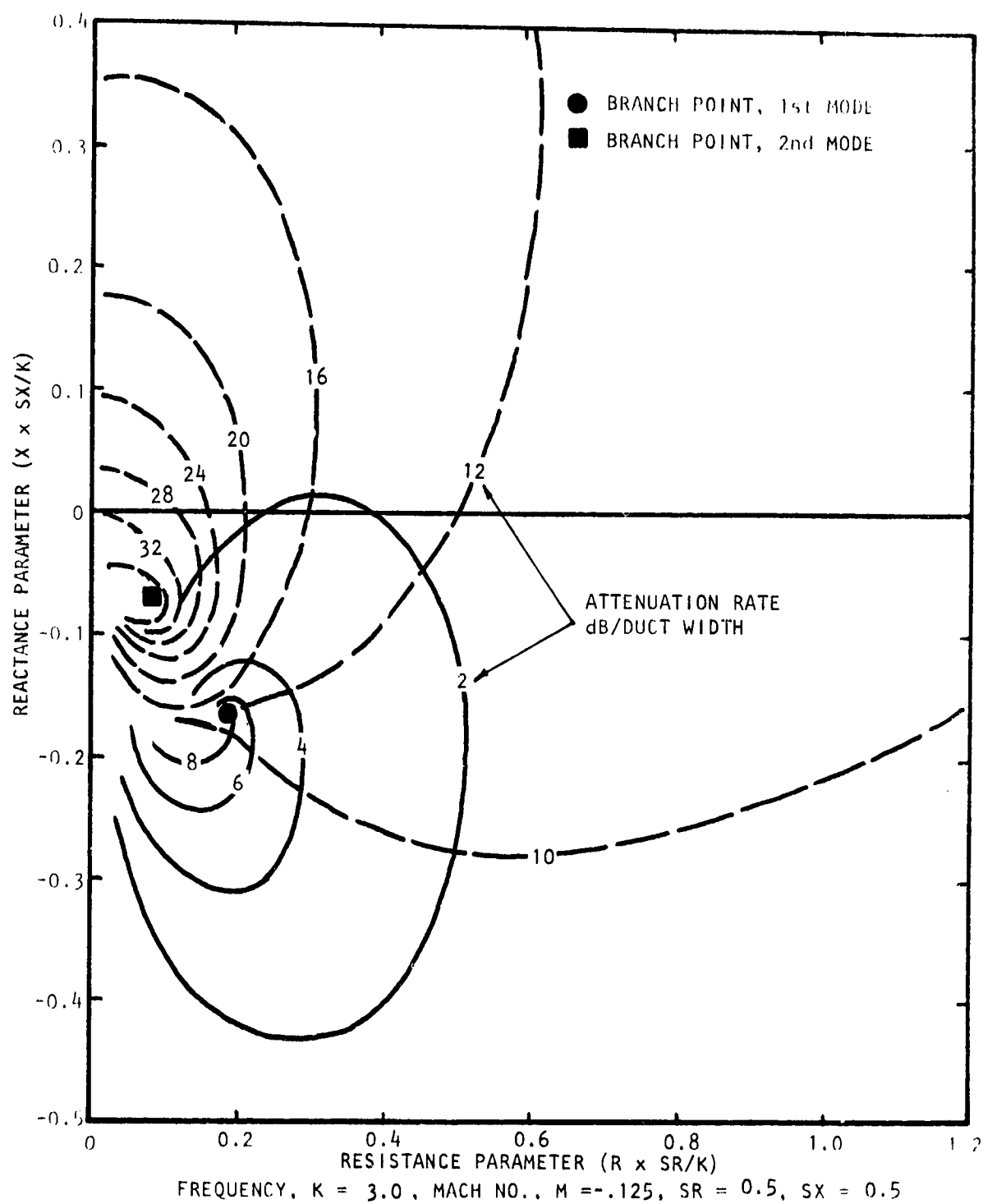


Figure A.73 Contours of Constant Attenuation for First Two Modes of Propagation (First Mode —, Second Mode ----)

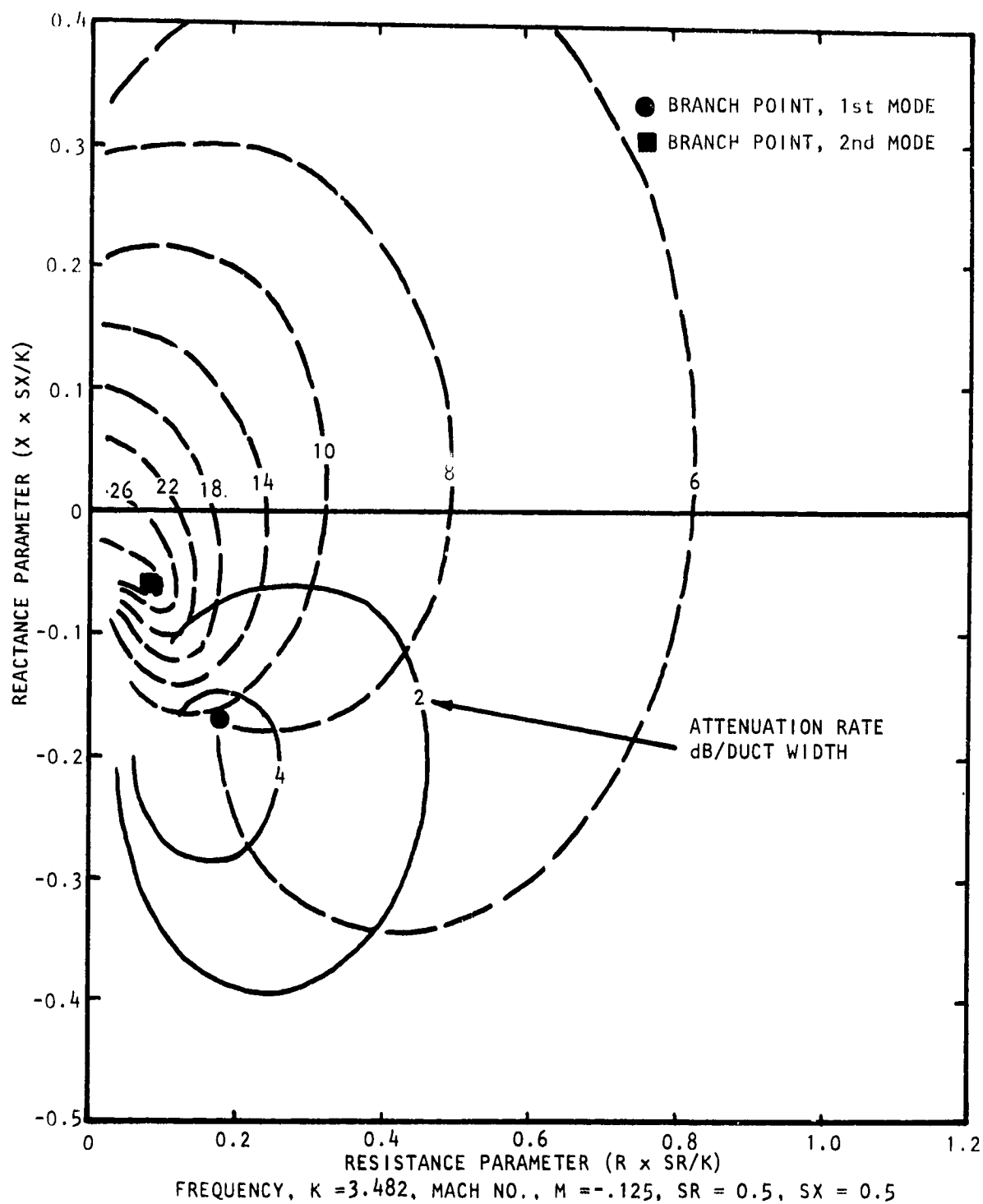


Figure A.74 Contours of Constant Attenuation for First Two Modes of Propagation (First Mode —, Second Mode ----)

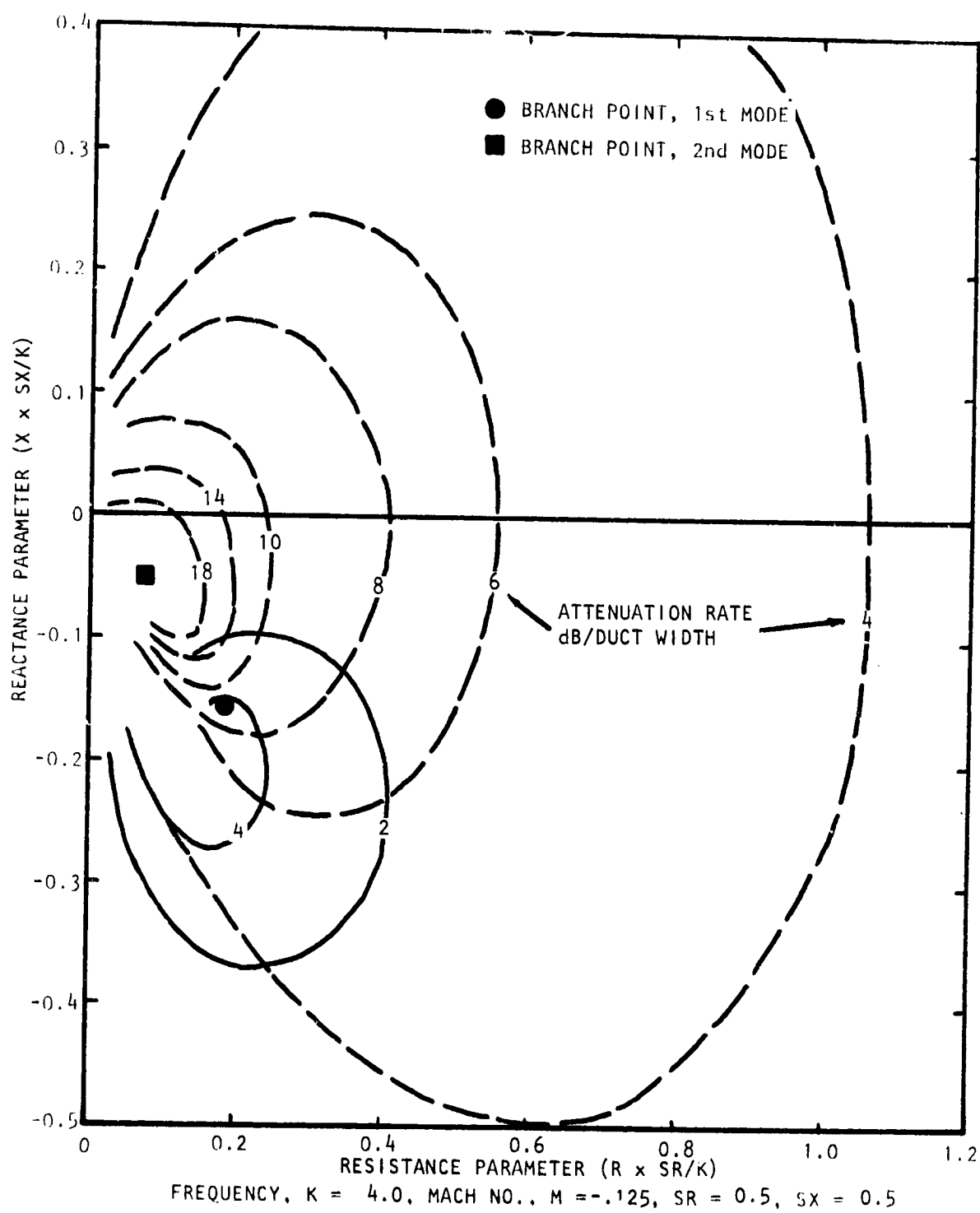


Figure A.75 Contours of Constant Attenuation for First Two Modes of Propagation (First Mode —, Second Mode ----)

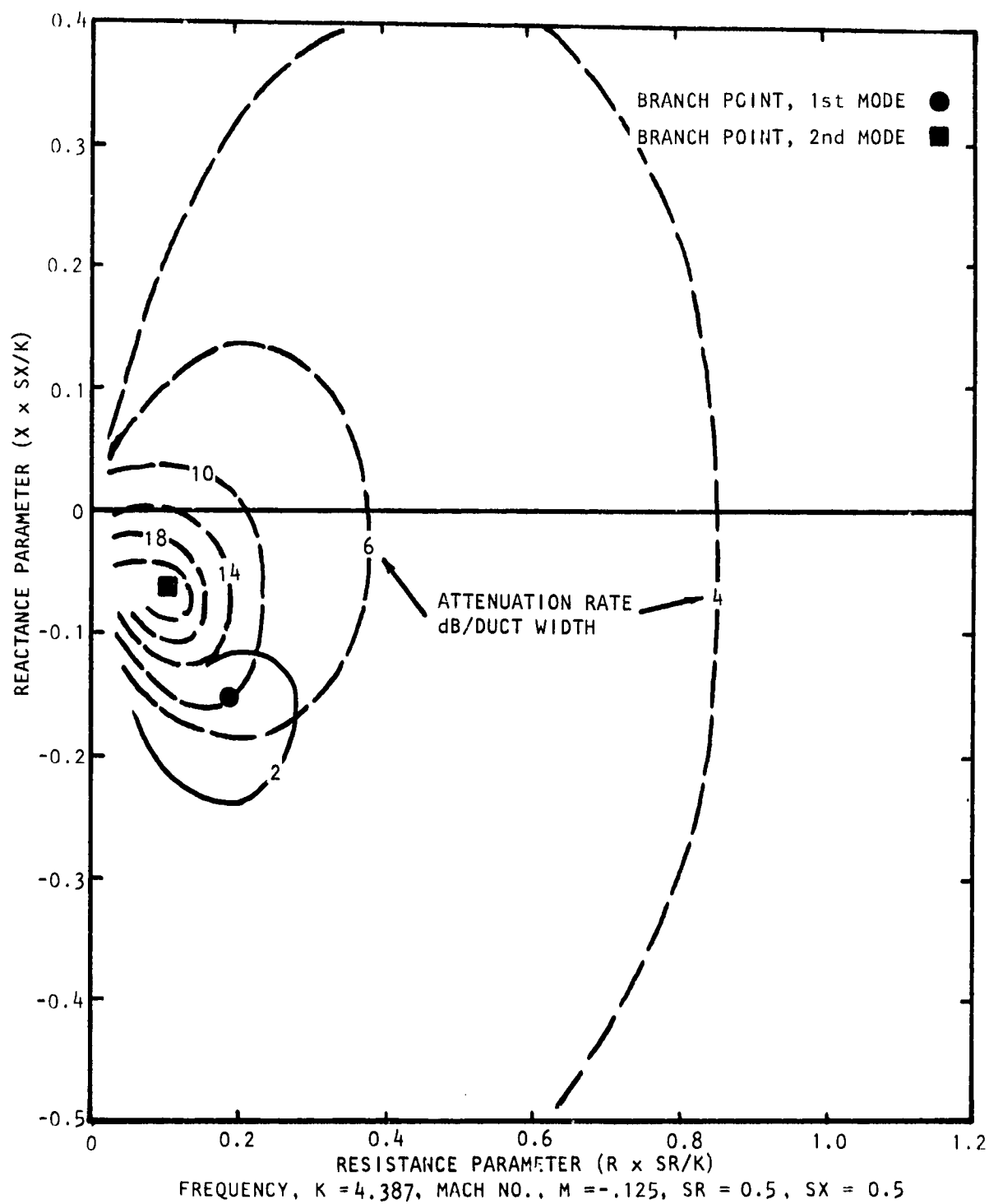


Figure A.76 Contours of Constant Attenuation for First Two Modes of Propagation (First Mode —, Second Mode ----)

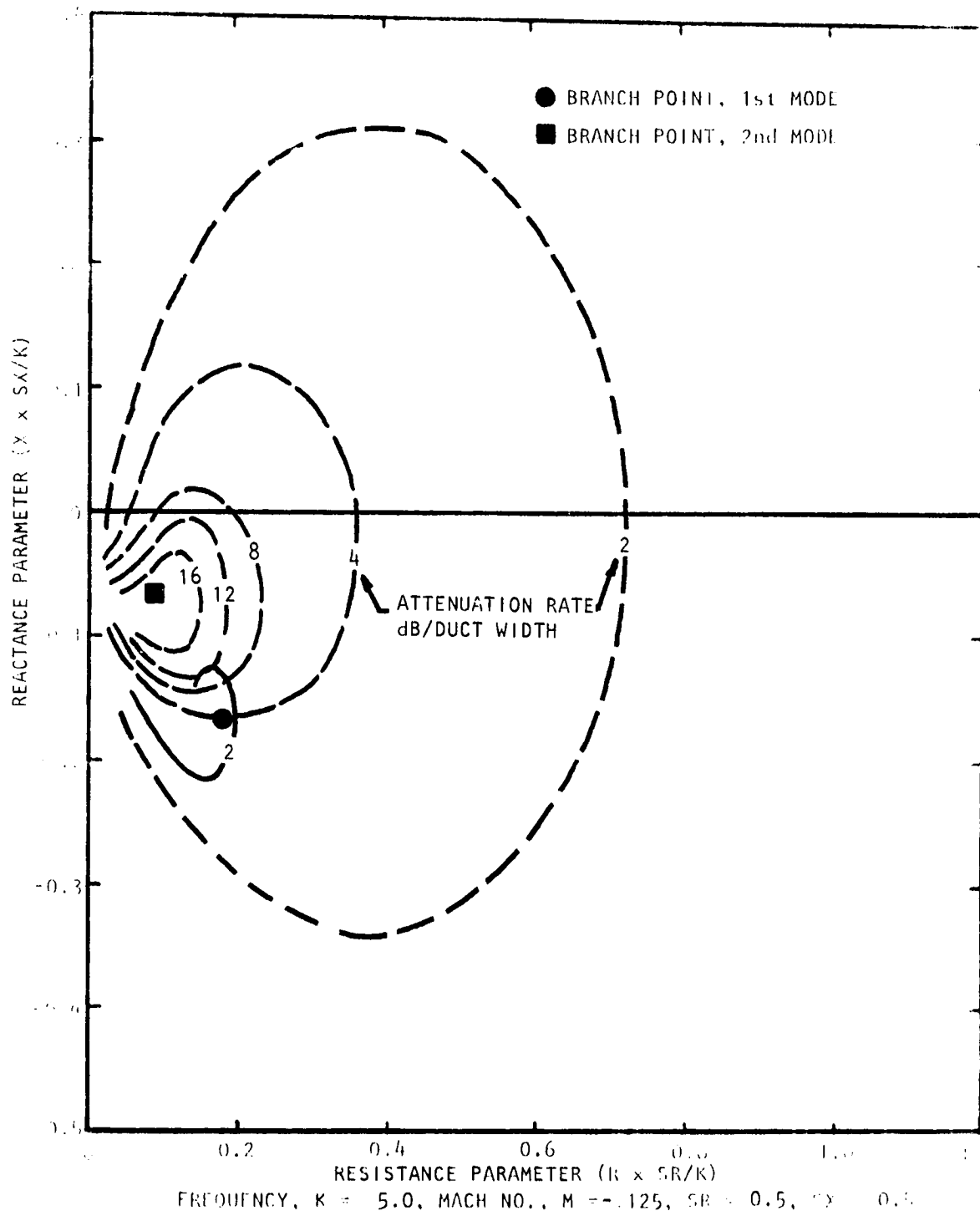


Figure A.77 Contours of Constant Attenuation for First Two Modes of Propagation (First Mode —, Second Mode ---)

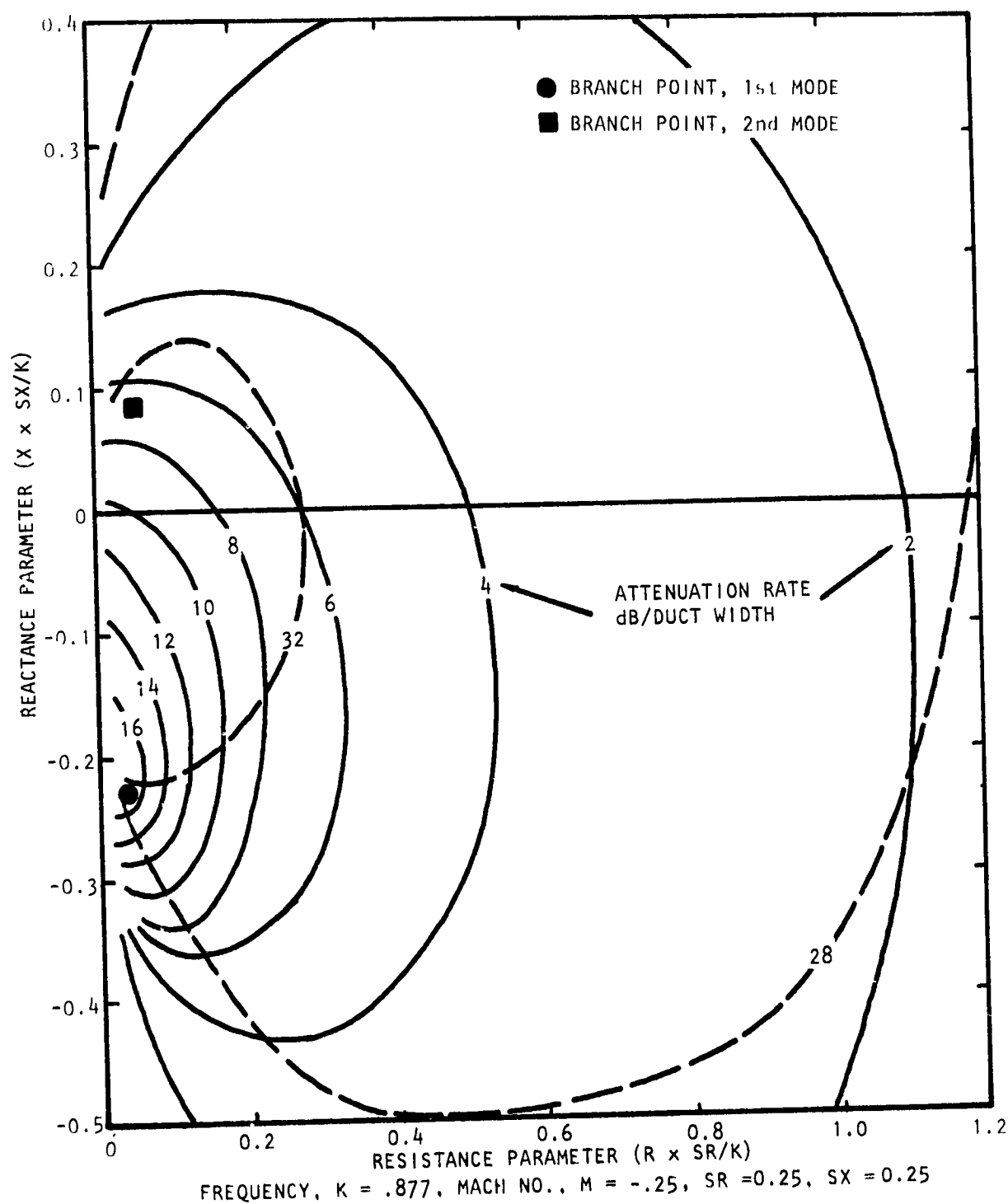


Figure A.78 Contours of Constant Attenuation for First Two Modes of Propagation (First Mode —, Second Mode ----)

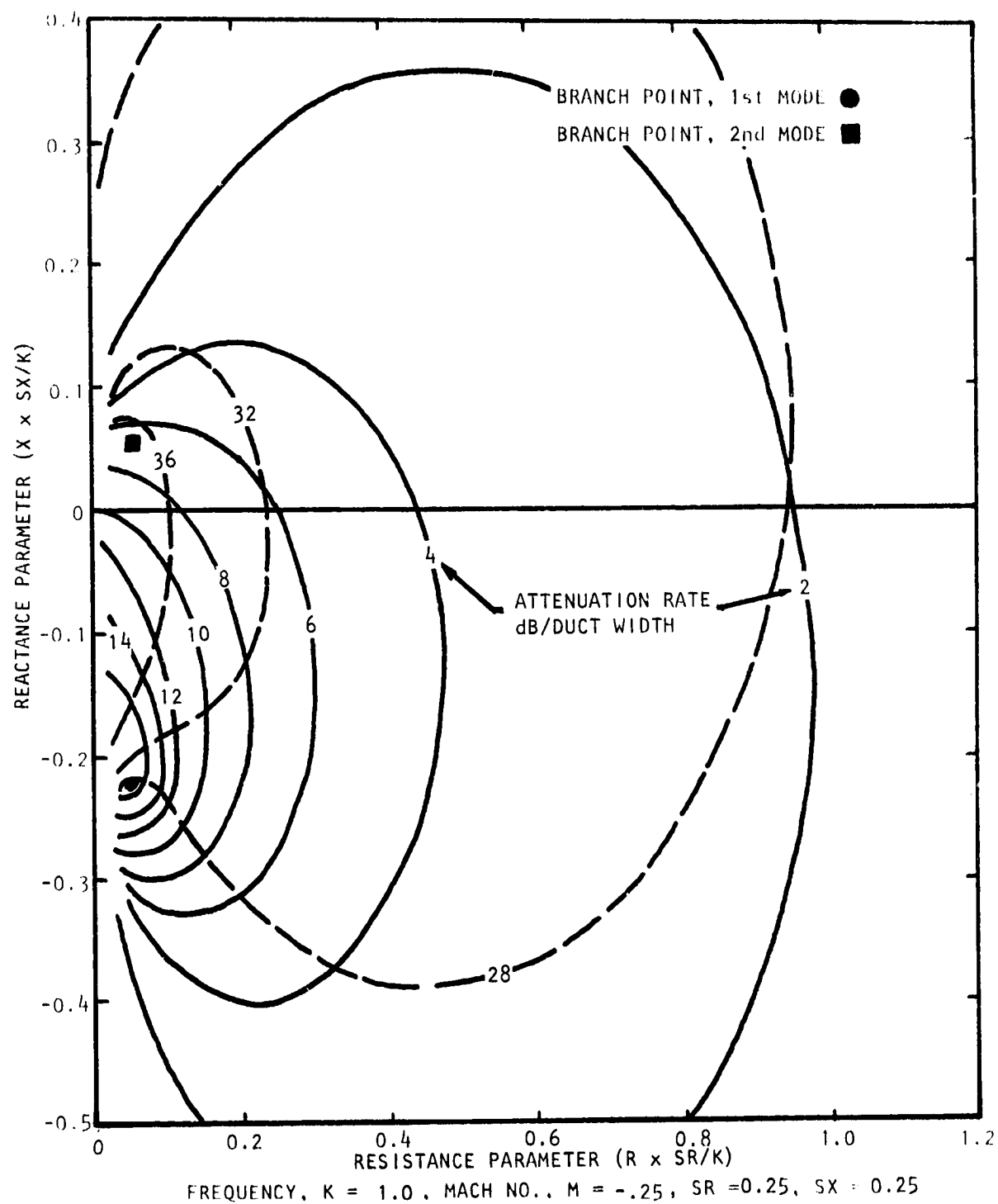


Figure A.79 Contours of Constant Attenuation for First Two Modes of Propagation (First Mode —, Second Mode ----)

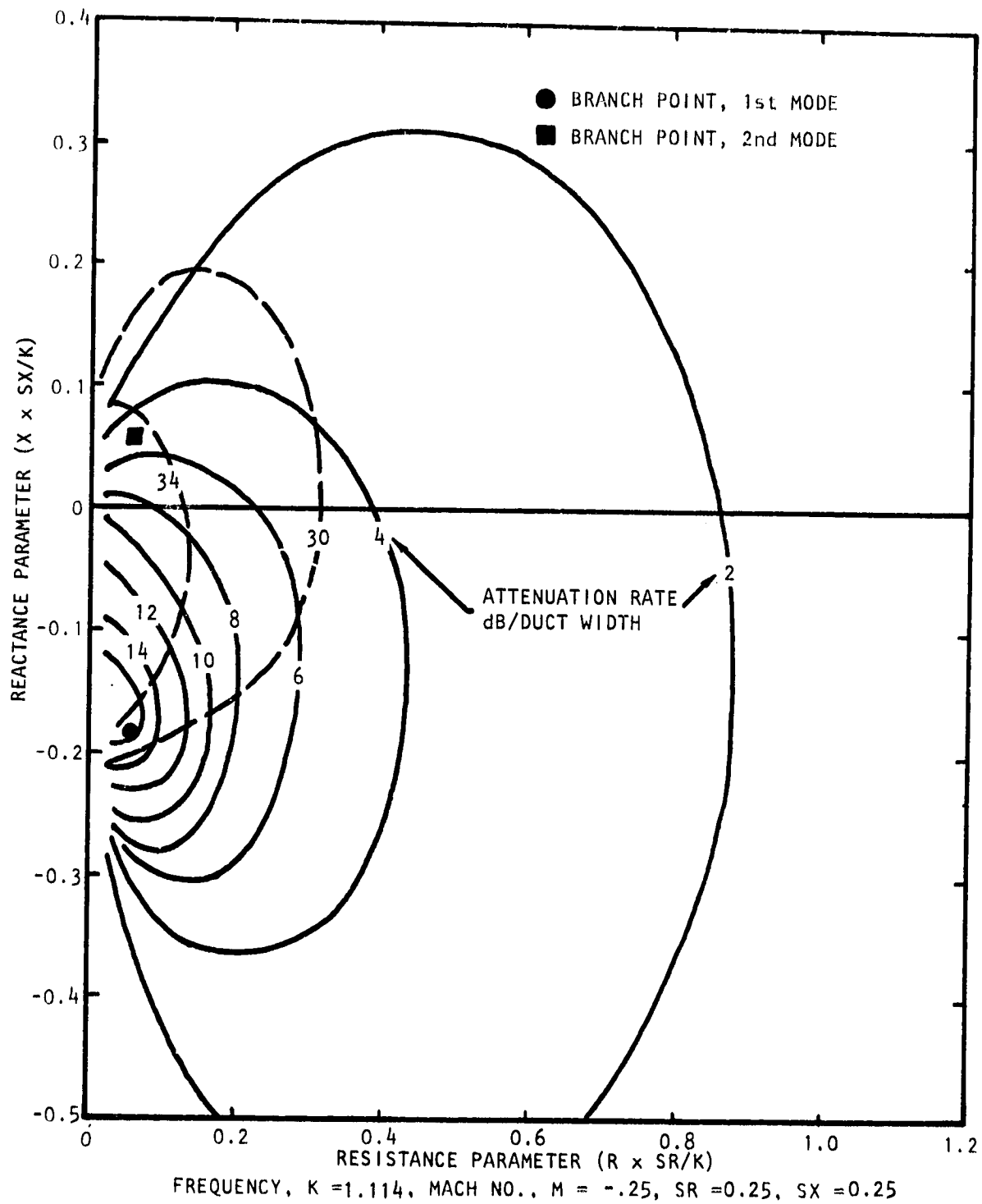


Figure A.80 Contours of Constant Attenuation for First Two Modes of Propagation (First Mode —, Second Mode ----)

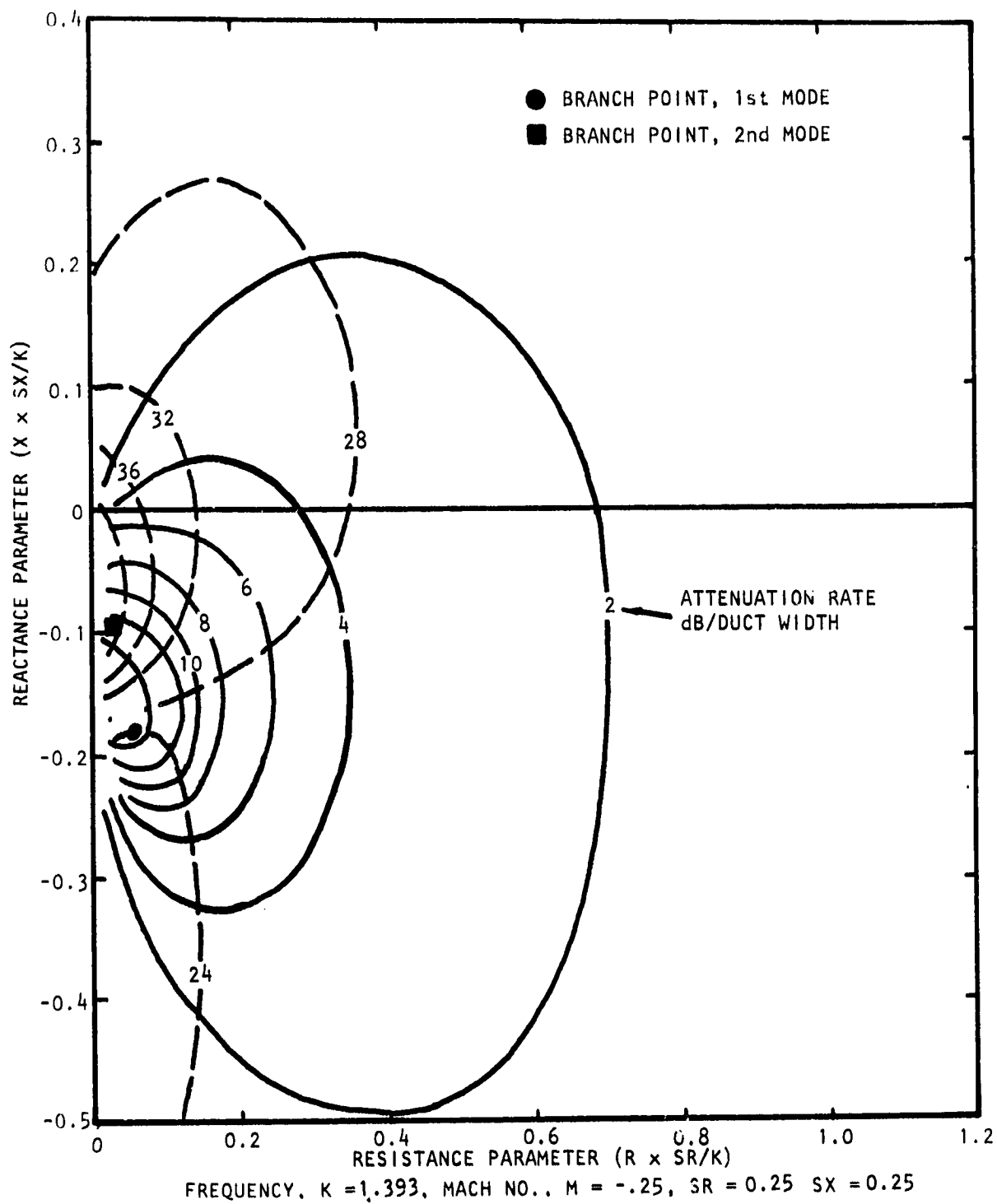


Figure A.81 Contours of Constant Attenuation for First Two Modes of Propagation (First Mode —, Second Mode ----)

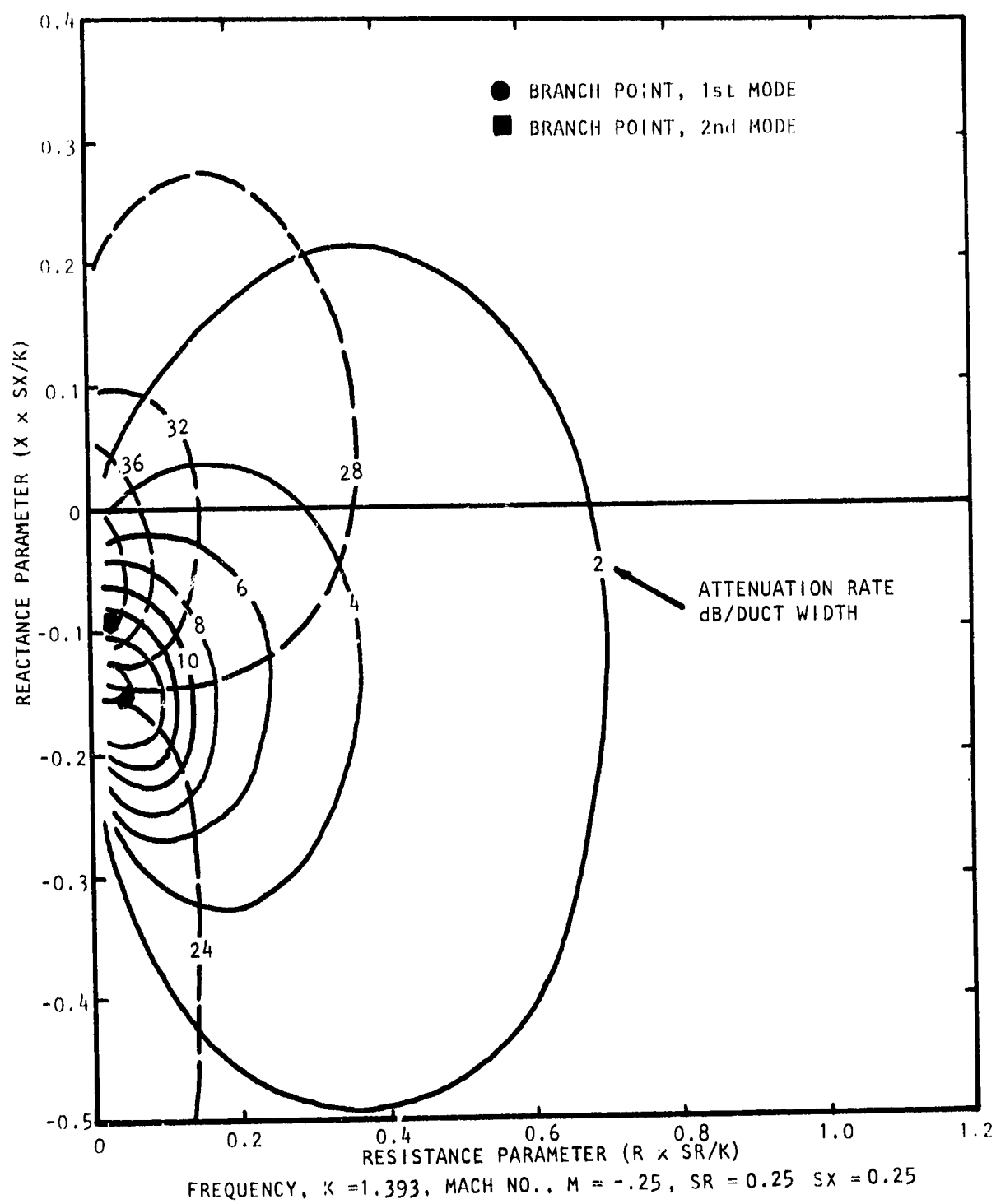


Figure A.82 Contours of Constant Attenuation for First Two Modes of Propagation (First Mode —, Second Mode ----)

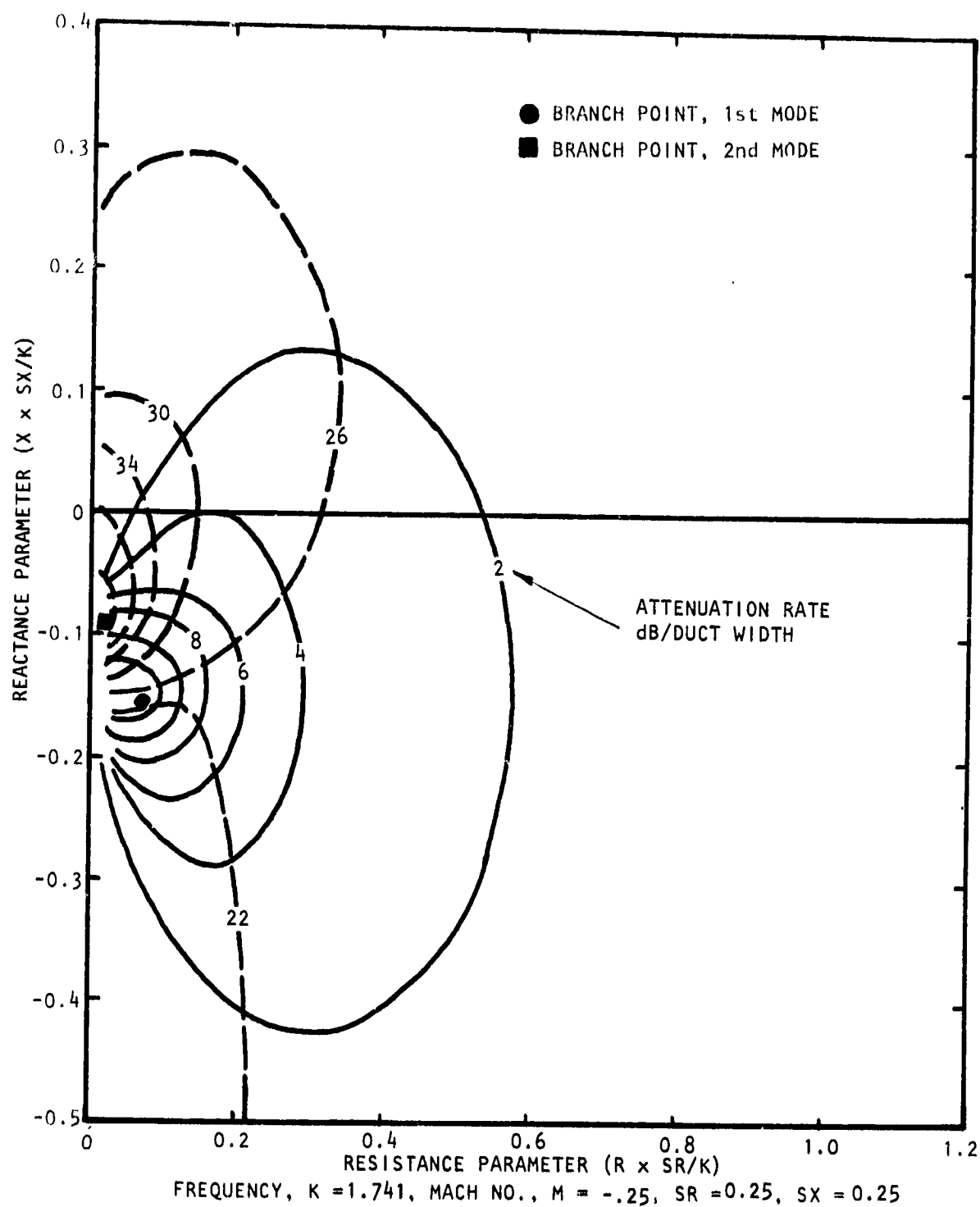


Figure A.83 Contours of Constant Attenuation for First Two Modes of Propagation (First Mode —, Second Mode ----)

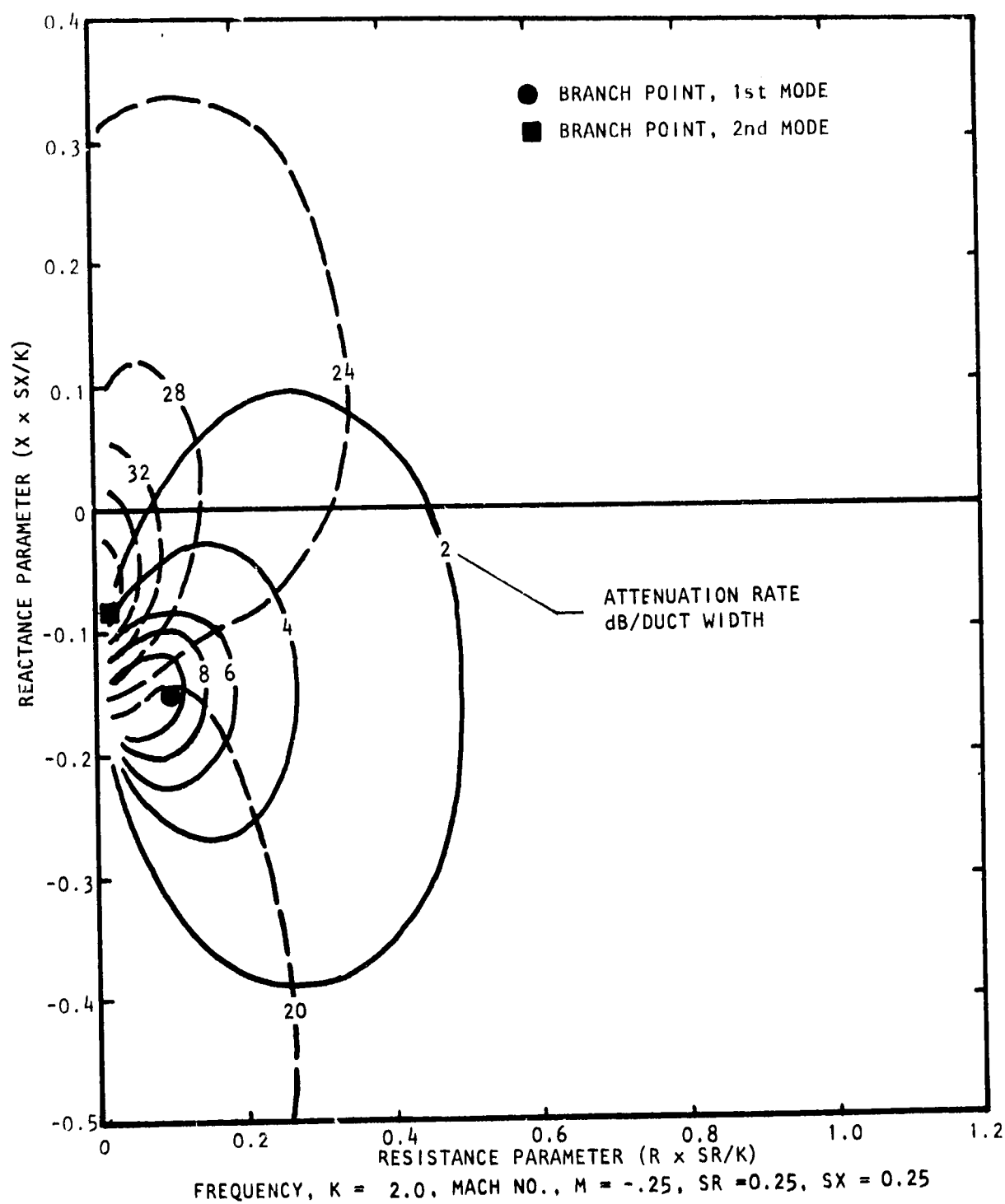


Figure A.84 Contours of Constant Attenuation for First Two Modes of Propagation (First Mode —, Second Mode ----)

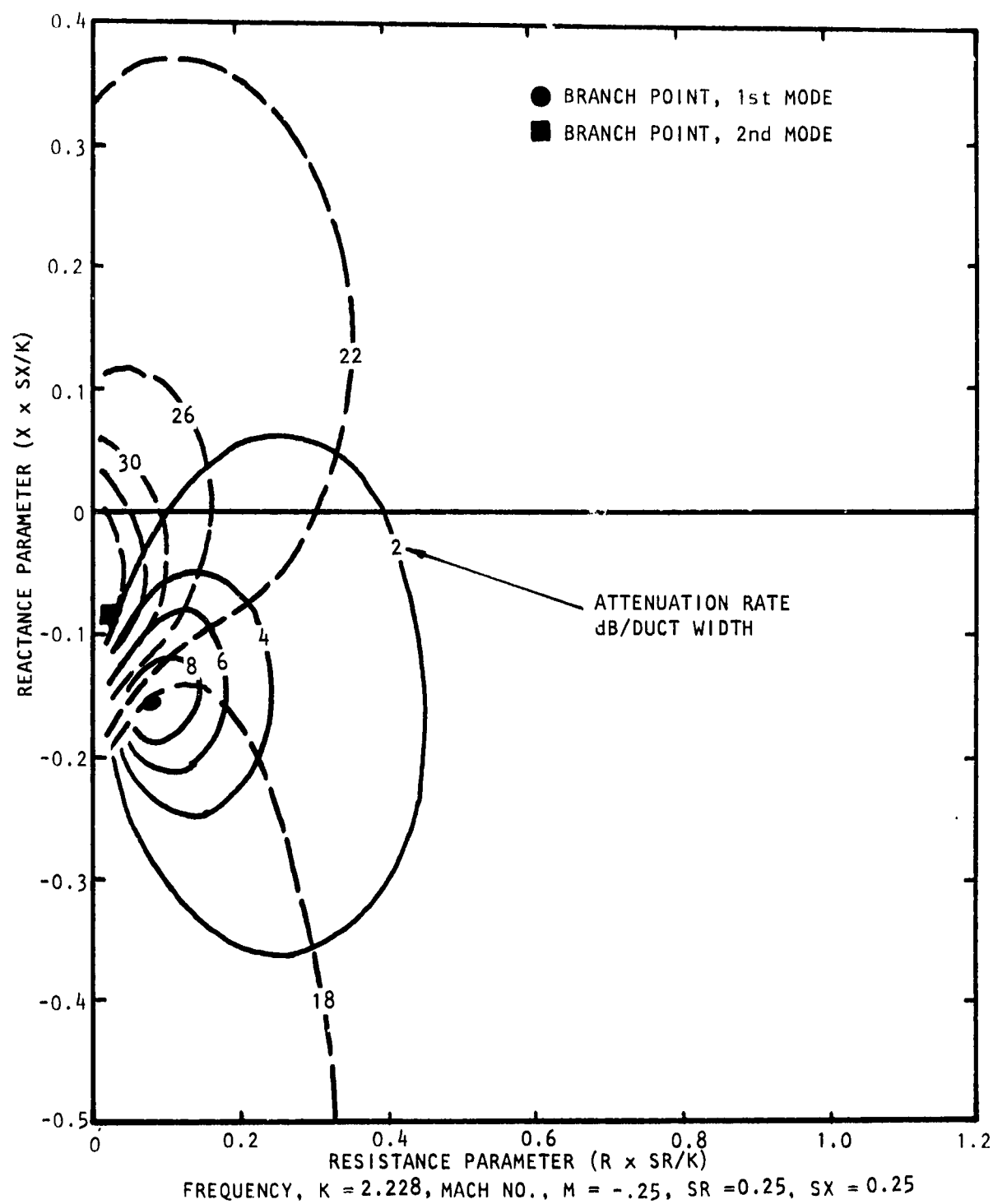


Figure A.85 Contours of Constant Attenuation for First Two Modes of Propagation (First Mode —, Second Mode ----)

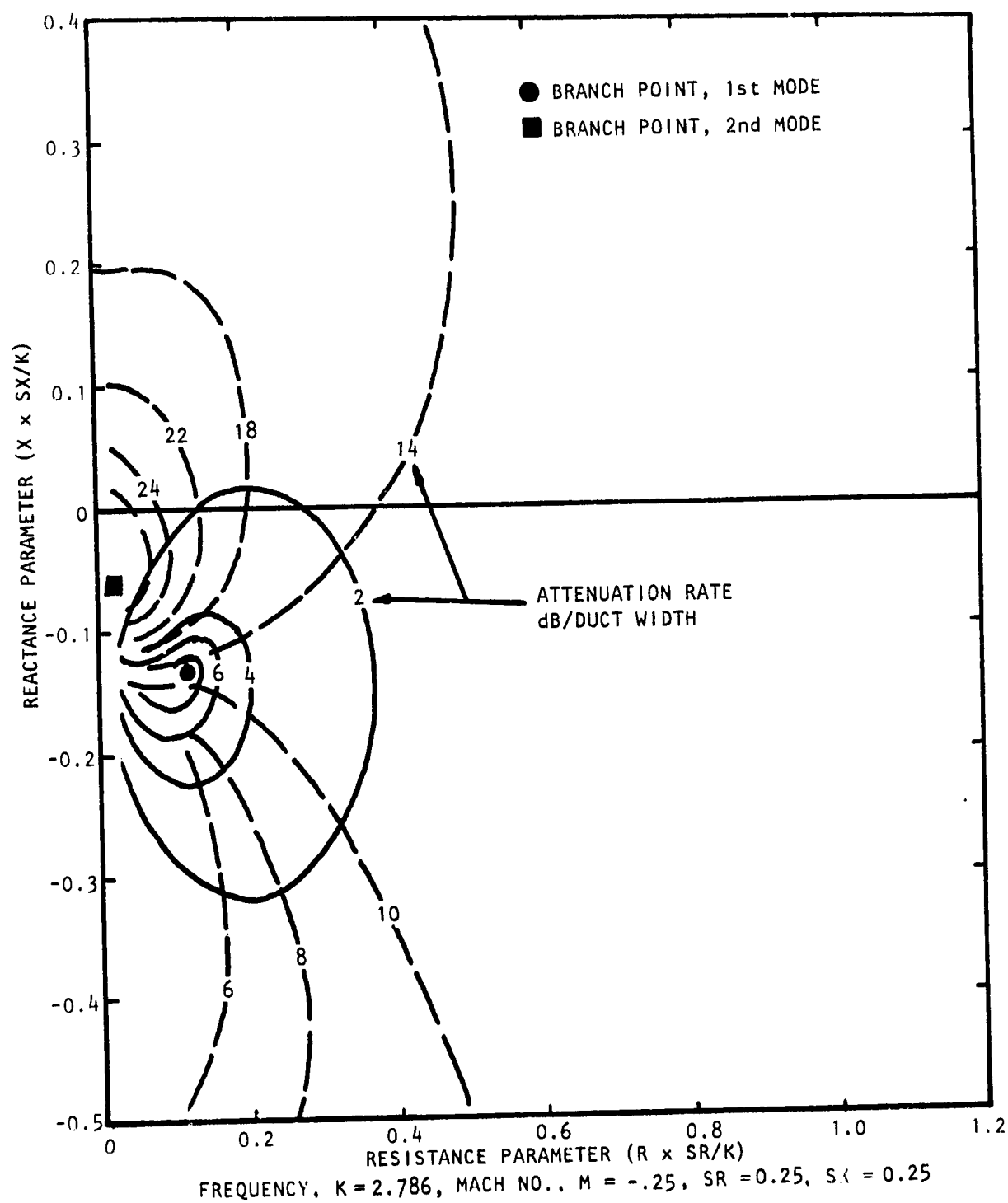


Figure A.86 Contours of Constant Attenuation for First Two Modes of Propagation (First Mode —, Second Mode ----)

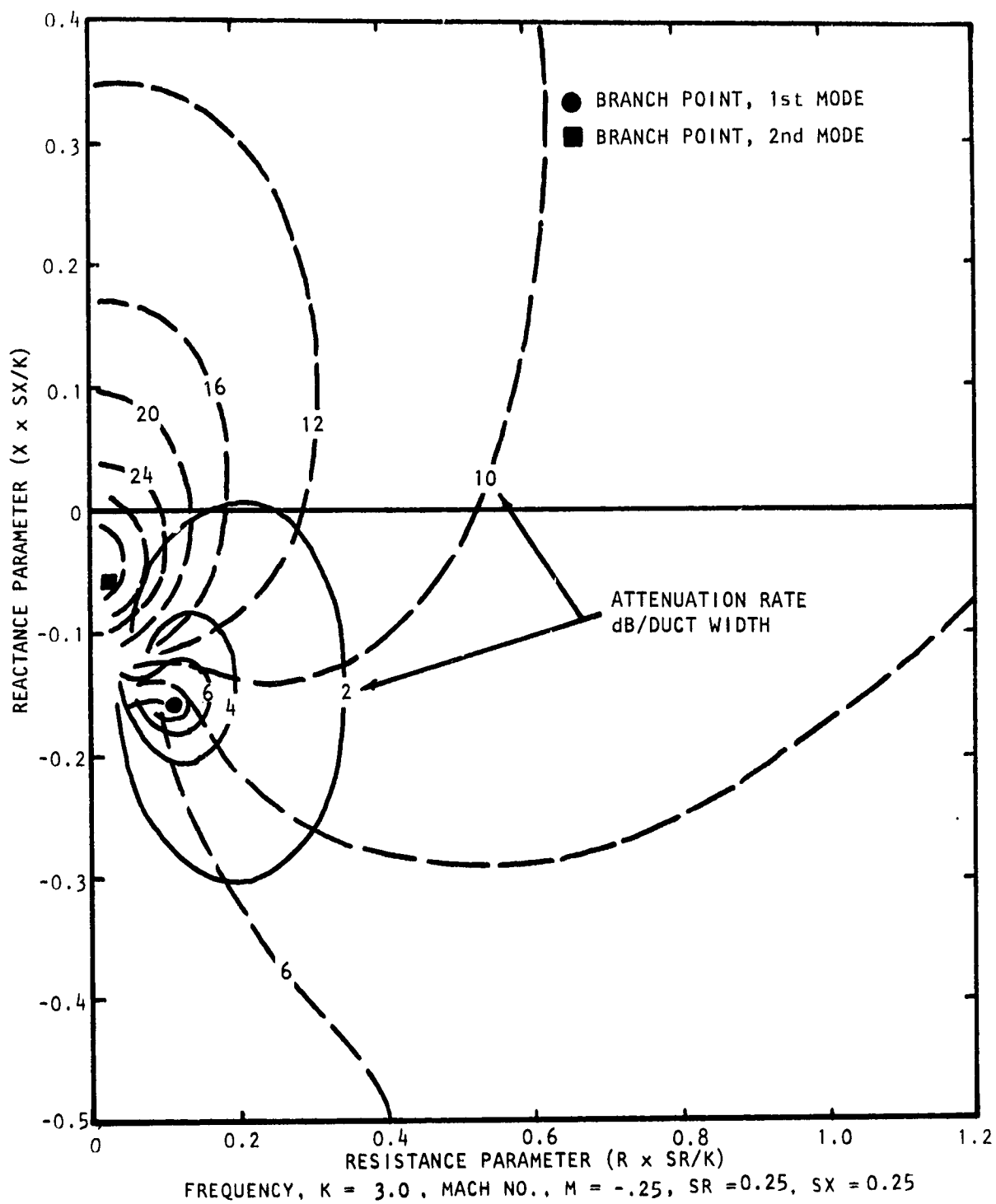


Figure A.87 Contours of Constant Attenuation for First Two Modes of Propagation (First Mode —, Second Mode ----)

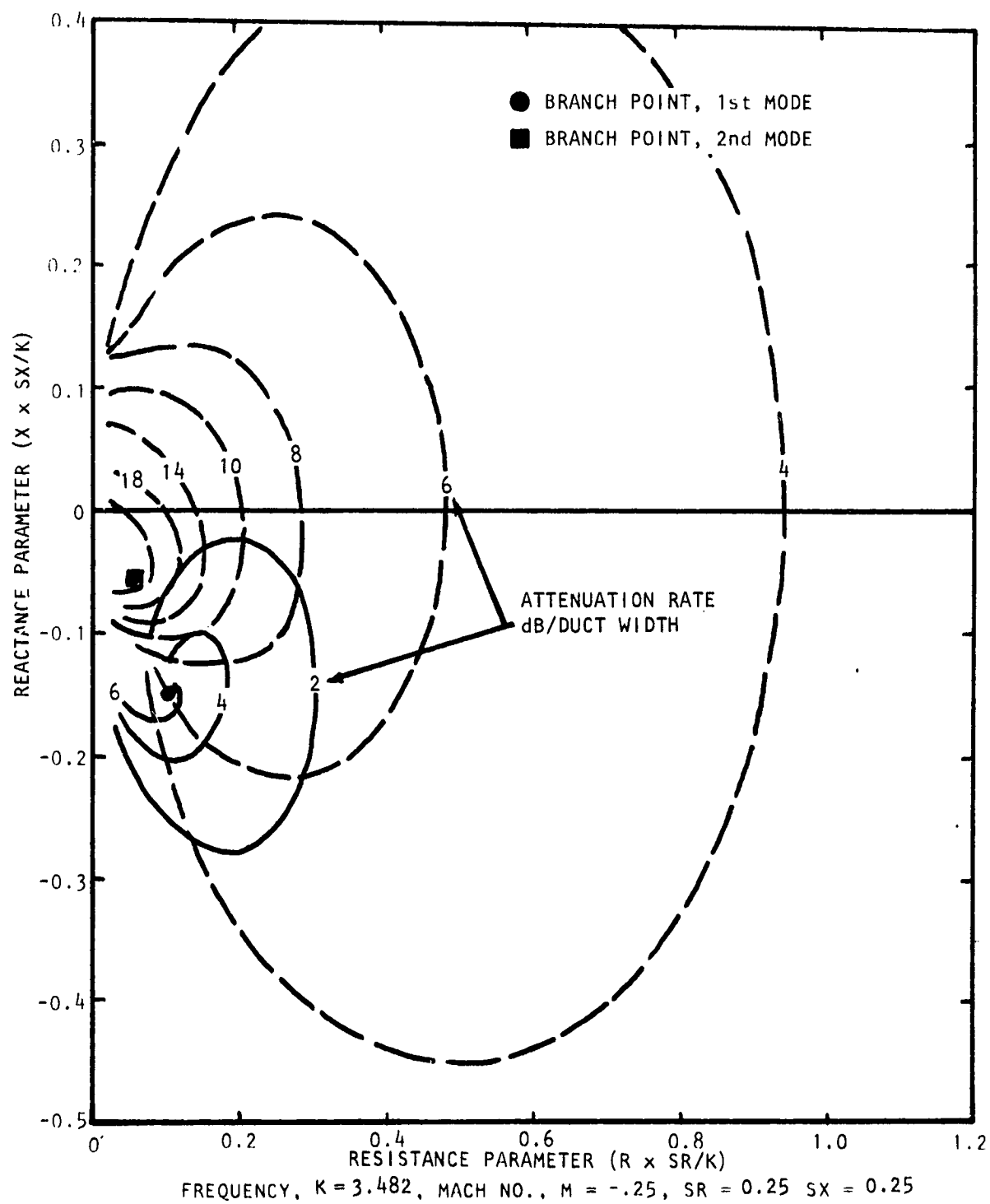


Figure A.88 Contours of Constant Attenuation for First Two Modes of Propagation (First Mode —, Second Mode ----)

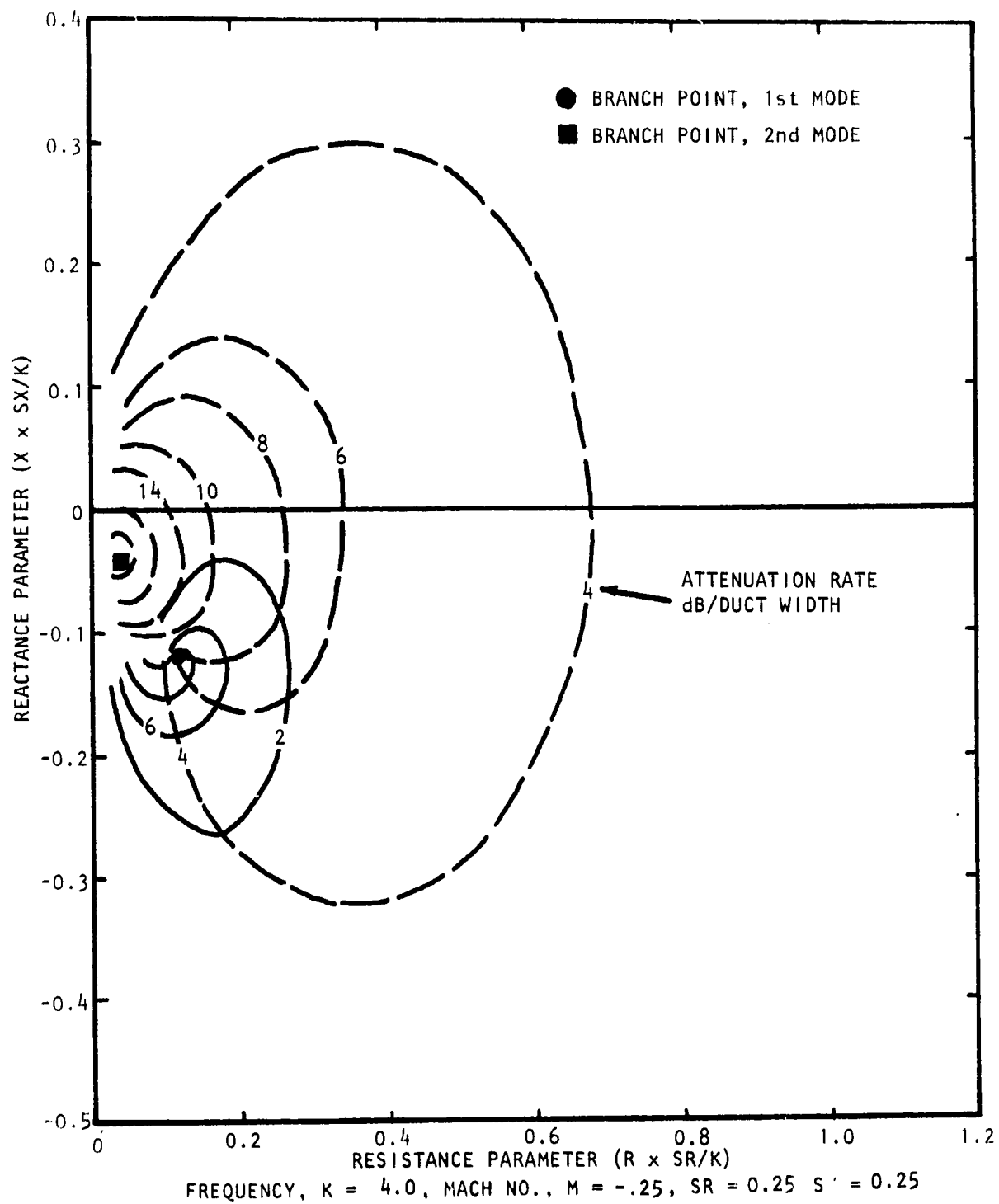


Figure A.89 Contours of Constant Attenuation for First Two Modes of Propagation (First Mode —, Second Mode ----)

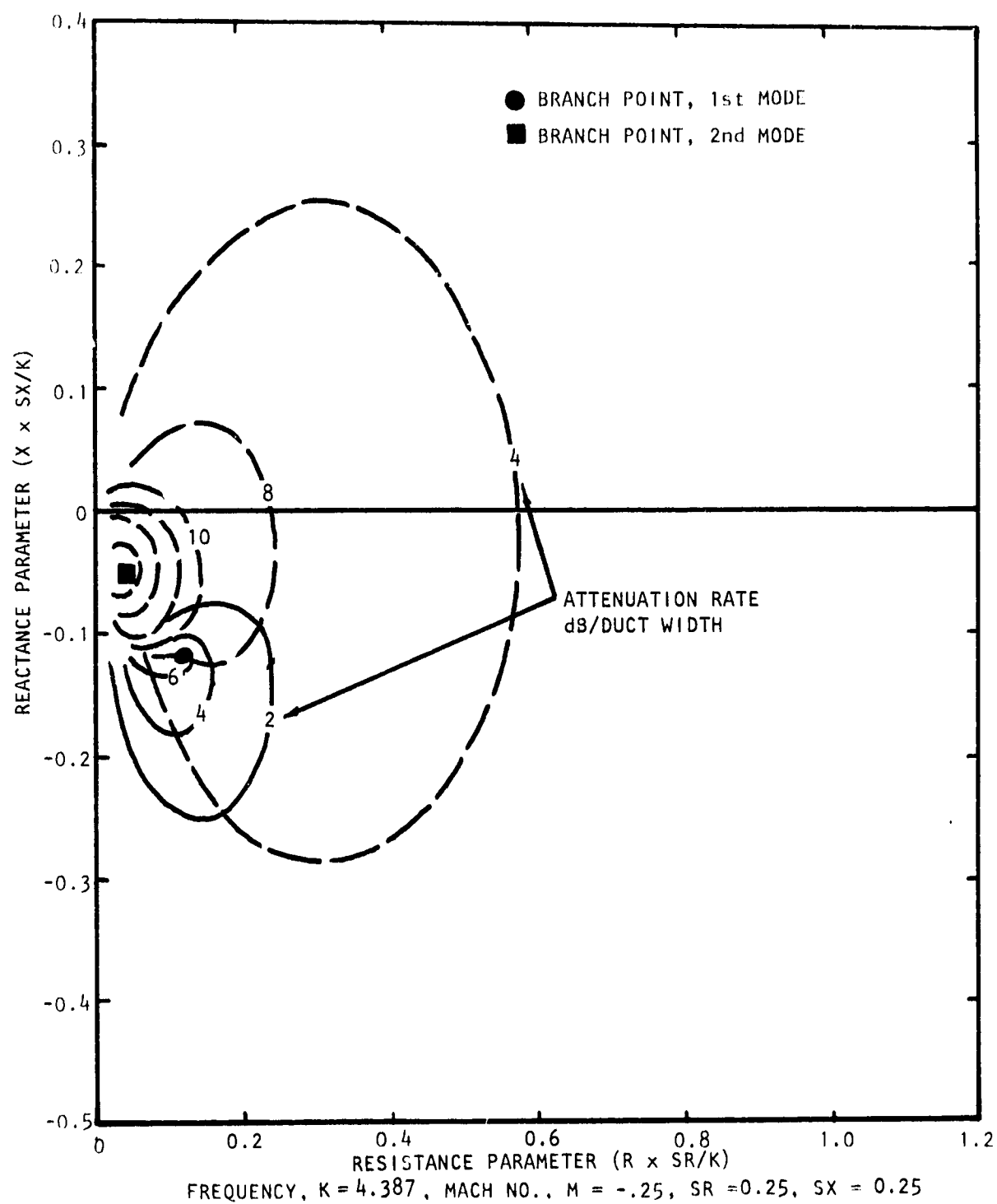


Figure A.90 Contours of Constant Attenuation for First Two Modes of Propagation (First Mode —, Second Mode ----)

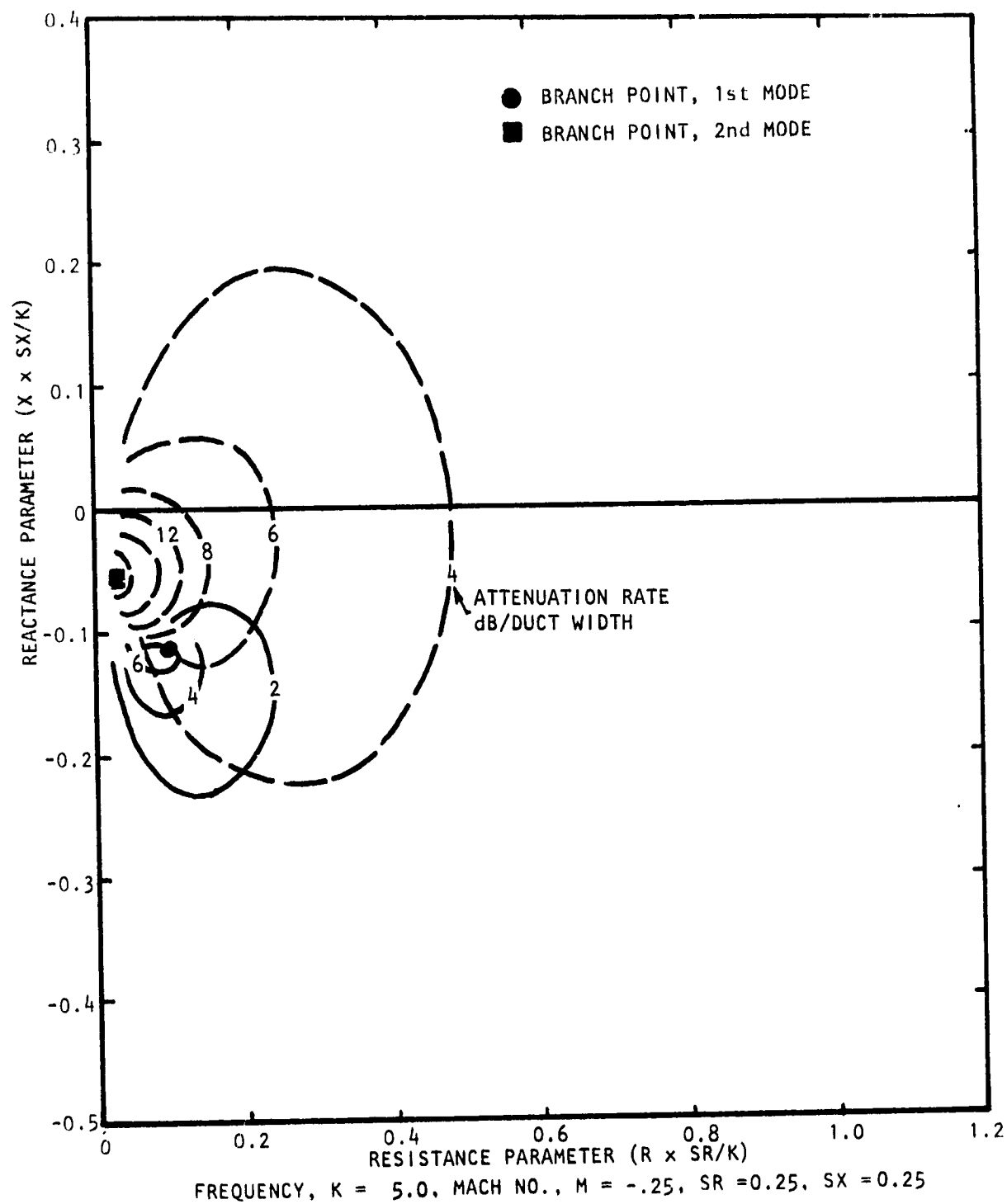


Figure A.91 Contours of Constant Attenuation for First Two Modes of Propagation (First Mode —, Second Mode ----)

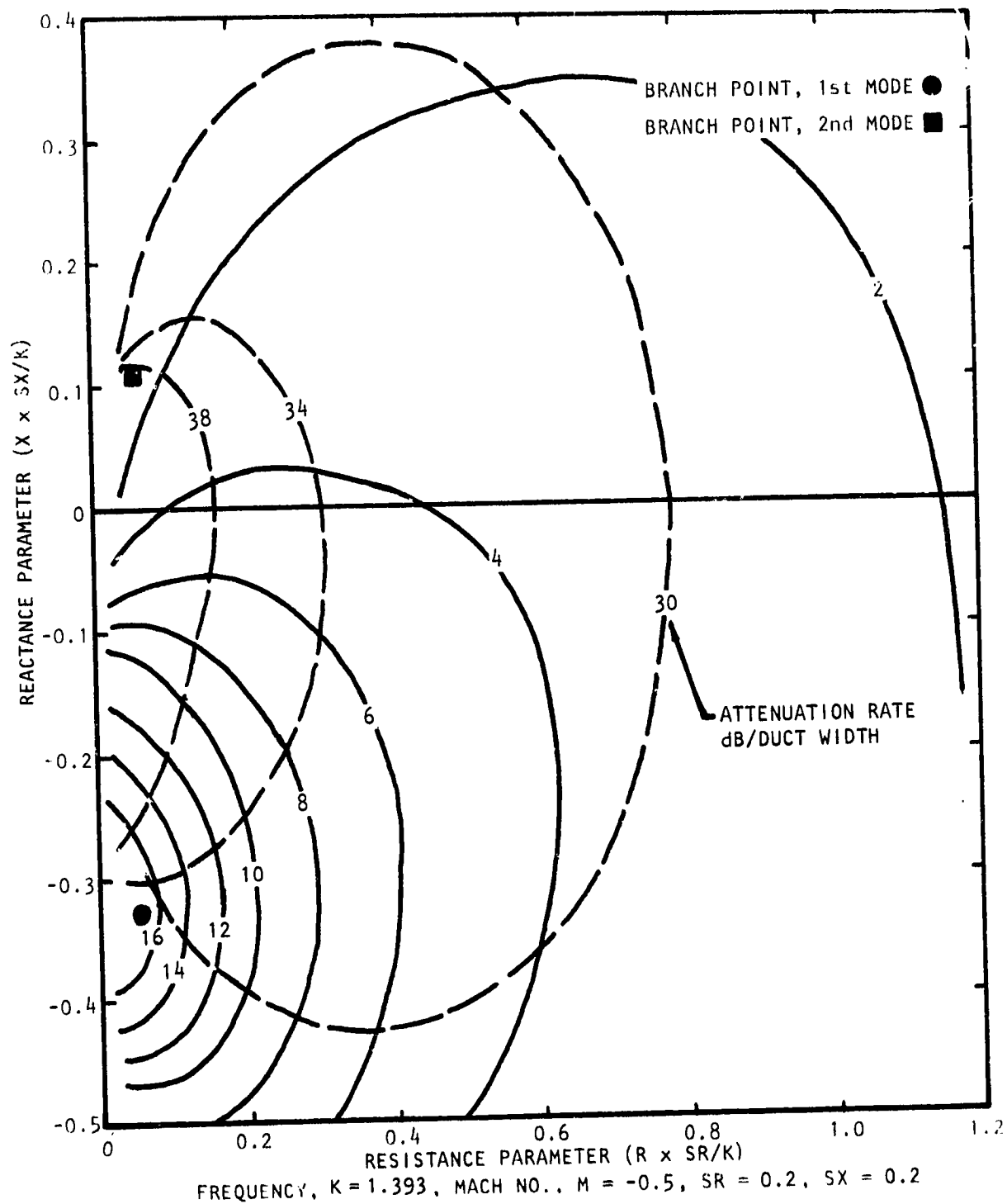


Figure A.92 Contours of Constant Attenuation for First Two Modes of Propagation (First Mode —, Second Mode ----)

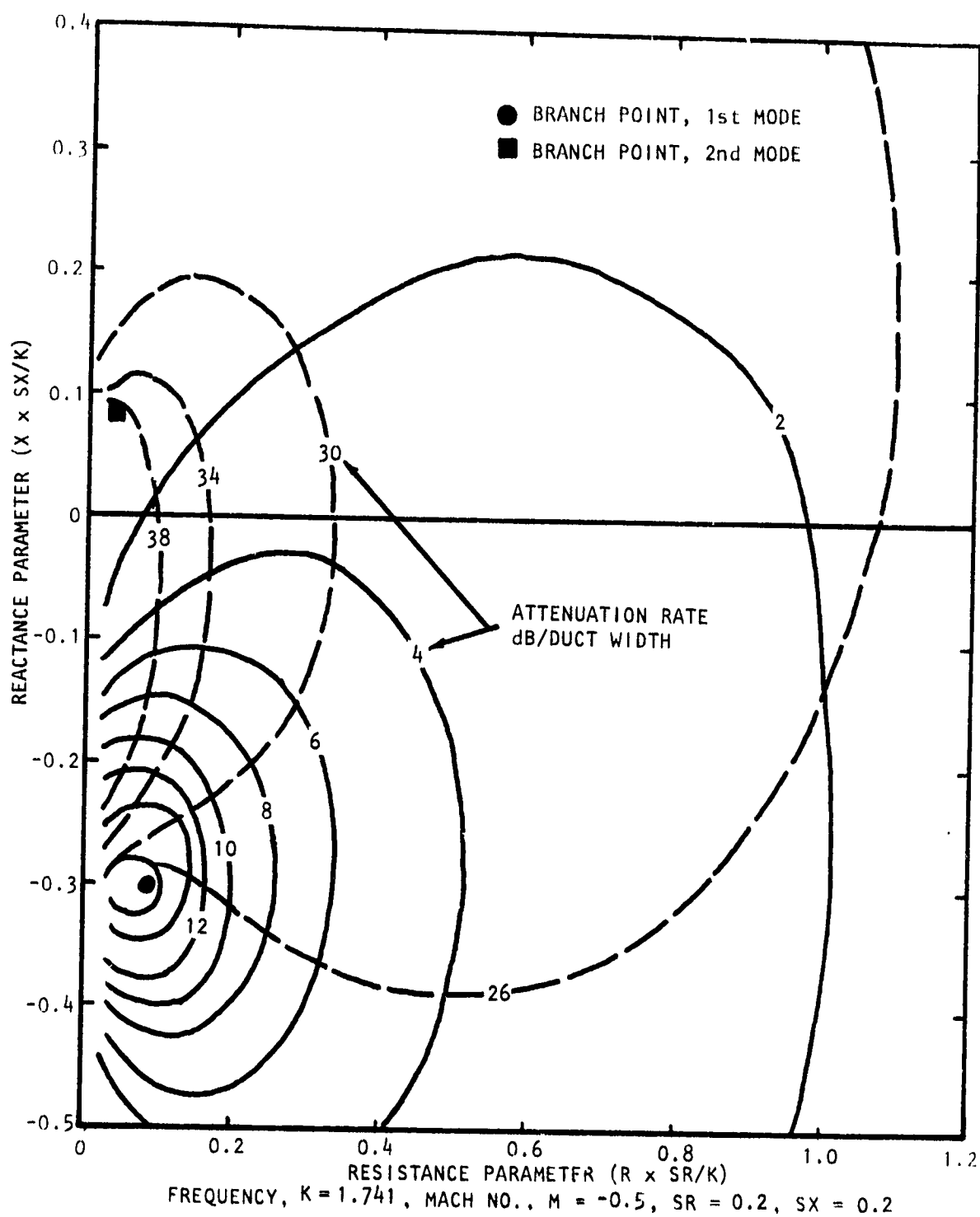


Figure A.93 Contours of Constant Attenuation for First Two Modes of Propagation (First Mode —, Second Mode ----)

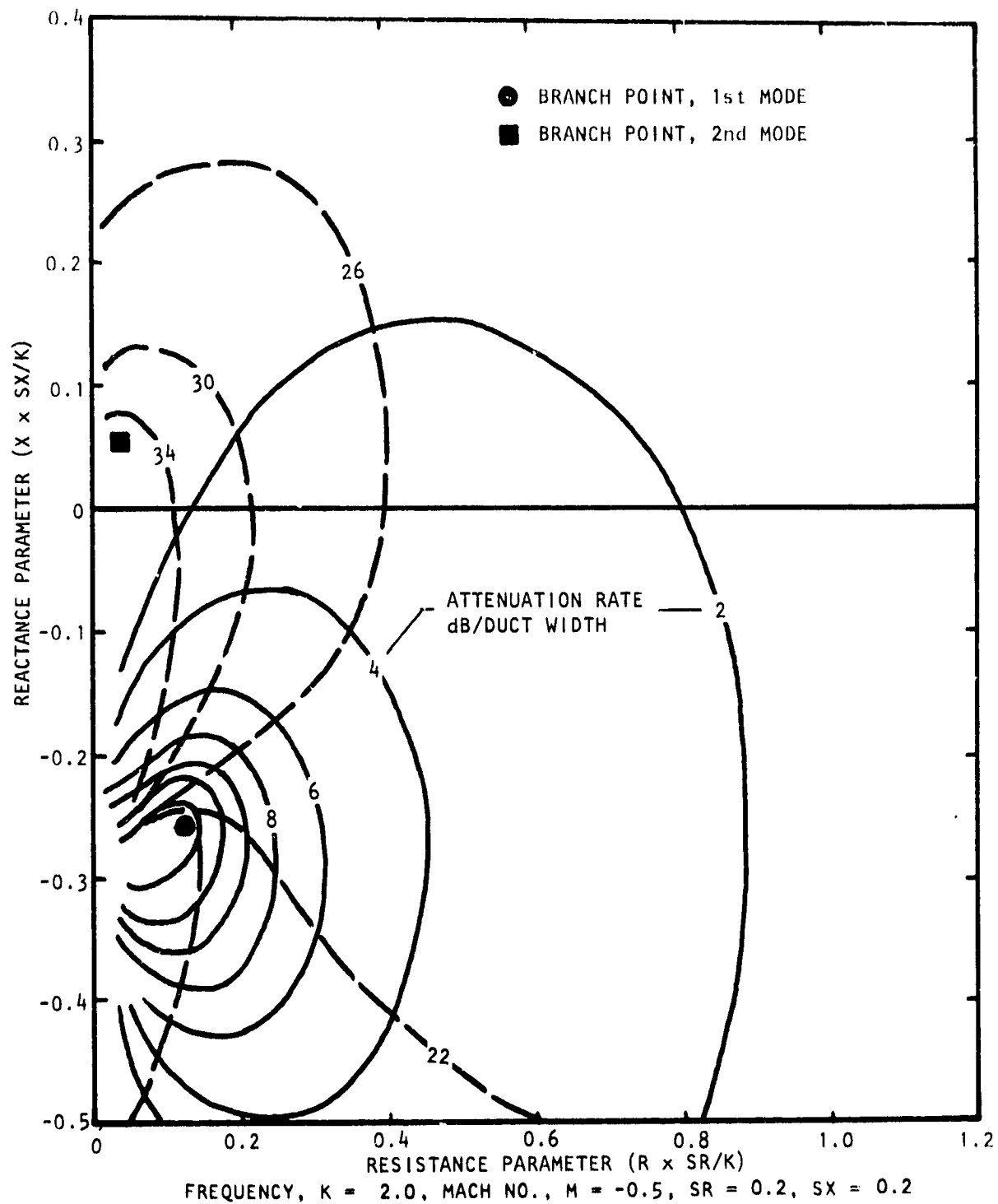


Figure A.94 Contours of Constant Attenuation for First Two Modes of Propagation (First Mode —, Second Mode ----)

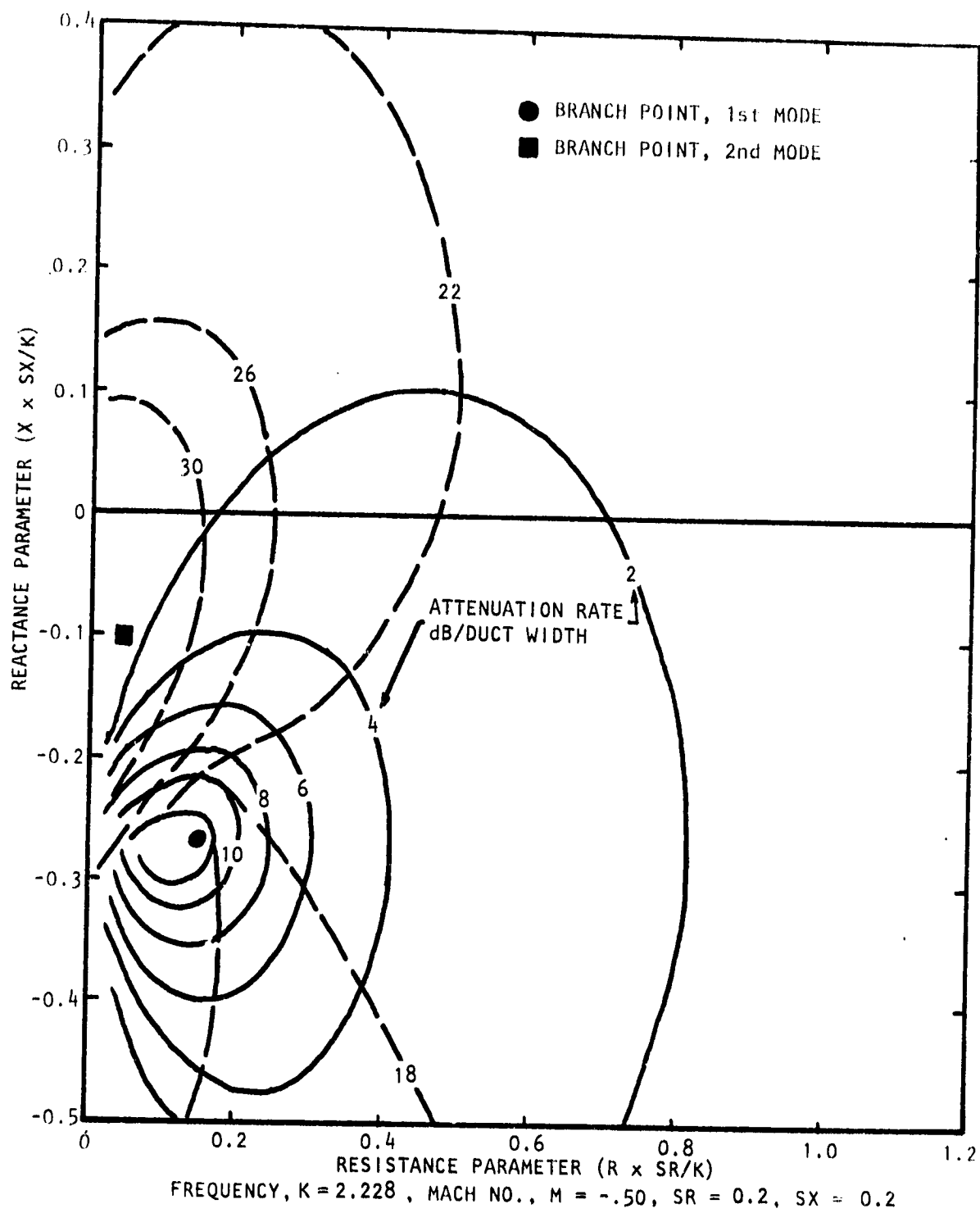


Figure A.95 Contours of Constant Attenuation for First Two Modes
 of Propagation (First Mode —, Second Mode ----)

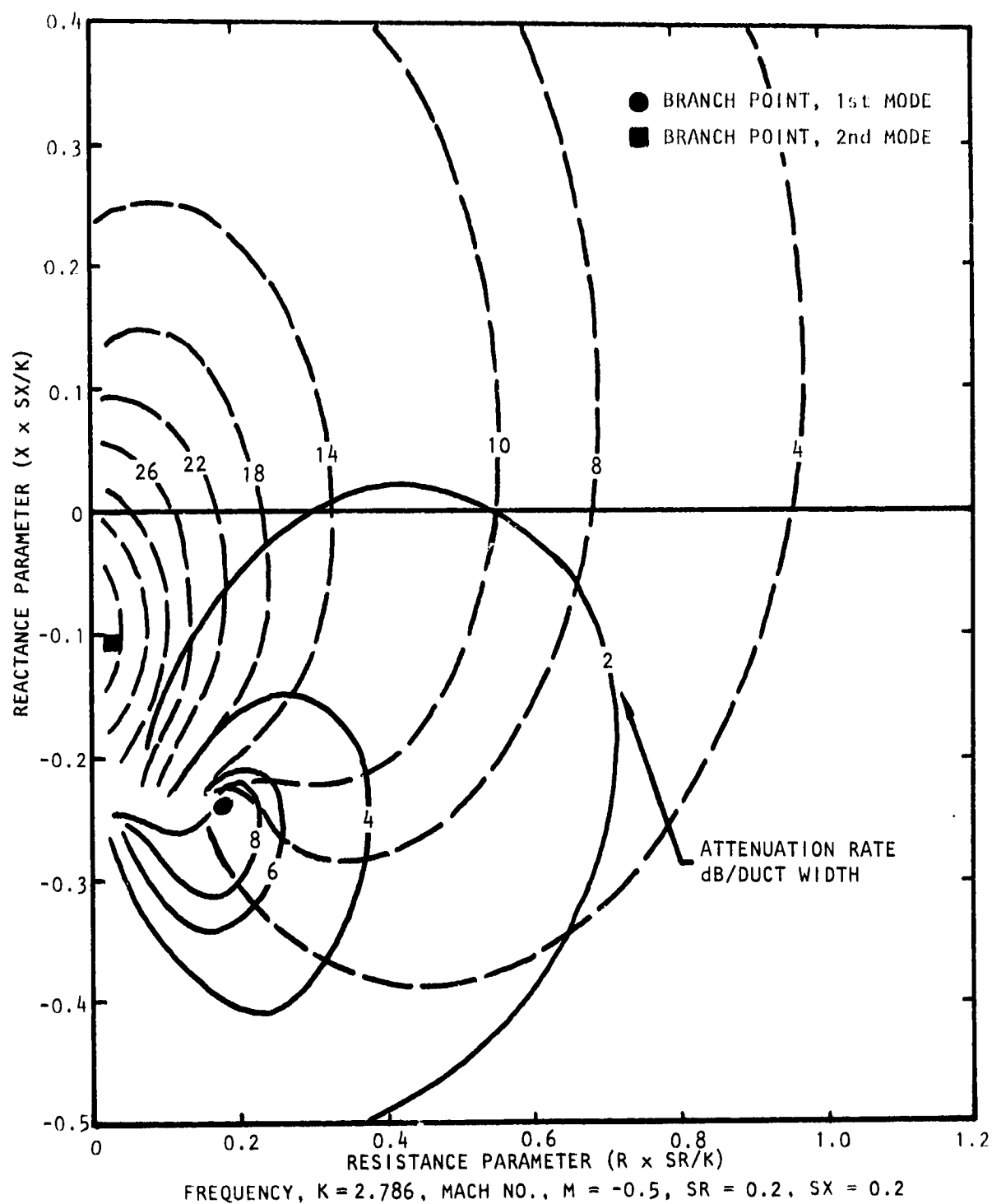


Figure A.96 Contours of Constant Attenuation for First Two Modes of Propagation (First Mode —, Second Mode ----)

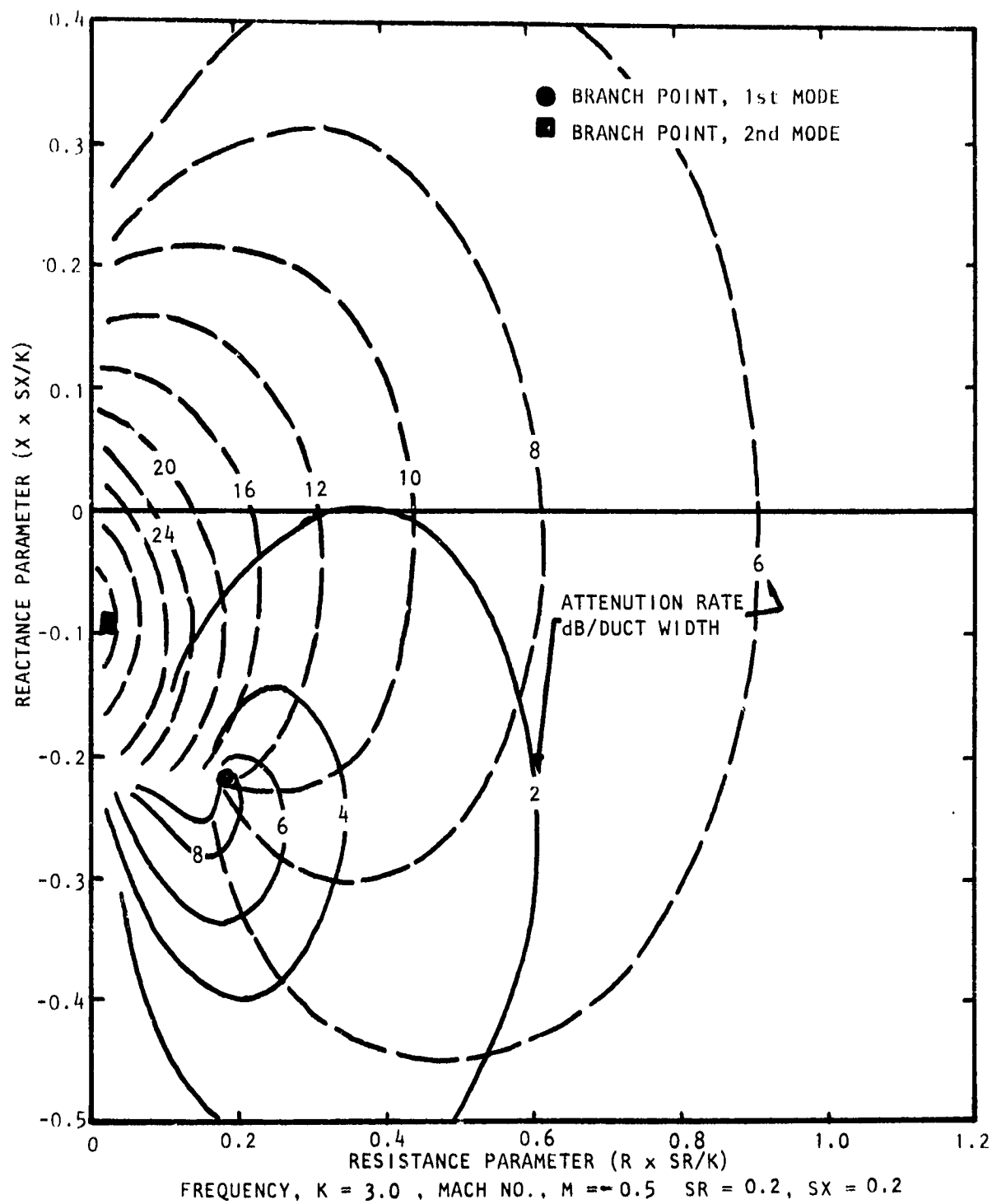


Figure A.97 Contours of Constant Attenuation for First Two Modes
 of Propagation (First Mode —, Second Mode ----)

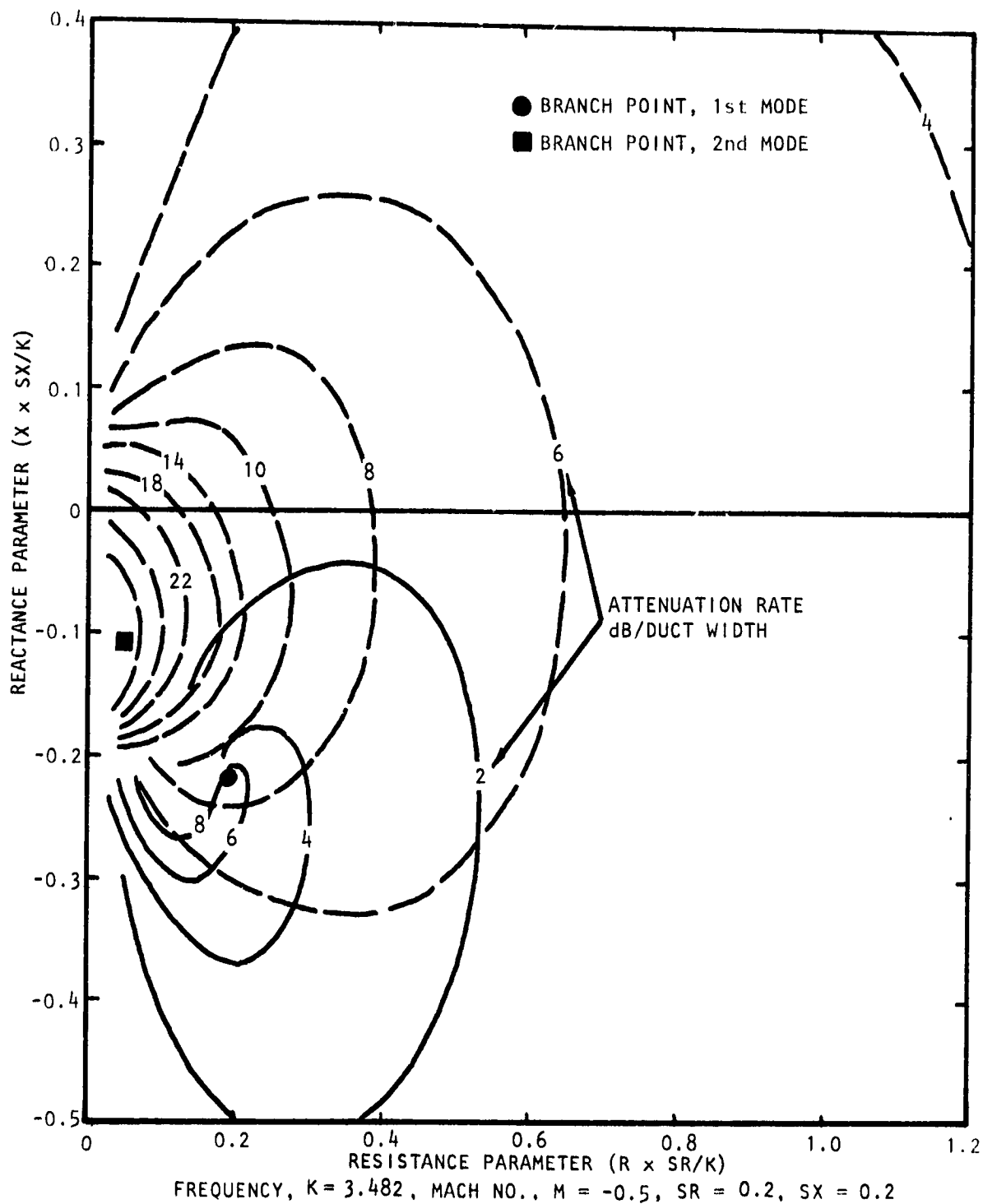


Figure A.98 Contours of Constant Attenuation for First Two Modes of Propagation (First Mode —, Second Mode ----)

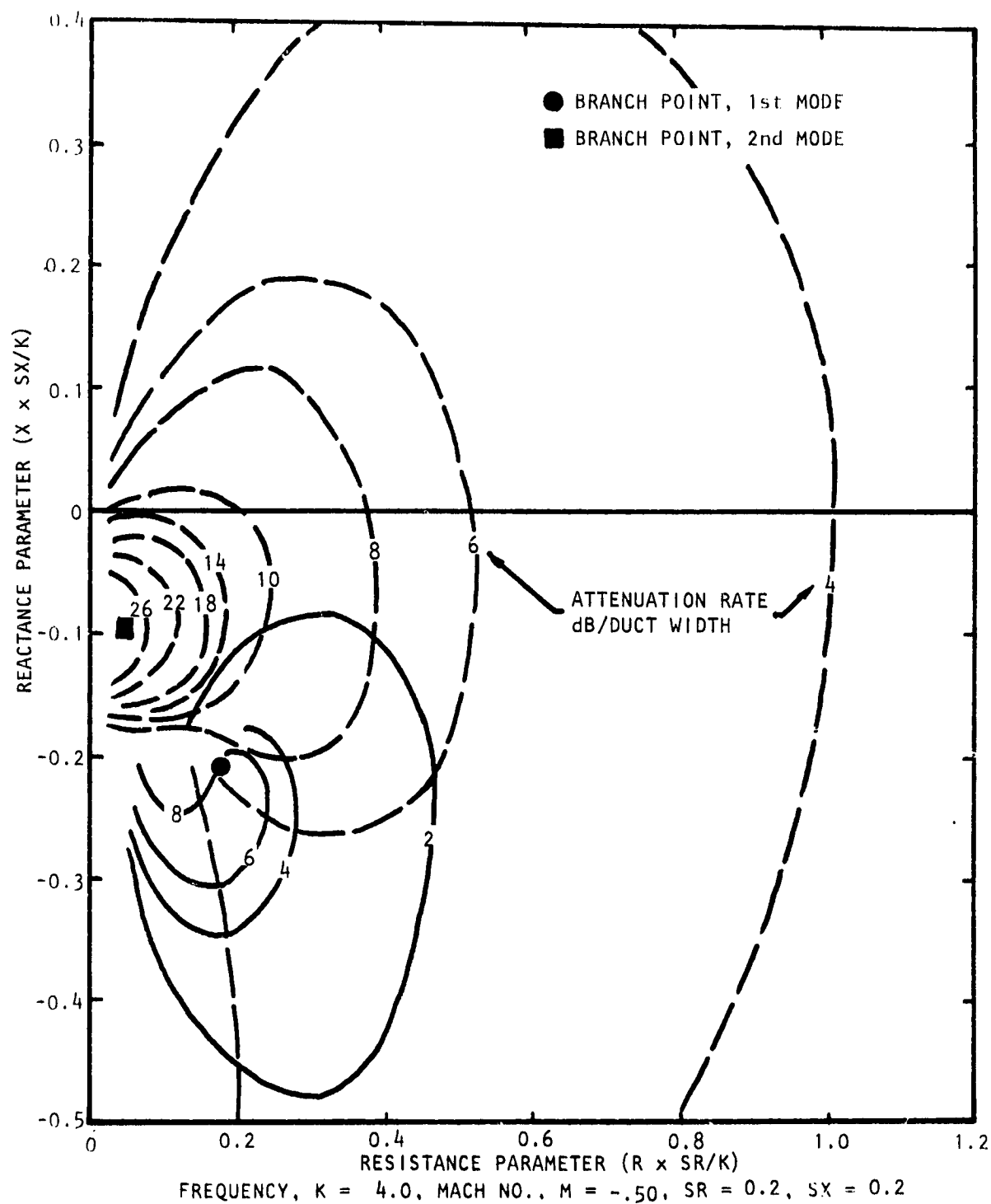


Figure A.99 Contours of Constant Attenuation for First Two Modes of Propagation (First Mode —, Second Mode ----)

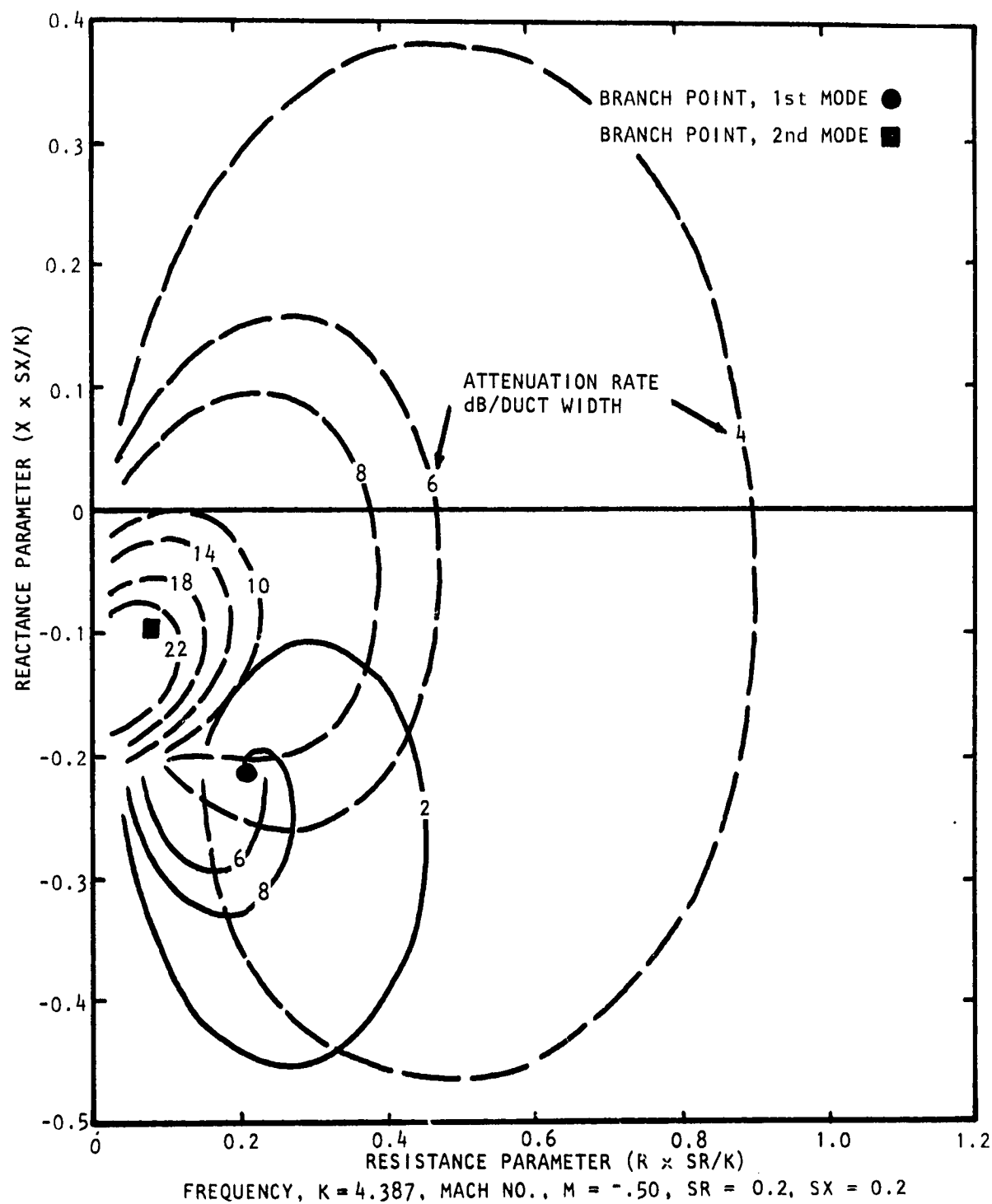


Figure A.100 Contours of Constant Attenuation for First Two Modes of Propagation (First Mode —, Second Mode ----)

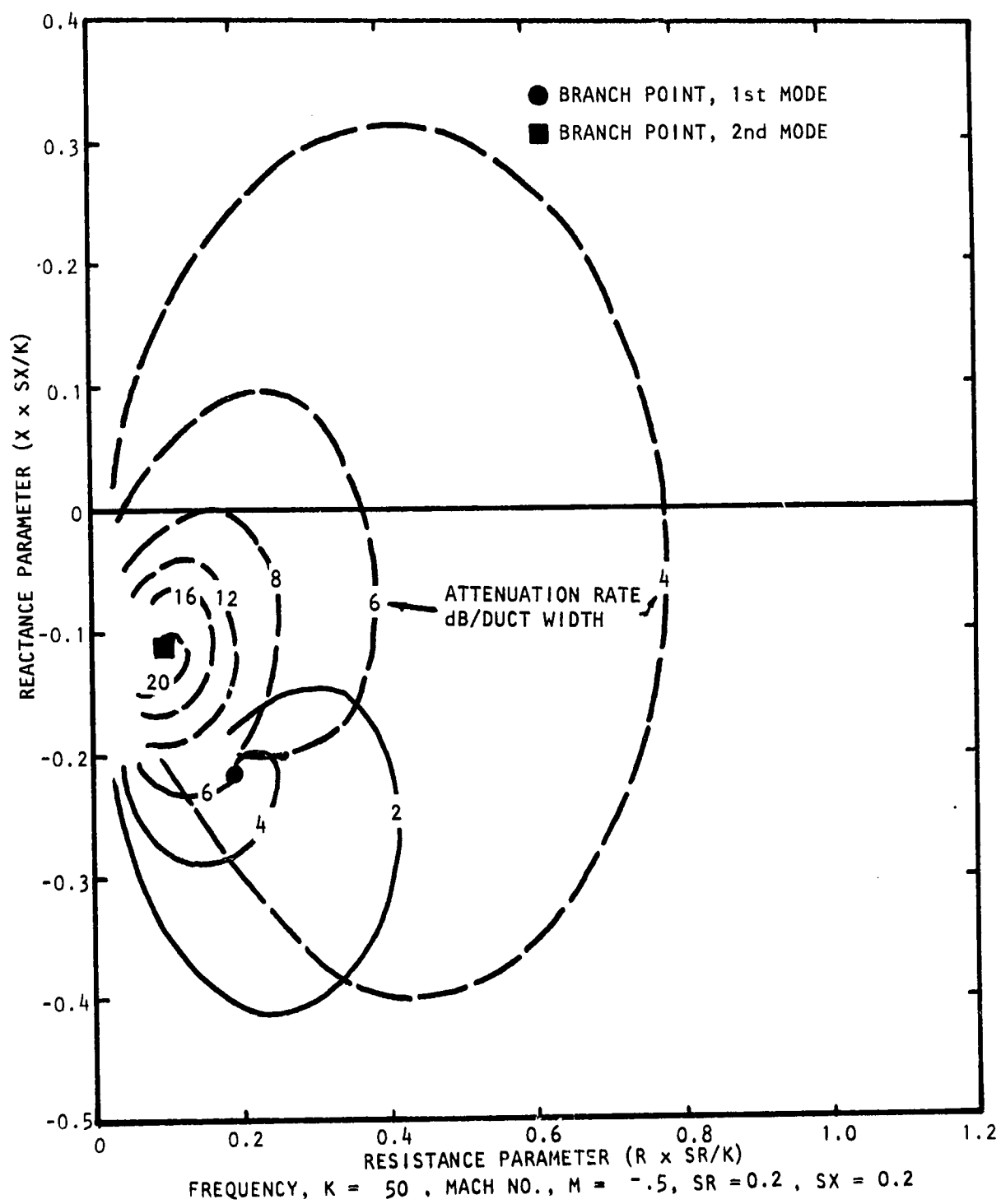


Figure A.101 Contours of Constant Attenuation for First Two Modes of Propagation (First Mode —, Second Mode ----)

APPENDIX B

MATHEMATICAL OUTLINE OF PREDICTION FORMULATIONS FOR IMPEDANCE EVALUATION IN THE PRESENCE OF BIAS OUTFLOW AND GRAZING FLOW *

**Based on work described in (1) Hersh, A. S.; and Rogers, T.: Fluid Mechanical Model for the Acoustic Impedance of Small Orifices, AIAA Paper 75-495, AIAA Second Aeroacoustics Conference, March 1975, and (2) Rogers, T.; and Hersh, A. S.: The Effect of Grazing Flow on the Steady State Resistance of Square-Edged Orifices, AIAA Paper 75-493, AIAA Second Aeroacoustics Conference, March 1975.*

FOR THE REGIME WHERE $V_0/\omega d$ IS LESS THAN 1.0

The perforate resistance is given by

$$\begin{aligned} \frac{R}{\rho c} = & \frac{1}{\sigma} \left[\frac{k(d+l)}{C_D^2 (1.0 + \frac{l}{d})} \left(\frac{0.4244 V_n}{C_D^2 (1.0 + \frac{l}{d})} \right) + \sqrt{\frac{1.0}{2Re}} \right] \\ & \times \left[\frac{0.8488 V_n}{C_D^2 (1.0 + \frac{l}{d})} - 1.0 - \sqrt{\frac{2}{Re}} \right] \\ & + \left\{ \frac{C M_i}{\sigma^2} \text{ or } \frac{M_{GF}}{0.845\sigma} \right\} \text{ -whichever is greater-} \end{aligned}$$

and the reactance by

$$\frac{X}{\rho c} = \frac{k(d+l)}{\sigma} \left[1.0 + \sqrt{\frac{1}{2Re}} \left(1.0 - \frac{0.8488 V_n}{C_D^2 (1 + \frac{l}{d})} \right) \right].$$

FOR THE REGIME WHERE $V_0/\omega d$ IS GREATER THAN 1.0

The perforate resistance is given by

$$\begin{aligned} \frac{R}{\rho c} = & k \frac{(d+l)}{\sigma C_D^2 (1.0 + \frac{l}{d})} \left[1.0 - \left(\frac{1.03 C_D (1.0 + \frac{l}{d})}{V_n} \right)^2 \right] \\ & + \left\{ \frac{C M_i}{\sigma^2} \text{ or } \frac{M_{GF}}{0.845\sigma} \right\} \text{ -whichever is greater -} \end{aligned}$$

and the reactance by

$$\begin{aligned} \frac{X}{\rho c} = & \frac{k(d+l)}{\sigma C_D} \left[1.0 + \frac{2.6 C_D (1 + \frac{l}{d})}{V_n} \right] \\ & \times \left[1.0 - \left(\frac{1.03 C_D (1 + \frac{l}{d})}{V_n} \right)^2 \right] \end{aligned}$$

where

k = free space wave number [= K /duct width, if formulation dictates use in reduced frequency (K) terms]

d, l = orifice diameter and length, respectively

σ = perforate porosity

V_o = velocity in orifice

ω = radian frequency

$V_n = M_i / \sigma k d$

M_i = incident Mach number to perforate holes

M_{GF} = grazing flow Mach number

C_D = empirical discharge coefficient defined by

$$C_D = \sqrt{0.25 - \left(\frac{V_o}{\omega d} - 0.5 \right)^2 + 0.28}$$

if $V_o / \omega d < 0.5$ or

$$C_D = 0.78 \quad \text{if} \quad \frac{V_o}{\omega d} \geq 0.5$$

Re = flow field Reynolds number [= $\omega(d+l)^2 / \nu$]

C = empirical constant (usually between 1.0 and 2.0)

c = ambient speed of sound

ρ = ambient air density

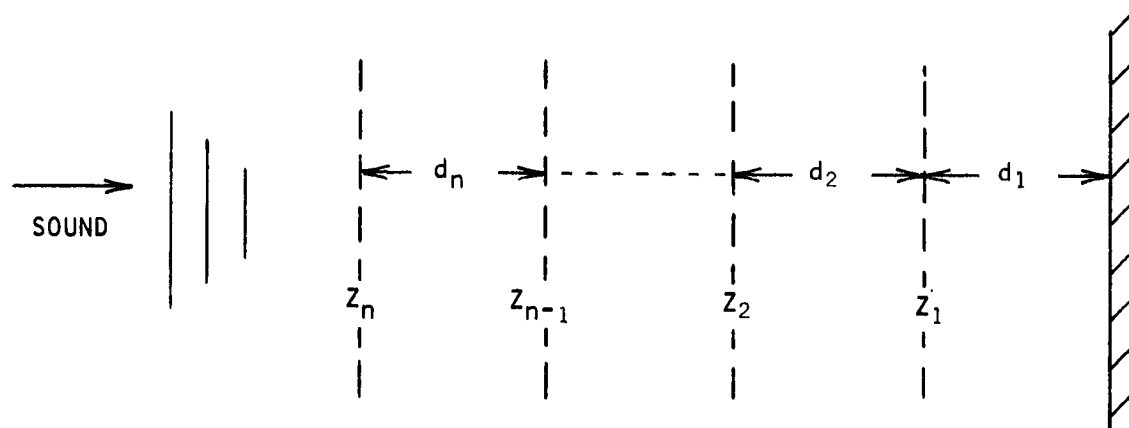
ν = kinematic viscosity

APPENDIX C

EVALUATION OF OVERALL ACOUSTIC IMPEDANCE SEEN AT SURFACE OF A MULTI-LAYER, LOCALLY REACTING, RESONANT CAVITY LINER SYSTEM*

*After Reschevkin, S. N., "A Course of Lectures on the Theory of Sound,"
Macmillan, N. Y., 1963.

Consider the multilayer liner system as shown below where Z is the impedance of the layer facing (resistance R and reactance X) normalized to ρc (the product of air density and speed of sound) and each layer is separated by distance d .



The input impedance of the first cavity and facing sheet is given by the facing sheet impedance plus the cavity impedance (considered purely reactive) i.e.

$$Z_1^{in} = R_1 + j(X_1 - \cot kd_1)$$

$$\begin{aligned} \text{where } k &= \text{free space wave number} = \frac{2\pi \text{ frequency}}{c} \\ &= Z_1 - \cot kd_1 \end{aligned}$$

Now the input impedance of the closed tube of length d terminated by a finite arbitrary impedance Z_a can be shown* to be of the form

$$Z^{in} = Z_{(\text{tube face})} + \frac{j \sin kd + Z_a \cos kd}{j Z_a \sin kd + \cos kd}$$

Thus, using this transformation extended to the second layer

$$Z_2^{in} = Z_2 + \frac{j \sin kd_2 + Z_1^{in} \cos kd_2}{j Z_1^{in} \sin kd_2 + \cos kd_2}$$

$$\begin{aligned}
&= Z_2 - j \cot kd_2 \\
&\quad + \frac{j \cot kd_2 (j Z_1^{in} \sin kd_2 + \cos kd_2) + j \sin kd_2 + Z_1^{in} \cos kd_2}{j Z_1^{in} \sin kd_2 + \cos kd_2} \\
&= Z_2 - j \cot kd_2 + \frac{j(\cot kd_2 \cos kd_2 + \sin kd_2)}{j \sin kd_2 (Z_1^{in} - j \cot kd_2)} \\
&= Z_2 - j \cot kd_2 + \frac{(\cos^2 kd_2 + \sin^2 kd_2)}{\sin^2 kd_2 (Z_1^{in} - j \cot kd_2)} \\
&= Z_2 - j \cot kd_2 + \frac{1}{\sin^2 kd_2 (Z_1^{in} - j \cot kd_2)} .
\end{aligned}$$

Now if we apply this procedure up to the nth layer the following continued fractional relationship results.

$$Z_n^{in} = Z_n^c + \frac{1}{\sin^2 kd_n \left[Z_{n-1}^c + \frac{1}{\sin^2 kd_{n-1} \left[Z_{n-2}^c \dots \right]} \right]}$$

where $Z_m^c = Z_m - j \cot kd_{m+1} - j \cot kd_m$, $m \neq n$

$$Z_n^c = Z_n - j \cot kd_n .$$

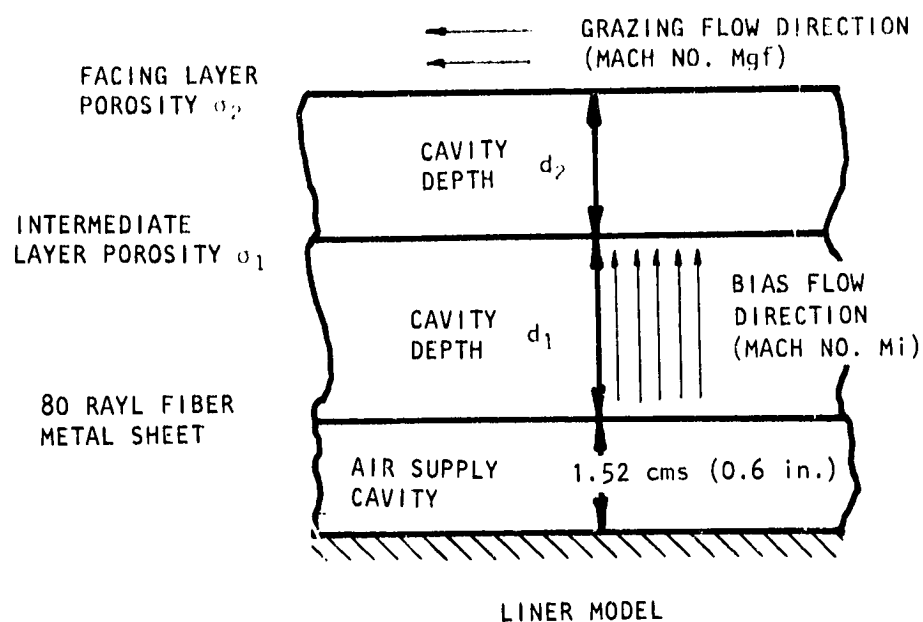
Thus, specifically for a triple layer cavity

$$\begin{aligned}
Z_3^{in} &= Z_3 - j \cot kd_3 \\
&\quad + \frac{1}{\sin^2 kd_3 \left[Z_2 - j \cot kd_3 - j \cot kd_2 + \frac{1}{\sin^2 kd_2 \left[Z_1 - j \cot kd_2 - j \cot kd_1 \right]} \right]} .
\end{aligned}$$

APPENDIX D

EFFECTS OF BIAS FLOW ON IMPEDANCE OF
MULTICAVITY LINER AT VARIOUS REDUCED FREQUENCIES.
GRAZING FLOW VELOCITIES, FACING SHEET POROSITIES,
AND CAVITY DEPTHS

The basic configuration and bias flow Mach number coding is shown in Figure D.1.



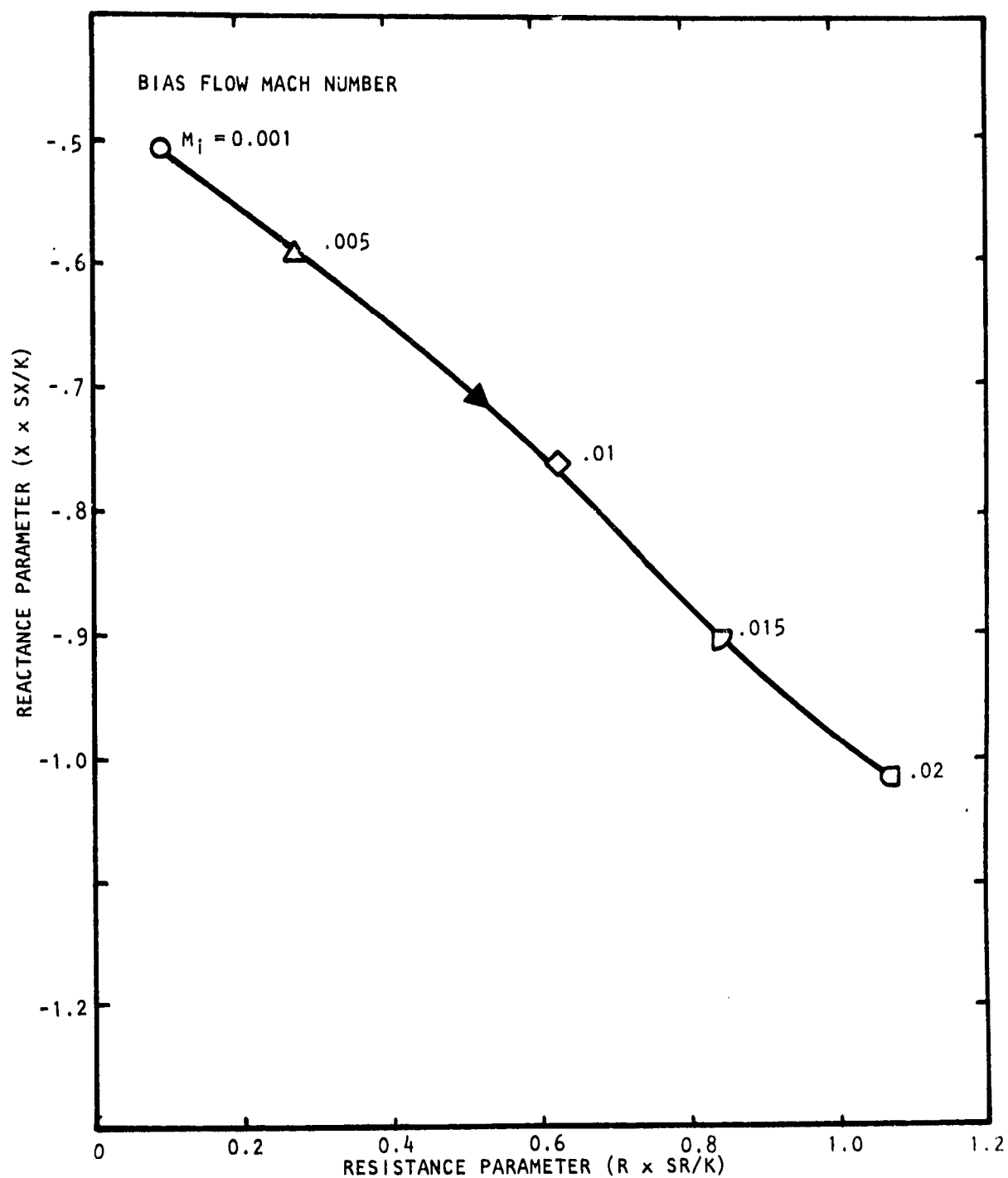
BIAS FLOW CODE

MACH NO.	SYMBOL
0.001	○
0.003	□
0.005	△
0.010	◇
0.015	◐
0.020	◑

NOTE: 1) SYMBOL ARROW (▶) DENOTES DIRECTION OF INCREASING BIAS FLOW

2) SR, SX ARE SCALE FACTORS ON RESISTANCE AND REACTANCE, RESPECTIVELY

Figure D.1 Impedance Model Layout, Parameter Nomenclature and Bias Flow Symbol Coding for Figures 105 to 147



FREQUENCY, $K = 0.5$, MACH NO., $M = 0.0$, $SR = 0.2$, $SX = 0.2$

Figure D.2 Effect of Bias Flow on Impedance of Multi-cavity Liner with Porosities $\sigma_1 = 10\%$, $\sigma_2 = 20\%$, and Cavity Depths $d_1 = 3.81$ cms. (1.5 ins.) and $d_2 = 3.81$ cms. (1.5 ins.)

REPRODUCIBILITY OF THE
ORIGINAL PAGE IS POOR

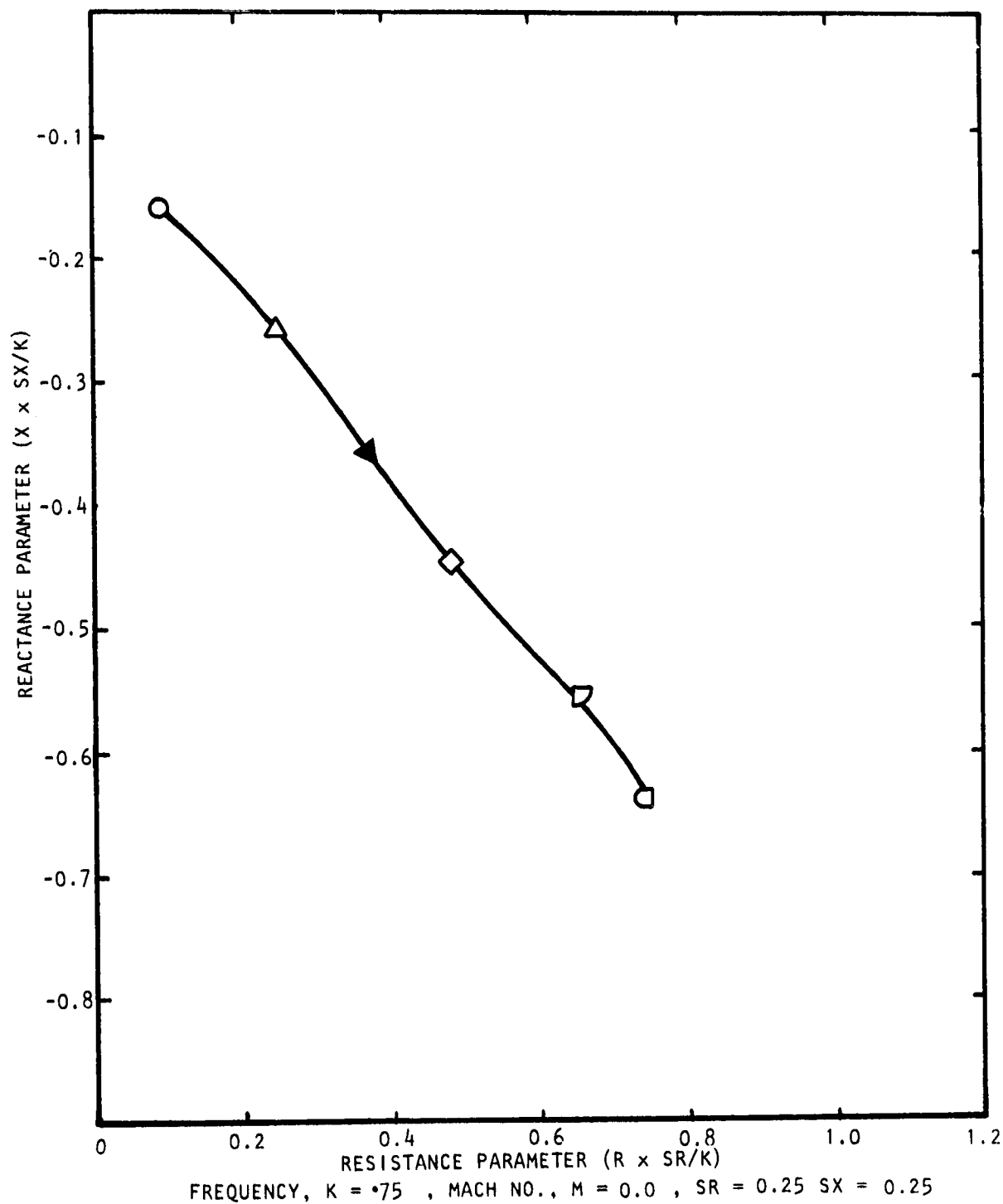


Figure D.3 Effect of Bias Flow on Impedance of Multi-Cavity Liner with Porosities $\sigma_1 = 10\%$, $\sigma_2 = 20\%$, and Cavity Depths $d_1 = 3.81$ Cms. (1.5 in.) and $d_2 = 3.81$ Cms. (1.5 in.)

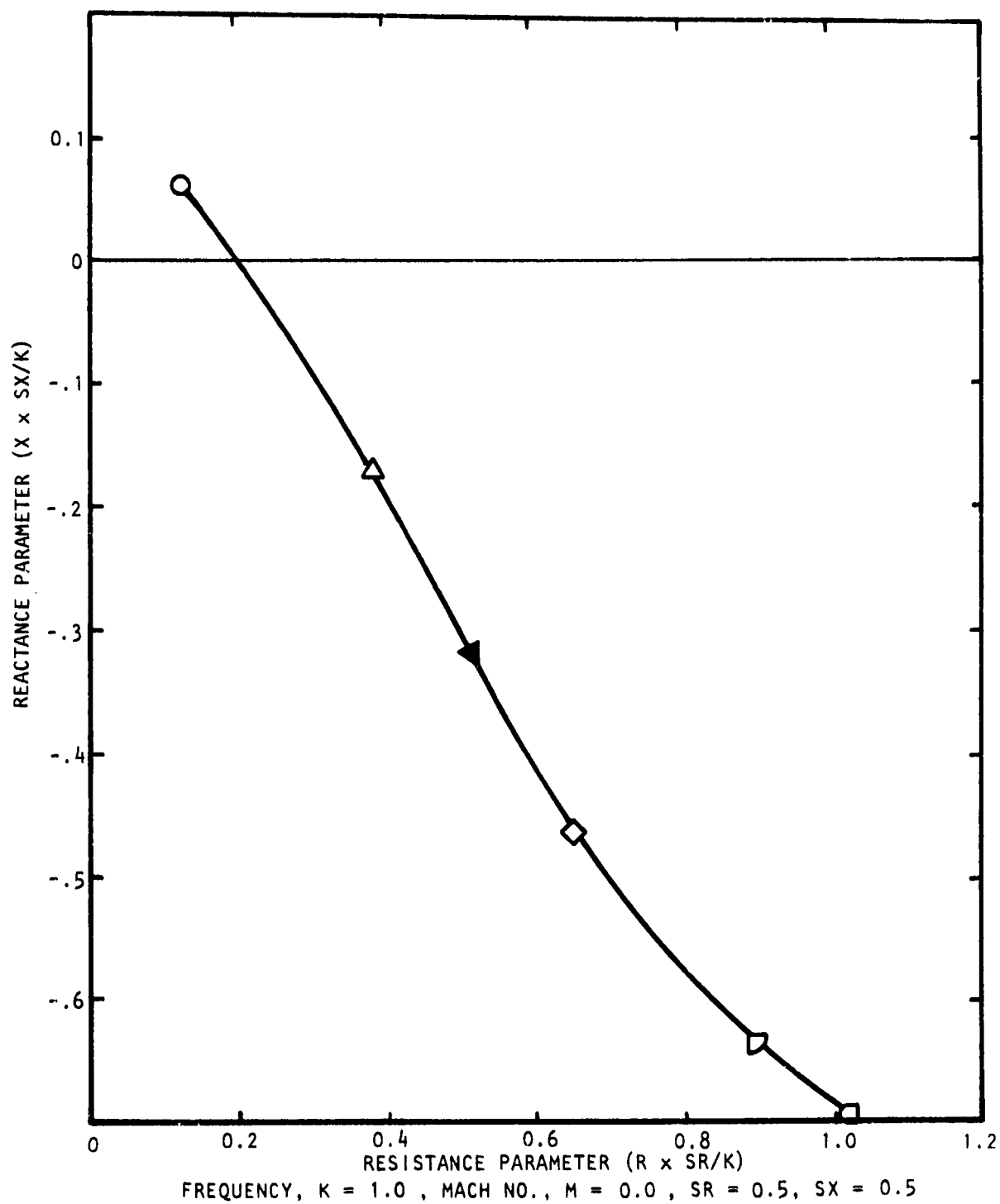


Figure D.4 Effect of Bias Flow on Impedance of Multi-Cavity Liner with Porosities $\sigma_1 = 10\%$, $\sigma_2 = 20\%$, and Cavity Depths $d_1 = 3.81$ cms. (1.5 in.) and $d_2 = 3.81$ cms. (1.5 in.)

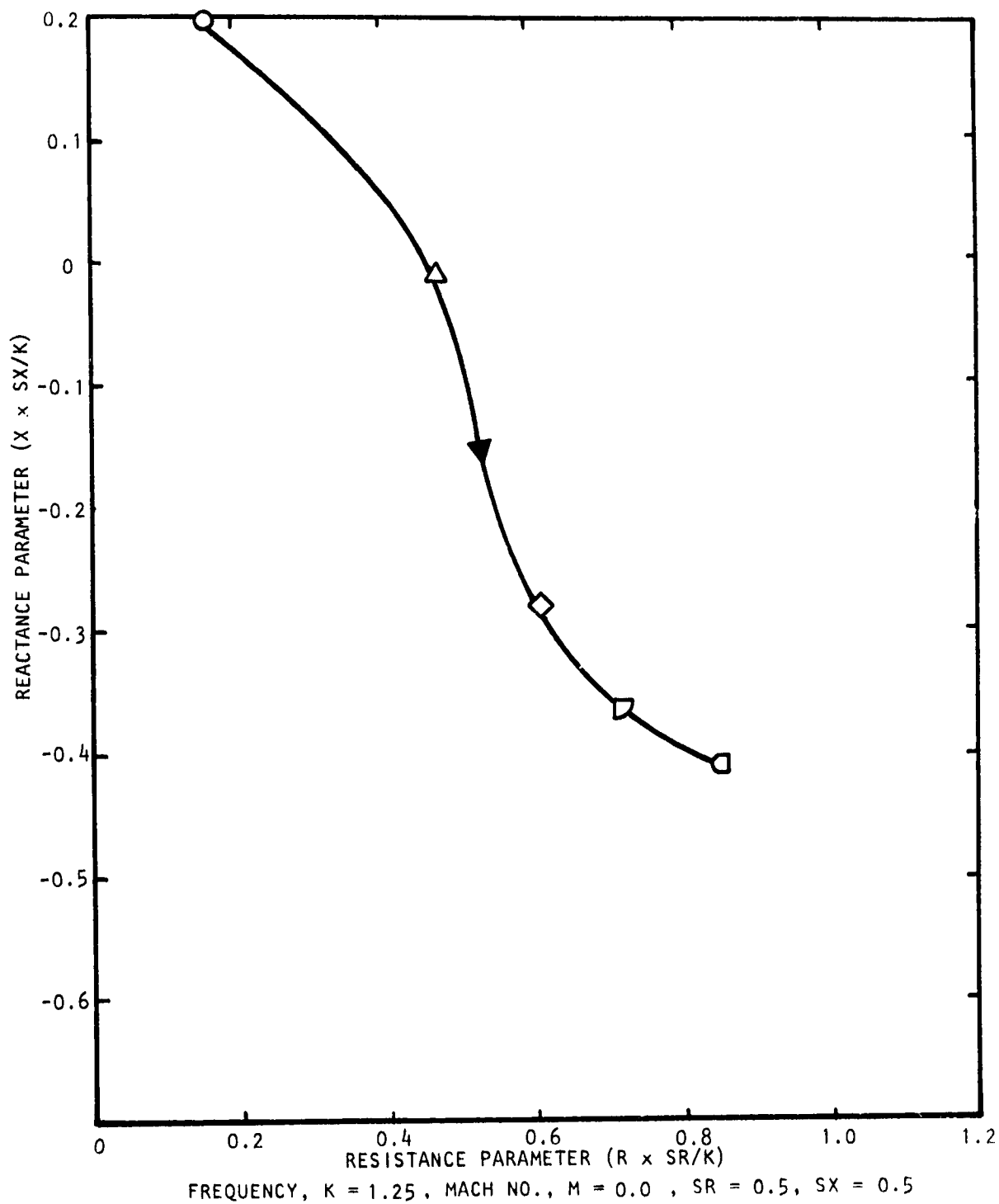


Figure D.5 Effect of Bias Flow on Impedance of Multi-Cavity Liner with Porosities $\sigma_1 = 10\%$, $\sigma_2 = 20\%$, and Cavity Depths $d_1 = 3.81$ Cms. (1.5 in.) and $d_2 = 3.81$ Cms. (1.5 in.)

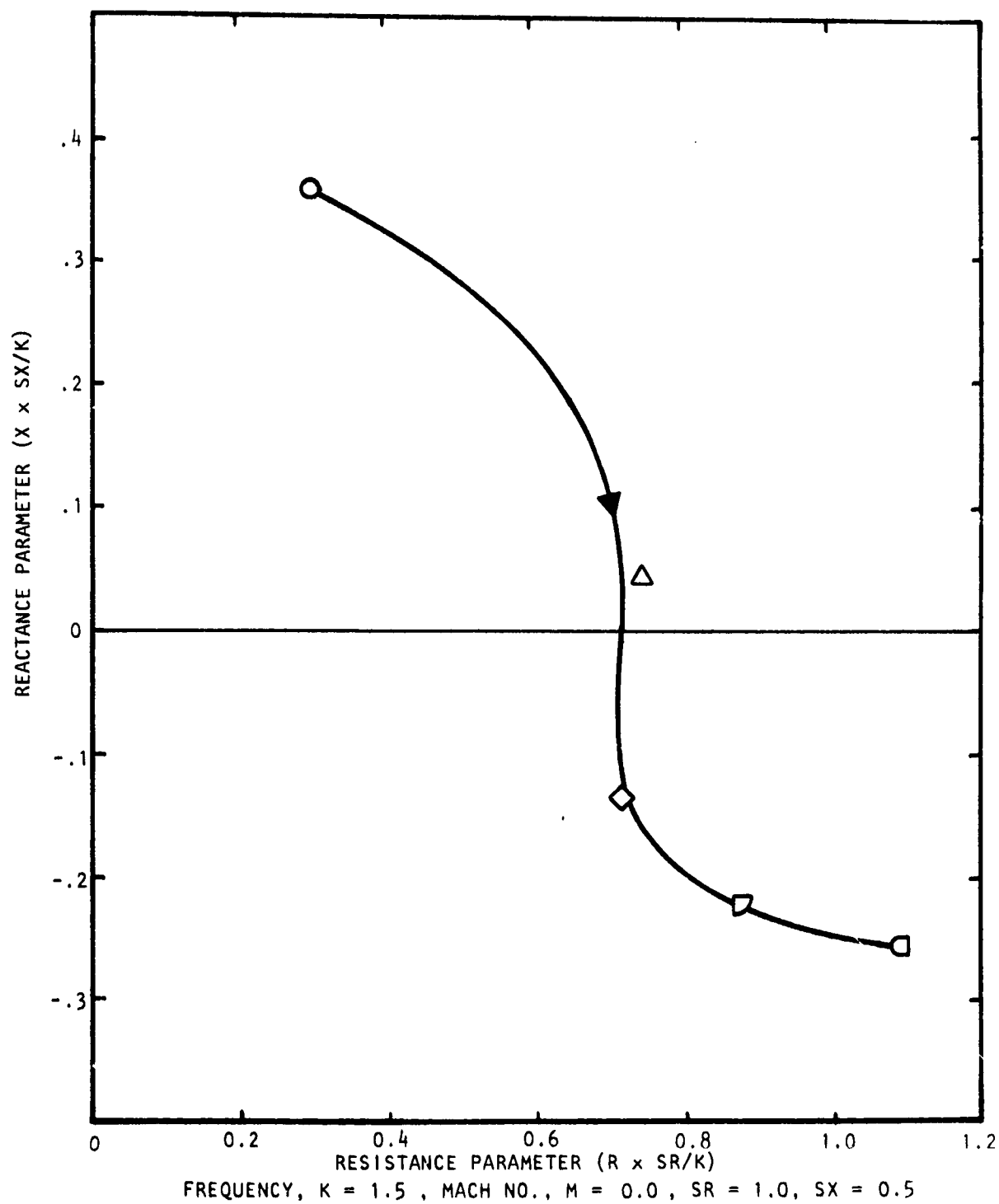


Figure D.6 Effect of Bias Flow on Impedance of Multi-Cavity Liner with Porosities $\sigma_1 = 10\%$, $\sigma_2 = 20\%$, and Cavity Depths $d_1 = 3.81$ cms. (1.5 in.) and $d_2 = 3.81$ cms. (1.5 in.)

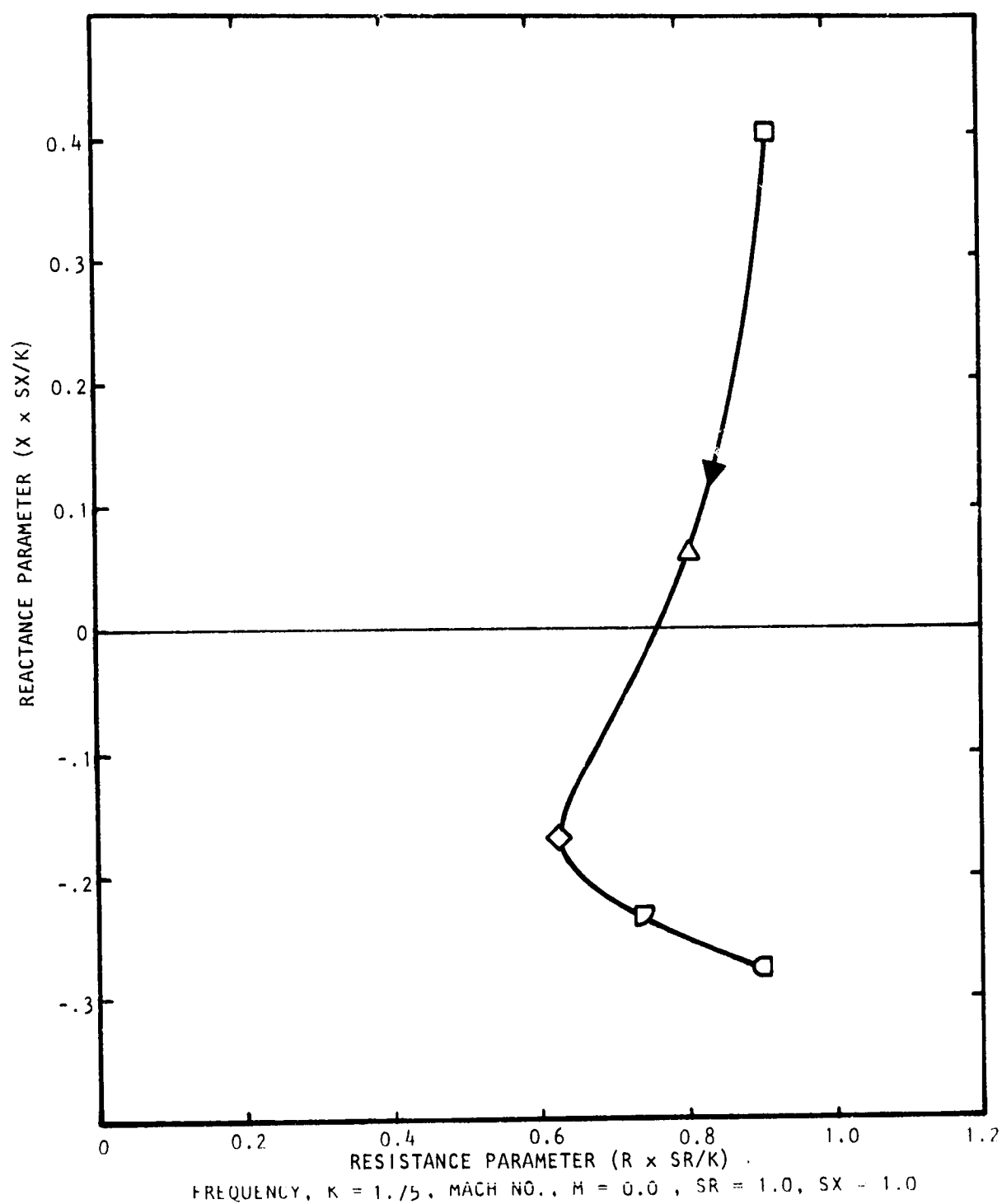


Figure D.7 Effect of Bias Blow on Impedance of Multi-Cavity Liner with Porosities $\alpha_1 = 10\%$, $\alpha_2 = 20\%$, and Cavity Depths $d_1 = 3.81$ cms. (1.5 in.) and $d_2 = 3.81$ cms. (1.5 in.)

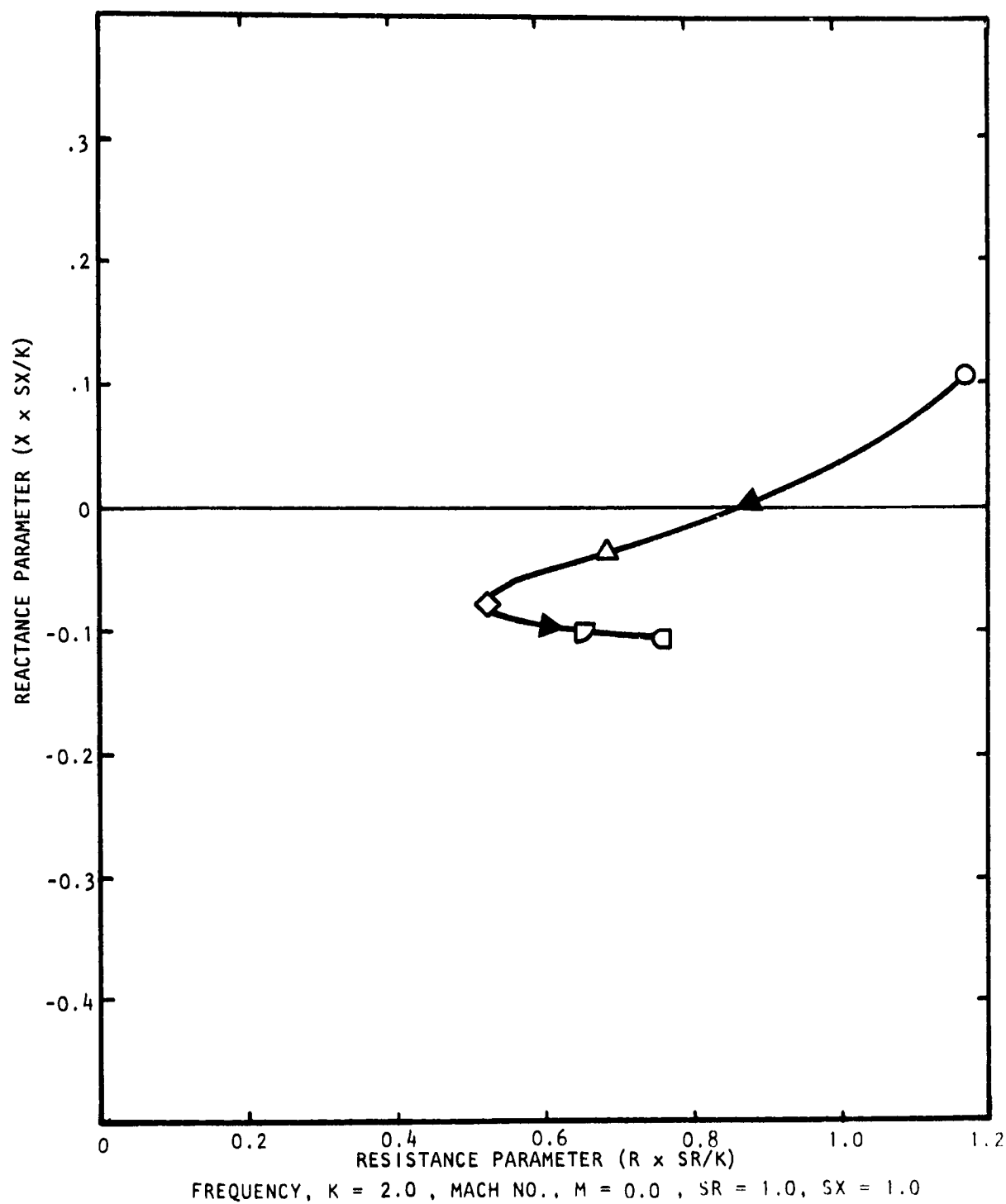


Figure D.8 Effect of Bias Flow on Impedance of Multi-Cavity Liner with Porosities $\alpha_1 = 10\%$, $\alpha_2 = 20\%$, and Cavity Depths $d_1 = 3.81$ cms. (1.5 in.) and $d_2 = 3.81$ cms. (1.5 in.)

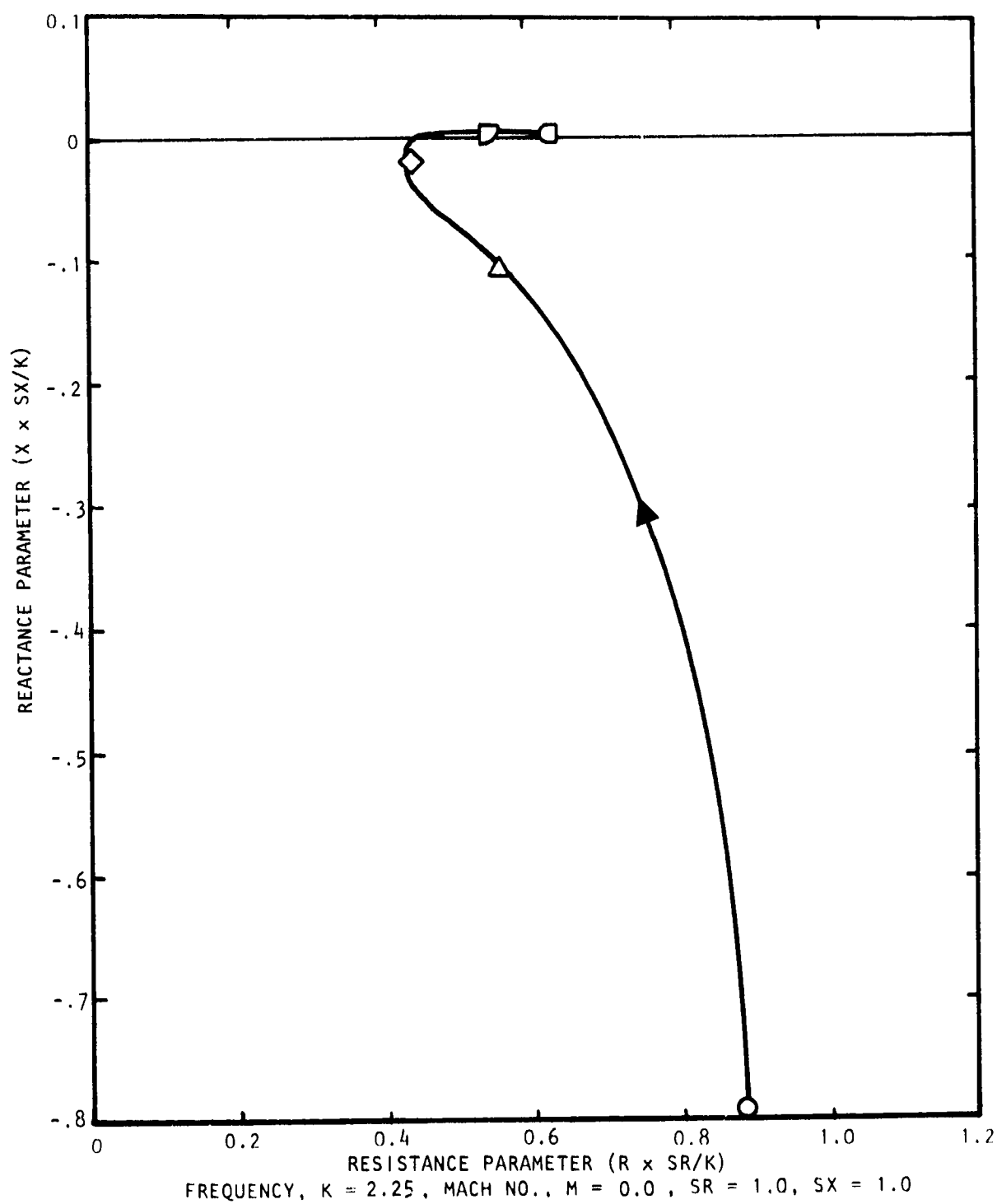


Figure D.9 Effect of Bias Flow on Impedance of Multi-Cavity Liner with Porosities $\alpha_1 = 10\%$, $\alpha_2 = 20\%$, and Cavity Depths $d_1 = 3.81$ cms. (1.5 in.) and $d_2 = 3.81$ cms. (1.5 in.)

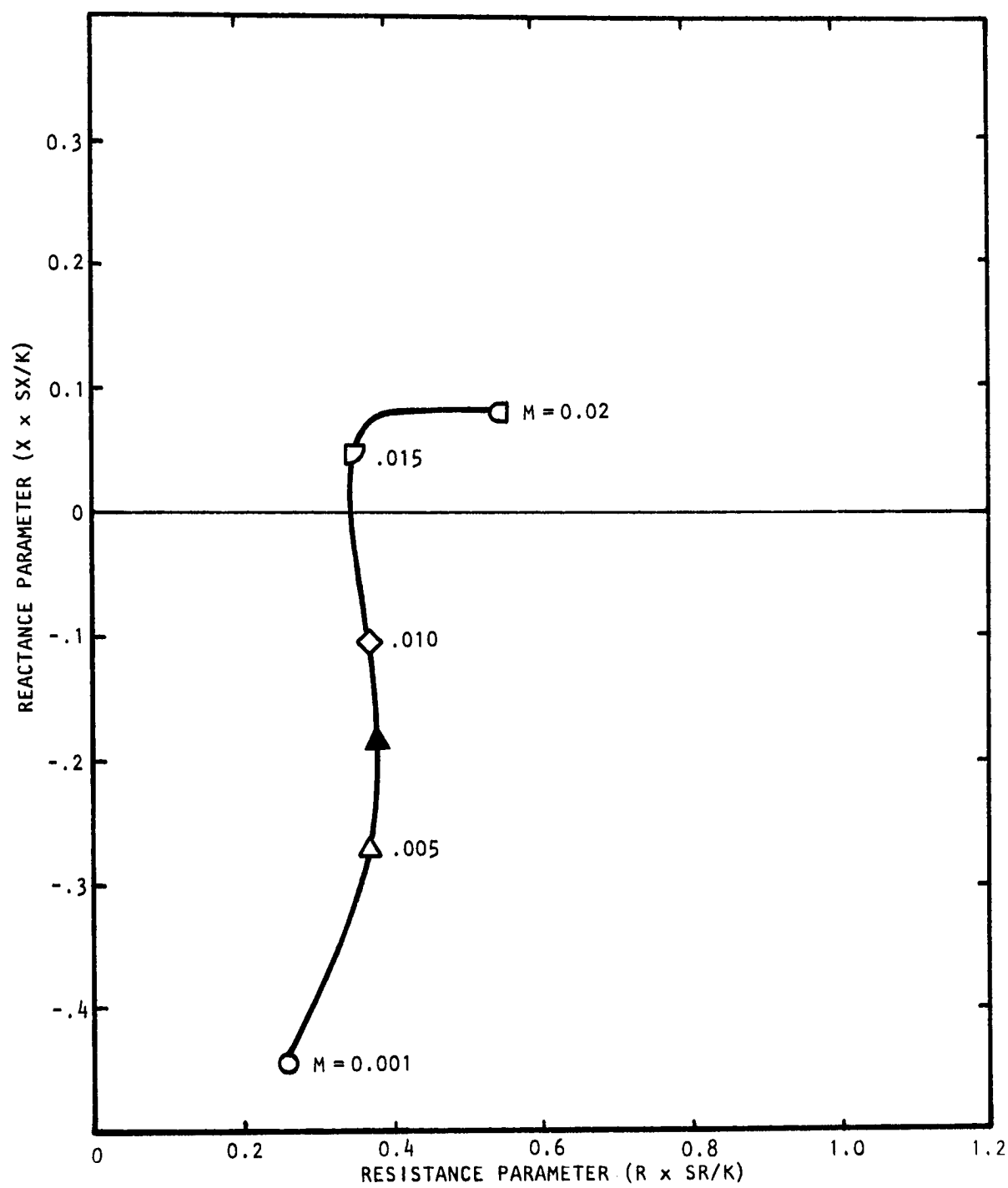


Figure D.10 Effect of Bias Flow on Impedance of Multi-Cavity Liner with Porosities $\sigma_1 = 10\%$, $\sigma_2 = 20\%$, and Cavity Depths $d_1 = 3.81$ cms. (1.5 in.) and $d_2 = 3.81$ cms. (1.5 in.)

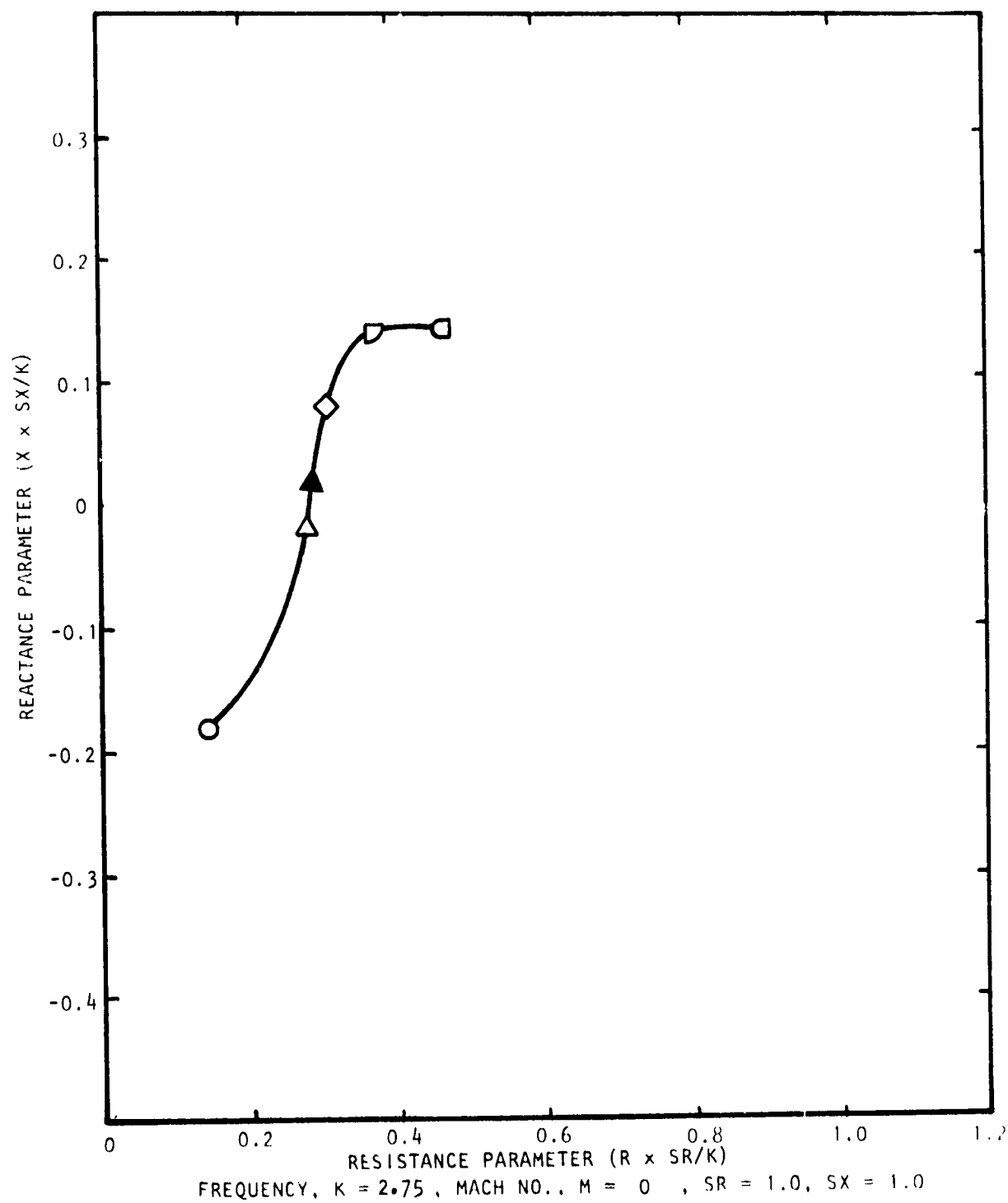
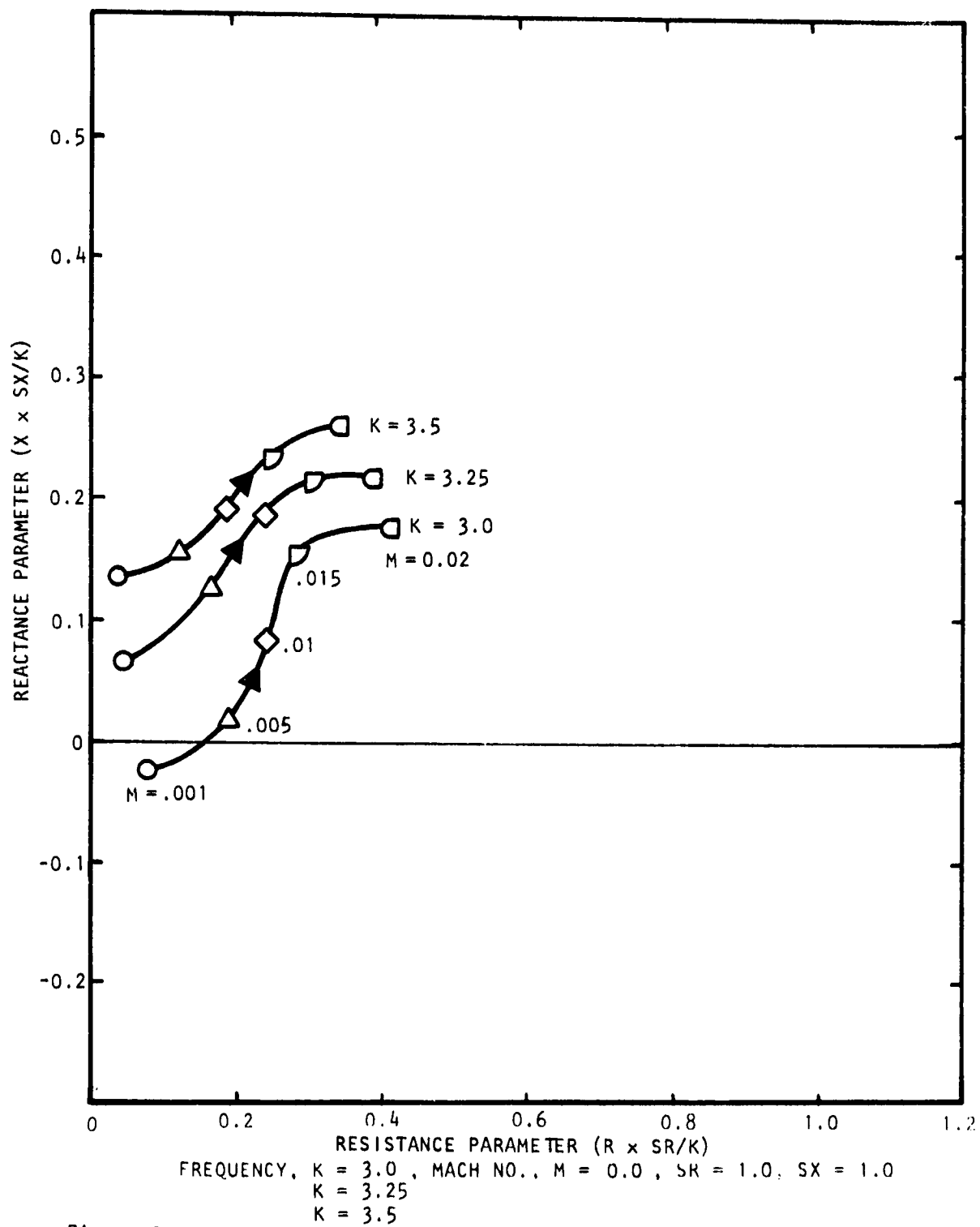


Figure D.11 Effect of Bias Flow on Impedance of Multi-Cavity Liner with Porosities $\sigma_1 = 10\%$, $\sigma_2 = 20\%$, and Cavity Depths $d_1 = 3.81$ Cms. (1.5 in.) and $d_2 = 3.81$ Cms. (1.5 in.)



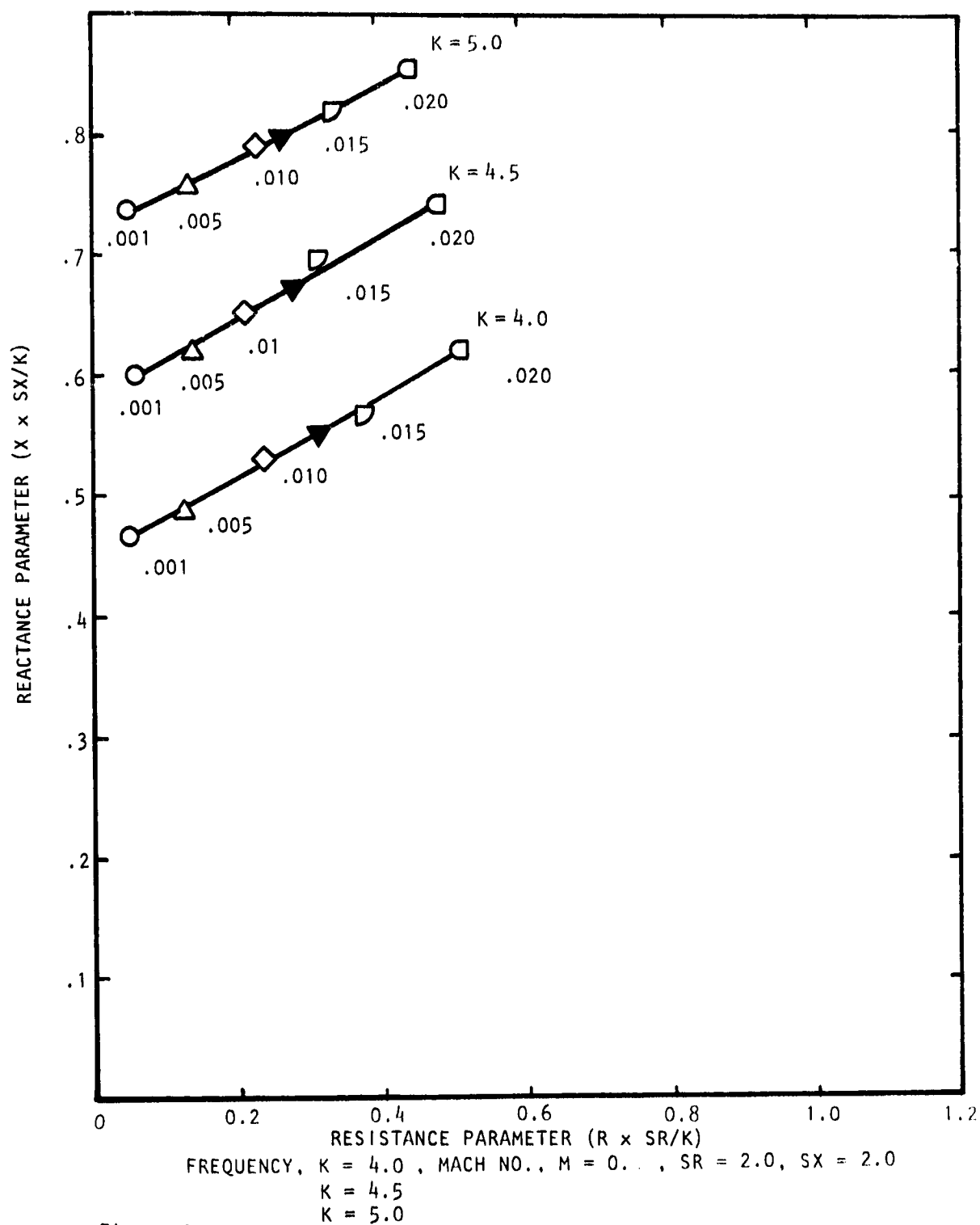
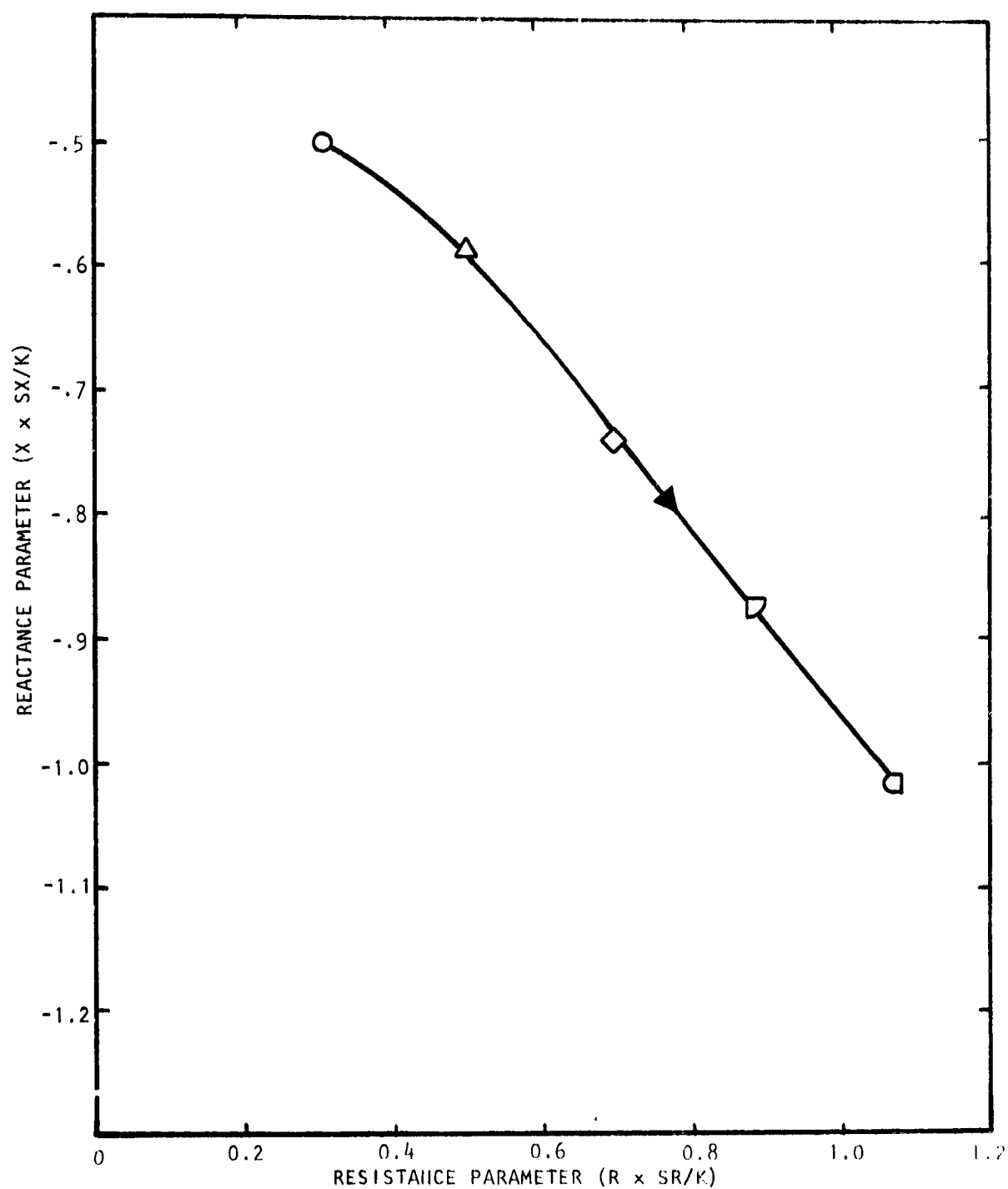
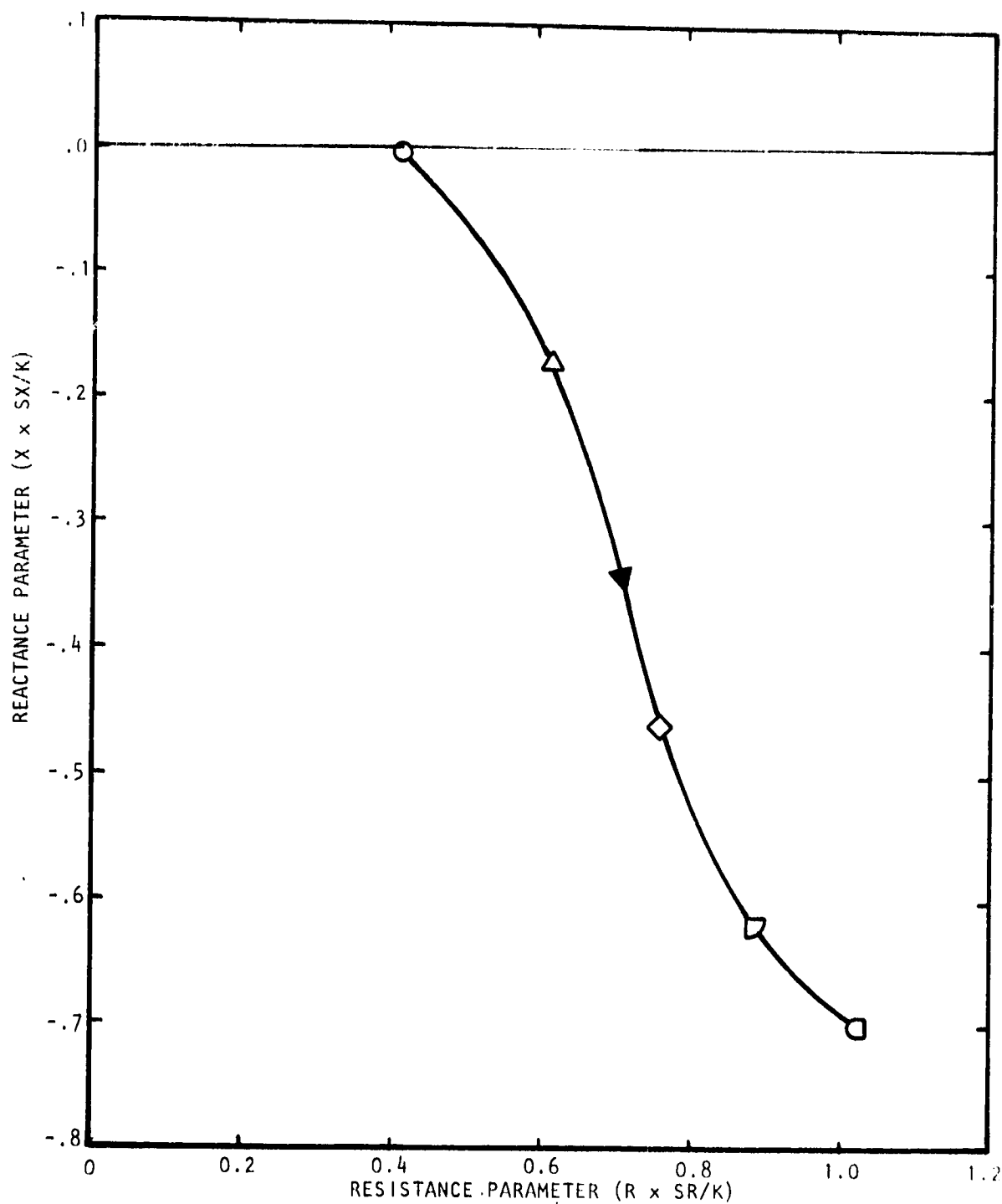


Figure D.13 Effect of Bias Flow on Impedance of Multi-Cavity Liner with Porosities $\sigma_1 = 10\%$, $\sigma_2 = 20\%$, and Cavity Depths $d_1 = 3.81$ cms. (1.5 in.) and $d_2 = 3.81$ cms. (1.5 in.)



FREQUENCY, $K = 0.5$, MACH NO., $M = .25$, $SR = 0.2$, $SX = 0.2$

Figure D.14 Effect of Bias Flow on Impedance of Multi-Cavity Liner with Porosities $\phi_1 = 10\%$, $\phi_2 = 20\%$, and Cavity Depths $d_1 = 3.81$ cms. (1.5 in.) and $d_2 = 3.81$ cms. (1.5 in.)



FREQUENCY, $K = 1.0$, MACH NO., $M = .25$, $SR = 0.5$, $SX = 0.5$
 Figure D.15 Effect of Bias Flow on Impedance of Multi-Cavity Liner with
 Porosities $\sigma_1 = 10\%$, $\sigma_2 = 20\%$, and Cavity Depths $d_1 = 3.81$ cms.
 (1.5 in.) and $d_2 = 3.81$ cms. (1.5 in.)

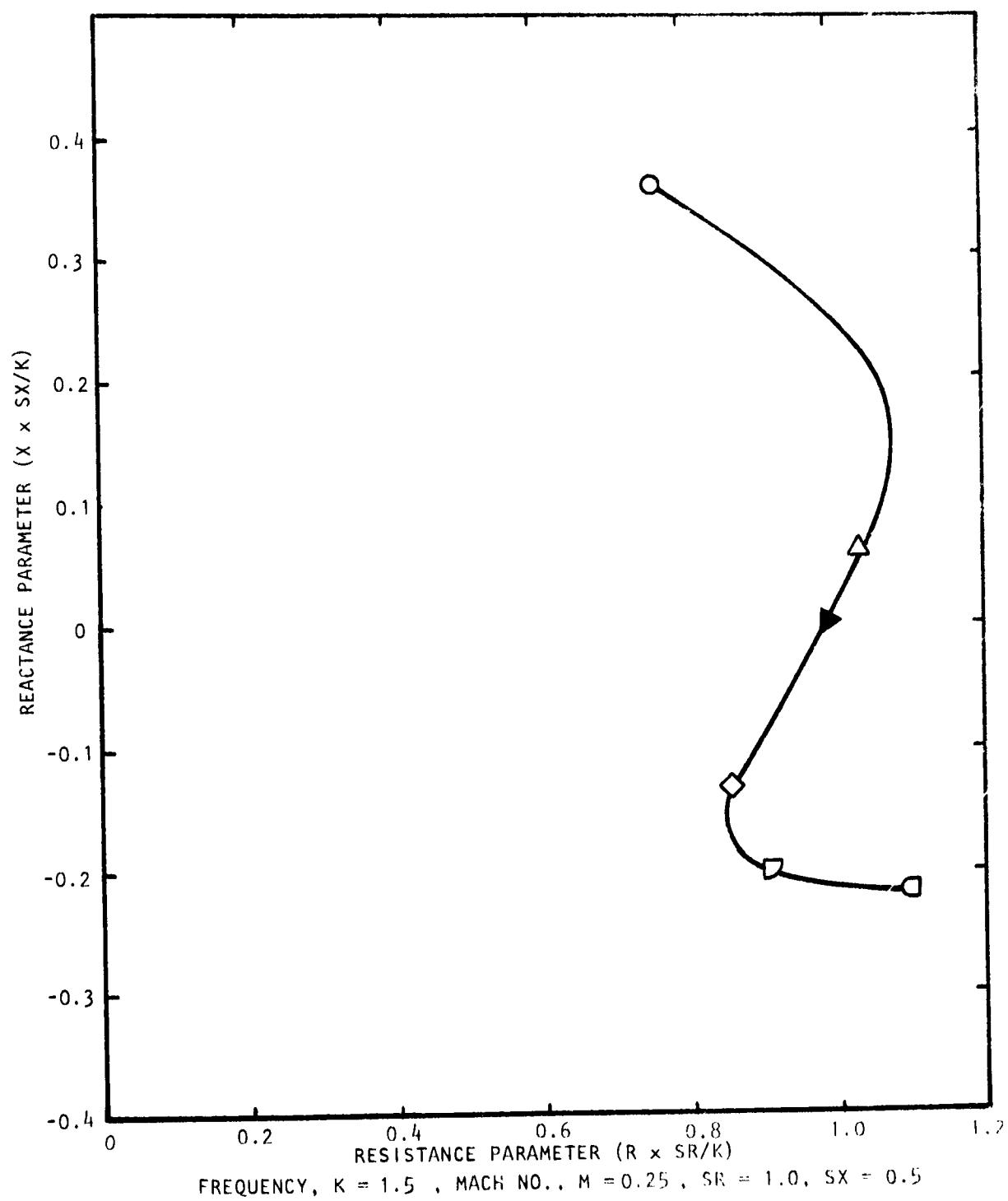


Figure D.16 Effect of Bias Flow on Impedance of Multi-Cavity Liner with Porosities $\sigma_1 = 10\%$, $\sigma_2 = 20\%$, and Cavity Depths $d_1 = 3.81$ Cms. (1.5 in.) and $d_2 = 3.81$ Cms. (1.5 in.)

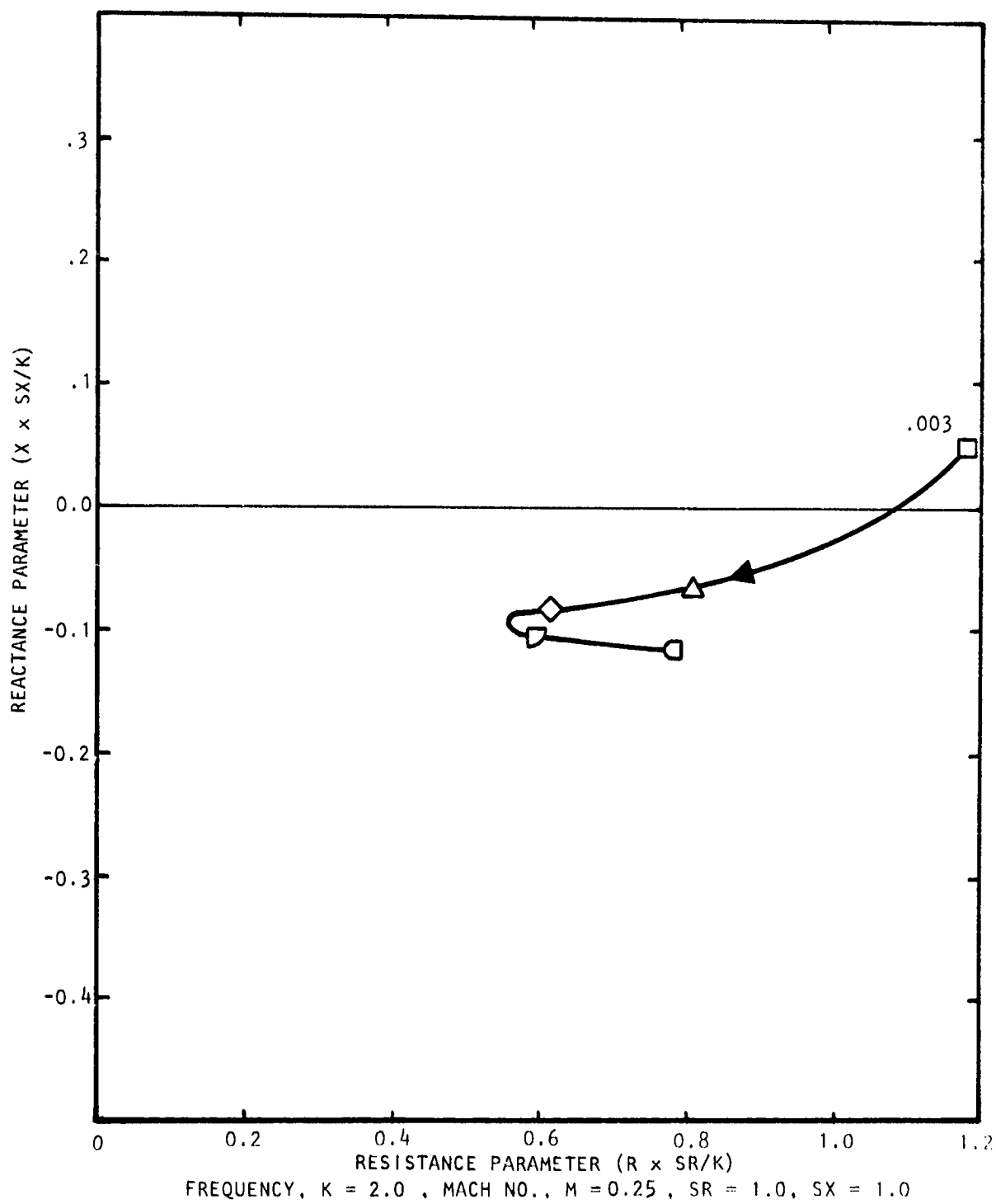
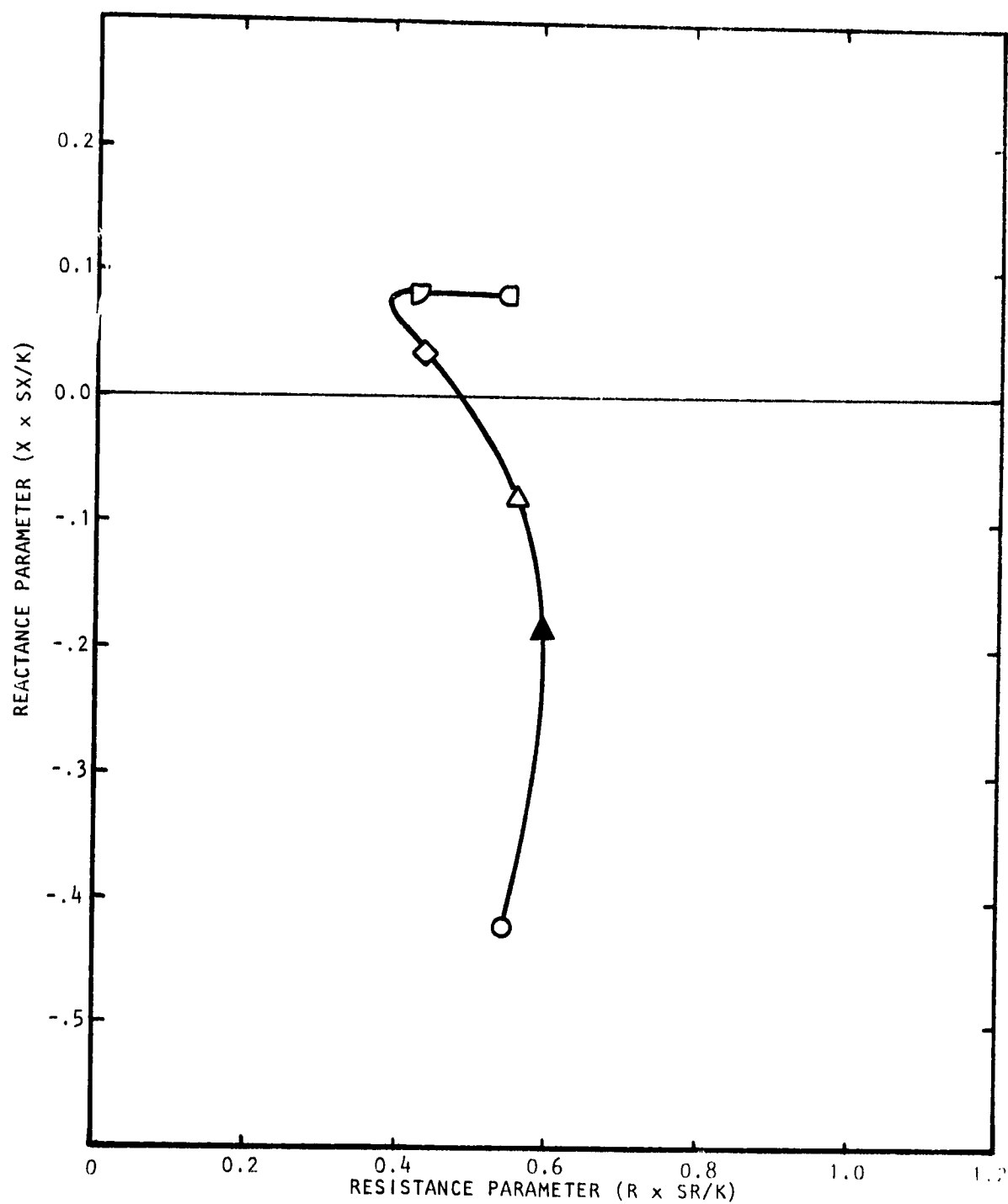


Figure D.17 Effect of Bias Flow on Impedance of Multi-Cavity Liner with Porosities $\alpha_1 = 10\%$, $\alpha_2 = 20\%$, and Cavity Depths $d_1 = 3.81$ cms. (1.5 in.) and $d_2 = 3.81$ cms. (1.5 in.)



FREQUENCY, $K = 2.5$, MACH NO., $M = 0.25$, $SR = 1.0$, $SX = 1.0$

Figure D.18 Effect of Bias Flow on Impedance of Multi-Cavity Liner with Porosities $\phi_1 = 10\%$, $\phi_2 = 20\%$, and Cavity Depths $d_1 = 3.81$ cms. (1.5 in.) and $d_2 = 3.81$ cms. (1.5 in.)

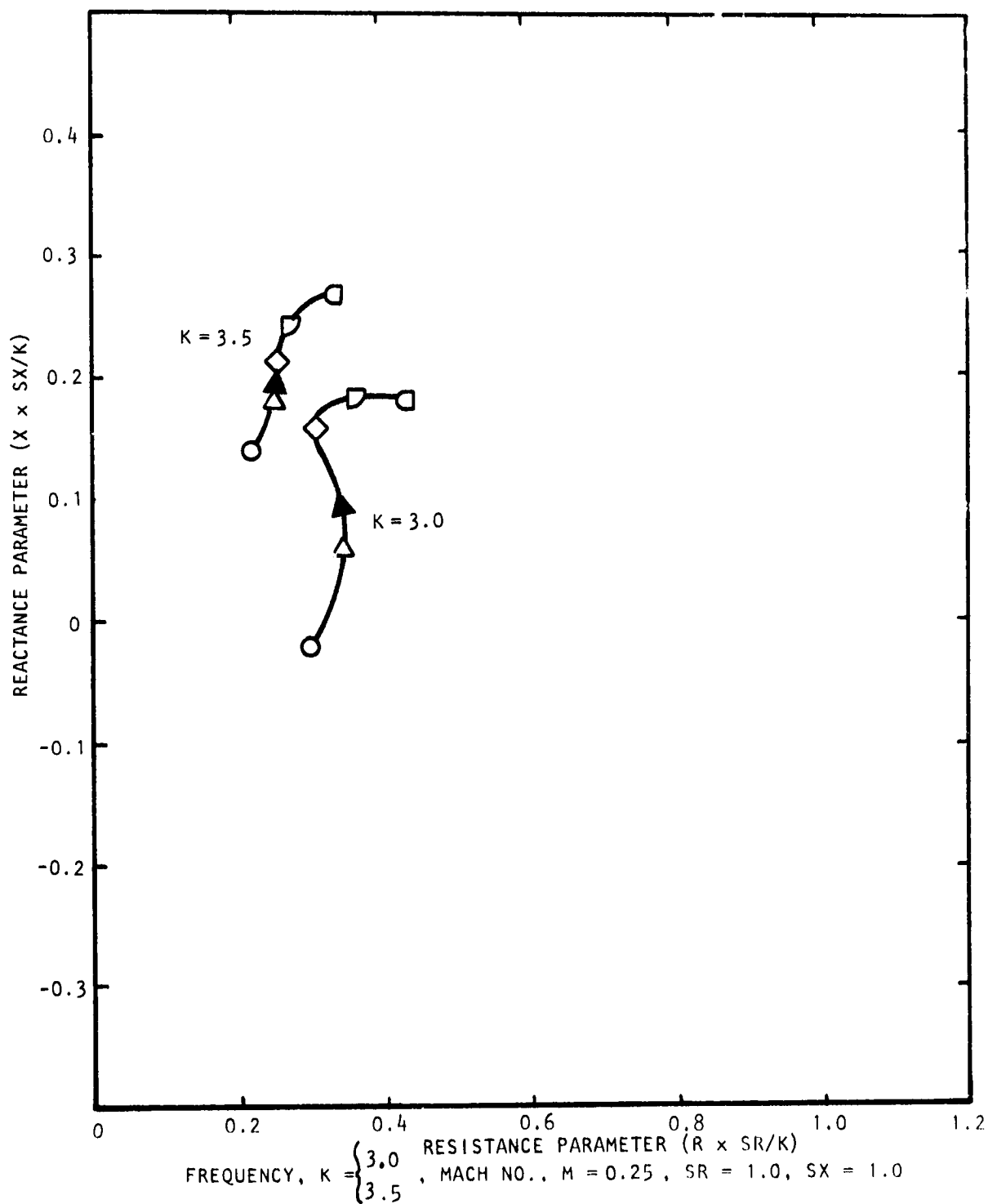


Figure D.19 Effect of Bias Flow on Impedance of Multi-Cavity Liner with Porosities $\sigma_1 = 10\%$, $\sigma_2 = 20\%$, and Cavity Depths $d_1 = 3.81$ Cms. (1.5 in.) and $d_2 = 3.81$ Cms. (1.5 in.)

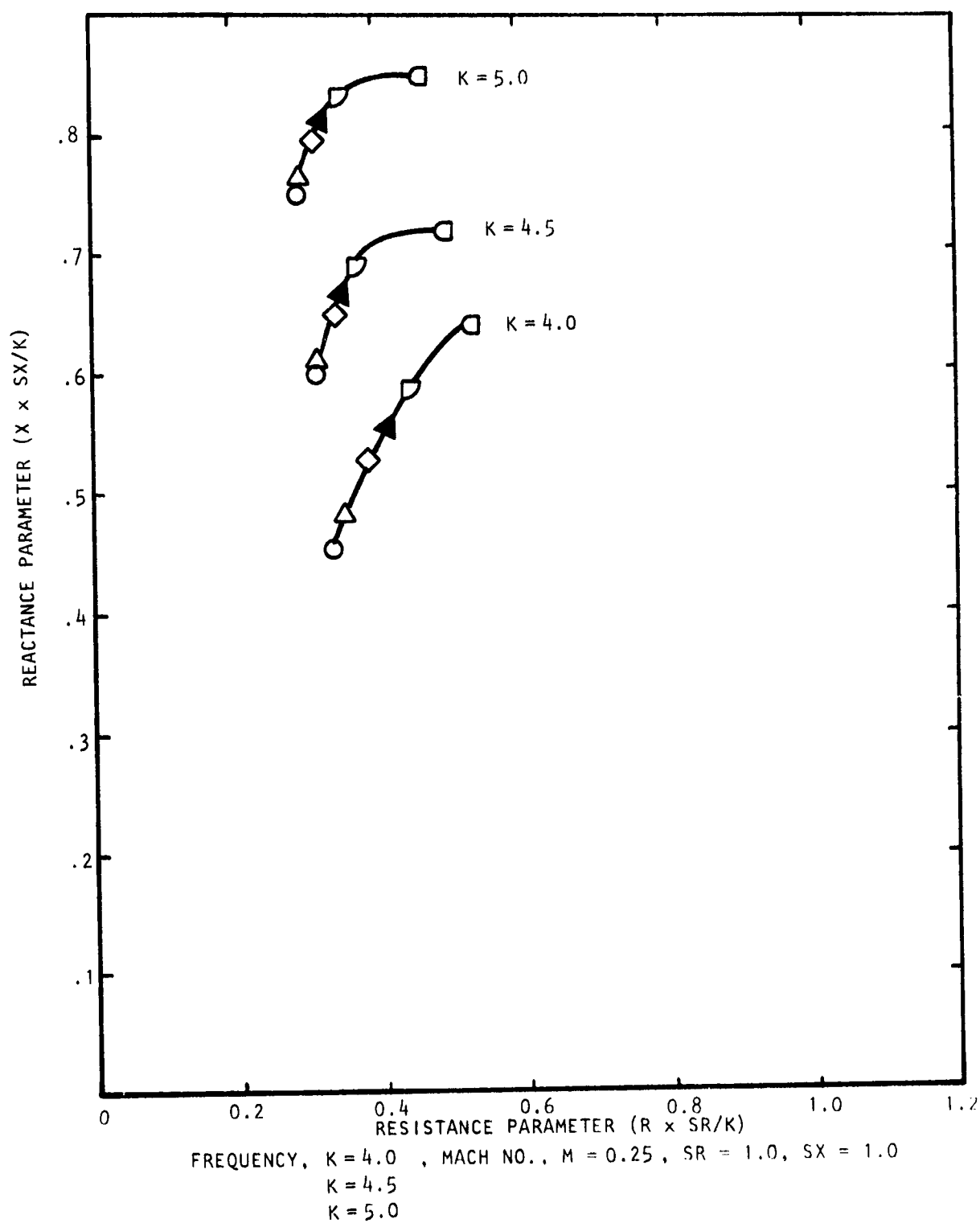


Figure D.20 Effect of Bias Flow on Impedance of Multi-Cavity Liner with Porosities $\sigma_1 = 10\%$, $\sigma_2 = 20\%$, and Cavity Depths $d_1 = 3.81$ cms. (1.5 in.) and $d_2 = 3.81$ cms. (1.5 in.)

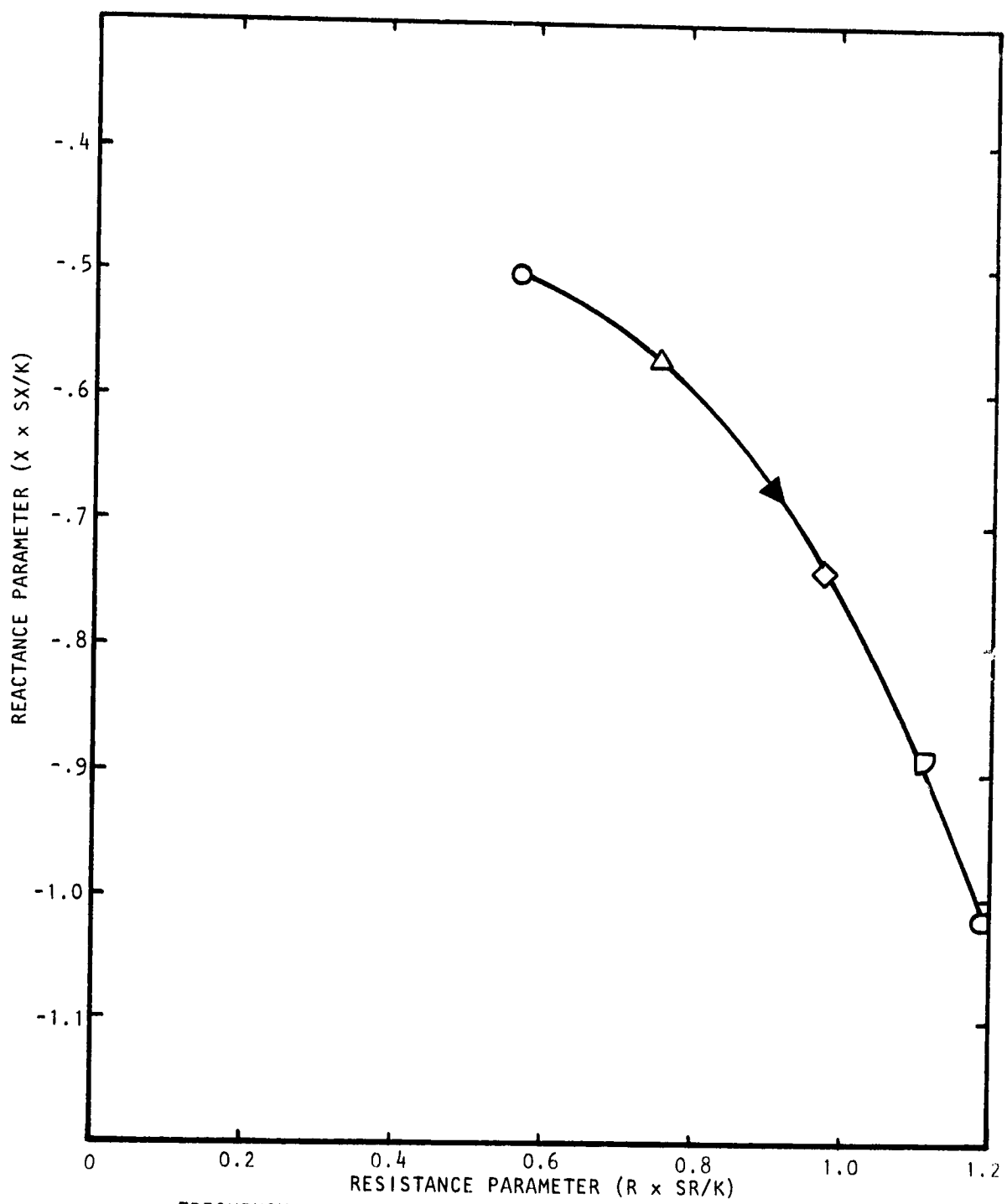


Figure D.21 Effect of Bias Flow on Impedance of Multi-Cavity Liner with Porosities $\alpha_1 = 10\%$, $\alpha_2 = 20\%$, and Cavity Depths $d_1 = 3.81$ cms. (1.5 in.) and $d_2 = 3.81$ cms. (1.5 in.)

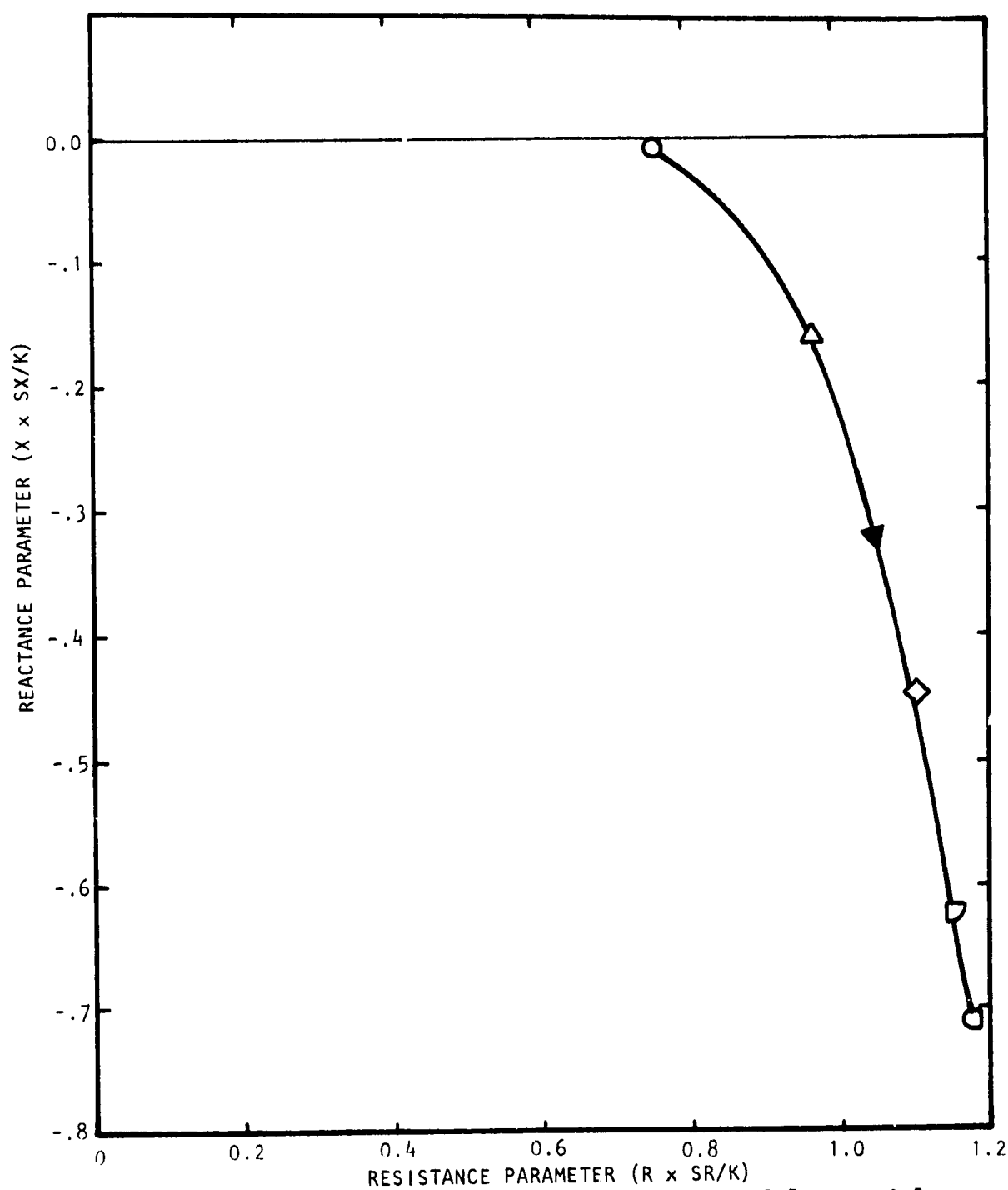
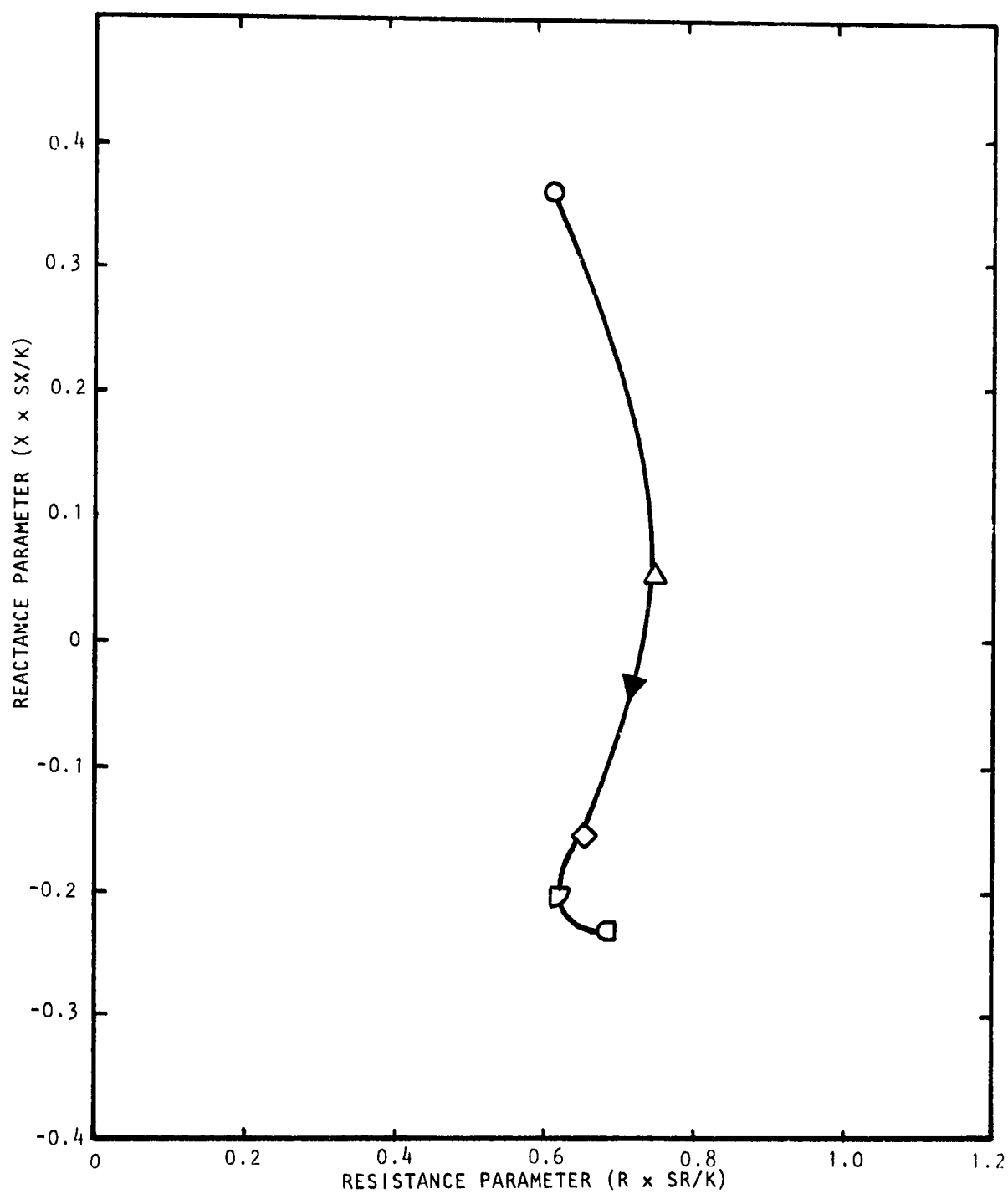
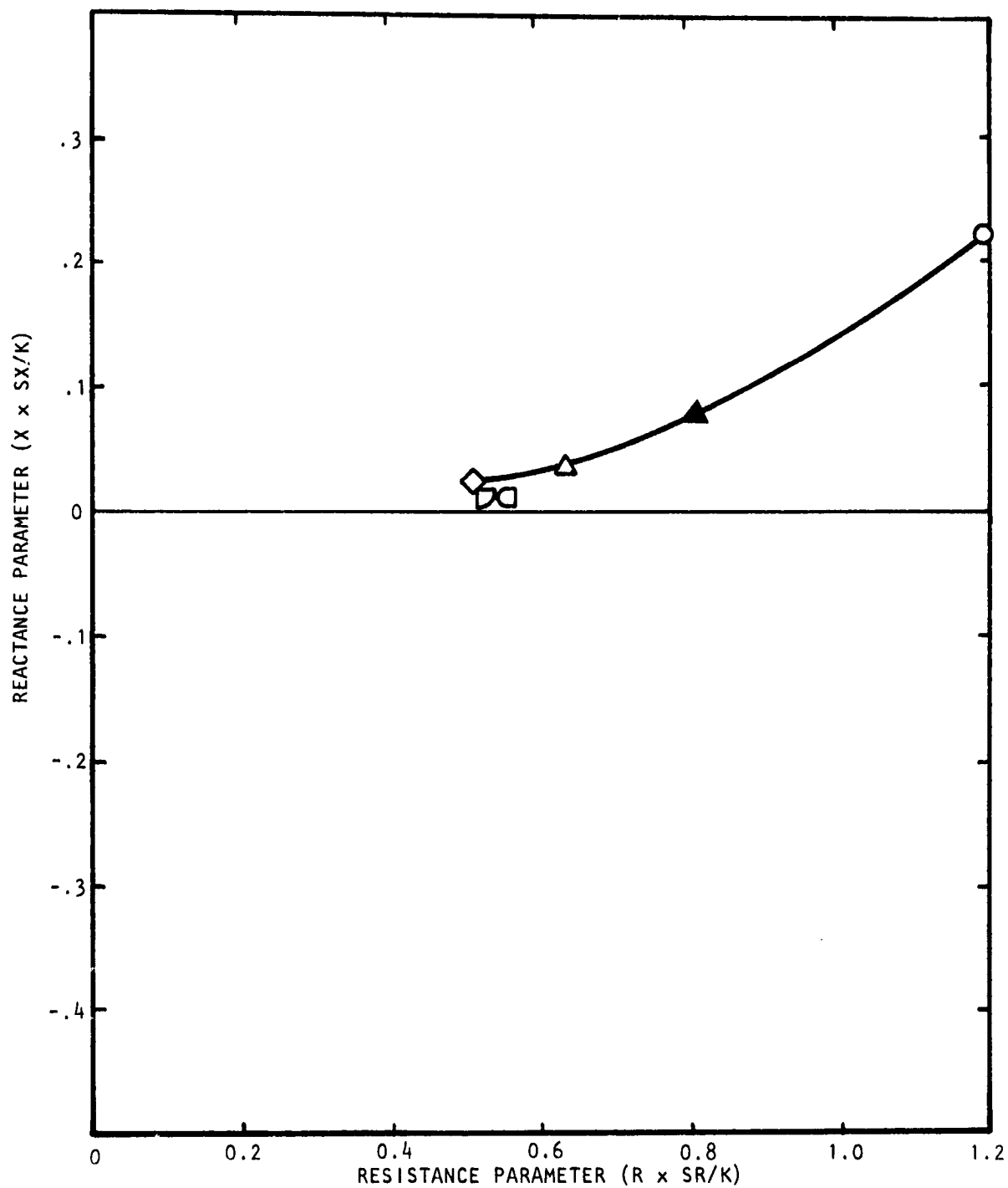


Figure D.22 Effect of Bias Flow on Impedance of Multi-Cavity Liner with Porosities $\alpha_1 = 10\%$, $\alpha_2 = 20\%$, and Cavity Depths $d_1 = 3.81$ cms. (1.5 in.) and $d_2 = 3.81$ cms. (1.5 in.)



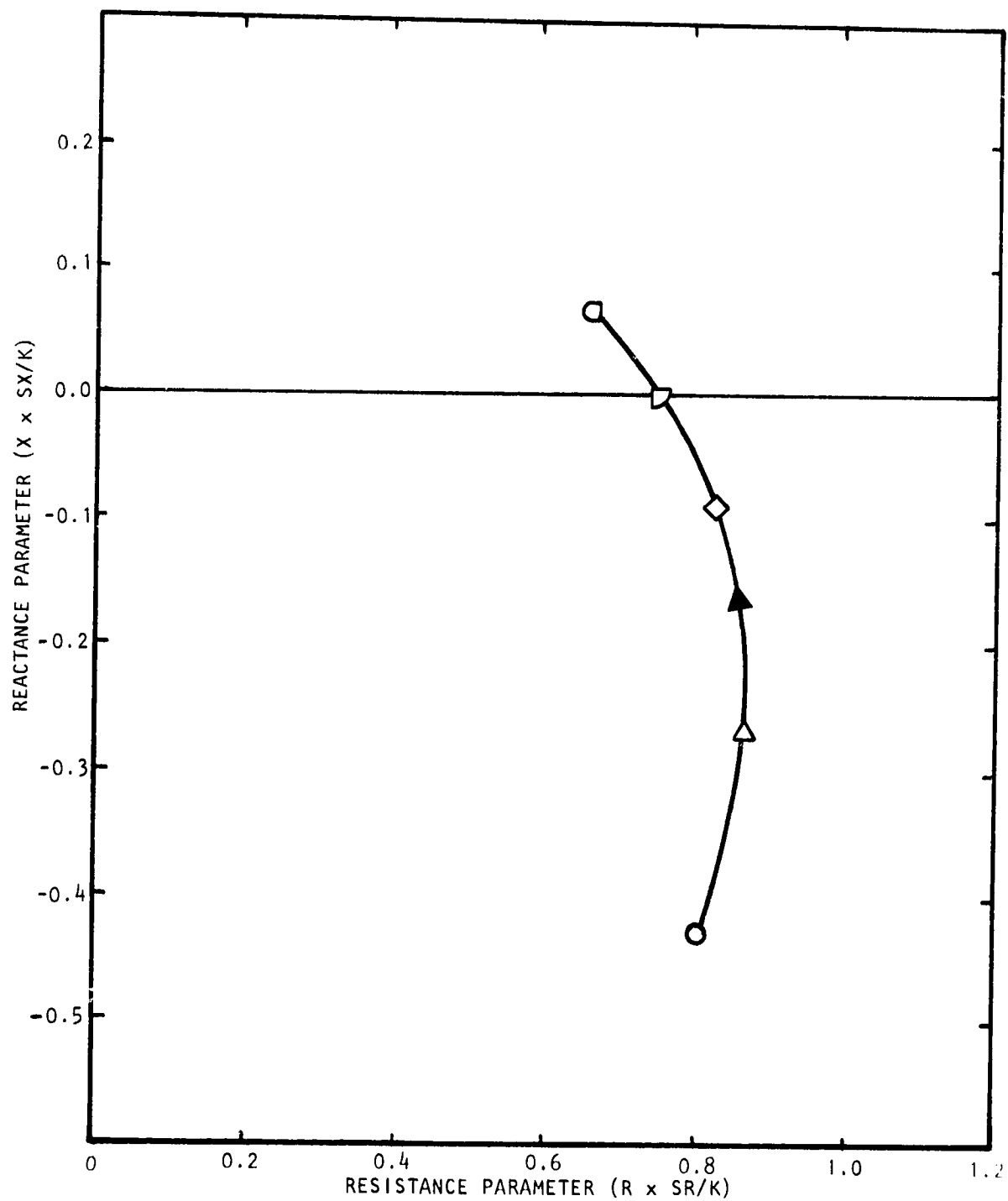
FREQUENCY, $K = 1.5$, MACH NO., $M = 0.5$, $SR = 0.5$, $SX = 0.5$

Figure D.23 Effect of Bias Flow on Impedance of Multi-Cavity Liner with Porosities $\sigma_1 = 10\%$, $\sigma_2 = 20\%$, and Cavity Depths $d_1 = 3.81$ Cms. (1.5 in.) and $d_2 = 3.81$ Cms. (1.5 in.)



FREQUENCY, $K = 2.0$, MACH NO., $M = 0.5$, $SR = 0.5$, $SX = 1.0$

Figure D.24 Effect of Bias Flow on Impedance of Multi-Cavity Liner with Porosities $\sigma_1 = 10\%$, $\sigma_2 = 20\%$, and Cavity Depths $d_1 = 3.81$ cms. (1.5 in.) and $d_2 = 3.81$ cms. (1.5 in.)



FREQUENCY, $K = 2.5$, MACH NO., $M = 0.5$, $SR = 1.0$, $SX = 1.0$

Figure D.25 Effect of Bias Flow on Impedance of Multi-Cavity Liner with Porosities $\sigma_1 = 10\%$, $\sigma_2 = 20\%$, and Cavity Depths $d_1 = 3.81$ cms. (1.5 in.) and $d_2 = 3.81$ cms. (1.5 in.)

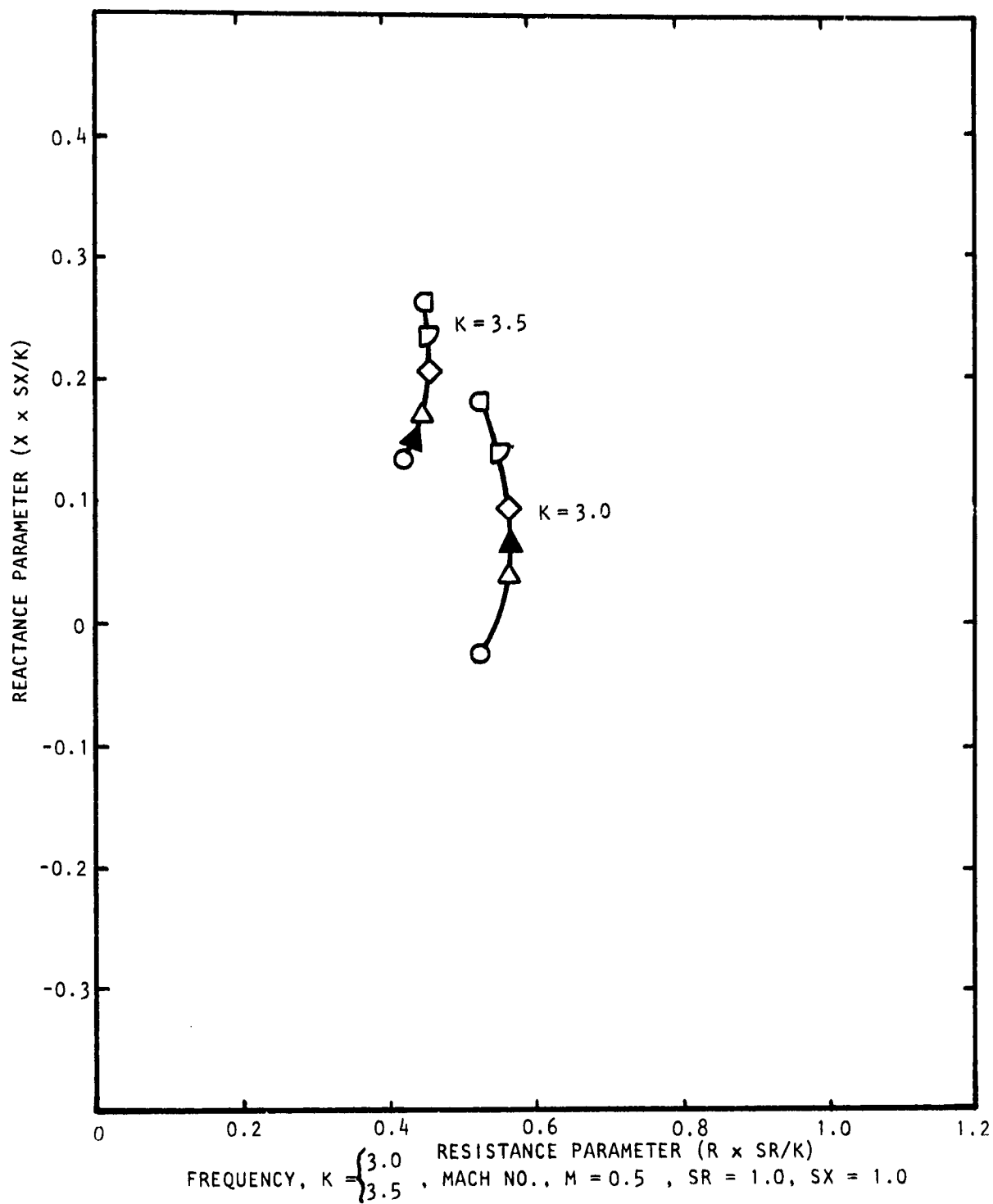


Figure D.26 Effect of Bias Flow on Impedance of Multi-Cavity Liner with Porosities $\sigma_1 = 10\%$, $\sigma_2 = 20\%$, and Cavity Depths $d_1 = 3.81$ Cms. (1.5 in.) and $d_2 = 3.81$ Cms. (1.5 in.)

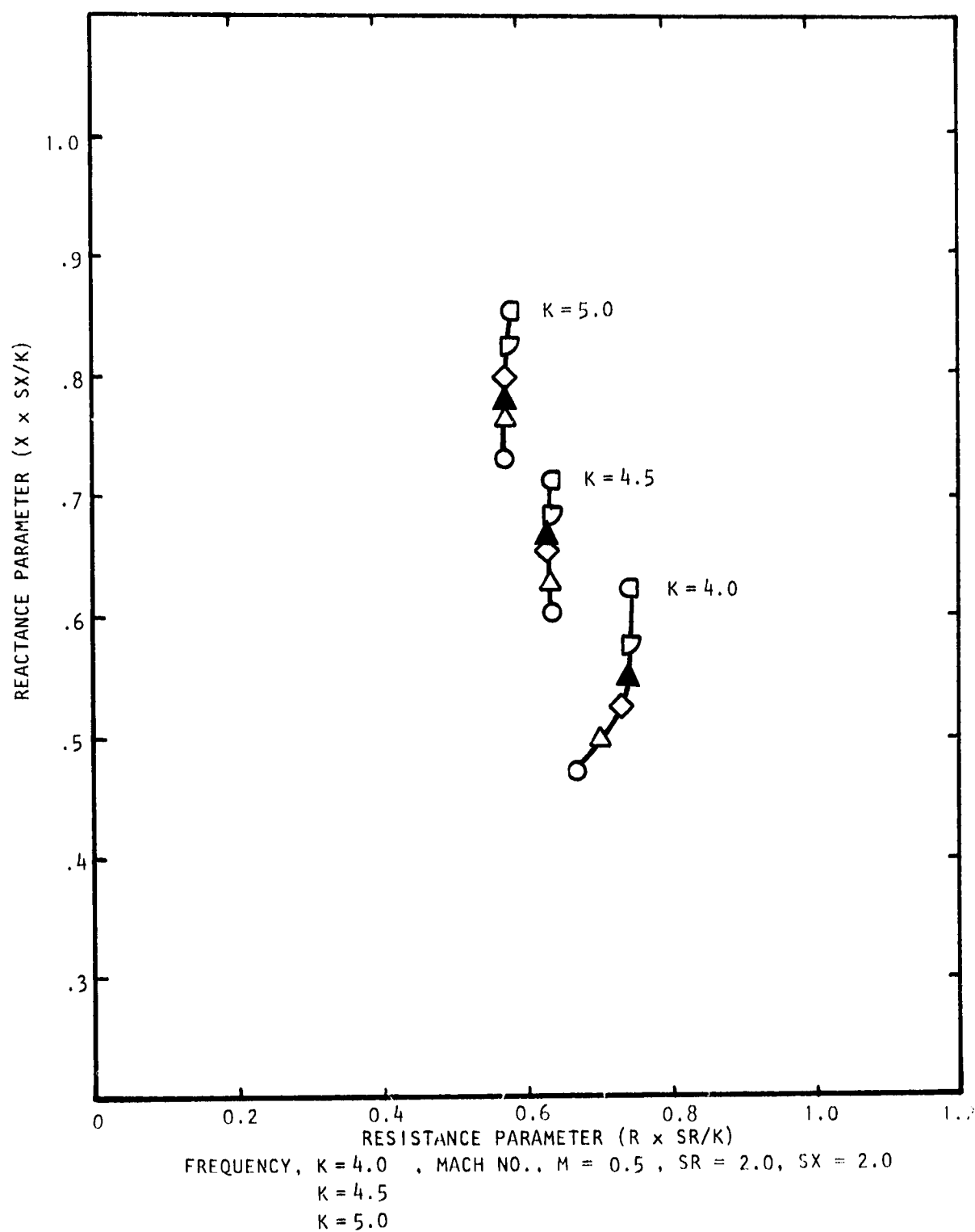


Figure D.27 Effect of Bias Flow on Impedance of Multi-Cavity Liner with Porosities $\sigma_1 = 10\%$, $\sigma_2 = 20\%$, and Cavity Depths $d_1 = 3.81$ cms. (1.5 in.) and $d_2 = 3.81$ cms. (1.5 in.)

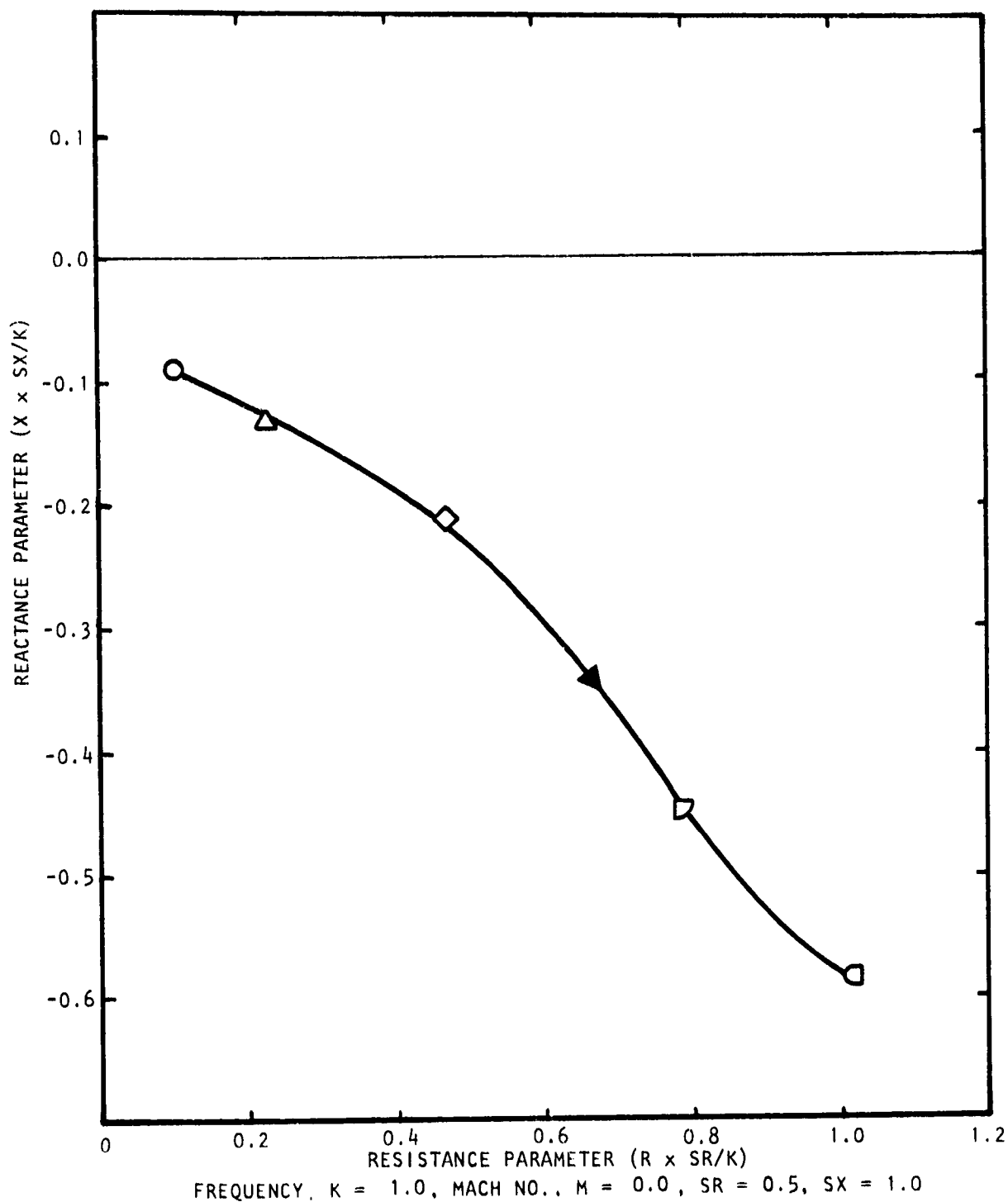


Figure D.28 Effect of Bias Flow on Impedance of Multi-cavity Liner with Porosities $\alpha_1 = 20\%$, $\alpha_2 = 20\%$, and Cavity Depths $d_1 = 3.81$ cms. (1.5 in.) and $d_2 = 3.81$ cms (1.5 in.)

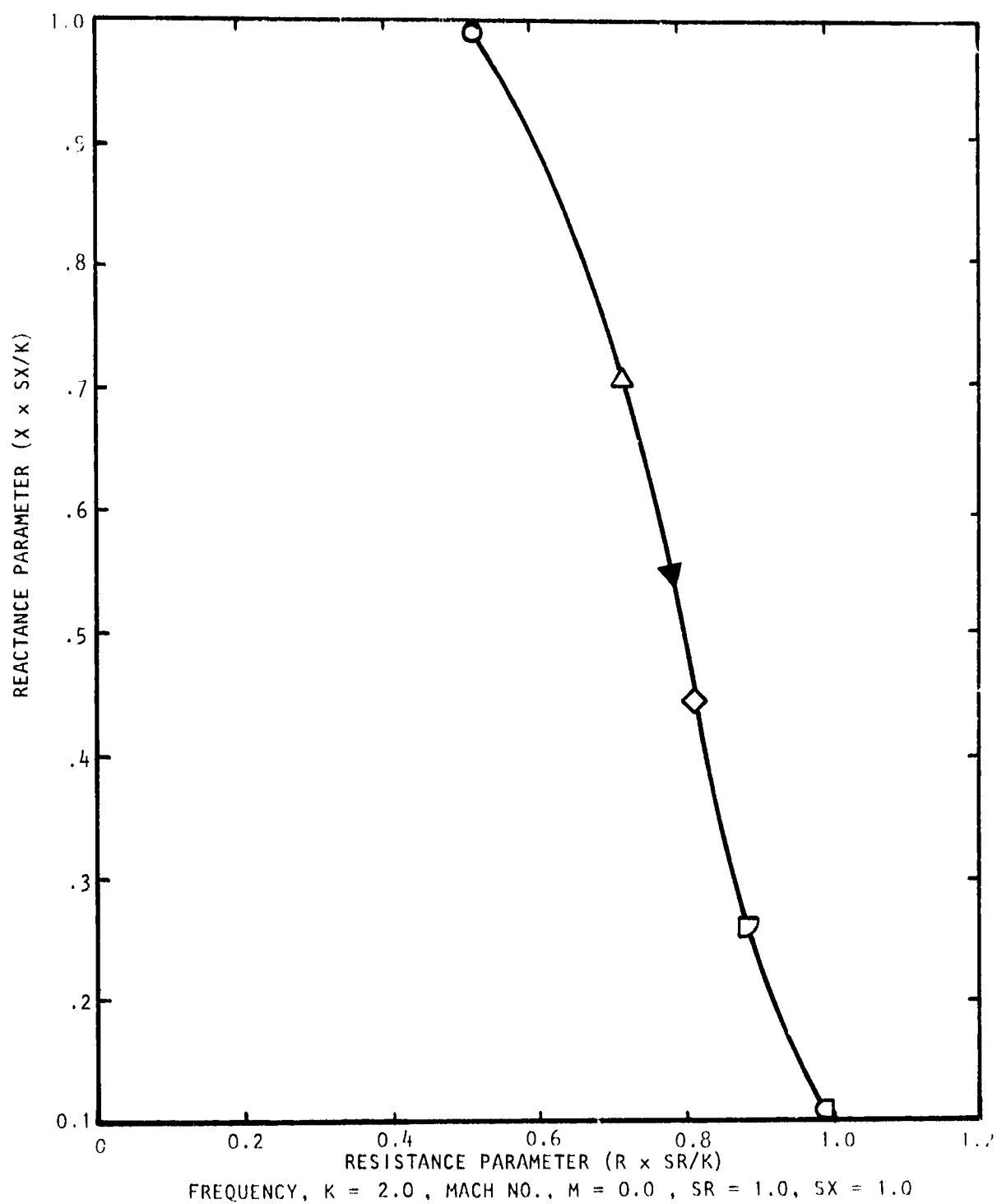
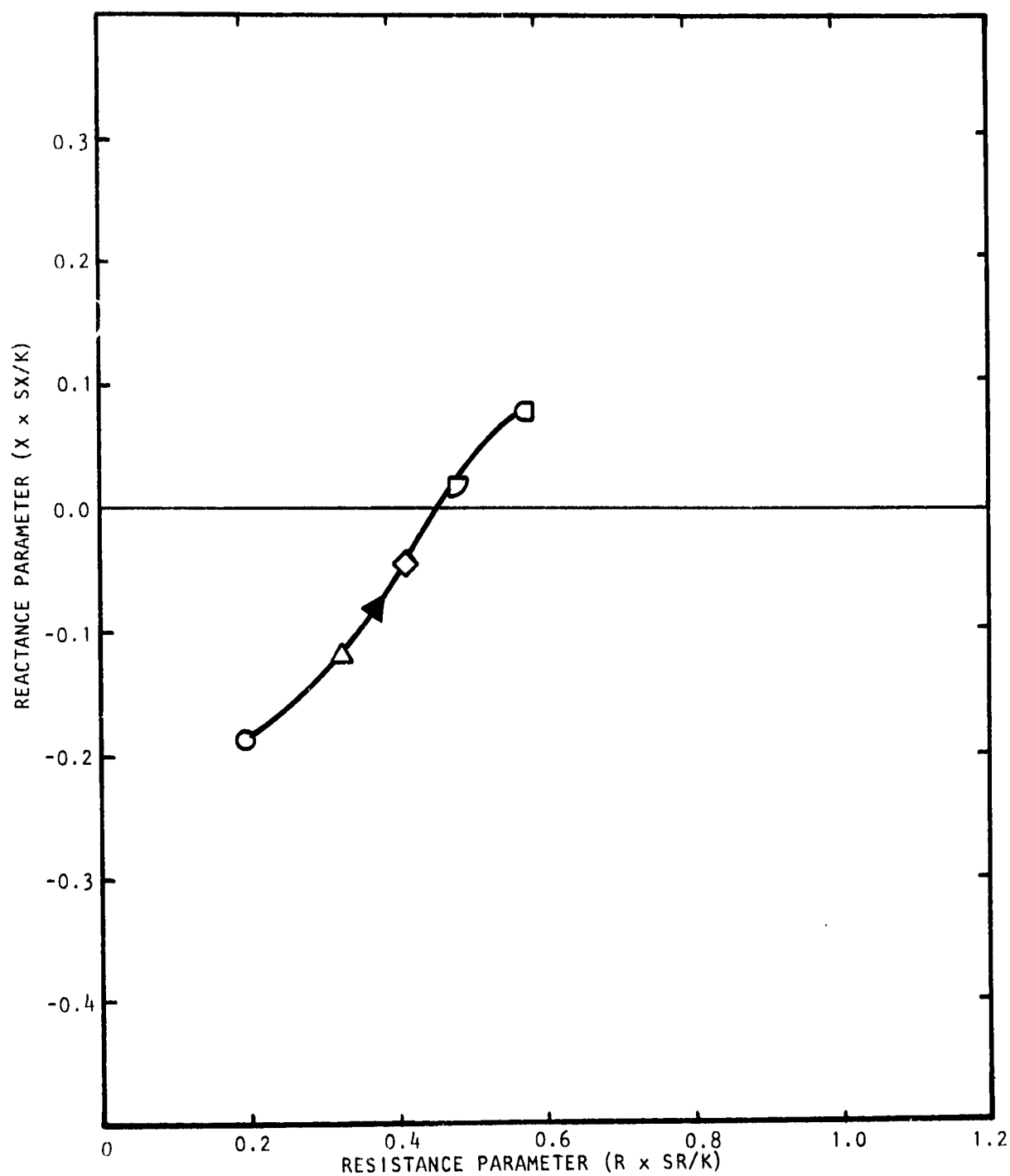


Figure D.29 Effect of Bias Flow on Impedance of Multi-Cavity Liner with Porosities $\alpha_1 = 20\%$, $\alpha_2 = 20\%$, and Cavity Depths $d_1 = 3.81$ cms. (1.5 in.) and $d_2 = 3.81$ (1.5 in.)



FREQUENCY, $K = 3.0$, MACH NO., $M = 0.0$, $SR = 1.0$, $SX = 1.0$

Figure D.30 Effect of Bias Flow on Impedance of Multi-Cavity Liner with Porosities $\sigma_1 = 20\%$, $\sigma_2 = 20\%$, and Cavity Depths $d_1 = 3.81$ cms. (1.5 in.) and $d_2 = 3.81$ (1.5 in.)

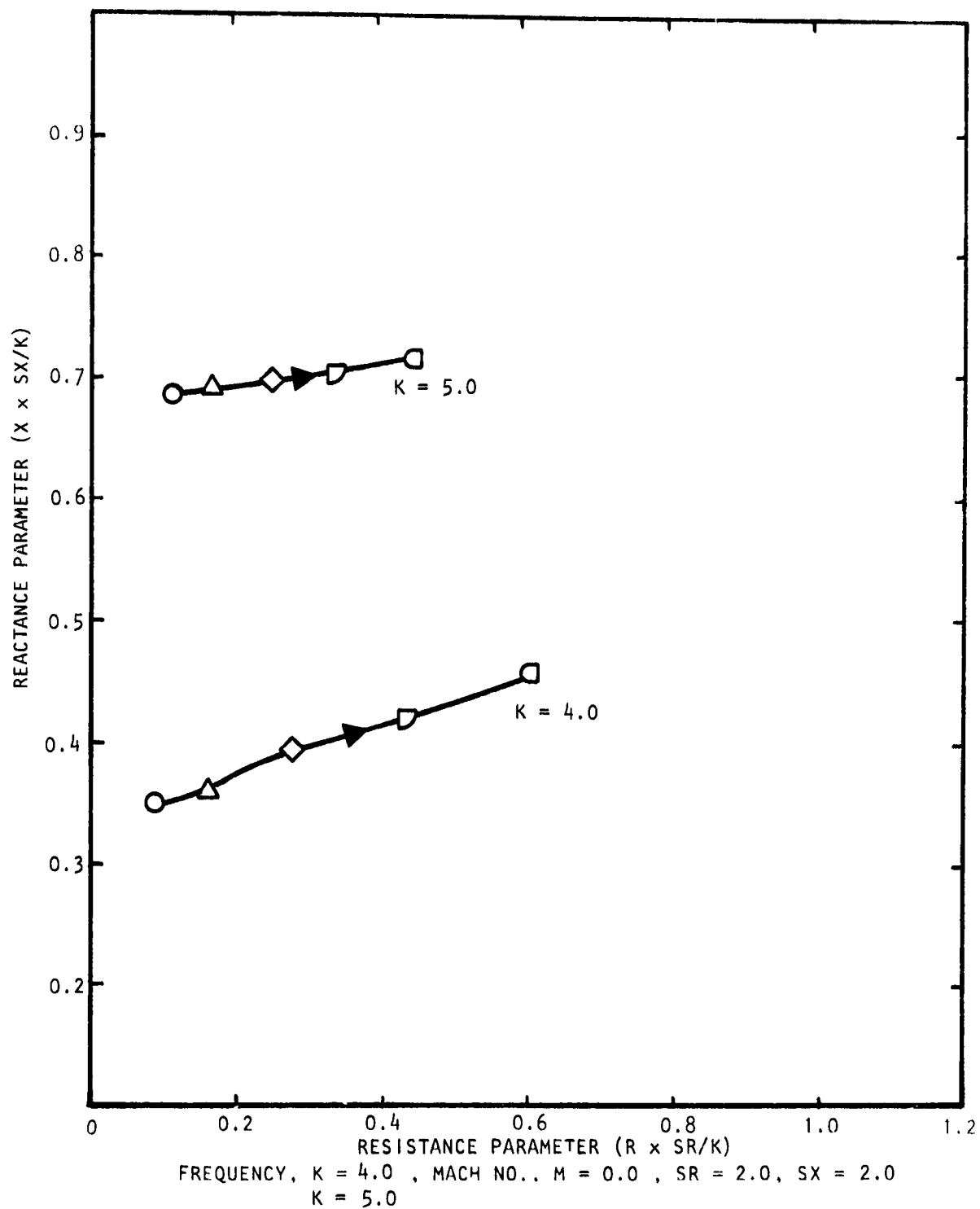


Figure D.31 Effect of Bias Flow on Impedance of Multi-Cavity Liner with Porosities $\sigma_1 = 20\%$, $\sigma_2 = 20\%$, and Cavity Depths $d_1 = 3.81$ cms. (1.5 in.) and $d_2 = 3.81$ (1.5 in.)

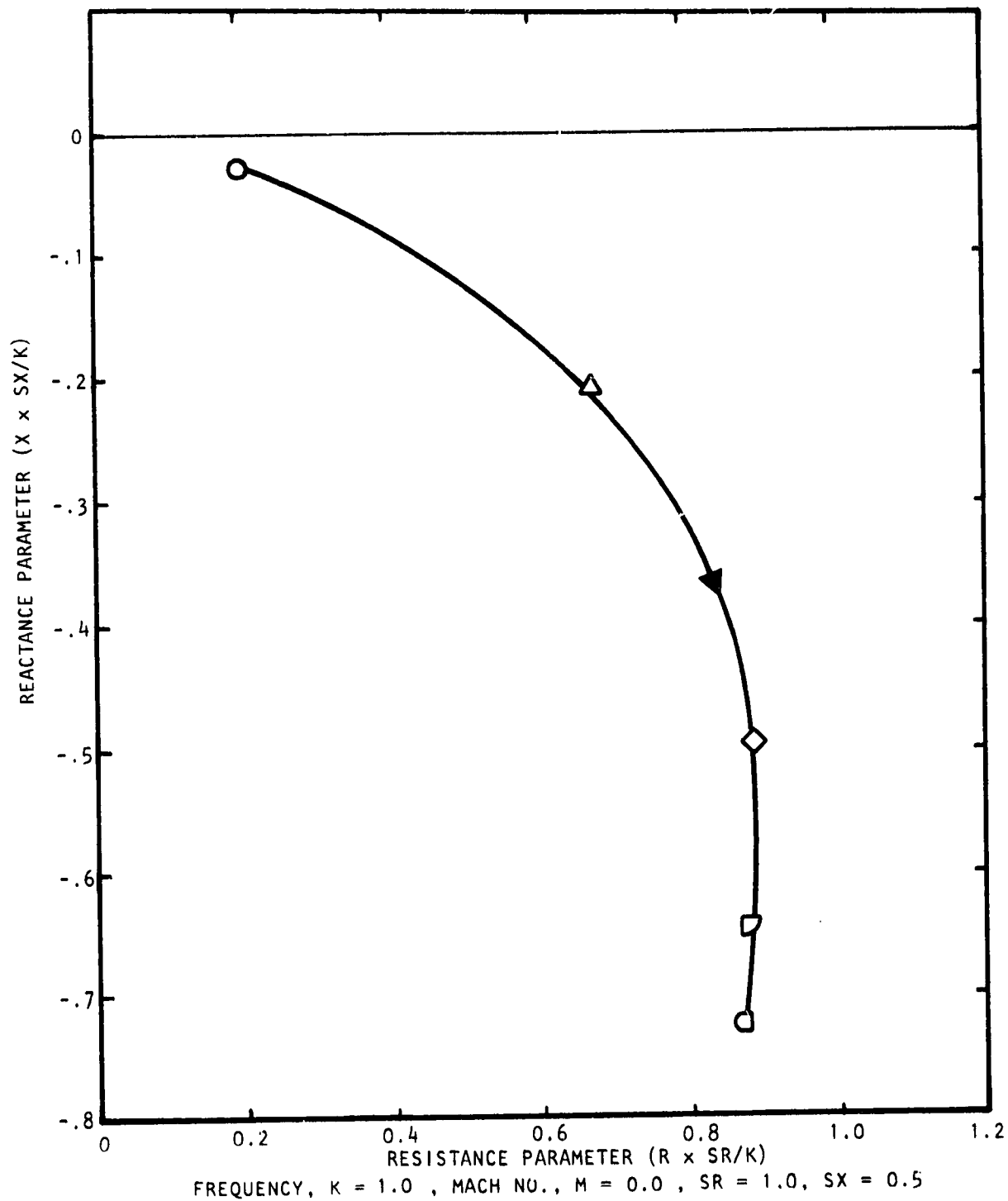


Figure D.32

Effect of Bias Flow on Impedance of Multi-cavity Liner with Porosities $\sigma_1 = 10\%$, $\sigma_2 = 40\%$, and Cavity Depths $d_1 = 3.81$ cms. (1.5 in.) and $d_2 = 3.81$ cms. (1.5 in.)

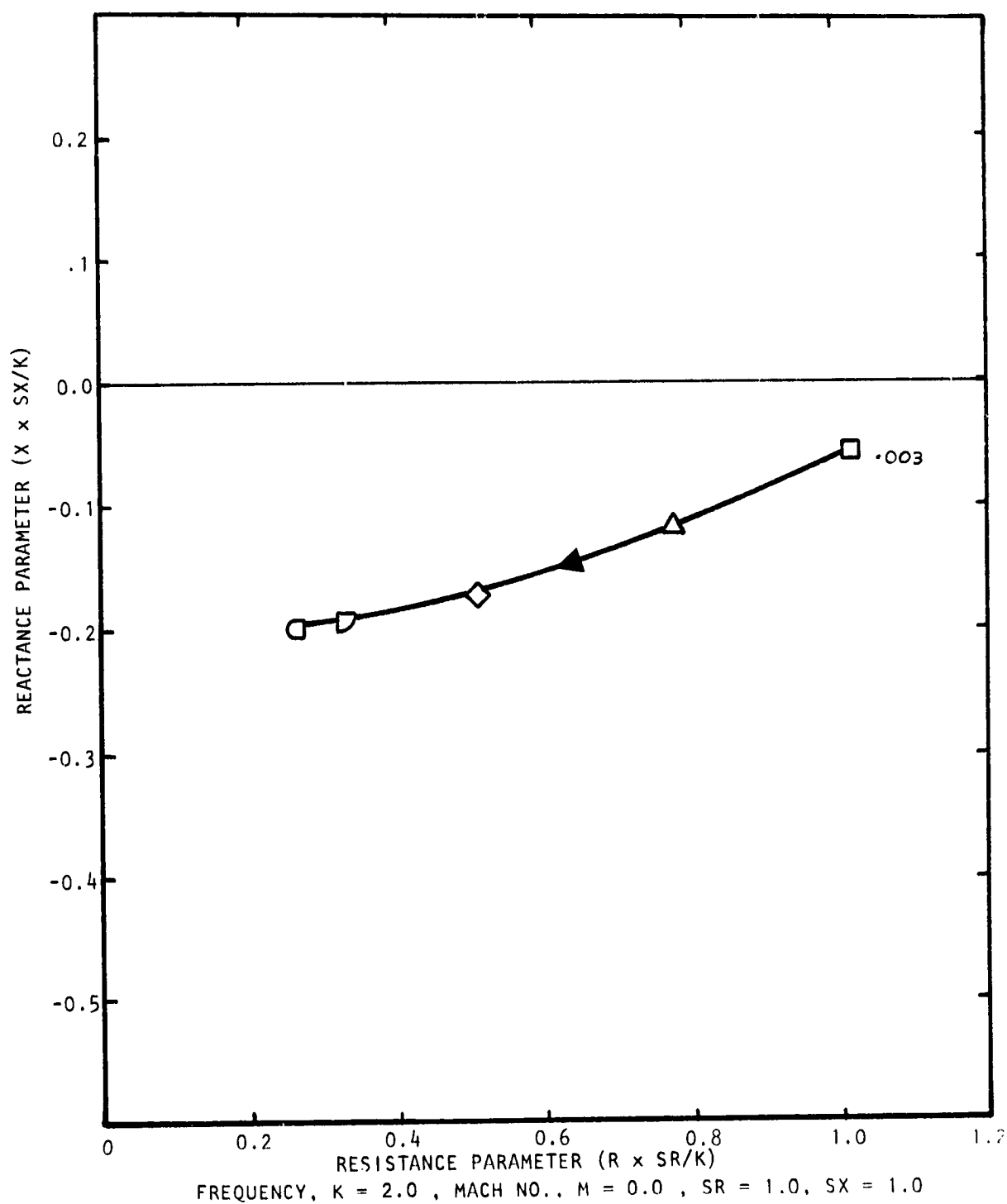
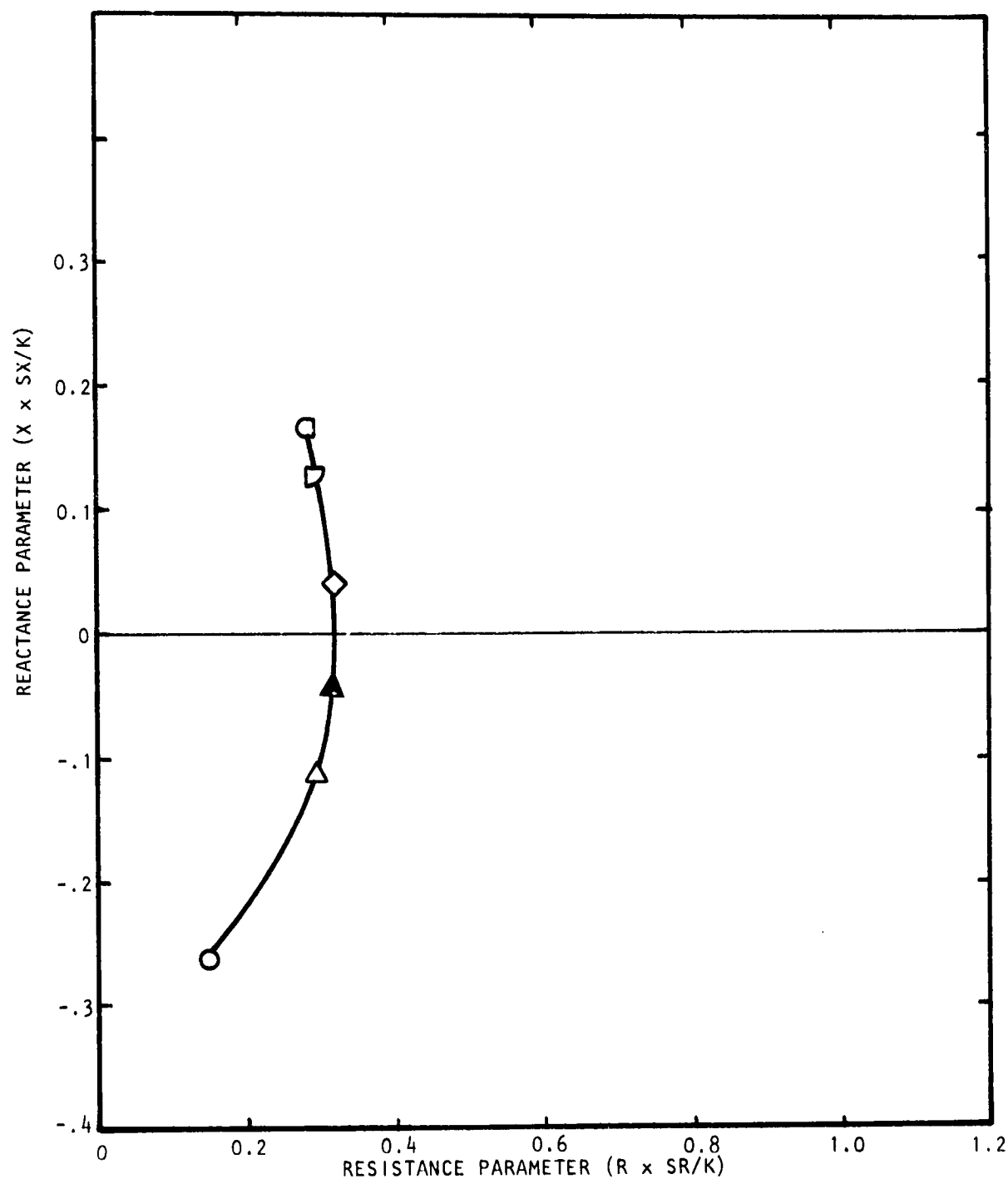


Figure D.33 Effect of Bias Flow on Impedance of Multi-Cavity Liner with Porosities $\sigma_1 = 10\%$, $\sigma_2 = 40\%$, and Cavity Depths $d_1 = 3.81$ cms. (1.5 in.) and $d_2 = 3.81$ cms. (1.5 in.)



FREQUENCY, $K = 3.0$, MACH NO., $M = 0.0$, $SR = 2.0$, $SX = 2.0$

Figure D.34 Effect of Bias Flow on Impedance of Multi-Cavity Liner with Porosities $\sigma_1 = 20\%$, $\sigma_2 = 20\%$, and Cavity Depths $d_1 = 3.81$ cms. (1.5 in.) and $d_2 = 3.81$ (1.5 in.)

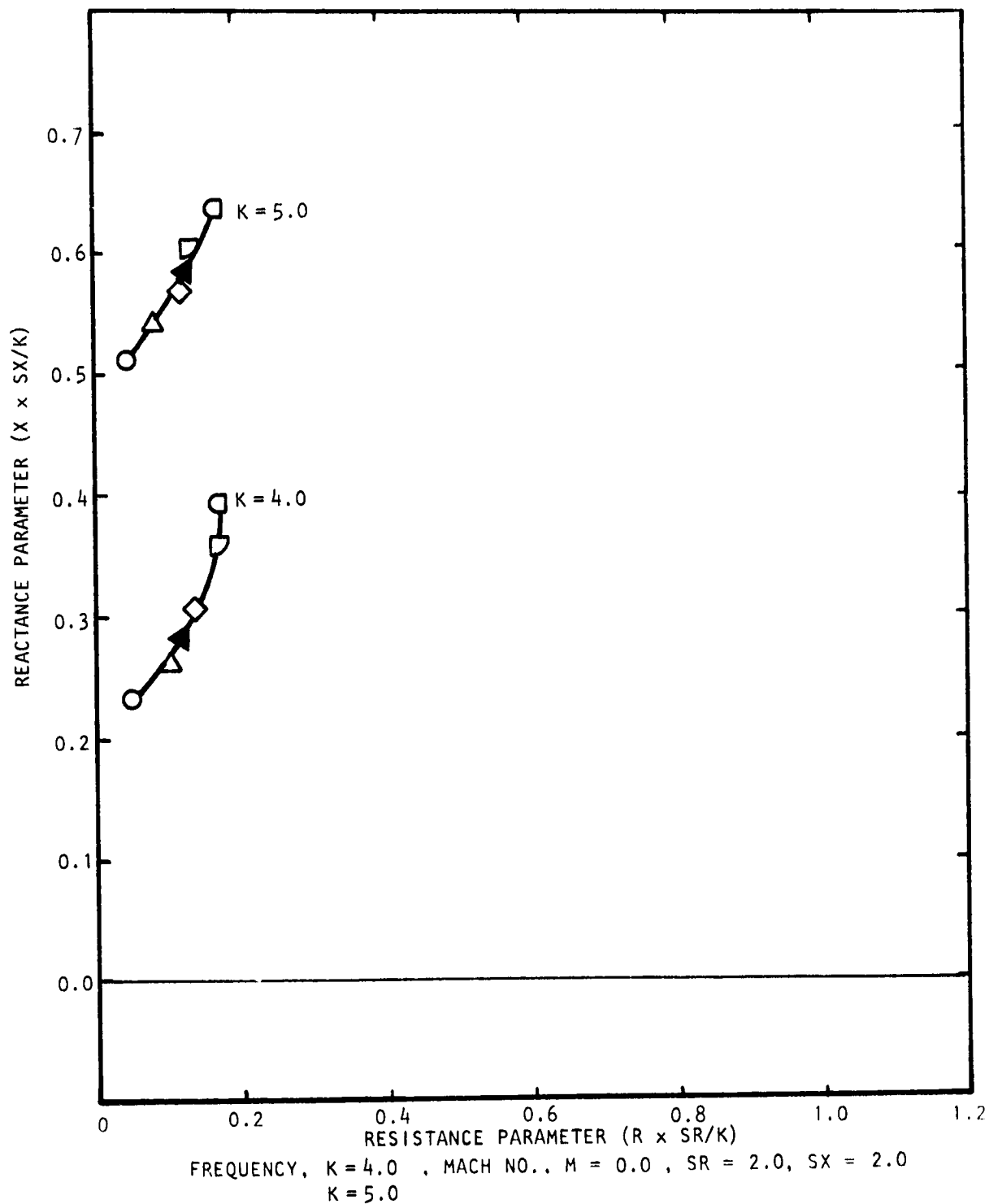


Figure D.35 Effect of Bias Flow on Impedance of Multi-Cavity Liner with Porosities $\sigma_1 = 10\%$, $\sigma_2 = 40\%$, and Cavity Depths $d_1 = 3.81$ cms. (1.5 in.) and $d_2 = 3.81$ cms. (1.5 in.)

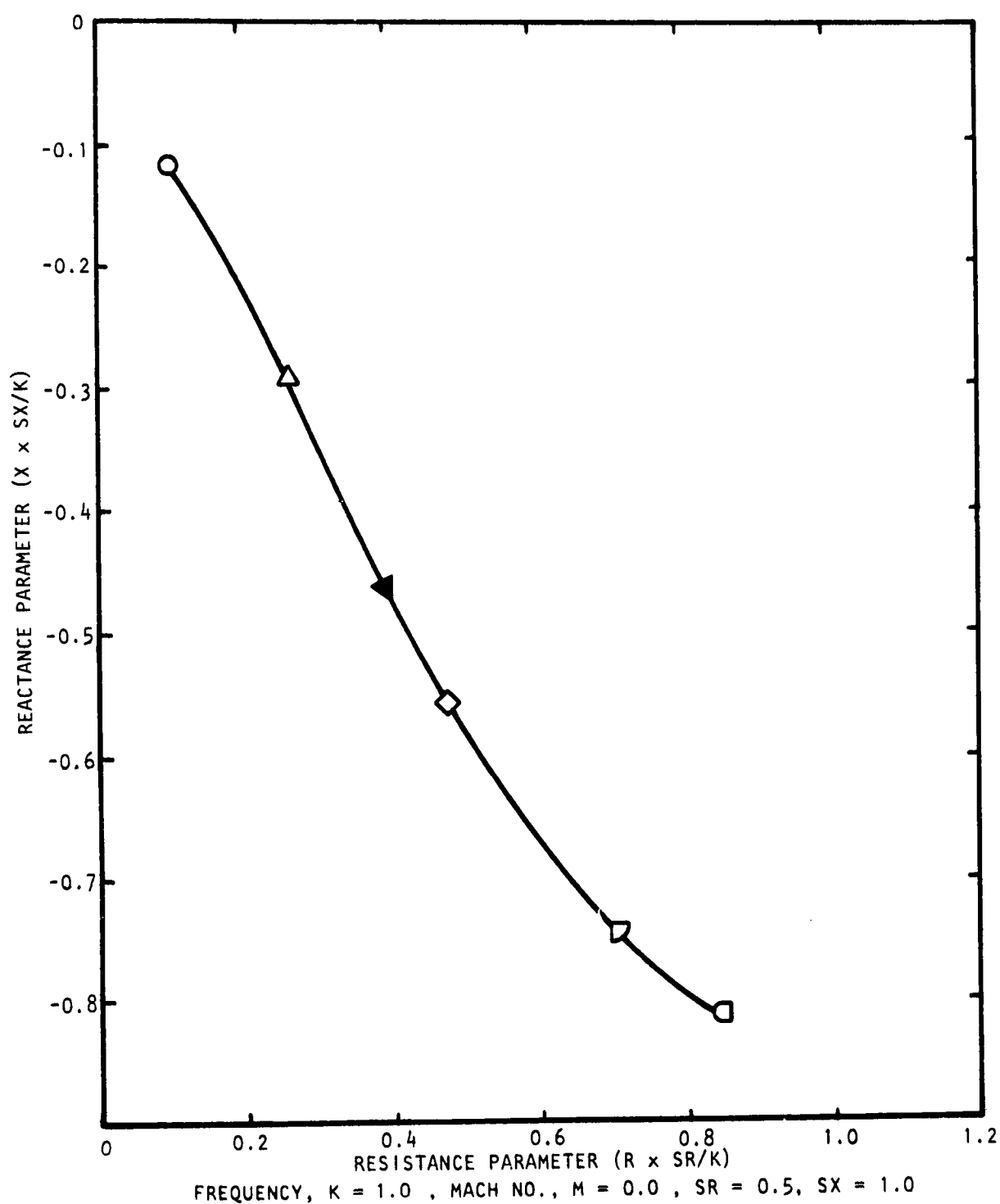


Figure D.36 Effect of Bias Flow on Impedance of Multi-cavity Liner with Porosities $\sigma_1 = 10\%$, $\sigma_2 = 20\%$, and Cavity Depths $d_1 = 1.91$ cms. (0.75 in.) and $d_2 = 5.72$ cms. (2.25 in.)

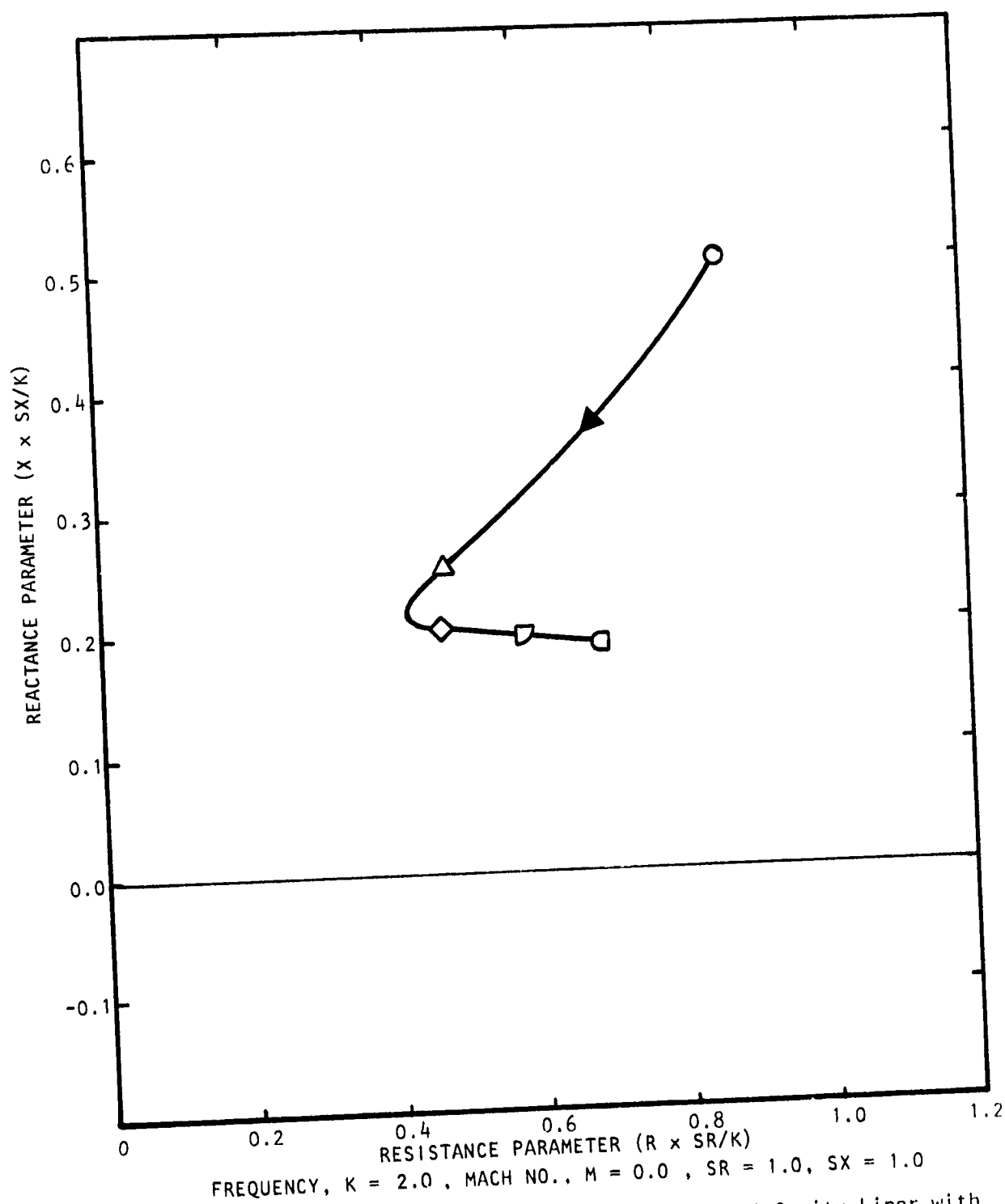
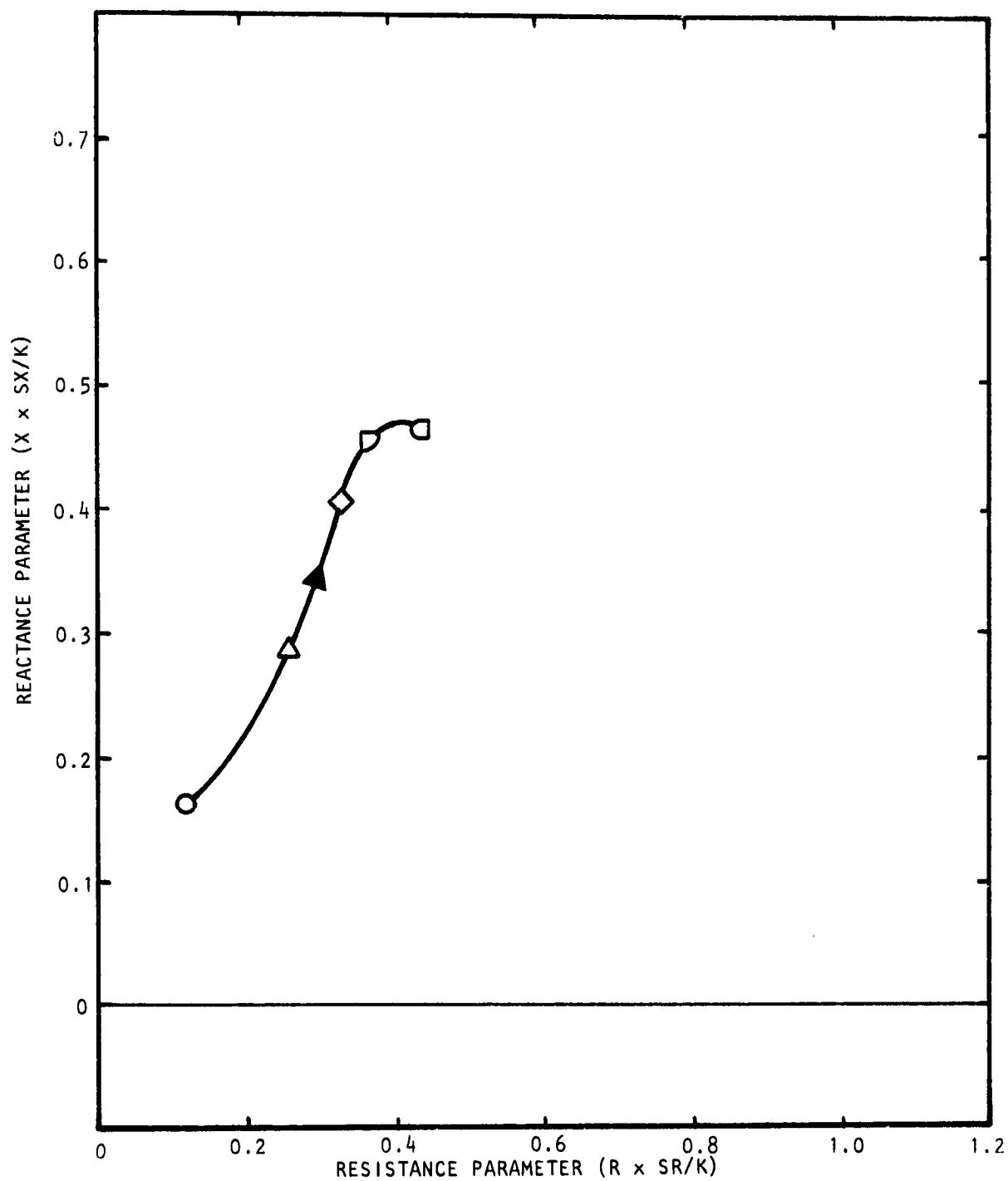
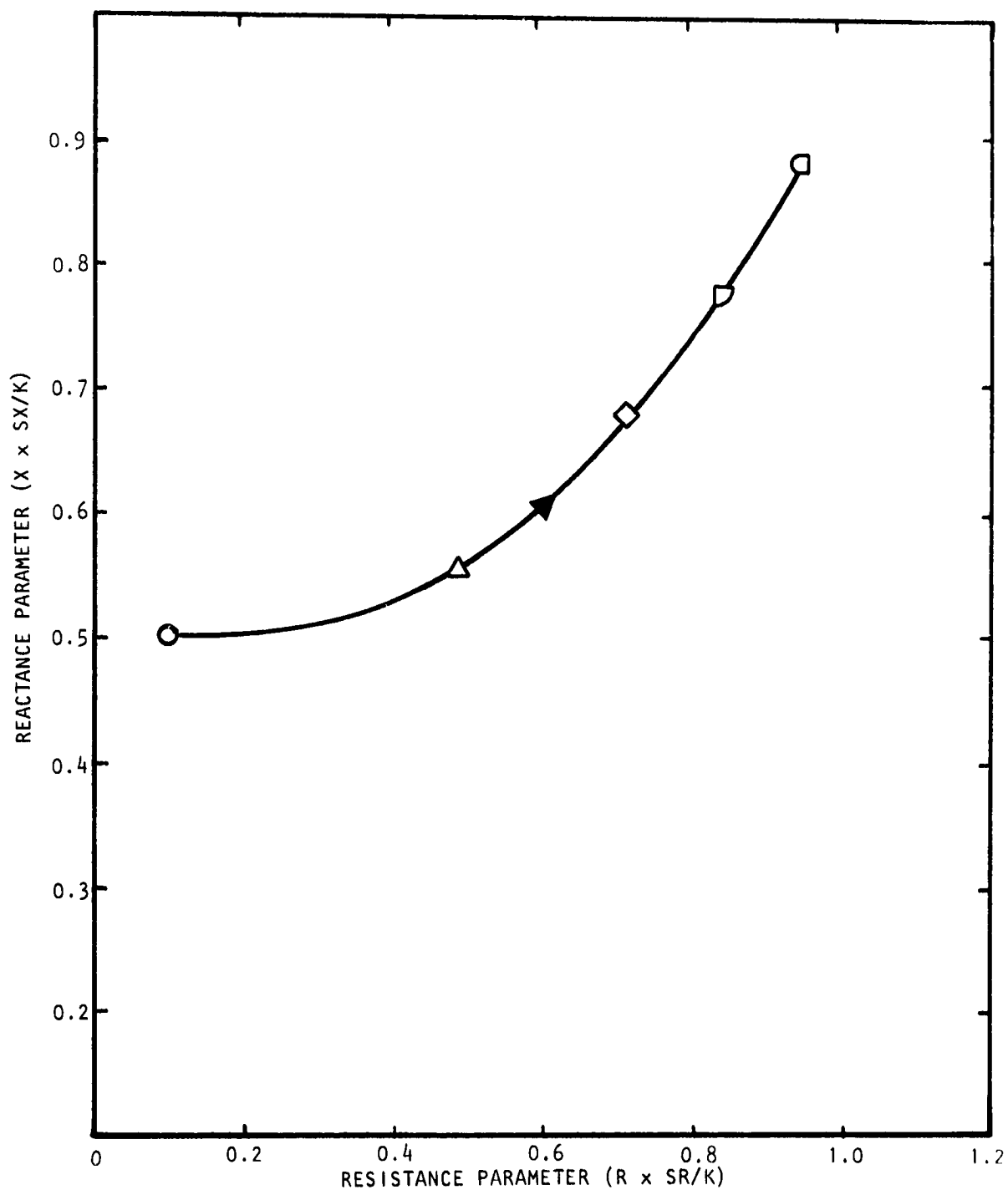


Figure D.37 Effect of Bias Flow on Impedance of Multi-Cavity Liner with Porosities $\sigma_1 = 10\%$, $\sigma_2 = 20\%$, Cavity Depths $d_1 = 1.91$ cms. (0.75 in.) and $d_2 = 5.72$ cms. (2.25 in.)



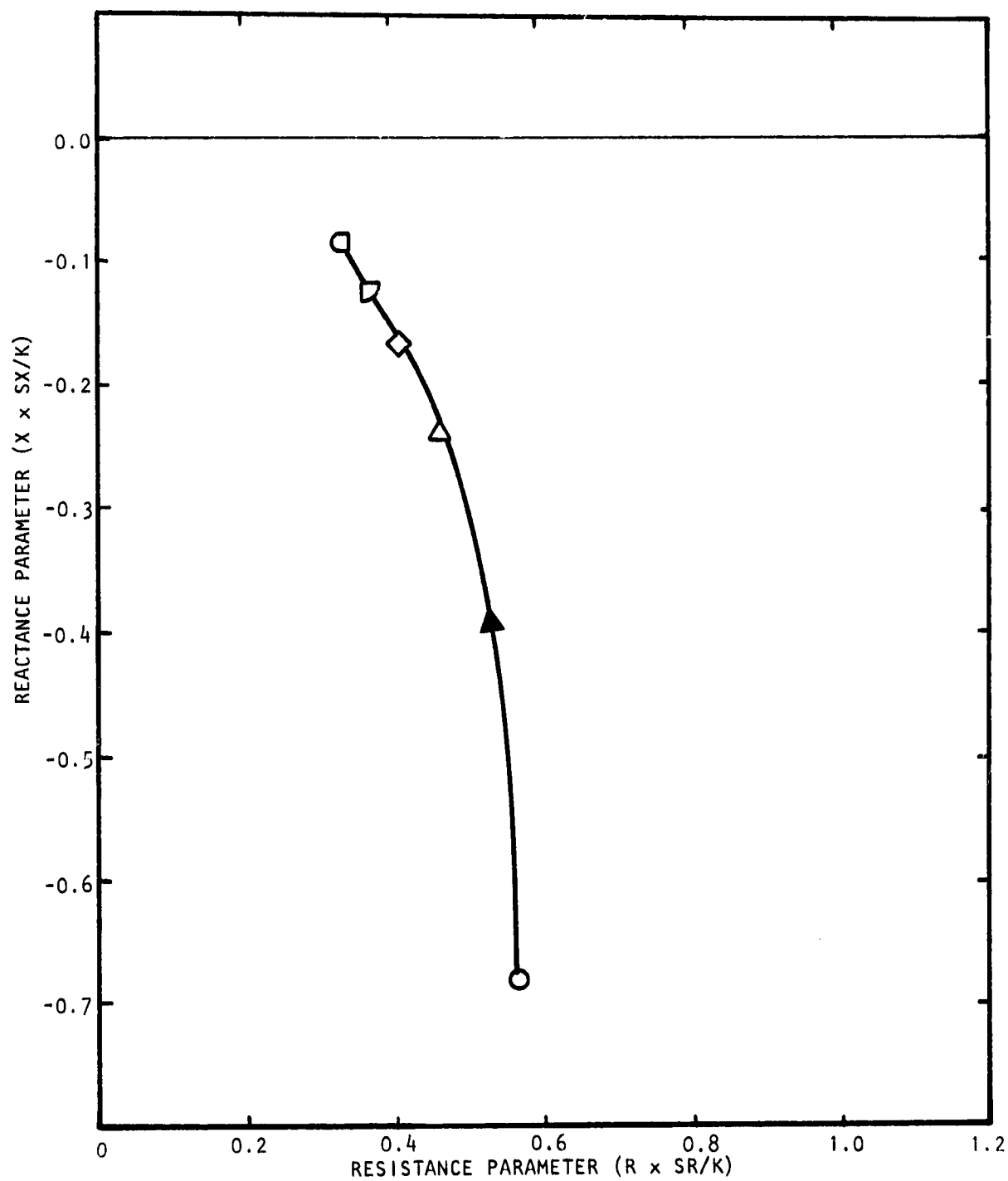
FREQUENCY, $K = 3.0$, MACH NO., $M = 0.0$, $SR = 1.0$, $SX = 1.0$

Figure D.38 Effect of Bias Flow on Impedance of Multi-Cavity Liner with Porosities $\sigma_1 = 10\%$, $\sigma_2 = 20\%$, Cavity Depths $d_1 = 1.91$ cms. (0.75 in.) and $d_2 = 5.72$ cms. (2.25 in.)



FREQUENCY, $K = 4.0$, MACH NO., $M = 0.0$, $SR = 1.0$, $SX = 1.0$

Figure D.39 Effect of Bias Flow on Impedance of Multi-Cavity Liner with Porosities $\sigma_1 = 10\%$, $\sigma_2 = 20\%$, Cavity Depths $d_1 = 1.91$ cms. (0.75 in.) and $d_2 = 5.72$ cms. (2.25 in.)



FREQUENCY, $K = 5.0$, MACH NO., $M = 0.0$, $SR = 1.0$, $SX = 1.0$

Figure D.40 Effect of Bias Flow on Impedance of Multi-Cavity Liner with Porosities $\sigma_1 = 10\%$, $\sigma_2 = 20\%$, Cavity Depths $d_1 = 1.91$ cms. (0.75 in.) and $d_2 = 5.72$ cms. (2.25 in.)

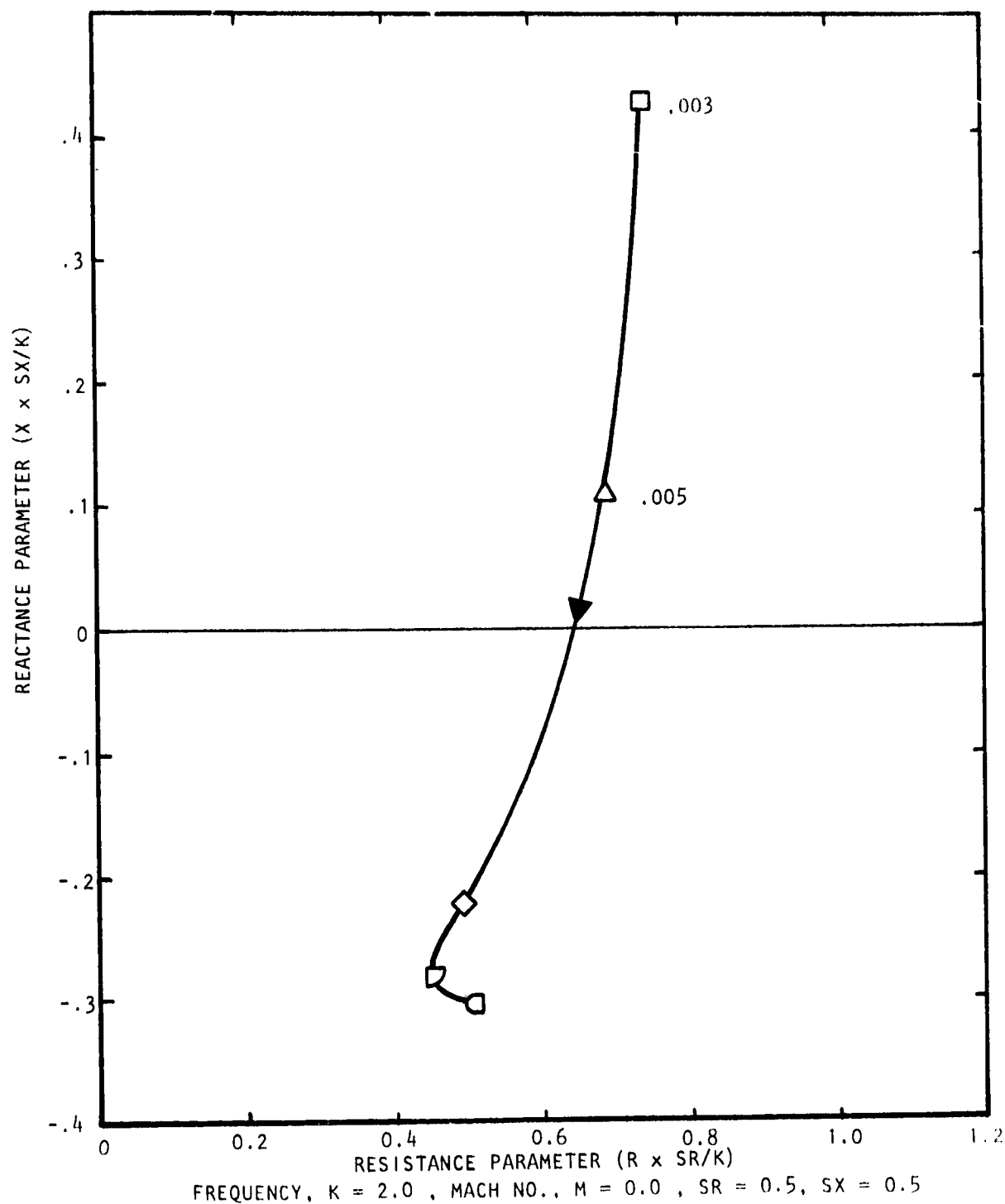
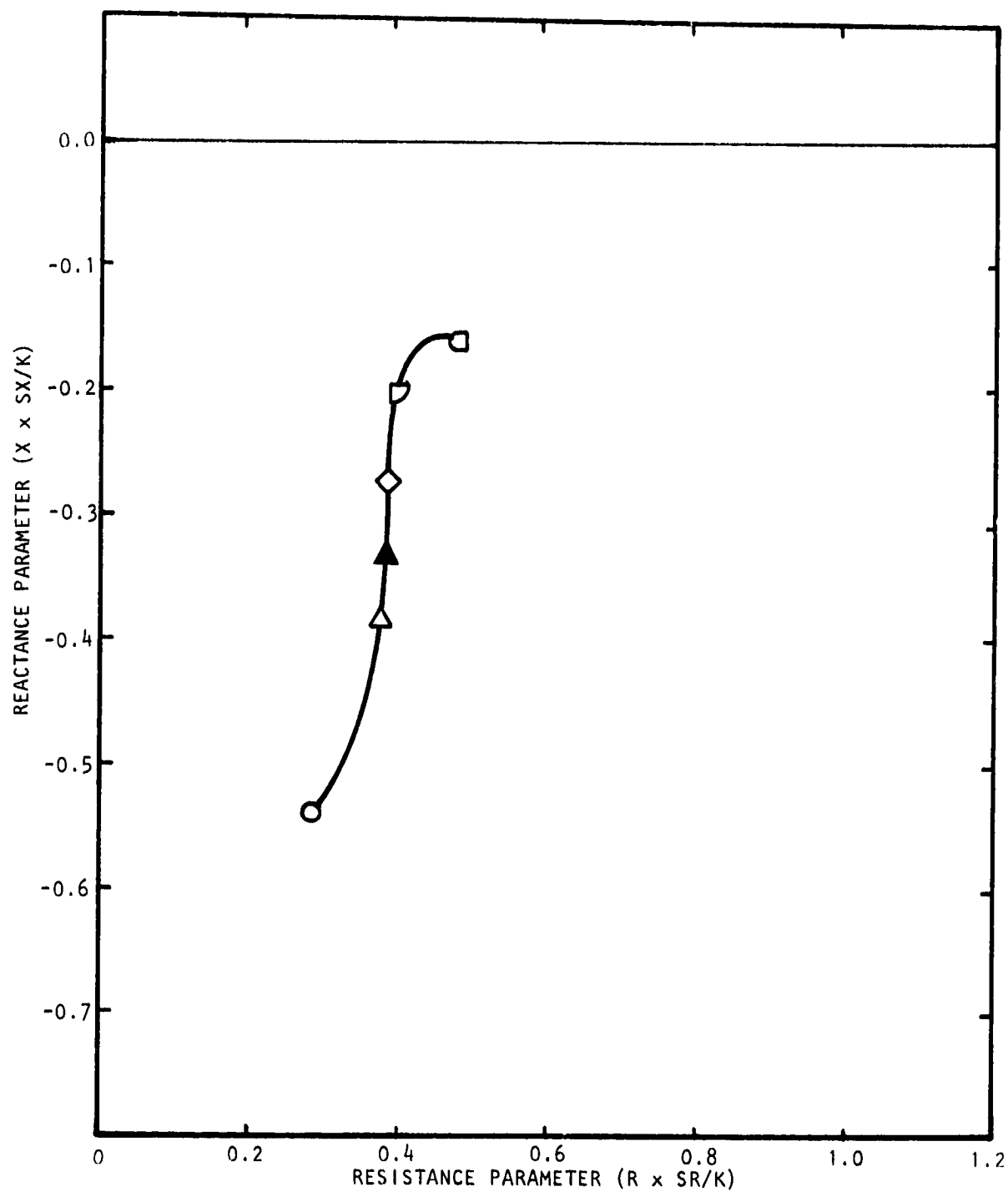


Figure D.41 Effect of Bias Flow on Impedance of Multi-Cavity Liner with Porosities $\sigma_1 = 10\%$, $\sigma_2 = 20\%$, and Cavity Depths $d_1 = 5.72$ cms. (2.25 in.) and $d_2 = 1.91$ cms. (0.75 in.)



FREQUENCY, $K = 3.0$, MACH NO., $M = 0.0$, $SR = 1.0$, $SX = 1.0$

Figure D.42 Effect of Bias Flow on Impedance of Multi-Cavity Liner with Porosities $\alpha_1 = 10\%$, $\alpha_2 = 20\%$, and Cavity Depths $d_1 = 5.72$ cms. (2.25 in.) and $d_2 = 1.91$ cms. (0.75 in.)

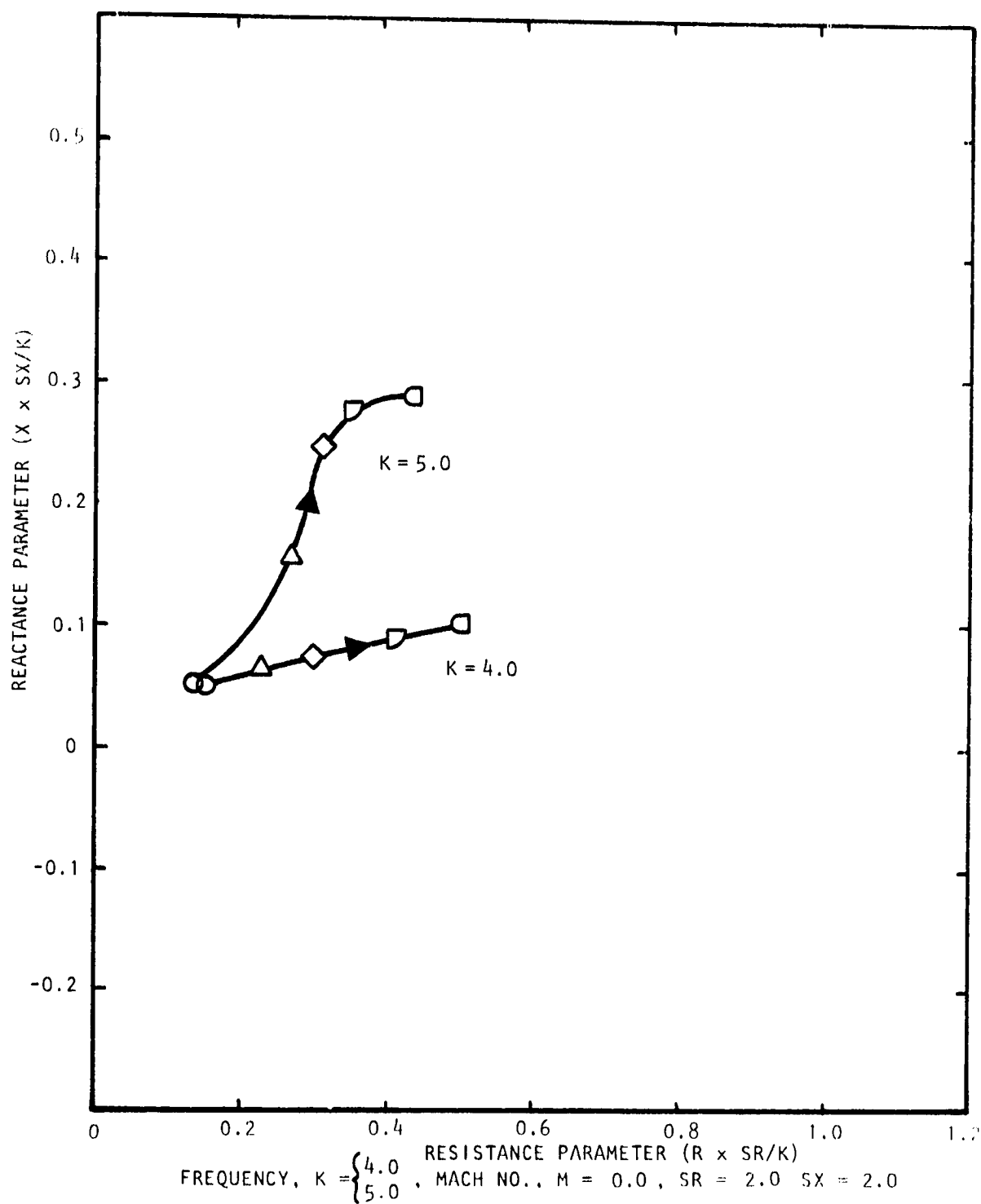


FIGURE D.43 Effect of Bias Flow on Impedance of Multi-Cavity Liner with Porosities $\alpha_1 = 10\%$, $\alpha_2 = 20\%$, and Cavity Depths $d_1 = 5.72$ Cms. (2.25 in.) and $d_2 = 1.91$ Cms. (0.75 in.)

APPENDIX E

THE CALCULATION OF NORMAL INCIDENCE IMPEDANCE IN A STANDING WAVE TUBE

The resistance is given by

$$\frac{R}{\rho c} = \frac{10^{SWR/20} [1 + \tan^2 2\pi(d_1/\lambda - 0.25)]}{1 + 10^{SWR/20} \tan^2 2\pi(d_1/\lambda - 0.25)}$$

and the reactance by

$$\frac{X}{\rho c} = \frac{[10^{SWR/10} - 1] \tan 2\pi(d_1/\lambda - 0.25)}{1 + 10^{SWR/10} \tan^2 2\pi(d_1/\lambda - 0.25)}$$

where SWR = Standing Wave Ratio (dB difference of maximum and minimum pressures)

d_1 = distance from first standing wave minima to the front face of the sample

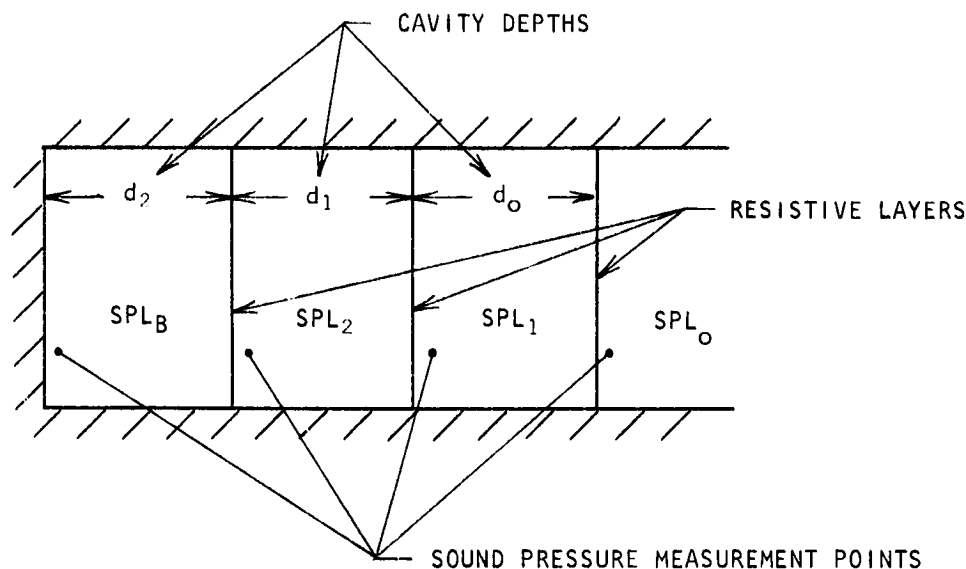
λ = free space wavelength (speed of sound/frequency)

APPENDIX F

CALCULATION OF ACOUSTIC IMPEDANCE FOR A LOCALLY REACTING RESONANT CAVITY TYPE TRIPLE-LAYER LINER SYSTEM*

**Procedure is based on theoretical extension of work described by Dean, P. D.: An In-Situ Method of Wall Acoustic Impedance Measurement in Flow Ducts, J. Sound Vib., Vol. 34(1), pp. 97-130, 1974.*

Consider the generalized triple cavity liner system as shown in the figure below where the cavity depths are denoted by d_0 , d_1 , and d_2 , the sound pressure levels at the front face of each liner denoted by SPL_0 , SPL_1 , SPL_2 , and SPL_B at the back wall, and the corresponding phase differences denoted by ϕ_{10} , ϕ_{20} and ϕ_{30} .



Then the admittance (9) is given by

$$\begin{aligned}
 G = & -j10 \frac{SPL_1 - SPL_0}{20} \left(\sin kd_0 \sin \phi_{10} \right) - j10 \frac{SPL_2 - SPL_0}{20} \left(\sin kd_1 \cos kd_0 \sin \phi_{20} \right) \\
 & - j10 \frac{SPL_B - SPL_0}{20} \left(\sin kd_2 \cos kd_1 \cos kd_0 \sin \phi_{30} \right) \\
 & + j10 \frac{SPL_1 - SPL_0}{20} \left(\sin kd_0 \cos \phi_{10} \right) + j10 \frac{SPL_2 - SPL_0}{20} \left(\sin kd_1 \cos kd_0 \cos \phi_{20} \right) \\
 & + j10 \frac{SPL_B - SPL_0}{20} \left(\sin kd_2 \cos kd_1 \cos kd_0 \cos \phi_{30} \right)
 \end{aligned}$$

and the impedance $Z = 1/G$, where

k = free space wave number = 2π frequency/speed of sound.

APPENDIX G

AXIAL SOUND PRESSURE AND PHASE TRAVERSES ON
CENTERLINE OF TEST FLOW DUCT AT VARIOUS FREQUENCIES
AT VARIOUS COMBINATIONS OF TWO EXTREMES OF BIAS FLOW
(MACH NUMBER = 0.0 AND 0.015) AND GRAZING FLOW
(MACH NUMBER = 0.0 AND 0.25)

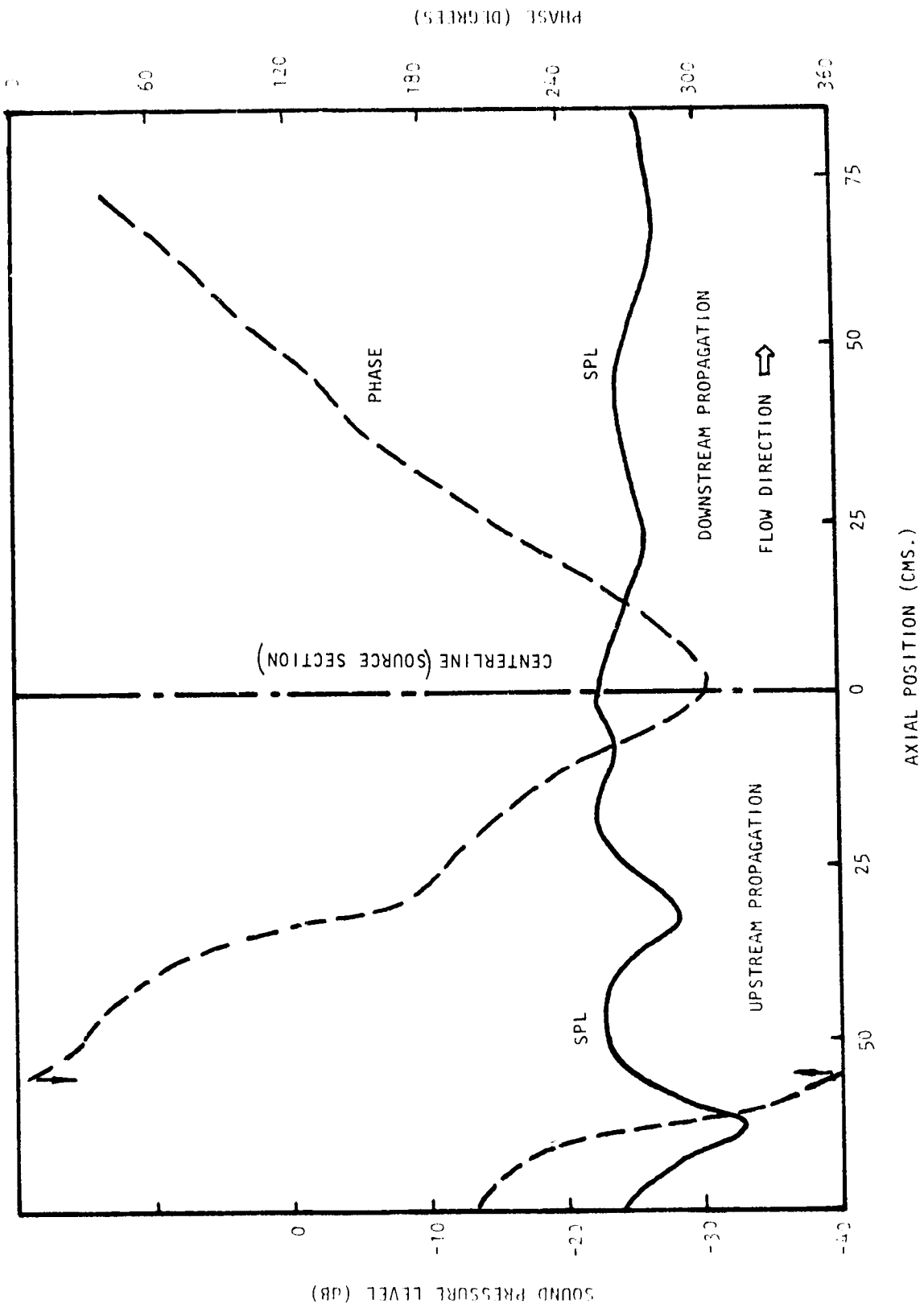


Figure G.1(a) Axial Sound Pressure and Phase Traverses on Duct Centerline at 315 Hz. p_{ias} Flow $M_i = 0.0$, Grazing Flow $M_{GF} = 0.0$

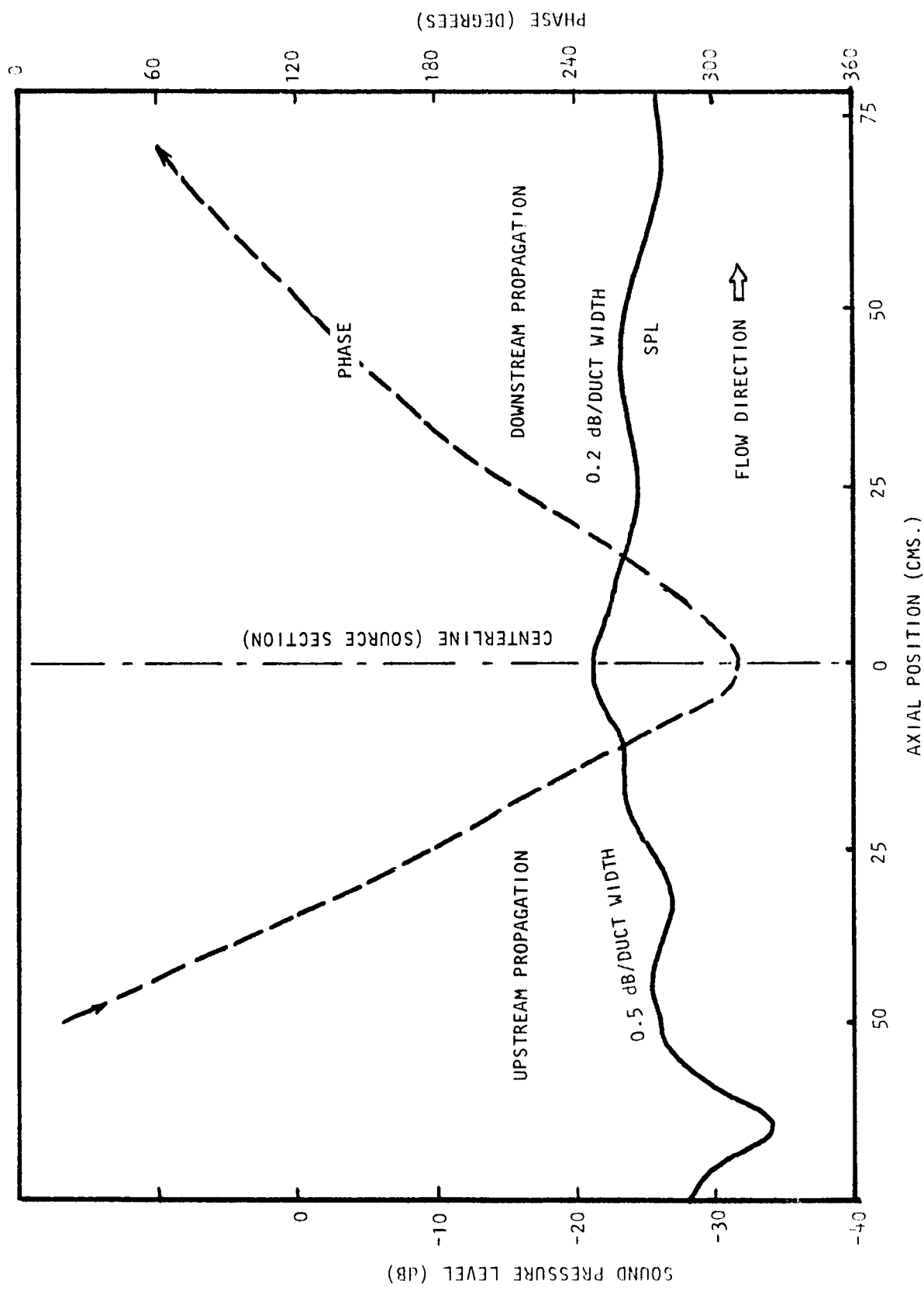


Figure 5.1(b) Axial Sound Pressure and Phase Traverses on Duct Centerline at 315 Hz. Bias Flow $M_i = 0.015$, Grazing Flow $M_{GF} = 0.0$

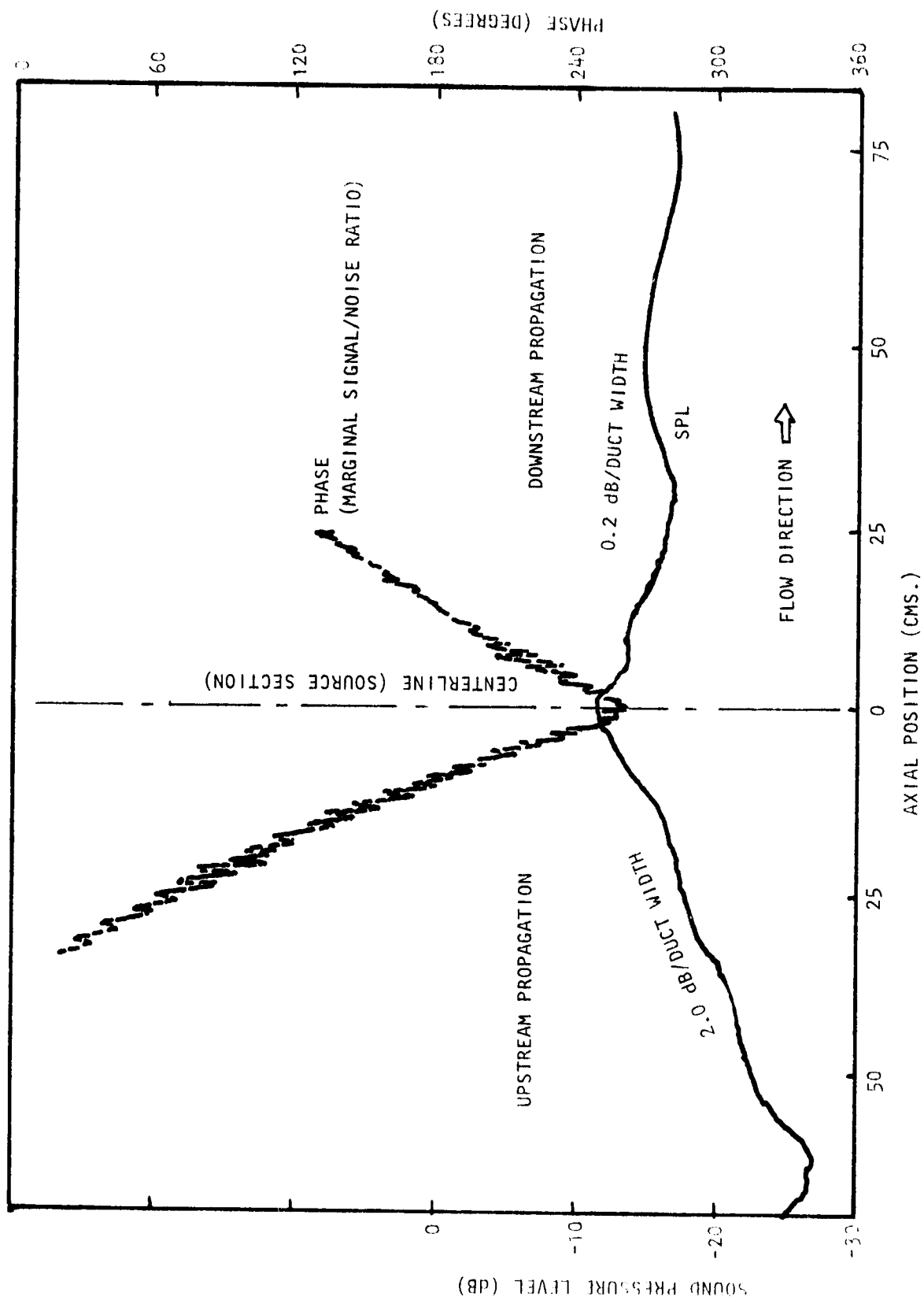


Figure 3.1(c) Axial Sound Pressure and Phase Traverses on Duct Centerline at 315 Hz. Bias Flow $M_i = 0.015$, Grazing Flow $M_{GF} = 0.25$

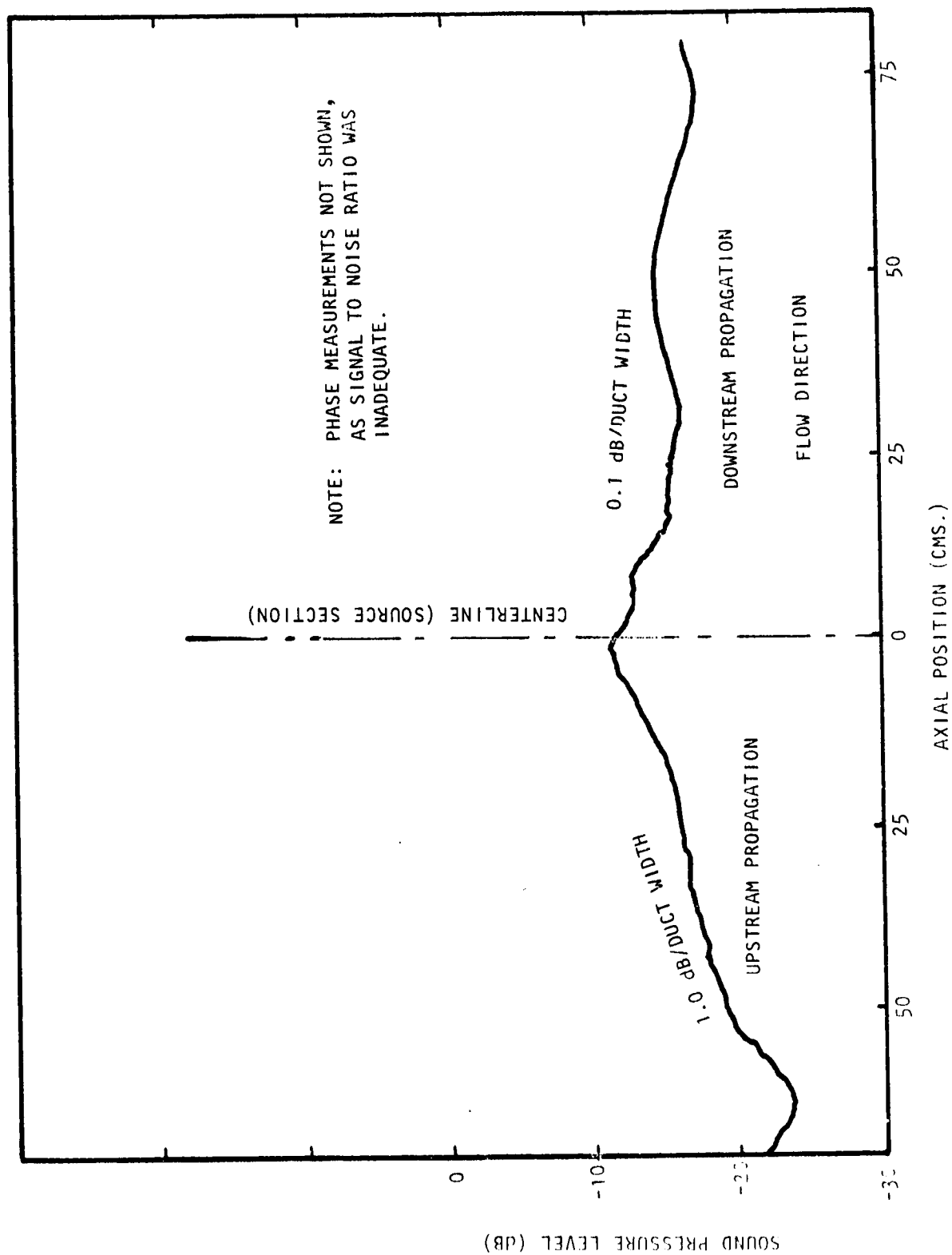


Figure G.1(d) Axial Sound Pressure Traverse on Duct Centerline at 315 Hz.
Bias Flow $M_i = 0.0$, Grazing Flow $M_{GF} = 0.25$

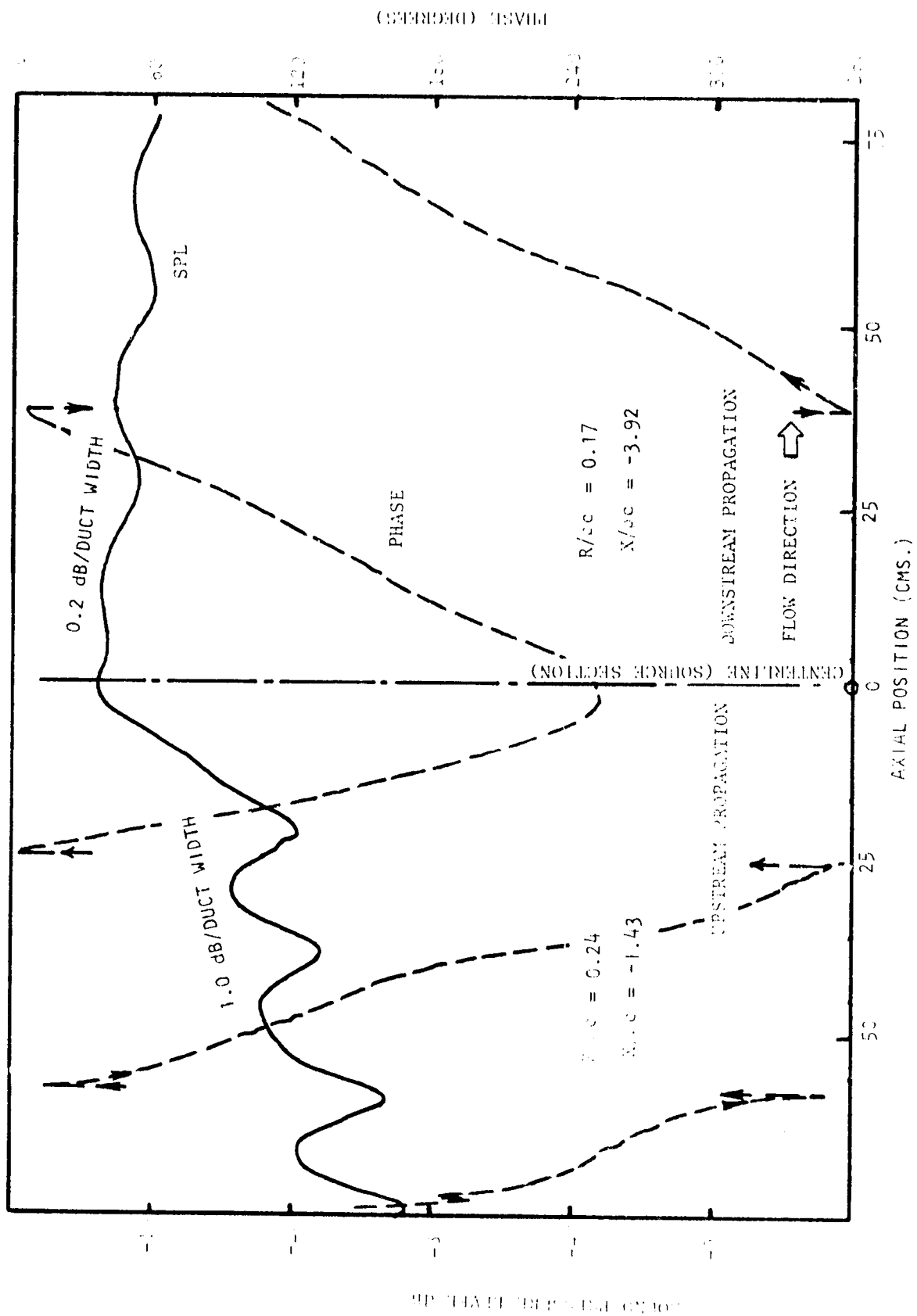


Figure 3.2(a) Axial Sound Pressure and Phase Traverses on Duct Centerline at 500 Hz. Bias Flow $M_i = 0.0$, Grazing Flow $M_{GF} = 0.0$

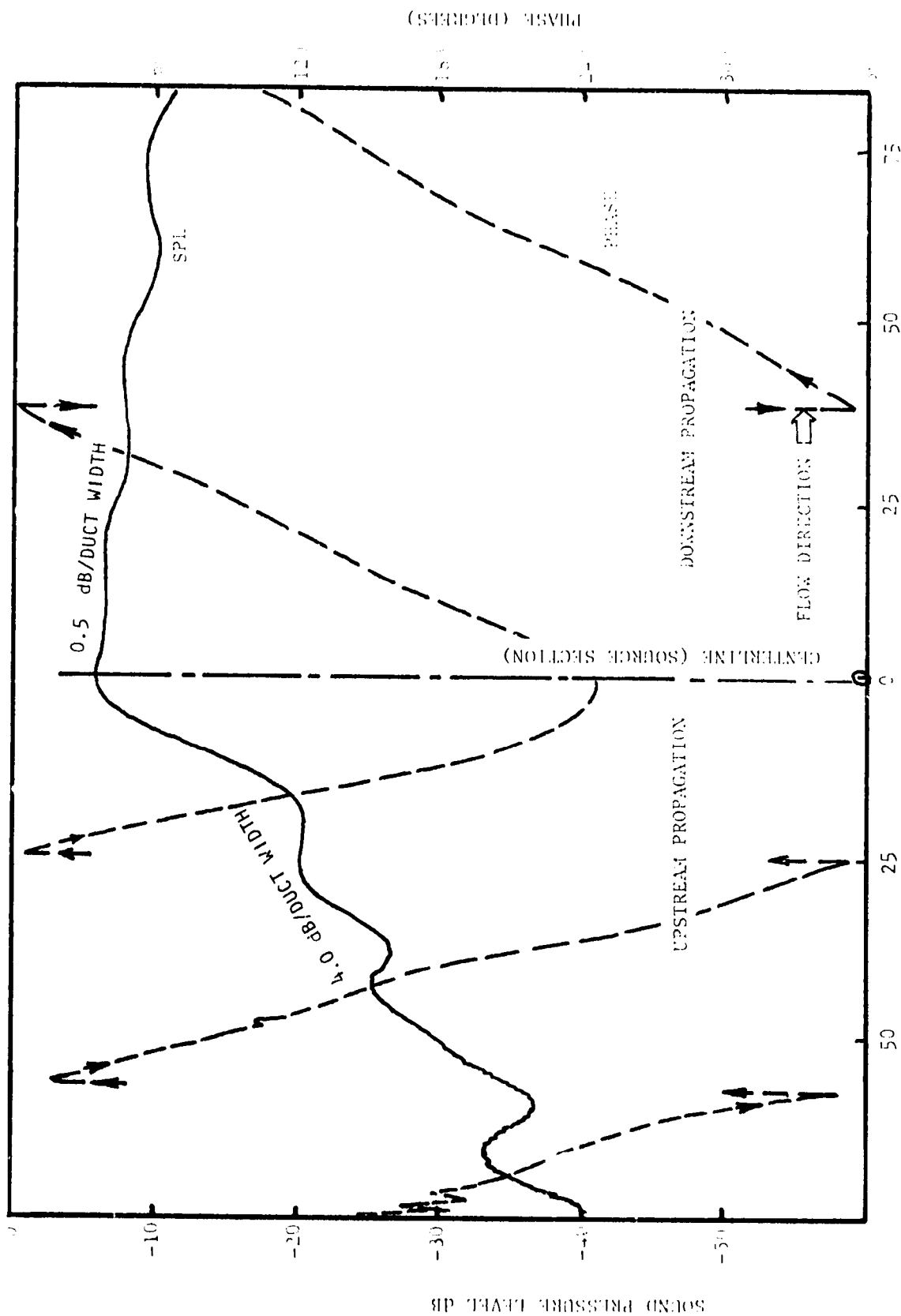


Figure G.2(b) Axial Sound Pressure and Phase Traverses on Duct Centerline at 500 Hz. Bias Flow $M_1 = 0.015$ Grazing Flow $M_{GF} = 0.3$

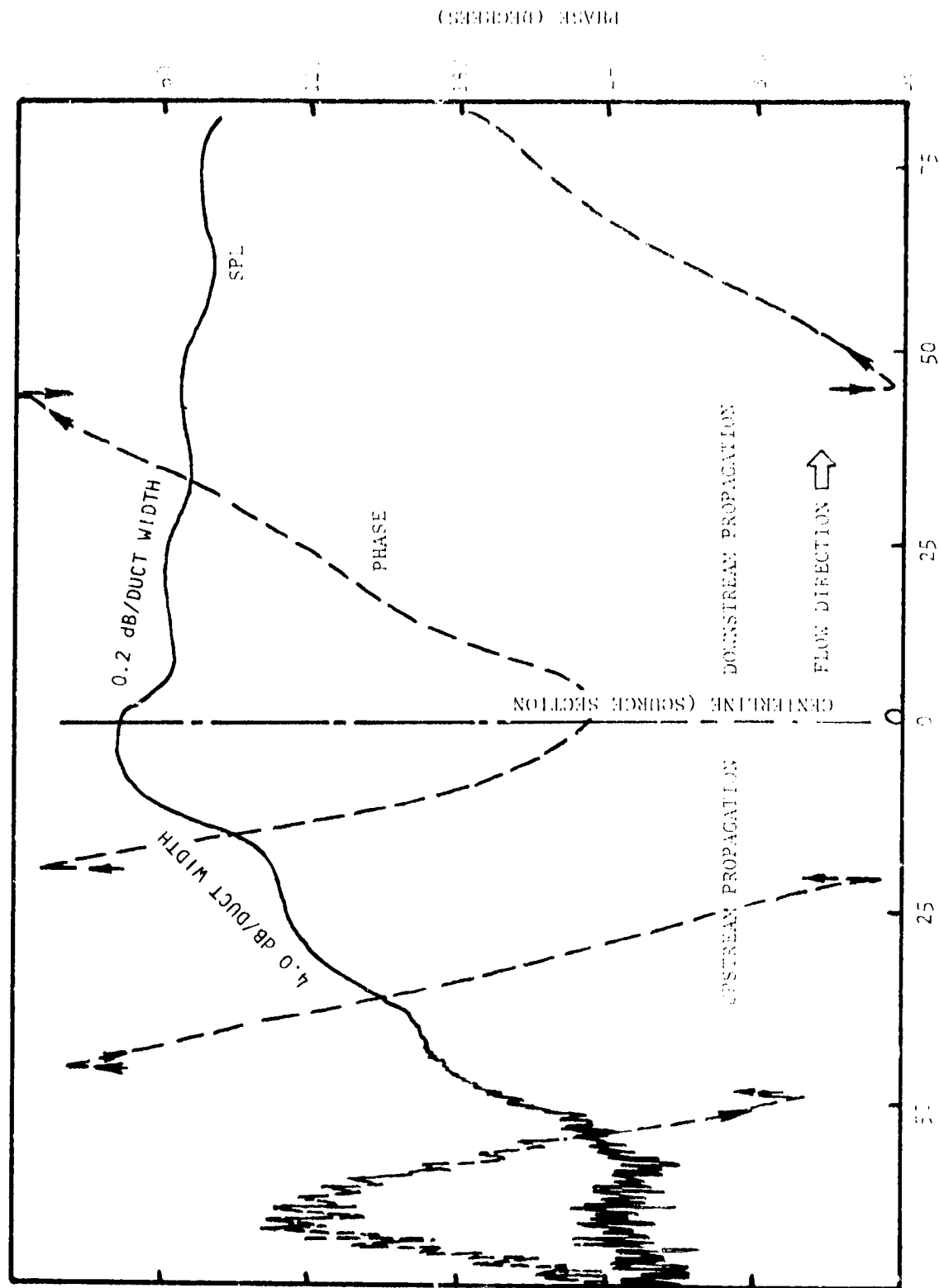


Figure 5.2(c) Axial Sound Pressure and Phase Traverses on Duct Centerline at 500 Hz. Bias Flow $M_j = 0.015$, Grazing Flow $M_{GF} = 0.25$

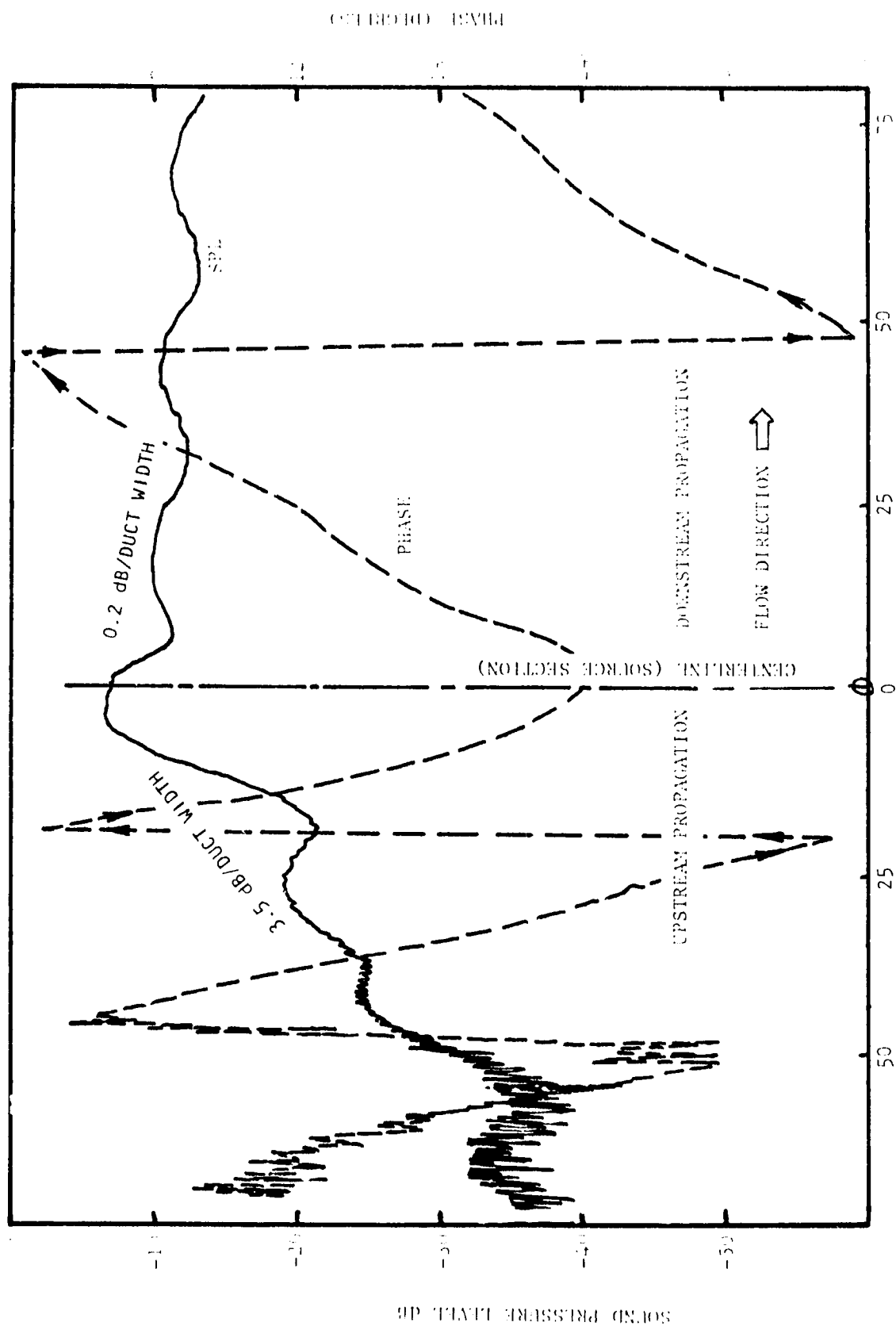


Figure G.2(d) Axial Sound Pressure and Phase Traverses on Duct Centerline at 500 Hz. Bias Flow $M_i = 0.0$, Grazing Flow $M_{GF} = 0.25$

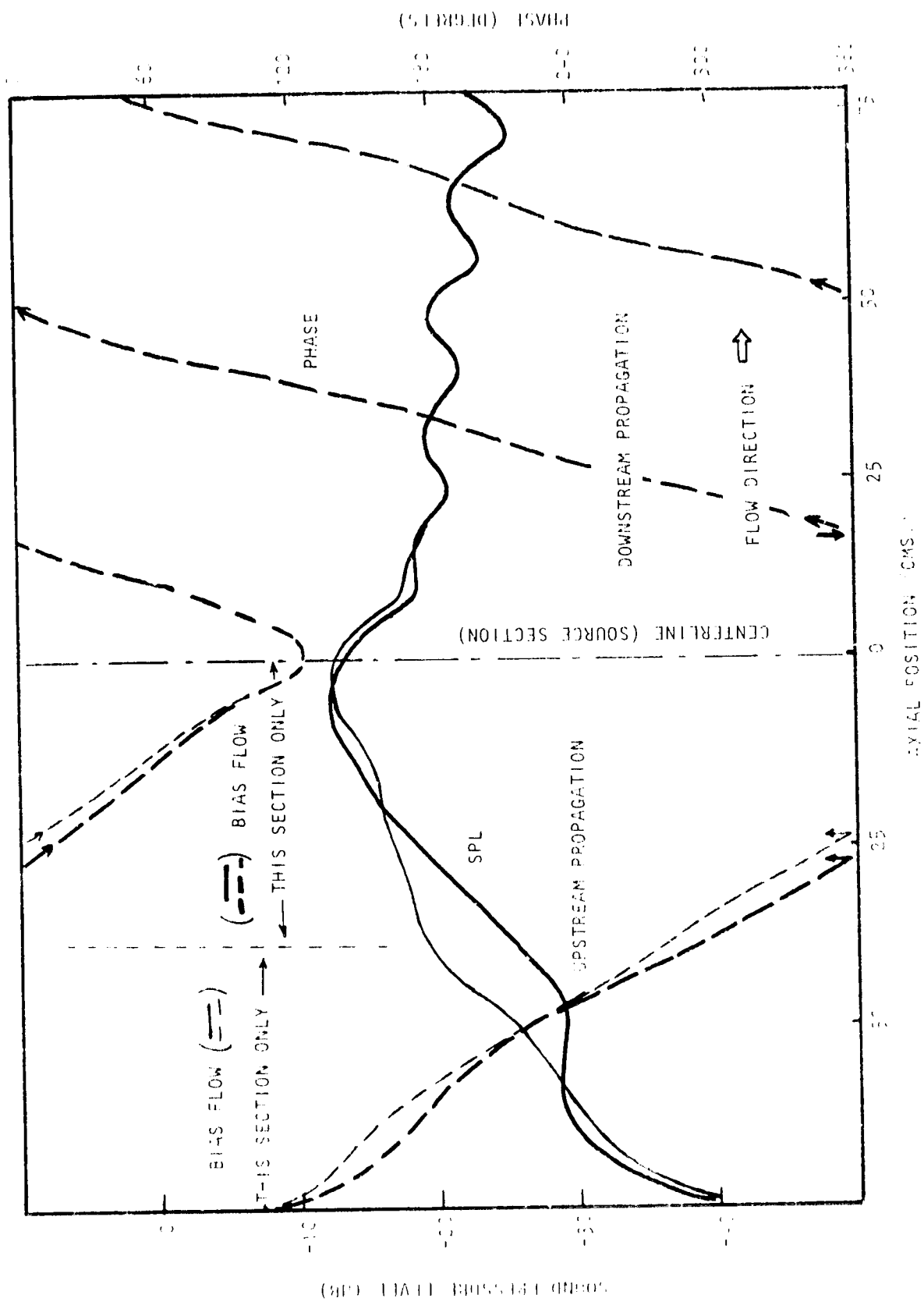


FIGURE 8.218 Axial Sound Pressure and Phase Traverses on Duct Centerline at 50 Hz. Bias flow, $M = 0.15$ (stream only, grazing flow, $M = 0.1$)

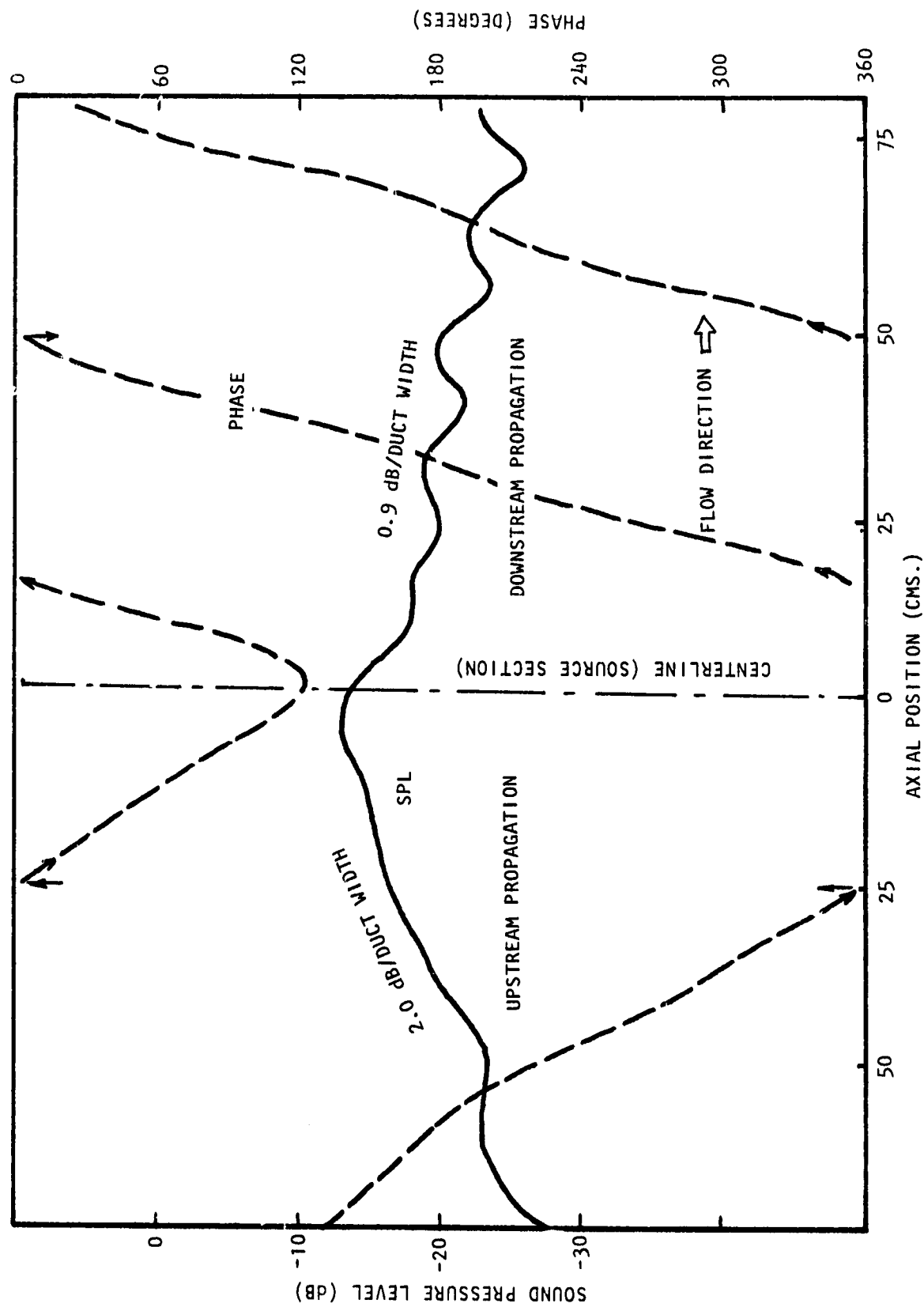


Figure 6.3(a) Axial Sound Pressure and Phase Traverses on Duct Centerline at 800 Hz. Bias Flow $M_i = 0.0$, Grazing Flow $M_{GF} = 0.0$

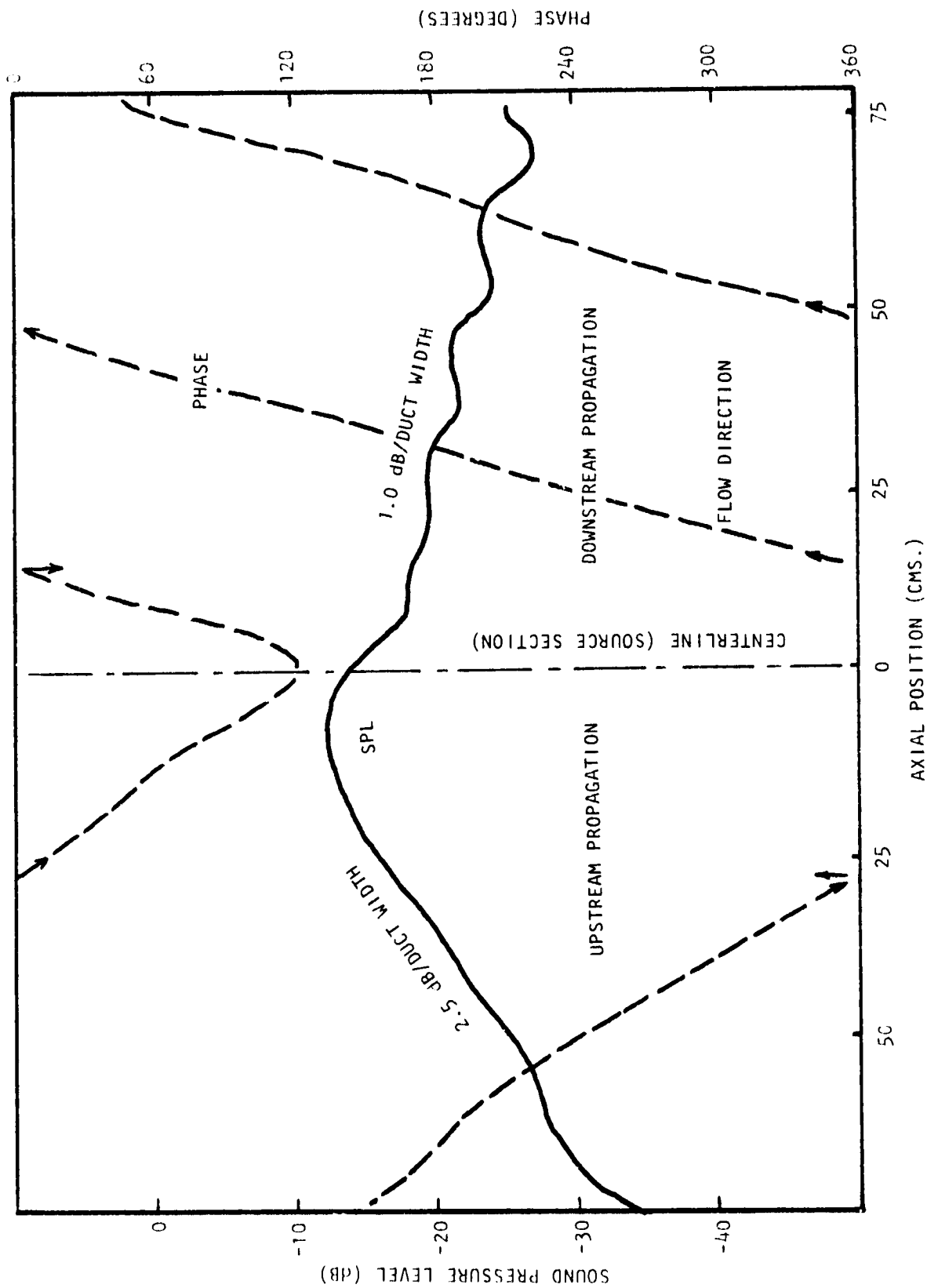


Figure G.3(b) Axial Sound Pressure and Phase Traverses at Duct Centerline at 800 Hz. Bias Flow $M_i = 0.015$, Grazing Flow $M_{GF} = 0.0$

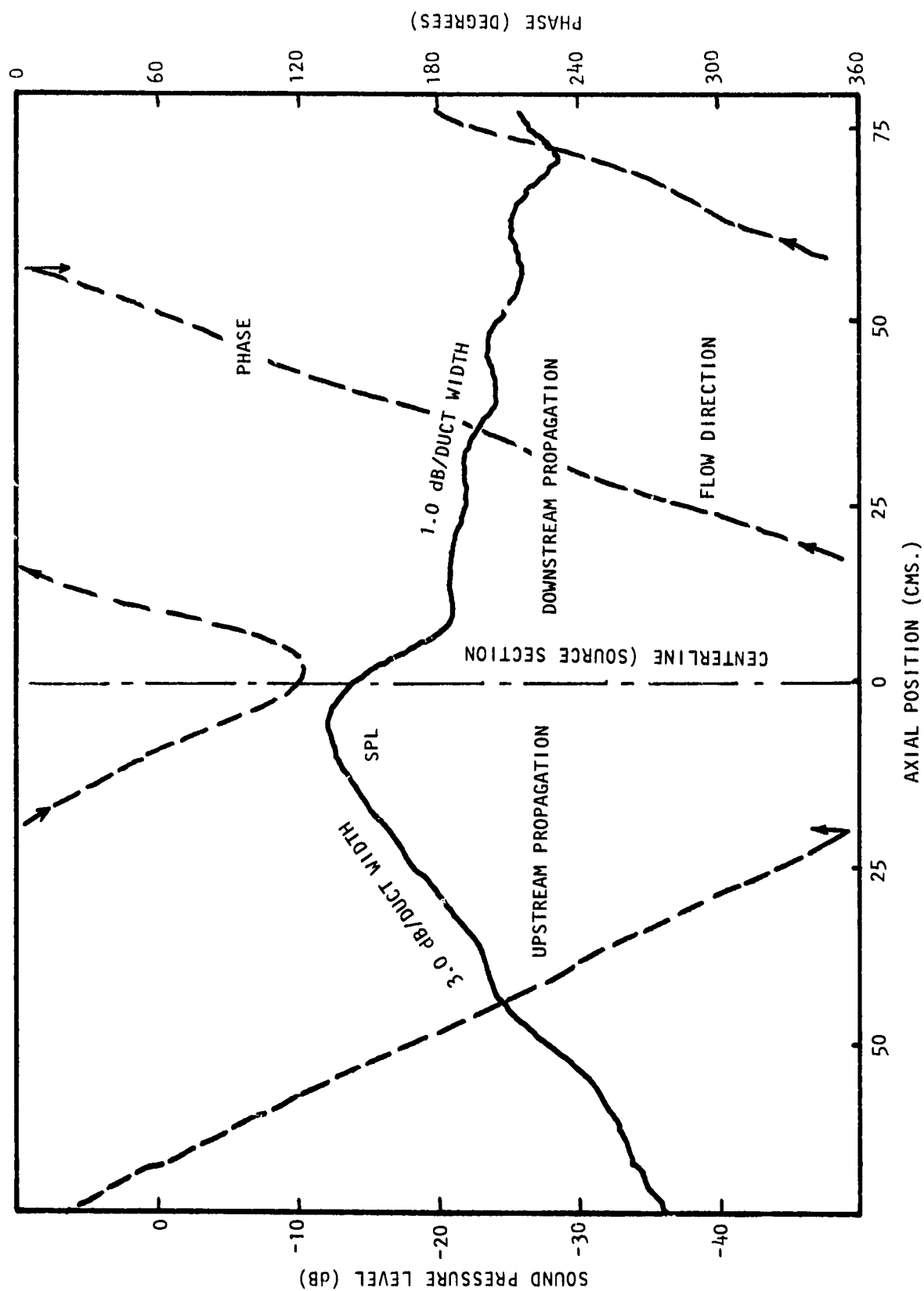


Figure G.3(c) Axial Sound Pressure and Phase Traverses on Duct Centerline at 800 Hz. Bias Flow $M_i = 0.015$, Grazing Flow $M_{GF} = 0.25$

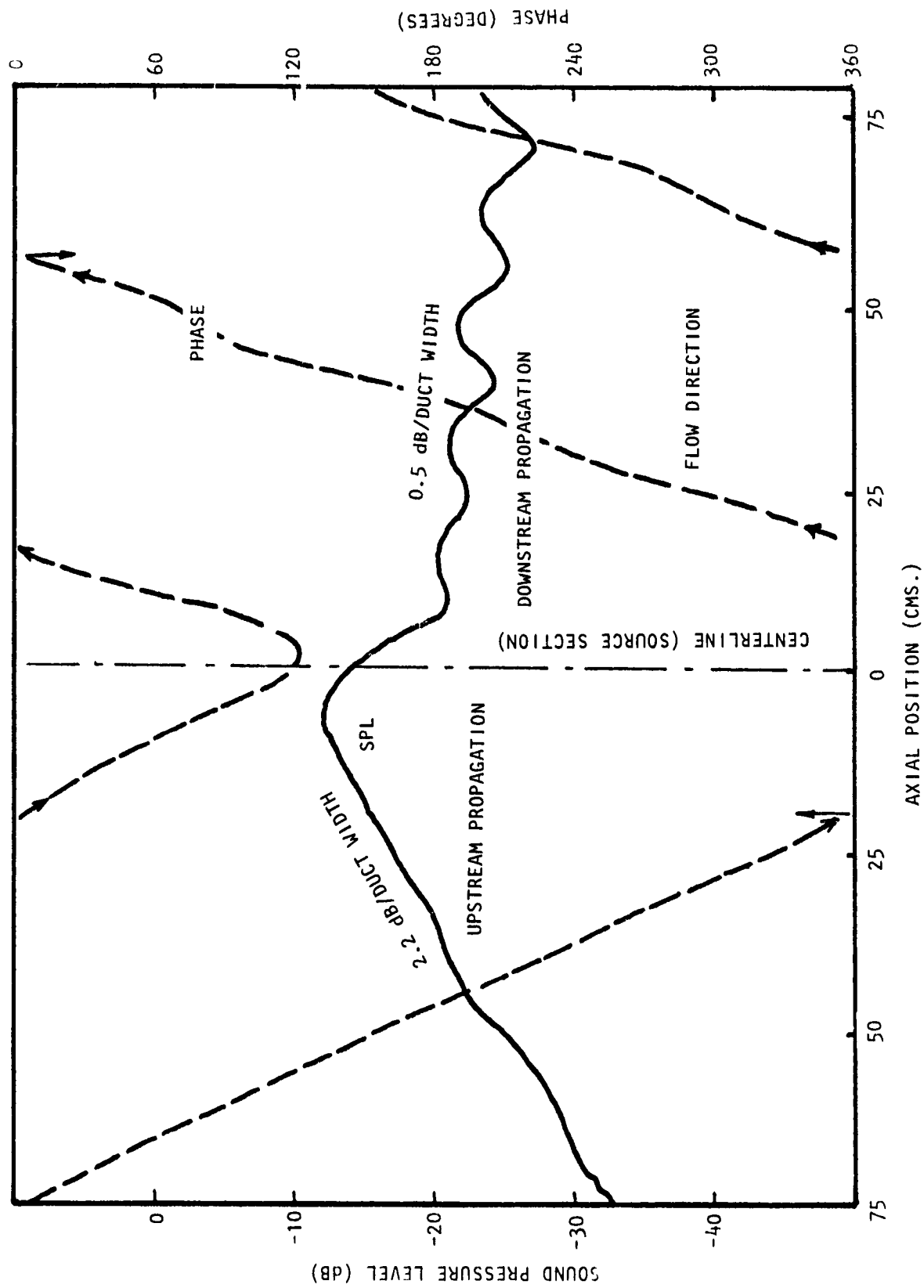


Figure G.3(d) Axial Sound Pressure and Phase Traverses on Duct Centerline at 800 Hz. Bias Flow $M_i = 0.0$, Grazing Flow $M_{GF} = 0.25$

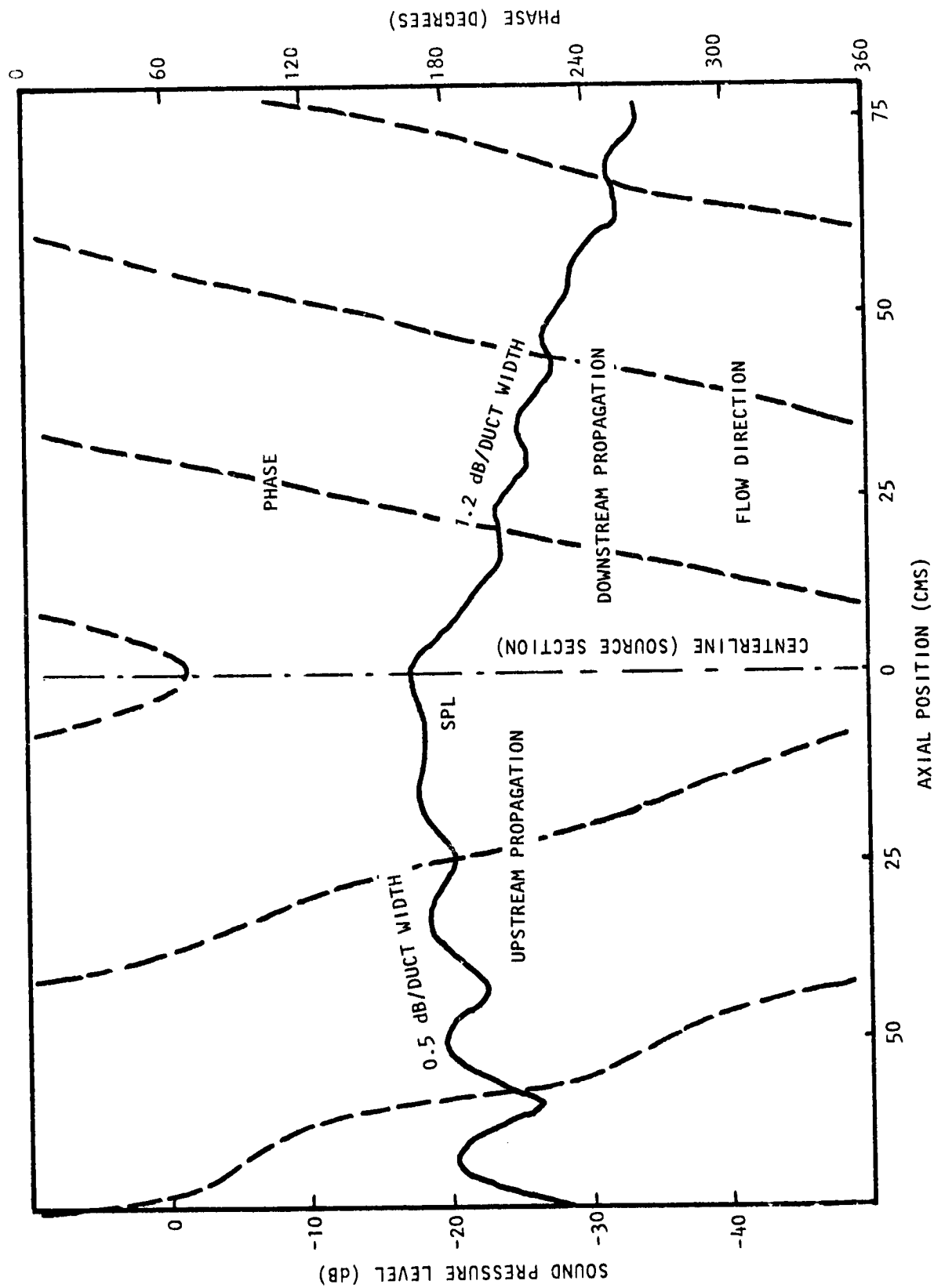


Figure G.4(a) Axial Sound Pressure and Phase Traverses on Duct Centerline at 1000 Hz. Bias Flow $M_i = 0.0$, Grazing Flow $M_{GF} = 0.0$

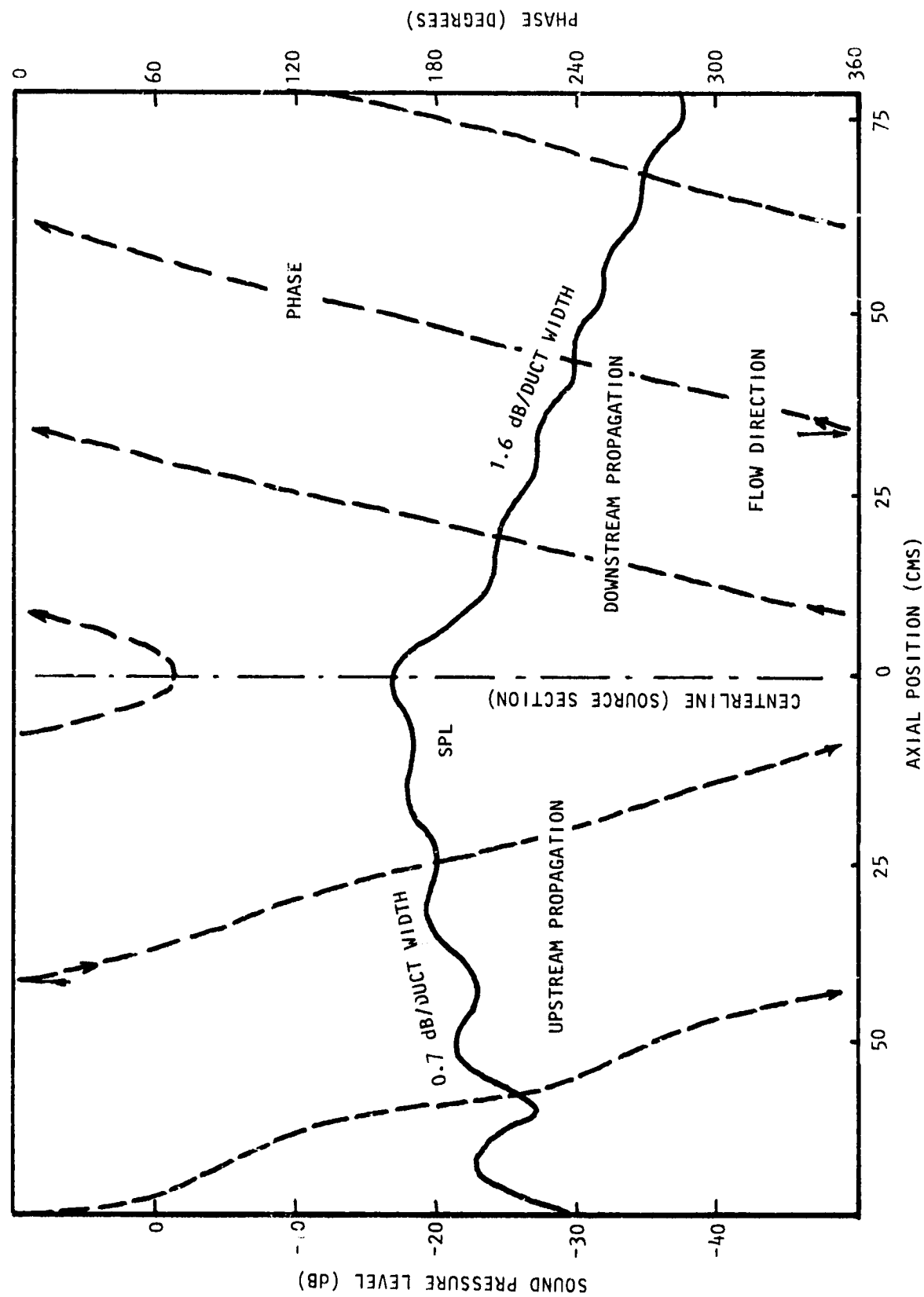


Figure G.4(b) Axial Sound Pressure and Phase Traverses on Duct Centerline at 1000 Hz Bias Flow. $M_j = 0.015$, Grazing Flow $M_{GF} = 0.0$

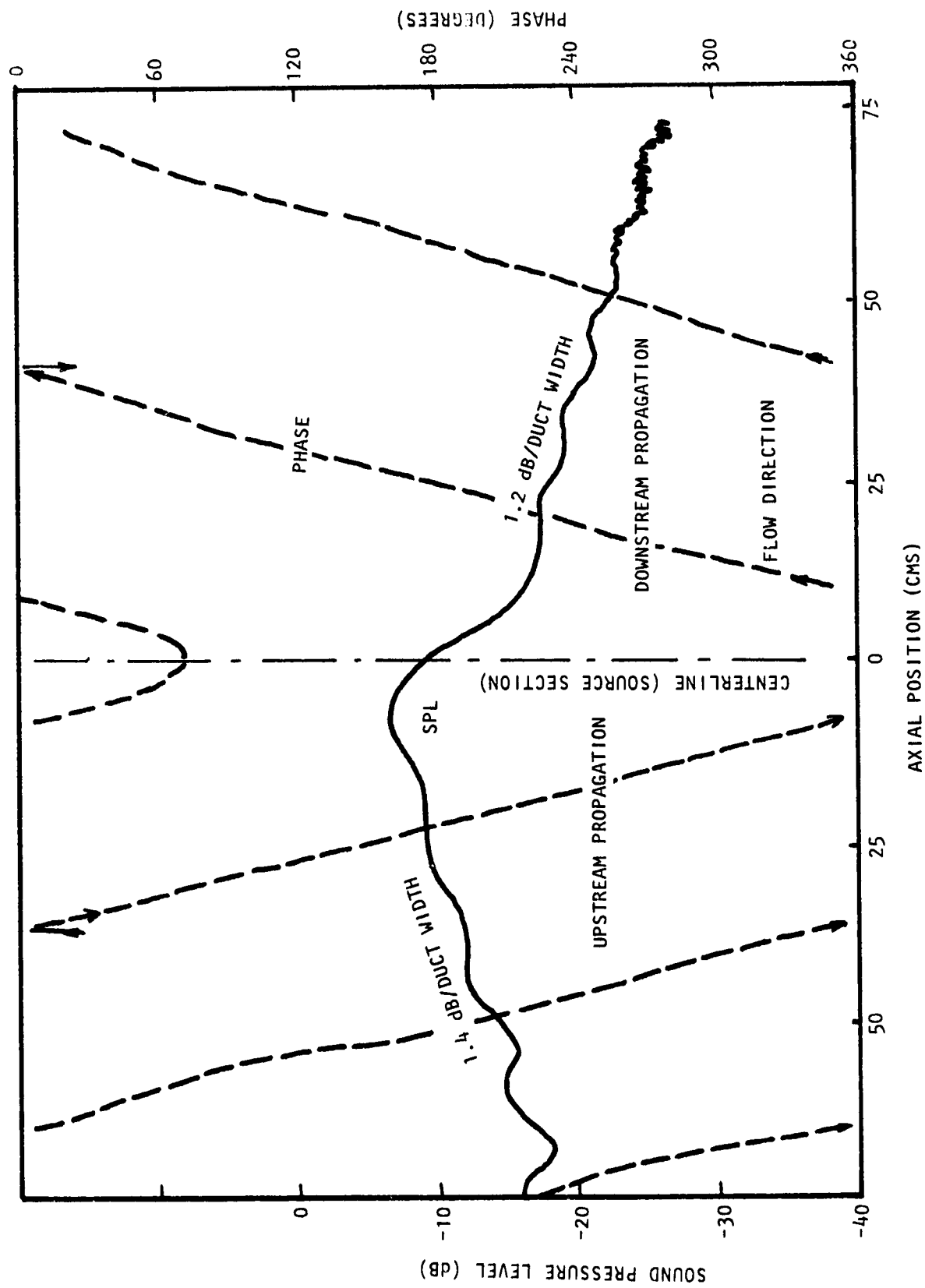


Figure G.4(c) Axial Sound Pressure and Phase Traverses on Duct Centerline at 1000 Hz Bias Flow $M_j = 0.015$, Grazing Flow $MGF = 0.25$

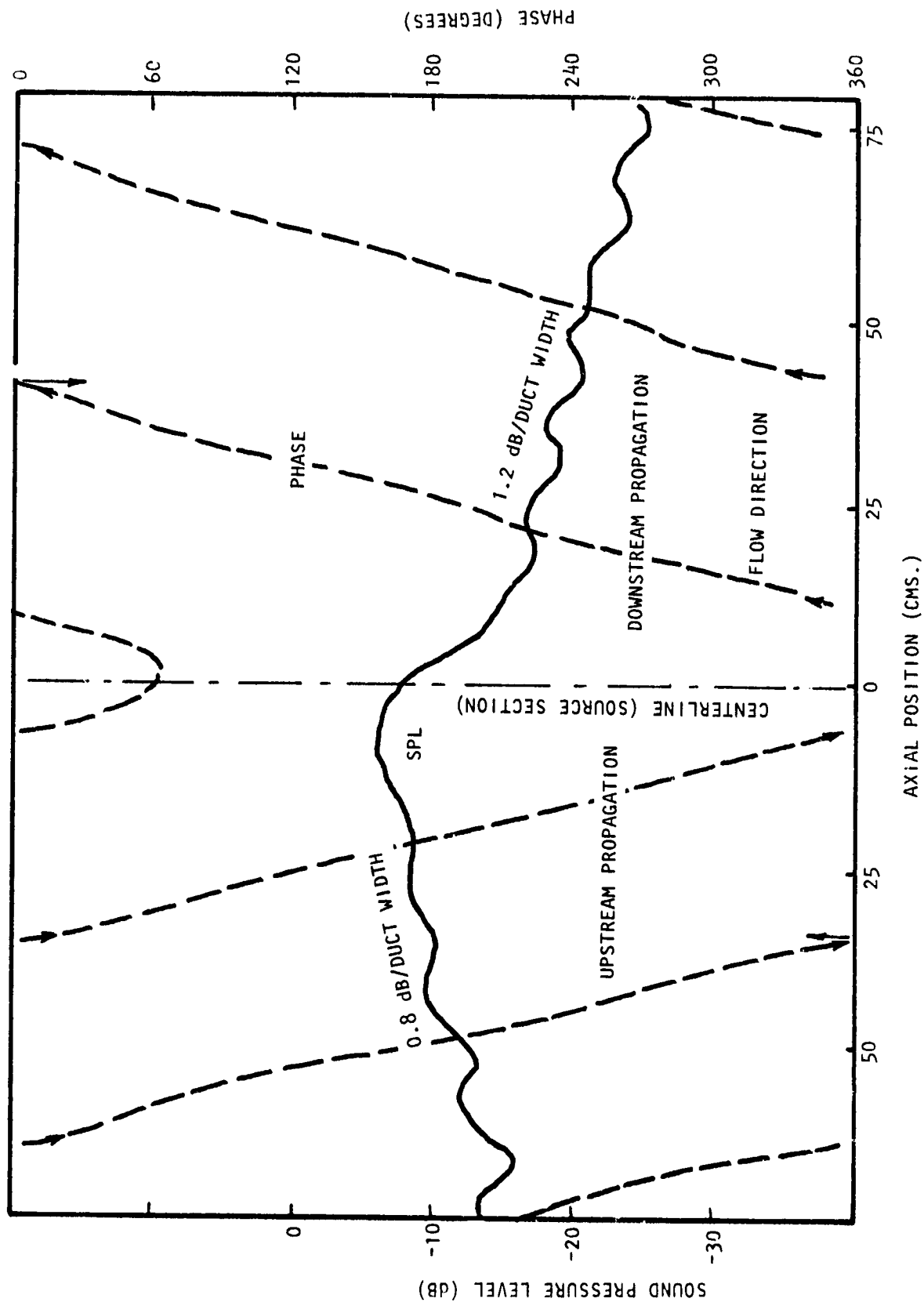


Figure G.4(d) Axial Sound Pressure and Phase Traverses on Duct Centerline at 1000 Hz. Bias Flow $M_i = 0.0$, Grazing Flow $M_{GF} = 0.25$

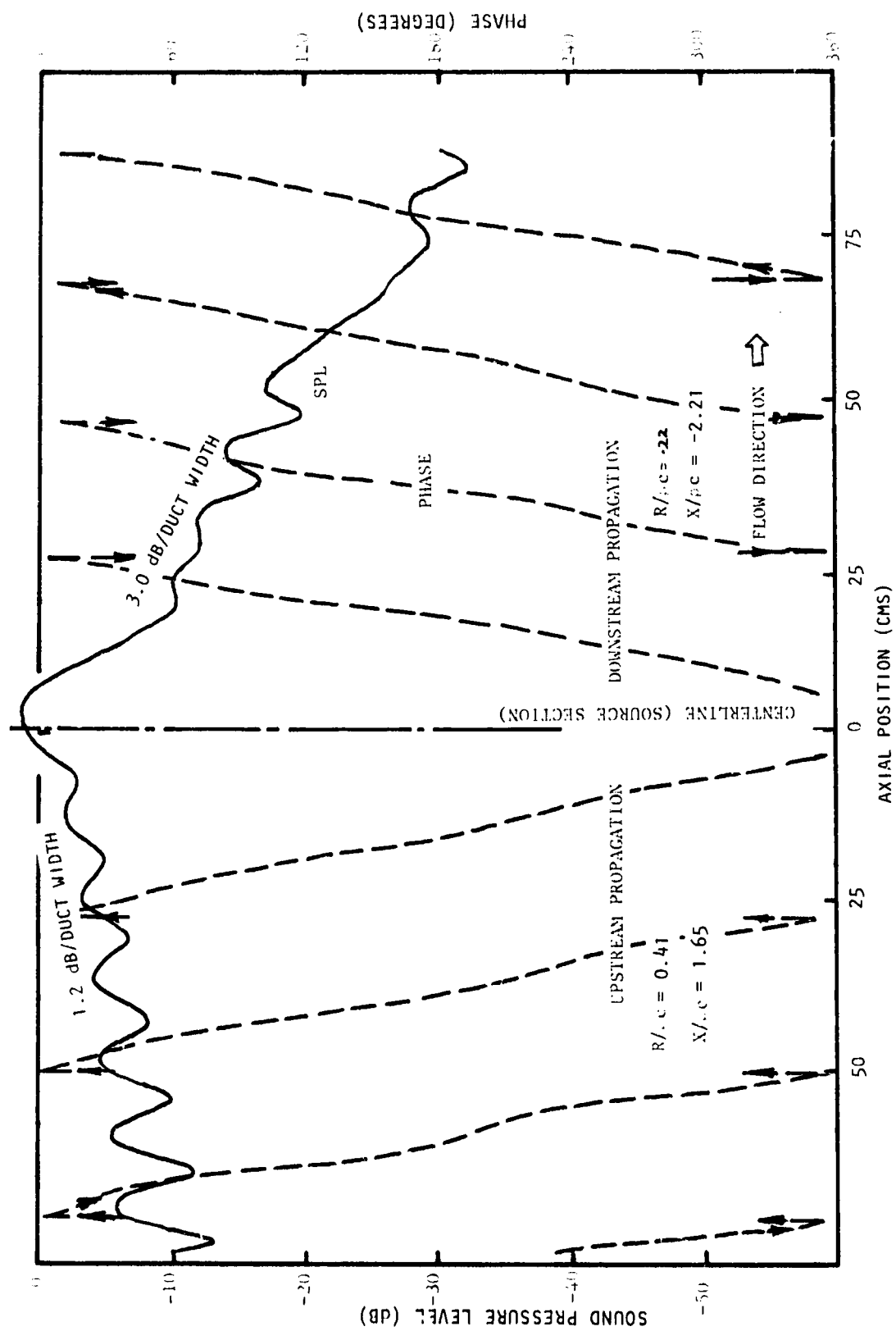


Figure G.5(a) Axial Sound Pressure and Phase Traverses on Duct Centerline at 1250 Hz. Bias Flow $M_i = 0.0$, Grazing Flow $M_{GF} = 0.0$

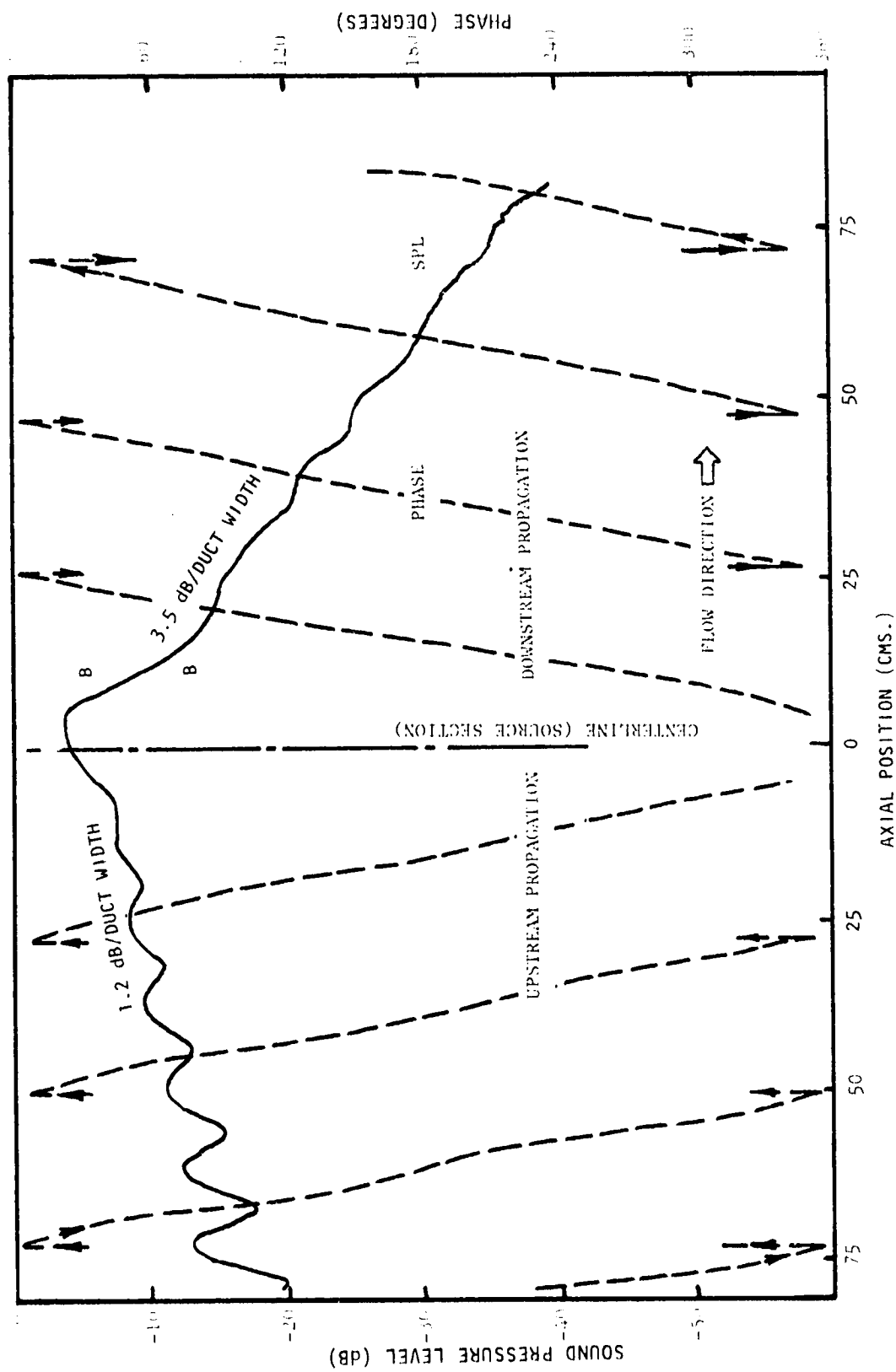


Figure 6.5(b) Axial Sound Pressure and Phase Traverses on Duct Centerline at 1250 Hz. Bias Flow $M_1 = 0.015$, Grazing Flow $M_{GF} = 0.0$

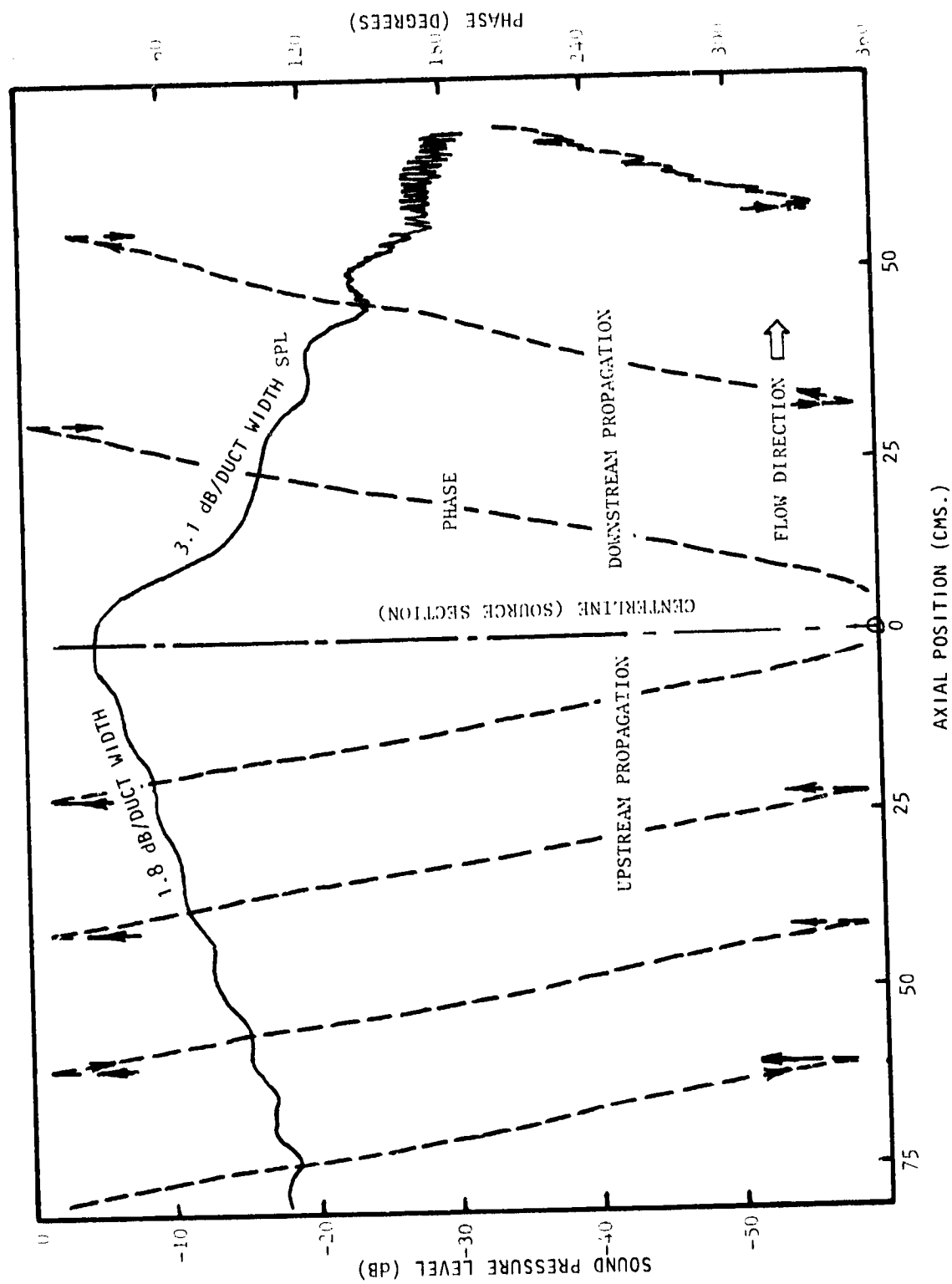


Figure G.5(c) Axial Sound Pressure and Phase Traverses on Duct Centerline at 1250 Hz. Bias Flow $M_i = 0.015$, Grazing Flow $M_{GF} = 0.25$

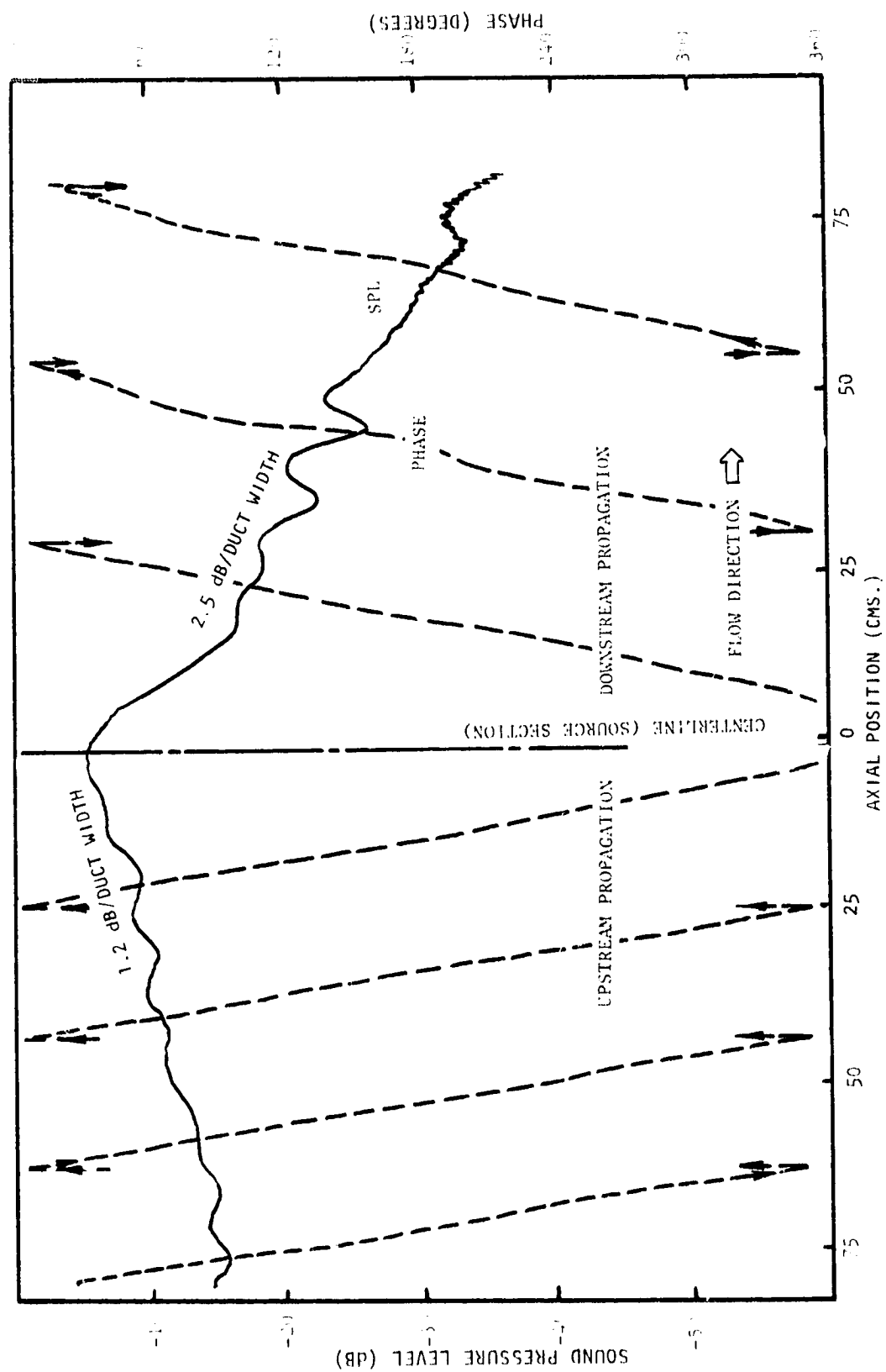


Figure G.5(d) Axial Sound Pressure and Phase Traverses on Duct Centerline at 1250 Hz. Bias Flow $M_i = 0.0$, Grazing Flow $M_{GF} = 0.25$

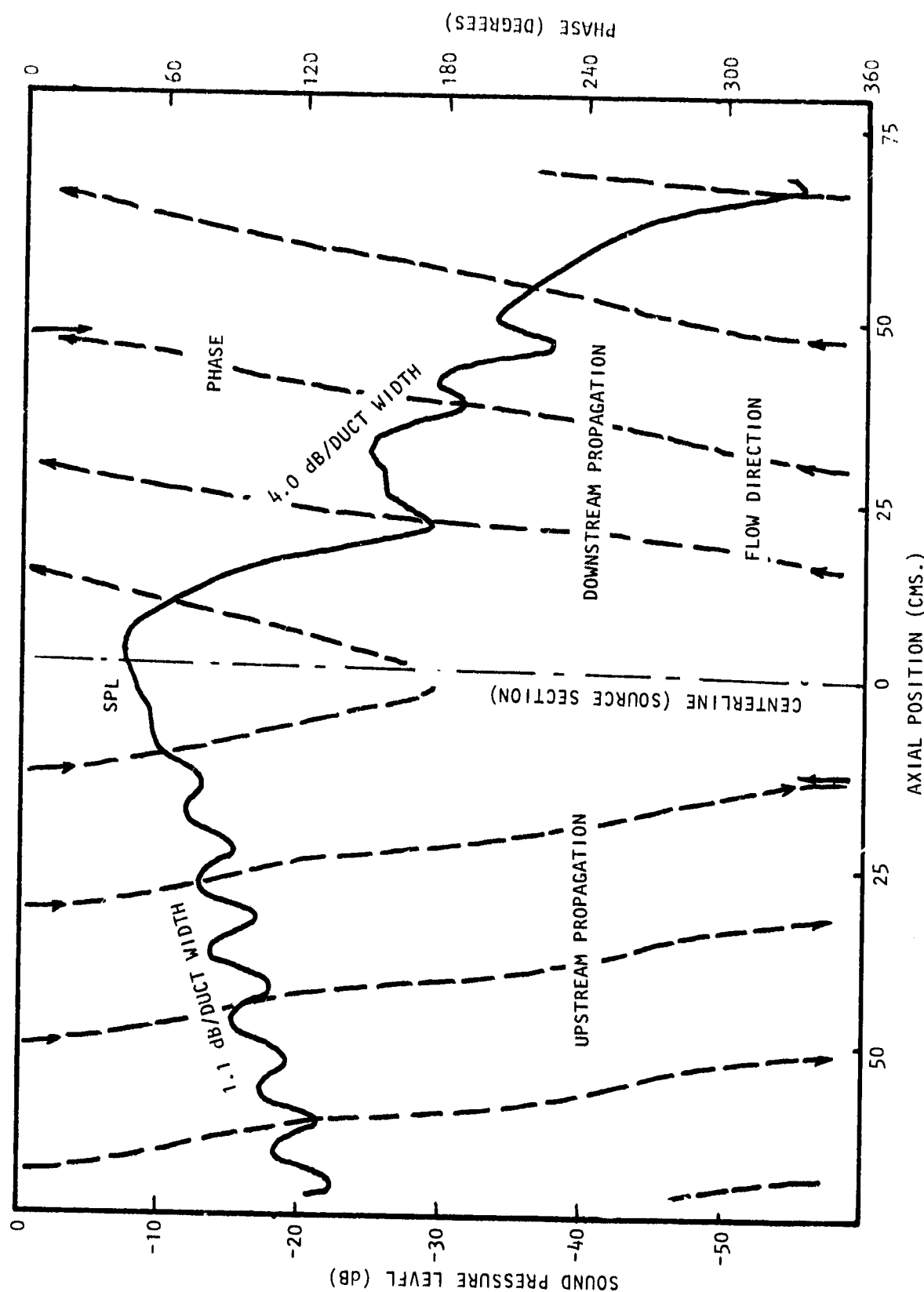


Figure G.6(a) Axial Sound Pressure and Phase Traverses on Duct Centerline at 1400 Hz. Bias Flow $M_i = 0.0$, Grazing Flow $M_{GF} = 0.0$

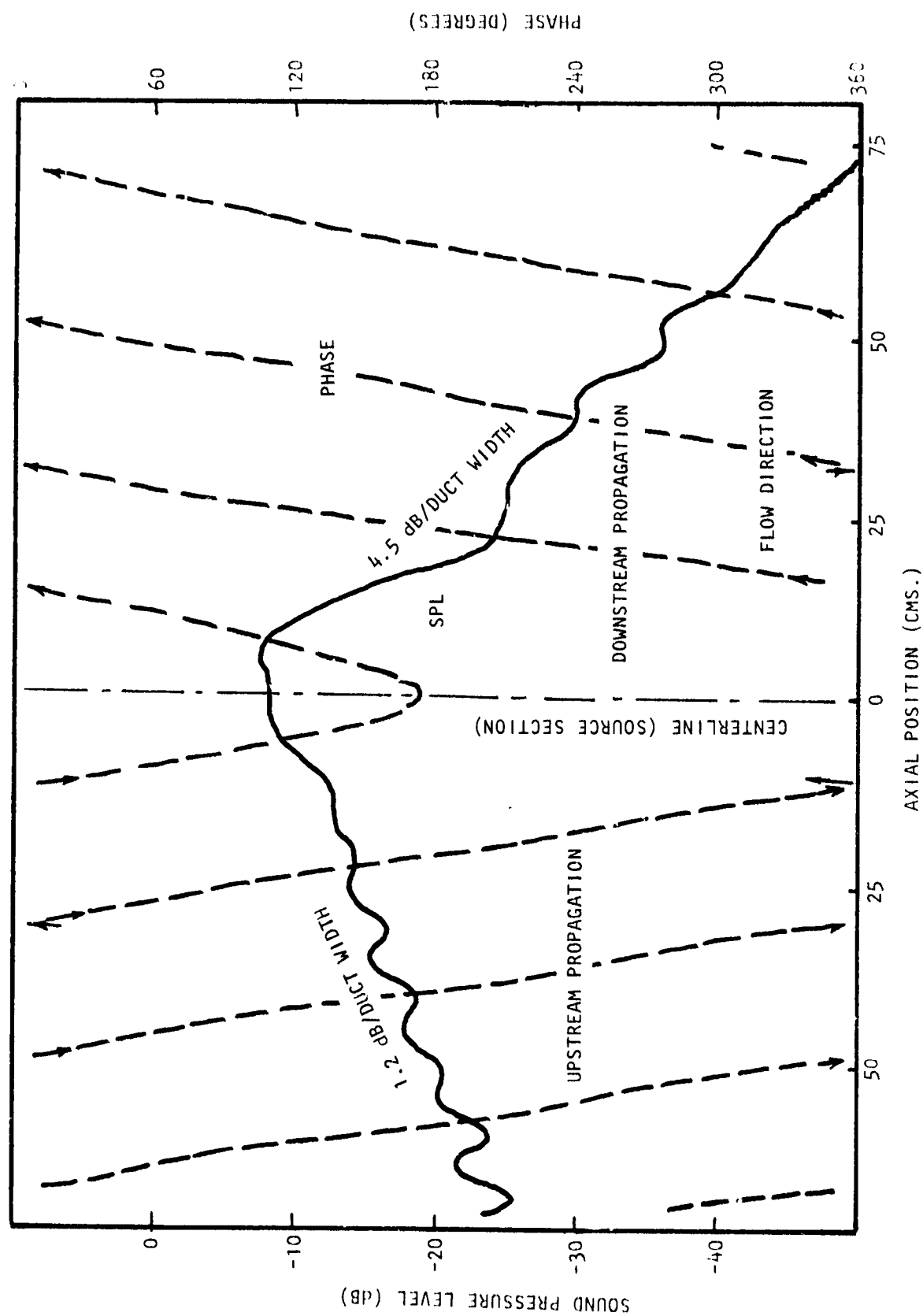


Figure G.6(b) Axial Sound Pressure and Phase Traverses on Duct Centerline at 1400 Hz. Bias Flow $M_i = 0.015$, Grazing Flow $M_{GF} = 0.0$

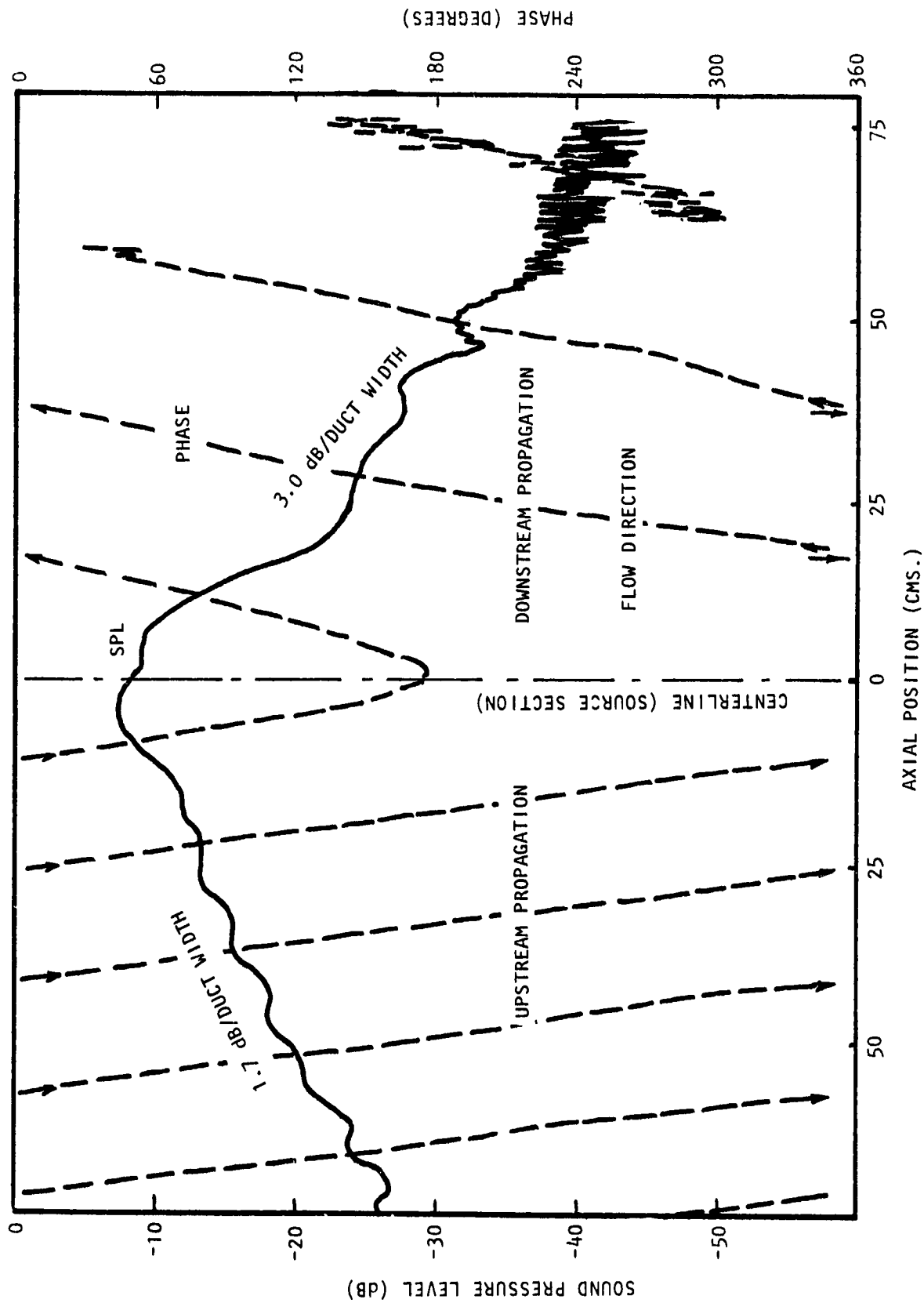


Figure G.6(c) Axial Sound Pressure and Phase Traverses on Duct Centerline at 1400 Hz. Bias Flow $M_j = 0.015$, Grazing Flow $M_{GF} = 0.25$

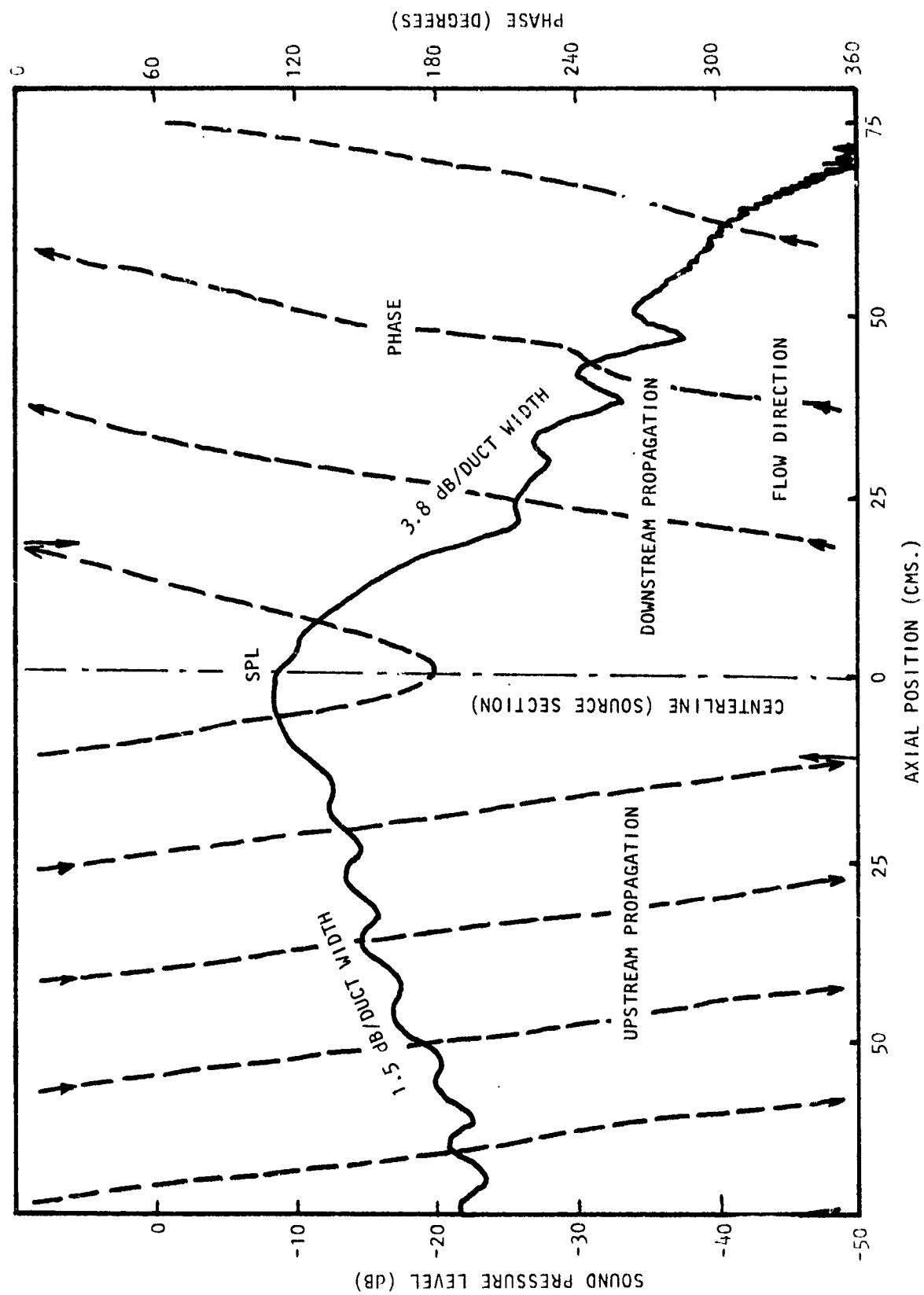


Figure 6.6(d) Axial Sound Pressure and Phase Traverses on Duct Centerline at 1400 Hz. Bias Flow $M_i = 0.0$, Grazing Flow $M_{GF} = 0.25$

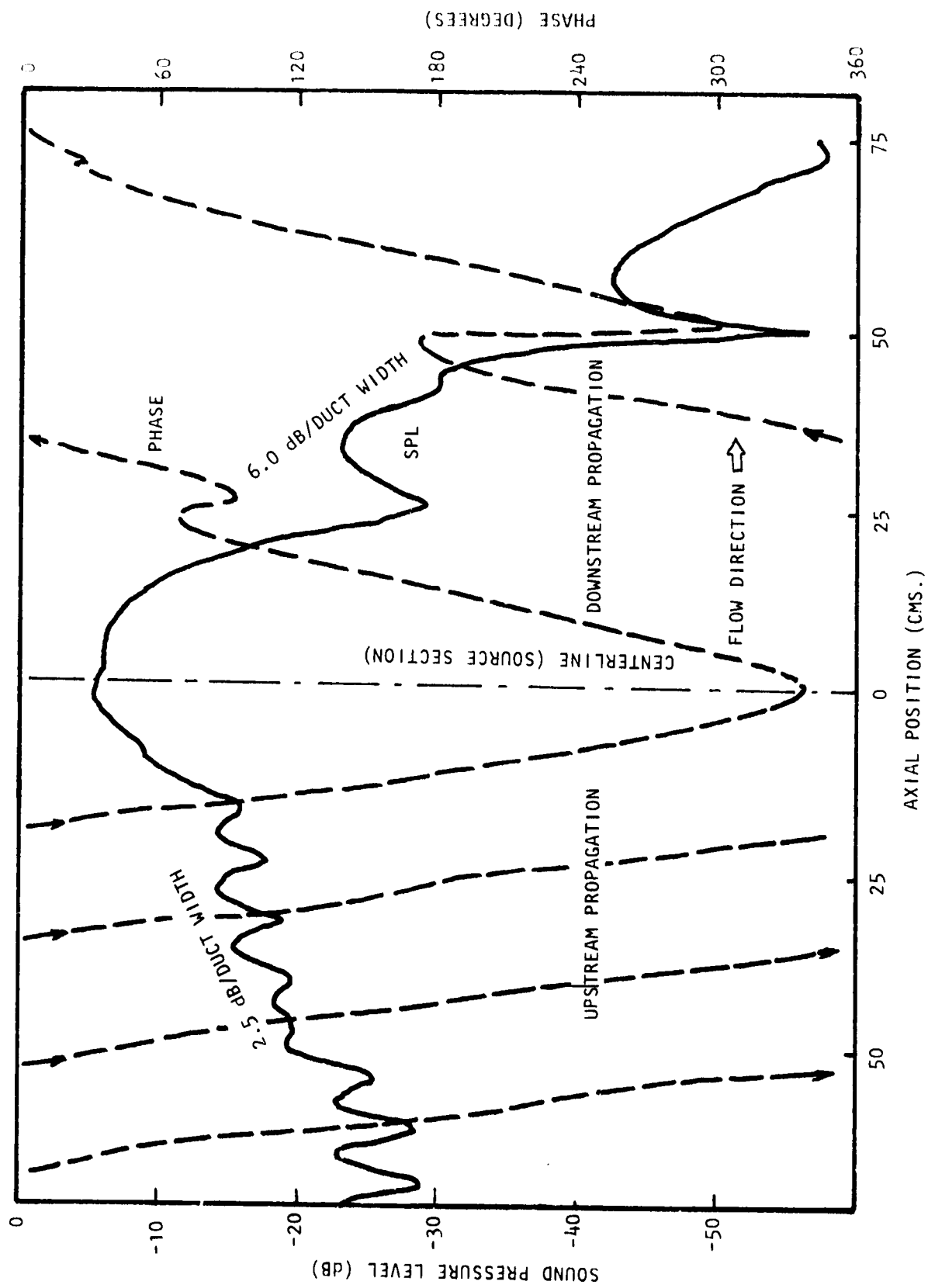


Figure 6.7(a) Axial Sound Pressure and Phase Traverses on Duct Centerline at 1500 Hz. Bias Flow $M_i = 0.0$, Grazing Flow $M_{GF} = 0.0$

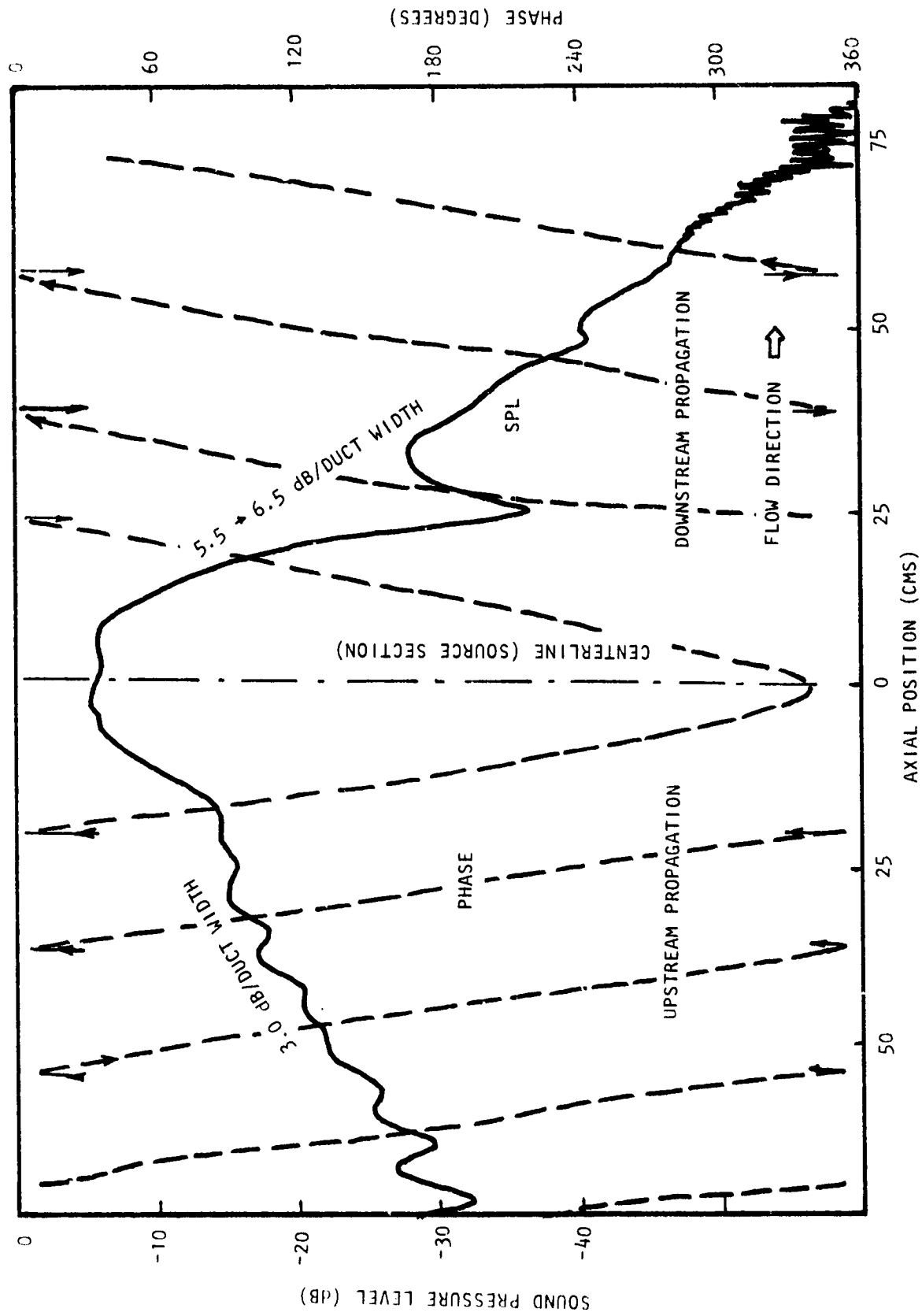


Figure G.7(b) Axial Sound Pressure and Phase Traverses on Duct Centerline at 1500 Hz. Bias Flow $M_i = 0.015$, Grazing Flow $M_{GF} = 0.0$

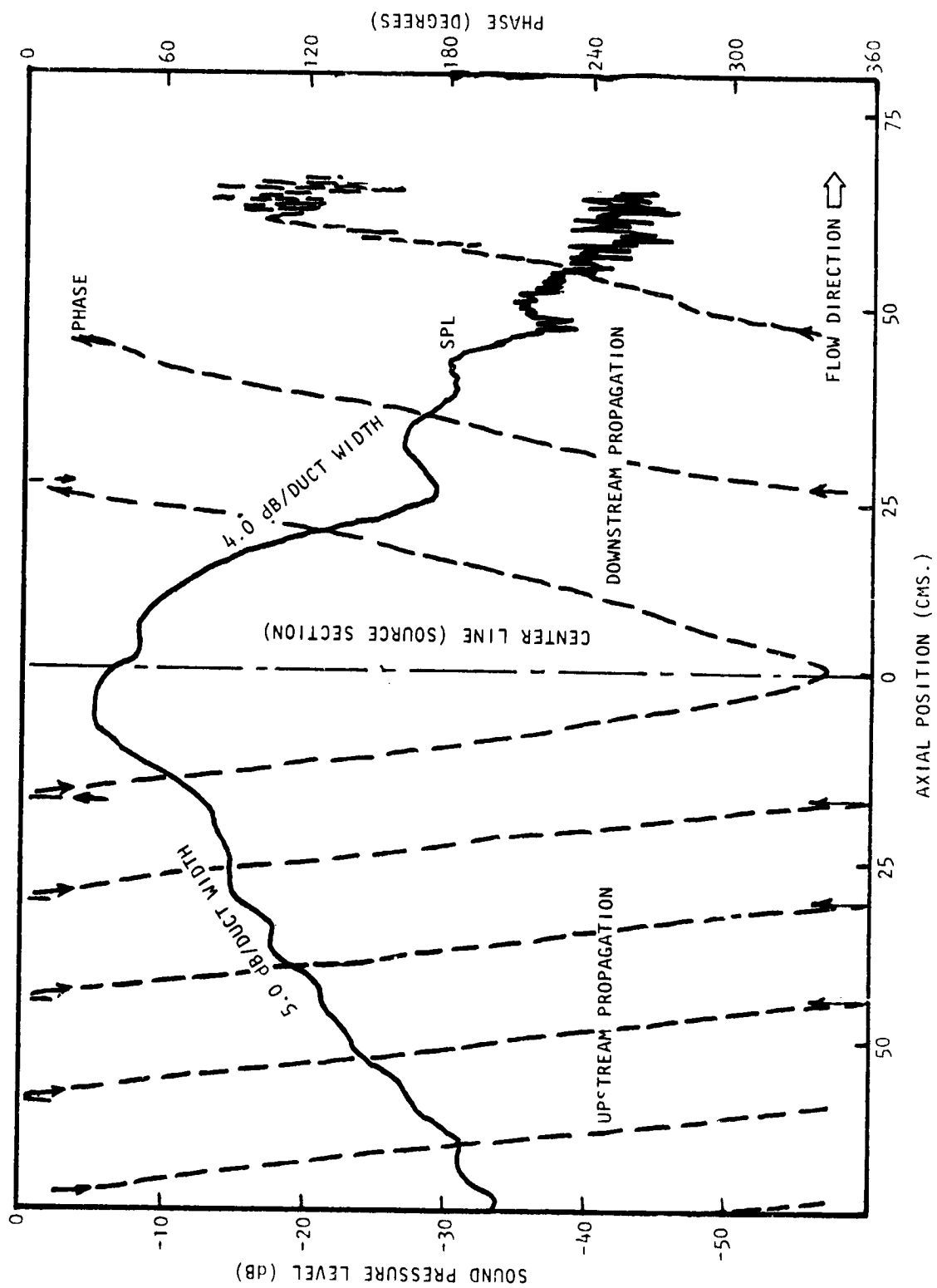


Figure 6.7(c) Axial Sound Pressure and Phase Traverses on Duct Centerline at 1500 Hz. Bias Flow $M_i = 0.015$, Grazing Flow $M_{GF} = 0.25$

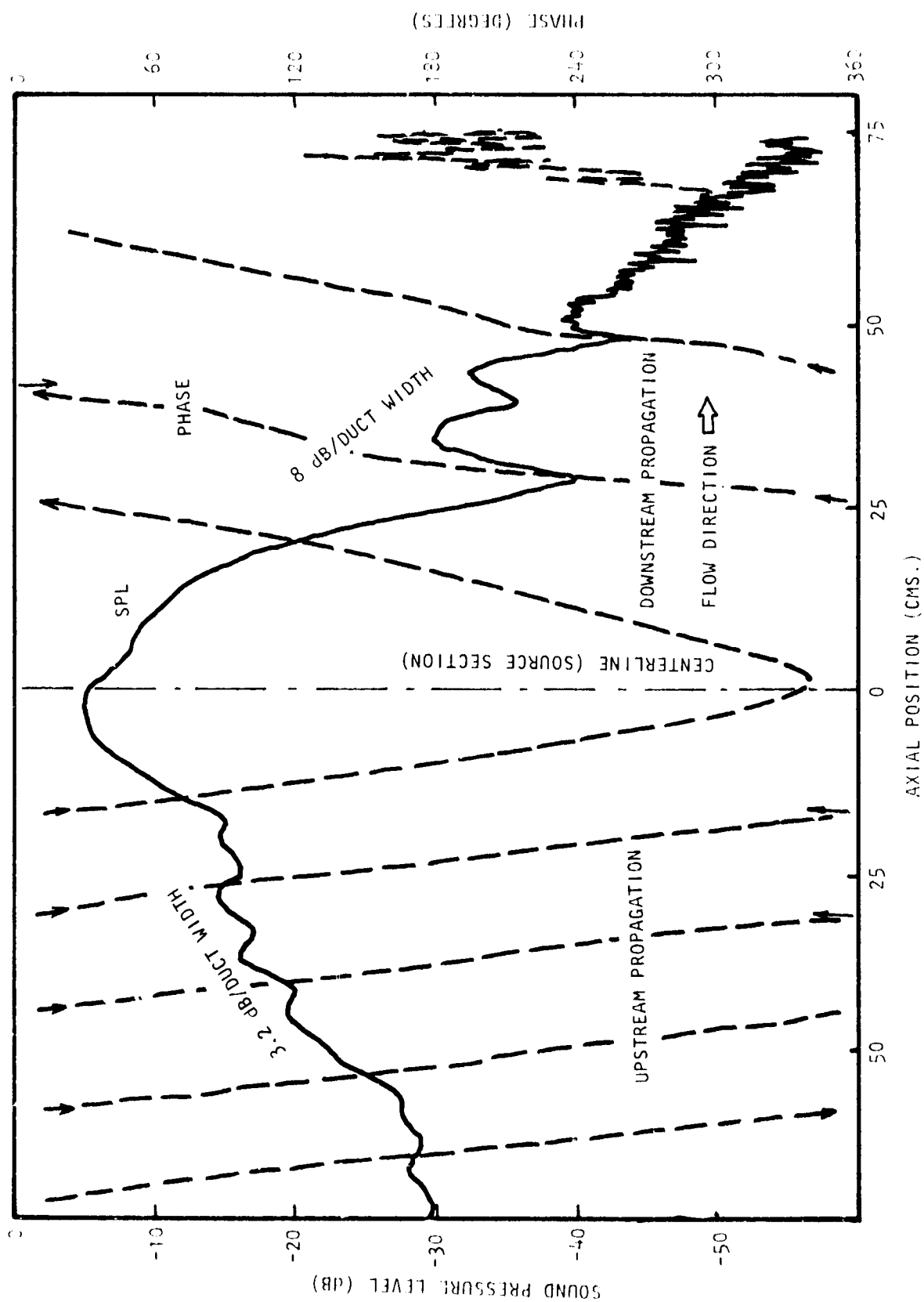


Figure G.7(d) Axial Sound Pressure and Phase Traverses on Duct Centerline at 1500 Hz. Bias Flow $M_i = 0.0$, Grazing Flow $M_{GF} = 0.25$

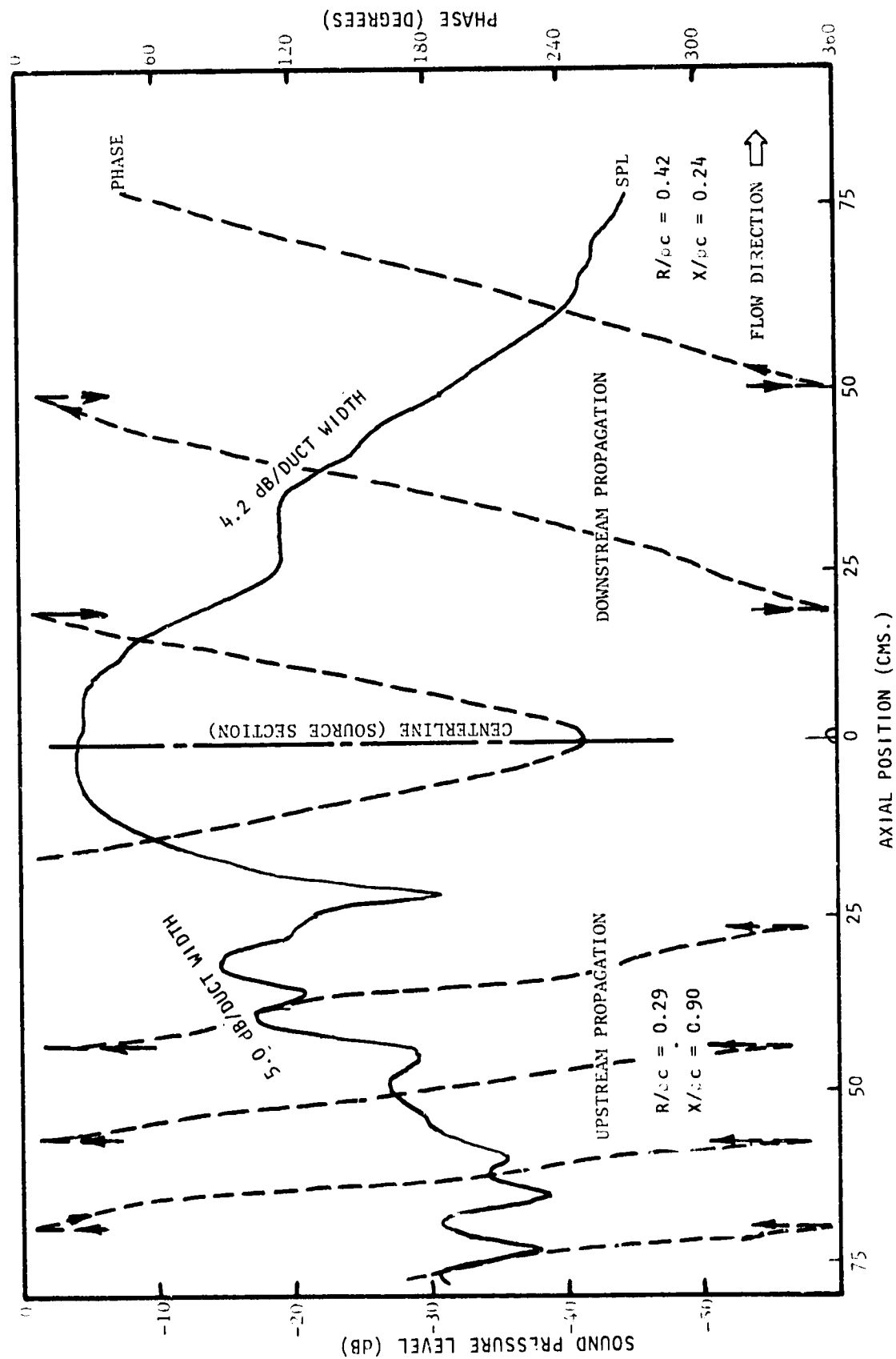


Figure G.8(a) Axial Sound Pressure and Phase Traverses on Duct Centerline at 1600 Hz. Bias Flow $M_i = 0.0$, Grazing Flow $M_{GF} = 0.0$

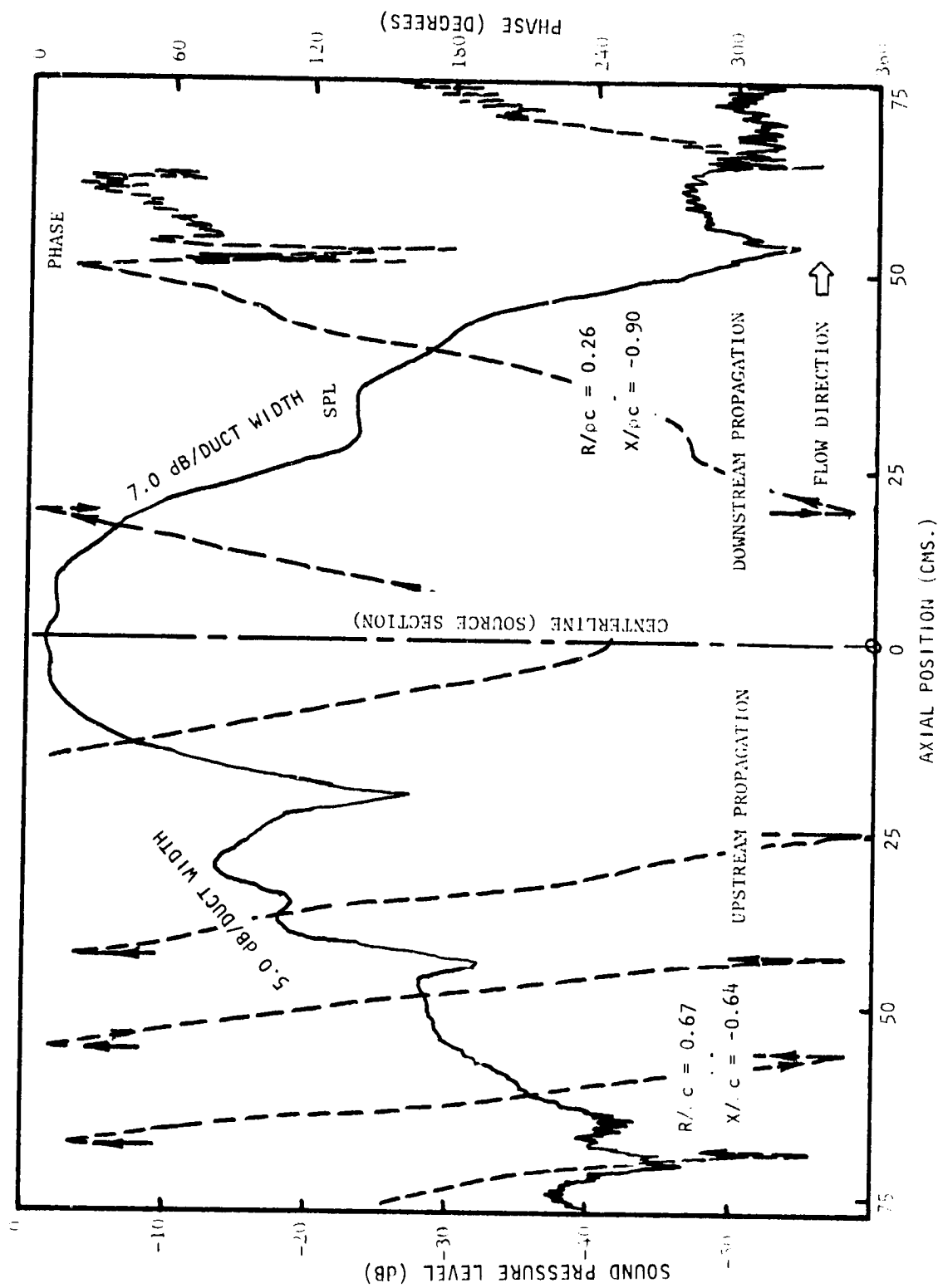


Figure G.8(b) Axial Sound Pressure and Phase Traverses on Duct Centerline at 1600 Hz. Bias Flow $M_i = 0.015$, Grazing Flow $M_{GF} = 0.0$

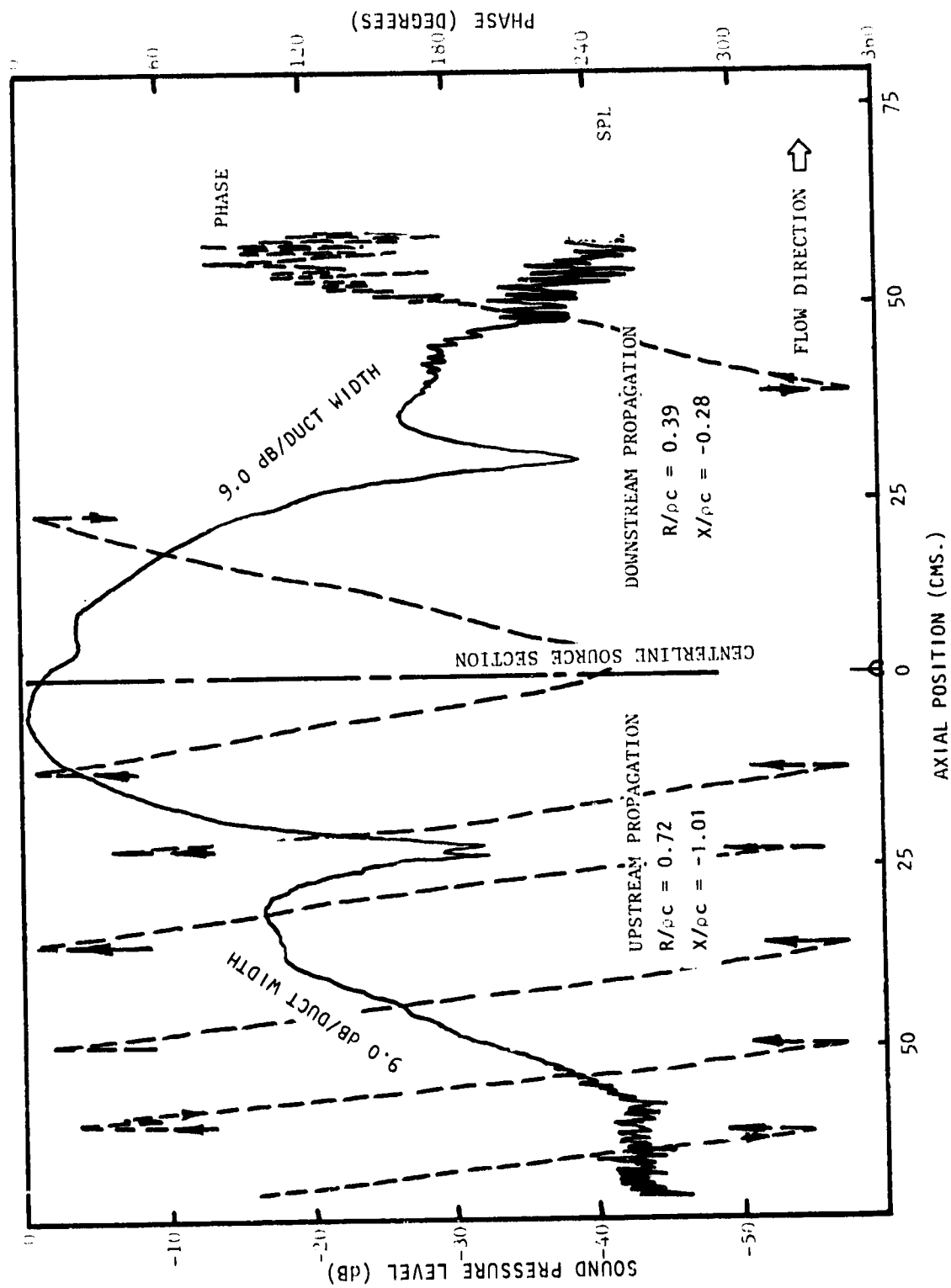


Figure G.8(c) Axial Sound Pressure and Phase Traverses on Duct Centerline at 1600 Hz. Bias Flow $M_j = 0.015$, Grazing Flow $M_{GF} = 0.25$

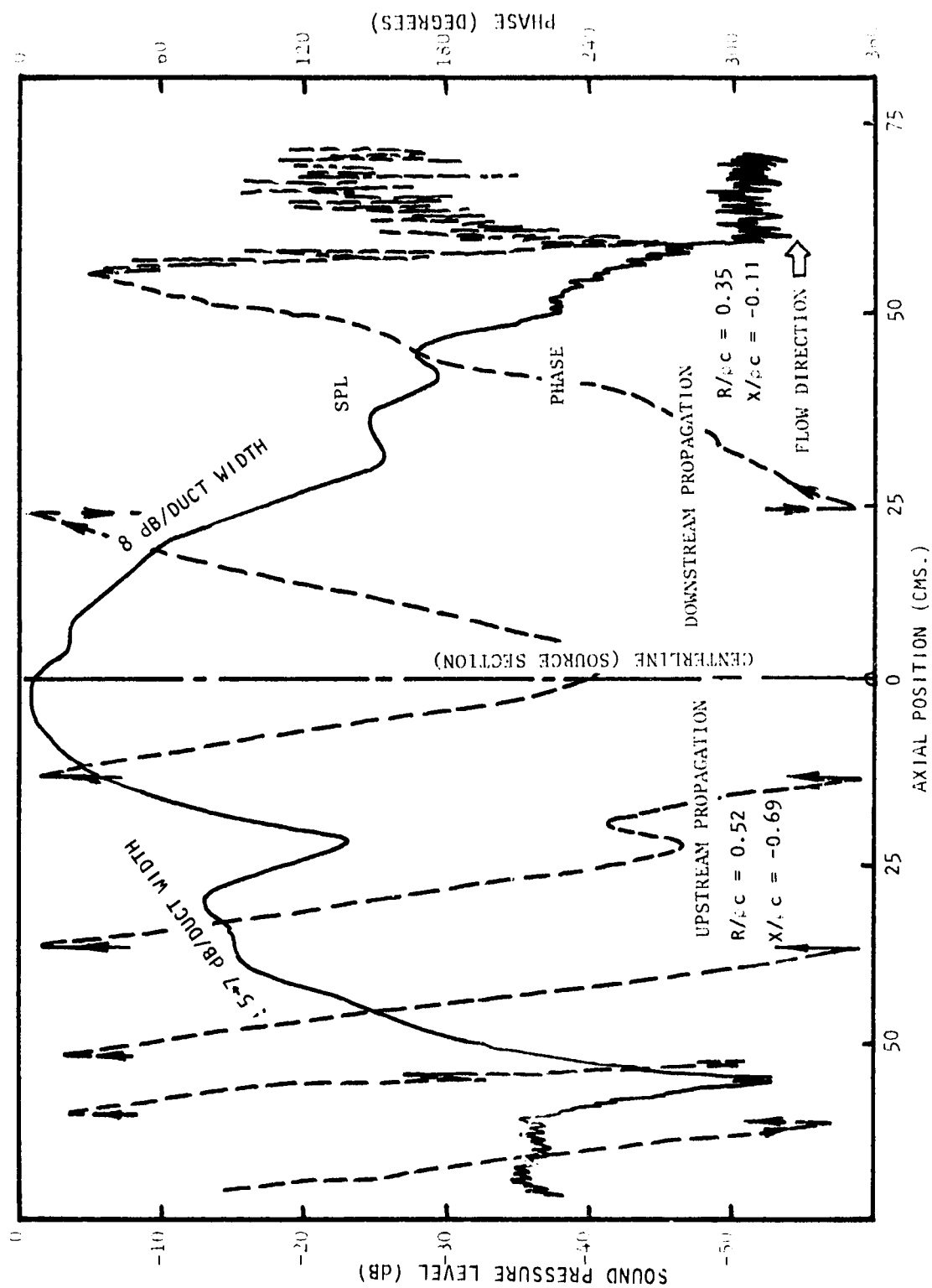


Figure G.8(d) Axial Sound Pressure and Phase Traverses on Duct Centerline at 1600 Hz Bias Flow $M_j = 0.0$, Grazing Flow $M_{GF} = 0.25$

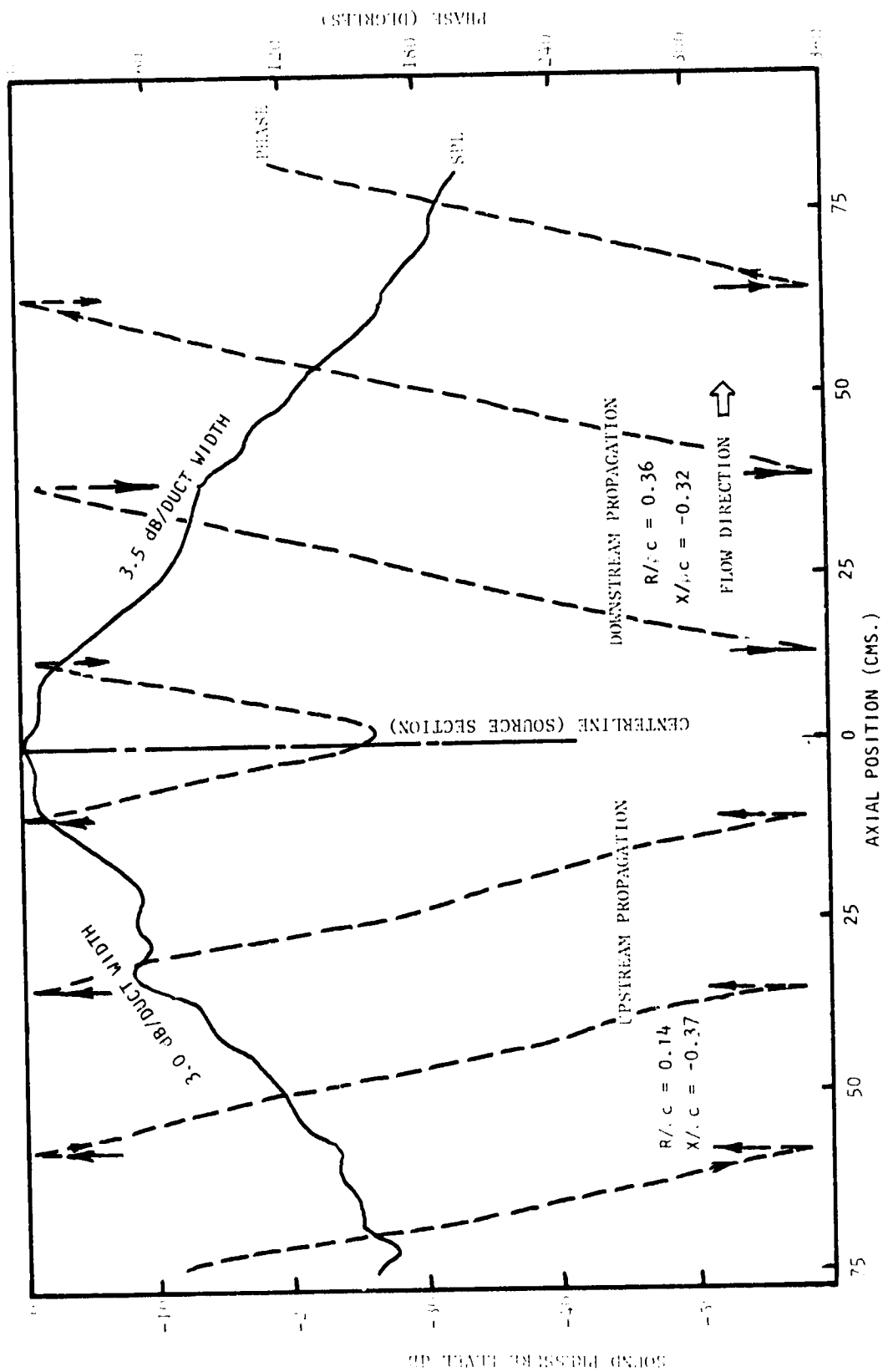


Figure 6.9(a) Axial Sound Pressure and Phase Traverses on Duct Centerline at 1700 Hz. Bias Flow $M_i = 0.0$, Grazing Flow $M_g = 0.0$

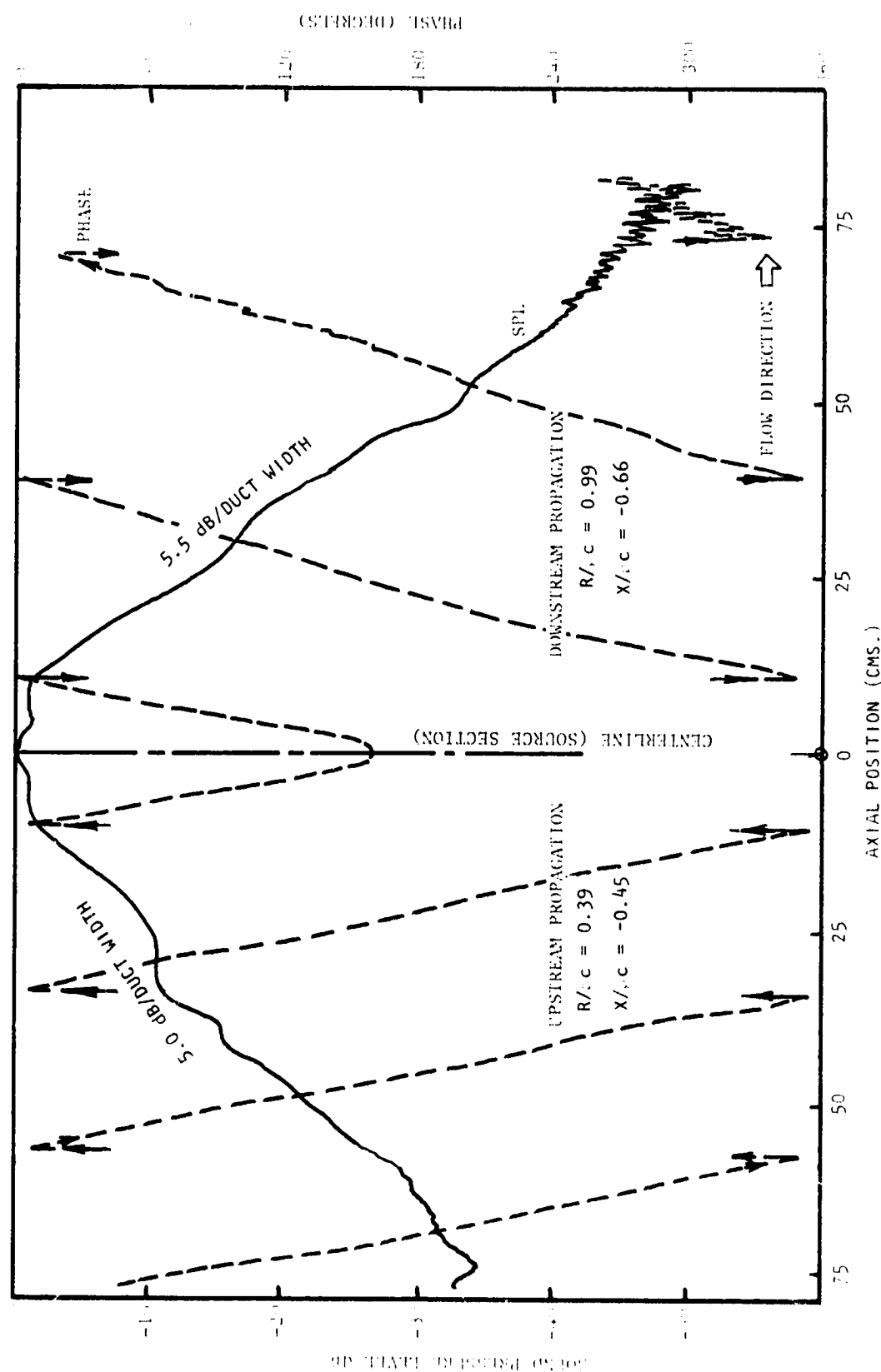


Figure G.9(b) Axial Sound Pressure and Phase Traverses on Duct Centerline at 1700 Hz. Bias Flow $M_j = 0.015$, Grazing Flow, $M_{GF} = 0.0$

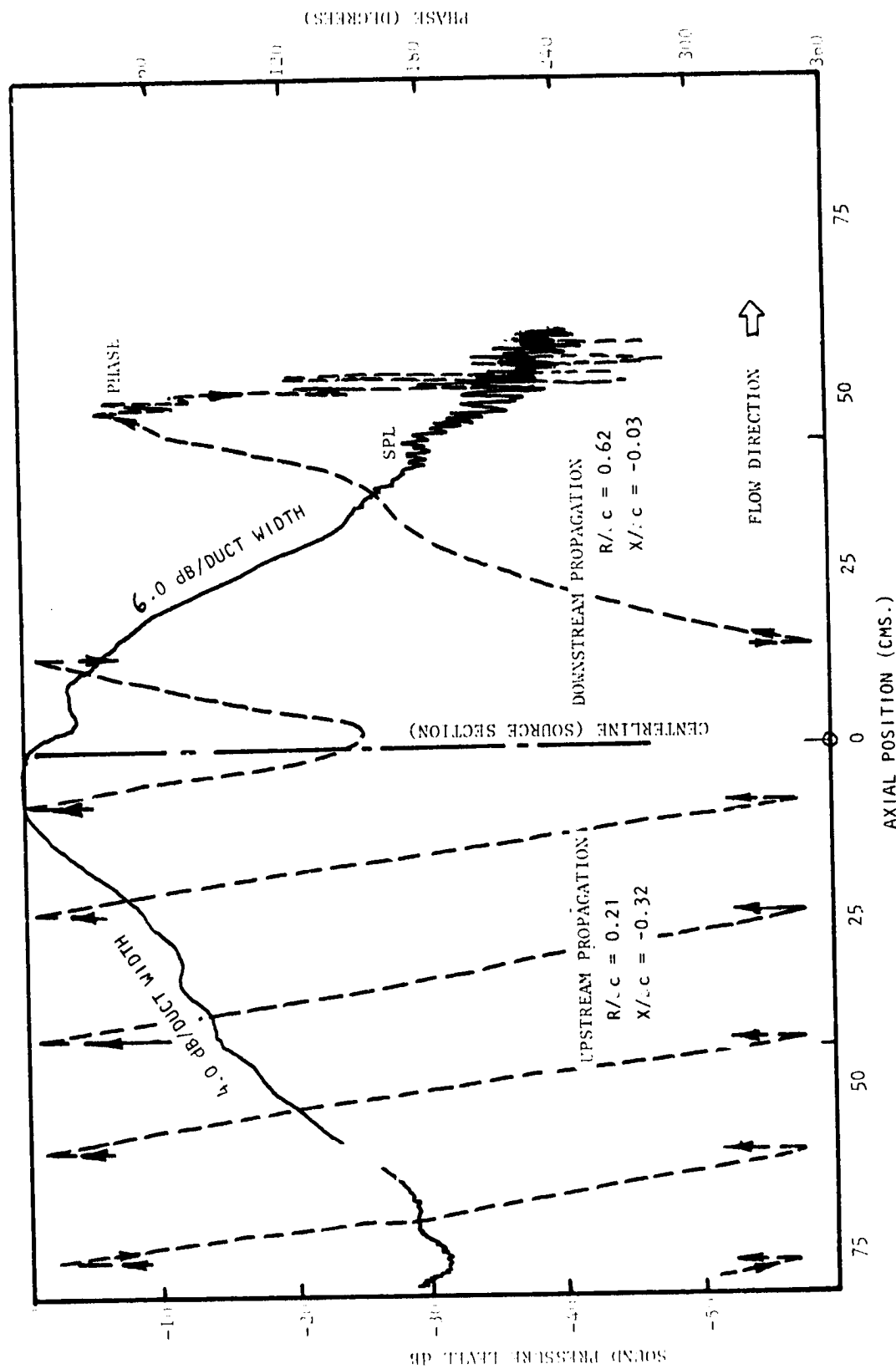


Figure G.9(c) Axial Sound Pressure and Phase Traverses on Duct Centerline at 1700 Hz. Bias Flow $M_j = 0.015$, Grazing Flow $M_{GF} = 0.25$

(STEP 10) FWH

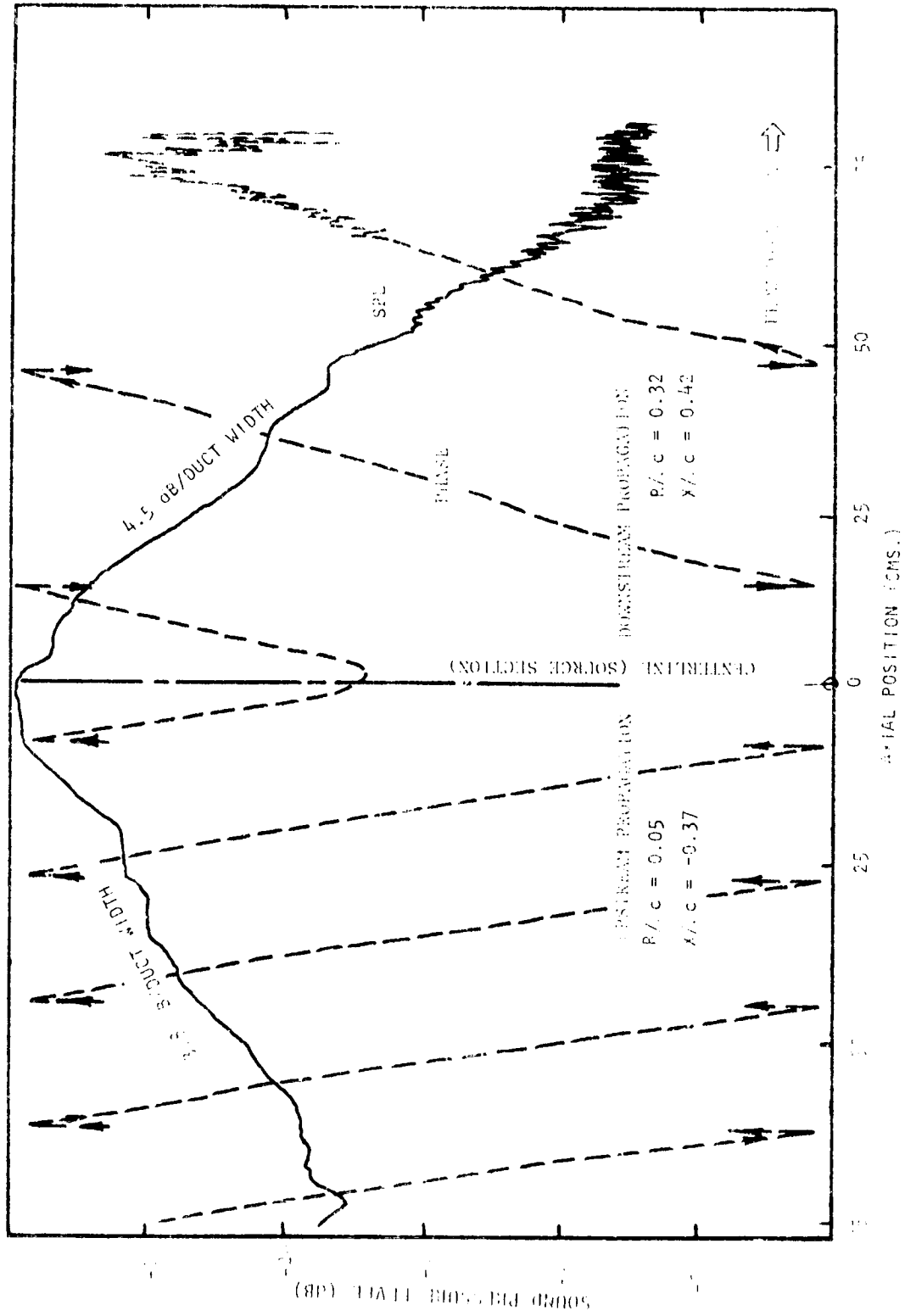


FIGURE 10.2 Axial Sound Pressure and Phase Transverse in Duct Centerline
 (1) $R/c = 0.05$, $X/c = -0.37$; (2) $R/c = 0.32$, $X/c = 0.42$

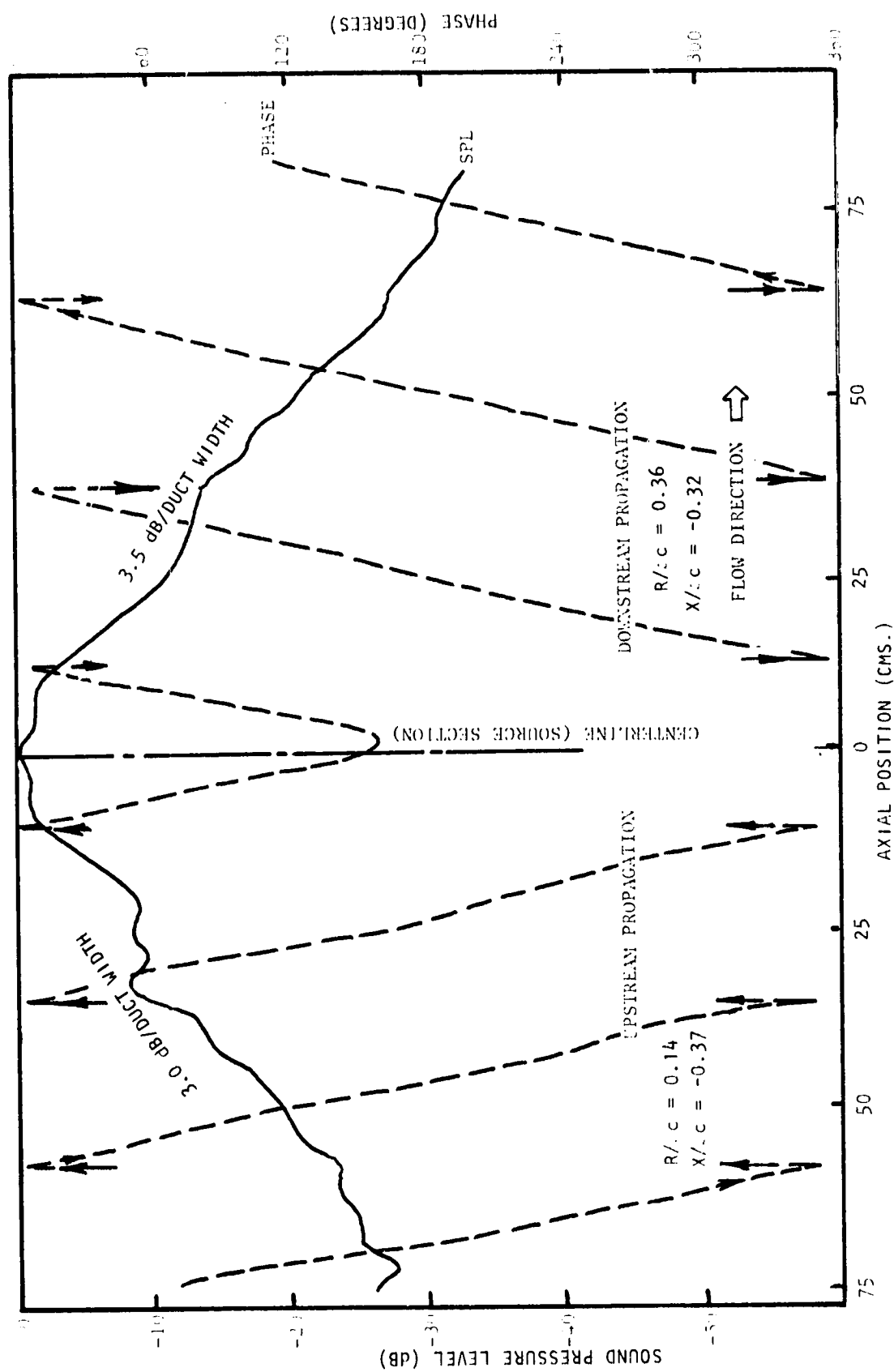


Figure 6.10(a) Axial Sound Pressure and Phase Traverses on Duct Centerline at 1700 Hz. Bias Flow $M_i = 0.0$, Grazing Flow $M_{GF} = 0.0$

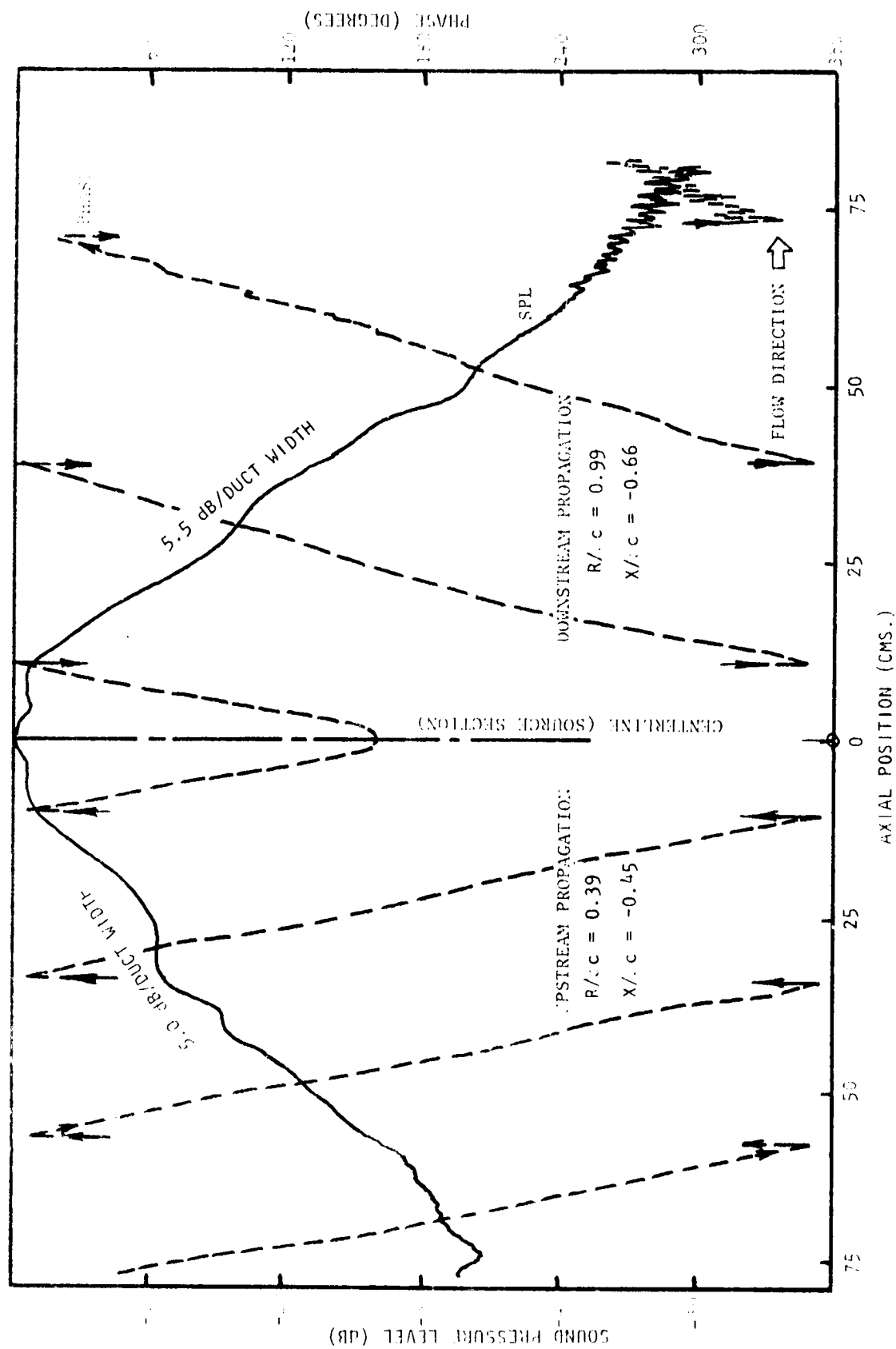


Figure G.10(b) Axial Sound Pressure and Phase Traverses on Duct Centerline at 1700 Hz. Bias Flow $M_i = 0.015$, Grazing Flow, $M_{GF} = 0.0$

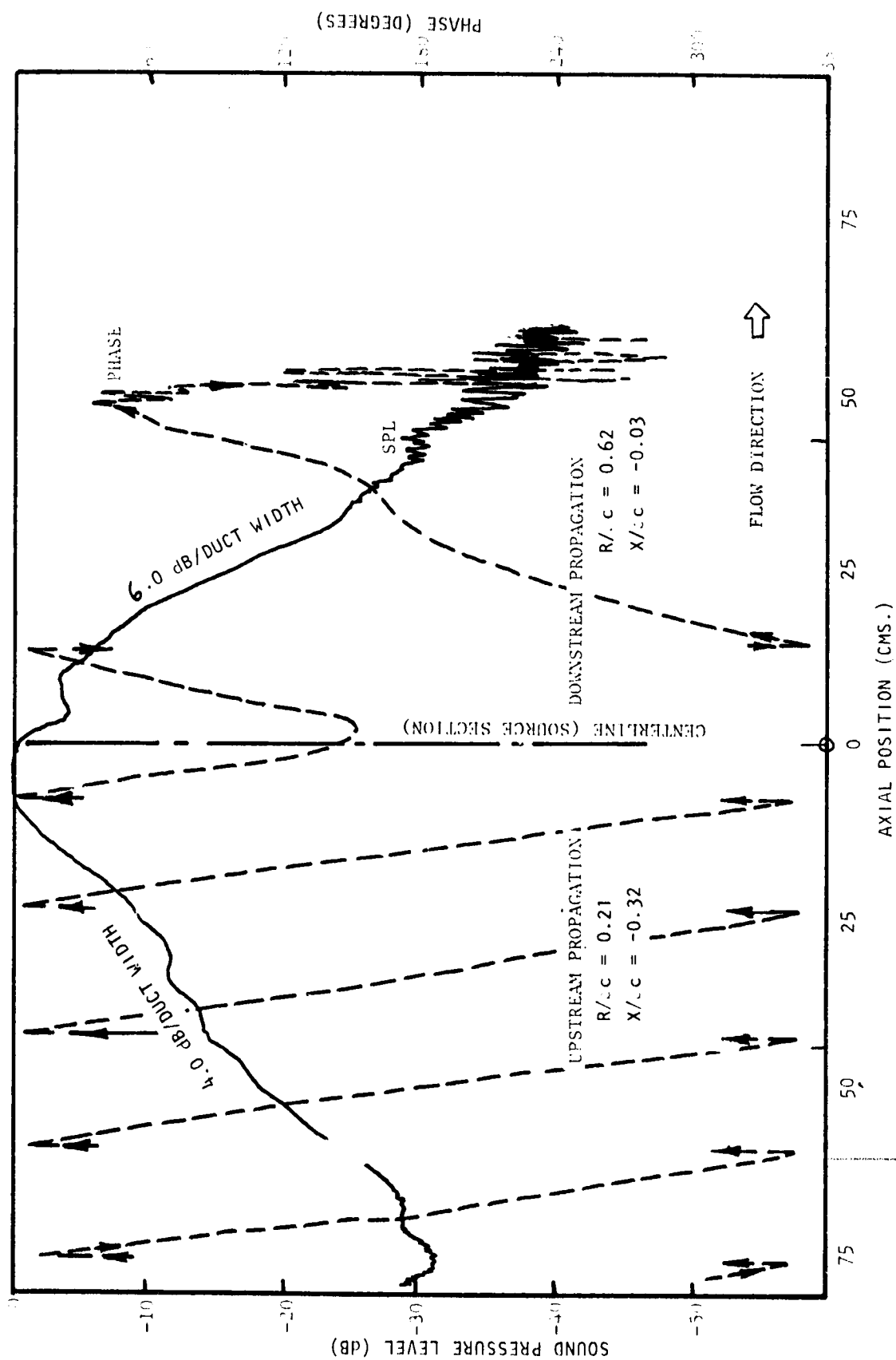


Figure G.10(c) Axial Sound Pressure and Phase Traverses on Duct Centerline at 1700 Hz. Bias Flow $M_i = 0.015$, Grazing Flow $M_g = 0.25$

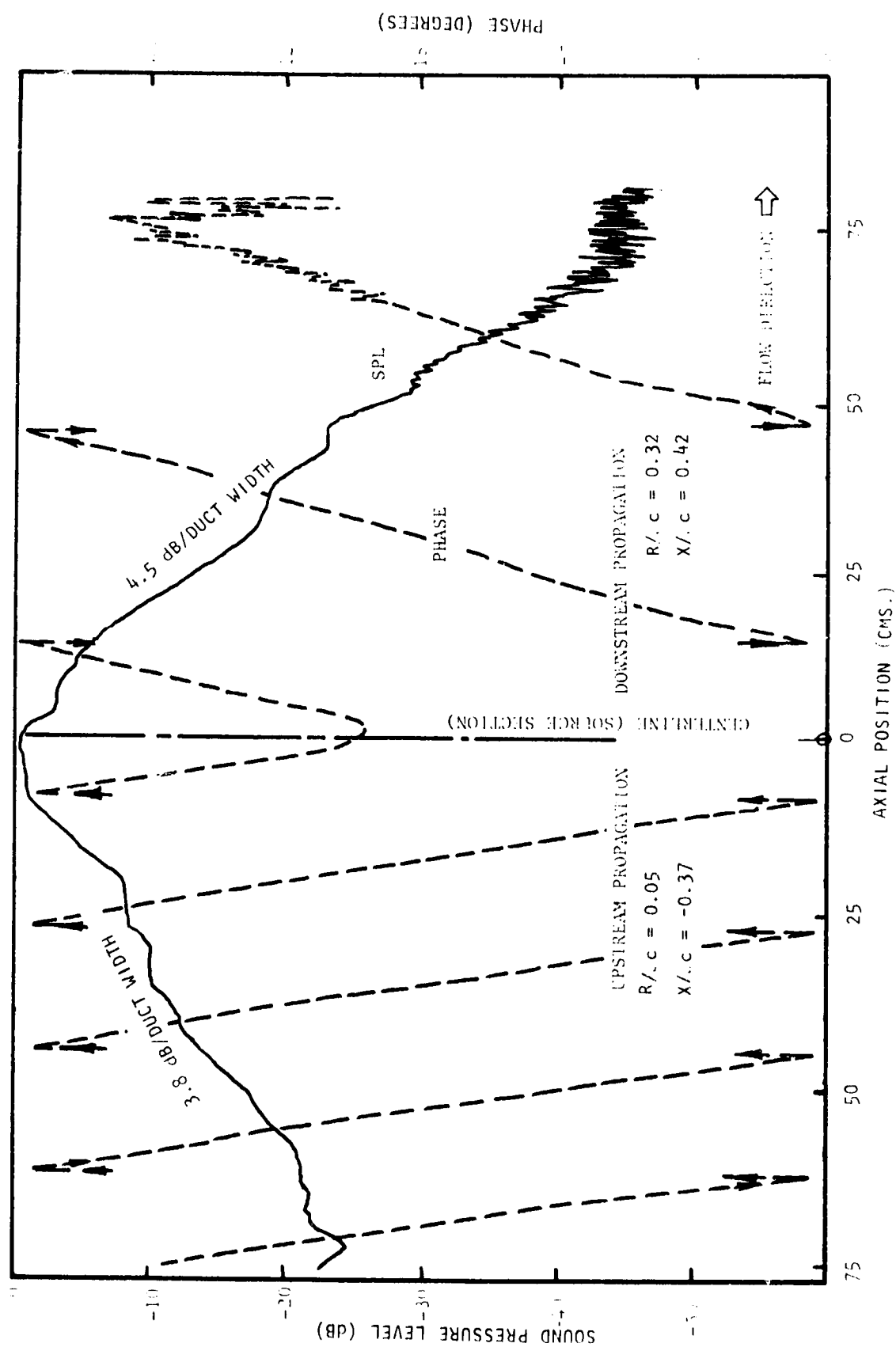


Figure 6.10(d) Axial Sound Pressure and Phase Traverses on Duct Centerline at 1700 Hz. Bias Flow $M_1 = 0.0$, Grazing Flow $M_2 = 0.25$

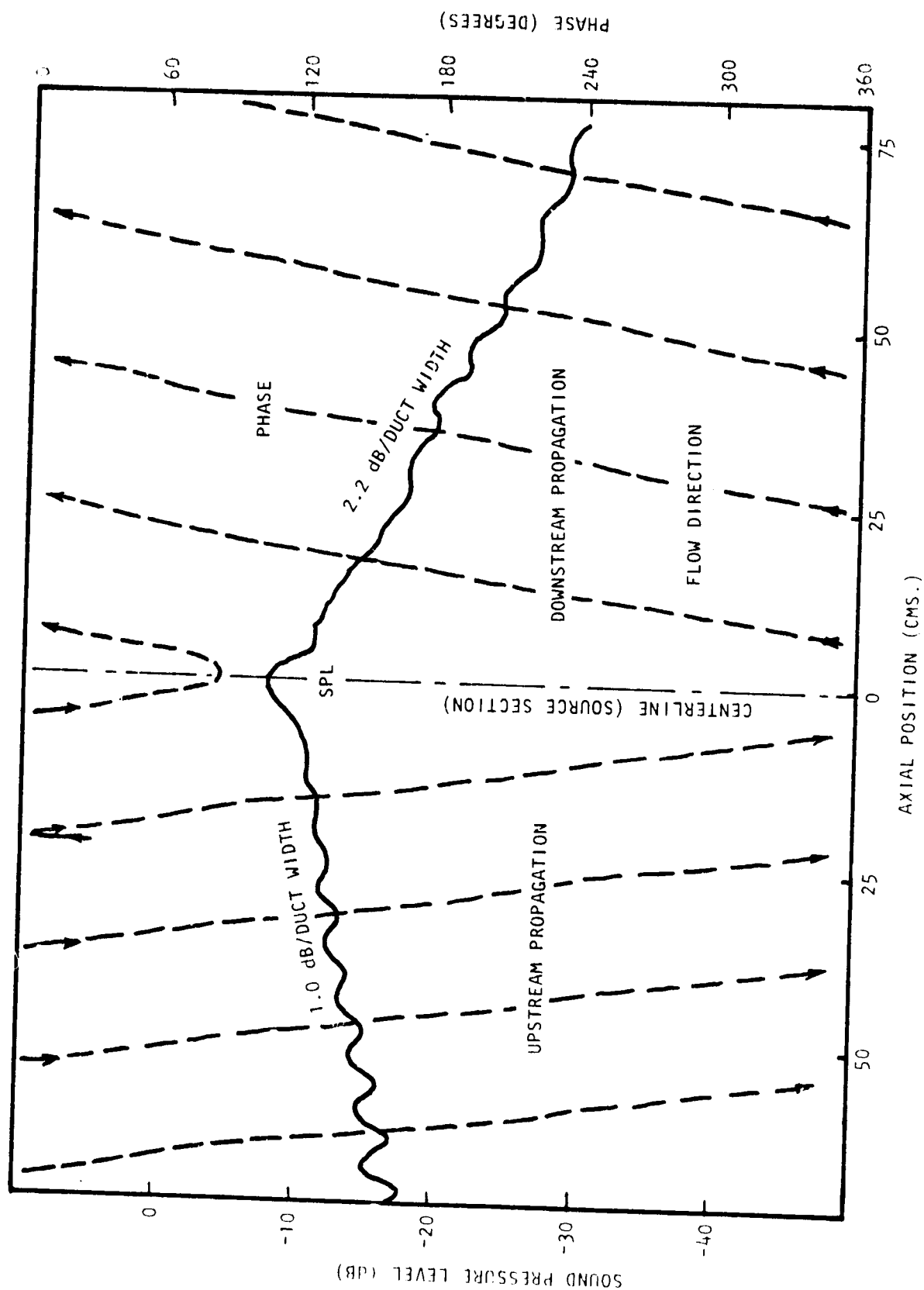


Figure G.11(a) Axial Sound Pressure and Phase Traverses on Duct Centerline at 2 KHz. Bias Flow $M_i = 0.0$, Grazing Flow $M_{GF} = 0.0$

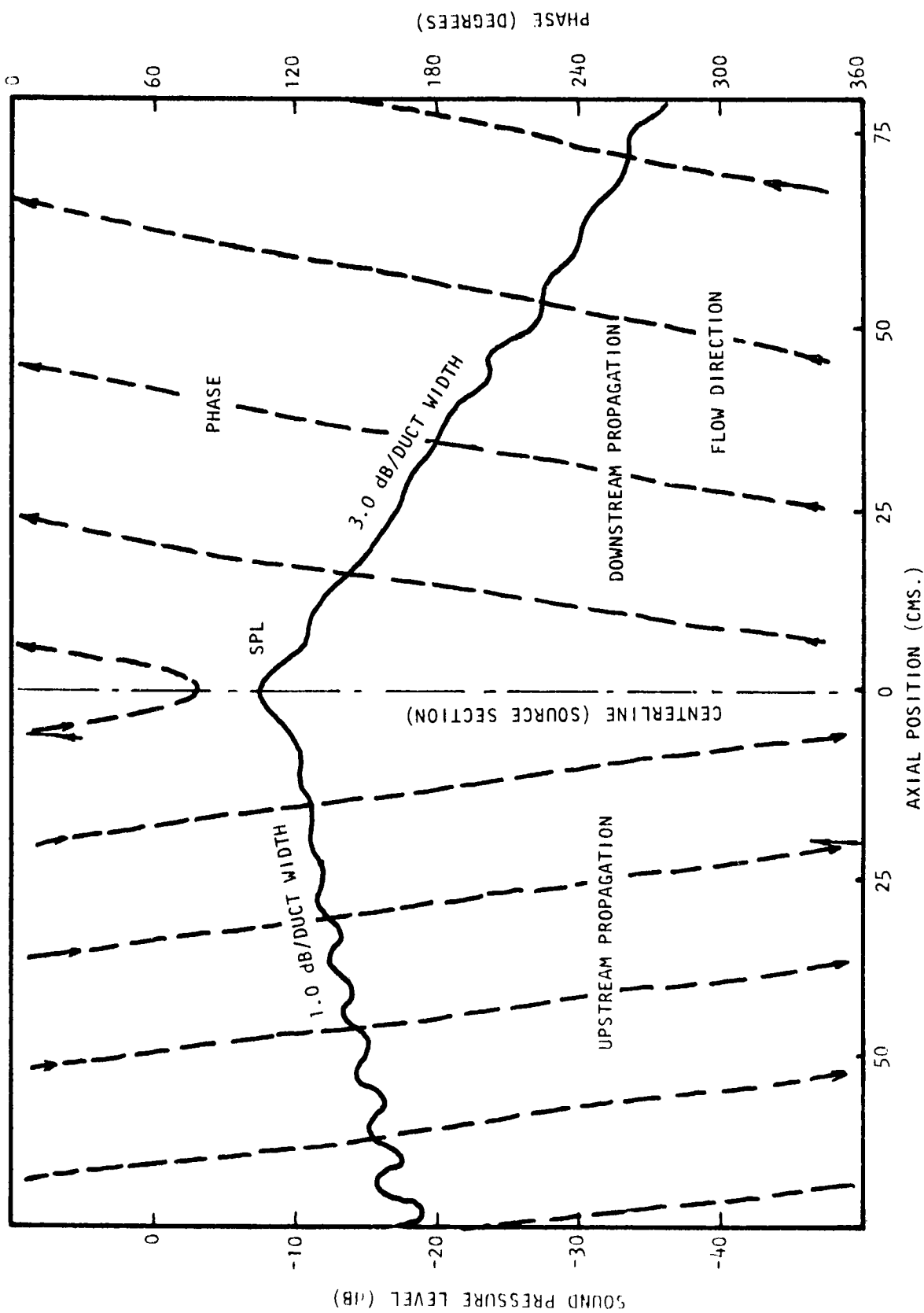


Figure 6.11(b) Axial Sound Pressure and Phase Traverses on Duct Centerline at 2 KHz. Bias Flow $M_i = 0.015$, Grazing Flow $M_{GF} = 0.0$

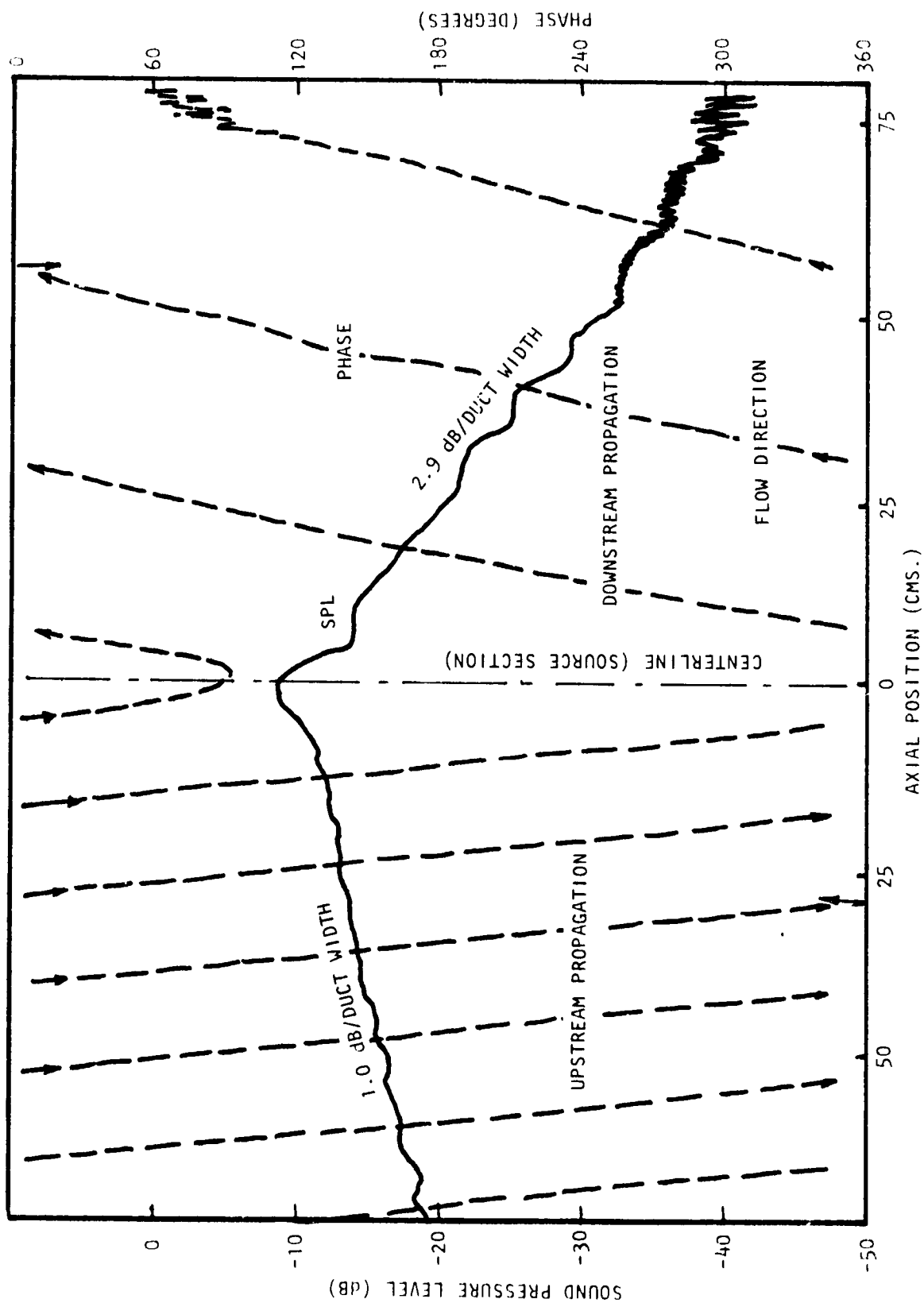


Figure G.11(c) Axial Sound Pressure and Phase Traverses on Duct Centerline at 2 KHz. Bias Flow $M_i = 0.015$, Grazing Flow $M_{GF} = 0.25$

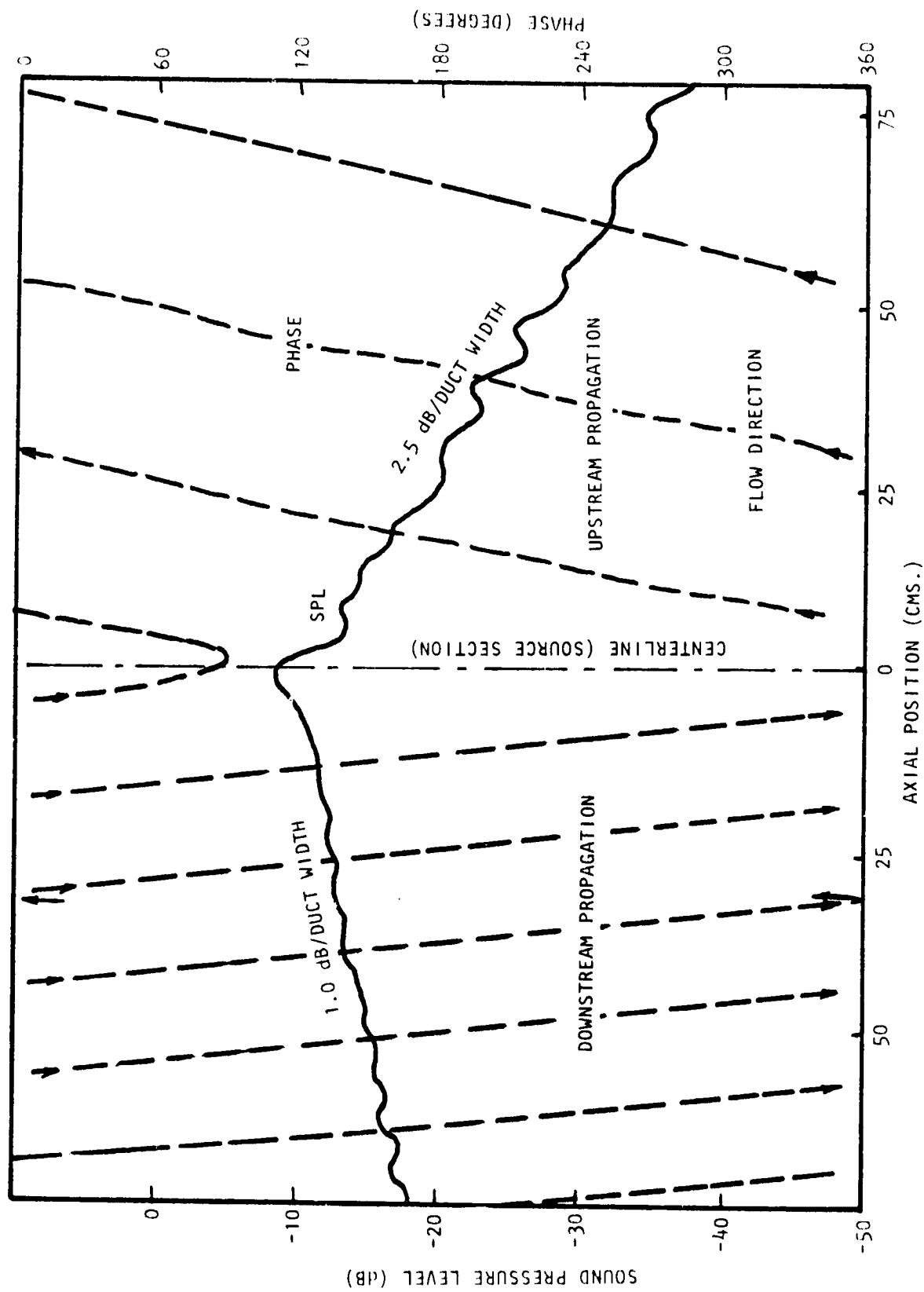


Figure G.11(d) Axial Sound Pressure and Phase Traverses on Duct Centerline at 2 KHz. Bias Flow $M_i = 0.0$, Grazing Flow $M_{GF} = 0.25$

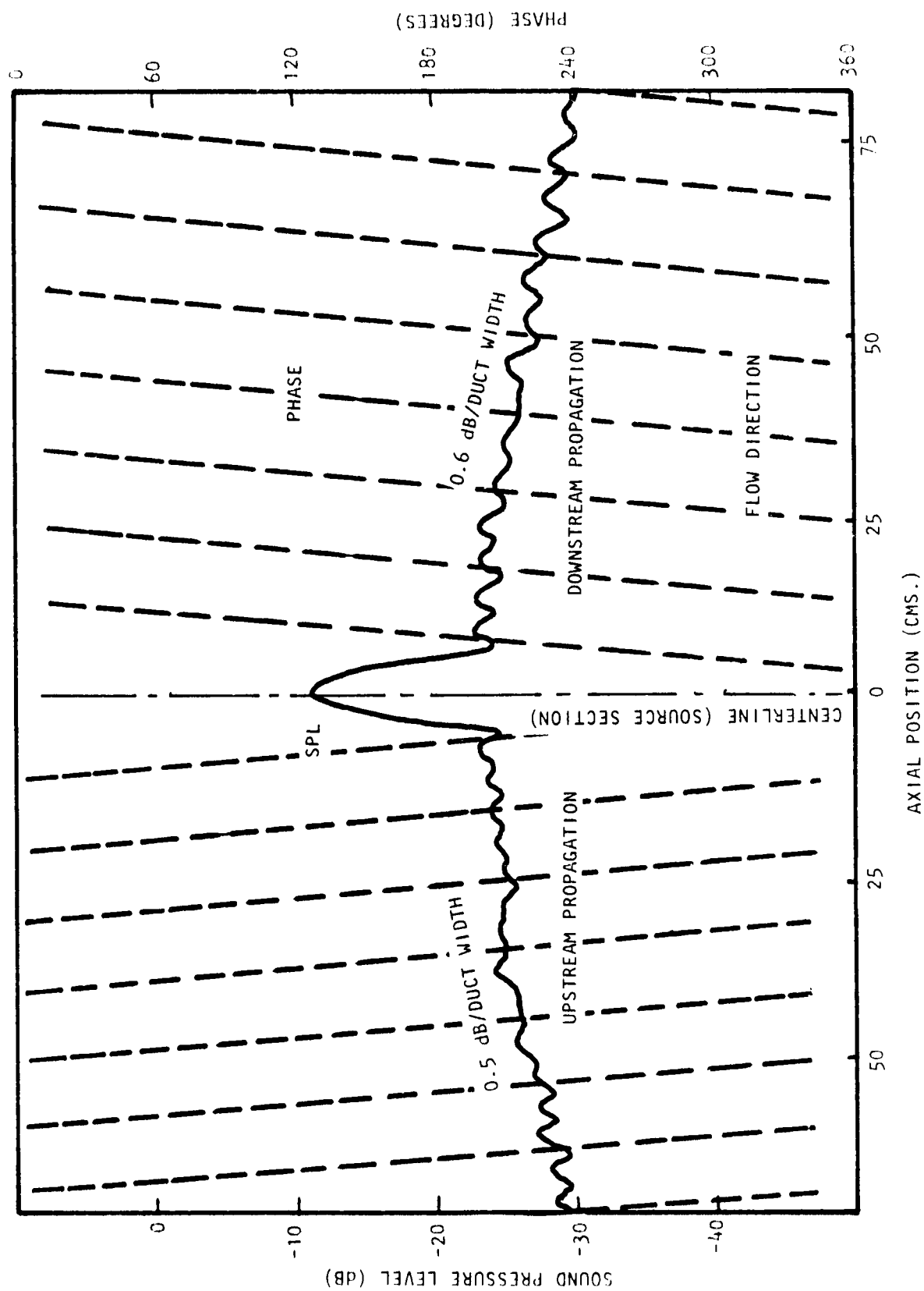


Figure G.12(a) Axial Sound Pressure and Phase Traverses on Duct Centerline at 3.15 KHz. Bias Flow $M_i = 0.0$, Grazing Flow $M_{GF} = 0.0$

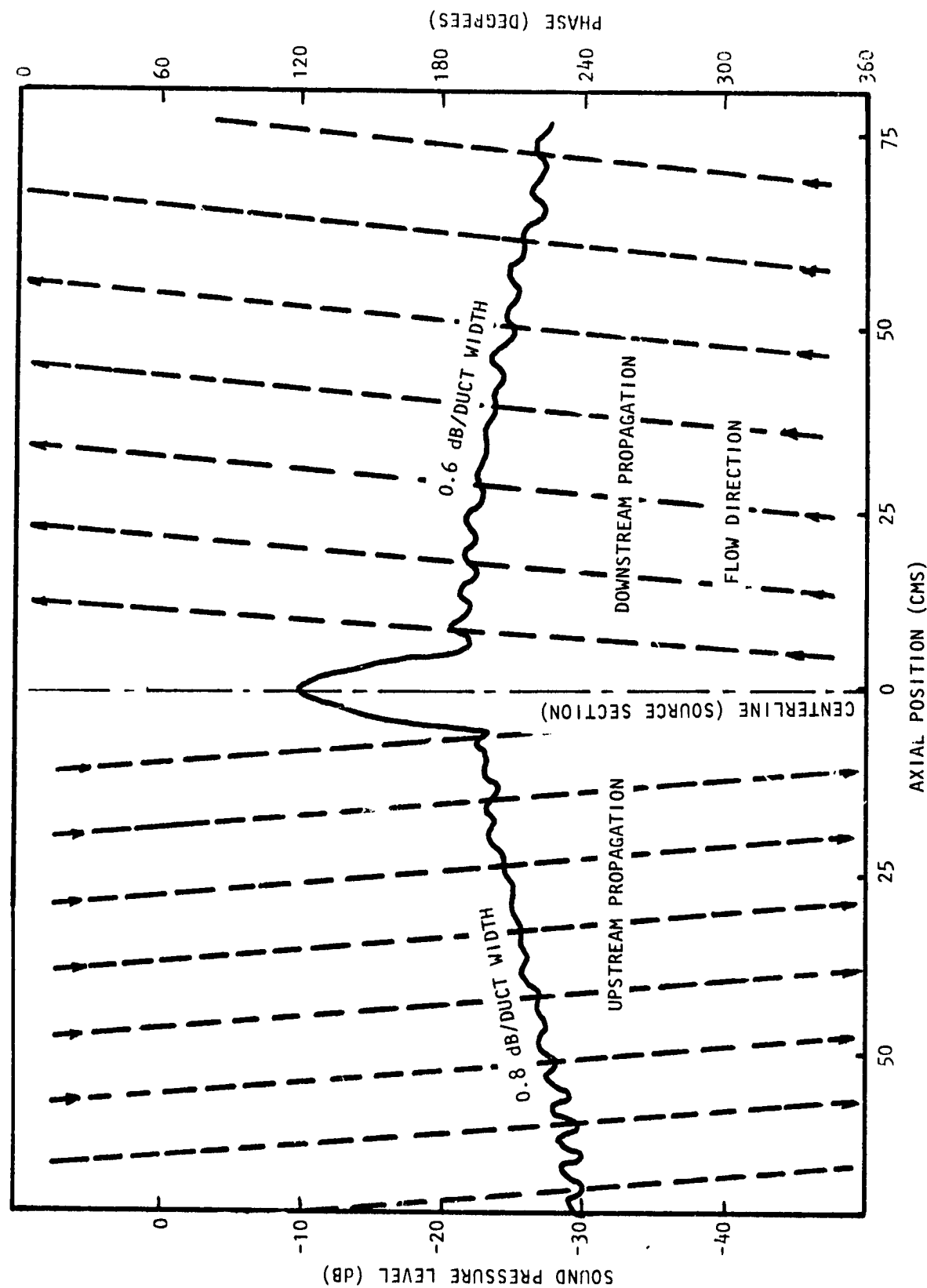


Figure 6.12(b) Axial Sound Pressure and Phase Traverses on Duct Centerline at 3.15 KHz. Bias Flow $M_i = 0.015$, Grazing Flow $M_{GF} = 0.0$

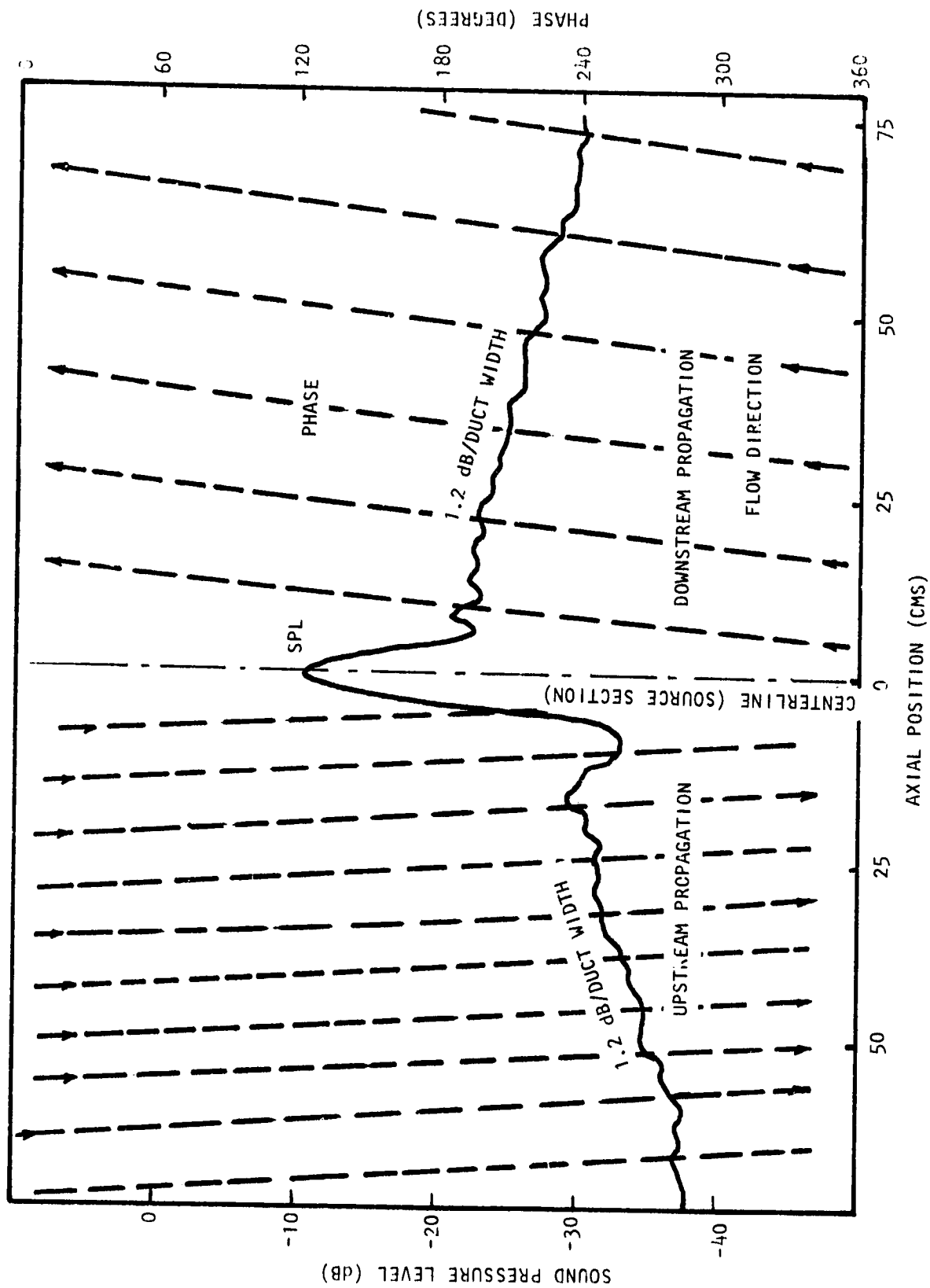


Figure 6.12(c) Axial Sound Pressure and Phase Traverses on Duct Centerline at 3.15 KHz. Bias Flow $M_i = 0.015$, Grazing Flow $M_{GF} = 0.25$

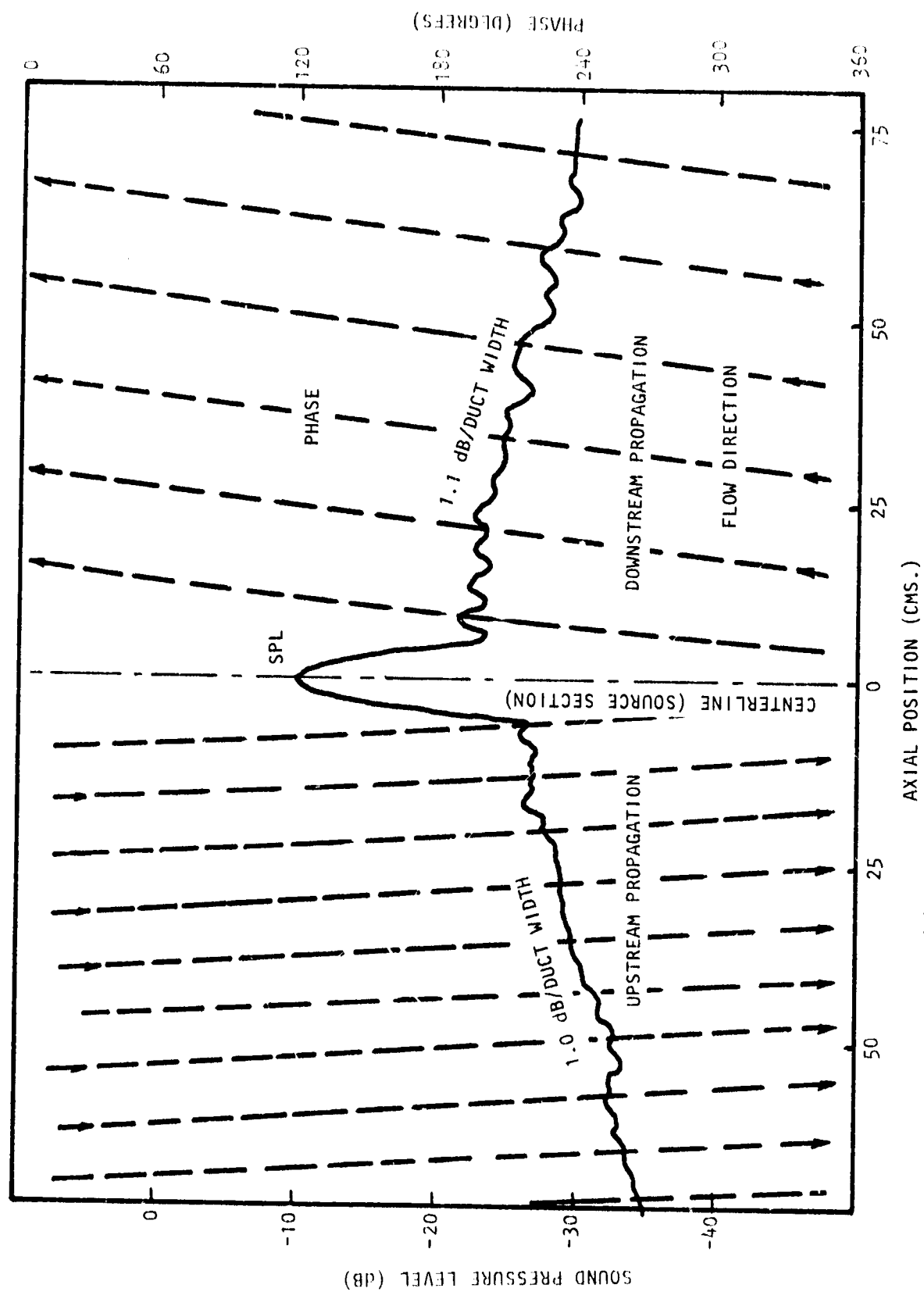


Figure 6.12(d) Axial Sound Pressure and Phase Traverses on Duct Centerline at 3.15 KHz. Bias Flow $M_i = 0.0$, Grazing Flow $M_{GF} = 0.25$

APPENDIX H

SOUND PRESSURE AND PHASE TRAVERSES WITHIN UPSTREAM
AND DOWNSTREAM SECTIONS OF FLOW DUCT LINER AT
VARIOUS FREQUENCIES AT VARIOUS COMBINATIONS OF
TWO EXTREMES OF BIAS FLOW (MACH NUMBER = 0.0 AND
0.015) AND GRAZING FLOW (MACH NUMBER = 0.0 AND 0.25)

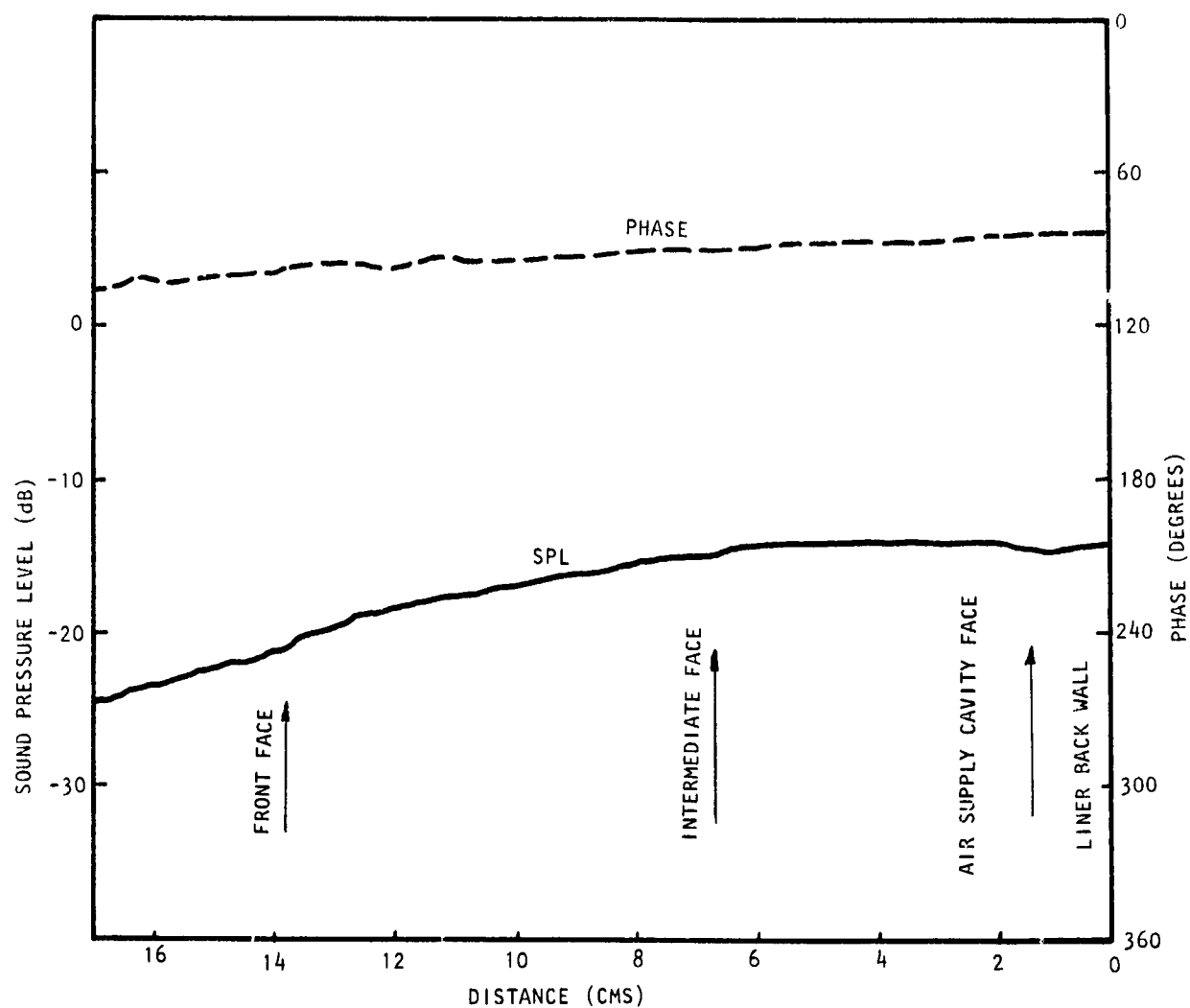


Figure H.1(a) Sound Pressure and Phase Traverses within Upstream Liner at 500 Hz. Bias Flow $M_i = 0.0$, Grazing Flow $M_{GF} = 0.0$

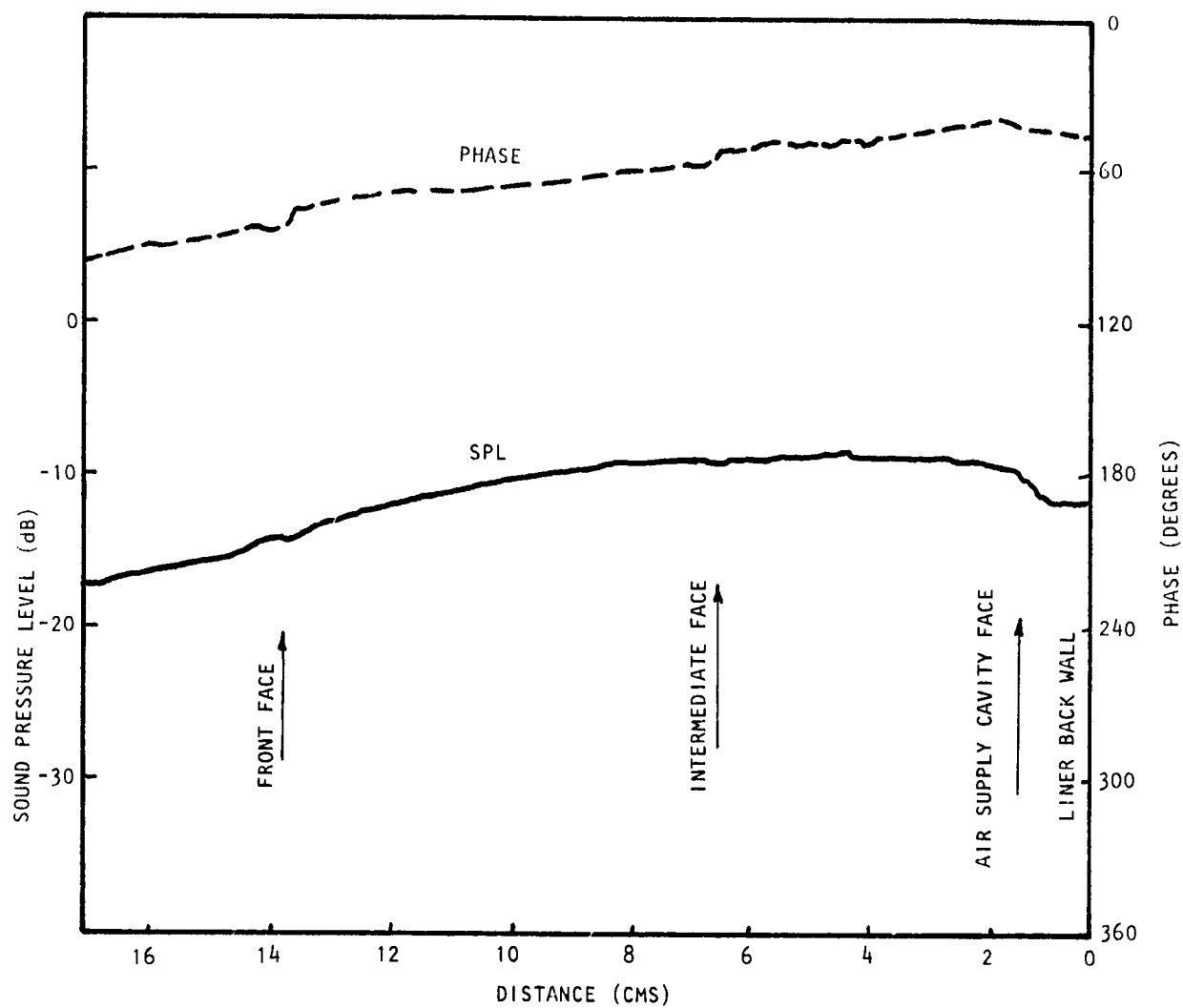


Figure H.1(b) Sound Pressure and Phase Traverses within Upstream Liner at 500 Hz. Bias Flow $M_i = 0.015$, Grazing Flow $M_{GF} = 0.0$

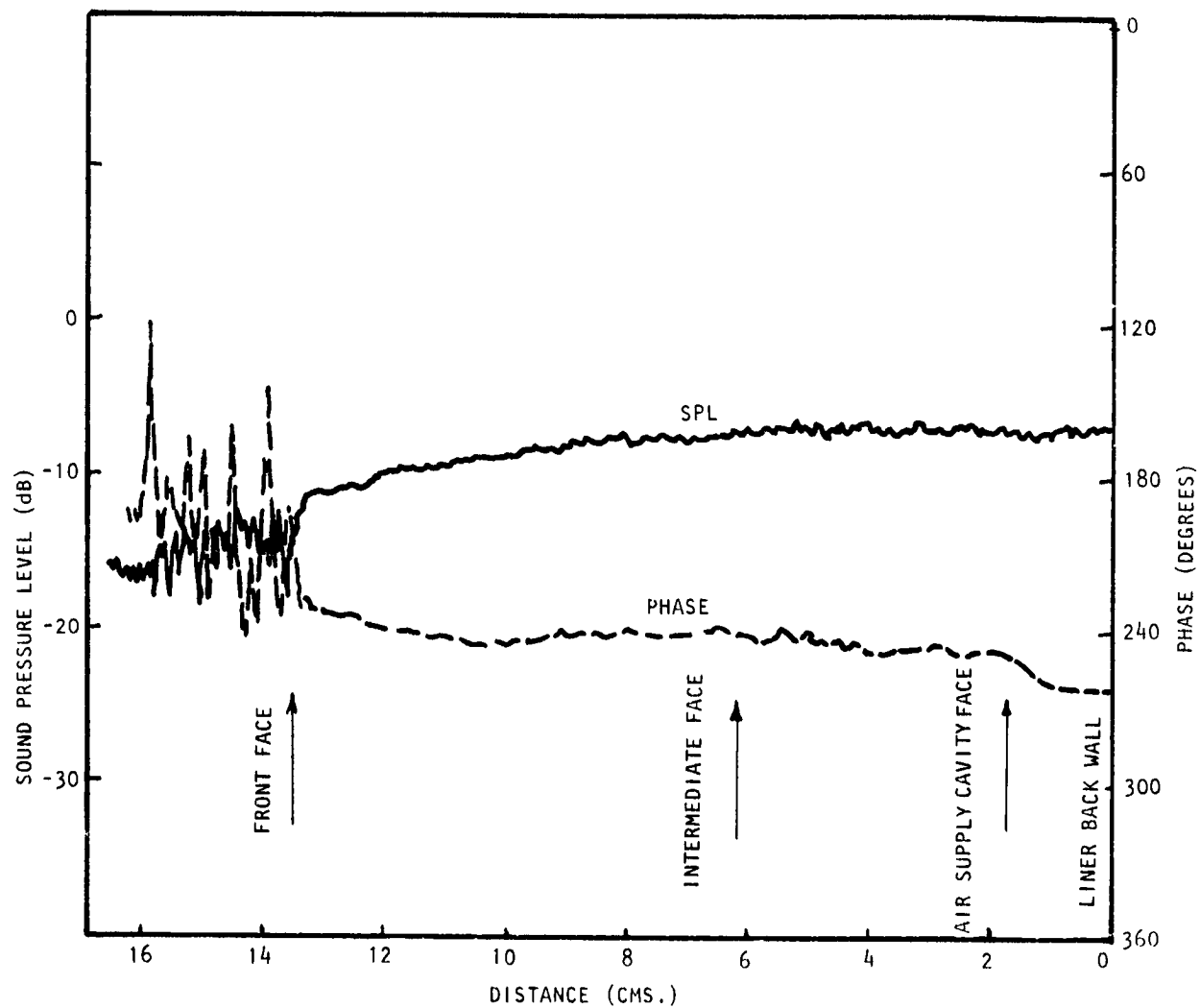


Figure H.1(c) Sound Pressure and Phase Traverses within Upstream Liner at 500 Hz. Bias Flow $M_b = 0.0$, Grazing Flow $M_{GF} = 0.25$

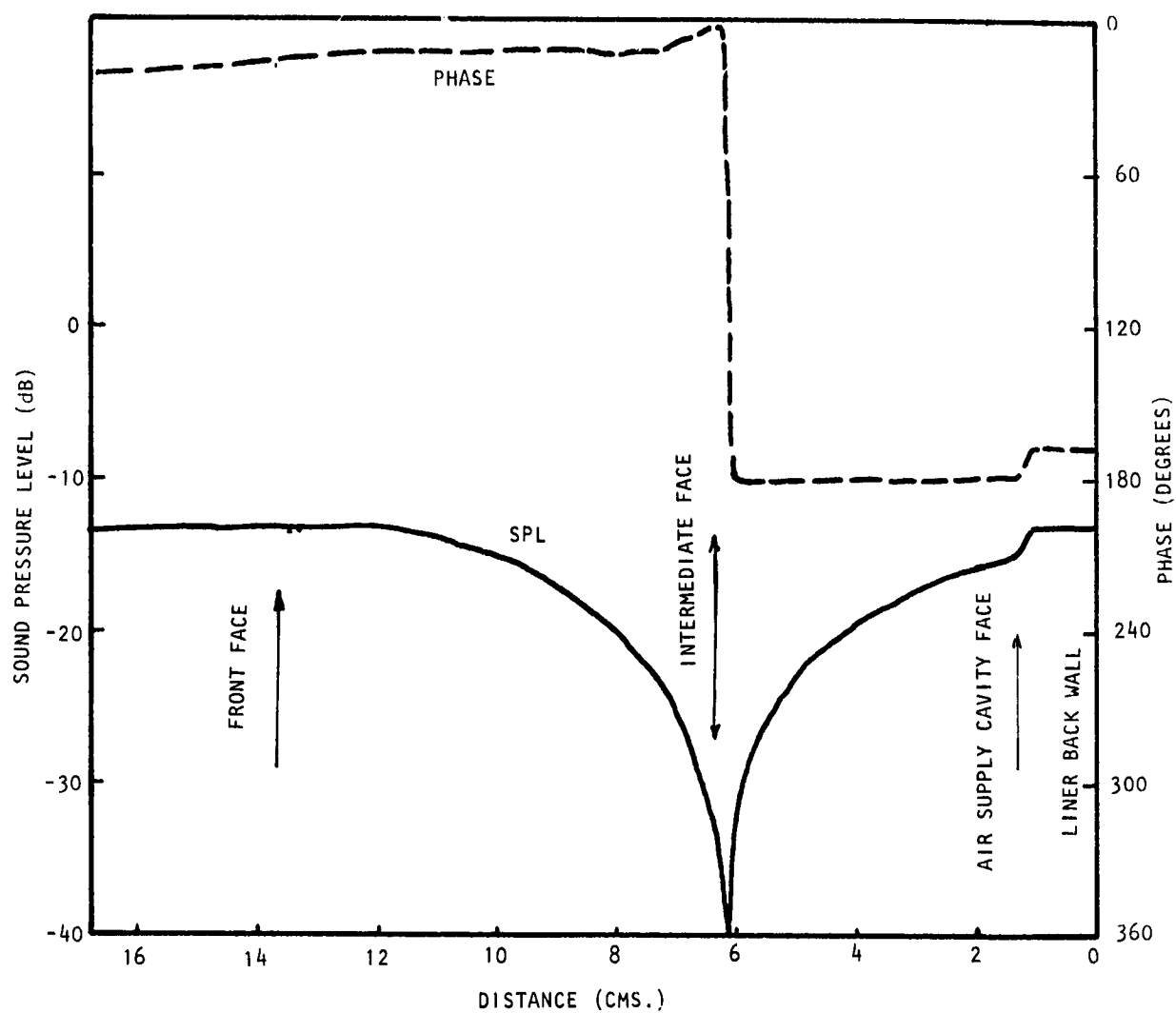


Figure H.2(a) Sound Pressure and Phase Traverses within Upstream Liner at 1250 Hz, Bias Flow $M_i = 0.0$, Grazing Flow $M_{GF} = 0.0$

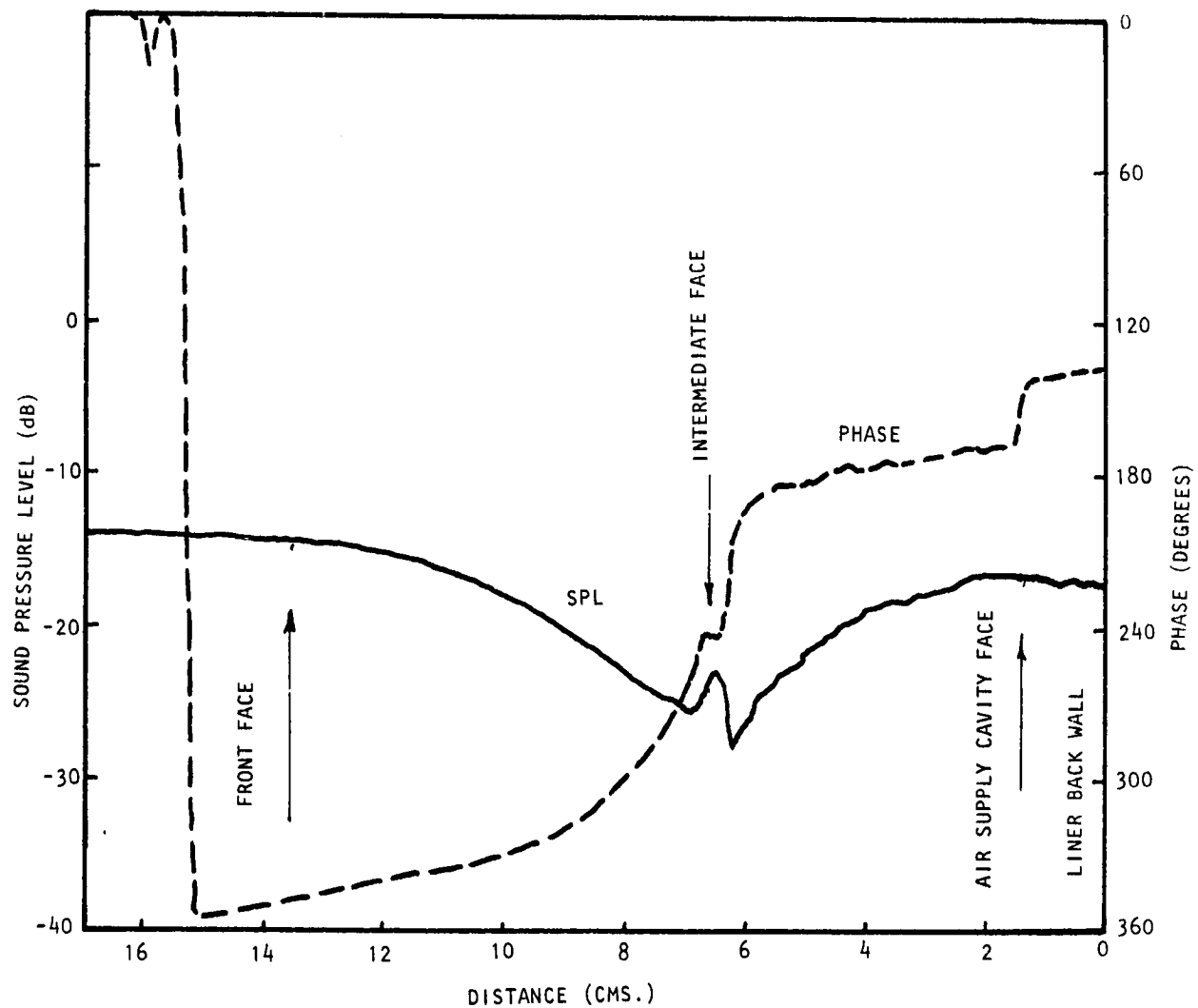


Figure H.2(b) Sound Pressure and Phase Traverses within Upstream Liner at 1250 Hz, Bias Flow $M_i = 0.15$, Grazing Flow $M_{GF} = 0.0$

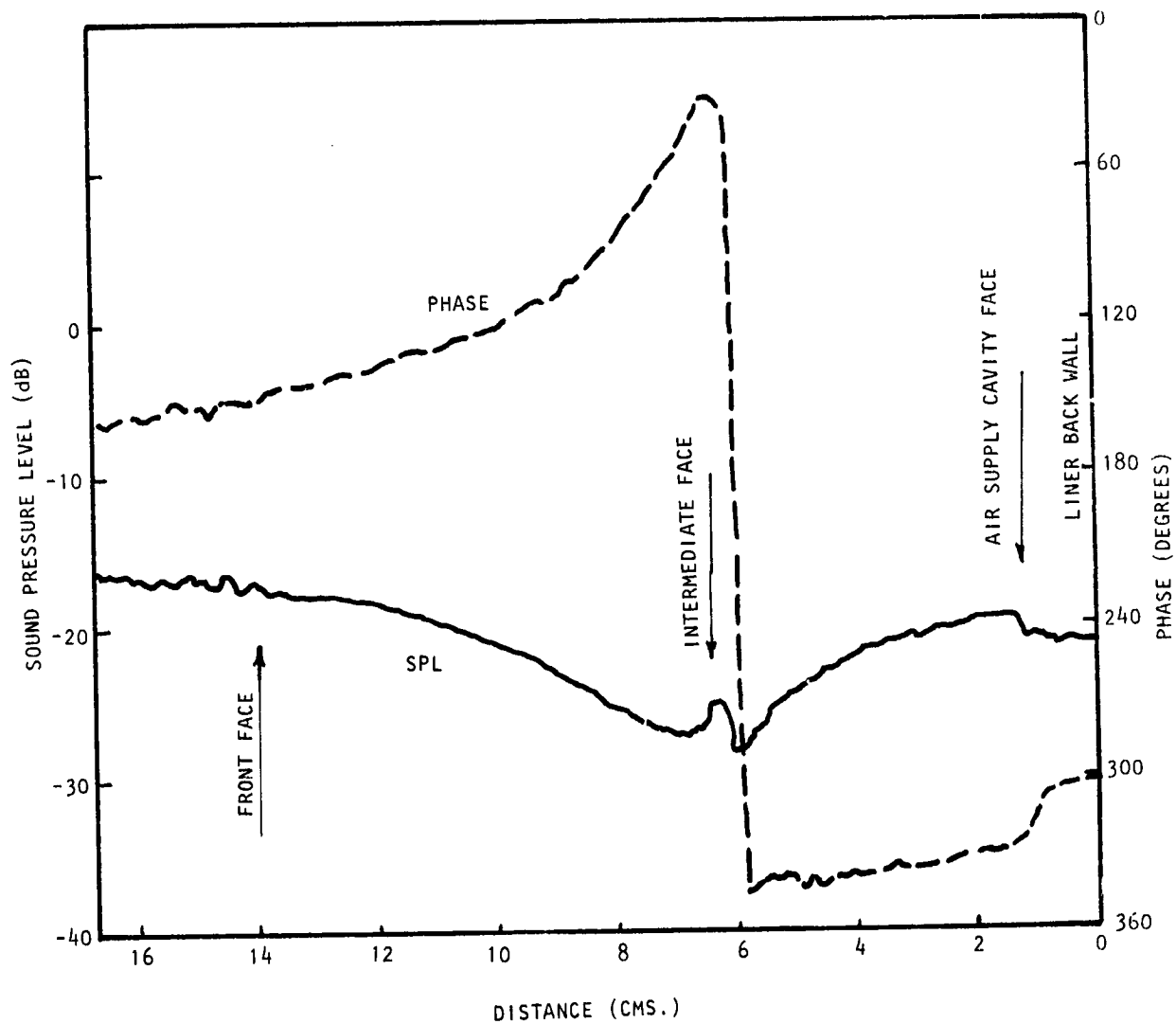


Figure H.2(c) Sound Pressure and Phase Traverses within Upstream Liner at 1250 Hz. Bias Flow $M_i = 0.015$, Grazing Flow $M_{GF} = 0.25$

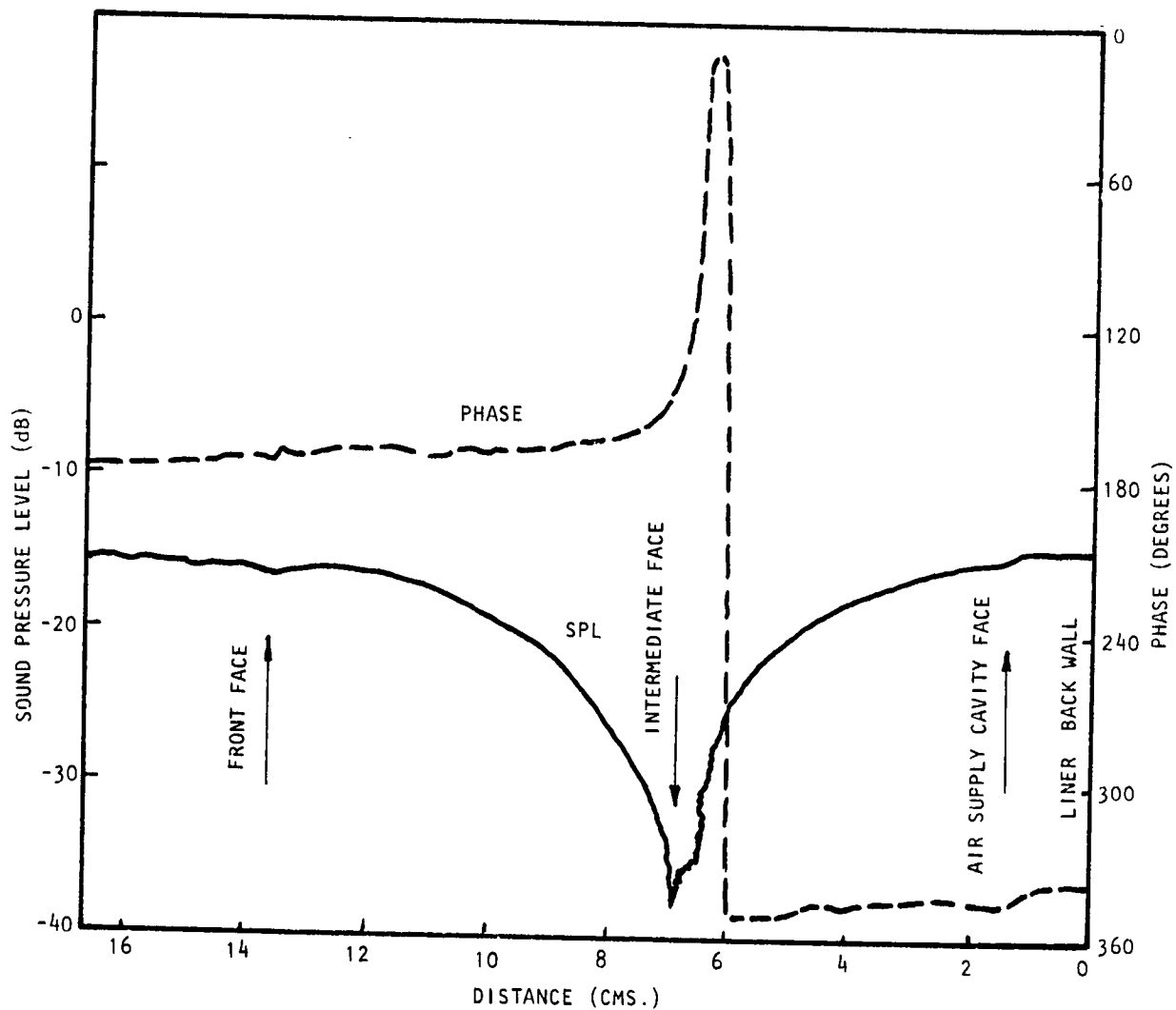


Figure H.2(d) Sound Pressure and Phase Traverses within Upstream Liner at 1250 Hz. Bias Flow $M_b = 0.0$, Grazing Flow $M_{gf} = 0.25$

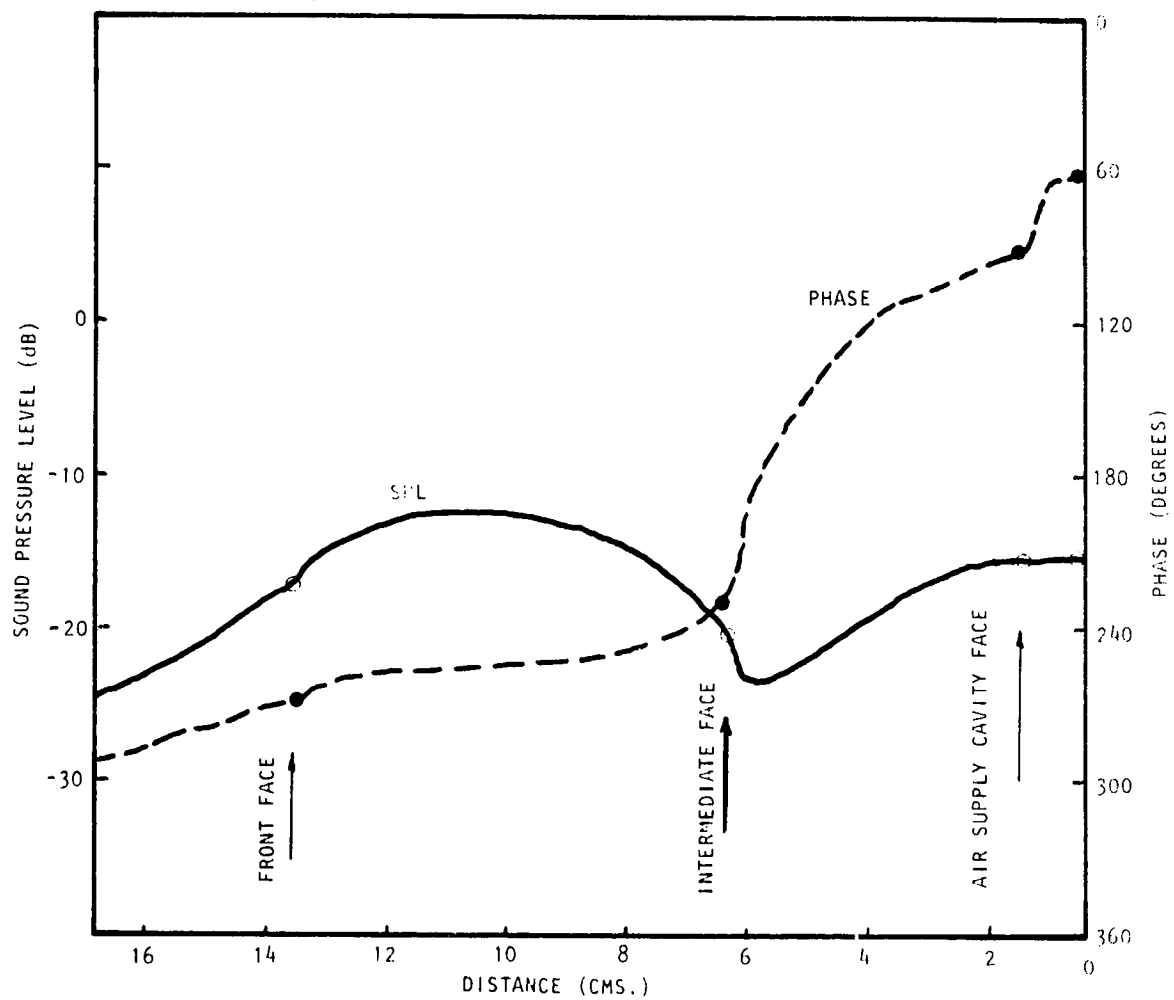


Figure H.3(a) Sound Pressure and Phase Traverses within Upstream Liner at 1600 Hz. Bias Flow $M_b = 0.0$, Grazing Flow $M_{GF} = 0.0$

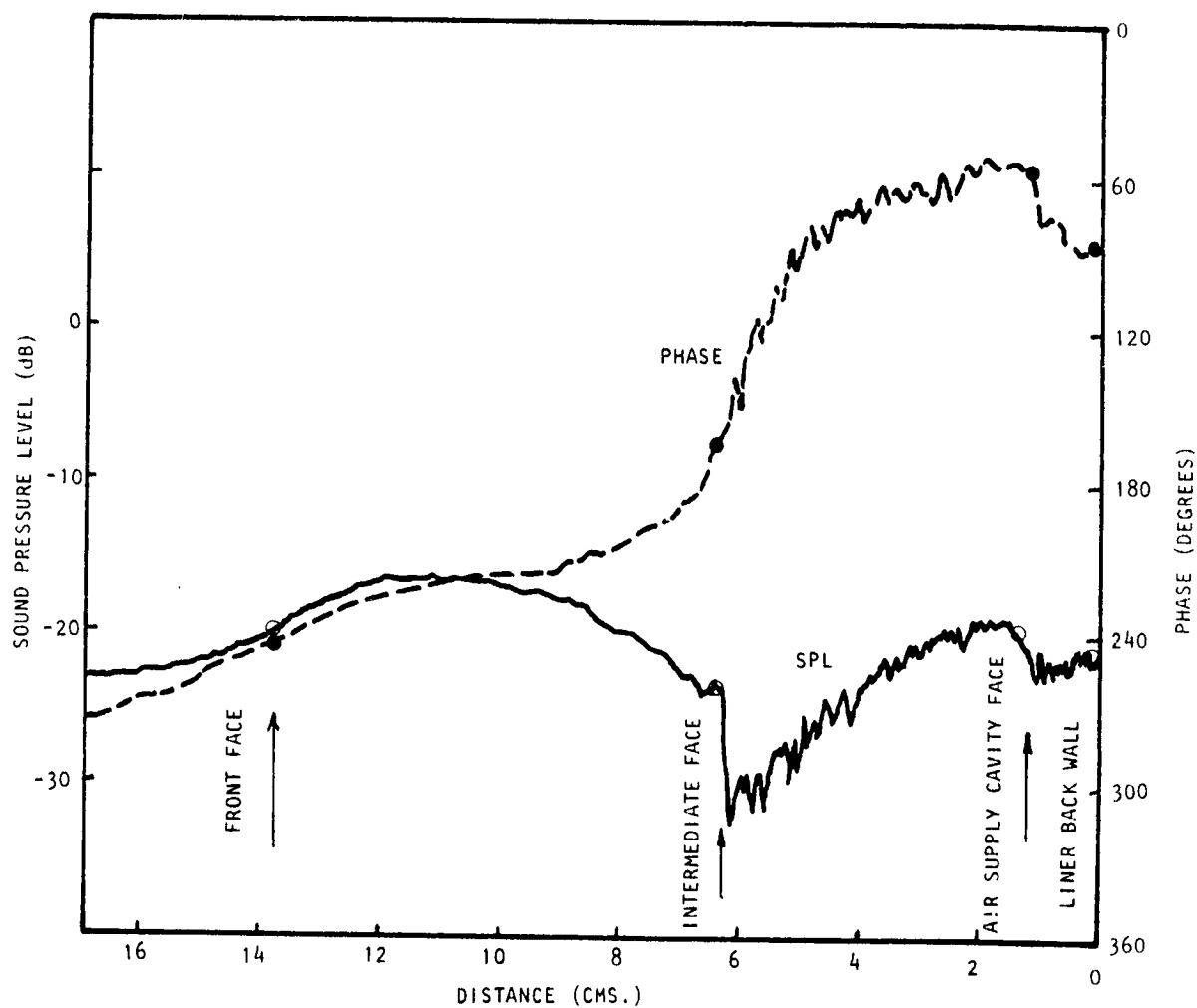


Figure H.3(b) Sound Pressure and Phase Traverses within Upstream Liner at 1600 Hz. Bias Flow $M_j = 0.015$, Grazing Flow = 0.0

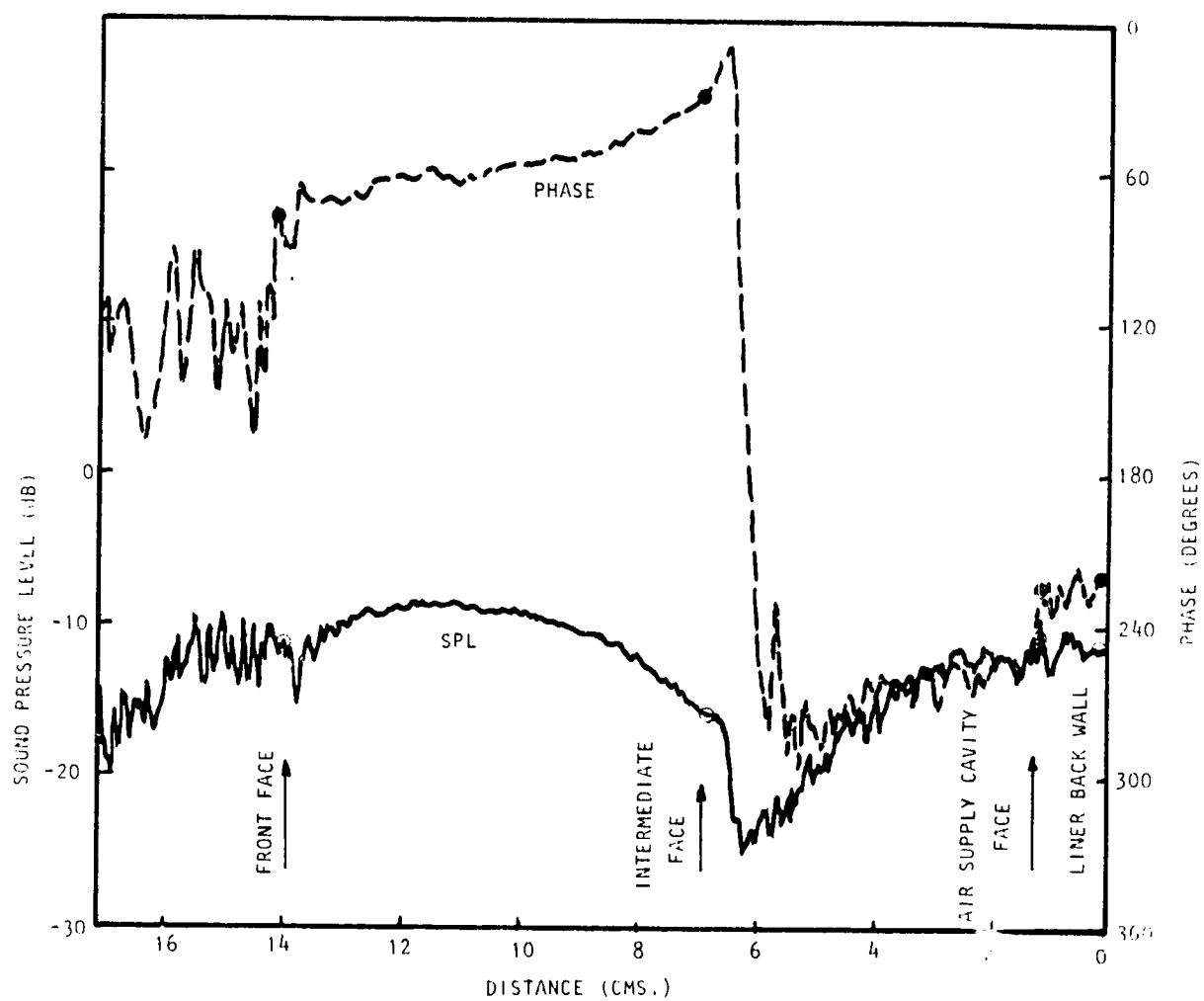


Figure H.3(c) Sound Pressure and Phase Traverses within Upstream Liner at 1600 Hz. Bias Flow $M_j = 0.015$, Grazing Flow = 0.25

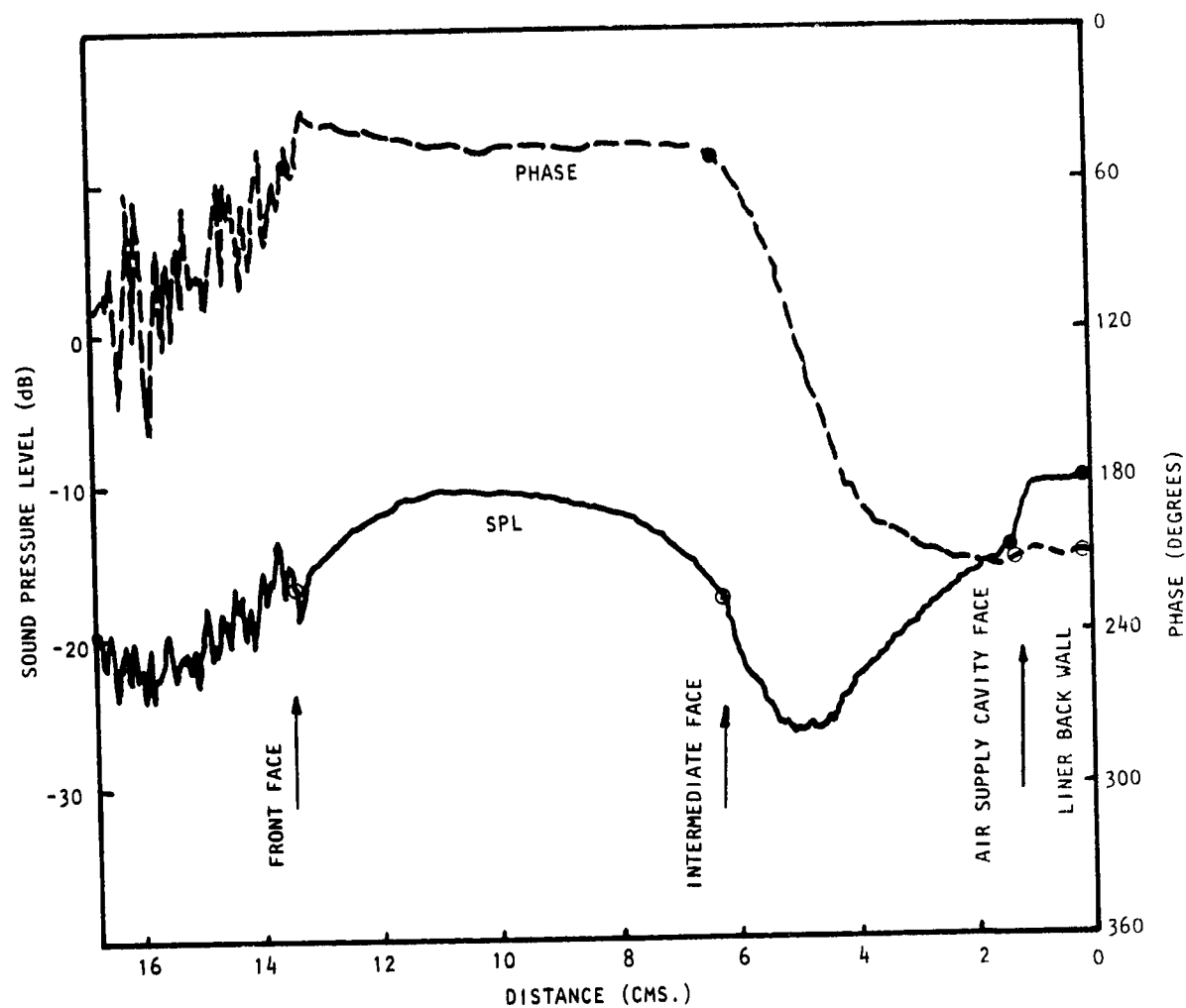


Figure H.3(d) Sound Pressure and Phase Traverses within Upstream Liner at 1600 Hz. Bias Flow $M_i = 0.0$, Grazing Flow = 0.25

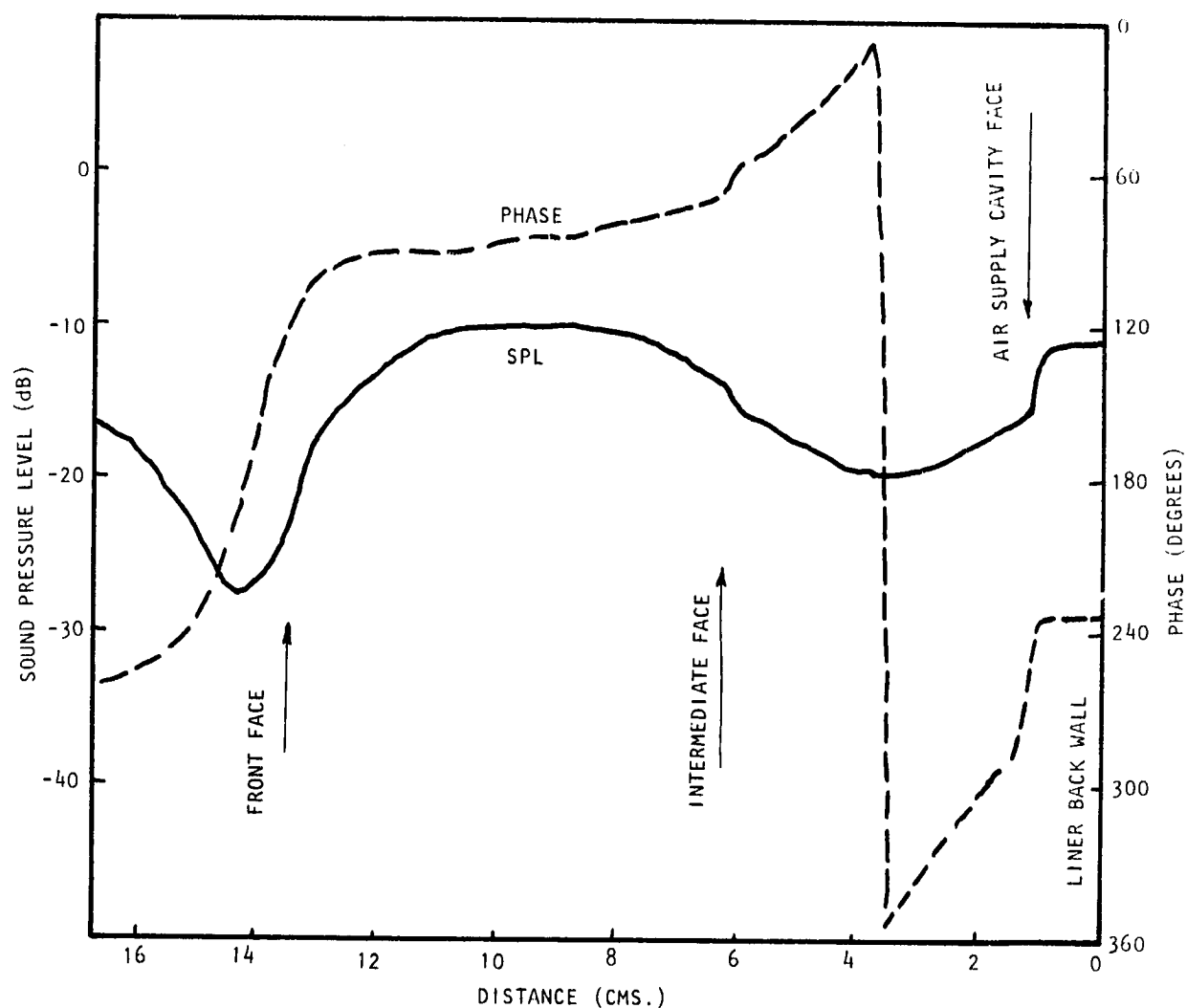


Figure H.4(a) Sound Pressure and Phase Traverses within Upstream Liner at 1700 Hz. Bias Flow $M_i = 0.0$, Grazing Flow $M_{GF} = 0.0$

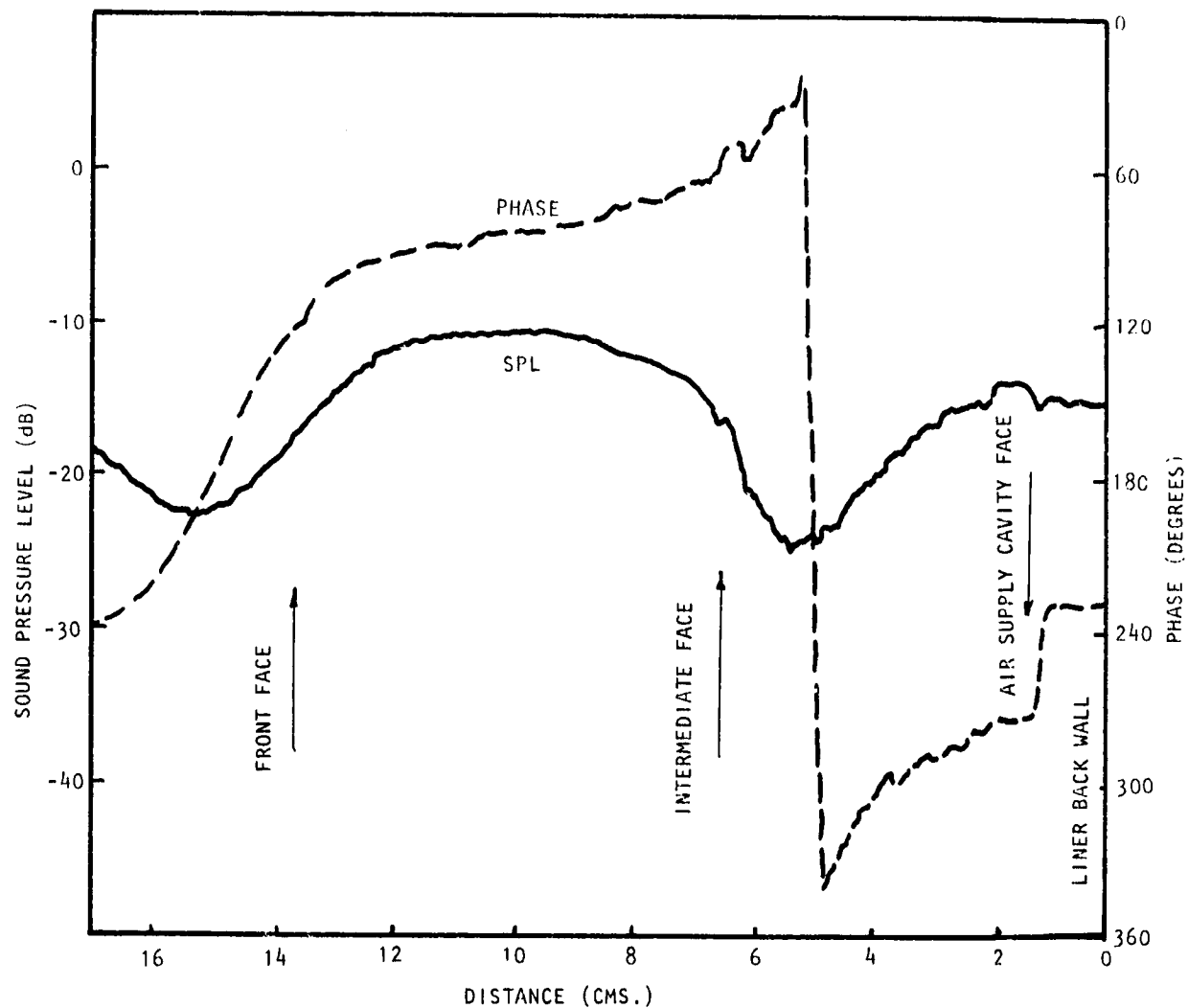


Figure H.4(b) Sound Pressure and Phase Traverses within Upstream Liner at 1700 Hz. Bias Flow $M_i = 0.015$, Grazing Flow $M_{GF} = 0.0$

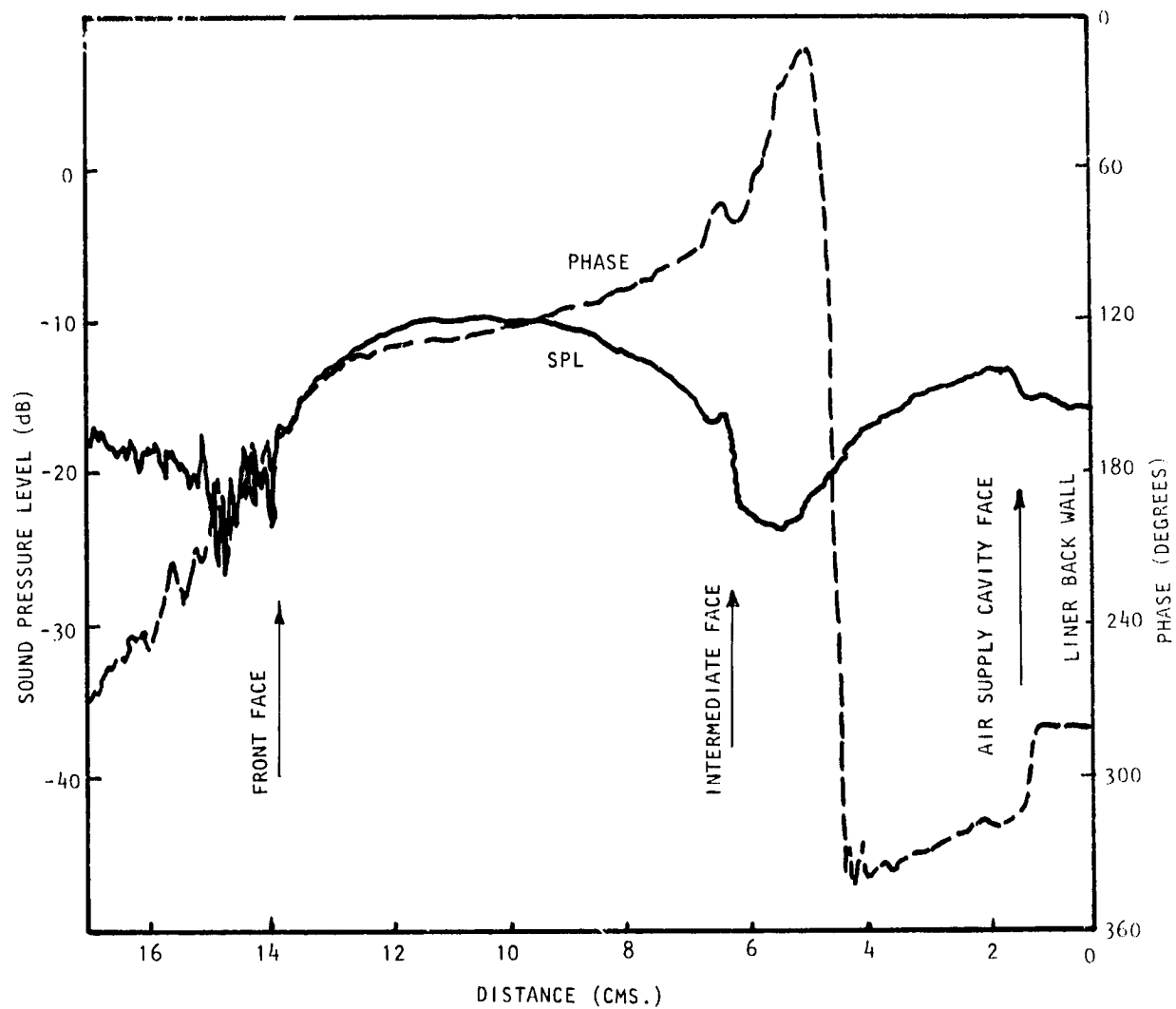


Figure H.4(c) Sound Pressure and Phase Traverses within Upstream Liner at 1700 Hz. Bias Flow $M_i = 0.015$, Grazing Flow $M_{GF} = 0.25$

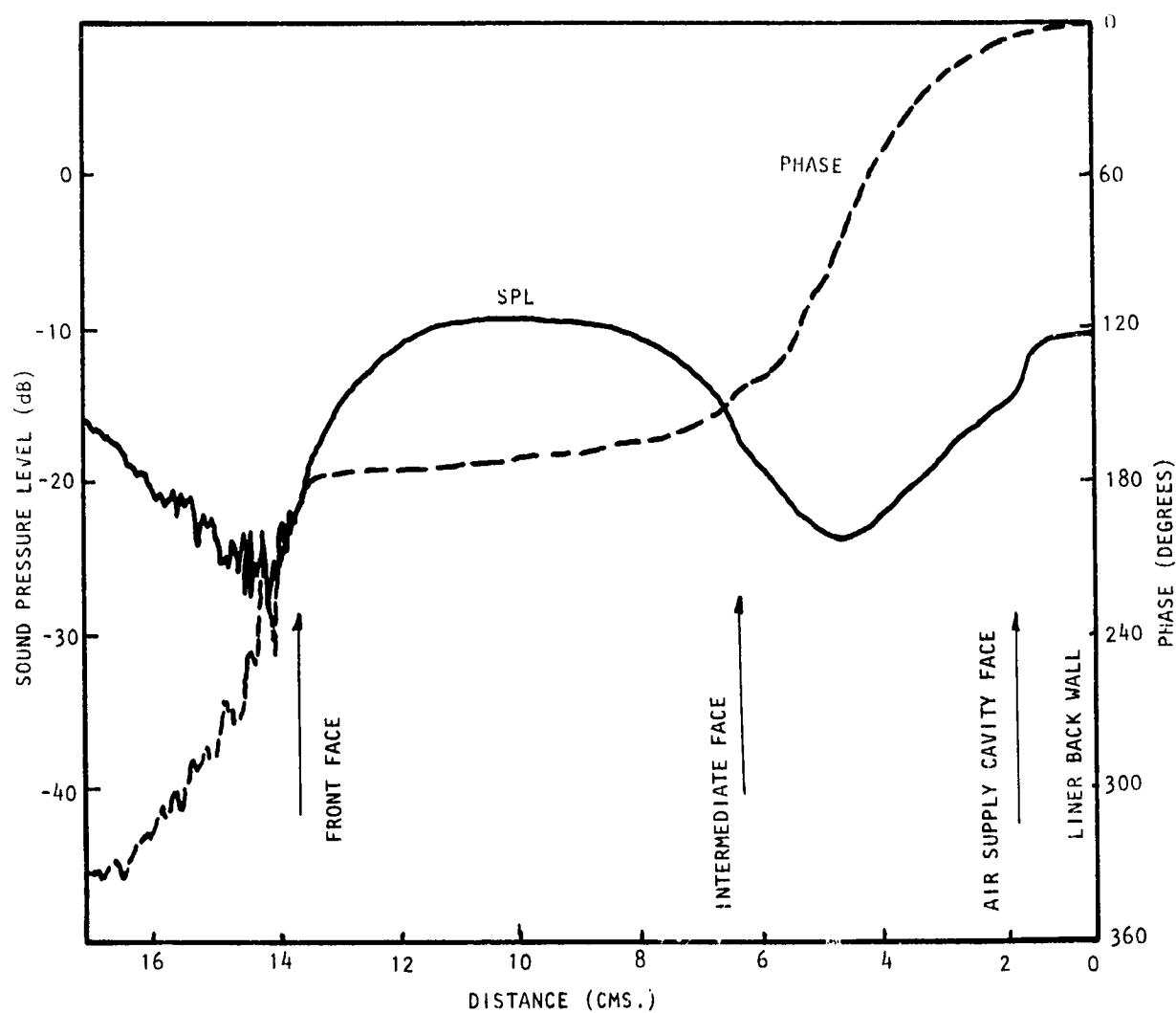


Figure H.4(d) Sound Pressure and Phase Traverses within Upstream Liner at 1700 Hz. Bias Flow $M_i = 0.0$, Grazing Flow $M_{GF} = 0.25$

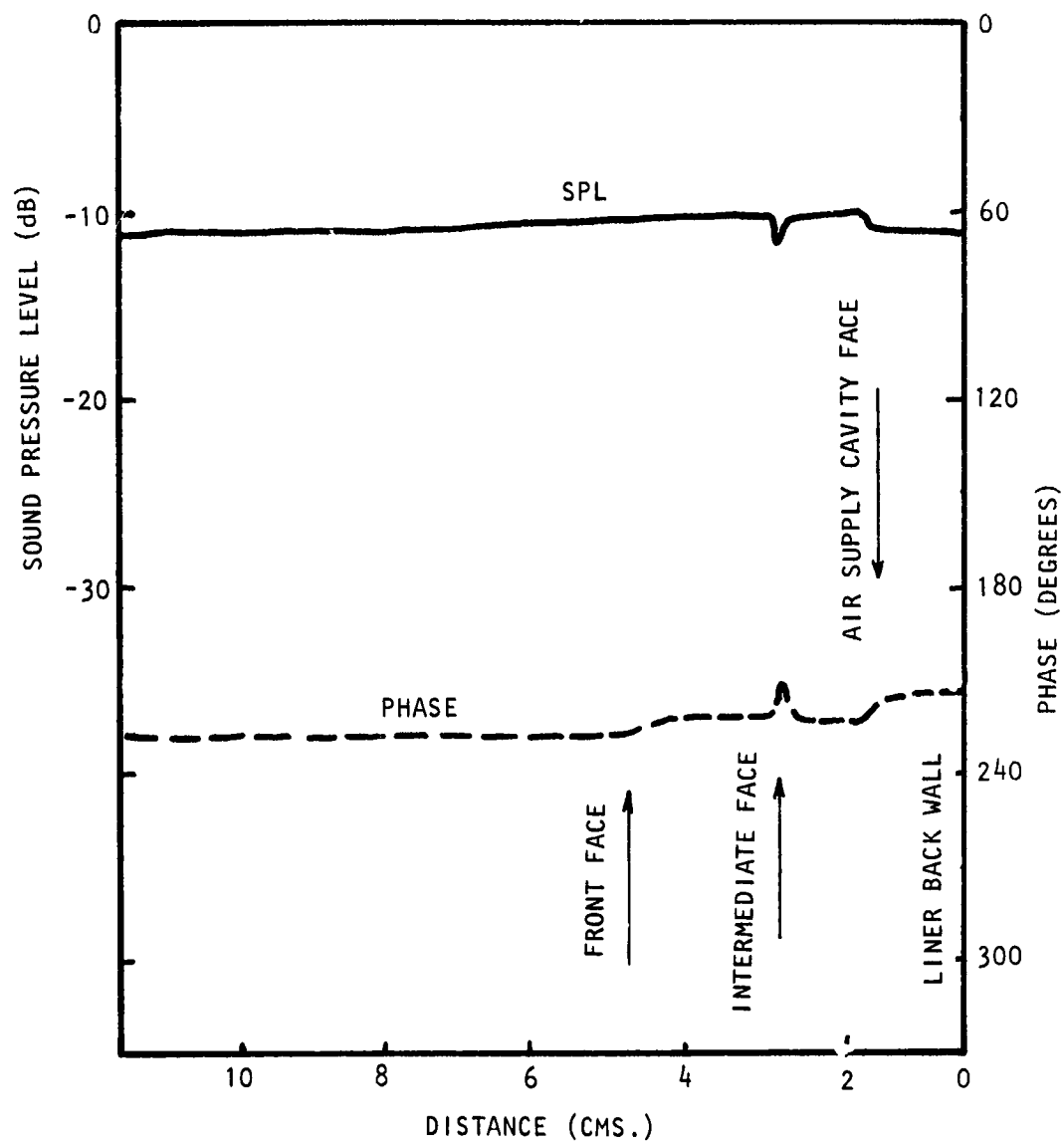


Figure H.5 Sound Pressure and Phase Traverses within Downstream Liner at 500 Hz. Bias Flow $M_i = 0.0$, Grazing Flow $M_{GF} = 0.0$

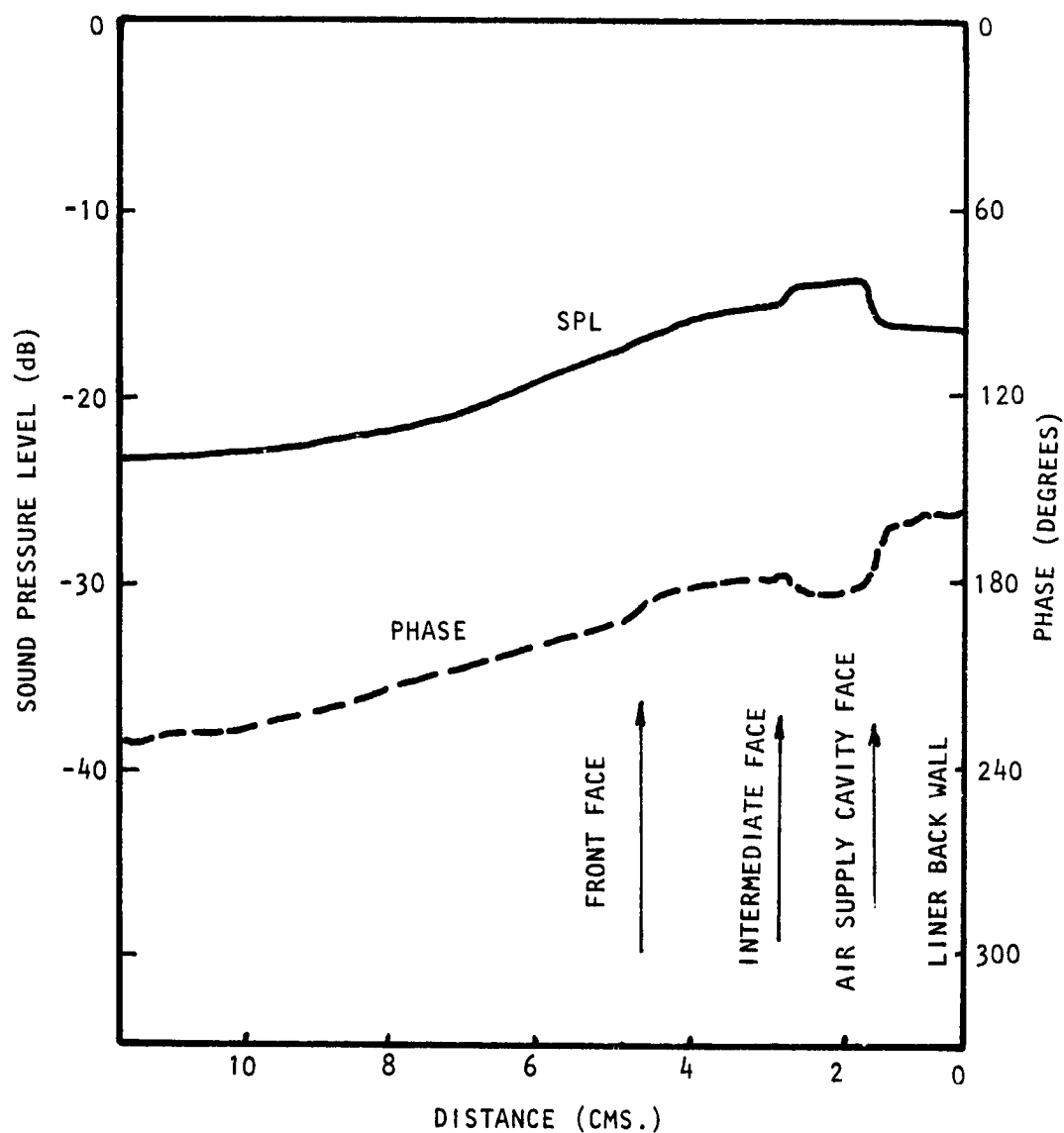


Figure H.6(a) Sound Pressure and Phase Traverses within Downstream Liner at 1.50 Hz. Bias Flow $M_i = 0.0$, Grazing Flow $M_{GF} = 0.0$

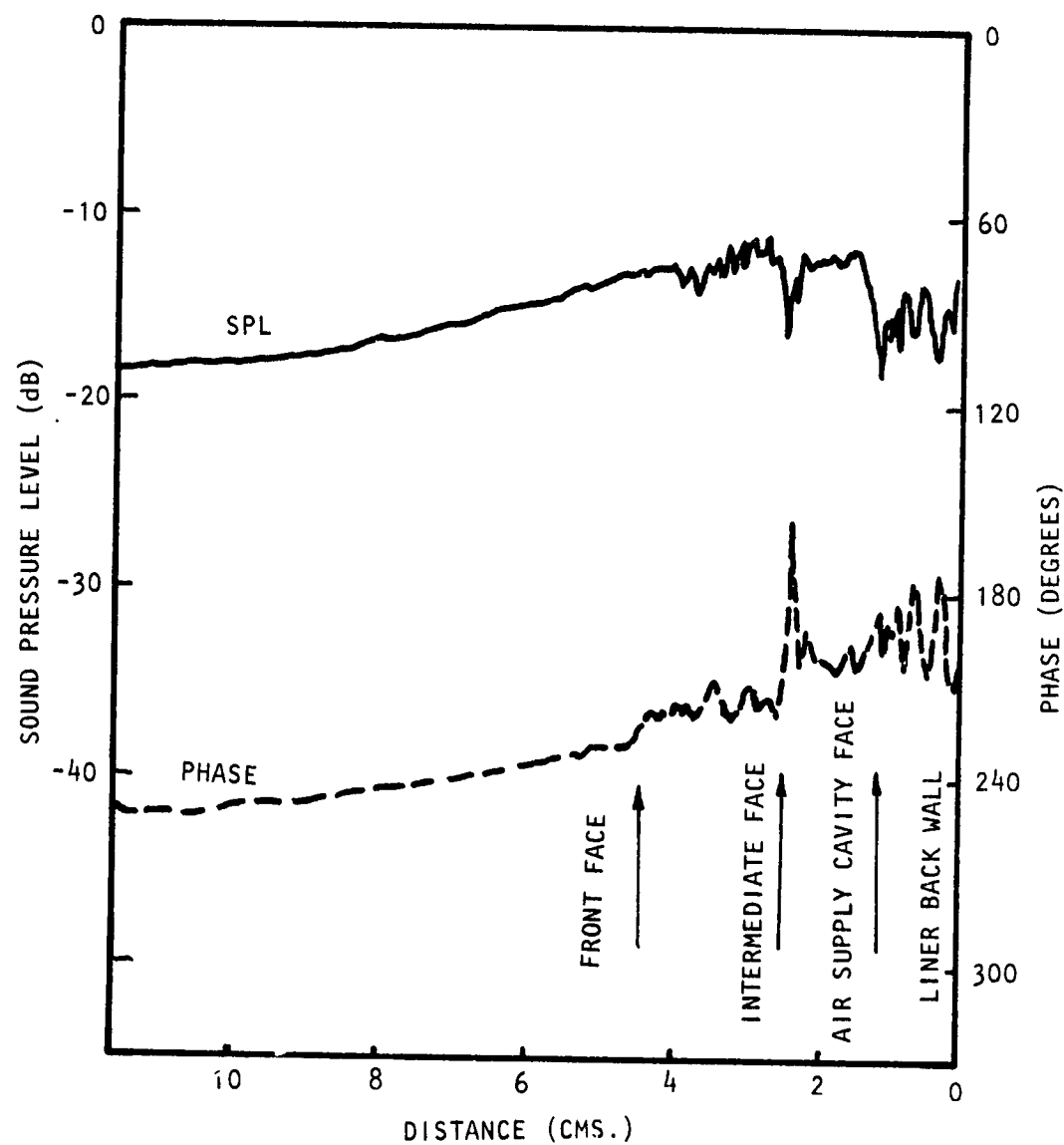


Figure H.6(b) Sound Pressure and Phase Traverses within Downstream Liner at 1250 Hz. Bias Flow $M_i = 0.015$, Grazing Flow $M_{GF} = 0.0$

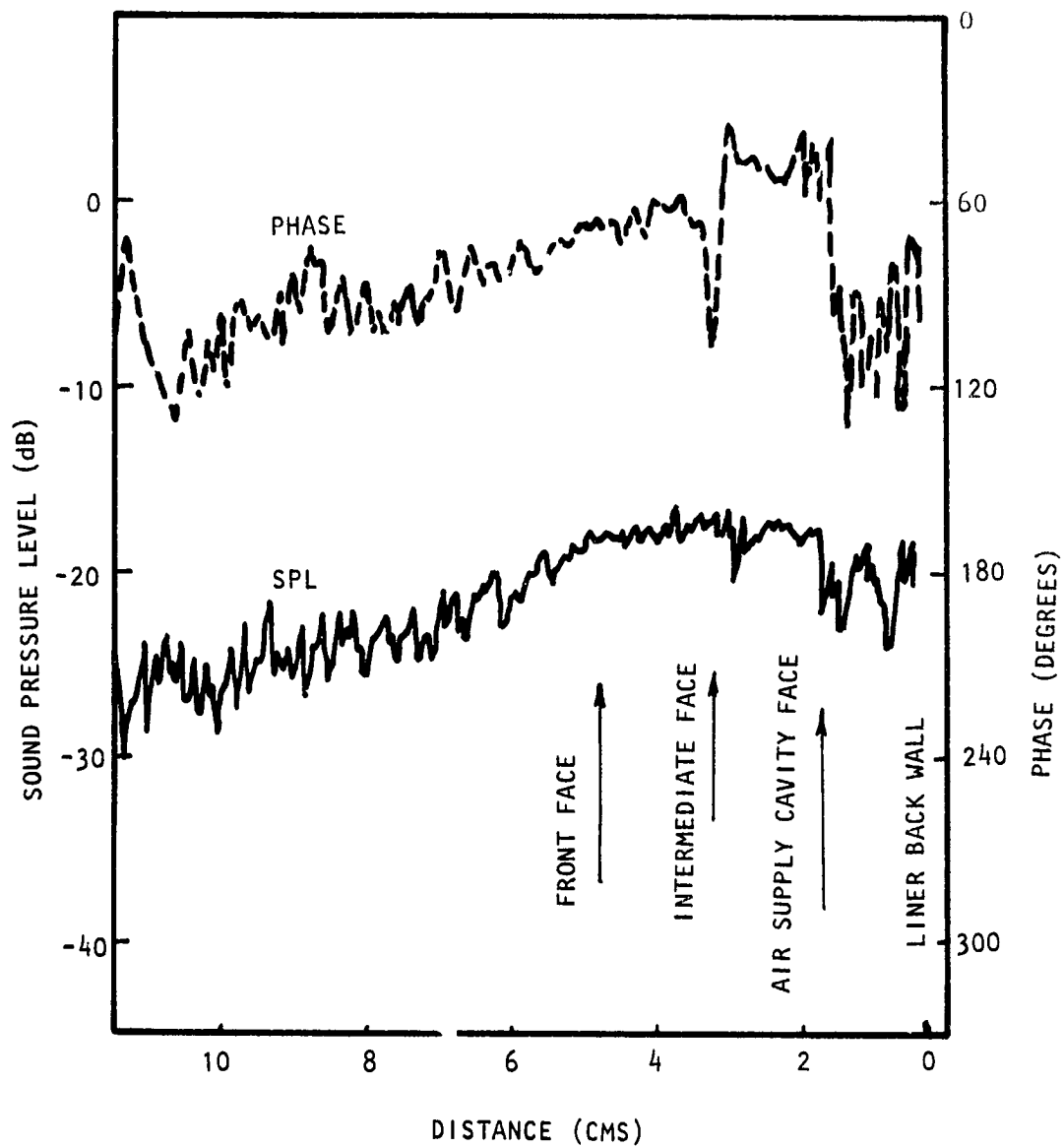


Figure H.6(c) Sound Pressure and Phase Traverses within Downstream Liner at 1250 Hz. Bias Flow $M_i = 0.015$, Grazing Flow $M_{GF} = 0.25$

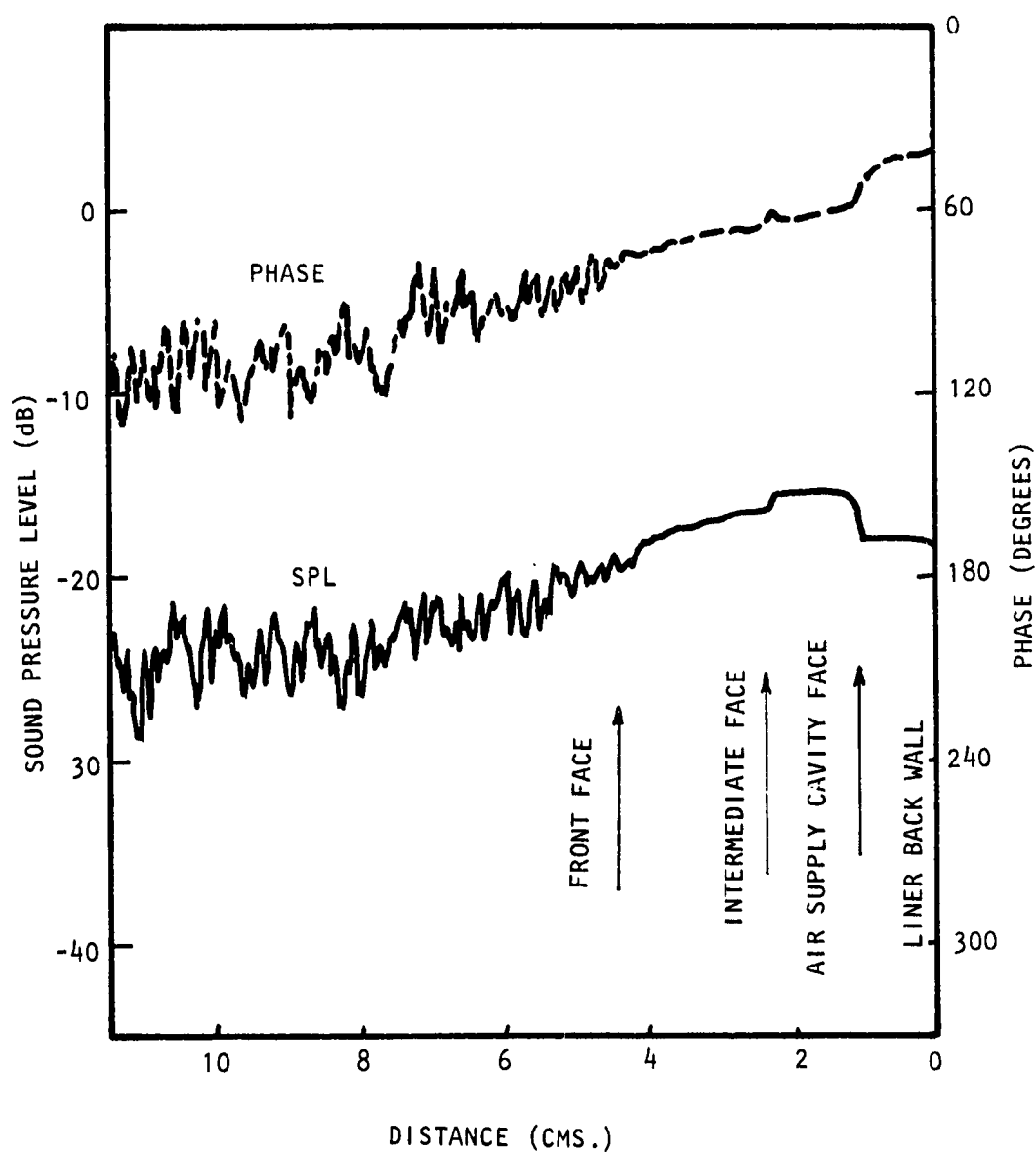


Figure H.6(d) Sound Pressure and Phase Traverses within Downstream Liner at 1250 Hz. Bias Flow $M_i = 0.0$, Grazing Flow $M_{GF} = 0.25$

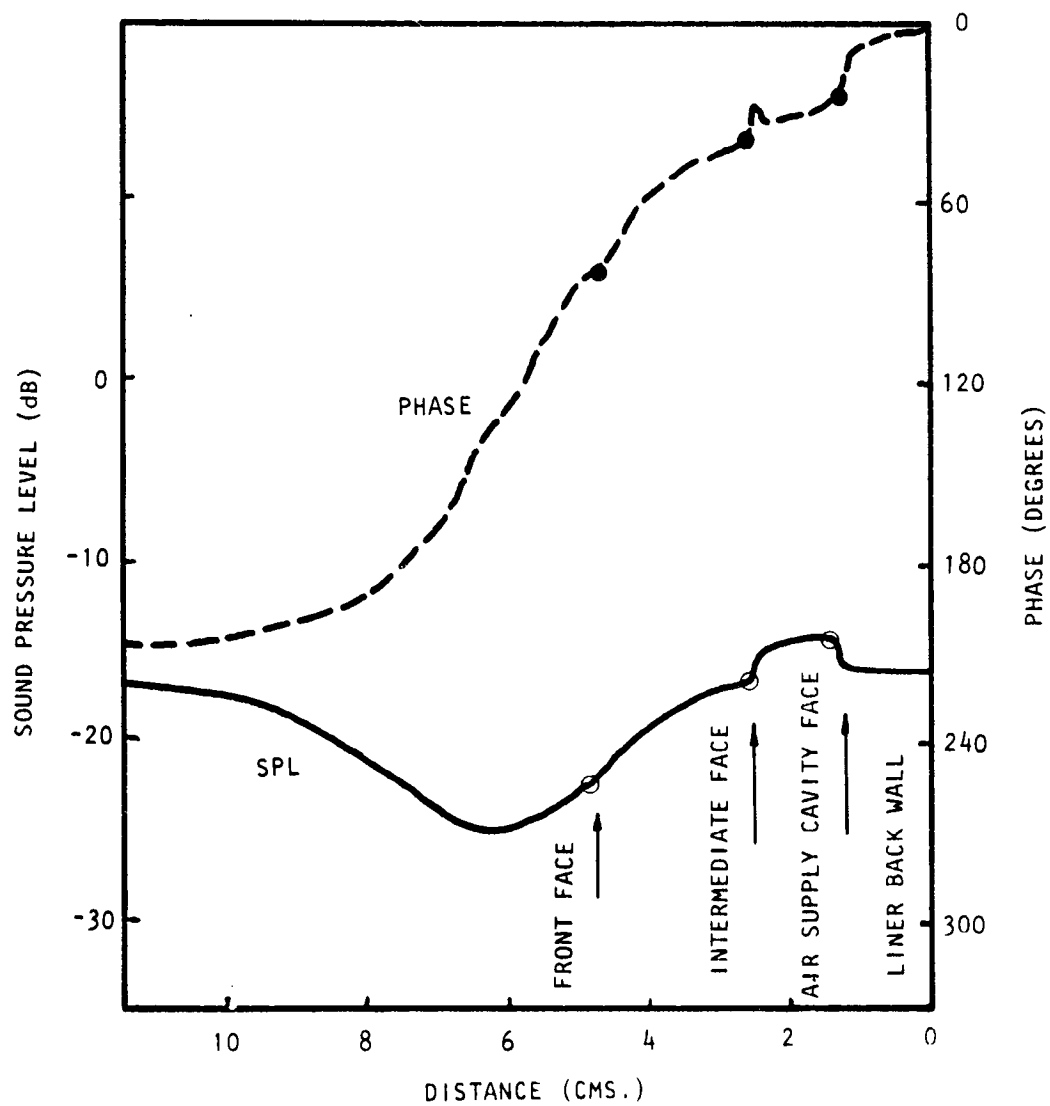


Figure H.7(a) Sound Pressure and Phase Traverses within Downstream Liner at 1600 Hz. Bias Flow $M_i = 0.0$, Grazing Flow $M_{GF} = 0.0$

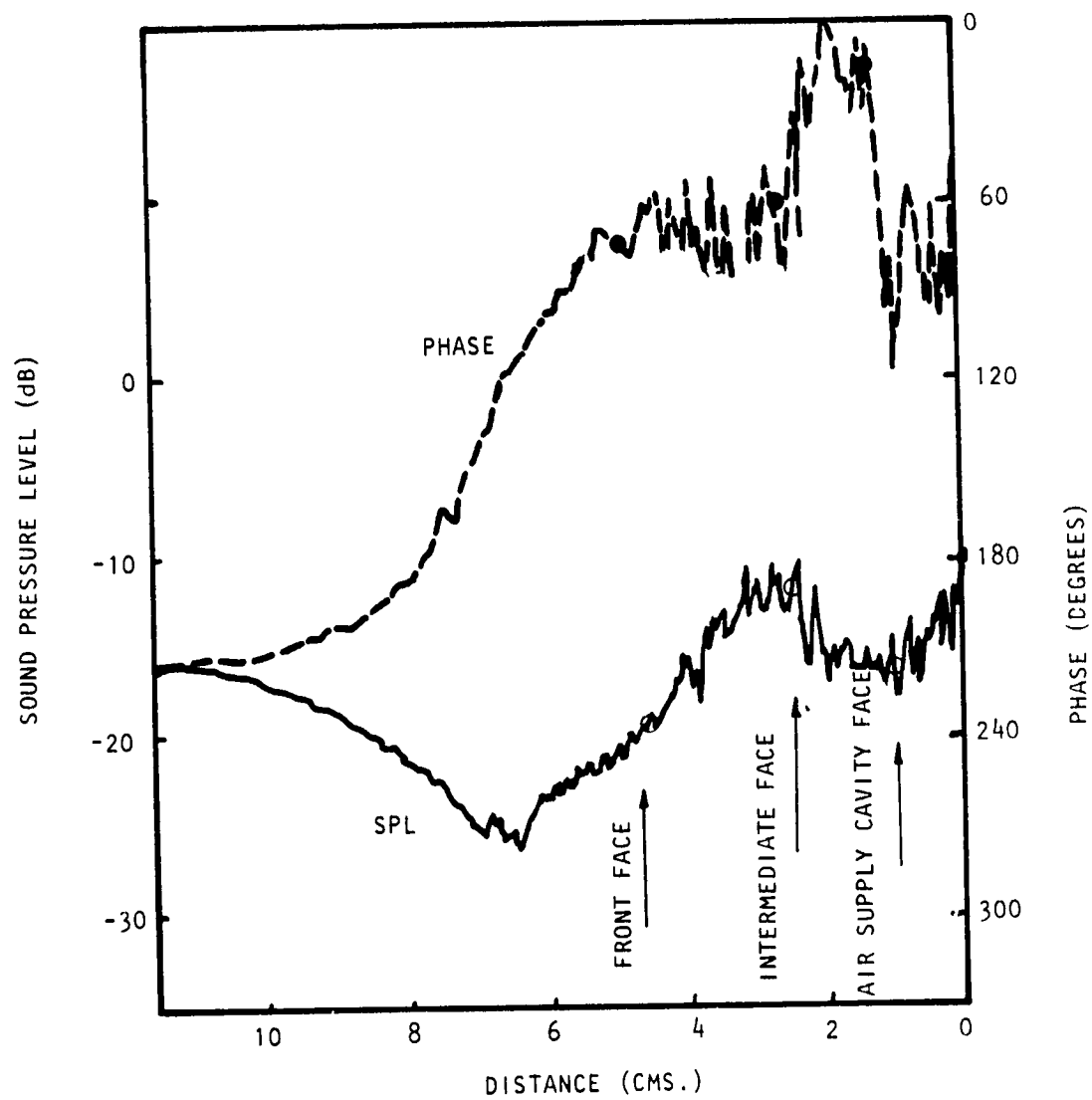


Figure H.7(b) Sound Pressure and Phase Traverses within Downstream Liner at 1600 Hz, Bias Flow $M_i = 0.015$, Grazing Flow $M_{GF} = 0.0$

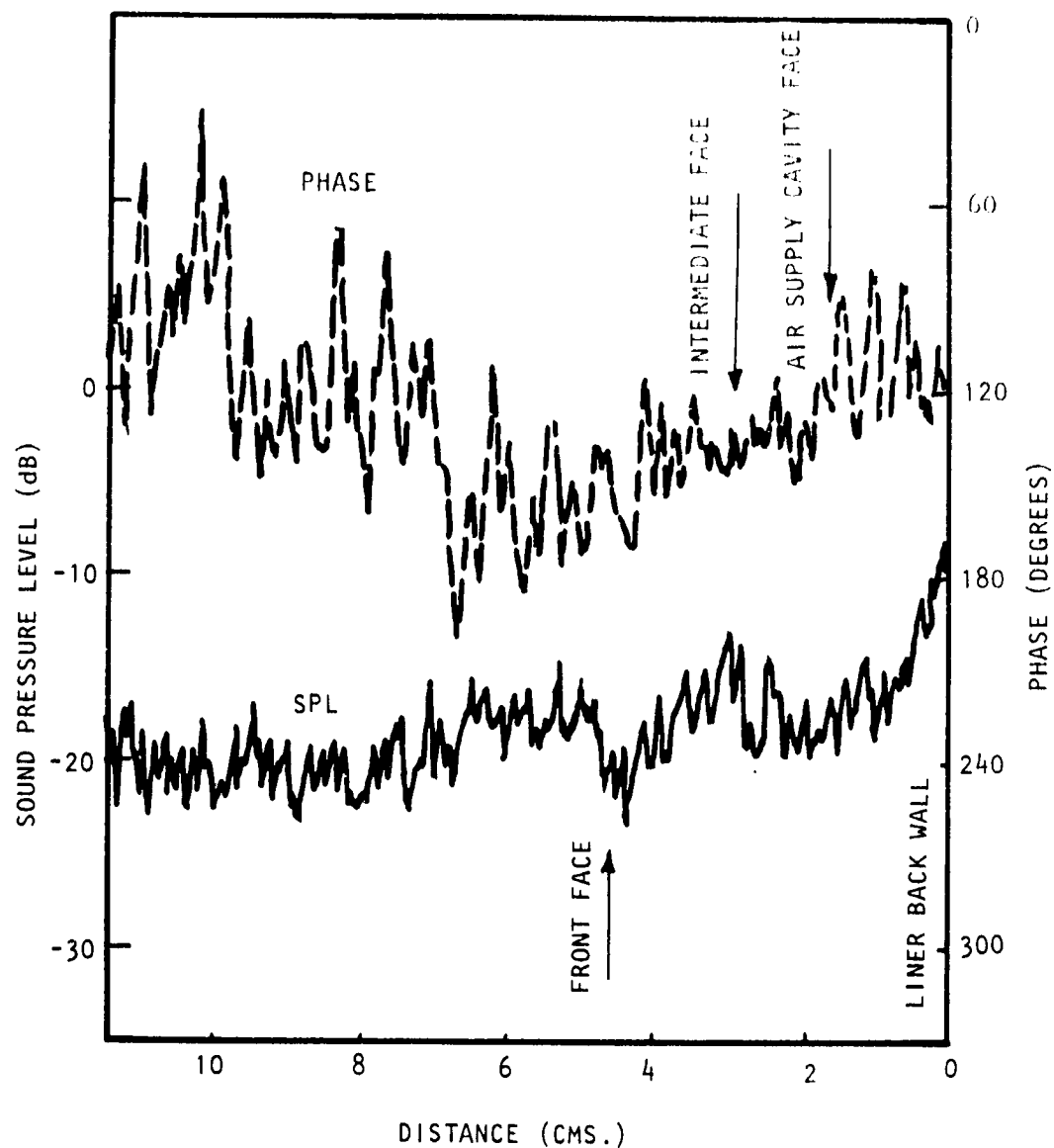


Figure H.7(c) Sound Pressure and Phase Traverses within Downstream Liner at 1600 Hz. Bias Flow $M_i = 0.015$, Grazing Flow $M_{GF} = 0.25$

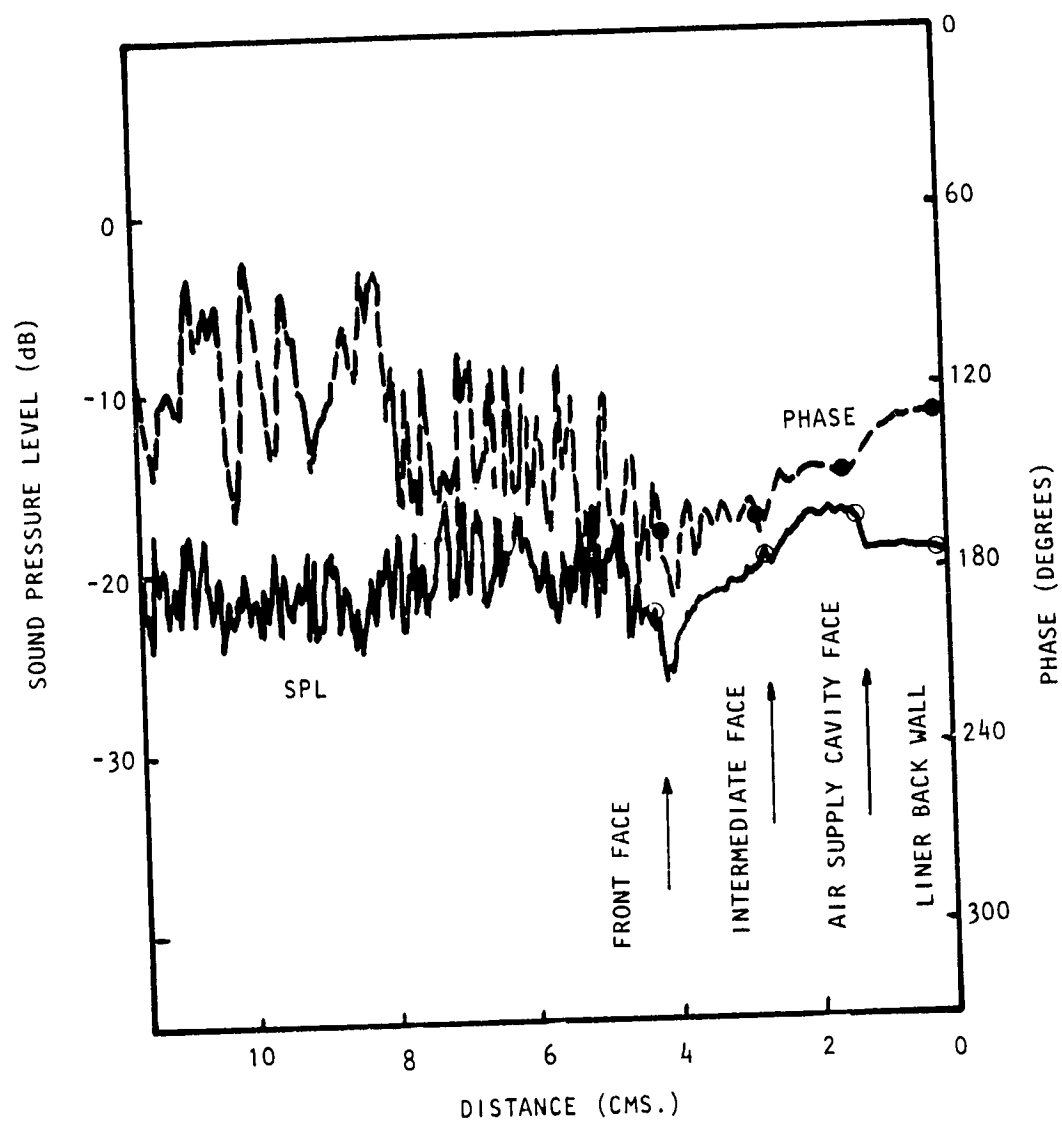


Figure H.7(d) Sound Pressure and Phase Traverses within Downstream Liner at 1600 Hz. Bias Flow $M_i = 0.0$, Grazing Flow = 0.25.

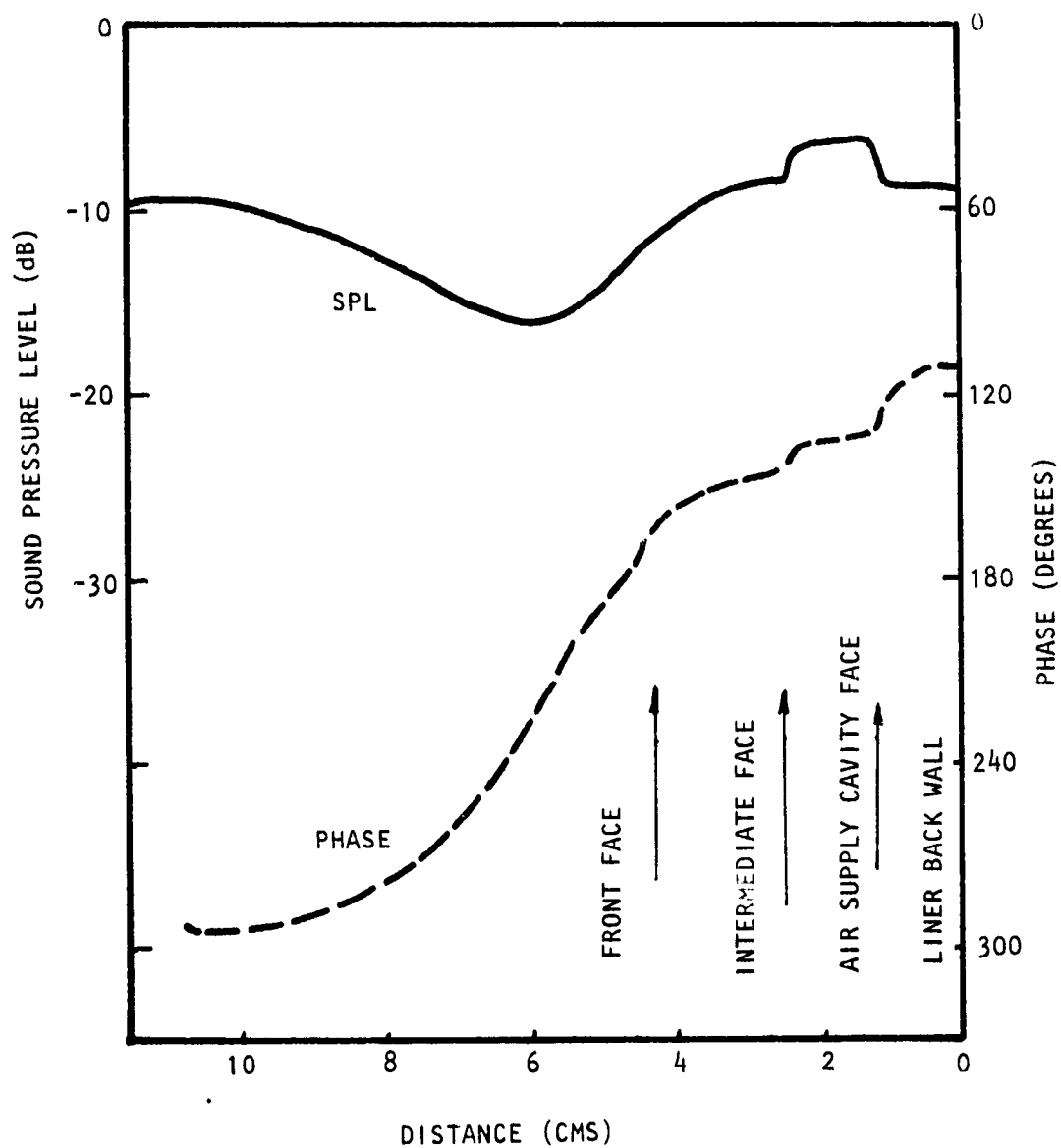


Figure H.8(a) Sound Pressure and Phase Traverses within Downstream Liner at 1700 Hz. Bias Flow $M_i = 0.0$, Grazing Flow $M_{GF} = 0.0$

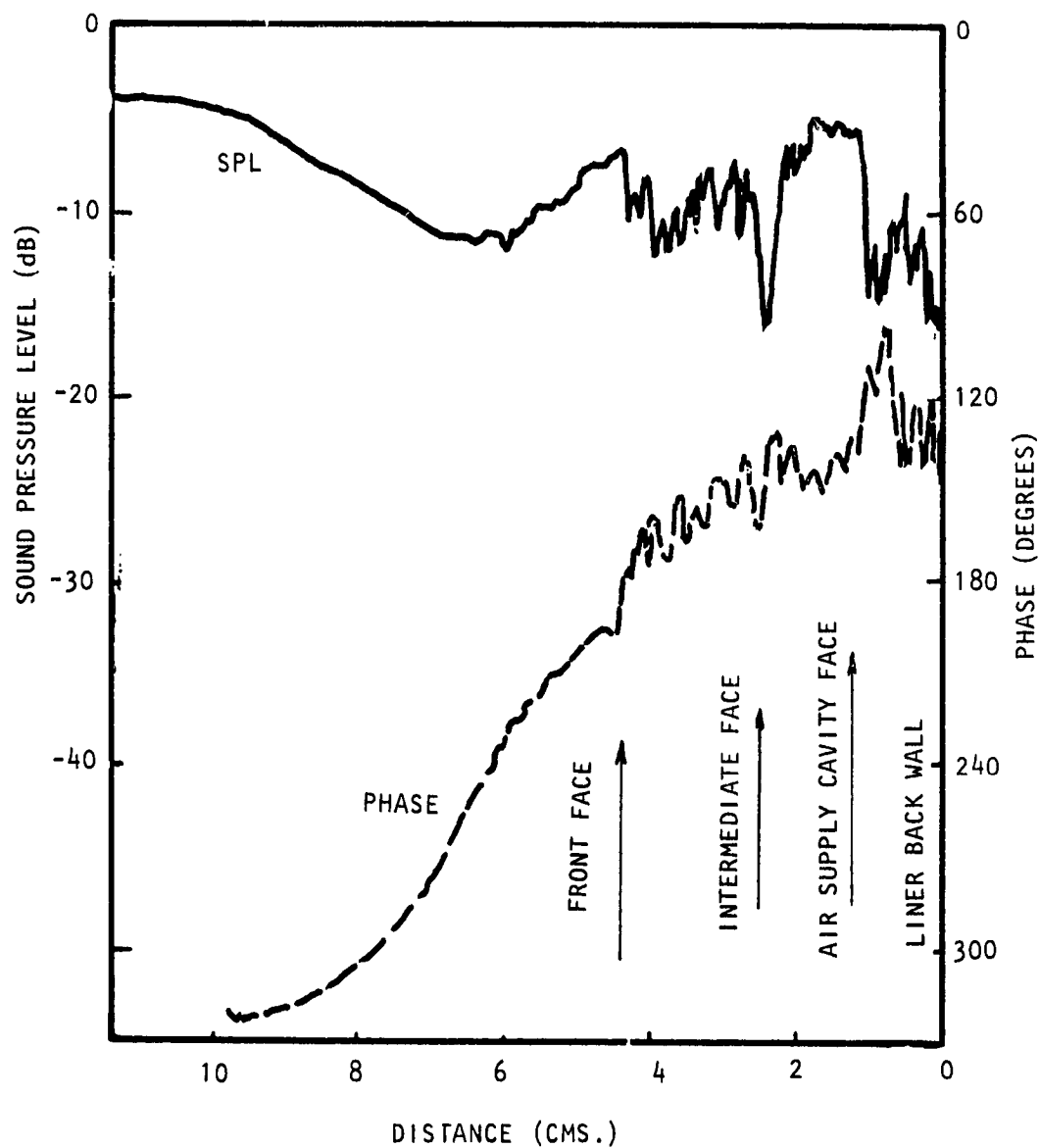


Figure H.8(b) Sound Pressure and Phase Traverses within Downstream Liner at 1700 Hz. Bias Flow $M_i = 0.015$, Grazing Flow $M_{GF} = 0.0$

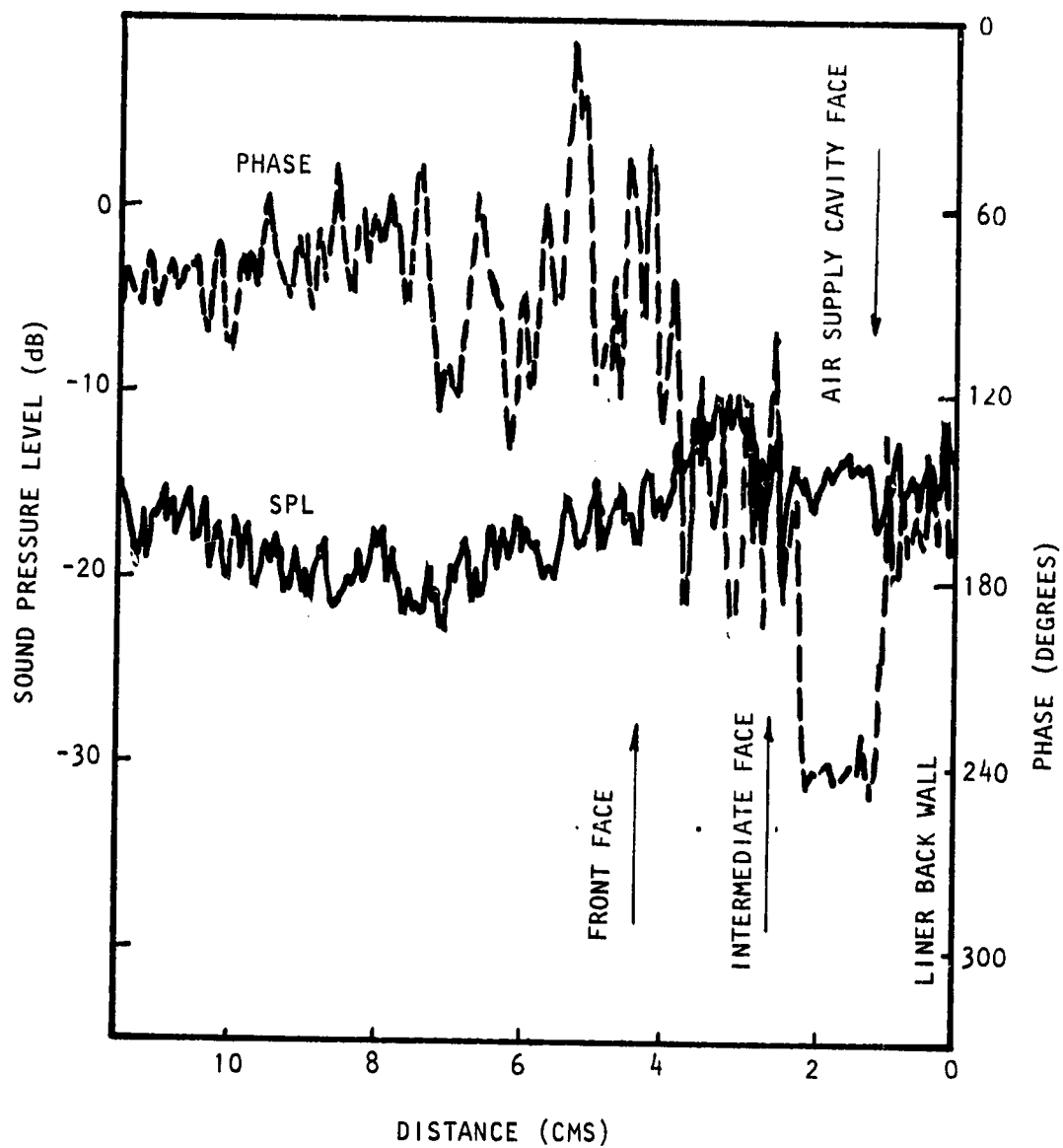


Figure H.8(c) Sound Pressure and Phase Traverses within Downstream Liner at 1700 Hz. Bias Flow $M_i = 0.015$, Grazing Flow $M_{GF} = 0.25$

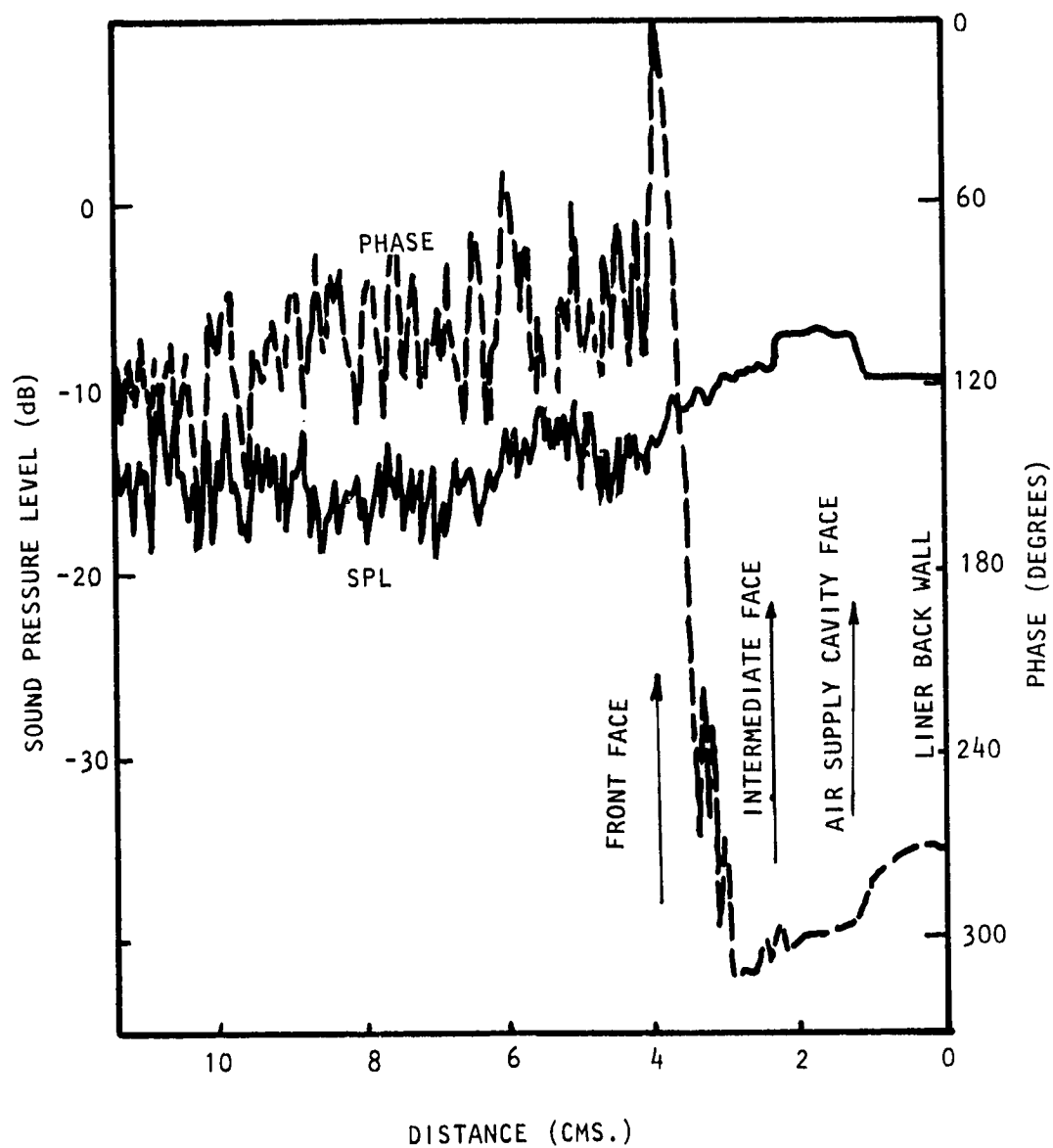


Figure H.8(d) Sound Pressure and Phase Traverses within Downstream Liner at 1700 Hz. Bias Flow $M_i = 0.0$, Grazing Flow $M_{GF} = 0.25$

REFERENCES

1. Feder, E.; and Dean, L. W.: Analytical and Experimental Studies for Predicting Noise Attenuation in Acoustically Treated Ducts for Turbofan Engines. NASA CR-1373, September 1969.
2. Morse, P. M.; and Ingard, K. U.: *Theoretical Acoustics*. McGraw-Hill, 1968.
3. Ko, S.-H.: Sound Attenuation in Acoustically Lined Circular Ducts in the Presence of Uniform Flow and Shear Flow. *J. Sound Vib.*, (1972), 22(2), 193-210.
4. Schauer, J. J.; and Hoffman, E. P.: Optimum Duct Wall Impedance - Shear Sensitivity, AIAA 13th Aerospace Sciences Meeting, California, AIAA Paper 75-129, 1975.
5. Hersh, A. S.; and Rogers, T.: Fluid Mechanical Model for the Acoustic Impedance of Small Orifices. AIAA Paper 75-495, AIAA Second Aeroacoustics Conference, March 1975.
6. Ingard, U.; and Ising, H.: Acoustic Nonlinearity of an Orifice. *J. Acous. Soc. Am.*, Vol. 42(1), pp. 6-17, 1967.
7. Rogers, T.; and Hersh, A. S.: The Effect of Grazing Flow on the Steady State Resistance of Square-Edged Orifices. AIAA Paper 75-493, AIAA Second Aeroacoustics Conference, March 1975.
8. Rice, E. J.: A Model of the Acoustic Impedance of a Perforate Plate Liner with Multiple Frequency Excitation, NASA TMX-67950, 1975.
9. Dean, P. D.: An In-Situ Method of Wall Acoustic Impedance Measurement in Flow Ducts. *J. Sound Vib.*, Vol. 34(1), pp. 97-130, 1974.
10. Guess, A. V.: Calculation of Perforated Plate Liner Parameters from Specified Acoustic Resistance and Reactance. *J. Sound Vib.*, Vol. 40(1), pp. 119-137, 1975.
11. Rschevkin, S. N.: *A Course of Lectures on the Theory of Sound*. McMillan, p. 261, 1963.
12. Melling, T. H.: The Acoustic Impedance of Perforates at Medium and High Sound Pressure Levels. *J. Sound Vib.*, Vol. 29(1), pp. 1-65, 1973.
13. Plumblee, H. E. *et al*: Sound Propagation in and Radiation from Acoustically Lined Flow Ducts: A Comparison of Experiment and Theory. NASA CR-2306, October 1973.
14. Tester, B. J.: The Optimization of Modal Sound Attenuation in Ducts, in the Absence of Mean Flow. *J. Sound Vib.*, Vol. 27(4), 477-513, 1973.
15. Tester, B. J.: Ray Models for Sound Propagation and Attenuation in Ducts in the Absence of Mean Flow. *J. Sound Vib.*, Vol. 27(4), 515-531.